X-ray Sources and the Evolution of Galaxies

Cumulative Habilitation

for Receiving the *venia legendi*

for Astronomy and Astrophysics

by

Dr. Manami Sasaki

Institut für Astronomie und Astrophysik
Kepler Center for Astro and Particle Physics
Mathematisch-Naturwissenschaftliche Fakultät
Eberhard Karls Universität Tübingen

Tübingen, 2015

Contents

1 Introduction

Galaxies present themselves to our eyes as a grand assembly of stars. Already in the ancient times, the Milky Way was observed by humans as a bright and broad band in the sky. It was Galileo Galilei who, in 1610, verified that the Milky Way consists of numerous stars. A century later, Thomas Wright postulated that the stars in the Milky Way form a disc (1750, *'An Original Theory or New Hypothesis of the Universe'*). As we are located in this disc, it is visible to us as a large, luminous circle across the sky. William Herschel performed a survey of stars in 1781 and published a drawing of the Milky Way, in which the position of the Solar system was indicated. Further observations of stars and star clusters by, e.g., Jacobus Kapteyn, Harlow Shapley, and Robert Julius Trumpler followed and, finally, revealed the real structure of the Milky Way in the 20th century.

Stars emit light because they generate energy through thermonuclear burning throughout their lifetime. Hydrogen is first burned into helium in the stellar core, helium to carbon and oxygen, and ultimately, if the star is massive enough, the nuclear burning continues up to iron. Stars with high masses have an onion-like structure consisting of shells of different elements (silicon, oxygen, neon, carbon, helium, and hydrogen in the outermost layer). At the end of its life, the core of a massive star with an initial mass higher than $\sim$8 $M_{\odot}$[a] collapses, resulting in an explosion called a 'supernova' (SN). A strong shock arises, which ejects the outer layers outwards. This shock is additionally driven by neutrinos created in the transformation of protons and electrons to neutrons. In the centre a neutron star (NS) or a black hole (BH) remains.

Astronomical observations enable us to access the places of stellar birth to stellar death, as well as the largest structures in the interstellar space to the tiniest objects in the Galaxy. Observations over the entire electromagnetic spectrum provide crucial diagnostics for our understanding of the structure and evolution of our Galaxy and the objects that form it. However, since we are located inside the Galactic disc, our view is badly compromised by dust and gas, a lack of accurate distance measurements, and a confusing welter of numerous features along each line of sight. Thus, to test realistic models for the flow and evolution of matter through the various components of the interstellar medium (ISM) to stars and back again, we must look beyond the Milky Way.

The Milky Way, the Andromeda galaxy (M 31), and the Triangulum galaxy (M 33) are the only spiral galaxies in the Local Group and its most dominant members. M 31 and M 33, as well as two of our closest neighbours, the Large and Small Magellanic Clouds (LMC, SMC), are among the best studied external galaxies, owing to their proximity and modest extinction along the line of sight. The underlying reason for this is obvious. All of the objects in each of these galaxies are at approximately the same distances of 48 kpc[b], 60 kpc, 760 kpc, and 860 kpc for the SMC, LMC, M 31, and M 33, respectively (Hilditch et al.,

[a] Solar mass $M_{\odot} = 1.98892 \times 10^{30}$ kg

[b] Kiloparsec. 1 Parsec = $3.08567758 \times 10^{16}$ m

2005; van Leeuwen et al., 2007; Clementini et al., 2011; Sarajedini et al., 2006). All the sources in each galaxy are subject to roughly the same amount of absorption. Furthermore, because they are nearby, one can study fainter objects than in any other galaxy outside the Local Group, and determine their relative location to other components in the galaxy. Studies of X-ray sources in these galaxies are essential to our understanding of the X-ray properties of normal galaxies and by extension, of our own Galaxy.

In the following, I will present my recent projects on Galactic and extragalactic X-ray sources with the aim to study the physical processes in these objects and the evolution of galaxies. I would like to point out that all the presented publications, also those for which I am not the first author, are based on projects initiated by myself and I have contributed significantly to the analysis as well as to the interpretation of the results. The Emmy Noether research group led by myself, which started its activities in September 2010, has also carried out additional studies. These projects have also resulted in numerous additional publications. The entire list of the studies that have been completed so far can be found in the publication list.

2 X-ray Source Population in Galaxies

The first X-ray observation carried out with a rocket flight in 1962 led to the discovery of the powerful X-ray source Sco X-1. Further detections of X-ray sources resulted from satellite missions in the 1970s. Optical observations showed that the stars associated with the bright X-ray sources are relatively faint in the optical (13th to 15th magnitude) and show a blue continuum without absorption features, but emission lines of hydrogen and ionised helium. The presence of ionised helium in the so-called X-ray stars indicates high temperature for the origin of emission lines. The *Uhuru* X-ray satellite discovered that some 'X-ray stars' show permanent X-ray pulsations with periods of a few seconds and additional eclipses. They were recognised to be interacting close binary systems, in which mass is transferred from one component to the other more compact object. Since the periods of the pulsations are so short, it was concluded that the compact object is a spinning NS and the sources were hence called 'X-ray pulsars'.

Satellite observations resulted in the discovery of more X-ray binaries (XRBs) and established the following classes of interacting binary systems that can be bright X-ray sources: high-mass X-ray binaries (HMXBs) and low-mass X-ray binaries (LMXBs) mainly differing in the respective mass and type of the companion star (e.g., Verbunt, 1993; Bildsten et al., 1997). In these systems, a compact object, which is a NS or a BH, accretes matter from the companion. X-rays are generally produced when gravitational energy of the infalling matter is released. Galaxies like the Milky Way host both old and young X-ray source populations, similar to their stellar content. The prompt evolution of HMXBs with lifetimes of $\sim 10^{6-7}$ yr makes them a good tracer of the very recent star-formation activity in a galaxy while the LMXBs with lifetimes of $\sim 10^{8-9}$ yr reflect the total stellar content of a galaxy defined by all the star-formation episodes that the galaxy has experienced during its lifetime. Observations of the distribution of XRBs in our Galaxy have told us that the HMXBs are mainly found in spiral arms. This is not surprising, since this is the place where young stars are born. In contrast, LMXBs are found in the bulge or globular clusters and are associated with the older population of a galaxy (Verbunt, 1993; van der Klis, 2000).

Luminosity functions of X-ray sources can be used to characterise the X-ray binary populations in galaxies (review by Fabbiano, 2006). The comparison of X-ray luminosity functions (XLFs) of different galaxies show that they scale with the star-formation rate (SFR) or the mass of the galaxy (Zezas & Fabbiano, 2002; Kilgard et al., 2002). The cumulative luminosity functions of the XRBs in the Milky Way are well-described by a power law with a high luminosity cut-off for LMXBs. Grimm et al. (2003) suggest that the XLFs of HMXBs can be described by a universal luminosity function, i.e., by a power law with a slope of $\sim$1.6 and a cut-off at $\log(L_X) \approx 40.5$ with a normalisation that is proportional to the star-formation rate. Gilfanov et al. (2004) find a correlation of the normalisation of LMXB XLFs and the stellar mass of the galaxy. Early-type galaxies in general have steeper XLFs than late-type galaxies with more active star formation (Kilgard et al., 2002; Colbert et al., 2004).

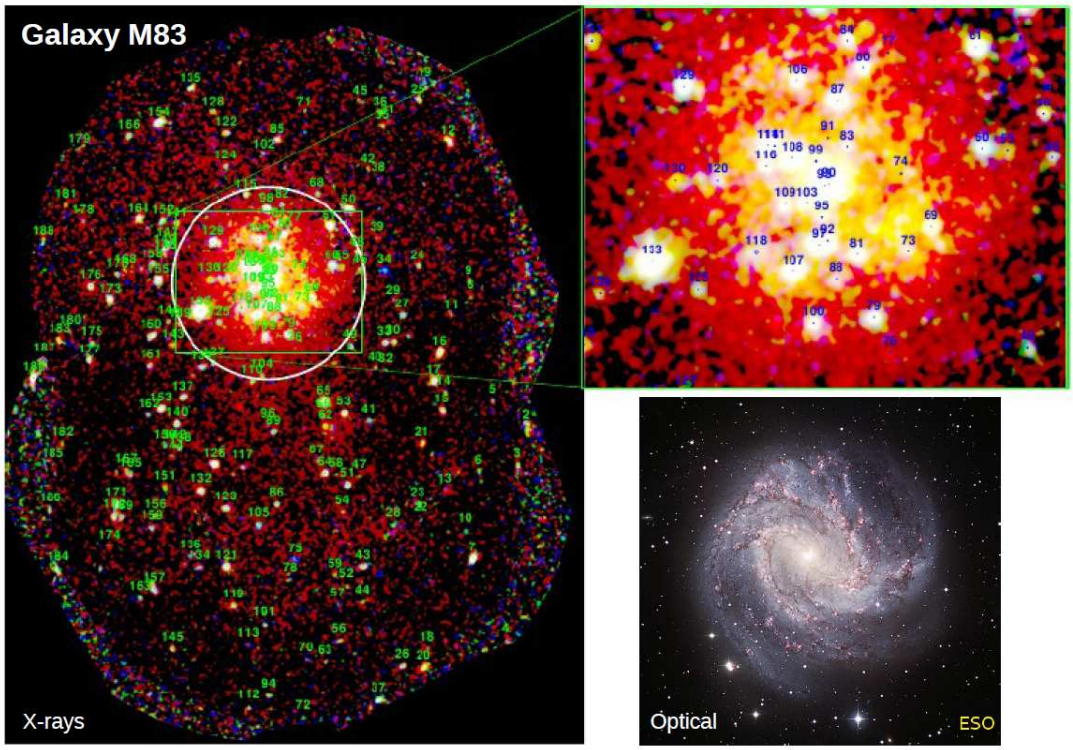

Figure 1: *XMM-Newton* image of M 83 with X-ray sources (left) and a zoom-in on the nuclear region (upper right, both taken from Ducci et al., 2013) with an optical image of the same area (lower right, ESO/IDA/Danish 1.5 m/Gendler, Guisard, Thöne).

These results indicate that it may be possible to determine the star formation history from luminosity functions of X-ray sources in a galaxy, which are more easily measured for distant galaxies than their resolved stellar populations. We test the XLFs of galaxies in the nearby Universe with well-known star-formation histories down to fainter luminosities to build a reliable basis for the study of more distant, less resolved galaxies.

2.1 M 83

DUCCI, SASAKI, ET AL., 2013, A&A, 553, 7

The starburst galaxy M 83 is a barred spiral galaxy oriented nearly face-on and located at a distance of 4.5 ± 0.3 Mpc. M 83 is experiencing starburst activity with a present-day star-formation rate of $3-4 M_{\odot}$ yr^{-1}. Ultraviolet (UV) images of M83 obtained with the Galaxy Evolution Explorer (*GALEX*) satellite revealed the presence of extended spiral arms and a population of young stars ($<$ 400 Myr) in the outer disc of M83.

We have analysed three archival observations of M 83 taken with the X-ray telescope X-ray Multi-Mirror Mission *XMM-Newton* (Jansen et al., 2001; Aschenbach et al., 2000) using the European Photon Imaging Cameras (EPICs, Strüder

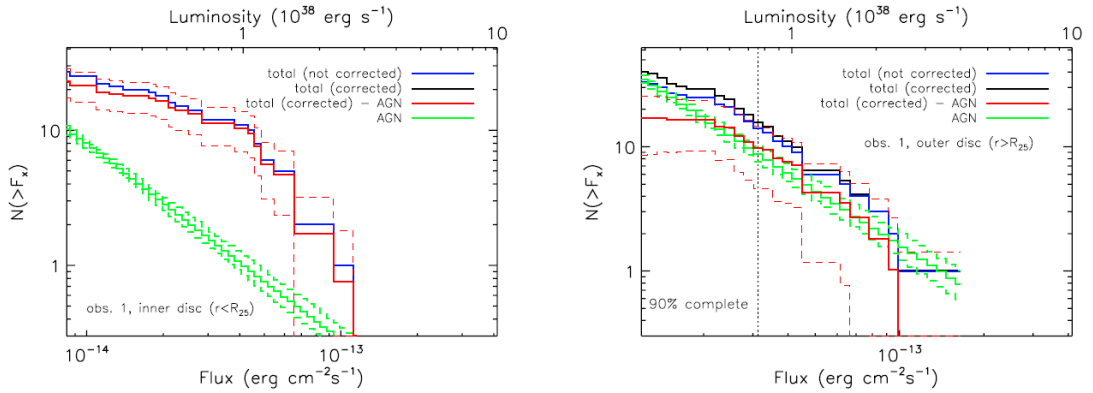

Figure 2: Cumulative XLFs of the *XMM-Newton* sources in M 83 inside (left) and outside (right) the D_{25} ellipse in the 2 – 10 keV band. The red (solid) line shows the corrected XLFs with errors (dashed). Taken from Ducci et al. (2013).

et al., 2001; Turner et al., 2001) in order to study its X-ray source population (Ducci et al., 2013). In total, 189 sources were detected in the energy range of 0.2 – 12.0 keV (Fig. 1). We performed a spectral analysis, studied the hardness ratios and X-ray variability, and searched for cross-correlations with catalogues at X-ray, optical, infrared (IR), and radio wavelengths to constrain the nature of the X-ray sources. Among the identified sources are background galaxies and active galactic nuclei (AGNs), Galactic foreground stars, and objects in M 83.

The XLFs were calculated for sources inside and outside the optical D_{25} ellipse of M 83, after correcting the total XLF for incompleteness and subtracting the AGN contribution (Fig. 2). As can be seen in Figure 2 (left), the XLF does not change significantly after the subtraction of the contribution by the background AGNs. Therefore, the majority of sources in the D_{25} ellipse are most likely M 83 sources. Using a relation between the XLF of HMXBs and the SFR in a galaxy as suggested by Mineo et al. (2012), we calculate a SFR of 3.1 $M_{\odot}$ yr^{-1}, in agreement with the SFR derived from data taken at other wavelengths.

In the outer arms outside the disc (Fig. 2, right diagram), there is also a clear excess above the population of background AGNs (red line), indicating the existence of XRBs in the outer arms of M 83 (Ducci et al., 2013). The Kosmogorov-Smirnov test to compare the distribution of the detected X-ray sources with that of the AGNs, which is assumed to be homogeneous, showed that the population of the *XMM-Newton* sources is significantly different from that of the background AGNs. Therefore, we conclude that a significant fraction of the observed, yet unidentified X-ray sources are X-ray binaries in the outer disc of M83.

We thus compiled the first complete catalogue of X-ray sources detected with *XMM-Newton* in the field of M 83, which is now available on the VizieR On-line Data Catalogue website (Data Catalogue J/A+A/553/A7) and in the HEASARC database[c]. In addition, we found indications for the existence of X-ray binaries in the extended arms of M 83 detected in the UV.

[c]http://heasarc.gsfc.nasa.gov/W3Browse/all/m83xmm.html

3 Accreting X-ray Pulsars

If a neutron star accretes matter from a companion in a binary system, the accreted matter, which is ionised gas, is directed along the strong magnetic field of the NS and eventually falls onto its surface. Energy is released as high-energy radiation. If the magnetic axis of the NS is not aligned to the rotational axis, the observer sees pulsed emission. Therefore, these objects are called accreting X-ray pulsars. In HMXBs, a NS or a BH forms a binary system with a massive star, i.e., an O or a B star. A large fraction of the companions of NSs in HMXBs are Be stars, which are B stars that are believed to have enhanced mass loss around the equator due to the fast rotation of the star. This forms an equatorial ring around the star. Every time the NS passes through the ring, an outburst is observed in X-rays, which is called type I outburst. These sources also sometimes show X-ray outbursts with much higher luminosities, called type II or giant outbursts. The giant outbursts are thought to be caused by a sudden increase in mass ejection and thus accretion rate due to instabilities in the companion star.

The pulse profiles of accreting X-ray pulsars are not always sinusoidal, as expected from an axially symmetric emitter. Instead, most of them have complicated pulse profiles that differ from object to object and even show changes if the luminosity of an object changes. The latter is believed to be caused by the change of structures in the accretion flow. When the accretion rate is low, which is the case for low-luminosity intervals, the matter falls freely on the magnetic poles of the NS. If the accretion rate is higher, the accreted matter forms an accretion column with a structure that is defined by the magnetic field of the NS. In the accretion column a shock forms above the surface of the NS and the X-ray luminosity is enhanced. Thus, the luminosity dependence of pulse profiles is indicative of the change of the emission components and thus the variation of accretion rate.

In the last few decades a wealth of data of accreting X-ray pulsars have been collected and analysed. However, there is yet no consistent, comprehensive model that can reproduce the observed emission and provide us with physical parameters of the X-ray pulsars. We have therefore started to study the pulse profiles of accreting X-ray pulsars using the available abundant data taken with the Rossi X-ray Timing Explorer (*RXTE*), INTErnational Gamma Ray Astrophysics Laboratory (*Integral*), or *BeppoSAX*, and compare the observed pulse profiles with those obtained from a set of comprehensive multi-component models (Kraus et al., 1995, 2003). These models include a number of important physical effects, like the different types of accretion column/walls, the formation of halo at the bottom of the accretion flow, or the scattering of radiation in the upper accretion stream. The emitted radiation is calculated by taking relativistic light-bending around the NS into account. The comparison of the observed pulse profiles with the simulated profiles allows us to derive parameters like the mass accretion rate or the inclination angle between the magnetic axis and the rotation axis of the NS, as well as the configuration of the magnetic fields. This information will also allow us to estimate the mass and the radius of a NS.

3.1 Pulse Decomposition Analysis

Pulsed emission is observed from an accreting X-ray pulsar because the magnetic field of the NS, which is primarily believed to be a dipole field, is not aligned to its rotation axis. If the emission regions are axially symmetric with respect to the magnetic axis, the observer should see symmetric pulses. However, the observed pulse profiles have complex structures and are in general highly asymmetric.

One of the reasons, which have been suggested for the asymmetry of pulse profiles, is a distortion of the magnetic dipole (Parmar et al., 1989a; Leahy, 1991; Riffert et al., 1993; Bulik et al., 1995). In this case the two magnetic poles on the surface of the NS are not antipodal and the superposition of the symmetric pulse profiles from each of the pole results in an asymmetric total pulse profile. The decomposition method developed by Kraus et al. (1995) is based on this assumption. Using this method we can find the two symmetric emission components from the two poles. We have successfully applied the pulse-profile decomposition method to the pulse profiles of the X-ray pulsars EXO 2030+375 (Sasaki et al., 2010), A 0535+26 (Caballero et al., 2011), 4U 0115+63 (Sasaki et al., 2012a), and V 0332+53 (Diplom thesis by D. Müller, second part of paper by Sasaki et al., 2012a) and derived emission patterns and NS geometries, as presented in the following.

3.1.1 EXO 2030+375

SASAKI ET AL., 2010, A&A, 517, 8

The source EXO 2030+375 is a Be/X-ray binary showing pulsations in X-rays with a period of $\sim$42 s (Parmar et al., 1989b). An orbital period of 46 days has been measured (Wilson et al., 2002). It shows normal outbursts at almost every periastron passage of the NS (Wilson et al., 2005). In 2006, EXO 2030+375 underwent a giant outburst, which was the first since the discovery of the source in 1985 (Corbet & Levine, 2006; Krimm et al., 2006; McCollough et al., 2006). During this giant outburst, it was monitored by *RXTE* and also observed with *Integral*. We have analysed the pulse profiles of EXO 2030+375 during its giant outburst using the pulse-profile decomposition method of Kraus et al. (1995) for different luminosities of the source. Data were divided into several spectral bands to study the energy dependence of the pulse profiles and their changes between different energies for varying luminosities. We used the *RXTE* data in the energy bands of 2 – 9 keV, 9 – 14 keV, 14 – 20 keV, 20 – 30 keV, and 30 – 115 keV. For *Integral*, we used the pulse profiles published by Klochkov et al. (2008) in the energy bands of 3 – 9 keV, 9 – 14 keV, 14 – 20 keV, 20 – 23 keV, 23 – 26 keV, 26 – 30 keV, 30 – 34 keV, 34 – 39 keV, 39 – 45 keV, 45 – 55 keV, 55 – 70 keV, and 70 – 120 keV. In total, we analysed 26 pulse profiles from *Integral* and *RXTE* observations. As can be seen in Figure 3, the pulse profiles before the maximum and after the maximum of the giant outburst taken when the source had similar luminosities are almost identical.

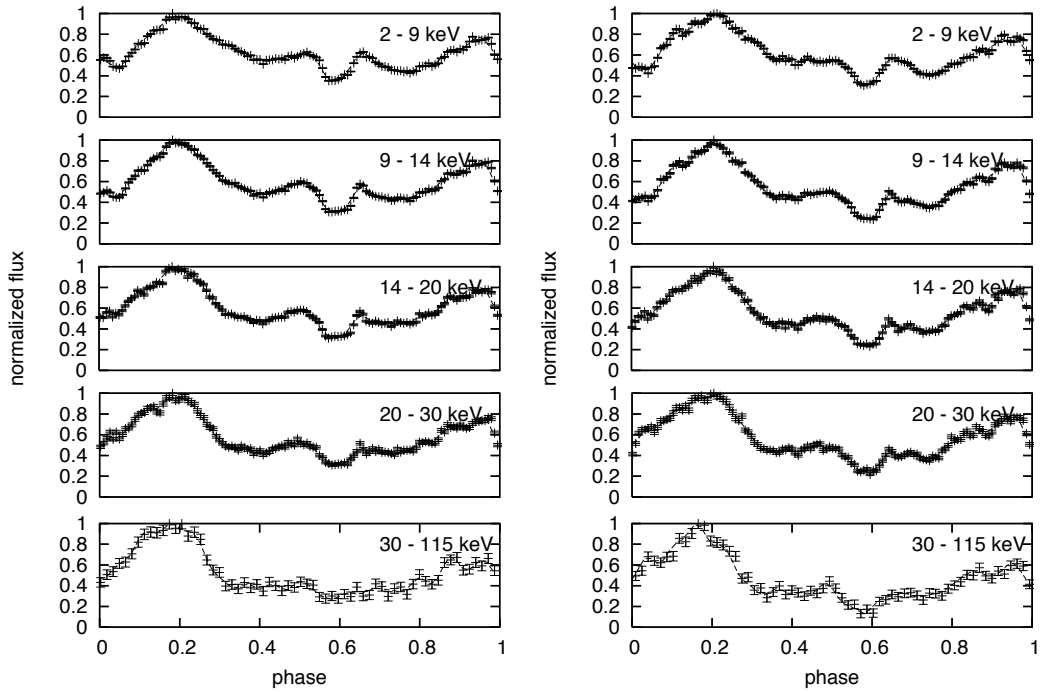

Figure 3: Pulse profiles of EXO 2030+375 during the rise (left) and the decay (right) of the giant outburst in 2006 observed with *RXTE*. The source had similar luminosities at the times when the data were taken. Taken from Sasaki et al. (2010).

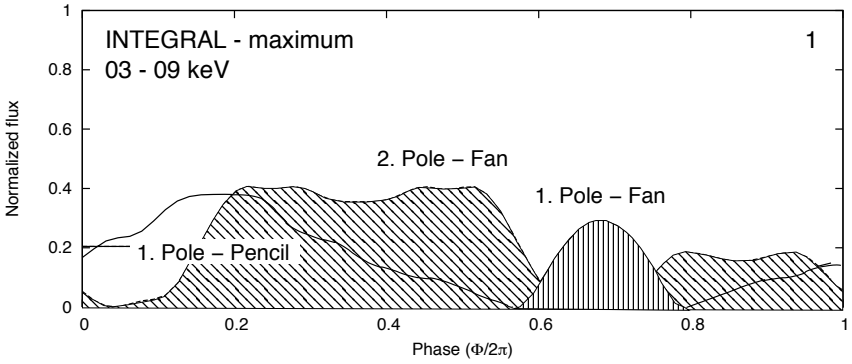

Figure 4: Decomposed single pole pulse profiles of EXO 2030+375 from the data taken near the maximum of the giant outburst for the lowest energy band with 'pencil beam' (mostly forward directed) emission component and 'fan beam' (wide, directed mostly to the side) emission component from each pole. 'Fan beam' emission is hatched with vertical stripes for the first pole, whereas the diagonally striped component shows the 'fan beam' from the second pole. The second pole never faces the observer, therefore, the observer only sees its 'fan beam' emission. Taken from Sasaki et al. (2010).

The pulse-profile decomposition method is a backward analysis of the observed emission, based on the assumption that i) the emission arises from the magnetic poles of the NS and the accretion flow forming a symmetric pattern and ii) the magnetic field is distorted resulting in an asymmetric geometry of the NS. We model asymmetric pulse profiles as superposition of two symmetric pulse profiles based on Fourier analysis. We thus obtain two symmetric functions $f_{1,2}$, symmetry points $\Phi_{1,2}$ for each function, and their offset Δ. The symmetry point corresponds to the pulse phase when the magnetic pole is either closest to or most distant from the observer on the observer's line of sight. Once we have found the two symmetry points, their offset, and the two functions, we can calculate the location of the emission regions and the beam pattern of the emission around each pole.

Based on the decomposition analysis of EXO 2030+375 we have shown that the magnetic field of the NS is indeed distorted and that the observed emission is a composition of that of the two emission regions. For this source only a part of the emission of each region is visible. The origin of the main peak at phase 0.2 in the observed pulse profile seems to be the harder pencil beam from the magnetic pole when it is closer to the observer (see Fig. 4). In addition, a fan beam from the pole on the other side is also observed at this phase owing to gravitational line bending. Fan beam is most likely caused by the halo on the surface of the NS and emission from the wall of the accretion column. Our analysis indicates that, due to the distorted configuration, both poles are located on the back side of the NS between phase $\sim$0.5 and $\sim$0.7, resulting in a sharp minimum seen at phase 0.6. The observer never looks on the second pole. However, its harder emission component can be observed as an additional maximum at phase 0.95, which is more pronounced at lower luminosities.

3.1.2 4U 0115+63

SASAKI ET AL., 2012, A&A, 540, 35 (part 1)

The object 4U 0115+63 was detected in the early years of X-ray astronomy with the satellites *Uhuru* (Forman et al., 1976), *Vela 5B* (Whitlock et al., 1989), *SAS 3* (Cominsky et al., 1978), and *HEAO-1* (Johnston et al., 1978). It is a binary system consisting of a NS and a Be star. An orbital period of 24.3 d and a pulse period of 3.61 s were measured. A giant outburst of 4U 0115+63 was observed in 1999. We analysed its pulse profiles obtained from observations with *RXTE* and *BeppoSAX*, which show strong energy and luminosity dependence (see Fig. 5).

The decomposition of the pulse profiles allowed us to find the symmetric pulse profiles of two single emission regions. By putting the two emission profiles together, we then reconstructed the total observed beam pattern of the source. We removed the effect of the gravitational light deflection to obtain the intrinsic beam pattern by assuming a standard NS with $R_{\rm NS}$ = 10 km and $M_{\rm NS}$ = 1.4 $M_{\odot}$. Two of the resulting intrinsic beam patterns are shown in Figure 6 in polar diagrams.

We conclude that the emission of 4U 0115+63 during the giant outburst can

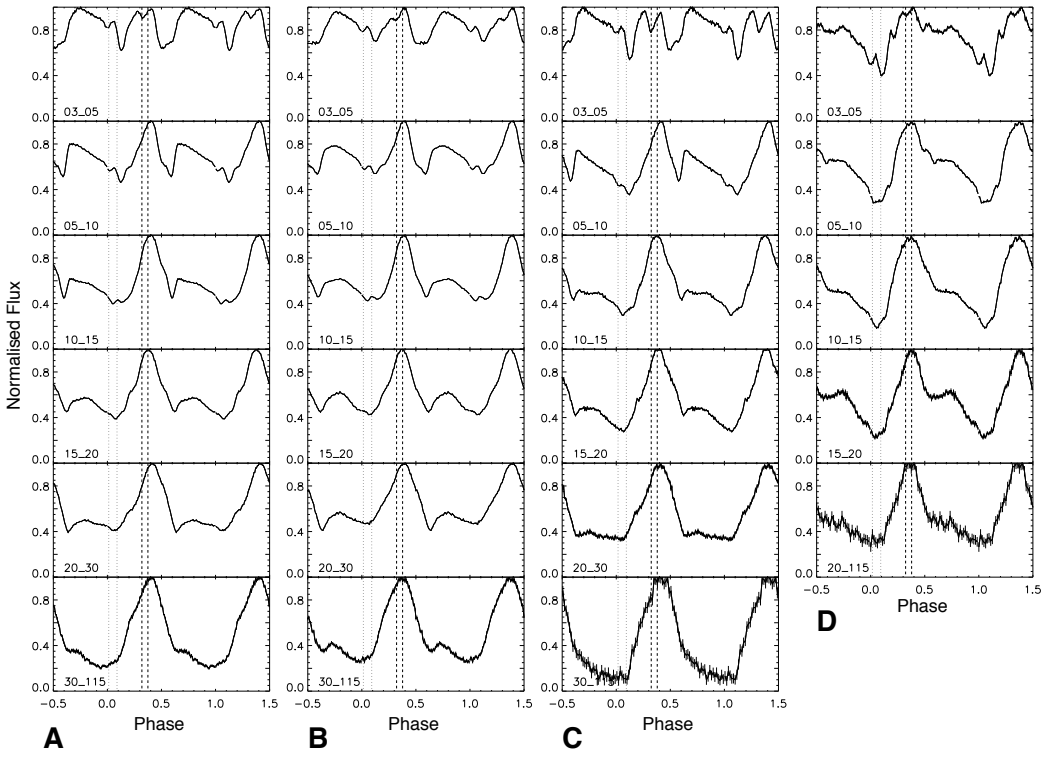

Figure 5: Pulse profiles of 4U 0115+63 during the giant outburst in 1999 observed with *RXTE* for the observations A (during the rise before the maximum), B (at the maximum, $L_{3-100\mathrm{keV}} = 1.5 \times 10^{38}$ erg s^{-1}), C (during the decay), and D (at the end of the decay). We analysed two additional data taken after the observation D at the very end of the decay (E and F), when the luminosity of the source was $L_{3-100\mathrm{keV}} \leq 2 \times 10^{37}$ erg s^{-1}. Energy bands are soft to hard from top to bottom for each observation. The numbers in the plots indicate the bands (lower energy – upper energy in keV). The dotted and dashed lines show the ranges in which the symmetry points Φ_1, Φ_2 are found. Taken from Sasaki et al. (2012a).

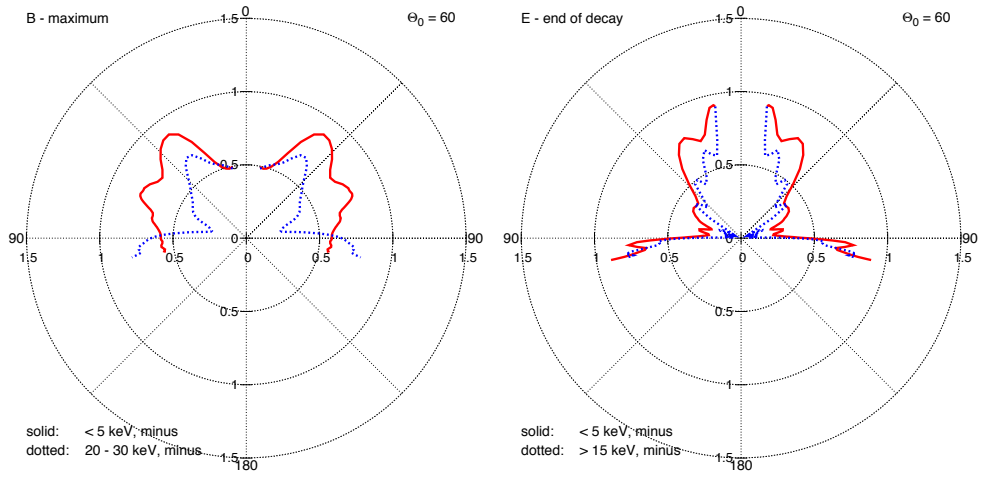

Figure 6: Polar diagrams of the intrinsic beam patterns of 4U 0115+63 for the observations B (maximum) and E (end of decay) for the softest band (red solid) and the hard band above ∼20 keV (blue dotted). Up (0°) is the direction straight up from the magnetic pole, 90° and 270° are the directions tangential to the neutron star surface at the magnetic pole. Taken from Sasaki et al. (2012a).

be explained as that of an accretion stream that has a column and a halo at the bottom. The halo emission dominates the softest bands and has a broad feature at an intrinsic angle of $\sim$30 – 45° with respect to the magnetic axis (see Fig. 6, left, solid line). This component is less prominent for higher energies and becomes also fainter when the luminosity of the source drops. The emission from the accretion column and the upper accretion stream is seen at higher angles (rather perpendicular to the magnetic axis).

For this source we clearly detect the transition from higher to lower accretion states, since the decomposition of the pulse profiles at the end of the giant outburst suggests that the emission from the halo and accretion column has disappeared. When the source becomes fainter the observer sees the pencil beam from the hot spot at the magnetic pole (at lower angles) and radiation scattered in the upper accretion stream (at $> 90^\circ$).

4 Supernovae

Before massive stars end their lives in supernovae (SNe) they have undergone phases of mass loss. Not only does the evolution of a star strongly depend on its mass loss rate but also the evolution of the SN is predetermined by the density distribution around the progenitor star. After the SN shock wave breaks out of the stellar surface it propagates into the surrounding stellar wind and creates an expanding hot region. While the hot plasma emit X-ray emission, electrons, which are accelerated in the shock front, produce radio synchrotron emission. No SN was observed in the Milky Way since the advent of X-ray Astronomy. However, a large number of SNe are detected in nearby galaxies, which allow us to study the X-ray emission during the early phases after an SN explosion.

4.1 SN 2011dh

SASAKI & DUCCI, 2012, A&A, 546, 80

On May 31, 2011, a supernova occurred in the nearby galaxy M 51 (Silverman et al., 2011) at a distance of 8.4±0.7 Mpc (Vinkó et al., 2012) and was classified as a type IIb SN (Arcavi et al., 2011a). The SN was monitored with the X-ray telescope (XRT) of the *Swift* satellite (Gehrels et al., 2004). Furthermore, two observations with *XMM-Newton* were performed 7 and 11 days after the detection of SN 2011dh (see Fig. 7).

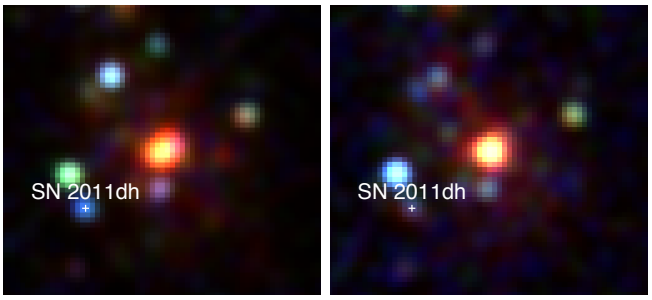

Figure 7: *XMM-Newton* EPIC-PN images ∼7 d (*left*) and ∼11 d (*right*) after the SN explosion in the colours red (0.3 – 1.0 keV), green (1.0 – 2.0 keV), and blue (2.0 – 8.0 keV). Taken from Sasaki & Ducci (2012).

We analysed the two *XMM-Newton* observations and *Swift* observations taken 3 to 30 days after the SN explosion to study possible changes in the X-ray spectrum of SN 2011dh (Sasaki & Ducci, 2012). Since the X-ray emission of the SN was very faint, only the EPIC-PN spectra have high enough statistics and are useful. Hereafter, we call the EPIC-PN spectra of 2011/06/07 and 2011/06/11 spectrum XMM1 and XMM2, respectively. We merged the data taken with the *Swift* XRT from 2011/06/03 to 10 and extracted a spectrum (called spectrum Swift1) that represents an average spectrum of before 2011/06/10. Similarly, we extracted an average spectrum taken with *Swift* XRT after 2011/06/11 (spectrum Swift2). We thus have four spectra with the following chronological order: Swift1, XMM1, XMM2, and Swift2, with Swift1 and XMM1 being spectra taken at similar times.

The spectra were analysed using the X-ray spectral fitting package XSPEC.

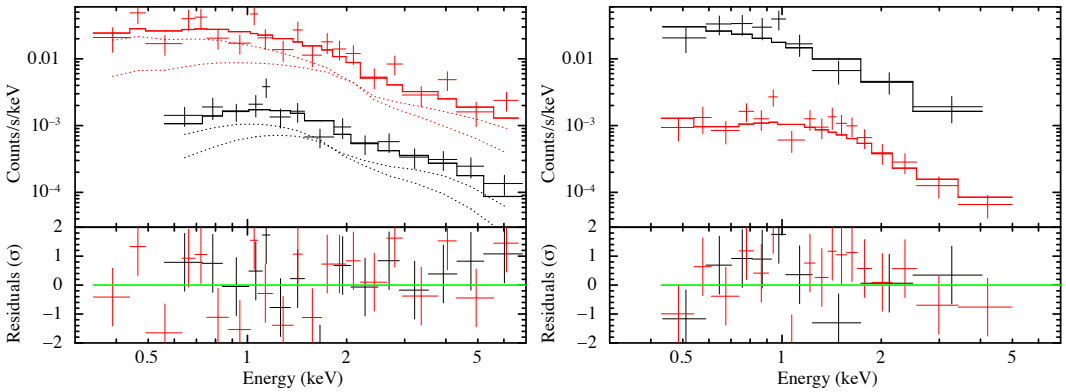

Figure 8: *Left*: Merged *Swift* spectrum of SN 2011dh for $t < 10$ d (Swift1, black) and *XMM-Newton* EPIC-PN spectrum taken at $t = 7$ d (XMM1, red). *Right*: *XMM-Newton* EPIC-PN spectrum taken at $t = 11$ d (XMM2, black) and stacked *Swift* spectrum for $11 < t < 30$ d (Swift2, red). The fitted model in the *left* diagram is a combination of a power-law and a Bremsstrahlung spectrum. For the spectra in the *right* diagram, only a power-law spectrum was used. The *Swift* spectra appear at a lower countrate per energy bin due to the lower effective area of the detector. Taken from Sasaki & Ducci (2012).

The first two spectra Swift1 and XMM1 (before 2011/06/11) can be fitted with a single power-law model with a photon index of $\Gamma = 1.1$ $(1.0 - 1.3)$[d] with a reduced $\chi^2 = 1.1$ and degrees of freedom (d.o.f.) $= 33$. The spectra XMM2 and Swift2 (after 2011/06/11) are also fitted well with a power-law spectrum but with a higher index of $\Gamma = 1.8$ $(1.5 - 2.0)$ with red. $\chi^2 = 1.1$ and d.o.f. $= 23$. It is obvious that the spectra taken on the first $\sim$10 days after the SN differ significantly from the spectra thereafter.

If we used a single thermal Bremsstrahlung model instead, the temperature is unconstrained for the first two spectra ($t < 10$ d) with $kT_{\rm brems,Swift1} > 9$ keV and $kT_{\rm brems,XMM1} > 22$ keV, respectively. For the two later spectra we get temperatures of $kT_{\rm brems,XMM2} = 3(1 - 18)$ keV and $kT_{\rm brems,Swift2} = 3(2 - 8)$ keV (red. $\chi^2 = 1.1$ at d.o.f. $= 56$).

4.1.1 Spectral Components

X-ray observations of SNe in the last decades have shown that the X-ray spectrum seems to become softer days to months after the SN event (e.g., Immler & Kuntz, 2005, and references therein). Possible causes for the softening are changes in the number spectrum of electrons, resulting in a change in the slope of the inverse-Compton (IC) emission of relativistic electrons, or changes in the emission of the forward and the reverse shock due to the propagation of the shock through the circumstellar medium. A change in the slope of the power-law spectrum on a timescale of days is rather unlikely for IC emission. Therefore, the spectral change in the X-ray emission of SN 2011dh seems to indicate a change in the underlying emission components.

[d] All errors given in brackets are at 90% confidence level.

After the shock breaks out of a star, it runs into the circumstellar medium. The interaction of the shock with denser parts of the stellar wind will form a reverse shock that propagates back inwards. Right behind the SN blast wave, the shocked gas has high temperatures of 100 keV or higher. On the contrary, the gas behind the reverse shock is believed to be cooler (1 – 10 keV, Immler, 2003). Therefore, a softening of the X-ray spectrum is probably observed if the reverse shock emission becomes brighter.

The fits of the *XMM-Newton* EPIC-PN and *Swift* XRT spectra have clearly shown that the X-ray spectrum changes at around 10 d after the SN. If the longer persistent X-ray emission can be ascribed to thermal Bremsstrahlung, the temperature is $\sim$3 keV after $t \approx$11 d, i.e., $\sim 3 \times 10^7$ K. This temperature corresponds to a shock velocity of 1 500 km s^{-1}, which is much lower than the velocity of 10 000 km s^{-1} measured from optical spectra (Arcavi et al., 2011b). Therefore, we conclude that this component is most likely reverse shock emission.

The additional hard component observed only until $\sim$10 d after the SN can be interpreted as emission from shocked circumstellar gas. The temperature, if Bremsstrahlung emission is assumed for this hard component, is not well constrained. As the *XMM-Newton* and *Swift* spectra do not extend to energies higher than $\sim$10 keV, we only obtain a lower limit of $kT_{\rm brems} > 42$ keV for the hard component of the early spectra, corresponding to a lower limit for the shock velocity:

$$v_{\rm s} = \sqrt{\frac{16 kT_{\rm brems}}{3\bar{m}}} > 9\,800 \text{ km s}^{-1}, \quad (1)$$

with a mean mass per free particle for fully ionised plasma of $\bar{m} = 0.61\ m_{\rm p}$. From radio and X-ray observations Soderberg et al. (2012) estimated $v_{\rm s} \approx 0.1\ c$, which is about three times higher than this lower limit. If we use a shock velocity of $v_{\rm s} \approx 0.1\ c$, the shock must have reached a radius of $R_{\rm s} \approx v_{\rm s} t \approx 1.8 \times 10^{15}$ cm at $t = 7$ d. From the flux derived from the spectra, we can estimate the down-stream density to be $n = 6.4 \times 10^7$ cm^{-3} at $R_{\rm s} \approx 1.8 \times 10^{15}$ cm. We have thus shown that the hard emission component is consistent with the picture in which the shock has propagated into the stellar wind extending up to a distance of $\sim 10^{15}$ cm.

5 Supernova Remnants

In supernova explosions, a large amount of energy is released and transferred to its surroundings. Stellar matter is expelled with a velocity of $\sim$10 000 km s^{-1}, and the initially spherically expanding shock wave produces a cavity filled with low-density, high-temperature (10^{6-7} K) gas called the supernova remnant (SNR). First, the SNR expands more or less freely through the circumstellar and interstellar medium. As soon as the forward moving blast wave has swept-up as much mass as the ejecta mass, the expansion of the SNR becomes adiabatic (Sedov, 1946a,b; Taylor, 1950a,b). Due to the pressure difference between the shocked ISM and the hot ejecta a second shock wave is formed that propagates inward, which is called the reverse shock (Ardavan, 1973; McKee, 1974; Mansfield & Salpeter, 1974). The reverse shock makes the expanding ejecta decelerate. The forward and the reverse shocks are responsible for the heating of the ISM and the ejecta to X-ray emitting temperatures. Typically after $\sim$10 000 years, radiative cooling in the outer-most shell of the SNR becomes non-negligible and forms a thin shell of colder gas. From then on, the SNR continues to expand as a 'pressure-driven snowplow' and optical line emission can be observed from the radiative shell. Finally, the temperature inside the remnant becomes also so low that radiative cooling cannot be neglected any more in the whole interior. The SNR is now in the 'momentum-driven snowplow' phase and in the end merges with the ISM. The low-density cavity of the SNR persists for $\sim 10^{5-6}$ yr radiating X-rays with a luminosity of $L_X = 10^{35-37}$ erg s^{-1}. The remnant is also visible in radio during almost the entire lifetime, since electrons that are accelerated in the shock fronts of the SNR and interact with the magnetic fields, emit synchrotron emission.

A SN explosion releases energy and matter into the ISM almost instantaneously. Due to interactions between the blast wave and dense clouds in the ISM small clouds may be destroyed, while in larger clouds star formation can be triggered owing to the shocks that are driven into the dense medium. Bubbles formed by stellar winds of massive stars and multiple SNRs can merge with other bubbles and form superbubbles and shells of hundreds of parsecs in diameter. In addition, particles can be accelerated to energies up to 10^{15} eV or higher in the shock waves of SNRs (Bell, 1978a,b; Blandford & Ostriker, 1978; Hillas, 2005). Therefore, SNRs, together with pulsars, are believed to be sources of Galactic cosmic rays.

Multi-frequency studies of SNRs from radio to X-rays help to understand the interaction between the SNRs and the ISM, i.e., the propagation of shock waves, the heating of the surrounding material, and the spreading of material that was processed in stellar interior and was expelled by the SN explosion. In doing so we will not only improve our knowledge of the physics of an SNR itself, but also of the composition, the structure, and the evolution of the ISM as well as the origin of cosmic rays in a galaxy.

Using data taken with today's X-ray telescopes *XMM-Newton* and the *Chandra* X-ray Observatory as well as with radio and optical telescopes, we study SNRs

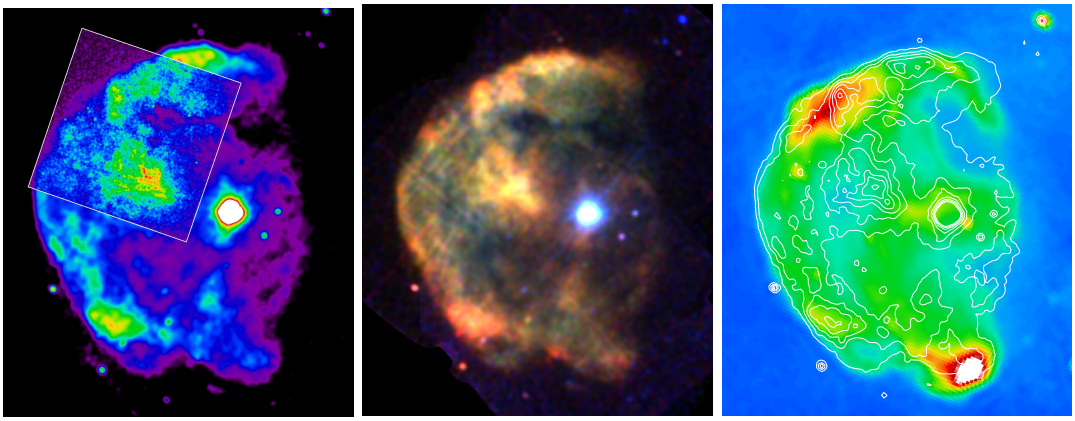

Figure 9: *Left:* Intensity map of the *XMM-Newton* mosaic of the SNR CTB 109 (Sasaki et al., 2004) shown with an inset of a *Chandra* image (Sasaki et al., 2006) of the bright interior region called the Lobe and the northeastern shell. CTB 109 is located next to a giant molecular cloud complex in the west and is one of the most striking example of an interaction of an SNR with cold ISM (see Sect. 5.1). *Middle: XMM-Newton* mosaic three-colour image of the SNR CTB 109 (red = 0.3 – 0.9 keV, green = 0.9 – 1.5 keV, blue = 1.5 – 4.0 keV). *Right:* Radio continuum image (Canadian Galactic Plane Survey, CGPS) with *XMM-Newton* contours.

in the Milky Way and in nearby galaxies to get a better understanding of their physics and the interaction with the ISM.

5.1 The Galactic Supernova Remnant CTB 109

The Galactic supernova remnant (SNR) CTB 109 (G109.2–1.0) was discovered in X-rays with the *Einstein* Observatory by Gregory & Fahlman (1980). The radio counterpart was identified by Hughes et al. (1981) in the Galactic plane survey at 49 cm with the Westerbork Synthesis Radio Telescope. The spectral index in radio is $\alpha = 0.50 \pm 0.04$ and does not vary across the SNR (Hughes et al., 1984). The shell of the SNR is incomplete in the west, both in radio and in X-rays (see Fig. 9). Larger bright spots are found along the rim in radio and in X-rays, but the regions do not coincide in the two energy ranges.

SNR CTB 109 is the host remnant of the anomalous X-ray pulsar (AXP) 1E 2259+586. With its semi-circular morphology, CTB 109 is one of the most exotic objects in the X-ray sky. The SNR and the AXP are located near a giant molecular cloud (GMC) complex (Israel, 1980). Based on CO observations Heydari-Malayeri et al. (1981) and Tatematsu et al. (1985) suggested that this GMC complex and the SNR are associated with each other. Also with the Position Sensitive Proportional Counter (PSPC) of the Röntgensatellit *ROSAT* no X-ray emission was detected in the west (Rho & Petre, 1997). Since no radio emission has been detected in the west either and absorption is negligible in the radio continuum, the SNR shell does not seem to extend further to the west behind the GMC. The SNR shock has most likely been stopped by the GMC complex on one side. Tatematsu et al. (1987) have found an arm-like CO ridge ('CO arm'), which extends eastwards from the GMC and is anti-correlated with

the X-ray emission.

There is a region bright in X-rays inside the shell of CTB 109 known as the 'Lobe' (see Fig. 9). Gregory & Fahlman (1983) suggested that the X-ray bright Lobe is a jet of the AXP. However, as shown by Rho & Petre (1993, 1997) the *ROSAT* PSPC spectrum of the Lobe is thermal in origin with no evidence of synchrotron emission, arguing against a jet interpretation.

5.1.1 The Evolution of the SNR CTB 109

SASAKI ET AL., 2004, APJ, 617, 322

We performed observations of the SNR CTB 109 with *XMM-Newton* EPICs to study the X-ray emission of the entire remnant. A mosaic of all observations using data of all EPICs (PN, MOS1, and MOS2) is shown in Figure 9 (Sasaki et al., 2004). As can be seen in this deep mosaic image of CTB 109 there is no X-ray emission in the western part of the remnant. Since the morphology of the remnant is also similar in radio, the blast wave has most likely been stopped completely in the west. There is also no indication for a molecular shock in the GMC (Koralesky et al., 1998, and references therein). Therefore, there is probably enough unshocked dense medium along the line of sight in front of where the SNR shock hit the GMC, and absorbs the emission.

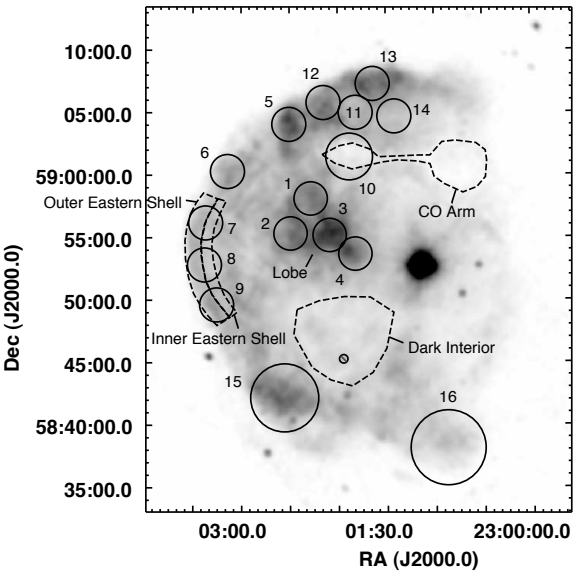

Figure 10: Mosaic of all five *XMM-Newton* observations of CTB 109 in the energy band of 0.3 – 4.0 keV with regions used for the spectral analysis. Taken from Sasaki et al. (2004).

On the eastern side, the blast wave of the SNR shock seems to be expanding into a lower-density medium. The smaller radii of the northern and southern shells indicate that CTB 109 might be confined by denser material also in the north and the south (Fesen & Hurford, 1995). The difference, however, is relatively small ($\sim$5 – 10%) and the overall morphology of the X-ray shell of CTB 109 can be considered a semi-sphere. As calculations have shown, the forward shock of an SNR located next to a molecular cloud is almost unaffected on the low-density side (e.g. Tenorio-Tagle et al., 1985; Wang et al., 1992) and can be modelled as a spherical problem on this side.

We extracted spectra from EPIC-PN, EPIC-MOS1, and MOS2 in different regions of the SNR (see Figs.10, 11). We fitted the spectra in XSPEC using the

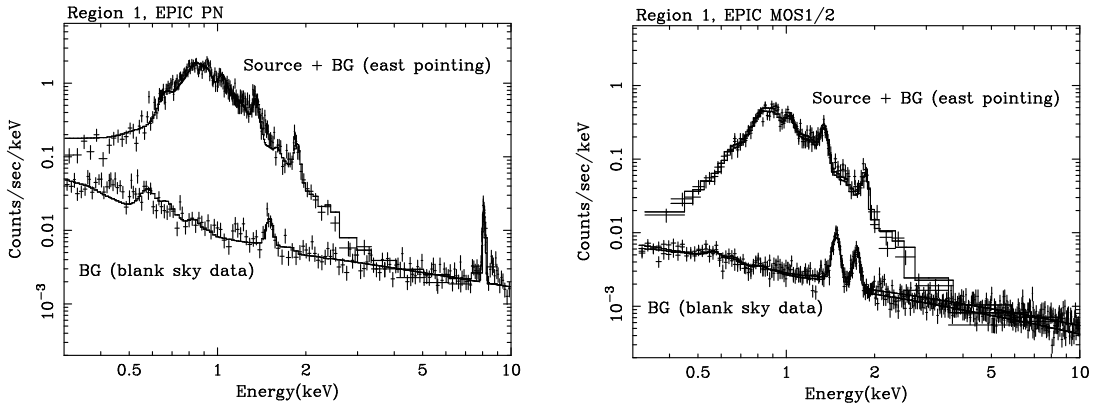

Figure 11: *XMM-Newton* EPIC spectra of the Lobe region 1 are shown with VNEI model fits (left: PN, right: MOS1/2). The background spectrum was not subtracted from the source spectrum, but was modelled simultaneously and is included in the spectral model of the source spectrum. Taken from Sasaki et al. (2004).

model VNEI, which is a model for non-equilibrium ionisation (NEI) plasma with variable abundances (Hamilton et al., 1983; Borkowski et al., 1994; Liedahl et al., 1995; Borkowski et al., 2001), absorbed with a column density $N_{\rm H}$ in the foreground. Fit parameters of the VNEI model are the average X-ray temperature kT, abundances, the ionisation timescale, $\tau = \int n_{\rm e} dt$ (which is an integral of the density over time since the gas was shocked), and the normalisation. The ionisation timescale τ is an indicator of the state of the plasma after the gas has been ionised. For small ionisation timescales $\tau = n_{\rm e} t < 10^{12}\,{\rm s\,cm^{-3}}$, the electrons and ions are still not in ionisation equilibrium.

The hydrodynamics of shock waves like that of an SNR can be described assuming the conservation of mass flow, energy flow, and momentum flow. The entropy of the fluid or gas rises by the passage of a shock wave. Furthermore, the expansion of the blast wave shock of an SNR can be described by the Sedov-Taylor-von Neumann similarity solution (Sedov, 1959; Taylor, 1950a; von Neumann, 1947). Therefore, we can calculate the physical parameters of CTB 109 using the fit results of the spectra of the eastern shell and applying the similarity solution. For the distance to CTB 109 we use $D = 3.0 \pm 0.5$ kpc (Kothes et al., 2002) together with a scaling factor $d_3 = D/3.0$ kpc. To estimate the radius of the SNR, we measure the distance of the shell in the east from the pulsar on the EPIC image: $R_{\rm s} = 18\farcm5 \pm 1\farcm0 = (16 \pm 1)\ d_3$ pc $= (4.9 \pm 0.2) \times 10^{19}\ d_3$ cm. The gas density (excluding electrons) for cosmic abundances (Anders & Grevesse, 1989) can be written as $n = 1.1\ n_{\rm H}$ with $n_{\rm H}$ being the atomic H number density. Assuming that all elements are almost completely ionised, we get $n_{\rm e} \approx 1.2\ n_{\rm H}$. Therefore, the total number density, including electrons, is $n_{\rm tot} = n_{\rm e} + n = 2.3\ n_{\rm H}$. The corresponding mean mass per free particle is $\bar{m} = 0.61\ m_{\rm p}$[e]. The mean mass per nucleus is $\bar{m}_{\rm n} = 1.4\ m_{\rm p}$. In the following, we use the suffix '0' for pre-shock values and 's' for post-shock values.

[e]Proton mass $m_{\rm p} = 1.67 \times 10^{-24}$ g

We use the temperature obtained from the fits of the spectra in regions of the outer blast wave with a VNEI model: $kT_X = 0.62 \pm 0.10$ keV, which corresponds to $(7.2 \pm 1.2) \times 10^6$ K. According to the shock jump condition the density jump at the shock front is $n = 4\ n_0$ with n_0 being the pre-shock ambient density of nuclei. Inside the remnant the density decreases towards the centre because of the adiabatic expansion of the remnant (Heiles, 1964; Cox & Anderson, 1982). Cox & Anderson (1982) calculated the distribution of the normalised density of the nuclei $n(R)/n_0 = n_H(R)/n_{H,0}$. Using their values one can estimate the emissivity at different locations in the SNR. We model the emitting volume of the circular regions as a cylinder intersecting a sphere with the axis of the cylinder aligned to the line of sight. The radius of the cylinder is the radius of the extraction region, i.e., $r = 80'' = 1.2$ pc for $D = 3.0$ kpc.

The normalisation of the VNEI model in XSPEC is

$$norm = \frac{10^{-14}}{4\pi D^2} \times \int 1.2\ n_{H,s}^2\ dV. \tag{2}$$

For the blast wave, we obtain $norm = (1.6 \pm 0.5) \times 10^{-3}$ cm^{-5}. We can thus write

$$norm = \frac{1.2 \times 10^{-14} n_{H,0}^2}{4\pi D^2} \int \left(\frac{n_H}{n_{H,0}}\right)^2 dV. \tag{3}$$

We estimate $V = 42\ d_3^3$ pc^3 for the projected volume and $\int (n_H/n_{H,0})^2\ dV = 240\ d_3^3$ pc^3. Therefore, we obtain the pre-shock densities $n_{H,0} = (0.14 \pm 0.02)\ d_3^{-0.5}$ cm^{-3} and $n_0 = 1.1\ n_{H,0} = (0.16 \pm 0.02)\ d_3^{-0.5}$ cm^{-3}.

If there is full equilibration between the electrons and the nuclei, the measured temperature is equal to the post-shock temperature and is thus related to the shock velocity as

$$T_X \approx T_s = \frac{3\bar{m}}{16k} v_s^2, \tag{4}$$

with $k = 1.38 \times 10^{-16}$ ergs K^{-1} being the Boltzmann's constant. Since the mean mass per free particle is $\bar{m} = 0.61\ m_p$ for a fully ionised plasma, the shock velocity can be estimated as $v_s = [(16kT_X)/(3 \times 0.61 m_p)]^{\frac{1}{2}} = 720 \pm 60$ km s^{-1} for $kT_X = 0.62 \pm 0.10$ keV.

However, in young and most middle-age SNRs like CTB 109 the electrons and ions are not fully equilibrated. In this case the ion temperature T_{ion} is higher but close to the mean plasma temperature T, and the electron temperature T_e is lower. Since the X-ray emissivity of the plasma primarily depends on the electron temperature, the observed emissivity and the derived velocity do not correspond to each other. Itoh (1978) studied the evolution of the electron temperature and its ratio to the mean post-shock temperature in two-fluid phase SNR shocks assuming the Sedov similarity solution and Coulomb equilibration between electrons and ions. It was shown that the ratio $g = T_e/T$ can be written as a function of a reduced time variable $\nu = t_3(n_0^8/E_{51}^3)^{1/14}$ that describes the thermal structure of the blast wave, with t_3 being the time elapsed since the explosion (in units of 10^3 yrs), n_0 the pre-shock density of the nuclei (in units of cm^{-3}), and E_{51} the initial

explosion energy (in units of 10^{51} ergs). We can obtain the X-ray temperature T_X, the ambient density n_0, and the radius R_s of the SNR from the X-ray data. These three values are related to each other as $f = T_X/T = 0.043 T_X (R_s n_0)^{-1/2} \nu^{7/5}$. Therefore, the value of $f = T_X/T$ can be obtained from the intersection of the curve $f(\nu)$ with the theoretical curve for Coulomb equilibration $g(\nu) = T_e/T$. Using the same method, we obtain a lower limit for the ratio $T_e/T_s \approx T_X/T_s \approx 0.4$, resulting in an upper limit for the velocity of $v_s = [(16kT_X)/(3 \times 0.4 \times 0.61 m_p)]^{\frac{1}{2}} = 1\,140 \pm 90$ km s^{-1}.

Using the Sedov similarity solution we estimate the age of the SNR from the shock velocity:

$$v_s = \dot{R}_s = \frac{2R_s}{5t}. \tag{5}$$

Assuming full equilibration of electron and ion temperatures, we get an age estimate of $t = (2.7 \pm 0.2) \times 10^{11}\ d_3$ s $= (8.6 \pm 0.8) \times 10^3\ d_3$ yrs. In the case of non-equilibrium the age would be lower. For the lower limit of $T_e/T_s = 0.4$, the age is $t = (1.7 \pm 0.2) \times 10^{11}\ d_3$ s $= (5.4 \pm 0.5) \times 10^3\ d_3$ yrs.

The initial energy of the explosion can be estimated using the relation of the self-similar solution:

$$R_s = \left(\frac{2.02 E_0 t^2}{\bar{m}_n n_0} \right)^{\frac{1}{5}}. \tag{6}$$

We thus get $E_0 = \frac{1}{2.02} R_s^5 \bar{m}_n n_0 t^{-2} = (7.0 \pm 2.2) \times 10^{50}\ d_3^{2.5}$ ergs for full equilibration between the electrons and ions, and $E_0 = (17.4 \pm 5.5) \times 10^{50}\ d_3^{2.5}$ ergs, for partial equilibration with a lower limit of the temperature ratio of $T_e/T_s = 0.4$.

5.1.2 The Shocked Cloud

SASAKI ET AL., 2006, APJL, 642, 149

The analysis of the spectra of SNR CTB 109 taken with *XMM-Newton* has shown that the X-ray emission of the Lobe is thermal and similar to that of the SNR shell (Sasaki et al., 2004). The enhanced X-ray brightness of the Lobe suggests an interaction of the SNR shock wave with a dense molecular cloud.

We therefore performed an observation with the *Chandra* X-ray Observatory (Weisskopf et al., 2002) using the Advanced CCD Imaging Spectrometer (ACIS, Garmire et al., 2003) in order to study this interaction region in more detail. We observed the northeast part of the SNR in an 80 ks pointing of *Chandra* with ACIS-I as the prime instrument. The high-resolution data from the *Chandra* X-ray Observatory in combination with the new high-resolution CO data from the Five College Radio Observatory revealed the interaction region with the cloud complex in greater detail (see Fig. 12, Sasaki et al., 2006).

Three CO clouds have been found around the Lobe. At the position where one of the CO clouds and the Lobe overlap, the velocity profile of the cloud has an additional component towards higher negative velocities. The molecular hydrogen density in this part of the cloud is relatively high ($N_{H_2} \approx 1.9 \times 10^{20}$ cm^{-2}), whereas

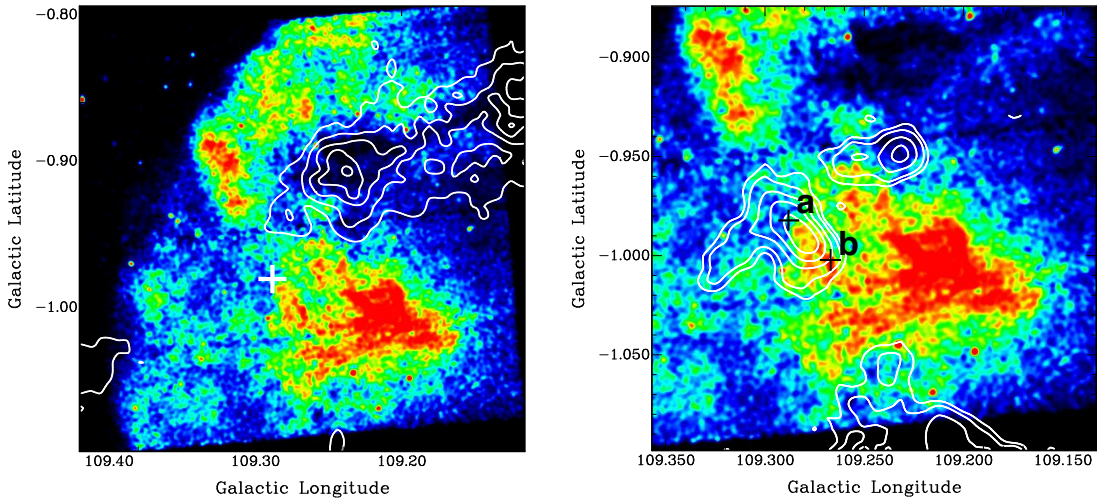

Figure 12: The distribution of molecular gas in the vicinity of the X-ray Lobe as seen in the light of the ^{12}CO($1-0$) line (white contours) overlaid on a *Chandra* image (0.35 – 10.0 keV) taken from Sasaki et al. (2006). These images are presented in Galactic coordinates and are hence rotated by about 25 degrees anti-clockwise with respect to the images in Figure 9. *Left:* The CO data are averaged over the velocity range from -51 to -44.5 km s^{-1} and show the absorbing CO in the foreground. The white cross marks the position of the IR source IRAS 23004+5841. *Right:* The CO data are averaged over the velocity range from -57 to -52 km s^{-1}. There are three clouds Galactic north (up), east (left), and south (down) of the Lobe. The positions at which the velocity profiles have been studied are marked with black crosses.

the foreground absorption in X-rays ($N_{\rm H} \approx 4.5 \times 10^{21}$ cm^{-2}), obtained from *Chandra* data, is lower than in other parts of the cloud and in other clouds. We estimate a mass of about 50 $M_{\odot}$ for the east cloud. These results indicate that this cloud has been hit by the SNR blast wave on its western side, corroborating that the shock-cloud interaction caused the bright X-ray Lobe.

5.1.3 The Lobe and the Northeastern Shell

SASAKI ET AL., 2013, APJ, 552, 45

To study the X-ray emission at and around the Lobe, we divided the emission of the SNR into small regions with similar surface brightness and X-ray colour and extracted spectra for each region (Sasaki et al., 2013). All the spectra can be fitted well with a two-component thermal model consisting of two thermal VNEI models. The first component is used to model the emission from the shocked ISM, while the second component models the emission from the ejecta (Fig. 13). The temperature of the ISM component (Fig. 14, x-axis in the left diagram) is $\sim$0.1 – 0.3 keV in all regions. The temperature of the ejecta component is higher ($\sim$0.4 – 0.9 keV, Fig. 14, x-axis in the middle diagram). The ionisation timescale of the ejecta component is $\tau_2 = n_{\rm e,2} t_2 = 10^{11-12}$ s cm^{-3} except for regions at and around the CO arm, in which τ_2 tends to be higher. The higher values for τ_2 in the CO arm regions indicate a higher density as we can assume that these regions have been

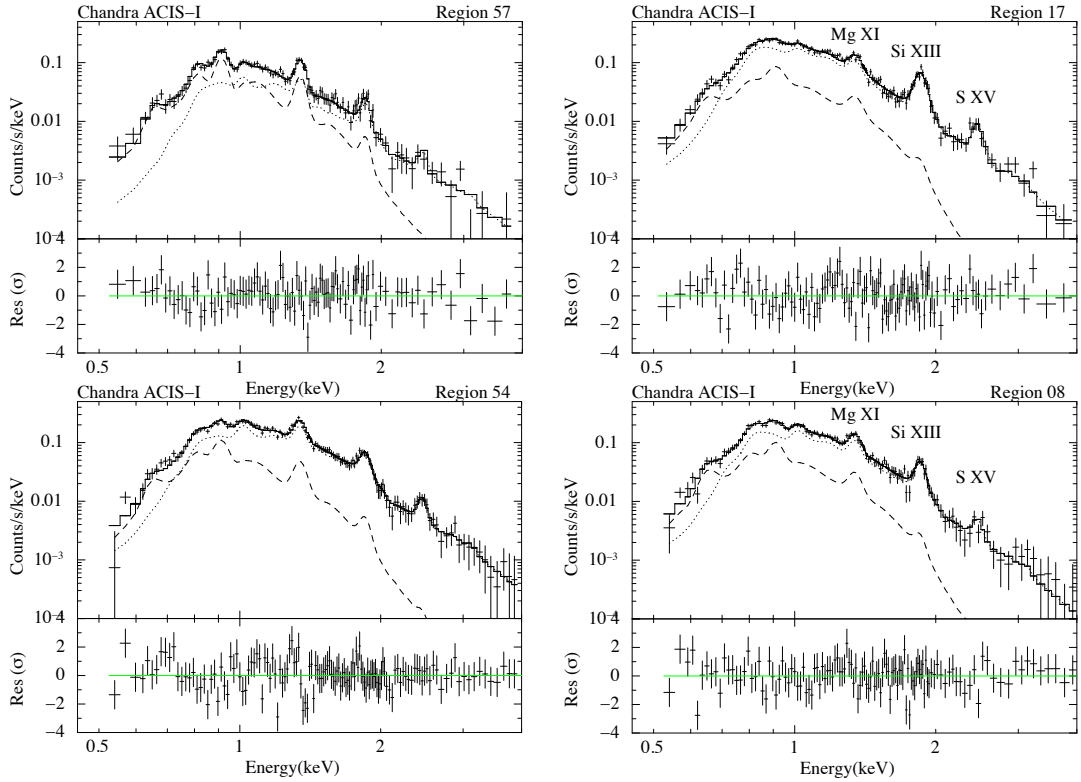

Figure 13: *Left*: Spectrum of the outermost region 57 in the east (upper) and an interior region 54 (lower) with the best fit 2 VNEI model. The relative flux of the ejecta component (dotted) with respect to the ISM component (dashed) in region 57 is lower than in most other regions. *Right*: Spectrum of region 17 with enhanced Si XIII emission (upper diagram). The Mg XI, Si XIII, and S XV triplets are marked. For comparison, the spectrum of region 08, which is the brightest region in the Lobe next to region 17, is shown (lower diagram). The best fit 2 VNEI model is additionally plotted in the diagrams. Taken from Sasaki et al. (2013).

shocked at a similar time to the rest of the remnant. The foreground absorption $N_{\rm H}$ is high around the CO arm ($N_{\rm H} > 1.1 \times 10^{22}$ cm^{-2}). Around and, in particular, west of the Lobe, the foreground absorption is lower ($N_{\rm H} < 1.0 \times 10^{22}$ cm^{-2}), while it seems to be higher southeast of the Lobe.

Pressure The normalisation of the emission model fitted to the observed spectra is given by the parameter

$$norm_{1,2} = \frac{10^{-14}}{4\pi D^2} \times \int n_{1,2}\, n_{e\,1,2}\, f_{1,2}\, dV. \qquad (7)$$

The values f_1 and f_2 are the filling factors of the ISM and ejecta components, respectively ($f_1 + f_2 = 1$). We show the dependence of the $norm_{1,2}$ per extracted area A on the temperature $kT_{1,2}$ in Figure 14 (left and middle diagrams). In addition, we calculated lines of constant pressure with $p/k = 10^6$ cm^{-3} K (blue) and 10^7 cm^{-3} K (green) for different values of filling factors and depths of the assumed emitting volume in the SNR. We assumed pressure equilibrium between

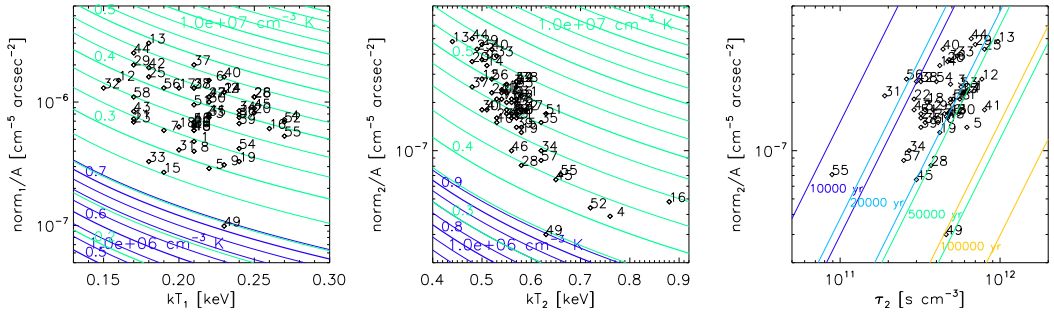

Figure 14: Distribution of the parameter values for the fit with two VNEI components. The labels of the data points are region numbers. The lines in the diagrams for surface brightness $norm_{1,2}/A$ over temperature $kT_{1,2}$ show the isobars for p/k = 10^6 cm^{-3} K (blue) and 10^7 cm^{-3} K (green) for different values of the filling factors in the remnant and the size of the emitting volume along the line of sight. The lines in the diagram showing the surface brightness as $norm_2/A$ over the ionisation timescale τ_2 are isochrones for t = 10000, 20000, 50000, and 10000 yr. There is not only one line but a range for all isochrones for the lowest to the highest depth of the emitting volume. Taken from Sasaki et al. (2013).

the shocked ISM and the shocked ejecta. The data are consistent with a thermal pressure of $p/k \approx 10^7$ cm^{-3} K, corresponding to 1.4 $\times 10^{-13}$ dyne cm^{-2}.

Age Estimate The relation between the ionisation timescale of the ejecta τ_2 and the surface brightness given by $norm_2/A$ is shown in Figure 14 (right). If we replace n_e by τ/t in Equation 7 we get $norm_2/A$ as a function of τ for a given t. The calculated isochrones for different values of t are also shown in the τ_2-$norm_2/A$ diagram. The two lines for each time t show the possible ranges for the possible projected depth of the SNR. The diagram indicates that the age of the shocked plasma, derived from the ejecta component is $\sim 2 \times 10^4$ yr.

The temperature of the ISM component was determined to be between 0.1 keV and 0.3 keV, with kT = 0.25 keV in the outermost regions. The ionisation timescale τ of the ISM component is high and not well-constrained, indicating that the plasma of the shocked ISM is close to collisional ionisation equilibrium (CIE). Using the temperature of this component as that of the shocked ISM, the blast wave velocity is

$$v = \sqrt{\frac{16kT_1}{3\bar{m}}}, \tag{8}$$

with a mean mass per free particle for a fully ionised plasma of $\bar{m}$ = 0.61 m_p. For kT_1 = 0.25 $\pm$ 0.03 keV, we get v = 460 $\pm$ 30 km s^{-1}. Using the Sedov similarity solution and a radius of $R = 5.0 \pm 0.8 \times 10^{19}$ cm (Sasaki et al., 2004), the age of the remnant can be estimated as

$$t = \frac{2R}{5v} = (14 \pm 2) \times 10^3 \text{yr}. \tag{9}$$

This value is a little higher than the age estimated from the *XMM-Newton* data (Sasaki et al., 2004), for which only one spectral component was assumed. The

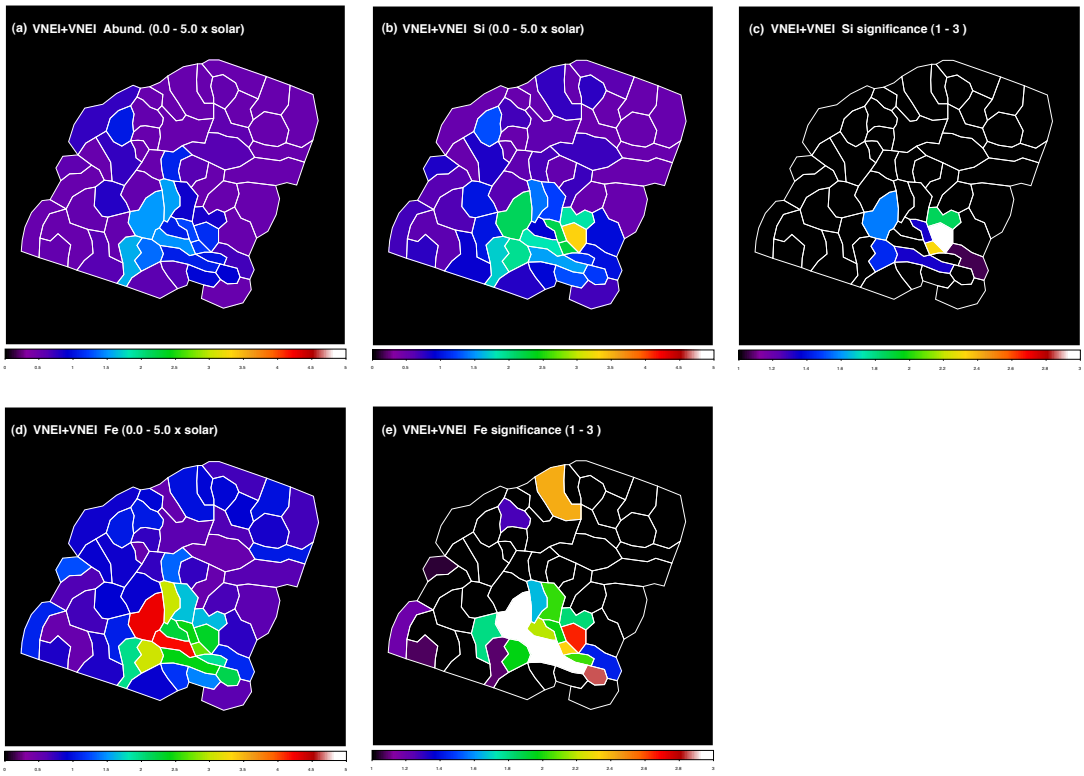

Figure 15: Best fit values for the abundances relative to solar values assuming a two-component VNEI model. Upper panel: abundances for elements other than Si, S, and Fe fitted for the ejecta emission (a), Si abundance fitted for the ejecta emission (b) and its significance calculated as (abundance of the Si – abundance of the other elements)/error of the abundance of Si (c). Lower panel: Fe abundance and its significance (d, e, respectively). Taken from Sasaki et al. (2013).

new value for the SNR age is in good agreement with the age estimate obtained from the fits of the ejecta component.

Abundances In Figure 15, we show the distribution of the fitted Si abundance and Fe abundance for the ejecta emission in the SNR. To create these images, we filled the regions in which the spectra were extracted with the best fit values. The overall abundance measured for the ejecta is comparable to or lower than solar values outside the Lobe, whereas the Si and Fe abundances are higher especially in the Lobe (Fig. 15a, b, d). The higher abundances in the Lobe suggest that its emission has its origin in a shocked ejecta clump or a mix of ejecta clumps and dense clouds. One region northwest of the Lobe in particular has a significantly enhanced Si abundance (3.3 [2.6 – 4.0], see Fig. 15b, c).

5.1.4 Summary

Using proprietary X-ray data obtained with *XMM-Newton* and *Chandra*, we have confirmed shock-cloud interaction in the SNR CTB 109 and detected ejecta emis-

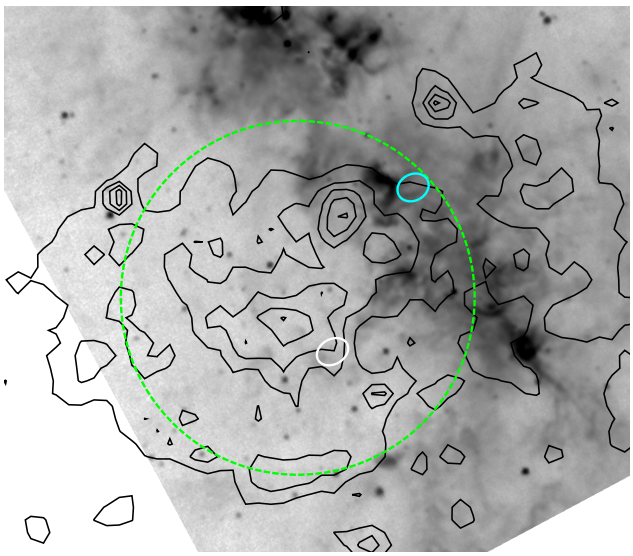

Figure 16: A Midcourse Space Experiment (MSX, Egan et al., 2003) image in the IR taken at 8.3 μm, together with *ROSAT* PSPC (0.1 – 2.4 keV) contours. The IR image shows the emission from interstellar dust. The green dashed circle shows the FOV of the *XMM-Newton* EPICs. The cyan ellipse in the north shows the position of the PWN candidate HX3 west, the white ellipse that of the PWN candidate CXO J1923 (Koo et al., 2005).

sion inside the remnant. The element abundances are enhanced in the X-ray bright Lobe and next to it. From both the ISM and the ejecta emission we derived an age of $\sim$10 – 20 kyr for the SNR. The bright X-ray feature called the Lobe is indicative of an interaction of the SNR with molecular clouds and suggests the following scenario: the blast wave hit a dense cloud evaporating and maybe encompassing it. Due to the interaction with the cloud, a reverse shock was formed and propagated towards the centre heating the ejecta. The evaporated cloud is now visible as the Lobe with stronger X-ray emission.

5.2 The Galactic Supernova Remnant W51C

SASAKI, ET AL., 2014, A&A, 563, 9

The Galactic SNR W51C (G49.2–0.7) is part of the W51 complex, located at the tangential point of the Sagittarius arm. In addition to the SNR, the W51 complex consists of the sources W51A and B, which both harbour compact H II regions. A high-velocity molecular gas stream, which is almost parallel to the Galactic plane (Mufson & Liszt, 1979), has been found on the western side of the SNR (see Fig. 16).

Since SNR W51C is located in a region with a large number of H II regions and dense molecular gas, this object is a prime example for the interaction of the SNR blast wave with the multi-phase ISM in our Galaxy and an ideal target to study the compact remnant of the SN explosion which was presumably caused

Table 1: Fit parameters for the SNR emission (Sasaki et al., 2014).

ID	N_H	kT	τ	Ne	Mg	red. χ^2
	[10^{22} cm^{-2}]	[keV]	[10^{11} s cm^{-3}]	$\times$ solar	$\times$ solar	DOF*
Region 1	1.6	0.68	1.1	1.0*	1.0*	1.3
	(1.5 – 1.7)	(0.66 – 0.74)	(0.8 – 1.5)			1034
Region 2	2.0	0.59	8.1	3.7	2.0	1.2
	(1.9 – 2.1)	(0.56 – 0.61)	(6.2 – 11.)	(3.5 – 4.2)	(1.9 – 2.2)	970

Errors are 90% confidence limits.
*Degrees of freedom.
*Fixed to solar values like all the other abundances.

by core-collapse. The shell of the SNR is clearly visible on the eastern side as an arc-like structure in the radio with an extent of about 30′ (Copetti & Schmidt, 1991; Subrahmanyan & Goss, 1995). In X-rays, the outer shock region is rather faint but follows the shape of the radio shell (Koo et al., 1995). Inside this shell there is an additional interior X-ray arc and a region in the northwest, which is bright in X-rays (see Fig. 16). Assuming a Sedov model, Koo et al. (1995) derived an SNR age of $\sim 3 \times 10^4$ yrs. Between the SNR and the high-velocity stream of molecular gas, OH(1720 MHz) masers have been found (Green et al., 1997), which are indicative of shock-cloud interactions.

5.2.1 SNR Emission

The shell-type morphology in radio and the central enhancement in X-rays suggest that W51C is a mixed-morphology SNR. We have analysed an *XMM-Newton* observation of the inner part of W51C, covering the interior arc-shaped region inside the SNR shell and the bright central region (Sasaki et al., 2014). The outer blast wave shock was not covered by the field of view (FOV) of the EPICs.

The spectrum of the arc-shaped region is fitted well with a thermal VNEI model with solar abundances (Region 1, Table 1). The origin of this diffuse X-ray emission is therefore shocked ISM. Since this interior arc-like structure has a much higher surface brightness than the outer blast wave emission to the east, this emission is indicative of circumstellar medium around the progenitor, which has been shocked by the SN explosion.

A single thermal model with solar abundances did not yield a satisfactory fit to the X-ray spectrum of the central X-ray bright region (Region 2). Instead, the fit improved significantly, when we freed the element abundances. We have confirmed enhanced abundances for the elements Ne and Mg, suggesting emission from the ejecta.

5.2.2 Pulsar Wind Nebula Candidate

The SNR W51C is very likely the result of a core-collapse SN and should have an associated compact object. In the *Chandra* studies, Koo et al. (2005) discovered

the point source CXO J192318.5+140305 (CXO J1923 hereafter) surrounded by an extended emission in the hard band (2.1 – 10.0 keV) and suggested that it might be a candidate pulsar wind nebula (PWN); its position is indicated in Figure 16 with a white ellipse. The analysis of the *XMM-Newton* data by Sasaki et al. (2014) has confirmed that the extended emission around CXO J1923 is consistent with a PWN. However, we have also found an additional source at the northern border of the SNR, which has similar properties with a hard point source surrounded by an extended hard emission with an extent of about 1′; this source is called HX3 west, following the nomenclature of Koo et al. (2002), who discovered this source in ASCA data. The *XMM-Newton* EPIC spectra of the hard diffuse emission of both sources are consistent with a power law with a photon index of $\Gamma \approx 1.8$. Radio sources were detected at both positions (Condon et al., 1998; Koo et al., 2002). The X-ray luminosities of these two PWN candidates are $L_{0.3-10.0\mathrm{keV}} \approx 4 \times 10^{33}$ erg s^{-1} with an assumed distance of D = 6 kpc.

5.2.3 Summary

The *XMM-Newton* data allowed us to 1) confirm shocked circumstellar matter inside the SNR W51C, 2) measure enhanced abundances in the most interior region indicative of ejecta emission, and 3) identify an additional PWN candidate HX3 west with a spectrum and luminosity similar to the known PWN candidate CXO J1923. Additional observations with higher spatial resolution and higher statistics are necessary to clarify the origin of the mixed-morphology emission of the SNR and to pin down the nature of the PWN candidates.

5.3 Supernova Remnants in the Large Magellanic Cloud

The hot plasma inside SNRs can best be studied in soft X-ray line and continuum emission owing to its high temperature ($10^6 - 10^7$ K). However, due to absorption by matter in the Galactic plane, it is difficult to study these soft X-ray sources in our own Galaxy.

The LMC is an irregular galaxy with spiral structures and is one of the closest neighbours of our Galaxy. Its proximity with a distance of 48 kpc (Macri et al., 2006) and modest extinction in the line of sight (average Galactic foreground $N_{\mathrm{H}} = 0.6 \times 10^{21}$ cm^{-2}) make it an ideal laboratory for a detailed study of a large sample of SNRs. The proximity enables spatially resolved studies of the SNRs, and the accurately known distance allows for analysis of the energetics of each SNR. In addition, the wealth of wide-field multi-wavelength data available, from radio maps to optical emission-line images as well as infrared surveys to global X-ray mosaics, provides information about the environments in which these SNRs are born and evolve.

With an improved sample of SNRs in the LMC, we are able to study not only the global properties of the SNRs but also the subclasses in detail (e.g., sorted by X-ray and radio morphology, diameter, or progenitor supernova type). Toward this goal, we have been studying SNRs in the Magellanic Clouds (MCs) using

combined optical, radio, and X-ray observations. From a thorough investigation of the X-ray properties of known, identified X-ray sources in the LMC, Haberl & Pietsch (1999, HP99 hereafter) derived classification criteria for new candidates for SNRs based on spatial extent, extent likelihood, hardness ratios, and X-ray (non-) variability. In addition, we also identified candidates based on optical and radio emission. There are over 50 confirmed SNRs in the LMC and another 25 – 30 candidates (HP99, Sasaki et al., 2000; Payne et al., 2008). An extensive study of SNRs observed with *ROSAT* has also been carried out by, e.g., Williams et al. (1999).

Most of the SNRs in the LMC that have been studied in the past years were identified as such based on *ROSAT* data. Only a few new SNRs were discovered so far using *Chandra*, *Suzaku*, or *XMM-Newton* in observations of other fields in the LMC than those with well-known X-ray sources (e.g., Williams et al., 2004b; Hughes et al., 2006; Klimek et al., 2010). We therefore proposed and have been granted new *XMM-Newton* observations to study bona-fide SNR candidates in the LMC (PI: M. Sasaki). The new X-ray data are compared with data in radio (e.g., taken at the Australia Telescope Compact Array [ATCA]) and optical (Magellanic Cloud Emission Line Survey [MCELS]). These studies allowed us to confirm and study a number of LMC SNRs in detail (Grondin et al., 2012; Haberl et al., 2012; de Horta et al., 2012; Bozzetto et al., 2012; Maggi et al., 2012; Kavanagh et al., 2013; Bozzetto et al., 2013; Maggi et al., 2014; Bozzetto et al., 2014; Warth et al., 2014; Kavanagh et al., 2015).

5.3.1 SNR XMMU J0541.8–6659 in the LMC

GRONDIN, SASAKI, ET AL., 2012, A&A, 539, 15

The *ROSAT* source [HP99] 456 was one of our brightest SNR candidates with a large extent. Therefore, we observed the source with *XMM-Newton* (Grondin et al., 2012). Morphological and spectral analyses of the source, which was detected and called XMMU J0541.8–6659, revealed the existence of two emission components, which dominate below and above 0.9 keV: a thermal emission, with a morphology of an SNR shell, and a non-thermal, hard emission region with a narrower but elongated structure (Fig. 17, left).

The X-ray emission below 0.9 keV is dominated by a shell-like source with a diameter of $\sim$5′, as seen in Fig. 17 (left). Its spectrum is well fitted in XSPEC with a single-temperature non-equilibrium ionisation model VNEI with a temperature of $kT = 0.49 \pm 0.12$ keV, ionisation timescale of $n_e t = (1.5 \pm 0.7) \times 10^{10}$ s cm^{-3}, absorbed by the foreground $N_{\rm H} = 6 \times 10^{20}$ cm^{-2} of the Milky Way (reduced χ^2 = 1.27 for 86 degrees of freedom). The abundances were fixed to 0.5 of the solar abundances, which is the mean value for the LMC. The morphology and the thermal X-ray spectrum strongly support the identification of the soft extended source as an SNR. At a distance of 50 kpc, the extent of the thermal shell corresponds to a diameter of $\sim$70 pc, which makes XMMU J0541.8–6659 one of the largest SNRs in the LMC, and thus one of the oldest. Applying the Sedov solution, we

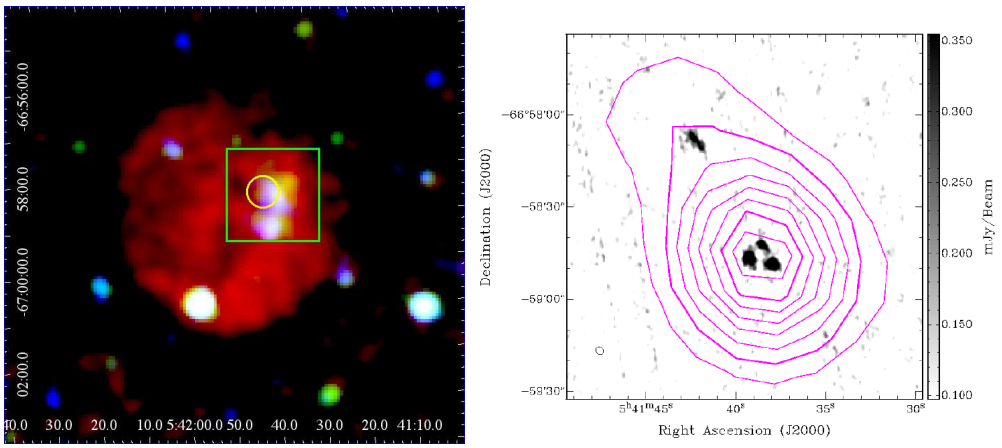

Figure 17: *Left:* Smoothed three-colour image of combined exposure-corrected data of *XMM-Newton* EPICs (red: 0.2 – 1.0 keV; green: 1.0 – 2.0 keV; blue: 2.0 – 4.5 keV) showing the LMC SNR XMMU J0541.8–6659. *Right:* High-resolution ATCA radio-continuum image at 6 cm with 20 cm contours of the low-resolution mosaic image (magenta, from 3 to 18 mJy/beam in steps of 1 mJy/beam). The 6 cm beam size is shown in the bottom left corner. In the X-ray image (left) the field of view of the radio image (right) is shown as a green square and the position of the *ROSAT* source [HP99] 456 by a yellow circle. Taken from Grondin et al. (2012).

obtain a dynamic age of $\sim$23 kyr for the remnant. The age and the low ionisation timescale indicate that the SNR is expanding in a medium of fairly low density.

The X-ray emission above 0.9 keV is dominated by an elongated structure located $\sim$1′ to the west of the centre of the shell-like thermal emission. The spectrum of this hard emission with $\sim$320 cts is well modelled with an absorbed power law with a spectral index of $\Gamma = 1.8 \pm 0.3$ and an additional intrinsic column density of $N_{\rm H} \approx (5.8 \pm 0.53) \times 10^{20}$ cm^{-2} (reduced χ^2 = 0.22 for 6 degrees of freedom).

We have also analysed the radio emission at the position of the SNR XMMU J0541.8–6659 from data taken at ATCA. These radio data reveal several bright sources within the X-ray emitting regions. Figure 17 (right) shows the high-resolution radio image at 6 cm with contours of the low resolution image at 20 cm. Three bright sources are found inside the non-thermal emitting region. One of them presents a spectral index of $\alpha \approx$ –0.5 and a flux density of 0.85 mJy at 6 cm, while the two other bright radio sources have indices of $\alpha \leq$ –1.0. These indices are consistent with a pulsar scenario. The extended hard X-ray emission then could be a PWN. However, the indices are also consistent with that of background AGNs. Therefore, the nature of these sources remains unclear and more data are required to clarify the origin of the hard X-ray emission.

5.4 Supernova Remnants in M 31

SASAKI ET AL., 2012, A&A, 544, 144

The Andromeda galaxy (M 31) is the largest galaxy in the Local Group and the

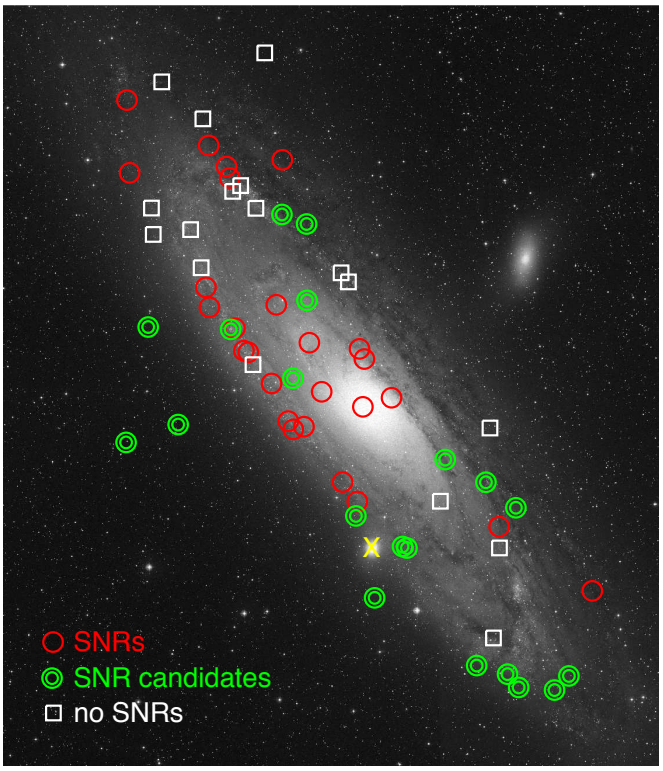

Figure 18: Positions of X-ray SNRs and candidates detected with *XMM-Newton* are shown on a Digitised Sky Survey 2 (*B*) image. Sources are marked according to our new classifications. In addition, the position of the dwarf elliptical M 32, which is a satellite galaxy of M 31, is indicated by a yellow cross. Taken from Sasaki et al. (2012b).

nearest spiral galaxy to the Milky Way, located at a distance of 790 kpc (Tully et al., 2009). Its size and mass are comparable to those of our Galaxy. Therefore, this archetypal spiral galaxy provides a unique opportunity to study and understand the nature and the evolution of a galaxy similar to our own. The entire M 31 was observed with *XMM-Newton* in a large programme (LP) between June 2006 and February 2008 (PI: W. Pietsch, Max-Planck-Institute for Extraterrestrial Physics, MPE) with the EPICs, revealing a total of 1897 *XMM-Newton* sources (Stiele et al., 2011).

During the evolution of SNRs, the shock waves, which run into the ISM and through the ejecta in the interior, produce a cavity filled with a low-density, high-temperature plasma, which emits predominantly soft X-ray radiation. Relativistic electrons and heavier particles in SNRs emit synchrotron emission that can be detected in radio and, in some cases, in X-rays. After a few thousand years, SNRs become radiative, i.e., the radiative losses in SNR shocks expanding into the ambient ISM become non-negligible. A shell of dense swept-up gas is formed around the hot gas, which emits ultraviolet and optical line emission. If a neutron star is created in the supernova explosion, a pulsar and/or a PWN can be found inside the SNR, in which particles are accelerated in the strong magnetic field of the neutron star and thus non-thermal emission is produced.

Supernova remnants in M 31 have been mainly detected in the optical (e.g., D'Odorico et al., 1980; Dennefeld & Kunth, 1981; Blair et al., 1981) and combined optical and radio studies (Braun & Walterbos, 1993). The X-ray survey performed with *ROSAT* led to the detection of 16 X-ray SNRs (Supper et al., 2001), while 21 were detected and identified with *XMM-Newton* (Pietsch et al., 2005). Kong et al. (2002) presented the first resolved X-ray image of an SNR in M 31 taken with *Chandra*, while Kong et al. (2003) and Williams et al. (2004a) reported on the discovery of additional SNRs in M 31 based on *Chandra* data.

We studied the population of SNRs in M 31 using the *XMM-Newton* survey data as well as optical data of the Local Group Galaxy Survey (LGGS) performed at the Kitt Peak National Observatory (KPNO, Massey et al., 2006) and compiled a list of SNRs confirmed in X-rays and the optical as well as bona-fide candidates (Sasaki et al., 2012b). For the optical analysis, we used Hα, [S II], and [O III] emission-line images and *UBVRI* band images of the LGGS. We newly calibrated the LGGS data to obtain optical fluxes and computed the [S II]/Hα flux ratio, which is an indicator of SNR emission in the optical.

Combining the X-ray flux and spectral properties with the [S II]/Hα flux ratio and the morphology in the optical, we confirmed new SNRs in M 31. The brightest SNRs have X-ray luminosities of $\sim 8 \times 10^{36}$ erg s^{-1} in the 0.35 – 2.0 keV band.

6 The Hot Interstellar Medium

It was known from observations in the radio and the optical, that the vast space between the stars and stellar remains in the Milky Way are filled with cool clouds ($T \lesssim 10^2$ K) of neutral hydrogen atoms with densities of $n \approx 10$ cm^{-3}, embedded in warm ($T \simeq 10^4$ K, $n \approx 0.1$ cm^{-3}) intercloud medium of partially ionised hydrogen (Cox, 2005, and references therein). Since the 1970s, observations in the UV and X-rays showed the presence of hot gas at coronal temperatures ($T \approx 10^6$ K) in the ISM. Such high temperatures in the ISM were already suggested by Spitzer (1956) in a work based on observational evidences of the presence of clouds at large distances from the Galactic plane. Observed as absorption features in optical spectra of bright stars at high Galactic latitudes, these clouds can only persist in an environment with pressure comparable to that in the Galactic plane, and indicate the existence of hot tenuous gas. Massive OB stars inject energy to the ISM through their radiation, stellar winds, and finally by supernova explosions. These processes are often correlated in space and time, generating superbubbles with sizes of typically $100 - 1000$ pc. Cox & Smith (1974) suggested that SNRs may also produce an interconnecting tunnel system of coronal gas in the ISM. Cooling of the coronal gas is very inefficient, and thus once heated, the hot gas of the ISM may persist for millions of years or longer, and forms a structure like a foam within the galaxy. Review on the hot phase of the ISM is given by Spitzer (1990).

First UV observations of coronal gas with temperatures of $\sim 5 \times 10^5$ K were reported by Rogerson et al. (1973), Jenkins & Meloy (1974), and York (1974). Coronal gas at even higher temperatures was found in the soft X-ray background (Williamson et al., 1974; Tanaka & Bleeker, 1977). Inoue et al. (1979) who observed the emission line of O VII at 0.57 keV, confirmed the thermal nature of the soft X-ray emission and determined a temperature of $\sim 5 \times 10^6$ K. The German Röntgensatellit *ROSAT* carried out an all-sky survey of the X-ray sky for the first time, in which a complete data set of the soft X-ray background at an angular resolution of about 2° was obtained. Galactic halo emission was identified as one component of the soft X-ray background, based on shadowing effects of H I clouds (Burrows & Mendenhall, 1991; Snowden et al., 1991).

The LMC, with its low foreground absorption and small distance, offers an ideal laboratory for exploring the global structures of the ISM in a galaxy. In addition, it is known to host a large number of H II regions, bubbles, and superbubbles of various sizes (Henize, 1956; Davies et al., 1976). To study these objects, we use data from X-ray observations and compare these to observations in radio and optical. Owing to the high sensitivity and good spatial and spectral resolution, *XMM-Newton* is the ideal telescope for studying extended, soft X-ray sources. We analyse observational data of selected superbubbles and SNRs in the LMC (see also Sect. 5.3) to study their emission and the underlying physics and to confirm their nature.

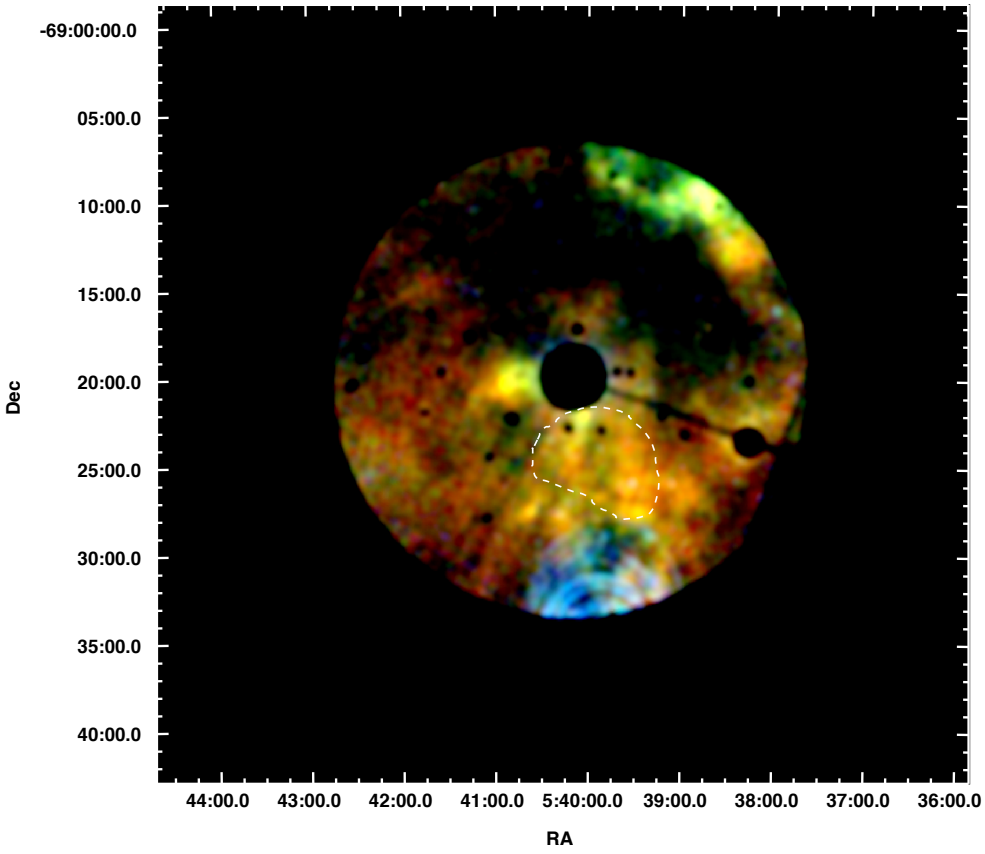

Figure 19: *XMM-Newton* EPIC mosaic image of the pulsar B 0540−69 and its surroundings in three-colour presentation (red: 0.3 – 0.8 keV, green: 0.8 – 1.5 keV, blue: 1.5 – 2.3 keV). The bright X-ray emission from B 0540−69 at ∼RA = 05^h 40^m, Dec = –69° 20′, other point sources, and the out-of-time events have been removed from the data. The arc-shaped features in the south are caused by stray light from the nearby bright X-ray source LMC X-1. The position of the superbubble in the H II region N 158 is shown with a dashed line. Taken from Sasaki et al. (2011).

6.1 LMC Superbubble N 158

SASAKI ET AL., 2011, A&A, 528, 136

The LMC harbours the Tarantula Nebula, also called the 30 Doradus, which is the closest giant H II region. The 30 Doradus region is the most active star forming site in the LMC and is host to many star forming regions, young star clusters, superbubbles, and SNRs.

The H II region N 158 (Henize, 1956) is located south of 30 Doradus. It is elongated in the north-south direction and consists of a superbubble in the north and a more compact bright region in the south. Two OB associations LH 101 and LH 104 (Lucke & Hodge, 1970) were found in N 158. LH 101 in the south is believed to power the very bright region in Hα in N 158, whereas LH 104 is located inside the superbubble in the northern part of N 158. The latter has a young stellar population with an age of 2 – 6 Myr (Testor & Niemela, 1998) and a large number

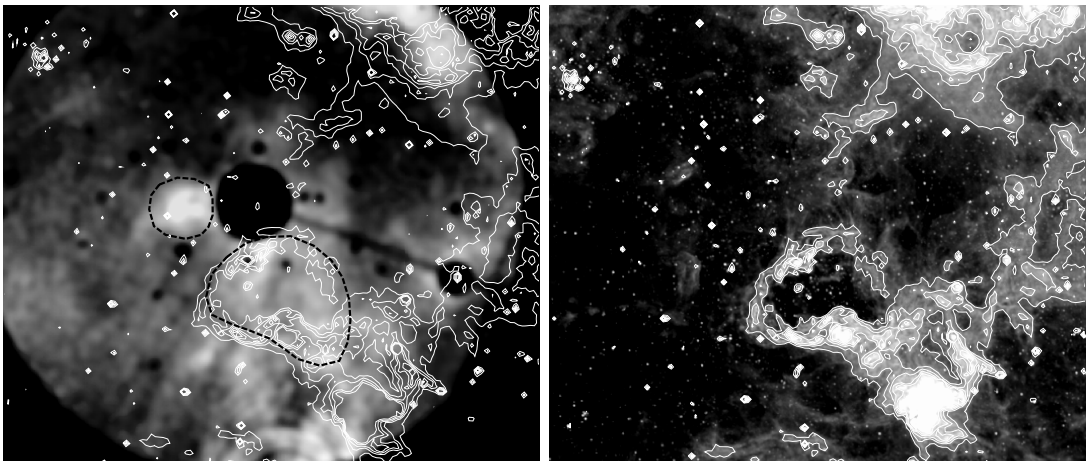

Figure 20: A zoom-in on the *XMM-Newton* EPIC mosaic image (left) with regions used for the spectral analysis (black dashed line) and Hα contours (MCELS) and the Hα image with the same contours (right). Taken from Sasaki et al. (2011).

of B stars (Schild & Testor, 1992). As N 158 is located near the X-ray bright pulsar B 0540−69 in the LMC, which is a calibration target of *XMM-Newton*, the northern part of N 158 was observed by the EPICs. This has allowed us to study the X-ray emission of the superbubble.

The mosaic image shown in Figure 19 is a three-colour image using red colour for the 0.3 – 0.8 keV band, green for 0.8 – 1.5 keV, and blue for 1.5 – 2.3 keV. As this three-colour image shows, there is soft extended emission below 1.5 keV coinciding with the superbubble in N 158, visible as a somewhat triangular shaped shell in Hα (Figs. 19, 20). For further analysis of the X-ray emission, we extracted spectra from the following two regions: region 1 that covers the brighter spot east of B 0540−69 and another region for the superbubble in N 158 (see left panel in Fig. 20).

The initial fits of the spectra of the diffuse emission indicated that the gas in the superbubble in N 158 is not in CIE. Therefore, we used a model for a plasma in NEI and for an NEI plasma shocked by a plane-parallel shock. We obtained a temperature of $\sim$1 keV for the plasma inside the superbubble. The estimated unabsorbed X-ray luminosity of the superbubble is $L_{\rm X}$(0.2 – 10.0 keV) = 1.5 $\times 10^{36}$ erg s^{-1}. From the X-ray temperature, we derived a pressure of

$$\begin{aligned} P/k &= (n_{\rm e} + 1.1n) f^{-1/2} T_a = 2.31 n f^{-1/2} T_a \\ &= (1.1 \pm 0.3) \times f^{-1/2} \times 10^6 \text{ cm}^{-3} \text{ K} \end{aligned} \quad (10)$$

for the hot gas inside the superbubble. Since the ISM in the LMC is believed to have a pressure of $P/k \approx 10^5$ cm^{-3} K (Oey & García-Segura, 2004) the superbubble in N 158 is over-pressured by about one order of magnitude with respect to the surrounding ISM. The ambient ISM of N 158 shows Hα emission, indicating that the temperature is $\sim$8000 K, as it is typical of the warm ionised medium (McKee & Ostriker, 1977). Using the calculated pressure inside the superbubble, we obtained an ambient density of $\sim$13 cm^{-3} and a compression factor of the

shock of $\sim$6 for the expansion of the shell around the superbubble. This allowed us to estimate the age of the superbubble of $t \simeq 1.1$ Myr and an energy input rate over this time interval of $L_{\rm superbubble} = 2.3 \times 10^{38}$ erg s^{-1} using the solution for a wind-blown bubble by Weaver et al. (1977). Taking the known stars inside the superbubble and the initial mass function of the OB association into account, we estimated the mass and energy inputs from the stars. The calculations have shown that 2 – 3 SNe must have occurred inside the superbubble around 1 Myr ago.

7 Summary and Outlook

Astronomy and Astrophysics are one of the few fields in science, in which the study of basic science questions, here mainly those of Physics, is combined with that of phenomena in nature on the largest possible range of scales, i.e., from particles to the entire Universe. Moreover, Astronomy and Astrophysics are tightly related to the fundamental questions of the evolution of the Universe and thus of our being. Physical phenomena that are important in this context are, e.g., gravitation, nuclear fusion, radiation, and shock waves. From the cosmological perspective, these already played a major role in the formation of the first structures.

The presented work consists of three major topics: 1) the population of X-ray sources and their X-ray luminosity functions to understand the underlying stellar populations in galaxies, 2) physics of SNRs as sources of matter and energy for the ISM, and 3) the heating and evolution of the ISM, best observed in its hot phase. Observational studies of the X-ray binary population give us insight into the stellar content and the star-formation history of galaxies. Supernova remnants are responsible for the chemical abundances, the energy budget, and the dynamics in the interstellar medium and provide us with information on the chemical and dynamical evolution of galaxies. The study of diffuse X-ray emission in galaxies reveals the global structure and the evolution, and hence the origin, of the hot ISM in a galaxy.

I analyse archival and new X-ray data and perform multi-wavelength studies using radio, infrared, optical, and ultraviolet data. I believe that the best way to understand the latest stages of cosmic evolution is to study the present Universe, i.e., the components in galaxies, their synthesis, and the evolution of galaxies, by putting these objects in context to each other and, at the same time, improving our knowledge of the underlying physics in these sources. In the coming years, the German-Russian *extended Roentgen Survey with an Imaging Telescope Array* (*eROSITA*) will perform an all-sky survey in the X-ray band of 0.3 – 10 keV and will provide us with new data of the X-ray emission of the entire sky with an unprecedented sensitivity and resolution. Observations of individual sources and the X-ray population of our Galaxy as well as sources in a large sample of nearby galaxies will enable us to study the evolution of galaxies by detailed modelling of the production of X-ray sources and the evolution of the ISM with reliable star-formation history constraints. In the more distant future, we will make a significant step forward in our efforts to grasp the physics of Galactic and extragalactic objects in the Universe using, among other next-generation telescopes, the *Athena X-ray Observatory*, which has been selected by the European Space Agency for the next large satellite mission to be launched in 2028.

References

Anders, E. & Grevesse, N. 1989, Geochimica et Cosmochimica Acta, 53, 197

Arcavi, I., Gal-Yam, A., Polishook, D., Yaron, O., Xu, D., et al. 2011a, The Astronomer's Telegram, 3413, 1

Arcavi, I., Gal-Yam, A., Yaron, O., Sternberg, A., Rabinak, I., et al. 2011b, ApJ, 742, L18

Ardavan, H. 1973, ApJ, 184, 435

Aschenbach, B., Briel, U. G., Haberl, F., Bräuninger, H., Burkert, W., Oppitz, A., Gondoin, P., & Lumb, D. 2000, Proc. SPIE, 4012, 731

Bell, A. R. 1978a, MNRAS, 182, 147

—. 1978b, MNRAS, 182, 443

Bildsten, L., Chakrabarty, D., Chiu, J., Finger, M. H., Koh, D. T., et al. 1997, ApJS, 113, 367

Blair, W. P., Kirshner, R. P., & Chevalier, R. A. 1981, ApJ, 247, 879

Blandford, R. D. & Ostriker, J. P. 1978, ApJ, 221, L29

Borkowski, K. J., Lyerly, W. J., & Reynolds, S. P. 2001, ApJ, 548, 820

Borkowski, K. J., Sarazin, C. L., & Blondin, J. M. 1994, ApJ, 429, 710

Bozzetto, L. M., Filipović, M. D., Crawford, E. J., Haberl, F., Sasaki, M., et al. 2012, MNRAS, 420, 2588

Bozzetto, L. M., Filipović, M. D., Crawford, E. J., Sasaki, M., Maggi, P., et al. 2013, MNRAS, 432, 2177

Bozzetto, L. M., Kavanagh, P. J., Maggi, P., Filipović, M. D., Stupar, M., et al. 2014, MNRAS, 439, 1110

Braun, R. & Walterbos, R. A. M. 1993, A&AS, 98, 327

Bulik, T., Riffert, H., Meszaros, P., Makishima, K., Mihara, T., & Thomas, B. 1995, ApJ, 444, 405

Burrows, D. N. & Mendenhall, J. A. 1991, Nature, 351, 629

Caballero, I., Kraus, U., Santangelo, A., Sasaki, M., & Kretschmar, P. 2011, A&A, 526, A131

Clementini, G., Contreras Ramos, R., Federici, L., Macario, G., Beccari, G., et al. 2011, ApJ, 743, 19

Colbert, E. J. M., Heckman, T. M., Ptak, A. F., Strickland, D. K., & Weaver, K. A. 2004, ApJ, 602, 231

Cominsky, L., Clark, G. W., Li, F., Mayer, W., & Rappaport, S. 1978, Nature, 273, 367

Condon, J. J., Cotton, W. D., Greisen, E. W., Yin, Q. F., Perley, R. A., Taylor, G. B., & Broderick, J. J. 1998, AJ, 115, 1693

Copetti, M. V. F. & Schmidt, A. A. 1991, MNRAS, 250, 127

Corbet, R. H. D. & Levine, A. M. 2006, The Astronomer's Telegram, 843, 1

Cox, D. P. 2005, ARA&A, 43, 337

Cox, D. P. & Anderson, P. R. 1982, ApJ, 253, 268

Cox, D. P. & Smith, B. W. 1974, ApJ, 189, L105

Davies, R. D., Elliot, K. H., & Meaburn, J. 1976, MmRAS, 81, 89

de Horta, A. Y., Filipović, M. D., Bozzetto, L. M., Maggi, P., Haberl, F., et al. 2012, A&A, 540, A25

Dennefeld, M. & Kunth, D. 1981, AJ, 86, 989

D'Odorico, S., Dopita, M. A., & Benvenuti, P. 1980, A&AS, 40, 67

Ducci, L., Sasaki, M., Haberl, F., & Pietsch, W. 2013, A&A, 553, A7

Egan, M. P., Price, S. D., Kraemer, K. E., Mizuno, D. R., Carey, S. J., et al. 2003, Air Force Research Laboratory Technical Report AFRL-VS-TR-2003-1589

Fabbiano, G. 2006, ARA&A, 44, 323

Fesen, R. A. & Hurford, A. P. 1995, AJ, 110, 747

Forman, W., Tananbaum, H., & Jones, C. 1976, ApJ, 206, L29

Garmire, G. P., Bautz, M. W., Ford, P. G., Nousek, J. A., & Ricker, Jr., G. R. 2003, in X-Ray and Gamma-Ray Telescopes and Instruments for Astronomy. Proceedings of the SPIE, Volume 4851, pp. 28-44 (2003)., ed. J. E. Truemper & H. D. Tananbaum, 28–44

Gehrels, N., Chincarini, G., Giommi, P., Mason, K. O., Nousek, J. A., et al. 2004, ApJ, 611, 1005

Gilfanov, M., Grimm, H.-J., & Sunyaev, R. 2004, MNRAS, 347, L57

Green, A. J., Frail, D. A., Goss, W. M., & Otrupcek, R. 1997, AJ, 114, 2058

Gregory, P. C. & Fahlman, G. G. 1980, Nature, 287, 805

Gregory, P. C. & Fahlman, G. G. 1983, in IAU Symp. 101: Supernova Remnants and their X-ray Emission, 429–436

Grimm, H.-J., Gilfanov, M., & Sunyaev, R. 2003, MNRAS, 339, 793

Grondin, M.-H., Sasaki, M., Haberl, F., Pietsch, W., Crawford, E. J., et al. 2012, A&A, 539, 15

Haberl, F., Filipović, M. D., Bozzetto, L. M., Crawford, E. J., Points, S. D., et al. 2012, A&A, 543, A154

Haberl, F. & Pietsch, W. 1999, A&AS, 139, 277

Hamilton, A. J. S., Chevalier, R. A., & Sarazin, C. L. 1983, ApJS, 51, 115

Heiles, C. 1964, ApJ, 140, 470

Henize, K. G. 1956, ApJS, 2, 315

Heydari-Malayeri, M., Kahane, C., & Lucas, R. 1981, Nature, 293, 549

Hilditch, R. W., Howarth, I. D., & Harries, T. J. 2005, MNRAS, 357, 304

Hillas, A. M. 2005, Journal of Physics G Nuclear Physics, 31, 95

Hughes, J. P., Rafelski, M., Warren, J. S., Rakowski, C., Slane, P., Burrows, D., & Nousek, J. 2006, ApJ, 645, L117

Hughes, V. A., Harten, R. H., Costain, C. H., Nelson, L. A., & Viner, M. R. 1984, ApJ, 283, 147

Hughes, V. A., Harten, R. H., & van den Bergh, S. 1981, ApJ, 246, L127

Immler, S. 2003, in IAU Symposium, Vol. 214, High Energy Processes and Phenomena in Astrophysics, ed. X. D. Li, V. Trimble, & Z. R. Wang, 113

Immler, S. & Kuntz, K. D. 2005, ApJ, 632, L99

Inoue, H., Koyama, K., Matsuoka, M., Ohashi, T., Tanaka, Y., & Tsunemi, H. 1979, ApJ, 227, L85

Israel, F. P. 1980, AJ, 85, 1612

Itoh, H. 1978, PASJ, 30, 489

Jansen, F., Lumb, D., Altieri, B., Clavel, J., Ehle, M., et al. 2001, A&A, 365, L1

Jenkins, E. B. & Meloy, D. A. 1974, ApJ, 193, L121

Johnston, M., Bradt, H., Doxsey, R., Gursky, H., Schwartz, D., & Schwarz, J. 1978, ApJ, 223, L71

Kavanagh, P. J., Sasaki, M., Bozzetto, L. M., Filipović, M. D., Points, S. D., Maggi, P., & Haberl, F. 2015, A&A, 573, A73

Kavanagh, P. J., Sasaki, M., Points, S. D., Filipović, M. D., Maggi, P., et al. 2013, A&A, 549, A99

Kilgard, R. E., Kaaret, P., Krauss, M. I., Prestwich, A. H., Raley, M. T., & Zezas, A. 2002, ApJ, 573, 138

Klimek, M. D., Points, S. D., Smith, R. C., Shelton, R. L., & Williams, R. 2010, ApJ, 725, 2281

Klochkov, D., Santangelo, A., Staubert, R., & Ferrigno, C. 2008, A&A, 491, 833

Kong, A. K. H., Garcia, M. R., Primini, F. A., & Murray, S. S. 2002, ApJ, 580, L125

Kong, A. K. H., Sjouwerman, L. O., Williams, B. F., Garcia, M. R., & Dickel, J. R. 2003, ApJ, 590, L21

Koo, B.-C., Kim, K.-T., & Seward, F. D. 1995, ApJ, 447, 211

Koo, B.-C., Lee, J.-J., & Seward, F. D. 2002, AJ, 123, 1629

Koo, B.-C., Lee, J.-J., Seward, F. D., & Moon, D.-S. 2005, ApJ, 633, 946

Koralesky, B., Frail, D. A., Goss, W. M., Claussen, M. J., & Green, A. J. 1998, AJ, 116, 1323

Kothes, R., Uyaniker, B., & Yar, A. 2002, ApJ, 576, 169

Kraus, U., Nollert, H.-P., Ruder, H., & Riffert, H. 1995, ApJ, 450, 763

Kraus, U., Zahn, C., Weth, C., & Ruder, H. 2003, ApJ, 590, 424

Krimm, H., Barthelmy, S., Gehrels, N., Markwardt, C., Palmer, D., Sanwal, D., & Tueller, J. 2006, The Astronomer's Telegram, 861, 1

Leahy, D. A. 1991, MNRAS, 251, 203

Liedahl, D. A., Osterheld, A. L., & Goldstein, W. H. 1995, ApJ, 438, L115

Lucke, P. B. & Hodge, P. W. 1970, AJ, 75, 171

Macri, L. M., Stanek, K. Z., Bersier, D., Greenhill, L. J., & Reid, M. J. 2006, ApJ, 652, 1133

Maggi, P., Haberl, F., Bozzetto, L. M., Filipović, M. D., Points, S. D., et al. 2012, A&A, 546, A109

Maggi, P., Haberl, F., Kavanagh, P. J., Points, S. D., Dickel, J., et al., & Pietsch, W. 2014, A&A, 561, A76

Mansfield, V. N. & Salpeter, E. E. 1974, ApJ, 190, 305

Massey, P., Olsen, K. A. G., Hodge, P. W., Strong, S. B., Jacoby, G. H., Schlingman, W., & Smith, R. C. 2006, AJ, 131, 2478

McCollough, M. L., Turler, M., Willis, D., & Shaw, S. E. 2006, The Astronomer's Telegram, 868, 1

McKee, C. F. 1974, ApJ, 188, 335

McKee, C. F. & Ostriker, J. P. 1977, ApJ, 218, 148

Mineo, S., Gilfanov, M., & Sunyaev, R. 2012, MNRAS, 419, 2095

Mufson, S. L. & Liszt, H. S. 1979, ApJ, 232, 451

Oey, M. S. & García-Segura, G. 2004, ApJ, 613, 302

Parmar, A. N., White, N. E., & Stella, L. 1989a, ApJ, 338, 373

Parmar, A. N., White, N. E., Stella, L., Izzo, C., & Ferri, P. 1989b, ApJ, 338, 359

Payne, J. L., White, G. L., & Filipović, M. D. 2008, MNRAS, 383, 1175

Pietsch, W., Freyberg, M., & Haberl, F. 2005, A&A, 434, 483

Rho, J. & Petre, R. 1997, ApJ, 484, 828

Rho, J.-H. & Petre, R. 1993, Bulletin of the American Astronomical Society, 25, 1442

Riffert, H., Nollert, H.-P., Kraus, U., & Ruder, H. 1993, ApJ, 406, 185

Rogerson, J. B., York, D. G., Drake, J. F., Jenkins, E. B., Morton, D. C., & Spitzer, L. 1973, ApJ, 181, L110

Sarajedini, A., Barker, M. K., Geisler, D., Harding, P., & Schommer, R. 2006, AJ, 132, 1361

Sasaki, M., Breitschwerdt, D., Baumgartner, V., & Haberl, F. 2011, A&A, 528, 136

Sasaki, M. & Ducci, L. 2012, A&A, 546, A80

Sasaki, M., Haberl, F., & Pietsch, W. 2000, A&AS, 143, 391

Sasaki, M., Heinitz, C., Warth, G., & Pühlhofer, G. 2014, A&A, 563, A9

Sasaki, M., Klochkov, D., Kraus, U., Caballero, I., & Santangelo, A. 2010, A&A, 517, A8

Sasaki, M., Kothes, R., Plucinsky, P. P., Gaetz, T. J., & Brunt, C. M. 2006, ApJ, 642, L149

Sasaki, M., Müller, D., Kraus, U., Ferrigno, C., & Santangelo, A. 2012a, A&A, 540, A35

Sasaki, M., Pietsch, W., Haberl, F., Hatzidimitriou, D., Stiele, H., Williams, B., Kong, A., & Kolb, U. 2012b, A&A, 544, 144

Sasaki, M., Plucinsky, P. P., Gaetz, T. J., & Bocchino, F. 2013, A&A, 552, A45

Sasaki, M., Plucinsky, P. P., Gaetz, T. J., Smith, R. K., Edgar, R. J., & Slane, P. O. 2004, ApJ, 617, 322

Schild, H. & Testor, G. 1992, A&AS, 92, 729

Sedov, L. I. 1946a, Dokl. Akad. Nauk SSSR, 42, 17

—. 1946b, Prikl. Mat. Mekh., 10, 241, No. 2

—. 1959, Similarity and Dimensional Methods in Mechanics, Academic Press, New York

Silverman, J. M., Filippenko, A. V., & Cenko, S. B. 2011, The Astronomer's Telegram, 3398, 1

Snowden, S. L., Mebold, U., Hirth, W., Herbstmeier, U., & Schmitt, J. H. M. 1991, Science, 252, 1529

Soderberg, A. M., Margutti, R., Zauderer, B. A., Krauss, M., Katz, B., et al. 2012, ApJ, 752, 78

Spitzer, Jr., L. 1990, ARA&A, 28, 71

Spitzer, L. J. 1956, ApJ, 124, 20

Stiele, H., Pietsch, W., Haberl, F., Hatzidimitriou, D., Barnard, R., Williams, B. F., Kong, A. K. H., & Kolb, U. 2011, A&A, 534, A55

Strüder, L., Briel, U., Dennerl, K., Hartmann, R., Kendziorra, E., et al. 2001, A&A, 365, L18

Subrahmanyan, R. & Goss, W. M. 1995, MNRAS, 275, 755

Supper, R., Hasinger, G., Lewin, W. H. G., Magnier, E. A., van Paradijs, J., Pietsch, W., Read, A. M., & Trümper, J. 2001, A&A, 373, 63

Tanaka, Y. & Bleeker, J. A. M. 1977, Space Science Reviews, 20, 815

Tatematsu, K., Fukui, Y., Nakano, M., Kogure, T., Ogawa, H., & Kawabata, K. 1987, A&A, 184, 279

Tatematsu, K., Nakano, M., Yoshida, S., Wiramihardja, S. D., & Kogure, T. 1985, PASJ, 37, 345

Taylor, G. I. 1950a, Proc. R. Soc. London A, 201, 159

—. 1950b, Proc. R. Soc. London A, 201, 175

Tenorio-Tagle, G., Bodenheimer, P., & Yorke, H. W. 1985, A&A, 145, 70

Testor, G. & Niemela, V. 1998, A&AS, 130, 527

Tully, R. B., Rizzi, L., Shaya, E. J., Courtois, H. M., Makarov, D. I., & Jacobs, B. A. 2009, AJ, 138, 323

Turner, M. J. L., Abbey, A., Arnaud, M., Balasini, M., Barbera, M., 2001, A&A, 365, L27

van der Klis, M. 2000, ARA&A, 38, 717

van Leeuwen, F., Feast, M. W., Whitelock, P. A., & Laney, C. D. 2007, MNRAS, 379, 723

Verbunt, F. 1993, ARA&A, 31, 93

Vinkó, J., Takáts, K., Szalai, T., Marion, G. H., Wheeler, J. C., . 2012, A&A, 540, A93

von Neumann, J. 1947, Los Alamos Sci. Lab. Tech. Series, Vol. 7

Wang, Z., Qu, Q., Luo, D., McCray, R., & Mac Low, M. 1992, ApJ, 388, 127

Warth, G., Sasaki, M., Kavanagh, P. J., Filipović, M. D., Points, S. D., & Bozzetto, L. M. 2014, A&A, 567, A136

Weaver, R., McCray, R., Castor, J., Shapiro, P., & Moore, R. 1977, ApJ, 218, 377

Weisskopf, M. C., Brinkman, B., Canizares, C., Garmire, G., Murray, S., & Van Speybroeck, L. P. 2002, PASP, 114, 1

Whitlock, L., Roussel-Dupre, D., & Priedhorsky, W. 1989, ApJ, 338, 381

Williams, B. F., Sjouwerman, L. O., Kong, A. K. H., Gelfand, J. D., Garcia, M. R., & Murray, S. S. 2004a, ApJ, 615, 720

Williams, R. M., Chu, Y.-H., Dickel, J. R., Gruendl, R. A., Shelton, R., Points, S. D., & Smith, R. C. 2004b, ApJ, 613, 948

Williams, R. M., Chu, Y.-H., Dickel, J. R., Petre, R., Smith, R. C., & Tavarez, M. 1999, ApJS, 123, 467

Williamson, F. O., Sanders, W. T., Kraushaar, W. L., McCammon, D., Borken, R., & Bunner, A. N. 1974, ApJ, 193, L133

Wilson, C. A., Fabregat, J., & Coburn, W. 2005, ApJ, 620, L99

Wilson, C. A., Finger, M. H., Coe, M. J., Laycock, S., & Fabregat, J. 2002, ApJ, 570, 287

York, D. G. 1974, ApJ, 193, L127

Zezas, A. & Fabbiano, G. 2002, ApJ, 577, 726

A&A 553, A7 (2013)
DOI: 10.1051/0004-6361/201321035

Astronomy & Astrophysics

X-ray source population study of the starburst galaxy M 83 with *XMM-Newton*⋆,⋆⋆,⋆⋆⋆

L. Ducci[1], M. Sasaki[1], F. Haberl[2], and W. Pietsch[2]

[1] Institut für Astronomie und Astrophysik, Eberhard Karls Universität, Sand 1, 72076 Tübingen, Germany
e-mail: ducci@astro.uni-tuebingen.de
[2] Max-Planck-Institut für Extraterrestrische Physik, Giessenbachstraße, 85741 Garching, Germany

Received 3 January 2013 / Accepted 5 March 2013

ABSTRACT

Aims. We present the results obtained from the analysis of three *XMM-Newton* observations of M 83. The aims of the paper are studying the X-ray source populations in M 83 and calculating the X-ray luminosity functions of X-ray binaries for different regions of the galaxy.
Methods. We detected 189 sources in the *XMM-Newton* field of view in the energy range of 0.2–12 keV. We constrained their nature by means of spectral analysis, hardness ratios, studies of the X-ray variability, and cross-correlations with catalogues in X-ray, optical, infrared, and radio wavelengths.
Results. We identified and classified 12 background objects, five foreground stars, two X-ray binaries, one supernova remnant candidate, one super-soft source candidate and one ultra-luminous X-ray source. Among these sources, we classified for the first time three active galactic nuclei (AGN) candidates. We derived X-ray luminosity functions of the X-ray sources in M 83 in the 2–10 keV energy range, within and outside the D_{25} ellipse, correcting the total X-ray luminosity function for incompleteness and subtracting the AGN contribution. The X-ray luminosity function inside the D_{25} ellipse is consistent with that previously observed by *Chandra*. The Kolmogorov-Smirnov test shows that the X-ray luminosity function of the outer disc and the AGN luminosity distribution are uncorrelated with a probability of ∼99.3%. We also found that the X-ray sources detected outside the D_{25} ellipse and the uniform spatial distribution of AGNs are spatially uncorrelated with a significance of 99.5%. We interpret these results as an indication that part of the observed X-ray sources are X-ray binaries in the outer disc of M 83.

Key words. galaxies: individual: M 33 – X-rays: galaxies

1. Introduction

M 83 (NGC 5236) is a grand-design barred spiral galaxy (SAB(s)c; de Vaucouleurs et al. 1992) located at 4.5 ± 0.3 Mpc from the Milky Way (Thim et al. 2003). M 83 is oriented nearly face-on ($i = 24°$; Rogstad et al. 1974) and shows a galactic disc spanning 12.9′ × 11.5′ (17 kpc × 15.2 kpc; Wofford et al. 2011).

M 83 is experiencing a starburst activity with a present-day star formation rate (SFR) of 3–4 $M_\odot\,\mathrm{yr}^{-1}$ (Boissier et al. 2005) in three regions: the nuclear region (galactocentric distance $d \lesssim 300$ pc; Harris et al. 2001), the inner disc (300 pc $\lesssim d \lesssim$ 7.5 kpc), and the outer disc (7.5 kpc $\lesssim d \lesssim$ 20 kpc; Dong et al. 2008). Ultraviolet (UV) images of M 83 obtained with the Galaxy Evolution Explorer (GALEX) satellite revealed a population of young stars (≲400 Myr) in the outer disc of M 83 (Thilker et al. 2005). Although this would indicate recent star-forming activity, using *Spitzer* and GALEX data, Dong et al. (2008) discovered that the star formation in the outer disc started at least 1 Gyr ago. These results are confirmed by the study of AGB stars of Davidge (2010). Bigiel et al. (2010) compared the HI data from the National Radio Astronomy Observatory (NRAO) Very Large Array (VLA) and far-ultraviolet (FUV) data from GALEX in the outer disc of M 83, and discovered that the star formation traced by the FUV emission and HI are spatially correlated out to almost four optical radii. Bigiel et al. (2010) also found that the star formation rate in the outer disc (∼0.01 $M_\odot\,\mathrm{yr}^{-1}$; Bresolin et al. 2009) implies that the star formation activity is not completely consuming the HI reservoir, which will be available as fuel for star formation in the inner disc.

M 83 was observed in the X-ray bands by *Einstein* in 1979–1981 (Trinchieri et al. 1985), Ginga in 1987 (Ohashi et al. 1990), ROSAT in 1992–1994 (Ehle et al. 1998; Immler et al. 1999), ASCA in 1994 (Okada et al. 1997), and *Chandra* in 2000 (Soria & Wu 2002; Soria & Wu 2003, SW03 hereafter). SW03 identified 127 discrete sources near the centre of M 83 (8.3′ × 8.3′) and resolved for the first time the nuclear region in X-rays. The diffuse X-ray emission of M 83 has been studied by Owen & Warwick (2009) with an *XMM-Newton* observation performed in January 27, 2003 (obsid 0110910201). They obtained a good fit to the spectrum assuming a two-temperature thermal model, which is typical of the diffuse emission in normal and starburst galaxies. They also found that the soft X-ray emission mainly overlaps with the inner spiral arm, and shows a strong correlation with the distribution of UV emission, indicative of a correlation between X-ray emission and recent star formation.

The recent high star formation activity experienced by the nucleus and the spiral arms of M 83 provided an unusually large number of supernova remnants (SNRs). In

⋆ Based on observations obtained with *XMM-Newton*, an ESA science mission with instruments and contributions directly funded by ESA Member States and NASA.
⋆⋆ Appendix A is available in electronic form at http://www.aanda.org
⋆⋆⋆ Appendix B is only available at the CDS via anonymous ftp to cdsarc.u-strasbg.fr (130.79.128.5) or via http://cdsarc.u-strasbg.fr/viz-bin/qcat?J/A+A/553/A7

Table 1. *XMM-Newton* observations of M 83.

	Obs. ID.	Date	Pointing direction		EPIC PN		EPIC MOS1		EPIC MOS2		Mode	
			RA	Dec	filter	T_{exp}	filter	T_{exp}	filter	T_{exp}	PN	MOS
1	0110910201	2003-01-27	13:37:05.16	–29:51:46.1	thin	21.2	medium	24.6	medium	24.6	EFF	FF
2	0503230101	2008-01-16	13:37:01.09	–30:03:49.9	medium	15.4	medium	19.0	medium	19.0	EFF	FF
3	0552080101	2008-08-16	13:36:50.87	–30:03:55.2	medium	25.0	medium	28.8	medium	28.8	EFF	FF

Notes. The exposure times after the screening for high background are given in units of ks. Mode: EFF = extended full frame imaging mode; FF = full frame imaging mode.

fact, the optical survey performed at the Cerro Tololo Inter-American Observatory in Chile by Blair & Long (2004) identified 71 sources as SNR candidates, the *Hubble* Space Telescope (HST) observations of the nuclear region of M 83 (Dopita et al. 2010) provided the identification of 60 SNR candidates, and the Magellan I survey 271 SNR candidates (Blair et al. 2012).

In a normal galaxy such as M 83, X-ray binaries (XRBs) are the most prominent class of X-ray sources. XRBs show X-ray luminosities ranging from $\sim 10^{32}$ erg s^{-1} to the Eddington luminosity, and sometimes they can exceed this limit (see e.g. White & Carpenter 1978). They are composed of a compact object (a neutron star or a black hole) and a companion star, which can be a main-sequence, giant, or supergiant star, and in some cases a white dwarf (e.g. van Paradijs 1998). The strong X-ray emission is produced by the accretion of matter from the companion star onto the compact object. XRBs are usually divided into two classes: low mass X-ray binaries (LMXBs), and high mass X-ray binaries (HMXBs). The companion stars of LMXBs have masses lower than $\sim 1\ M_{\odot}$. The lifetime of an LMXB is determined by the nuclear evolution time-scale of the companion star to 10^8–10^9 yr (e.g. Tauris & van den Heuvel 2006), and their number is correlated to the total stellar mass of a galaxy (Gilfanov 2004). The companion star of LMXBs usually tranfers mass by Roche-lobe overflow, and the compact object accretes from an accretion disc (e.g. van Paradijs 1998). The donors in HMXBs have masses $\gtrsim 8\ M_{\odot}$, and their typical lifetime does not exceed 10^6–10^7 yr. Therefore, the presence of HMXBs in a particular region of a galaxy is associated with a relatively recent star formation event (e.g. Fabbiano 2006). The X-ray emission from HMXBs is usually explained with the accretion of a fraction of the stellar wind ejected by the donor star onto the compact object, or through mass transfer via Roche-lobe overflow (see e.g. Treves et al. 1988 and references therein). As a first approximation, two standard models are commonly used to describe the X-ray spectra of XRBs in nearby galaxies: an absorbed disc-blackbody model, with temperatures ranging from ∼0.5 to ∼1 keV (e.g. Makishima et al. 1986), or an absorbed powerlaw model. X-ray spectra of LMXBs below 10 keV are described by absorbed powerlaw with photon indices 1–3. HMXBs usually show harder X-ray spectra in the energy range 1–10 keV, with photon indices 1–2 and a high intrinsic absorption (White et al. 1995). Within each of these classes, the properties of the X-ray spectra can also depend on the type of the accreting compact object. Accreting black holes can show states of high luminosity (e.g. Jones 1977), with very soft spectra, with slopes steeper than those shown by accreting neutron stars (see e.g. White & Marshall 1984). Given the wide variety of spectral shapes shown by XRBs, they can be confused with background AGNs, whose X-ray spectra have roughly a powerlaw shape, with indices ranging from 1.6 to 2.5 (see e.g. Walter & Fink 1993; Vignali et al. 1999; Turner et al. 1991).

In this paper we report the results obtained from a study of the X-ray source populations of M 83, using three *XMM-Newton* observations covering both the inner and outer disc regions. The higher spatial resolution and sensitivity of *XMM-Newton* compared to the previous observations of ROSAT and *Einstein* allowed an increase of the number of detected sources in M 83. While the spatial coverage of the *Chandra* observation was limited to a region located at the centre of M 83 with a size of $8.3' \times 8.3'$ (the ACIS S3 field of view), the *XMM-Newton* observations allowed us to obtain a complete coverage of M 83, and to study also the outer parts of the galaxy, which in total provided us with a more representative sample of X-ray sources in M 83.

The paper is organised as follows: in Sect. 2 we describe the data reduction and analysis of *XMM-Newton* observations. In Sect. 3 we show the astrometrical corrections that have been applied. In Sect. 4 we present the techniques adopted to classify the X-ray sources (X-ray variability, spectral analysis, and hardness ratios). In Sect. 5 we describe the properties and classification of the detected sources. In Sect. 6 we derive the X-ray luminosity functions (XLFs) of X-ray binaries within and outside the D_{25} ellipse, after correcting them for incompleteness and subtracting the AGN contribution, and we discuss our results. We examine in detail the properties of the sources that have been identified and classified in this work in Appendix A.

2. Reduction and data analysis

We analysed the public archival *XMM-Newton* data of M 83 (PIs: Watson, Kuntz). Table 1 lists the three observations that we analysed, one pointing at the centre of the galaxy (obs. 1) and two in the south, which covered the outer arms with a young population of stars discovered with GALEX. The data analysis was performed using the *XMM-Newton* Science Analysis System (SAS) 12.0. For each pointing we produced PN, MOS1, and MOS2 event files. We excluded times of high background due to soft proton flares as follows. For each observation and instrument, we created background lightcurves (with sources removed) in the 7−15 keV energy band. Good time intervals (GTIs) were determined by selecting count rates lower than 8 cts ks^{-1} arcmin^{-2} and 2.5 cts ks^{-1} arcmin^{-2} for PN and MOS, respectively.

For each observation, data were divided into five energy bands:

- *R1*: 0.2–0.5 keV;
- *R2*: 0.5–1 keV;
- *R3*: 1–2 keV;
- *R4*: 2–4.5 keV;
- *R5*: 4.5–12 keV.

For the PN data we used single-pixel events (PATTERN = 0) in the first energy band and for the other energy bands single- and double-pixel events (PATTERN ≤ 4) were selected. For the MOS data, single-pixel to quadruple-pixel events (PATTERN ≤ 12) were used for all five bands.

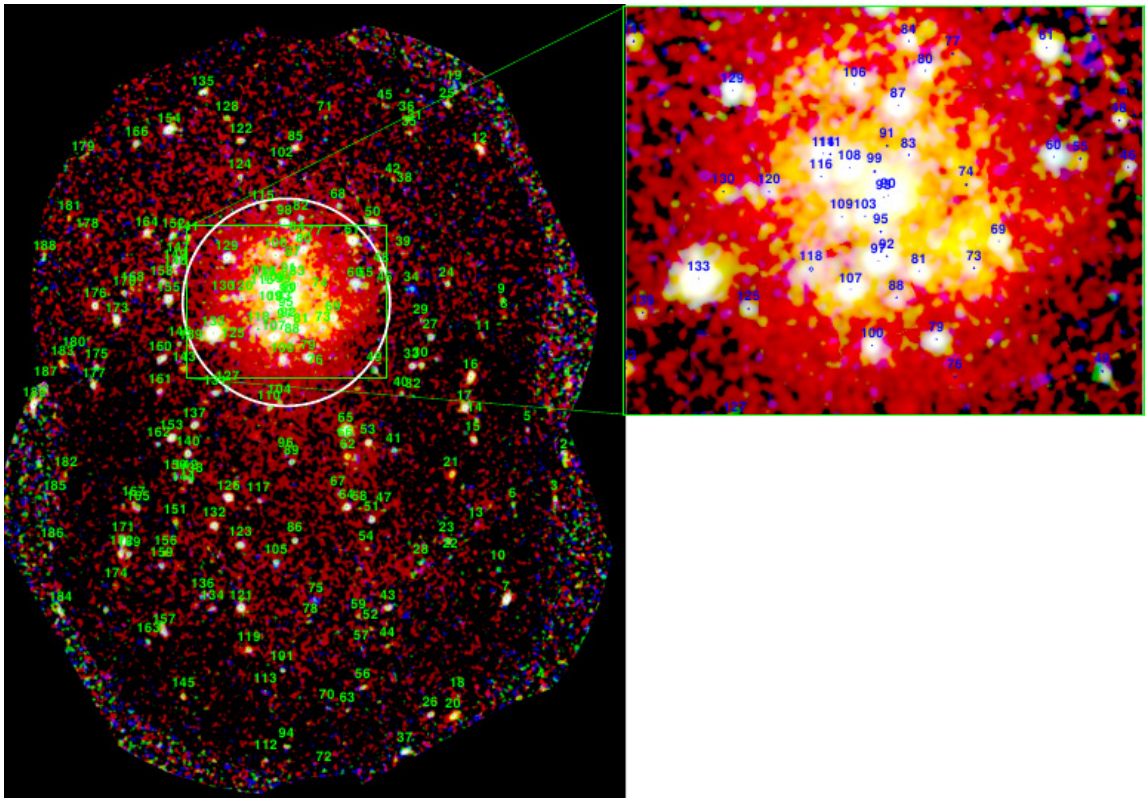

Fig. 1. Combined PN, MOS1, and MOS2 three-colour mosaic image of M 83. The crowded central region is shown in higher resolution. The white circle is the D_{25} ellipse (diameter = 11.5′; Tully 1988).

We ran the source detection procedure separately for images of each observation, and simultaneously for five energy bands and three instruments with the SAS task `edetect_chain`. The source detection consists of three steps. The first step provides a list of source positions used to create the background maps. We adopted a minimum-detection likelihood[1] of 7 to obtain this list of sources. After removing the sources, a two-dimensional spline with 20 nodes was fitted to the exposure-corrected image. In the second step the background maps are used to improve the detection sensitivity and hence to create a new source list, assuming a minimum-detection likelihood of 4. In the last step, a maximum-likelihood point-spread function (PSF) fit to the source count distribution is performed simultaneously in all energy bands and each EPIC instrument, from the input list of source positions obtained in the previous step (a description of this algorithm is given by Cruddace et al. 1988). For each observation we generated the final source list adopting a lower threshold for the maximum-detection likelihood of 6, which corresponds to a detection probability of ~99.75%. The source detection gives several parameters for each source, such as the coordinates, count rates, and likelihood of detection (see Table B.1). As mentioned above, 20 nodes (more than the default 16) for the background spline map were used to better follow the central diffuse emission and to minimise false detections. We removed the remaining false detections due to diffuse emission structures by visual inspection.

Figure 1 shows the combined PN, MOS1, and MOS2 three-colour mosaic image obtained from the three observations. The numbers of the detected sources are overplotted on the image. The red, green, and blue colours represent the 0.2–1 keV, 1–2 keV, and 2–4.5 keV energy bands.

[1] The detection likelihood L is defined by the relationship $L = -\ln(p)$, where p is the probability that a Poissonian fluctuation in the background is detected as a spurious source.

3. Astrometrical corrections

3.1. Corrections between XMM-Newton observations

We calculated the RA and Dec offsets of the three *XMM-Newton* observations using position of the sources detected in at least two observations. Sources were considered as detections in at least two different observations if their position was closer than 3× the combined statistical positional errors. We calculated the offsets of observations 2 and 3 with respect to the reference observation 1 as the weighted mean of RA and Dec of all sources, then recalculated all X-ray positions correcting for the shifts relative to the observation 1.

3.2. Correcting the position of the detected sources using X-ray and optical observations

We also applied the cross-correlation procedure described above to determine the systematic errors in the X-ray positions of the *XMM-Newton* observations by calculating the offsets in the X-ray positions of the *XMM-Newton* sources with respect to the X-ray sources observed by SW03 with *Chandra*. The offset between the *XMM-Newton* and *Chandra* positions (given as the weighted mean of RA and Dec in arcsec) is $\Delta\mathrm{RA} = -1.22 \pm 0.16$, $\Delta\mathrm{Dec} = -0.72 \pm 0.16$. We point out that SW03 corrected the *Chandra* positions using only the position of the infrared nucleus of M 83 deduced from HST/WFPC2 observations. Therefore, to

Table 2. Count rate to energy conversion factors for thin and medium filters of the EPIC instruments in the energy ranges *R*1–*R*5.

Detector EPIC	Filter	*R*1	*R*2	*R*3	*R*4	*R*5
			(10^{-12}) erg cm^{-2} ct^{-1}			
PN	Thin	0.8850	1.091	1.731	5.020	17.97
	Medium	1.055	1.110	1.730	4.977	17.47
MOS	Medium	6.796	5.582	5.189	13.71	69.63

Notes. We assumed an absorbed powerlaw with a photon index of 1.7 and the Galactic foreground absorption 3.69×10^{20} cm^{-2} in the direction of M 83.

obtain more accurate positions from possible optical counterparts, we cross-correlated the *XMM-Newton* list of sources with the optical catalogue of the United States Naval Observatory USNO-B1 (Monet et al. 2003). For this calculation we were interested in associations between X-ray sources and foreground stars. As discussed in Sect. 5.1, we classified five sources as foreground star candidates. The offset between the X-ray positions and optical positions corrected for proper motion (given as the weighted mean of RA and Dec in arcsec) is $\Delta\mathrm{RA} = -2.02 \pm 0.43$, $\Delta\mathrm{Dec} = -0.44 \pm 0.43$. The measured offset in RA agrees with the expected precision of the *XMM-Newton* Attitude Measurement System (Guainazzi 2012). We used these systematic offsets to correct the position of all detected sources.

4. Analysis

4.1. Variability of the sources

4.1.1. Short-term variability

For each *XMM-Newton* observation, we searched for pulsations of the brightest sources (counts $\gtrsim$200) on time scales between ~4 s and the time duration of each observation. After extracting the event files, we applied both a Fourier transform and a Z_n^2 analysis (Buccheri et al. 1983). No statistically significant variability from the analysed sources was detected.

4.1.2. Long-term variability

To study the long-term time variability of sources observable at least in two different observations, we calculated the average flux (or the 3σ upper limit in case of non-detection) at the source position in each observation. We considered fluxes in the 0.2–4.5 keV energy band because, as Pietsch et al. (2004) noted, the band 4.5–12 keV has a lower sensitivity and is contaminated by hard background. We calculated the fluxes with the energy conversion factors (ECFs) reported in Table 2. Then, we searched for variable sources by comparing their fluxes (or upper limits) in different observations. We measured the X-ray variability of each source by its variability factor $V_\mathrm{f} = F_\mathrm{max}/F_\mathrm{min}$, where F_max and F_min are the maximum and minimum (or upper-limit) fluxes. To estimate the significance of the variability between different observations, we calculated the significance parameter $S = (F_\mathrm{max} - F_\mathrm{min})/\sqrt{\sigma_\mathrm{max}^2 + \sigma_\mathrm{min}^2}$, where σ_max and σ_min are the errors of the maximum and minimum flux (Primini et al. 1993).

We also studied the X-ray variability considering the *Chandra* observation of M 83. We converted the *Chandra* counts (0.3–8 keV) of SW03 to 0.2–4.5 keV fluxes with the conversion factor calculated by SW03 and the distance of M 83 (d = 4.5 Mpc) assumed in this work. The conversion factor $CF = 8 \times 10^{37}/300$ erg s^{-1} counts^{-1} was calculated by SW03 assuming an absorbed powerlaw spectrum with $\Gamma = 1.7$, $N_\mathrm{H} = 10^{21}$ cm^{-2}, and a distance of 3.7 Mpc. For each *Chandra* source, we obtained the flux in the energy range 0.2–4.5 keV correcting the luminosity $L_{0.3-8\ \mathrm{keV}} = \mathrm{counts} \times CF$ by the absorption column density, the galaxy distance, and the energy range. The results are reported in Table 3.

Figure 2 shows the variability factor plotted versus the maximum detected flux and the hardness ratio $(R2 - R1)/(R1 + R2)$ (see Sect. 4.3) for each source. The left column shows the variability factors calculated for sources observed in at least two *XMM-Newton* observations. The right column shows the variability factors calculated for sources observed with *Chandra* and in at least one *XMM-Newton* observation.

Applying a variability significance threshold of $S = 3$, we found 35 variable sources. Like XRBs and AGNs, SSSs can show high variability, and because of their soft spectrum (see Sect. 5.6), they can be distinguished from the other sources: in Fig. 2 (lower panels), SSSs candidates should appear on the left-hand side, while XRBs (characterized by a much harder spectrum) are expected to appear on the right-hand side.

4.2. Spectral analysis

We extracted the X-ray spectra of sources with $\gtrsim$300 counts in the energy range 0.2–12 keV. For each source, we fitted all three EPIC spectra simultaneously with different models: powerlaw, disc-blackbody, thermal plasma model (APEC Smith et al. 2001), and blackbody, using XSPEC (ver. 12.7.0, Arnaud 1996). For the absorption we used the PHABS model.

A good fit with one of the above-mentioned spectral models can be used to classify the sources into one of the following classes of sources:

- X-ray binaries;
- supernova remnants;
- super-soft sources.

In total, we fitted the spectra of 12 sources (see Sect. A).

For sources that are not bright enough for spectral modelling, we only calculated their hardness ratios, as described in Sect. 4.3.

4.3. Hardness-ratio diagrams

We used the hardness-ratio diagrams to separate different classes of sources according to their X-ray properties. They are especially helpful for sources that are too faint, for which spectral fitting is not possible. For each source, we computed four hardness ratios, defined as

$$HR_i = \frac{R_{i+1} - R_i}{R_{i+1} + R_i} \quad \text{for } i = 1, \ldots, 4, \tag{1}$$

where R_i are the net source counts in five energy bands. To obtain the best statistics we combined the hardness-ratios of all three instruments.

When a source was detected in more than one observation, we considered the observation with the highest number of counts. Some sources can exhibit different spectral states (which can be correlated with the X-ray flux), resulting in hardness-ratio changes between different observations (see e.g. Done et al. 2007). Therefore, for some of these sources we only considered

Table 3. Variability factors (V_f) with errors of sources observed in at least two *XMM-Newton* observations and in *XMM-Newton* and *Chandra* observations.

XMM-Newton									
Source	Flux max.	V_f	Error V_f	S	Source	Flux max.	V_f	Error V_f	S
2	$(3.05 \pm 1.76) \times 10^{-14}$	3.0	0.6	1.2	104	$(8.29 \pm 3.25) \times 10^{-15}$	1.9	0.6	1.0
3	$(3.00 \pm 0.71) \times 10^{-14}$	3.1	0.2	2.9	107	$(1.36 \pm 0.12) \times 10^{-13}$	1.97	0.12	5.1
4	$(1.65 \pm 0.60) \times 10^{-14}$	1.7	0.4	1.2	108	$(1.79 \pm 0.15) \times 10^{-13}$	1.44	0.10	3.3
7	$(1.13 \pm 0.10) \times 10^{-13}$	7.16	0.09	9.4	109	$(3.43 \pm 0.34) \times 10^{-14}$	2.0	0.4	2.4
9	$(2.22 \pm 0.71) \times 10^{-14}$	1.5	0.3	1.1	110	$(1.79 \pm 0.44) \times 10^{-14}$	2.3	0.4	2.1
12	$(7.31 \pm 1.08) \times 10^{-14}$	3.95	0.14	5.0	111	$(5.91 \pm 1.28) \times 10^{-14}$	6.4	0.2	3.9
15	$(8.04 \pm 1.13) \times 10^{-14}$	3.1	0.2	4.4	113	$(3.05 \pm 1.76) \times 10^{-14}$	3.0	0.6	1.2
16	$(1.41 \pm 0.13) \times 10^{-13}$	10.6	0.3	9.5	114	$(1.27 \pm 0.17) \times 10^{-13}$	2.39	0.18	4.1
17	$(7.23 \pm 1.01) \times 10^{-14}$	2.1	0.2	3.3	116	$(3.32 \pm 0.51) \times 10^{-14}$	2.63	0.15	4.0
19	$(1.86 \pm 0.63) \times 10^{-14}$	1.9	0.3	1.4	118	$(3.41 \pm 1.21) \times 10^{-14}$	3.6	0.4	2.0
20	$(5.31 \pm 1.12) \times 10^{-14}$	3.3	0.2	3.3	119	$(1.64 \pm 0.29) \times 10^{-14}$	1.70	0.17	2.4
25	$(2.62 \pm 0.82) \times 10^{-14}$	1.8	0.3	1.4	121	$(2.82 \pm 0.50) \times 10^{-14}$	1.76	0.17	2.4
26	$(2.85 \pm 0.87) \times 10^{-14}$	1.8	0.3	1.4	122	$(2.21 \pm 0.38) \times 10^{-14}$	1.62	0.17	2.2
33	$(2.64 \pm 0.55) \times 10^{-14}$	1.4	0.3	1.1	123	$(2.76 \pm 0.49) \times 10^{-14}$	1.8	0.3	2.1
37	$(7.96 \pm 0.89) \times 10^{-14}$	8.58	0.11	7.9	126	$(4.84 \pm 0.62) \times 10^{-14}$	1.4	0.2	1.4
40	$(1.39 \pm 0.37) \times 10^{-14}$	1.7	0.5	1.2	129	$(4.96 \pm 0.58) \times 10^{-14}$	3.94	0.11	6.4
41	$(1.82 \pm 0.47) \times 10^{-14}$	2.4	0.4	2.0	131	$(2.26 \pm 0.45) \times 10^{-14}$	2.2	0.4	2.1
50	$(3.50 \pm 0.51) \times 10^{-14}$	2.77	0.14	4.4	133	$(7.64 \pm 0.29) \times 10^{-13}$	2.24	0.06	12.4
51	$(2.20 \pm 0.36) \times 10^{-14}$	1.8	0.3	2.0	135	$(5.26 \pm 1.29) \times 10^{-14}$	3.8	0.2	3.0
53	$(2.43 \pm 0.51) \times 10^{-14}$	1.5	0.3	1.3	136	$(1.57 \pm 0.51) \times 10^{-14}$	1.9	0.5	1.2
55	$(2.15 \pm 0.65) \times 10^{-14}$	2.5	0.3	2.0	140	$(2.39 \pm 0.48) \times 10^{-14}$	1.4	0.3	1.1
56	$(2.09 \pm 0.69) \times 10^{-14}$	2.2	0.3	1.7	143	$(1.50 \pm 0.39) \times 10^{-14}$	2.0	0.3	1.9
60	$(7.24 \pm 1.09) \times 10^{-14}$	1.46	0.19	1.8	144	$(9.08 \pm 3.86) \times 10^{-15}$	2.6	0.8	1.2
61	$(7.25 \pm 0.64) \times 10^{-14}$	4.28	0.08	8.6	145	$(1.92 \pm 0.56) \times 10^{-14}$	2.0	0.3	1.7
62	$(1.75 \pm 0.40) \times 10^{-14}$	1.7	0.3	1.6	153	$(3.52 \pm 0.43) \times 10^{-14}$	1.6	0.2	1.9
64	$(3.74 \pm 1.14) \times 10^{-14}$	2.5	0.4	1.9	154	$(1.08 \pm 0.12) \times 10^{-13}$	6.41	0.11	7.5
65	$(1.25 \pm 0.11) \times 10^{-13}$	3.90	0.15	7.8	155	$(4.55 \pm 0.58) \times 10^{-14}$	3.61	0.12	5.7
67	$(8.92 \pm 2.93) \times 10^{-15}$	2.4	0.5	1.6	157	$(3.34 \pm 0.66) \times 10^{-14}$	3.46	0.19	3.6
69	$(3.95 \pm 0.52) \times 10^{-14}$	3.13	0.13	5.1	160	$(8.04 \pm 1.13) \times 10^{-14}$	12.4	0.4	6.4
75	$(1.46 \pm 0.36) \times 10^{-14}$	1.7	0.5	1.1	162	$(1.97 \pm 0.56) \times 10^{-14}$	2.3	0.5	1.7
79	$(3.99 \pm 0.58) \times 10^{-14}$	1.4	0.2	1.5	163	$(1.40 \pm 0.50) \times 10^{-14}$	1.6	0.4	1.1
80	$(3.47 \pm 0.41) \times 10^{-14}$	1.53	0.11	2.9	166	$(1.96 \pm 0.39) \times 10^{-14}$	1.68	0.19	2.0
81	$(5.58 \pm 0.94) \times 10^{-14}$	2.5	0.3	3.0	171	$(7.03 \pm 0.98) \times 10^{-14}$	3.74	0.13	5.3
87	$(1.55 \pm 0.18) \times 10^{-13}$	1.31	0.13	1.9	172	$(3.32 \pm 0.68) \times 10^{-14}$	2.1	0.2	2.5
89	$(1.40 \pm 0.23) \times 10^{-14}$	2.1	0.5	1.8	173	$(3.95 \pm 0.55) \times 10^{-14}$	3.13	0.13	4.9
90	$(1.34 \pm 0.04) \times 10^{-12}$	1.35	0.03	8.1	177	$(5.01 \pm 0.83) \times 10^{-14}$	2.2	0.4	2.6
93	$(2.78 \pm 0.17) \times 10^{-13}$	16.42	0.06	15.6	183	$(2.71 \pm 0.60) \times 10^{-14}$	1.9	0.2	2.1
94	$(1.73 \pm 0.59) \times 10^{-14}$	1.9	0.3	1.4	184	$(2.83 \pm 0.60) \times 10^{-14}$	1.6	0.2	1.8
98	$(4.01 \pm 0.51) \times 10^{-14}$	3.18	0.12	5.4	186	$(2.44 \pm 0.74) \times 10^{-14}$	2.1	0.3	1.7
99	$(1.47 \pm 0.28) \times 10^{-13}$	15.29	0.18	5.0	187	$(1.78 \pm 0.63) \times 10^{-14}$	1.7	0.4	1.2
103	$(1.21 \pm 0.15) \times 10^{-13}$	12.78	0.12	7.2	189	$(7.96 \pm 0.89) \times 10^{-14}$	8.58	0.11	7.9
Chandra and *XMM-Newton*									
Source	Flux max.	V_f	Error V_f	S	Source	Flux max.	V_f	Error V_f	S
55	$(2.15 \pm 0.65) \times 10^{-14}$	3.3	0.3	2.3	97	$(1.30 \pm 0.12) \times 10^{-13}$	2.79	0.10	6.6
60	$(7.24 \pm 1.09) \times 10^{-14}$	2.35	0.16	3.8	98	$(4.01 \pm 0.51) \times 10^{-14}$	3.18	0.12	5.4
69	$(3.95 \pm 0.52) \times 10^{-14}$	3.13	0.13	5.1	99	$(1.47 \pm 0.28) \times 10^{-13}$	15.29	0.18	5.0
76	$(1.29 \pm 0.60) \times 10^{-14}$	4.5	0.5	1.7	106	$(4.21 \pm 0.52) \times 10^{-14}$	1.28	0.13	1.7
79	$(3.99 \pm 0.58) \times 10^{-14}$	1.4	0.2	1.5	107	$(1.36 \pm 0.17) \times 10^{-13}$	1.97	0.12	5.1
80	$(3.47 \pm 0.41) \times 10^{-14}$	1.53	0.11	2.9	108	$(1.79 \pm 0.15) \times 10^{-13}$	1.44	0.10	3.3
81	$(5.58 \pm 0.94) \times 10^{-14}$	2.5	0.3	3.0	109	$(3.43 \pm 0.34) \times 10^{-14}$	4.02	0.14	7.4
84	$(1.95 \pm 0.42) \times 10^{-14}$	2.7	0.3	2.8	114	$(1.27 \pm 0.17) \times 10^{-13}$	2.39	0.18	4.1
87	$(1.55 \pm 0.18) \times 10^{-13}$	1.35	0.11	2.2	116	$(3.32 \pm 0.51) \times 10^{-14}$	20.8	0.3	6.2
88	$(1.03 \pm 0.33) \times 10^{-14}$	4.6	0.4	2.5	125	$(7.23 \pm 0.27) \times 10^{-15}$	5.3	0.5	2.2
92	$(3.74 \pm 0.19) \times 10^{-14}$	2.7	0.4	4.3	129	$(4.96 \pm 0.58) \times 10^{-14}$	3.94	0.11	6.4
95	$(2.00 \pm 0.44) \times 10^{-14}$	1.9	0.2	2.0					

Notes. Table also includes maximum fluxes and errors in the energy range 0.2–4.5 keV in units erg cm^{-2} s^{-1}, and the significance of the difference S.

a state by adopting the highest number of counts when determining the hardness ratio. This approach allowed us to obtain the hardness ratios with small uncertainties for bright sources in their bright states. However, one has to be aware that if a source changes its state, the hardness-ratio may change as well. For fainter sources (with hardness ratio uncertainties $\gtrsim$0.2), the

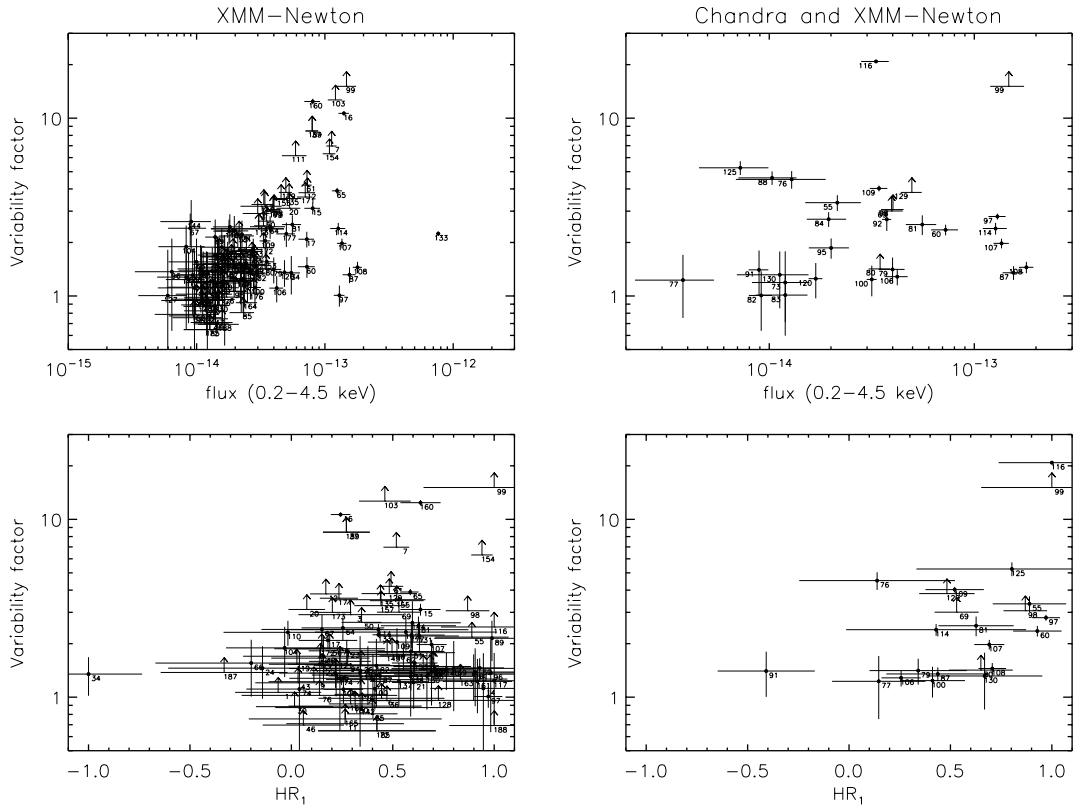

Fig. 2. *Left panels*: variability factor as a function of the maximum flux (*upper panel*) and hardness ratio HR_1 (*bottom panel*) based on *XMM-Newton* observations. *Right panels*: variability factor as a function of the maximum flux (*upper panel*) and hardness ratio HR_1 (*bottom panel*) based on *XMM-Newton* and *Chandra* observations. The lower limits of the variability factors are marked as arrows.

hardness ratios are not sensitive to changes of the state of the source within uncertainties. The hardness ratios calculated for each source are reported in Table B.1.

Figure 3 shows the hardness ratios of sources with errors smaller than 0.3, detected in the field of view of M 83. We plotted sources classified as XRBs, SNRs, SSSs, ultra-luminous X-ray sources (ULXs), foreground stars, and background objects (see Sect. 5) with different symbols. On the same plot we also overlaid grids of hardness ratios calculated for different spectral models: three absorbed powerlaws with photon-index $\Gamma = 1, 2, 3$ (XRBs in hard state), two absorbed disc-blackbody models with temperatures at the inner disc radius of $kT_{\rm in} = 0.5$ and 1 keV (XRBs in soft state), four thermal plasma models APEC with temperatures $kT_{\rm apec} = 0.2$, 0.5, 1, 1.5 keV (SNRs), and two blackbody models with temperatures $kT_{\rm bb} = 50$ and 100 eV (SSSs, see Sect. 5.6). The column densities range from $N_{\rm H} = 10^{20}$ cm^{-2} to $N_{\rm H} = 10^{24}$ cm^{-2}.

5. Source classification

We cross-correlated the list of sources observed with *XMM-Newton* with existing catalogues. For this purpose we used X-ray (Trinchieri et al. 1985; Ehle et al. 1998; Immler et al. 1999; SW03; Di Stefano & Kong 2003), optical (Blair & Long 2004; Dopita et al. 2010; Jones et al. 2004; Rumstay & Kaufman 1983; USNO-B1, Monet et al. 2003), radio (Maddox et al. 2006; Cowan et al. 1994; Condon et al. 1998), and infrared (2MASS, Skrutskie et al. 2006) catalogues.

We considered two sources as associated to each other if their positions were closer than the 3× combined statistical errors. The optical counterparts of several X-ray sources cannot be determined uniquely. In such cases we assumed as counterpart the brightest optical object within the error circle. The cross-correlations are reported in Table B.2.

We used the previous classifications in X-rays and other wavelengths and the methods of classification described in Sects. 4.1 (X-ray variability), 4.2 (spectral analysis), and 4.3 (hardness ratios), to identify and classify sources as background objects, foreground stars, XRBs, SNRs, SSSs, and ULXs.

In this section we describe the observational properties for each class of sources and define the classification criteria.

5.1. Foreground stars

X-ray observations of nearby galaxies are contaminated by foreground stars, which have X-ray luminosities ranging from $\sim 10^{26}$ to $\sim 10^{30}$ erg s^{-1} for stars of spectral type F to M, and $\sim 10^{29}$ to $\sim 10^{34}$ erg s^{-1} for stars of spectral types O and B (Vaiana et al. 1981; Rosner et al. 1985). Stars of spectral classes F to M emit X-rays because of the intense magnetic fields that form a corona, in which the plasma is heated to temperatures of about $\sim 10^6$–10^8 K (e.g. Güdel 2002). A mechanism proposed to explain the X-ray emission from stars of spectral types O-B is the formation of shocks in the coronal regions due to the instability of the wind-driven mechanism (see Puls et al. 2008 and references therein). In A-type stars, none of the above mechanisms for X-ray emission can operate efficiently. Therefore, A-type stars are expected to be weak X-ray sources (Schröder & Schmitt 2007) and only very few have been observed in X-rays (see e.g. Robrade & Schmitt 2010; Schröder et al. 2008).

The X-ray spectra of foreground stars are relatively soft and can be described by models of optically thin plasma in

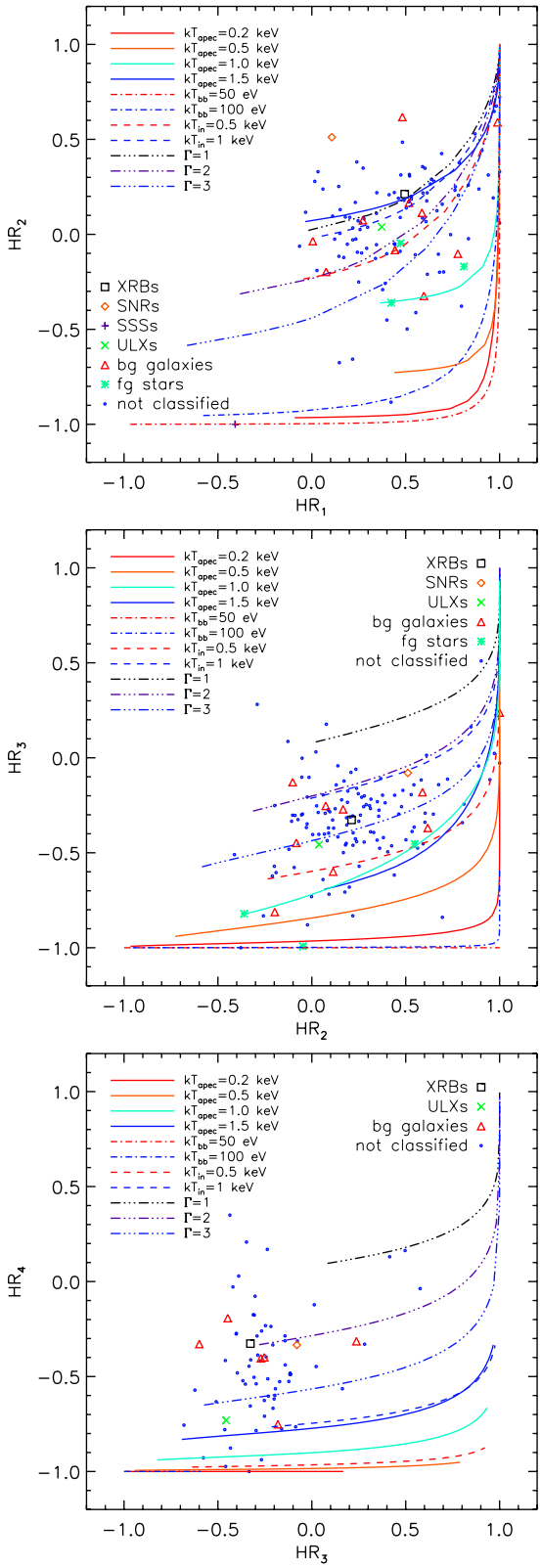

Fig. 3. Hardness-ratio diagrams of sources with error-bars smaller than 0.3. Black squares are sources classified as XRBs (Sect. 5.4), orange diamonds are SNRs (Sect. 5.5), violet plus signs are SSSs (Sect. 5.6), green crosses are ULXs (Sect. 5.8), cyan stars are foreground stars (Sect. 5.1), red triangles are background sources (Sect. 5.2), and blue circles are sources not classified. The lines are the hardness ratios calculated for different spectral models and column densities, as described in Sect. 4.3.

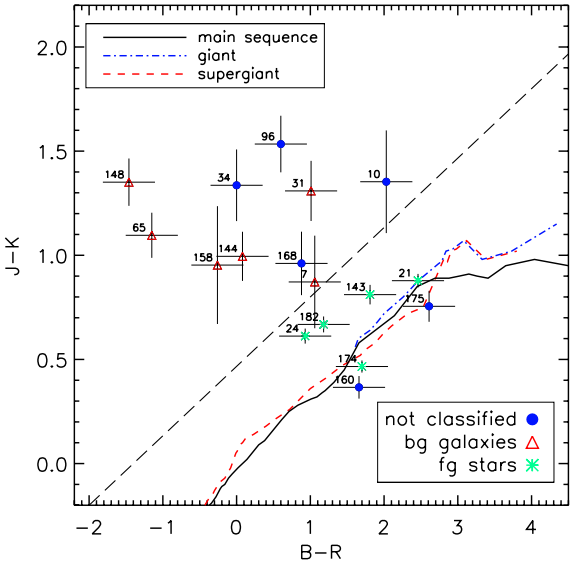

Fig. 4. Colour–colour diagram of *XMM-Newton* sources with optical (USNO-B1) and infrared (2MASS) counterparts. Sources located below the black dashed line are very likely foreground stars.

collisional equilibrium (e.g. Raymond & Smith 1977) with temperatures ranging from 10^6 to 10^7 K. A common method to distinguish stars from other X-ray sources is comparing the X-ray-to-optical flux ratio, as suggested by Maccacaro et al. (1988):

$$\log_{10}(f_x/f_{opt}) = \log_{10}(f_x) + \frac{m}{2.5} + 5.37, \quad (2)$$

where m is the visual magnitude m_v. In the USNO-B1 catalogue the red and blue magnitudes are given, thus we assumed $m_v \approx (m_{red} + m_{blue})/2$. We used the blue magnitude m_{blue} as magnitude m when the red magnitude was not available.

For each X-ray source with an optical counterpart, we distinguished foreground stars from other sources by plotting X-ray-to-optical flux ratios over the hardness ratios HR_2 and HR_3 (Fig. 5). The X-ray-to-optical flux ratios and the hardness ratios differ significantly between different classes of sources.

The soft X-ray flux of early-type stars (OB type) scales with $f_x \approx 10^{-7} f_{opt}$ (Kudritzki & Puls 2000 and references therein), while the ratio f_x/f_{opt} of late-type stars (F to M) usually ranges from 10^{-6} to 10^{-1} (e.g. Krautter et al. 1999). In contrast, sources such as SNRs, SSSs, and XRBs radiate mainly in X-rays.

We also used optical and near-infared magnitudes and colours to classify foreground stars (Figs. 4 and 6). Figure 4 is the colour–colour diagram for *XMM-Newton* sources with optical (USNO-B1) and infrared (2MASS) counterparts. Lines show the expected $(B - R)$ and $(J - K)$ colours for main-sequence, giant, and supergiant stars belonging to the Milky Way. We obtained these lines using intrinsic colours calculated by Johnson (1966). Stars located at the Galactic latitude of M 83 ($b \approx 32°$) have on average a colour excess per kiloparsec of $E(B - V) = 0.05 \pm 0.05$ mag kpc^{-1} (Gottlieb & Upson 1969). Therefore, the colour excesses $E(J-K)$ and $E(B-R)$ are negligible compared to the optical and infrared magnitude uncertainties (Schild 1977).

Figures 4 and 6 allow to separate foreground stars from other classes of sources. Foreground stars are brighter in R than background objects or members of M 83, and sources with $J - K \lesssim 1.0$ and $B - R \lesssim 2.0$ are most likely foreground stars.

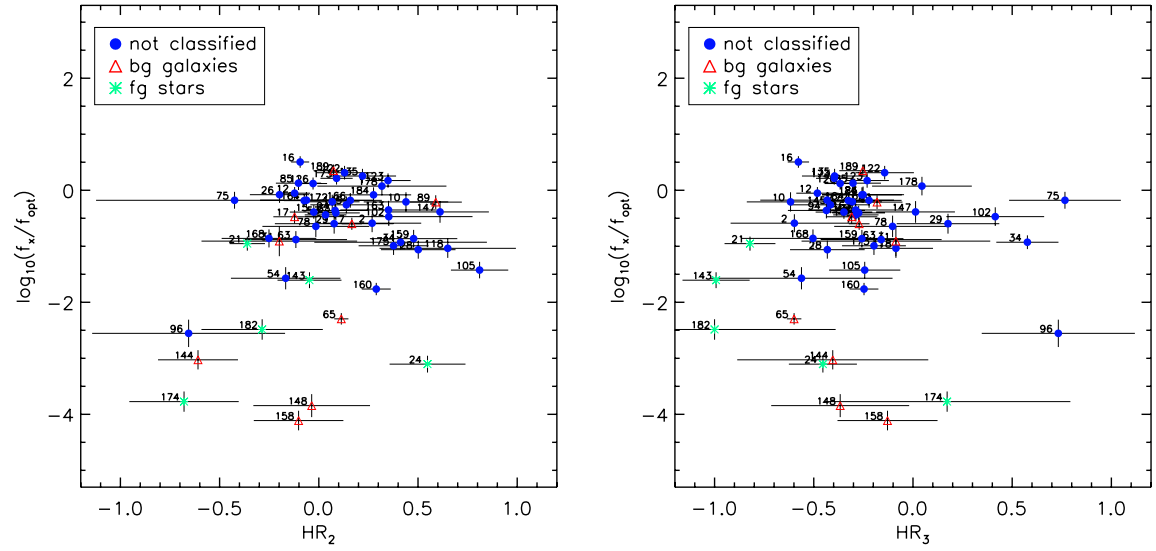

Fig. 5. Flux ratio $\log(f_x/f_{opt})$ over hardness ratios HR_2 and HR_3.

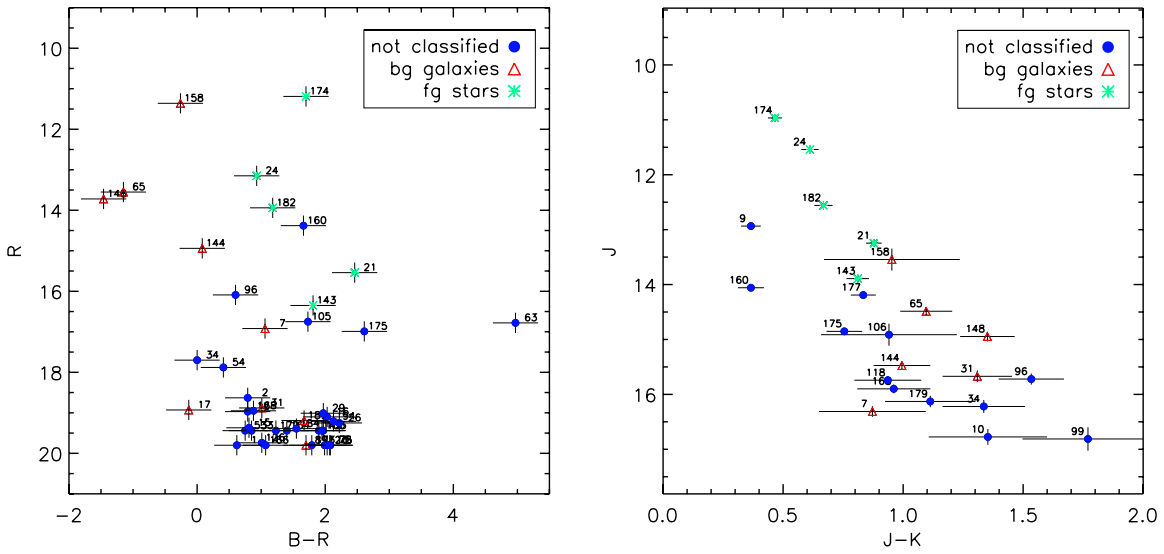

Fig. 6. Colour–magnitude diagrams of *XMM-Newton* sources correlating with sources in the USNO-B1 (*left panel*) and 2MASS (*right panel*) catalogues.

From previous considerations, we classified foreground stars when these conditions were met:

- $\log(f_x/f_{opt}) \lesssim -1$;
- $HR_2 \lesssim 0.3$;
- $HR_3 \lesssim -0.4$;
- $J - K \lesssim 1.0$;
- $B - R \lesssim 2.0$.

The five sources classified as foreground star candidates are reported in Table 4. A detailed discussion of the identification and classification of foreground stars is provided in Sects. A.1 and A.2.

5.2. Background objects

The identification of AGNs, normal galaxies, and galaxy clusters is based on SIMBAD and NED correlations, and is confirmed if there is an optical counterpart in the *2nd Digitized Sky Survey* (DSS2) image. New classifications are based on the radio counterpart and hardness ratio $HR_2 \geq -0.4$ (Pietsch et al. 2004).

Table 4. M 83 X-ray sources and their associated candidate sources in our Galaxy.

No.	RA (J2000)	Dec (J2000)	USNO-B1	*B* mag.	*R* mag.
21	13 36 18.73	–30 01 38.1	0599-0299962	18.0	15.5
24	13 36 19.95	–29 51 08.3	0601-0298625	14.1	13.2
143	13 37 27.29	–29 55 45.5	0600-0300561	18.2	16.4
174	13 37 44.79	–30 07 49.2	0598-0301638	12.9	11.2
182	13 37 57.77	–30 01 40.6	0599-0300696	15.1	13.9

We identified nine sources as background galaxies and AGNs (sources No. 7, 17, 31, 65, 83, 89, 144, 148, 158, see Table 5). We found radio counterparts of the sources Nos. 20, 37, 189 and classified them as AGN candidates for the first time (see Sect. A.3). Based on the $\log N - \log S$ calculated by Cappelluti et al. (2009) (see Sect. 6.2), about 40 observed sources (with a 2–10 keV flux $F_x > 10^{-14}$ erg cm^{-2} s^{-1}) are expected to be background objects in each *XMM-Newton* observation of

Table 5. X-ray sources identified and classified as galaxies or AGNs and their counterparts or previous X-ray classifications.

No.	RA (J2000)	Dec (J2000)	Name (SIMBAD)
		Identifications:	
7	13 36 04.66	–30 08 30.8	QSO B1333–298
17	13 36 15.42	–29 57 58.2	[I1999] 5[3]
31	13 36 28.13	–29 42 27.9	2MASS 13362821–2942266
65	13 36 45.78	–29 59 13.0	6dFGS gJ133645.8–295913
83	13 36 58.26	–29 51 04.3	[MCK2006] 28[1]
89	13 36 59.68	–30 00 58.8	[BRK2009] 7[2]
144	13 37 27.46	–30 02 28.3	6dFGS gJ133727.5–300228
148	13 37 29.36	–29 50 27.4	6dFGS gJ133729.5–295028
158	13 37 32.94	–29 51 01.2	ESO 444–85
		New classifications:	
20	13 36 18.21	–30 15 00.5	NVSS J133618–301459
37	13 36 30.53	–30 16 57.0	NVSS J133630–301651
189	13 38 05.57	–29 57 45.4	NVSS J133805–295748

References. [(1)] Maddox et al. (2006); [(2)] Bresolin et al. (2009); [(3)] Immler et al. (1999).

Table 1. From a comparison with other works (e.g. Misanovic et al. 2006), we expect a large difference between the predicted number of background objects from background surveys and the number of identified/classified background objects in an *XMM-Newton* observation. This difference is due to the difficulty in classifying sources which, because of their distance, are too faint (and therefore provide little information) to be classified with the methods at our disposal.

5.3. Nuclear sources

We detected two bright sources in the nuclear region of M 83 with the source detection procedure: sources No. 92 and No. 95. They are separated by ∼6.3″ and are the brightest sources detected with *XMM-Newton* in M 83 ($F_{\rm No.\,90} = [1.03 \pm 0.25] \times 10^{-12}$ erg cm^{-2} s^{-1}; $F_{\rm No.\,93} = [2.59 \pm 0.15] \times 10^{-13}$ erg cm^{-2} s^{-1}; 0.2–12 keV, assuming an absorbed powerlaw spectrum with index 1.8 and a foreground Galactic absorption of $N_{\rm H} = 3.69 \times 10^{20}$ cm^{-2}). The two nuclear sources coincide with ∼18 *Chandra* sources and the bright diffuse emission of the starburst nucleus, not resolved by *XMM-Newton* because of its high PSF, which causes source confusion in crowded regions, such as the nuclear region of M 83.

5.4. X-ray binaries

We classified sources as XRBs if the X-ray spectra or hardness ratios were compatible with the typical spectra of XRBs and we detected a flux periodicity.

We identified two X-ray binaries (Nos. 81 and 120), previously classified by SW03 using *Chandra* observations (Sect. A.4).

5.5. Supernova remnants

We assume that the X-ray spectra of SNRs are well described by the thermal plasma model APEC (Smith et al. 2001), with temperatures ranging from 0.2 to 1.5 keV. At this distance we are unable to resolve an SNR or to verify a more detailed spectral model assuming, e.g., a non-equilibrium ionisation.

We classified an X-ray source as SNR if $HR_1 > 0.1$, $HR_2 < -0.4$, the source was not a foreground star, and did not show a significant variability (Pietsch et al. 2004).

We identified the source No. 79 as source [SW03] 27, classified as a young SNR candidate by SW03 (Sect. A.5).

SN1957D. Long et al. (2012) reported the first detection of SN1957D in X-rays with *Chandra*. The source shows a luminosity of 1.7×10^{37} erg cm^{-2} s^{-1} ($d = 4.61$ Mpc, Saha et al. 2006; 0.3–8 keV), and the spectrum is well modelled with an absorbed powerlaw with an index ∼1.4, a foreground Galactic absorption of $N_{\rm H} = 4 \times 10^{20}$ cm^{-2} and an intrinsic column density of $N_{\rm H} = 2 \times 10^{22}$ cm^{-2}. We did not detect SN1957D in the *XMM-Newton* observations. In observation 1 the source is located near to the centre of the field of view, and in the other two observations the source is located at the edge of the field of view. Assuming the spectral parameters found by Long et al. (2012), we calculated a 3σ upper-limit in observation 1 of $\sim 2.4 \times 10^{-14}$ erg cm^{-2} s^{-1} (0.2–12 keV), corresponding to a luminosity of $\sim 5.8 \times 10^{37}$ erg s^{-1}, well above the luminosity detected by Long et al. (2012).

5.6. Super-soft sources

Super-soft sources are a class of sources that are believed to be binary systems containing a white dwarf. The white dwarf accretes matter from a Roche-lobe-filling companion at high rates ($\dot{M}_{\rm acc} \sim 10^{-7}\ M_\odot\,{\rm yr}^{-1}$), which leads to quasi-steady nuclear burning on its surface (see e.g. van den Heuvel et al. 1992). SSSs show soft spectra with blackbody temperatures of 15–150 eV and X-ray luminosities ranging from $\sim 10^{35}$ erg s^{-1} to 10^{38} erg s^{-1} (Di Stefano & Kong 2003; Kahabka & van den Heuvel 1997). An additional harder component, due to interactions of the radiation with matter near to the white dwarf or wind interactions can be observed (Di Stefano & Kong 2003). Moreover, SSSs are often observed as transient X-ray sources (see Greiner 2000). Other classes of sources with soft spectra can be confused with SSSs. For example, some X-ray pulsars observed outside the beam of the pulsed radiation can show a soft (∼30 eV) component (Hughes 1994; Di Stefano & Kong 2003). Moreover, stripped cores of giant stars can be classified as SSSs (Di Stefano et al. 2001).

As our classification criteria, we assumed blackbody temperatures of $kT_{\rm bb} \leq 100$ eV (in agreement with the selection procedure proposed by Di Stefano & Kong 2003) and hardness ratios that do not overlap with those of other classes of sources. These criteria are an $HR_1 \lesssim 0$ and $HR_2 - EHR_2 < -0.9$. We classified a source as SSS only if both criteria are fulfilled.

We identified source No. 91 as source M 83-50, classified as an SSS candidate by Di Stefano & Kong (2003) using *Chandra* observations (Sect. A.6).

5.7. Hard sources

Hard sources show hard X-ray spectra (or hard HRs, see Table 5 in Pietsch et al. 2004). Using their spectral properties and hardness ratios, we classified five hard sources (Nos. 16, 61, 103, 126, and 153; see Sect. A.8.1) and we identified 11 hard sources (Nos. 60, 80, 92, 97, 99, 106, 107, 108, 114, 116, 129; see Sect. A.8.2).

5.8. Ultra-luminous X-ray sources

ULXs are pointlike non-nuclear sources with X-ray luminosities in excess of the Eddington limit ($L_{\rm Edd} \simeq 10^{39}$ erg s^{-1}) for a stellar

mass black-hole (see e.g. Feng & Soria 2011). They are usually located in active star-forming environments (Miller & Colbert 2004), and their nature is still unclear; recent studies indicate that ULXs are a heterogeneous sample of objects (e.g. Gladstone 2010).

Several models have been proposed to explain the high X-ray luminosity of ULXs, but there are three models that are often used for this class of sources. The first model requires that ULXs are intermediate-mass black-hole systems (IMBHs) with masses $M \sim 10^2$–$10^4\ M_\odot$, accreting at sub-Eddington rates (e.g. Colbert & Mushotzky 1999). The other models assume that ULXs are stellar-mass black holes (with masses $M \lesssim 100\ M_\odot$) in a super-Eddington accretion regime (Poutanen et al. 2007) or with beamed radiation (see e.g. King 2009).

We identified ULX No. 133, discovered by Trinchieri et al. (1985) with *Einstein* (source H2), and previously observed in X-rays with ROSAT by Ehle et al. (1998) and Immler et al. (1999) (see Sect. A.7).

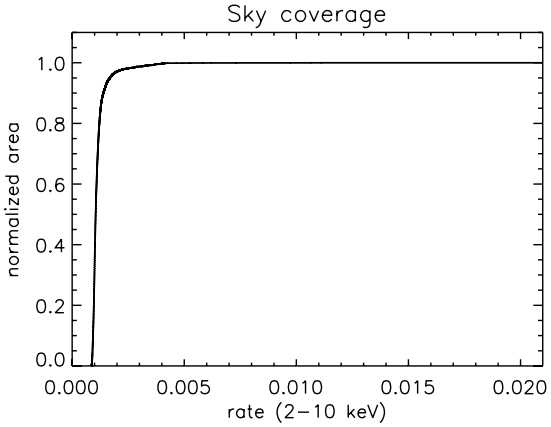

Fig. 7. Sky coverage as a function of the X-ray flux (2–10 keV) for the region inside the D_{25} ellipse (observation 1), calculated excluding the region within the circle centered on the nuclear region of M 83 with radius $R = 26''$.

6. X-ray luminosity functions

For each observation, we calculated the XLFs in the energy range 2–10 keV excluding the softer bands to reduce the effect of incompleteness of the observed source sample due to absorption. Moreover, from an XLF calculated in this energy band, it is possible to easily subtract the contribution of the $\log N - \log S$ of the AGNs, which was calculated from several surveys performed by *XMM-Newton* and *Chandra* (see Sect. 6.2).

We considered for XLFs only sources with a detection likelihood greater than 6 in the energy range 2–12 keV. For each source, we converted the count rates to the 2–10 keV fluxes using the ECFs of Table 2 for the energy bands *R*4 and *R*5.

We excluded the region inside a circle centred on the nuclear region of M 83 with radius $R = 26''$ from the XLF calculation, where the large PSF of EPIC in a crowded region causes source confusion effects (see Sect. 5.3). Since we were interested in obtaining XLFs of XRBs, we also excluded the sources previously classified as SNRs, SSSs, ULXs, and foreground stars (Sect. 5). For each observation, we calculated the XLFs of sources detected within two regions of M 83: the inner disc inside the D_{25} ellipse, and the outer disc outside the D_{25} ellipse.

6.1. XLFs corrected for incompleteness

The sensitivity of the EPIC instruments depends on the exposure, background, and PSF, which are not uniform across the FOV. Indeed, the exposure time is relatively high at the centre of the FOV and decreases with increasing off-axis angle (vignetting effect). The background, modelled by the task `esplinemap`, decreases with increasing angular distance from the nuclear region of M 83 (due to the diffuse emission in the disc of M 83), and the optical properties of the X-ray telescope introduce a degradation of the PSF with increasing off-axis angle. Therefore, the sensitivity also varies across the observed area, allowing the detection of the brightest sources across the entire observed area, whereas the effective area for the detection of faint sources is smaller. This effect leads to an underestimation of the number of sources observed at the faintest flux levels.

We corrected the XLFs by taking into account the incompleteness effect described above by calculating the *sky coverage function*, which is the effective area covered by the observation as a function of flux. For each observation, we first created the combined sensitivity maps of PN, MOS1, and MOS2 with the SAS task `esensmap`, which requires as input files the exposure maps, the background images, and the detection masks created by the source detection procedure. We used the sensitivity maps to calculate the sky coverage function for each observation (Fig. 7). The cumulative XLF corrected for incompleteness is given by

$$N(>F_\mathrm{x}) = A_\mathrm{tot} \sum_{i=1}^{N_\mathrm{s}} \frac{1}{\Omega(F_i)}\,, \tag{3}$$

where $N(>\ F_\mathrm{x})$ is the number of sources with a flux higher than F_x, weighted by the fraction of the surveyed area $\Omega(F_i)/A_\mathrm{tot}$ over which sources with flux F_i can be detected; A_tot is the total area of the sky observed by EPIC, $\Omega(F_i)$ is the sky coverage (Fig. 7), and N_s is the total number of the detected sources. Therefore, with Eq. (3), every source is weighted with a factor correcting for incompleteness at its flux. The variance of the source number counts is defined as

$$\sigma^2 = \sum_{i=1}^{N_\mathrm{s}} \left(\frac{1}{\Omega_i}\right)^2. \tag{4}$$

6.2. AGN-corrected XLFs

The XLFs obtained in Sect. 6.1 consist of sources belonging to M 83 (XRBs) and AGNs. We subtracted the AGN contribution using the AGN XLF of Cappelluti et al. 2009, who derived the XLFs from the 2 deg^2 of the XMM-COSMOS survey (Scoville et al. 2007). These authors found that the XLF of AGNs in the energy range 2−10 keV is described by a broken powerlaw:

$$\frac{\mathrm{d}N}{\mathrm{d}F} = \begin{cases} AF^{-\alpha_1} & F > F_\mathrm{b} \\ BF^{-\alpha_2} & F \le F_\mathrm{b}, \end{cases} \tag{5}$$

where $A = BF_\mathrm{b}^{\alpha_1-\alpha_2}$ is the normalisation, $\alpha_1 = 2.46 \pm 0.08$, $\alpha_2 = 1.55 \pm 0.18$, $F_\mathrm{b} = (1.05 \pm 0.16) \times 10^{-14}$ erg cm^{-2} s^{-1}, and $A = 413$.

Figure 8 shows the XLFs of sources detected within the D_{25} ellipse and outside, calculated for each *XMM-Newton* observation. Blue lines are the observed XLFs, and black lines are the XLFs corrected for incompleteness. Solid green lines are the AGN XLFs of Eq. (5) with relative uncertainties (dashed green

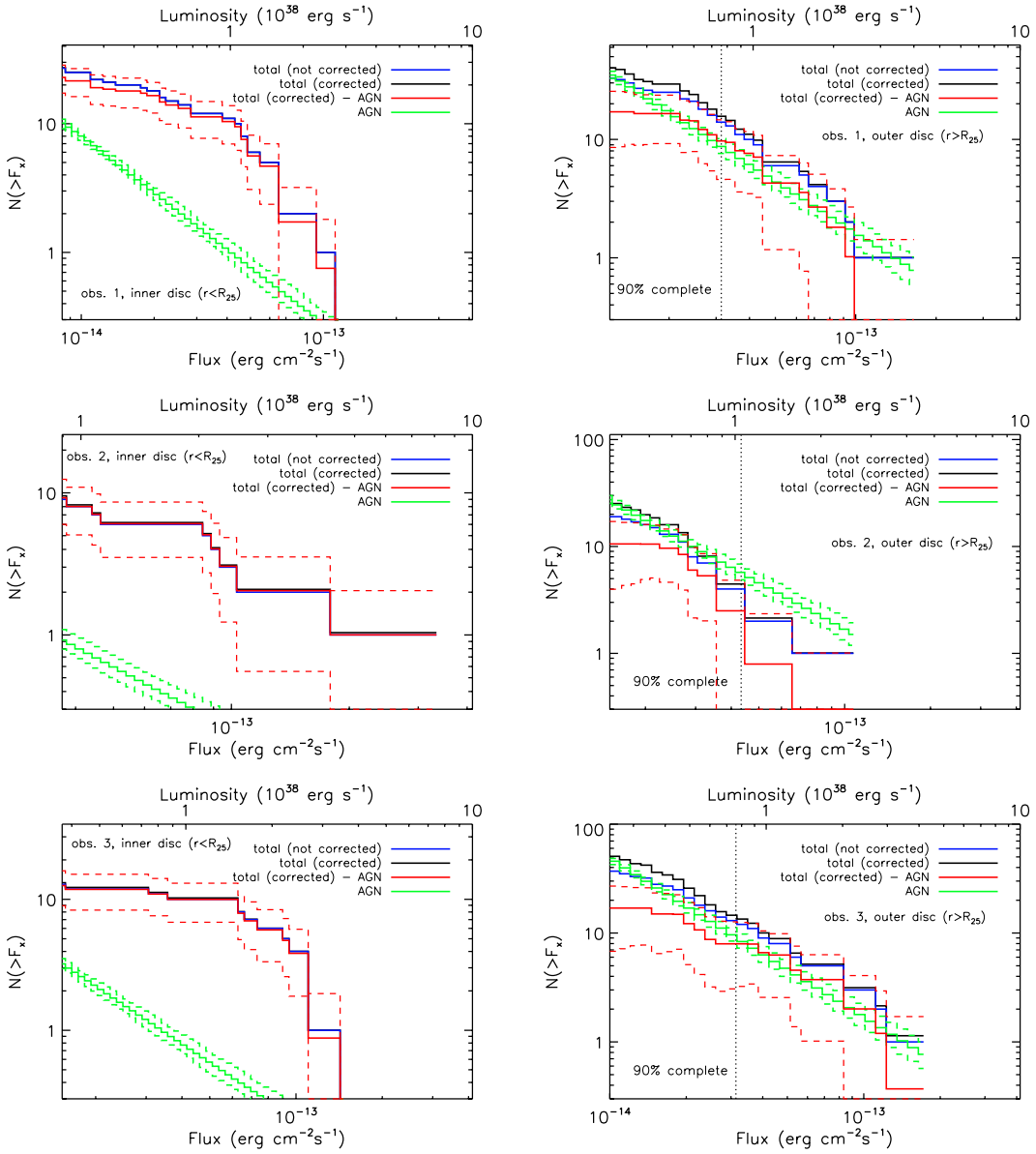

Fig. 8. Cumulative XLFs in the 2–10 keV energy band. Blue lines correspond to the XLFs without the contribution of SNRs, SSSs, ULX, and foreground stars, not corrected for incompleteness. Black lines are the XLFs corrected for incompleteness. Solid green lines are the AGN XLFs of Cappelluti et al. (2009), and dashed green lines are the 90% confidence errors. Solid red lines are the XLFs corrected for incompleteness and AGN-subtracted, and the dashed red lines are the resulting uncertainties.

lines). Solid red lines show the XLFs corrected for incompleteness and AGN-subtracted, and dashed red lines are the 90% confidence errors, obtained from Eq. (4) and the 90% confidence errors of the AGN distribution.

Vertical black lines in the right column of Fig. 8 show the level at which the survey is 90% complete (see Sect. 6.3.2), defined as the flux at which

$$\sum_{i=1}^{N_s} N(F_i) / \sum_{i=1}^{N_s} A_{\rm tot}/\Omega(F_i) = 0.9.$$

6.3. Fit

We fitted the differential XLFs corrected for incompleteness and AGN-subtracted with a powerlaw:

$$A(F) = kF^{\alpha}\ , \tag{6}$$

where k is the normalisation and α the powerlaw index. We also fitted the differential XLFs with a broken powerlaw:

$$A(F) = \begin{cases} kF_{\rm b}^{\alpha_2-\alpha_1}F^{\alpha_1} & F > F_{\rm b} \\ kF^{\alpha_2} & F \le F_{\rm b}\ , \end{cases} \tag{7}$$

where $F_{\rm b}$ is the break point. The resulting parameters obtained from the fit are reported in Table 6.

6.3.1. Inner disc

From *Chandra* observation, SW03 calculated the XLFs of sources located in the inner region (distance < 60″ from the nucleus) and outer region (60″ < d < R_{25}) of the optical disc. They found that the inner region sources have a powerlaw luminosity distribution with an differential index of −1.7, while the luminosity distribution of the outer region sources shows a lack of bright sources above ∼10^{38} erg s^{-1}. These authors modelled

Table 6. Best-fitting parameters of the differential XLFs of observations 1, 2, and 3, calculated for sources within and outside the D_{25} ellipse.

	$<R_{25}$		
	Obs. 1	Obs. 2	Obs. 3
	powerlaw[a]		
α	-1.0 ± 0.3	-1.8 ± 0.4	-1.6 ± 1.2
k	$10.4^{+1.8}_{-1.6}$	$11.2^{+5.9}_{-3.9}$	$21.4^{+38.9}_{-13.8}$
χ^2 (d.o.f.)	23.48 (15)	11.74 (5)	9.20 (5)
	broken powerlaw[b]		
α_1	$-3.0^{+0.9}_{-0.2}$	$-2.9^{+0.8}_{0.2}$	
α_2	$-1.1^{+0.1}_{-0.5}$	$-1.1^{+0.1}_{-0.4}$	
k	$20.9^{+13.0}_{-8.0}$	$37.2^{+48.0}_{-20.9}$	
F_b (10^{-14} erg cm^{-2} s^{-1})	$5.6^{+1.0}_{-0.4}$	$6.5^{+0.8}_{-0.7}$	
χ^2 (d.o.f.)	21.01 (13)	9.17 (3)	
	$> R_{25}$		
	Obs. 1	Obs. 2	Obs. 3
	powerlaw[a]		
α	-1.9 ± 0.5	-3.3 ± 1.1	-1.2 ± 0.4
k	$13.4^{+4.7}_{-3.5}$	$8.7^{+3.5}_{-2.5}$	$7.1^{+2.0}_{-1.6}$
χ^2 (d.o.f.)	11.62 (11)	4.41 (5)	8.68 (9)

Notes. For each observation, the best-fitting parameters were obtained using the total XLF corrected for incompleteness and AGN-subtracted. [(a)] See Eq. (6); [(b)] see Eq. (7).

the XLF of these sources with a broken powerlaw with a break around $\sim 10^{38}$ erg s^{-1} and differential indices of -1.6 and -2.6. They explained the XLF of the inner region sources in terms of current starburst activity, while the XLF of the outer region may result from an older population of disc sources mixing with a younger population.

We recall that we cannot study the innermost region because of poor spatial resolution of *XMM-Newton* compared to *Chandra*. We compared the best-fitting parameters of the XLF of the outer region sources ($60'' < d < R_{25}$) obtained by SW03 with those obtained from the *XMM-Newton* analysis (Table 6). In particular, we considered the broken powerlaw fit of sources detected in observation 1. Only during this observation was the whole optical disc of M 83 observed. We found that the indices α_1, α_2 and the break F_b of Eq. (7) agree within the uncertainties with the parameters found by SW03.

Grimm et al. (2003) studied the XLFs of a sample of galaxies and found the probable existence of a universal HMXB XLF (in the luminosity range $\sim 4 \times 10^{36}$–10^{40} erg s^{-1}), described by a powerlaw with differential slope of -1.6. They found that the number of HMXBs with $L_x > 2 \times 10^{38}$ erg s^{-1} in a star-forming galaxy is directly proportional to the SFR, and proposed that the number and the total X-ray luminosity of HMXBs can be used to measure the star formation rate of a galaxy. Based on a much larger sample of galaxies, Mineo et al. (2012) found that the properties of populations of HMXBs and their relation with the SFR agree with those obtained by Grimm et al. (2003). We estimated the SFR in the optical disc of M 83 using the $N_{\rm HMXBs}$–SFR relation of Mineo et al. (2012):

$$N(>10^{38}\text{erg s}^{-1}) = 3.22 \times SFR\,(M_\odot\ \text{yr}^{-1}). \quad (8)$$

We assumed that the XLF we used for this calculation provides a good approximation of the HXMB XLF in M 83. The contribution of LMXBs to the XLF is negligible for a starburst galaxy such as M 83 when $L_x \gtrsim 10^{38}$ erg s^{-1} (Grimm et al. 2003). Moreover, the contribution of LMXBs to the XLF is minimized by excluding the nuclear region of the galaxy, from which a strong contribution to the total number of LMXBs is expected. Using the XLF of sources detected in observation 1 within the D_{25} ellipse, from Eq. (8) we found an $SFR \approx 3.1\ M_\odot\ \text{yr}^{-1}$, in agreement with the SFR estimates obtained from observations in other wavelengths (see e.g. Boissier et al. 2005; Dong et al. 2008; Grimm et al. 2003 and references therein).

6.3.2. Outer disc

The XLFs of the outer disc ($d > R_{25}$) show an excess of sources (with respect to the expected number of AGNs) in the luminosity range $\sim 10^{37}$ to $\sim 2 \times 10^{38}$ erg s^{-1} (Fig. 8).

We are interested in calculating the probability of the luminosity distribution of the observed sources to be consistent with the luminosity distribution of Eq. (5) which represents the AGN distribution. Therefore, we compared for each observation the luminosity distribution of the sources detected in the outer disc ($d > R_{25}$) that was not corrected for incompleteness (see Sect. 6) with a distribution of simulated sources over the EPIC FOV obtained from a uniform spatial distribution of sources with a luminosity distribution given by Eq. (5), filtered to exclude sources with a flux below the detection threshold calculated at the position of each source in the sensitivity map. The Kolmogorov-Smirnov test applied to these source samples showed that the probabilities that the luminosity distributions of the observed sources are consistent with the luminosity distribution of AGNs (Eq. (5)) are almost zero, being 0.04% in observation 1, 0.7% in observation 2, and 0.6% in observation 3.

To quantify the probability that the set of X-ray sources located outside the D_{25} ellipse are AGNs (which are expected to be uniformly distributed across the sky) or XRBs (whose distribution should not be uniform, because the position of XRBs should correlate with the arms extending out of the optical disc), we performed a two-dimensional Kolmogorov-Smirnov test (Fasano & Franceschini 1987; Peacock 1983). This test is based on the statistic δ, which in the unidimensional Kolmogorov-Smirnov test represents the largest difference between two cumulative distributions. We applied this test to two data samples:

1. all X-ray sources detected in observation 1 that are located outside the D_{25} ellipse. The number of these sources is $N_1 = 39$;
2. a distribution of simulated sources in the EPIC FOV of observation 1, obtained from a uniform spatial distribution of sources (which represents the uniform spatial distribution of AGNs) modified to take into account the incompleteness effect described in Sect. 6.1. We obtained this spatial distribution of sources as follows. We first generated a uniform spatial distribution of sources with fluxes given by the XLF of AGNs described in Sect. 6.2. Then, we selected sources with flux higher than that corresponding to the position of each source in the sensitivity map. We additionally selected sources with luminosity $>10^{37}$ erg s^{-1} in the energy range 2–10 keV that are located outside the D_{25} ellipse. With this method, we generated a sample of $N_2 = 10^4$ coordinate pairs (RA, Dec) of sources (see Fig. 9).

From the number of data points N_1 and N_2 of the two data sets, the significance level was calculated from the probability distribution of the quantity

$$Z_n \equiv \delta \sqrt{n}, \quad (9)$$

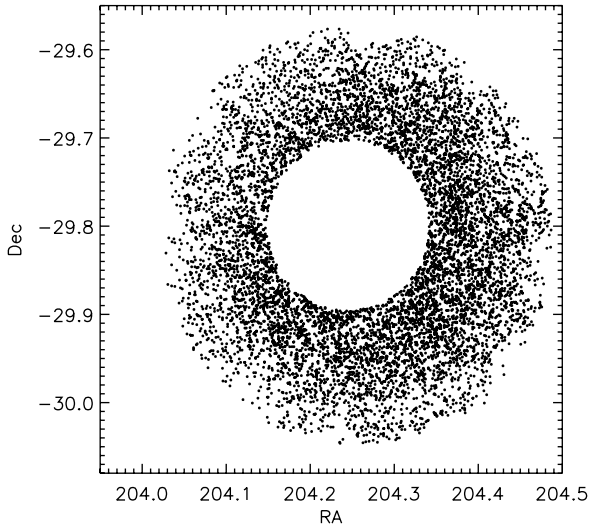

Fig. 9. Sample of 10^4 simulated sources, distributed over the EPIC field of view of observation 1 and located outside the D_{25} ellipse.

where $n = N_1N_2/(N_1 + N_2)$. The analytical formula for calculating of the probability that the two data samples come from the same distribution is accurate enough for large data sets with $n > 80$ (Fasano & Franceschini 1987). Since in our case $n \approx 39$, we needed to use Monte Carlo simulations. We generated many synthetic data samples simulating the uniformly distributed AGNs with the same method previously used to calculate sample 2; each of the synthetic data samples has the same number of sources as the observed data set 1 ($N_1 = 39$). For each data set we applied the 2D Kolmogorov-Smirnov test by comparing the synthetic data set with the set of 10^4 sources distributed across the EPIC FOV previously described, then we calculated the quantity Z_n using Eq. (9). The probability of the observed Z_n is given by the fraction of the times the simulated Z_n are larger than the observed Z_n.

Applying this statistical method to our data, we found a probability of 99.5% that the observed sample 1 and the simulated homogeneously distributed sample 2 are significantly different, which suggests a non-uniform distribution of the observed X-ray sources and therefore a possible correlation between the positions of these sources and the extended arms of M 83.

The incompleteness correction given by Eq. (3) is based on the hypothesis that sources are uniformly distributed. However, we have demonstrated that the X-ray sources located outside the D_{25} ellipse have a non-uniform distribution, hence the associated XLFs corrected for incompleteness of Fig. 8 (right column) are not reliable at low luminosities. Therefore we only considered the part of the XLFs with luminosities higher than the level at which the survey is 90% complete (to the right of the vertical black lines in Fig. 8). We found that the 90% complete XLFs of observations 1 and 3 (for which we have enough data points to find a good fit) are well fitted with a powerlaw with differential slopes $\alpha = -2.2 \pm 0.5$ (observation 1), and $\alpha = -1.7 \pm 0.4$ (observation 3), which are consistent with each other within errors. These are also consistent with the AGN slope of Cappelluti et al. (2009).

Assuming that the spatial distribution of AGNs and their number density are not subject to strong fluctuations on small angular scales corresponding to different directions in the M 83 field, the observed excess of sources (with respect to the AGN distribution) in the luminosity range $\sim 10^{37}$ to $\sim 2 \times 10^{38}$ erg s^{-1} (Fig. 8) can probably be ascribed to a population of XRBs located in the outer disc of M 83. The recent star-forming activity discovered by GALEX in this region indicates that a large portion of the observed X-ray sources are HMXBs. However, the observed XLF slope is steeper than the slope of the universal HMXB XLF inferred by Grimm et al. (2003). A possible explanation for the difference between the two slopes could be that the observed XLFs are the result of a mix of XRB populations formed after starbursts of different ages. An alternative explanation is that the mass distribution of the population of stars in the low-density regions of the outer disc of M 83 is described by a truncated initial mass function (IMF), whose existence was proposed to explain the production of fewer high-mass stars (compared to the standard IMF) in low-density environments (see e.g. Krumholz & McKee 2008; Meurer et al. 2009). The universality of the IMF is still a matter of debate (Bastian et al. 2010); in this context, a recent Subaru Hα observation of the outer disc of M 83 revealed O stars even in small clusters ($M \lesssim 10^3\ M_\odot$), which supports the hypothesis that the IMF is not truncated in low-density environments (Koda et al. 2012).

7. Summary

We presented an analysis of three *XMM-Newton* observations of M 83. We performed the source detection procedure separately for images of each observation, and we obtained a catalogue containing 189 sources.

Based on cross-correlations with other catalogues we identified counterparts for 103 sources, 12 of which were identified or classified as background objects and 5 as foreground stars (one as candidate CV). We performed spectral analysis of the sources with the largest number of counts, as well as studies of the X-ray variability and the hardness ratio diagrams. The spectral analysis of ULX No. 133 in observations 2 and 3 showed good fits with the standard IMBHs model as well as with accreting stellar-mass black-hole model, in agreement with the results obtained by Stobbart et al. (2006) from observation 1.

In Sect. 6 we presented the XLFs of sources in the 2–10 keV energy band, within and outside the D_{25} ellipse. We corrected the XLFs for incompleteness and subtracted the contribution of background AGNs from the total XLF to obtain the XLFs of XRBs. The XLF of the optical disc is well fitted with a powerlaw or a broken powerlaw, while the XLF of the outer disc is well fitted with a simple powerlaw. The broken powerlaw fit parameters agree (within the uncertainties) with the parameters found by SW03 with *Chandra*. From the *XMM-Newton* XLF, we obtained an $SFR \approx 3.1\ M_\odot\ \mathrm{yr}^{-1}$ in the optical disc of M 83, which agree with previous estimates obtained in other wavelengths.

The XLFs of these sources show an excess of sources (compared to the AGNs distribution) in the luminosity range $\sim 10^{37}$ to $\sim 2 \times 10^{38}$ erg s^{-1}. The application of the Kolmogorov-Smirnov test to the X-ray sources detected outside the D_{25} ellipse allowed us to find that this population of sources is significantly different from the population of background AGNs, which is supposed to have a homogeneous distribution. These results led us to suggest that a part of the X-ray sources observed outside the D_{25} ellipse belongs to the outer disc of M 83. The 90% complete XLFs of the outer disc are well fitted with a simple powerlaw with differential slope $\alpha = -2.2 \pm 0.5$ (observation 1), and $\alpha = -1.7 \pm 0.4$ (observation 3) steeper than the universal HMXB XLF discovered by Grimm et al. (2003). We proposed as a possible origin for the steep slope of the observed XLF that the observed XLFs are the result of a mix of XRB populations of different ages, or, as an alternative explanation, that the IMF in the low-density

regions of the outer disc of M 83 is truncated, as previously suggested by e.g. Krumholz & McKee (2008) and Meurer et al. (2009) to explain the low production of high-mass stars in low-density environments. Additional X-rays and UV observations of the outer disc of M 83, analysed with most effective methods such as the one used by Bodaghee et al. (2012) to measure the spatial cross-correlation of HMXBs and OB star-forming complexes in the Milky Way, will be fundamental to confirm our hypothesis.

Acknowledgements. We thank the referee Eric M. Schlegel for constructive comments, which helped to improve the manuscript. This research is funded by the Deutsche Forschungsgemeinschaft through the Emmy Noether Research Grant SA 2131/1. This research has made use of the SIMBAD database, operated at CDS, Strasbourg, France, and of the NASA/IPAC Extragalactic Database (NED), which is operated by the Jet Propulsion Laboratory, California Institute of Technology, under contract with the National Aeronautics and Space Administration. This publication has made use of data products from the Two Micron All Sky Survey, which is a joint project of the University of Massachusetts and the Infrared Processing and Analysis Center, funded by the National Aeronautics and Space Administration and the National Science Foundation. This research has made use of SAOImage DS9, developed by Smithsonian Astrophysical Observatory.

References

Arnaud, K. A. 1996, in Astronomical Data Analysis Software and Systems V, eds. G. H. Jacoby, & J. Barnes, ASP Conf. Ser., 101, 17
Bastian, N., Covey, K. R., & Meyer, M. R. 2010, ARA&A, 48, 339
Bigiel, F., Leroy, A., Seibert, M., et al. 2010, ApJ, 720, L31
Blair, W. P., & Long, K. S. 2004, ApJS, 155, 101
Blair, W. P., Winkler, P. F., & Long, K. S. 2012, ApJS, 203, 8
Bodaghee, A., Tomsick, J. A., Rodriguez, J., & James, J. B. 2012, ApJ, 744, 108
Boissier, S., Gil de Paz, A., Madore, B. F., et al. 2005, ApJ, 619, L83
Bresolin, F., Ryan-Weber, E., Kennicutt, R. C., & Goddard, Q. 2009, ApJ, 695, 580
Buccheri, R., Bennett, K., Bignami, G. F., et al. 1983, A&A, 128, 245
Cappelluti, N., Brusa, M., Hasinger, G., et al. 2009, A&A, 497, 635
Colbert, E. J. M., & Mushotzky, R. F. 1999, ApJ, 519, 89
Condon, J. J., Cotton, W. D., Greisen, E. W., et al. 1998, AJ, 115, 1693
Cowan, J. J., Roberts, D. A., & Branch, D. 1994, ApJ, 434, 128
Cruddace, R. G., Hasinger, G. R., & Schmitt, J. H. 1988, in European Southern Observatory Conference and Workshop Proceedings, eds. F. Murtagh, A. Heck, & P. Benvenuti, 28, 177
Davidge, T. J. 2010, ApJ, 718, 1428
de Vaucouleurs, G., de Vaucouleurs, A., Corwin, H. G., Jr., et al. 1992, VizieR Online Data Catalog: VII/137
Di Stefano, R., & Kong, A. K. H. 2003, ApJ, 592, 884
Di Stefano, R., Greiner, J., Murray, S., & Garcia, M. 2001, ApJ, 551, L37
Done, C., Gierliński, M., & Kubota, A. 2007, A&ARv, 15, 1
Dong, H., Calzetti, D., Regan, M., et al. 2008, AJ, 136, 479
Dopita, M. A., Blair, W. P., Long, K. S., et al. 2010, ApJ, 710, 964
Ehle, M., Pietsch, W., Beck, R., & Klein, U. 1998, A&A, 329, 39
Fabbiano, G. 2006, ARA&A, 44, 323
Fasano, G., & Franceschini, A. 1987, MNRAS, 225, 155
Feng, H., & Soria, R. 2011, New Astron. Rev., 55, 166
Gilfanov, M. 2004, MNRAS, 349, 146
Gladstone, J. C. 2010, International Conference on Binaries: In celebration of Ron Webbink's 65th Birthday, AIP Conf. Proc., 1314, 353
Gottlieb, D. M., & Upson, II, W. L. 1969, ApJ, 157, 611
Greiner, J. 2000, New Astron., 5, 137
Grimm, H.-J., Gilfanov, M., & Sunyaev, R. 2003, MNRAS, 339, 793
Guainazzi, M. 2012, *XMM-Newton* Calibration Technical Note; XMM-SOC-CAL-TN-0018
Güdel, M. 2002, Roy. Soc. London Phil. Trans. Ser. A, 360, 1935
Harris, J., Calzetti, D., Gallagher, III, J. S., Conselice, C. J., & Smith, D. A. 2001, AJ, 122, 3046
Hughes, J. P. 1994, ApJ, 427, L25
Immler, S., Vogler, A., Ehle, M., & Pietsch, W. 1999, A&A, 352, 415
Irwin, M., Maddox, S., & McMahon, R. 1994, IEEE Spectrum, 2, 14
Johnson, H. L. 1966, ARA&A, 4, 193
Jones, C. 1977, ApJ, 214, 856
Jones, D. H., Saunders, W., Colless, M., et al. 2004, MNRAS, 355, 747
Kahabka, P., & van den Heuvel, E. P. J. 1997, ARA&A, 35, 69
King, A. R. 2009, MNRAS, 393, L41
Koda, J., Yagi, M., Boissier, S., et al. 2012, ApJ, 749, 20
Krautter, J., Zickgraf, F.-J., Appenzeller, I., et al. 1999, A&A, 350, 743
Krumholz, M. R., & McKee, C. F. 2008, Nature, 451, 1082
Kudritzki, R.-P., & Puls, J. 2000, ARA&A, 38, 613
Long, K. S., Blair, W. P., Godfrey, L. E. H., et al. 2012, ApJ, 756, 18
Maccacaro, T., Gioia, I. M., Wolter, A., Zamorani, G., & Stocke, J. T. 1988, ApJ, 326, 680
Maddox, L. A., Cowan, J. J., Kilgard, R. E., et al. 2006, AJ, 132, 310
Makishima, K., Maejima, Y., Mitsuda, K., et al. 1986, ApJ, 308, 635
Meurer, G. R., Wong, O. I., Kim, J. H., et al. 2009, ApJ, 695, 765
Miller, M. C., & Colbert, E. J. M. 2004, Int. J. Mod. Phys. D, 13, 1
Mineo, S., Gilfanov, M., & Sunyaev, R. 2012, MNRAS, 419, 2095
Misanovic, Z., Pietsch, W., Haberl, F., et al. 2006, A&A, 448, 1247
Monet, D. G., Levine, S. E., Canzian, B., et al. 2003, AJ, 125, 984
Ohashi, T., Makishima, K., Tsuru, T., et al. 1990, ApJ, 365, 180
Okada, K., Mitsuda, K., & Dotani, T. 1997, PASJ, 49, 653
Owen, R. A., & Warwick, R. S. 2009, MNRAS, 394, 1741
Peacock, J. A. 1983, MNRAS, 202, 615
Pietsch, W., Misanovic, Z., Haberl, F., et al. 2004, A&A, 426, 11
Poutanen, J., Lipunova, G., Fabrika, S., Butkevich, A. G., & Abolmasov, P. 2007, MNRAS, 377, 1187
Primini, F. A., Forman, W., & Jones, C. 1993, ApJ, 410, 615
Puls, J., Vink, J. S., & Najarro, F. 2008, A&ARv, 16, 209
Raymond, J. C., & Smith, B. W. 1977, ApJS, 35, 419
Roberts, T. P., Warwick, R. S., Ward, M. J., Goad, M. R., & Jenkins, L. P. 2005, MNRAS, 357, 1363
Roberts, T. P., Levan, A. J., & Goad, M. R. 2008, MNRAS, 387, 73
Robrade, J., & Schmitt, J. H. M. M. 2010, A&A, 516, A38
Rogstad, D. H., Lockhart, I. A., & Wright, M. C. H. 1974, ApJ, 193, 309
Rosner, R., Golub, L., & Vaiana, G. S. 1985, ARA&A, 23, 413
Rumstay, K. S., & Kaufman, M. 1983, ApJ, 274, 611
Saha, A., Thim, F., Tammann, G. A., Reindl, B., & Sandage, A. 2006, ApJS, 165, 108
Sako, M., Liedahl, D. A., Kahn, S. M., & Paerels, F. 1999, ApJ, 525, 921
Schild, R. E. 1977, AJ, 82, 337
Schröder, C., & Schmitt, J. H. M. M. 2007, A&A, 475, 677
Schröder, C., Hubrig, S., & Schmitt, J. H. M. M. 2008, A&A, 484, 479
Scoville, N., Aussel, H., Brusa, M., et al. 2007, ApJS, 172, 1
Skrutskie, M. F., Cutri, R. M., Stiening, R., et al. 2006, AJ, 131, 1163
Smith, R. K., Brickhouse, N. S., Liedahl, D. A., & Raymond, J. C. 2001, ApJ, 556, L91
Soria, R., & Wu, K. 2002, A&A, 384, 99
Soria, R., & Wu, K. 2003, A&A, 410, 53
Soria, R., Long, K. S., Bianchi, L., et al. 2010, The Astronomer's Telegram, 3092, 1
Soria, R., Kuntz, K. D., Winkler, P. F., et al. 2012, ApJ, 750, 152
Stobbart, A.-M., Roberts, T. P., & Wilms, J. 2006, MNRAS, 368, 397
Tauris, T. M., & van den Heuvel, E. P. J. 2006, Formation and evolution of compact stellar X-ray sources, eds. W. H. G., Lewin, & M. van der Klis, 623
Thilker, D. A., Bianchi, L., Boissier, S., et al. 2005, ApJ, 619, L79
Thim, F., Tammann, G. A., Saha, A., et al. 2003, ApJ, 590, 256
Tilanus, R. P. J., & Allen, R. J. 1993, A&A, 274, 707
Treves, A., Maraschi, L., & Abramowicz, M. 1988, PASP, 100, 427
Trinchieri, G., Fabbiano, G., & Palumbo, G. G. C. 1985, ApJ, 290, 96
Tully, R. B. 1988, Nearby galaxies catalog
Turner, T. J., Weaver, K. A., Mushotzky, R. F., Holt, S. S., & Madejski, G. M. 1991, ApJ, 381, 85
Vaiana, G. S., Cassinelli, J. P., Fabbiano, G., et al. 1981, ApJ, 245, 163
van den Heuvel, E. P. J., Bhattacharya, D., Nomoto, K., & Rappaport, S. A. 1992, A&A, 262, 97
van Paradijs, J. 1998, in The Many Faces of Neutron Stars., eds. R. Buccheri, J. van Paradijs, & A. Alpar, NATO ASIC Proc., 515, 279
Vaughan, B. A., van der Klis, M., Wood, K. S., et al. 1994, ApJ, 435, 362
Vignali, C., Comastri, A., Cappi, M., et al. 1999, ApJ, 516, 582
Walter, R., & Fink, H. H. 1993, A&A, 274, 105
White, N. E., & Carpenter, G. F. 1978, MNRAS, 183, 11
White, N. E., & Marshall, F. E. 1984, ApJ, 281, 354
White, N. E., Nagase, F., & Parmar, A. N. 1995, in X-ray Binaries, 1
Wofford, A., Leitherer, C., & Chandar, R. 2011, ApJ, 727, 100

Pages 15 to 19 are available in the electronic edition of the journal at http://www.aanda.org

Appendix A: Classification and identification of the *XMM-Newton* sources

A.1. Foreground stars

Sources Nos. 21, 143, 182, and 174. Using the criteria in Sect. 5.1, we classified sources Nos. 21, 143, 182, and 174 as foreground stars according to their optical and infrared properties (Figs. 4, 6), and their optical-to-X-ray ratios as a function of the hardness ratios (Fig. 5). Although the hardness ratio criterion $HR_3 \lesssim -0.4$ of source No. 174 is not fulfilled, we classified this source as a foreground star because of the large uncertainty of the hardness ratio (see Fig. 5).

Source No. 24 has optical and infrared counterparts and $\log_{10}(f_x/f_{opt}) < -1$, but violates the hardness ratio HR_2 criterion (see Fig. 5). The optical counterpart is bright ($m_{B,No.24} = 14.1$), and the $B-R$ and $J-K$ colours are consistent with those of foreground stars (Figs. 4 and 6), thus this source most likely belongs to the Milky Way. It has been detected in observations 1 and 2 in all three EPIC cameras. In all cases, source No. 24 shows hard HR_2 (Fig. 5, left panel), inconsistent with the expected X-ray spectra of foreground stars. The properties of the optical companion and the hard X-ray spectra may indicate a cataclysmic-variable nature for this source. This class of sources can show short- and long-term time variability, therefore we produced the X-ray lightcurve in the energy range 0.5–4.5 keV to give more evidence for this identification. However, the resulting X-ray lightcurve (with a bin-time of 2000 s) shows neither short- nor long-term variability.

A.2. Sources that are not foreground stars

Sources Nos. 12, 137, 164, and 189 coincide with ROSAT sources H2, H31, H34 and H36. They were classified by Immler et al. (1999) as foreground stars based on positional coincidences with optical sources of the *APM Northern Sky Catalogue* (Irwin et al. 1994). We found possible optical counterparts in the USNO-B1 catalogue for source No. 164 (USNO−B1 0601 − 0299090) and source No. 12 (USNO−B1 0602 − 0301227). However, their X-ray-to-optical flux ratios (Eq. (2)) are $\log(f_x/f_{opt}) \approx 0.10$ and 0.11 respectively (f_{opt} of both sources was calculated using visual magnitude), hence the foreground star classification for these sources is ruled out. The refined positions of sources Nos. 137 and 189 obtained with *XMM-Newton*, allowed us to exclude their association with the optical counterparts proposed by Immler et al. (1999). Source No. 189 can be associated with a new optical counterpart, USNO−B1 0600 − 0300832, which is ∼3 orders of magnitude fainter than the previous one (USNO−B1 0600 − 0300831). However, the new X-ray-to-optical flux ratio is $\log(f_x/f_{opt}) \approx 0.68$ (f_{opt} was calculated using visual magnitude), too high for a foreground star (see Sect. A.3). Hardness ratios of sources Nos. 164 and 137 are consistent with a powerlaw or disk-blackbody spectrum. Therefore, the spectra of these sources are too hard to be classified as foreground stars.

A.3. Background objects

We found radio counterparts of the sources Nos. 20, 37, and 189 and classified them as AGN candidates for the first time.

Source No. 20 is located outside the D_{25} ellipse ($D_{25} = 11.5'$; Tully 1988) at ∼0.41° from the centre of the galaxy. It coincides with the radio source NVSS J133618−301459. We detected this source with *XMM-Newton* in observations 2 and 3 in the outer disc of M 83. Source No. 20 shows a significant long-term variability (Table 3), and the hardness ratios are roughly consistent with a spectrum described by an APEC model with a temperature of $kT_{apec} \sim 0.5$ keV ($HR_2 = -0.2 \pm 0.1$; $HR_3 = -0.81 \pm 0.11$). Therefore, source No. 20 can be classified as an AGN candidate (with a soft spectral component) or an SNR candidate. The distance of this source from the nuclear region of M 83 of ∼32 kpc rather indicates that source No. 20 does not belong to the galaxy, therefore it is more likely an AGN than an SNR candidate.

Sources Nos. 37 and 189 coincide with the radio sources NVSS J133630−301651 and NVSS J133805−295748, respectively. Source No. 189 was previously classified as a foreground star by Immler et al. (1999) (see Sect. A.2). We detected these sources with *XMM-Newton* in observation 3. Their hardness ratios are consistent with a spectrum described with a powerlaw or disc-blackbody model (No. 37: $HR_2 = 0.62 \pm 0.12$; $HR_3 = -0.37 \pm 0.13$; No. 189: $HR_2 = 0.07 \pm 0.10$; $HR_3 = -0.25 \pm 0.12$). Therefore, they can be classified as AGN candidates.

A.4. X-ray binaries

Source No. 81 coincides with the *Chandra* source [SW03] 33, classified as an accreting X-ray pulsar, with a hard spectrum ($\Gamma \approx 1.7$) and a spin period of 174.9 s.

We observed source No. 81 in all *XMM-Newton* observations. The hardness ratios are consistent with an absorbed powerlaw spectrum, and this source shows a significant long-term X-ray variability ($V_f = 2.5$, $S = 3.0$, Table 3). We applied a Fourier transform periodicity search and a Z_n^2 analysis (Sect. 4.1), which did not reveal any significant periodicity. We calculated the upper-limit on the pulsed fraction (defined as the semi-amplitude of the sinusoidal modulation divided by the mean count rate) using the procedure described by Vaughan et al. (1994). The upper limit on the pulsed fraction obtained from the combined PN and MOS events of observation 1 is 16% at the 99% confidence level. This upper limit is marginally compatible with the pulsed fraction of (50 ± 15)% of source [SW03] 33.

Source No. 120 corresponds to the X-ray source [SW03] 113. Using the spectral properties and the 201.5 s periodicity detected with *Chandra*, SW03 classified source [SW03] 113 as an XRB in a soft state.

We observed source No. 120 with *XMM-Newton* in observations 1 and 3. The hardness ratios of this source are consistent with an absorbed powerlaw spectrum with $N_H \sim 5 \times 10^{21}$ cm^{-2} and $\Gamma \sim 1.5$. Similarly to source No. 81, a Fourier transform periodicity search and a Z_n^2 analysis did not reveal any significant periodicity. At the 99% confidence level, the upper limit on the pulsed-fraction of source No. 120 derived from the MOS events is 49%. This upper limit is compatible with the (50±19)% pulsed fraction of [SW03] 113.

A.5. Supernova remnant candidates

Source No. 79. The position of this source corresponds to the position of the ROSAT source H15 (Immler et al. 1999) and the *Chandra* source [SW03] 27. The *Chandra* spectrum shows emission lines, suggesting the possibility of emission from optically thin thermal plasma, and has been fitted by SW03 with

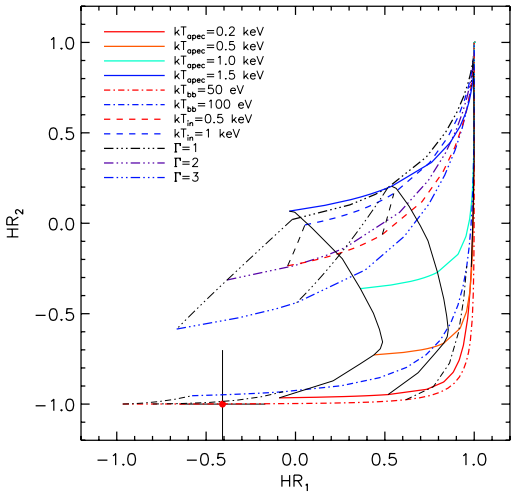

Fig. A.1. Hardness-ratio diagram of source No. 91 observed with *XMM-Newton*. Thick lines are different spectral models as function of the $N_{\rm H}$, thin lines are different column densities $N_{\rm H}$ (from left to right: 10^{20}, 10^{21}, 10^{22} cm^{-2}) as a function of the spectral parameters.

an absorbed powerlaw with $\Gamma \sim 1.4$ and $N_{\rm H} \sim 7 \times 10^{20}$ cm^{-2}. SW03 classified this source as a young SNR candidate. Another possible explanation for the hard powerlaw spectrum with superposition of emission lines of [SW03] 27 is that the source is an XRB surrounded by a photoionised nebula (SW03). However, XRBs showing these spectral properties usually have a higher absorbing column density than that of [SW03] 27 (see e.g. Sako et al. 1999).

The *XMM-Newton* hardness ratios of source No. 79 below 2 keV are consistent with an APEC model with temperature $kT_{\rm apec} \gtrsim 1.5$ keV, while at higher energies the hardness ratios are consistent with a powerlaw with photon index ∼2. The spectral shape of source No. 79 derived from *XMM-Newton* hardness-ratio diagrams agrees with the X-ray spectrum of [SW03] 27 presented by SW03 (see Fig. 6 in SW03) and can be interpreted as an SNR exhibiting both a thin-thermal emission (below ∼2 keV) and an additional hard component, which dominates at energies above ∼2 keV. Also, source No. 79 does not show any significant long-term variability (see Table 3).

A.6. Super-soft source candidates

Source No. 91 coincides with *Einstein* source 3 (Trinchieri et al. 1985) and *Chandra* source [SW03] 55 classified by Di Stefano & Kong (2003) as an SSS candidate (source M 83-50 in Di Stefano & Kong 2003). Di Stefano & Kong (2003) fitted the X-ray spectrum of M 83-50 with an absorbed blackbody with a temperature of $kT_{\rm bb} = 66^{+13}_{-24}$ eV, a column density of $N_{\rm H} = 2.4^{+7.4}_{-2.4} \times 10^{20}$ cm^{-2}, and a luminosity of $L_{\rm x} = 2.8 \times 10^{37}$ erg s^{-1} (0.3–7 keV, $d = 4.5$ Mpc).

We detected source No. 91 in observation 1, where the hardness ratios are consistent with a blackbody spectrum (with column density in the range ≈10^{20}–10^{21} cm^{-2}) and marginally compatible with an APEC spectrum with temperature in the range ≈0.2–0.5 keV (Fig. A.1). Source No. 91 has a 0.2–4.5 keV luminosity of $L_{\rm x} = (2.2 \pm 0.2) \times 10^{37}$ erg s^{-1} and does not show any significant variability compared to the *Chandra* observation.

A.7. Ultra-luminous X-ray sources

Two ULXs have been discovered in M 83: H2 (Trinchieri et al. 1985), and a transient ULX discovered with *Chandra* on 23 December 2010 with a luminosity of $L_{\rm x} \sim 4 \times 10^{39}$ erg s^{-1} (0.3–10 keV) by Soria et al. (2010), and classified as an accretion-powered black hole with mass $M_{\rm BH} \approx 40$–$100\ M_{\odot}$ (Soria et al. 2012). This ULX has not been detected in the *XMM-Newton* data. Soria et al. (2012) measured an upper limit to the X-ray luminosity of ∼10^{37} erg s^{-1} (0.3–10 keV) from the three *XMM-Newton* observations.

Source No. 133. We observed the ULX as source No. 133 in all *XMM-Newton* observations. Ehle et al. (1998) and Immler et al. (1999) found a faint extended optical source within the error circle of the ROSAT source position. Roberts et al. (2008) used HST images in three Advanced Camera for Survey (ACS) filters to find the counterparts to six ULXs in different galaxies. For the ULX in M 83, they compared the optical position with the X-ray position from a *Chandra* High Resolution Camera for Imaging (HRC-I) observation. They detected a counterpart to the ULX with magnitudes $B = 25.66 \pm 0.13$, $V = 25.36 \pm 0.17$. They also noticed that the ULX is located at ∼5″ from the centre of a background galaxy, and although the latter is outside the error circle, Roberts et al. (2008) did not completely rule out a possible association between the ULX and the background galaxy.

Stobbart et al. (2006) reported the *XMM-Newton* spectral analysis of source No. 133 during observation 1. They found that the X-ray spectrum is well fitted with a cool disc-blackbody ($kT_{\rm in} \sim 0.2$ keV) plus a powerlaw ($\Gamma \sim 2.5$), or with a cool blackbody ($kT_{\rm bb} \sim 0.2$ keV) plus a warm disc-blackbody ($kT_{\rm in} \sim 1.1$ keV). The first spectral model is the standard IMBH model, where the low disc temperature is due to a black hole with mass of ∼1000 $M_{\odot}$, while the origin of the powerlaw component is still not clear (see Roberts et al. 2005). Instead, the spectral parameters obtained with the second spectral model suggest that No. 133 is a stellar-mass black hole accreting close to the Eddington limit. In this model, the cool blackbody component represents the optically thick wind from the stellar-mass black-hole accreting at or above the Eddington limit, while the high temperature of the disc follows the standard trend $L_{\rm x} \propto T^4$ shown by the Galactic stellar-mass black-hole binaries.

We analysed all *XMM-Newton* observations of the ULX No. 133 and fitted the PN, MOS1 and MOS2 spectra simultaneously with a model assuming an IMBH (PHABS*[DISKBB + POWERLAW] in XSPEC), and a model assuming a stellar-mass BH (PHABS*[BBODY + DISKBB]). We used two absorption components: the Galactic absorption column density ($N_{\rm H} = 3.69 \times 10^{20}$ cm^{-2}) and the absorption within M 83 plus the intrinsic column density of the ULX. In all fits we obtained a good fit with both spectral models with the resulting spectral parameters in agreement with those obtained by Stobbart et al. (2006) from observation 1. However, the spectral parameters in observation 3 are only poorly constrained due to the poor statistics (only MOS1 and MOS2 data were available for this observation). Therefore, we fitted the spectrum of observation 3 with a single component model and found that an absorbed powerlaw can adequately fit the data (Fig. A.2, Table A.1).

A.8. Hard sources

A.8.1. New classifications

Source No. 16 coincides with the ROSAT source H3 discovered by Immler et al. (1999). This source is located outside the optical disc of M 83, and its position overlaps with the outer disc of M 83 observed by GALEX (e.g. Thilker et al. 2005).

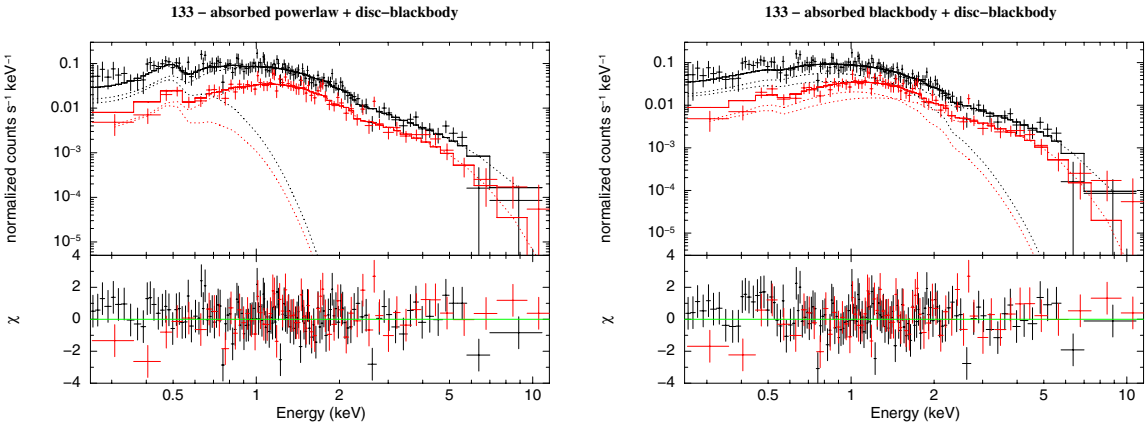

Fig. A.2. EPIC counts spectra, together with residuals in units of standard deviations for source No. 133 detected in the observation 2. *Left panel* shows the fit with an absorbed cool disc-blackbody plus hard powerlaw, while the *right panel* shows the fit with an absorbed cool blackbody plus a warm disc-blackbody (see Table A.1).

Table A.1. Best-fitting parameters of the X-ray spectra of source No. 133 (errors at 90% confidence level).

	Obs. 2		Obs. 3
Model	POWERLAW + DISKBB	BBODY + DISKBB	POWERLAW
$N_{\rm H}$ (10^{22} cm^{-2})	$0.30^{+0.12}_{-0.09}$	≤0.03	0.12 ± 0.05
Γ or $kT_{\rm bb}$ (keV)	$2.64^{+0.19}_{-0.18}$	$0.30^{+0.02}_{-0.04}$	$2.6^{+0.3}_{-0.2}$
Norm.	$4.4^{+1.0}_{-0.4} \times 10^{-4}$	$3.6^{+0.8}_{-0.9} \times 10^{-6}$	$1.4^{+0.3}_{-0.3} \times 10^{-4}$
$kT_{\rm in}$ (keV)	$0.09^{+0.02}_{-0.03}$	$1.4^{+0.3}_{-0.2}$	
Norm.	$4.8^{+47.4}_{-4.4} \times 10^{3}$	$7.8^{+9.7}_{-3.1} \times 10^{-3}$	
$\hat{\chi}^2_\nu$ (d.o.f.)	0.946 (184)	0.994 (184)	0.918 (62)
$F_{\rm x}$ (0.2–12 keV, erg cm^{-2} s^{-1})	$8.9^{+57.5}_{-3.7} \times 10^{-13}$	$8.5^{+24.5}_{-5.2} \times 10^{-13}$	$3.7^{+2.2}_{-1.4} \times 10^{-13}$
$L_{\rm x}$ (d = 4.5 Mpc, erg s^{-1})	$1.3^{+20.4}_{-0.6} \times 10^{40}$	$2.2^{+6.3}_{-1.3} \times 10^{39}$	$2.2^{+0.9}_{-0.5} \times 10^{39}$

Table A.2. Best-fitting parameters of sources No. 16, 61, 103, 126, 153.

Source	Parameters						Analysed data	
	$N_{\rm H}$ (10^{21} cm^{-2})	Γ	Norm.	$\hat{\chi}^2_\nu$ (d.o.f.)	$F_{\rm x}$ (erg cm^{-2} s^{-1})	$L_{\rm x}$ (erg s^{-1})	Obs.	Instrument
16	$0.8^{+0.4}_{-0.3}$	$2.6^{+0.3}_{-0.3}$	$4.1^{+0.9}_{-0.7} \times 10^{-5}$	0.928 (38)	$1.4^{+0.8}_{-0.5} \times 10^{-13}$	$6.3^{+2.7}_{-1.3} \times 10^{38}$	1	PN, MOS1, MOS2
61	$2.01^{+0.75}_{-0.65}$	$2.4^{+0.3}_{-0.3}$	$2.9^{+0.9}_{-0.6} \times 10^{-5}$	1.04 (36)	$8.0^{+6.8}_{-3.7} \times 10^{-14}$	$4.3^{+1.4}_{-0.6} \times 10^{38}$	1	PN, MOS1, MOS2
103	$0.7^{+1.0}_{-0.7}$	$1.8^{+0.4}_{-0.4}$	$3.7^{+1.8}_{-1.2} \times 10^{-5}$	0.876 (19)	$2.2^{+3.3}_{-1.3} \times 10^{-13}$	$6.6^{+6.7}_{-2.7} \times 10^{38}$	1	PN, MOS2
126	$0.01^{+0.56}_{-0.01}$	$1.8^{+0.4}_{-0.2}$	$8.8^{+2.7}_{-1.2} \times 10^{-6}$	0.743 (17)	$6.3^{+3.1}_{-2.9} \times 10^{-14}$	$1.5^{+0.8}_{-0.4} \times 10^{38}$	2	PN, MOS1, MOS2
153	$0 < N_{\rm H} \leq 1.5$	$1.4^{+0.7}_{-0.3}$	$7.6^{+5.8}_{-1.6} \times 10^{-6}$	1.027 (15)	$8.8^{+13.7}_{-6.2} \times 10^{-14}$	$2.1^{+3.3}_{-1.2} \times 10^{38}$	1	PN, MOS1, MOS2

Notes. We fitted the spectra with an absorbed powerlaw. Γ is the powerlaw photon-index, $F_{\rm x}$ is the absorbed flux in the energy range 0.2–12 keV, $L_{\rm x}$ is the X-ray luminosity in the same energy range of $F_{\rm x}$ (errors at 90% confidence level).

We detected source No. 16 in all *XMM-Newton* observations, but only in observation 1 was it bright enough to allow spectral analysis. The spectrum can be well fitted with an absorbed powerlaw with $\Gamma = 2.6^{+0.3}_{-0.3}$, compatible with that of an XRB or an AGN (see Table A.2). Source No. 16 shows a significant long-term variability ($S = 9.5$) with a variability factor of $V_{\rm f} = 10.6 \pm 0.3$ (Table 3). It also shows a significant variability within observation 1, with a variability factor of $V_{\rm f} = 6.6 \pm 4.5$ and significance $S = 4.0$.

Source No. 61 is in the field of view of *XMM-Newton* during observation 1, where it shows an X-ray luminosity of $L_{\rm x} \approx 4 \times 10^{38}$ erg s^{-1} (see Table A.2). It has not been previously detected in X-ray, optical, radio, infrared, or UV. The X-ray spectrum is well fitted with an absorbed powerlaw with $\Gamma = 2.4^{+0.3}_{-0.3}$ or a disc-blackbody model with temperature $kT_{\rm in} = 0.82^{+0.13}_{-0.11}$ keV (Table A.2). Source No. 61 shows a significant long-term variability ($S = 8.6$) with a variability factor of $V_{\rm f} = 4.3 \pm 0.1$ (Table 3).

Source No. 103 is located at a distance of ∼6″ from a radio source (6 in Cowan et al. 1994, 36 in Maddox et al. 2006), and at 1.6″ from the *Chandra* source [SW03] 84, which shows hardness ratios compatible with a powerlaw or a disc-blackbody spectrum.

Table A.3. Best-fitting parameters of sources Nos. 97, 106, 107, 108, 114, and 129.

Source	Parameters						Analysed data	
	N_H (10^{21} cm^{-2})	Γ	Norm.	$\hat{\chi}^2_\nu$ (d.o.f.)	F_x (erg cm^{-2} s^{-1})	L_x (erg s^{-1})	Obs.	Instrument
97	$4.4^{+1.1}_{-0.9}$	$2.4^{+0.3}_{-0.3}$	$7.4^{+2.3}_{-1.7} \times 10^{-5}$	1.03 (45)	$1.7^{+1.5}_{-0.8} \times 10^{-13}$	$1.1^{+0.4}_{-0.2} \times 10^{39}$	1	PN, MOS2
106	$0.3^{+0.5}_{-0.3}$	$1.8^{+0.4}_{-0.3}$	$8.3^{+2.5}_{-1.9} \times 10^{-6}$	1.38 (27)	$5.4^{+5.0}_{-2.7} \times 10^{-14}$	$1.5^{+1.0}_{-0.5} \times 10^{38}$	1	PN, MOS1, MOS2
107	$3.3^{+1.0}_{-0.8}$	$2.8^{+0.4}_{-0.3}$	$3.9^{+1.4}_{-1.0} \times 10^{-5}$	0.821 (43)	$6.5^{+6.5}_{-3.3} \times 10^{-14}$	$6.6^{+5.1}_{-2.3} \times 10^{38}$	1	PN, MOS1, MOS2
108	$3.3^{+0.7}_{-0.6}$	$2.7^{+0.3}_{-0.2}$	$8.0^{+1.9}_{-1.5} \times 10^{-5}$	0.91 (68)	$1.5^{+0.9}_{-0.6} \times 10^{-13}$	$1.3^{+0.5}_{-0.3} \times 10^{39}$	1	PN, MOS1
114	$4.5^{+3.8}_{-3.1}$	$1.7^{+0.4}_{-0.4}$	$1.8^{+1.3}_{-0.7} \times 10^{-5}$	0.952 (20)	$9.6^{+24.0}_{-6.9} \times 10^{-14}$	$3.5^{+5.68}_{-1.8} \times 10^{38}$	1	PN, MOS1, MOS2
129	$5.4^{+4.3}_{-3.0}$	$2.0^{+0.6}_{-0.5}$	$2.0^{+1.9}_{-0.9} \times 10^{-5}$	0.867 (18)	$6.7^{+20.9}_{-5.1} \times 10^{-14}$	$3.1^{+5.4}_{-1.4} \times 10^{38}$	1	PN, MOS1

Notes. We fitted the spectra with an absorbed powerlaw. Γ is the powerlaw photon-index, F_x is the absorbed flux in the energy range 0.2–12 keV, L_x is the X-ray luminosity in the same energy range of F_x (errors at 90% confidence level).

We detected source No. 103 only in the *XMM-Newton* observation 2, with a flux of $(2.23^{+3.26}_{-1.34}) \times 10^{-13}$ erg cm^{-2} s^{-1} (0.2–12 keV). The X-ray spectrum is well fitted with an absorbed powerlaw with $\Gamma = 1.8^{+0.4}_{-0.4}$ (Table A.2). We did not detect source No. 103 in observations 1 and 3, thus we calculated the flux upper-limits and we found a significant ($S = 7.2$) long-term variability, with a variability factor of $V_f = 12.78 \pm 0.12$ (Table 3, Fig. 2).

Source No. 126 coincides with X-ray source 30 (Ehle et al. 1998) discovered with ROSAT. Source No. 126 also cross-correlates with the optical counterpart USNO-B1 0599 − 0300335, but the ratio $\log_{10}(F_x/F_{opt})$ does not match the criteria previously specified to classify foreground stars. Source No. 126 is located outside the optical disc of M 83, and its position overlaps with an extended arm of the galaxy.

We observed source No. 126 in all *XMM-Newton* observations. The X-ray spectra extracted from each observation can be well fitted with an absorbed powerlaw with $\Gamma \approx 1.8$ and the flux is consistent with that measured by Ehle et al. (1998) (Table A.2).

Source No. 153 is detected in all *XMM-Newton* observations, and has not been previously detected in X-rays, optical, radio, infrared, or UV bands. It is located in the extended arms observed by *GALEX*, ≈10′ away from the nuclear region of M 83.

The spectra extracted from each observation can be well fitted with an absorbed powerlaw with $\Gamma \approx 1.5$, suggesting an XRB nature for this source (see Table A.2).

A.8.2. Identifications

Source No. 60 correlates with the *Chandra* source [SW03] 5 SW03 suggested that this source is an XRB candidate.

We observed source No. 60 in all *XMM-Newton* observations. The source shows a significant long-term variability ($V_f = 2.4$, $S = 3.8$, Table 3) with respect to the *Chandra* observation. X-ray colours of No. 60 are consistent with a powerlaw or disc-blackbody spectrum, in agreement with the spectral analysis of SW03.

Source No. 80 correlates with the *Chandra* source [SW03] 31. From the spectral properties, SW03 suggested that [SW03] 31 is an XRB candidate.

We observed source No. 80 with *XMM-Newton* in observation 1. The hardness ratios are consistent with a powerlaw or disc-blackbody spectrum with column density of $\sim 10^{21}$ cm^{-2}

Source No. 92 coincides with the *Chandra* source [SW03] 60. SW03 suggested that No. 92 is a XRB candidate because of its hard spectrum ($\Gamma \sim 1.6$).

We observed source No. 92 with *XMM-Newton* in observation 1. The hardness ratios are consistent with a spectrum described by an absorbed powerlaw model with $\Gamma \sim 2$. Source No. 92 also shows a high long-term variability by a factor of $V_f = 2.7$, with a variability significance of $S = 4.3$ (see Table 3).

Source No. 97 coincides with the *Chandra* source [SW03] 72 and with a ROSAT source (source 7 in Ehle et al. 1998 and source H20 in Immler et al. 1999).

We observed source No. 97 in all *XMM-Newton* observations. The spectra extracted from each observation can be well fitted with an absorbed powerlaw or a disc-blackbody model (Table A.3), with spectral parameters in agreement with the spectral analysis of SW03. Source No. 97 shows a significant long-term variability between *XMM-Newton* and *Chandra* observations ($V_f = 2.8 \pm 0.1$, $S = 6.6$; Table 3). Within observation 1 we found a variability of $V_f = 6.4 \pm 2.7$ with a significance of $S = 4.8$.

Source No. 99 coincides with the *Chandra* source [SW03] 73, and it is associated with the radio source MCK 34 (Maddox et al. 2006). located in a HII region (RK 137, Rumstay & Kaufman 1983). From a spectral study, SW03 proposed that [SW03] 73 is more likely an XRB than a young SNR.

We observed source No. 99 with *XMM-Newton* in observations 2 and 3. The source shows a significant variability ($S = 5.0$), with a variability factor of $V_f = 15.3$ (Table 3). and the hardness ratios are consistent with an absorbed powerlaw or disk-blackbody spectrum.

Source No. 106 corresponds to the X-ray source H25 observed by Immler et al. (1999) in a ROSAT observation and the *Chandra* source [SW03] 85.

We observed source No. 106 in all the observations. During observation 1 the source was bright enough to allow spectral analysis. The spectrum can be well fitted with an absorbed powerlaw (see Table A.3), with spectral parameters in agreement with those previously obtained by SW03.

Source No. 107 was detected by Ehle et al. (1998) (source 9) and Immler et al. (1999) (source H26) in ROSAT (PSPC and HRI) observations. Immler et al. (1999) found that H26 coincides with a compact radio source (source 8 in Cowan et al. 1994), and with a giant HII region (Rumstay & Kaufman 1983). Hence, they classified this source as an SNR candidate. Moreover, also the observation of Hα and Hβ emission anti-coincident with HI emission (Tilanus & Allen 1993) supports the SNR hypothesis. Source No. 107 was also observed in 2000 April 29 by *Chandra* (source [SW03] 86). From a spectral analysis, SW03 proposed that No. 110 is more likely an XRB (BH candidate) than an SNR.

We detected source No. 107 in all *XMM-Newton* observations with a luminosity of $\sim 7 \times 10^{38}$ erg s^{-1}. In observations 1 and 3 the source was bright enough to allow spectral analysis. The spectra can be well fitted with an absorbed powerlaw or a disc-blackbody (see Table A.3). The obtained spectral parameters are consistent with those previously found by SW03 with *Chandra*. Source No. 107 shows a significant long-term variability between *XMM-Newton* observations ($V_{\rm f} = 1.97 \pm 0.12$, $S = 5.1$).

Source No. 108 was first detected in X-rays by Trinchieri et al. (1985) (source 4) with the *Einstein* satellite and by Ehle et al. (1998) (source 8) and Immler et al. (1999) (source H27) with ROSAT. It also coincides with the *Chandra* source [SW03] 88.

We observed source No. 108 in all *XMM-Newton* observations. During observation 1 source No. 108 was in the centre of the field of view, providing enough statistic to allow spectral analysis. We extracted the PN and MOS1 spectra (the position of source No. 108 was in a gap of MOS2) and we found that an absorbed powerlaw or an absorbed disc-blackbody provide acceptable fits (Table A.3), with spectral parameters consistents with those obtained by SW03. Source No. 108 shows a significant long-term X-ray variability ($V_{\rm f} = 1.4 \pm 0.1$, $S = 3.3$, Table 3), and during observation 1 we found a variability of $V_{\rm f} = 4.2 \pm 1.5$, with a significance of $S = 4.4$.

Source No. 114 coincides with the *Chandra* source [SW03] 104.

We observed source No. 114 in all *XMM-Newton* observations. During observation 1 source No. 114 was in the centre of the field of view, providing enough statistics to allow a spectral analysis. The spectrum is well fitted with an absorbed powerlaw with spectral parameters consistent with those found by SW03 with *Chandra* (see Table A.3). Source No. 114 also shows a significant long-term variability ($V_{\rm f} = 2.4 \pm 0.2$, $S = 4.1$).

Source No. 116 coincides with [SW03] 105. Di Stefano & Kong (2003) observed [SW03] 105 with *Chandra* (source M 83-88 in Di Stefano & Kong 2003) and classified it as an SSS candidate. Blair & Long (2004) compared the list of *Chandra* sources of SW03 with a list of optical SNR candidates and associated [SW03] 105 with the optical SNR candidate BL53.

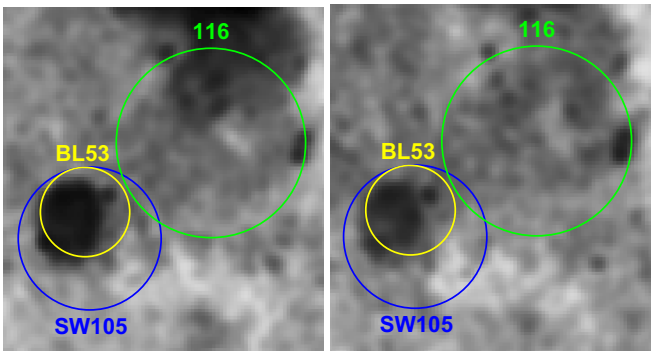

Fig. A.3. Emission line HST/WFC3 images of the region surrounding source No. 116. *Left panel*: WFC3 image with the narrowband filter F657N, corresponding to Hα line emission. *Right panel*: WFC3 image with the narrowband filter F673N, corresponding to SII line emission. The radii of the circles of *Chandra* (SW105) and *XMM-Newton* (116) sources give the 3σ accuracy of the position of the sources. The circle labelled BL53 gives the position of the opitcal SNR candidate.

We observed source No. 116 with *XMM-Newton* in observation 1, where it shows a significant X-ray variability ($V_{\rm f} = 20.8$, $S = 6.2$, Table 3) compared to the *Chandra* observation, and the X-ray hardness ratios are consistent with a hard spectrum. These properties indicate that source No. 116 is most likely an XRB. We overlaid the 3σ error circles of source No. 116, [SW03] 105, and BL53 on the emission line images Hα and SII obtained from the public *Wide Field Camera 3 (WFC3)* observation of 2009-08-20 (Fig. A.3). Hα and SII images are used in extragalactic searches of SNRs because their optical spectra show high [SII]:Hα ratios compared to the spectra of normal HII regions (see e.g. Blair & Long 2004). Fig. A.3 shows that the shell of the optical SNR is located only in the error circles of BL53 and [SW03] 105, indicating that source No. 116 and [SW03] 105 cannot be the same source.

Therefore, source No. 116 is more likely a transient source not associated with BL53.

Source No. 129 coincides with the *Chandra* source [SW03] 121 and with a ROSAT source (source 12 in the catalogue of Ehle et al. 1998, source H29 in the catalogue of Immler et al. 1999).

We observed source No. 129 during observation 1, where it was in the *XMM-Newton* field of view. The spectrum is well fitted with an absorbed powerlaw with spectral parameters consistent with those found by SW03 with *Chandra* (see Table A.3). We did not detect source No. 129 in observations 2 and 3, thus we calculated the flux upper limits and we found a significant ($S \gtrsim 6.4$) long-term variability with a variability factor of $V_{\rm f} = 3.94 \pm 0.11$ (Table 3).

A&A 517, A8 (2010)
DOI: 10.1051/0004-6361/200913863

Astronomy & Astrophysics

Analyzing X-ray pulsar profiles: geometry and beam pattern of EXO 2030+375

M. Sasaki[1], D. Klochkov[1], U. Kraus[2], I. Caballero[3], and A. Santangelo[1]

[1] Institut für Astronomie und Astrophysik, Universität Tübingen, Sand 1, 72076 Tübingen, Germany
e-mail: sasaki@astro.uni-tuebingen.de
[2] Institut für Physik und Technik, Universität Hildesheim, Marienburger Platz 22, 31141 Hildesheim, Germany
[3] CEA Saclay, DSM/IRFU/SAp – UMR AIM (7158) CNRS/CEA/Université P. Diderot, 91191 Gif-sur-Yvette, France

Received 14 December 2009 / Accepted 7 April 2010

ABSTRACT

Context. The pulse profiles of the transient Be/X-ray binary EXO 2030+375 show strong dependence on energy, as well as on its luminosity state, and are asymmetric in shape.
Aims. We want to identify the emission components of the two magnetic poles in the pulsed emission to understand the geometry of the neutron star and its beam pattern.
Methods. We utilize a pulse-profile decomposition method that enables us to find two symmetric pulse profiles from the magnetic poles of the neutron star. The symmetry characteristics of these single-pole pulse profiles give information about the position of the magnetic poles of the neutron star relative to its rotation axis.
Results. We find a possible geometry for the neutron star in EXO 2030+375 through the decomposition of the pulse profiles, which suggests that one pole gets closer to the line of sight than the other and that, during the revolution of the neutron star, both poles disappear behind the horizon for a short period of time. A considerable fraction of the emission arises from a halo while the pole is facing the observer and from the accretion stream of the other pole while it is behind the neutron star, but the gravitational line bending makes the emission visible to us.

Key words. stars: neutron – X-rays: binaries

1. Introduction

EXO 2030+375 is an accreting X-ray pulsar with a pulsation period of ~42 s, which was discovered with *EXOSAT* in 1985 during a giant outburst (Parmar et al. 1989b). A B0 Ve star was found as its counterpart in follow-up observations in the optical and infrared bands (Janot-Pacheco et al. 1988; Motch & Janot-Pacheco 1987; Coe et al. 1988). During the giant outburst, EXO 2030+375 showed a spin-up of $-P/\dot{P} \approx 30$ yr (Parmar et al. 1989b) and quasi-periodic oscillations with a frequency of ~0.2 Hz (Angelini et al. 1989) interpreted as caused by the formation of an accretion disk. Detailed analyses have shown that its rate of pulse-period change $\dot{P}$, energy spectrum, and pulse profile are strongly luminosity dependent (Parmar et al. 1989a,b; Reynolds et al. 1993). The orbital period is 46 days (Wilson et al. 2002), and a normal outburst has been detected for nearly every periastron passage since 1991 (Wilson et al. 2005). In 2006, EXO 2030+375 underwent the first giant outburst since its discovery in 1985 (Corbet & Levine 2006; Krimm et al. 2006; McCollough et al. 2006), during which it reached a maximum luminosity of $L_{1-20\ \mathrm{keV}} \approx 1.2 \times 10^{38}$ erg s^{-1} (Klochkov et al. 2008) and again showed a strong spin-up. Rossi X-ray Timing Explorer (*RXTE*) monitored EXO 2030+375 extensively during the 2006 giant outburst (Wilson et al. 2008). The source was also observed by the INTErnational Gamma Ray Astrophysics Laboratory (*INTEGRAL*, Winkler et al. 2003) and *Swift* (Gehrels et al. 2004). The spectra indicate a cyclotron absorption line (Klochkov et al. 2007; Wilson et al. 2008). Klochkov et al. (2008) have shown that the spectrum of EXO 2030+375 changes with pulse phase, suggesting a fan beam geometry during the maximum, while towards the end of the giant outburst, it changes to a combination of a fan beam and a pencil beam.

In X-ray pulsars, a neutron star accretes matter from a companion star via stellar wind or Roche lobe overflow. The accreted matter is channeled along the field lines of the strong magnetic field of the neutron star onto the magnetic poles. X-ray emission from the neutron star is produced in regions around the two magnetic poles. As the magnetic dipole axis is most likely inclined against the rotation axis of the neutron star, a distant observer sees pulsed emission. X-ray pulsars exhibit a wide variety of pulse shapes that differ from source to source. Generally, high-energy pulses have simpler shapes than low-energy pulses (White et al. 1983; Frontera & Dalfiume 1989; Bildsten et al. 1997, and references therein). If one assumes an axially symmetric geometry for the two emission regions of the neutron star in a dipole configuration, the observed pulse profile should be symmetric. However, the observed pulse profiles typically show an asymmetry. To explain the asymmetric shape of the total pulse profile, a distorted magnetic dipole field in which the two magnetic poles are not located opposite each other have been discussed (Parmar et al. 1989a; Leahy 1991; Riffert et al. 1993; Bulik et al. 1995). Kraus et al. (1995) shows that, starting from the observed, asymmetric pulse profile, it is possible to disentangle the contribution of the two emission regions of the neutron star. Once the pulsed emission from each of the poles has been obtained, one can derive the geometry of the neutron star. This again allows us to construct the beam pattern, i.e., the flux distribution from one emission region. Using this pulse-profile decomposition method, Kraus et al. (1996) have analyzed the

pulse profiles of Cen X-3 and find indications of both pencil and fan beam. In the case of Her X-1, the results of the pulse-profile decomposition by Blum & Kraus (2000) have not only shed light on the beam pattern of the magnetic poles, but have also confirmed that a warped and tilted accretion disk attenuates the emission from one pole of the neutron star. For A 0535+26, the reconstructed beam pattern suggests that the emission comes from a hollow column plus a halo of scattered radiation on the neutron star surface (Caballero et al. 2010).

In this paper we present the analysis of the energy-resolved pulse profiles of EXO 2030+375 utilizing the decomposition method developed by Kraus et al. (1995). Section 2 gives an overview of the data used for our analysis and Sect. 3 describes the analysis and the results obtained with the pulse-profile decomposition method. The results are discussed in Sect. 4. Section 5 summarizes the possible geometry of the neutron star and the origin of the observed emission.

2. Data

EXO 2030+375 experienced a giant outburst in 2006, during which the source was monitored continuously by *RXTE* and was also observed by *INTEGRAL*. We have used the pulse profiles obtained with the Joint European X-Ray Monitor (JEM-X, Lund et al. 2003) and the imaging system IBIS/ISGRI (Ubertini et al. 2003) as presented in Figs. 2 and 8 of Klochkov et al. (2008).

2.1. RXTE observations

For better statistics, we also used publicly available archival data from two observations with *RXTE* during the rise and the decay of the giant outburst when EXO 2030+375 showed about half of the maximum luminosity. The observations took place on June 28 and September 17, 2006 (observation IDs 91089-01-07-00 and 91089-01-19-01) when the luminosity of the source was $L_{1-20\,\mathrm{keV}} = 7 \times 10^{37}$ erg s^{-1} and 6×10^{37} erg s^{-1}, respectively. We started from the event files obtained with the Proportional Counter Array (PCA, Jahoda et al. 1996). We used the event encoded mode files in oder to have optimum binning. After filtering good time intervals and applying bitmasks, we created lightcurves with a time binning of 0.125 s in the following spectral bands: 2–9 keV, 9–14 keV, 14–20 keV, 20–30 keV, and 30–115 keV. After background subtraction, the lightcurves were corrected to solar barycenter and for orbitary motion of the binary. After folding the lightcurves with periods measured for each observation, we obtained pulse profiles with 128 phase bins. Phase 0.0 was fixed to agree with the *INTEGRAL* pulse profiles of Klochkov et al. (2008). The folded lightcurves from the *RXTE* observations are shown in Fig. 1.

During the two *RXTE* observations shown here, the luminosity of EXO 2030+375 was comparable. As can be seen in Fig. 1, the pulse profiles before the maximum and after the maximum of the giant outburst are very similar, corroborating that the shape of the pulse profiles only depends on the luminosity state (Parmar et al. 1989a).

3. The analysis

3.1. The method

A detailed description of the pulse-profile decomposition method, which is based on a backward tracing of the emission, can be found in Kraus et al. (1995). All major steps of our analysis and the criteria applied to obtain the best solution are described in the Appendix.

The basic assumption of the method is that the magnetic dipole field of the neutron star is distorted in such a way that the two magnetic poles do not lie on a straight line through the center of the neutron star. Therefore, even though the emission from each pole is axisymmetric, the sum of the emission from both poles results in an asymmetric pulse profile. Using Fourier analysis, we model the observed asymmetric pulse profiles with two symmetric functions $f_{1,2}$ to search for symmetry points $\Phi_{1,2}$ in the pulse profiles and their offset Δ (see Appendix for details). For each observation and energy range, the functions f_1 and f_2 correspond to the two single-pole pulse profiles that in total add up to the observed asymmetric pulse profile. Each symmetry point corresponds to the pulse phase where the respective pole is either closest to or most distant from the observer's line of sight. From the two symmetry points and functions, we then derive the location of the emission regions and the beam pattern.

Table 1. Parameters obtained from the decomposition for solutions 1 and 2.

	Φ_1	Δ	a	b	Θ_1[1]	Θ_2[1]	δ[1]
1	65°–75°	63°–70°	–2.1	1.0	39°	141°	40°
2	70°–80°	81°–88°	–0.1	1.0	87°	93°	85°

(1) Assuming $\Theta_0 = 50°$.

3.2. Decompositions

We have a total of 26 pulse profiles from *INTEGRAL* and *RXTE* observations. To perform pulse-profile decomposition, the maximum in each of the 26 pulse profiles is normalized to unity. Thereafter each pulse profile is modeled with two symmetric functions f_1 and f_2 based on Fourier analysis. After applying criteria 1 (*positive flux*, see Appendix A.1) and 2 (*no ripples*), we obtain a large number of possible values for the parameters Φ_1 and Δ. However, after combining the results for all pulse profiles (criterion 3), only two interesting solution regions remain in the parameter space of Φ_1-Δ. We call these solutions 1 and 2 and perform further analysis with these two possible solutions.

For each observation and energy band, the functions f_1 and f_2 correspond to the two single-pole pulse profiles that in total add up to the observed asymmetric pulse profile. The Fourier analysis finds more than one possible set of Φ_1 and Δ within a small region for one solution. For each total pulse profile, we have to look at the different sets of the single-pole pulse profiles to decide which one is consistent with the single-pole pulse profiles at other energies. The pulse profiles of the different observations are studied separately, because one should see a correlation between the different energy bands of one luminosity state, but not necessarily between two different observations. Figure 2 shows some of the selected single-pole pulse profiles and the derived beam patterns for each pole for solution 1. Within one observation, one can see an energy-dependent evolution of the single-pole pulse profiles. The values of Φ_1 and Δ for solutions 1 and 2 are ($65° < \Phi_1 < 75°$, $63° < \Delta < 70°$) and ($70° < \Phi_1 < 80°$, $81° < \Delta < 88°$), respectively. The parameters for the two solutions are listed in Table 1.

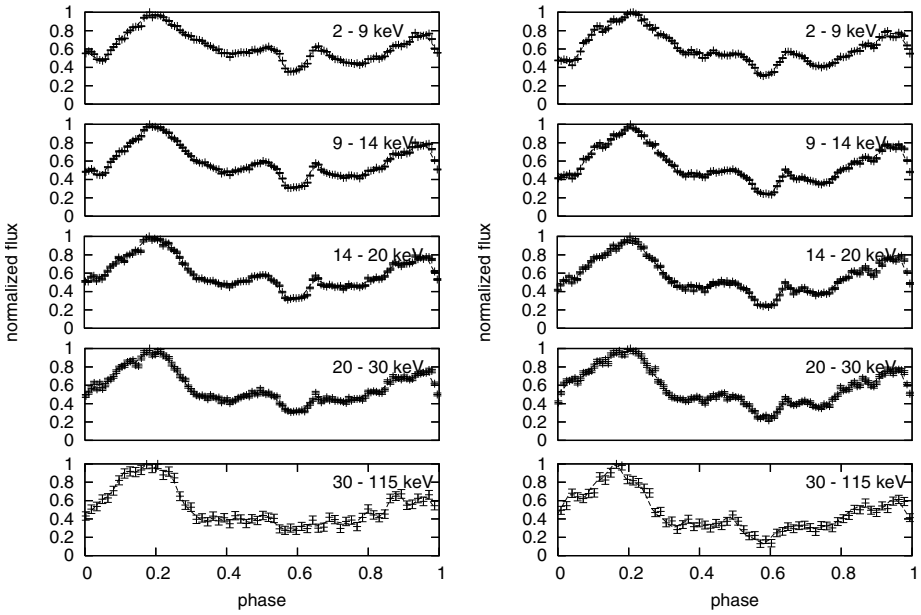

Fig. 1. Pulse profiles of EXO 2030+375 during the rise (*left*) and the decay (*right*) of the giant outburst in 2006 observed with *RXTE*.

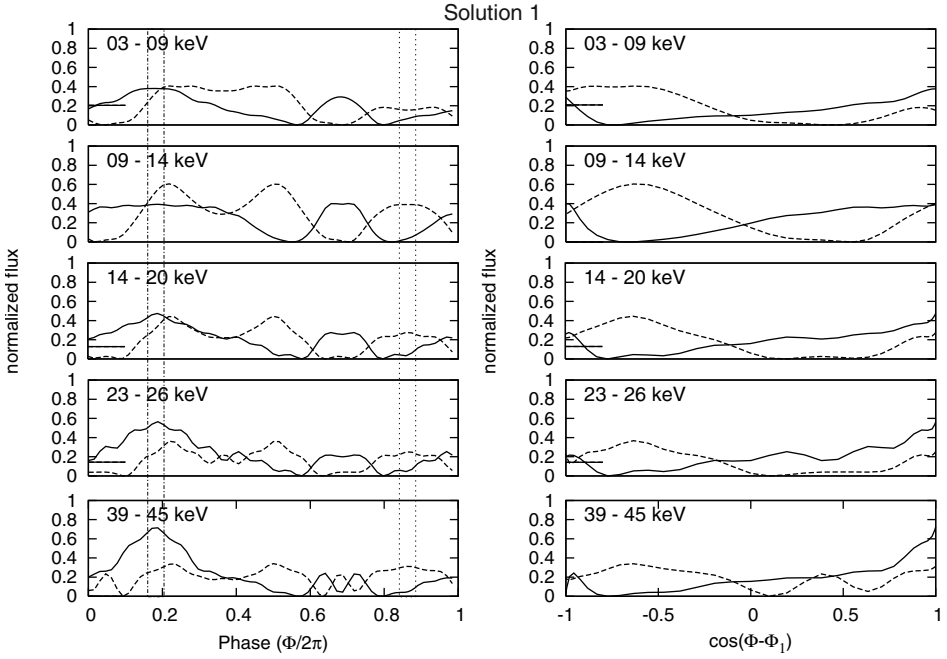

Fig. 2. A selection of single-pole pulse profiles (*left*) and corresponding beam patterns (*right*) obtained by the decomposition method for the Φ_1-Δ set for solution 1 for the energy bands 3–9 keV, 9–14 keV, 14–20 keV, 23–26 keV, and 39–45 keV of the *INTEGRAL* observation near maximum. The solid line is used for emission from the first pole, dashed line for the second pole. The vertical dash-dotted lines indicate the ranges for the symmetry point Φ_1, while the dotted lines show the ranges for Φ_2 obtained from pulse profiles of different energies and observations.

3.3. Overlaying beam patterns

As the neutron star rotates, the angle between the axis through one magnetic pole and the line of sight θ changes with phase, i.e., with rotation angle Φ. The decomposition has provided us with beam patterns as seen by the distant observer for each emission region as functions of the phase. Now we compare the two beam patterns derived from the two single-pole pulse profiles of each observed pulse profile and search for a range in $\cos(\Phi - \Phi_1)$, and thus θ, in which the two beam patterns seem to show the same emission (see Appendix A.2). We try to overlay the two beam patterns by using the relation:

$$\cos(\Phi - \Phi_1) = a + b\ \cos(\tilde{\Phi} - \Phi_2), \quad b > 0. \tag{1}$$

For solution 1 we are not able to find an overlap of the single-pole beam patterns. It is more likely that, in this case, the geometry only allows the observer to see two different parts of the total beam pattern. To assemble the two parts of the beam pattern, we use $a = -2.1$ and $b = 1.0$ (see Fig. A.2, upper panel). For solution 2, we find an overlap of the single-pole beam patterns for $a = -0.1, b = 1.0$, although the beam patterns do not seem to match perfectly.

A total beam pattern can be reconstructed from the beam patterns calculated from the single-pole pulse profiles. As shown in Kraus et al. (1995), there is an ambiguity in the relation between Φ and θ, as each single-pole pulse profile has two symmetry points at Φ_i and $\Phi_i + \pi$. Therefore, the solutions cannot tell us which ends of the sections of the beam patterns belong to, e.g., the lower values of θ. For each set of Φ_1 and Δ we obtain two possible solutions (called `plus` and `minus`) for the total beam pattern. The decomposition method cannot tell us which one is the real solution. We have to take results from other measurements of the source into consideration, e.g., luminosities or

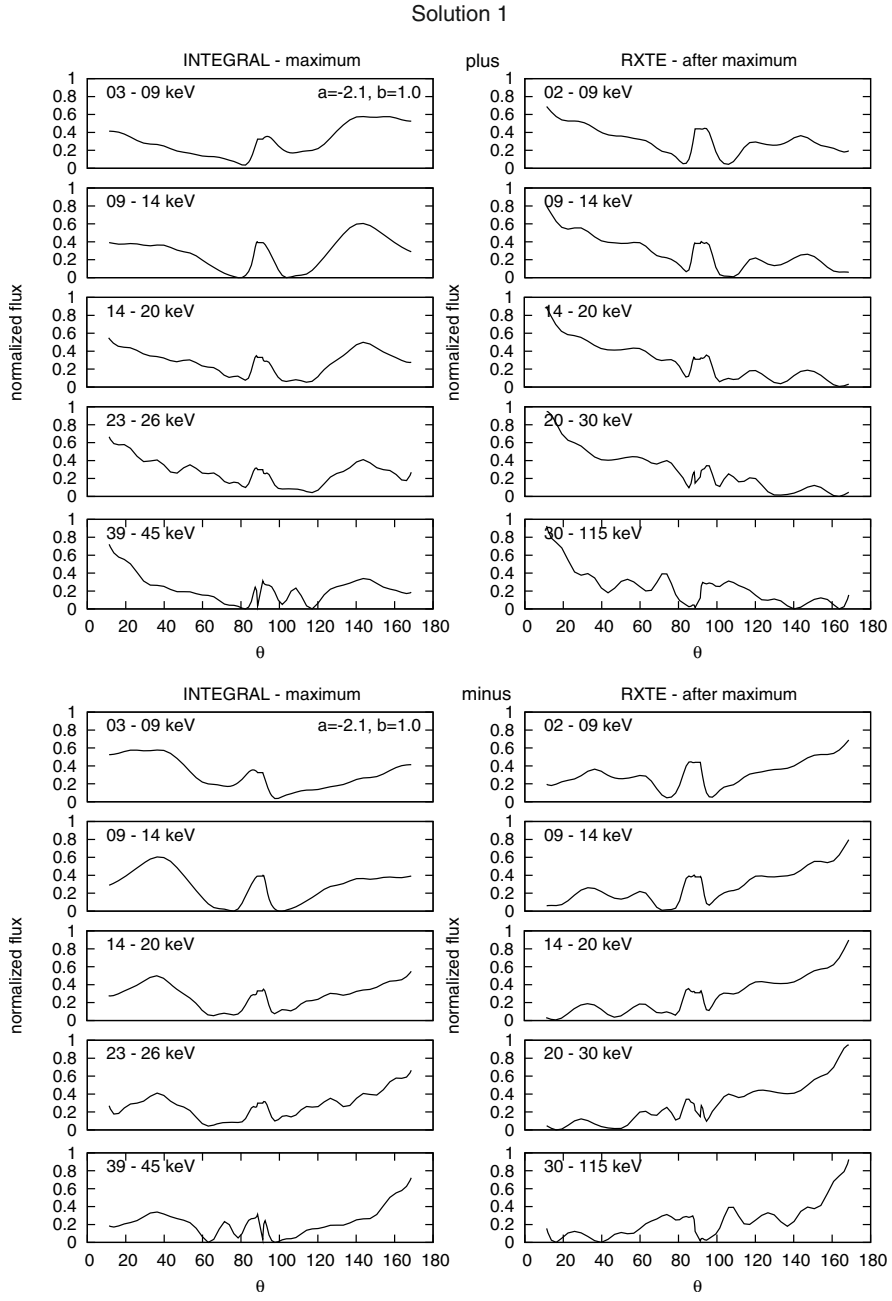

Fig. 3. Asymptotic beam patterns of the `plus` and `minus` solutions of solution 1 seen by the distant observer plotted over the angle θ between the first magnetic pole and the line of sight. *The left panel* shows the beam patterns of solution 1 of the observation near maximum as shown in Fig. 2. *The right panel* shows a selection of additional data from the observation after maximum with similar energy bands.

spectra that will give insight into the emission processes, to decide which of the two is the real solution. The reconstructed asymptotic beam patterns for solution 1 as seen by the distant observer are shown in Fig. 3. Here the beam patterns are plotted over the angle θ between the normal at the first magnetic pole and the line of sight.

That the beam patterns of the single-pole pulse profiles do not match in the overlap region of solution 2 might indicate that the emission from the two magnetic poles are not identical and cannot be described with one local beam pattern. Therefore, we take the mean of the two beam patterns and model a total averaged beam pattern, which we use to reconstruct the visible total pulse profile, i.e., assuming equal local emission pattern for the two poles. The reconstructed pulse profiles (Fig. A.3) show significant deviations from the observed profiles. In addition, this solution yields a very extreme geometry with the two magnetic poles located near the equator of the neutron star, forming an angle of ~90° between each other (see Table 1). Although, in principle, we cannot rule such a strongly distorted geometry out, especially not for young neutron stars like those expected in Be/X-ray binary systems, as they might have experienced some anisotropic conditions while their birth, this rather unlikely geometry also suggests that solution 2 is not appropriate for EXO 2030+375. Therefore, in the following, we focus on the discussion of solution 1.

3.4. Geometry of the neutron star

To derive the exact geometry of the neutron star, i.e., to determine the polar angles of the magnetic poles Θ_1 and Θ_2 as well as the offset angle δ, we need to know the inclination angle of the rotation axis of the neutron star. However, this angle

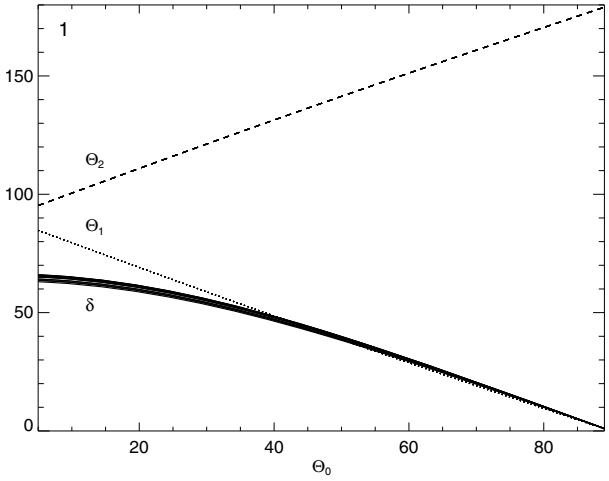

Fig. 4. Relation between the observing angle Θ_0 and the angles Θ_1 (dotted line), Θ_2 (dashed line), and δ (range of possible values) for solution 1.

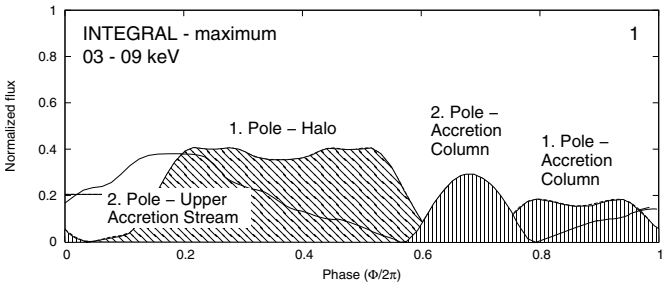

Fig. 5. Decomposed single-pole pulse profiles of the data taken near the maximum of the giant outburst for the lowest energy band (same as the upper left diagram of the upper [solution 1] panels in Fig. 2) with proposed emission components derived from the beam patterns of the `minus` solution (Fig. 3, lower panel). We suggest that the emission from the first pole consists of emission from the halo (diagonally striped component) and from the accretion column (vertically striped). The dominant emission from the second pole seems to have its origin in the scattered photons in the upper accretion stream, which is visible while the second pole is behind the horizon of the neutron star due to gravitational light bending, while there is also a contribution from the accretion column (vertically striped). In this solution, the first pole gets closer to the line of sight than the second.

is not known for most of the neutron stars, in particular not for EXO 2030+375. Figure 4 shows the dependence of the angles Θ_1, Θ_2, and δ on the angle Θ_0 between the rotation axis of the neutron star and the line of sight of the observer. To convert the phase parameter $\cos(\Phi - \Phi_1)$ into the angle θ between the first magnetic pole and the observer, we have to assume an inclination angle Θ_0 with respect to the rotation axis. Here, we use $\Theta_0 = 50°$, corresponding to $\Theta_1 = 39°$, $\Theta_2 = 141°$ (see Fig. 4 and Table 1).

4. Discussion

In this section we want to further examine the results of the decomposition method and present the possible geometry of the neutron star.

4.1. Disentangling the emission components

For solution 1, there is no overlap between the two beam patterns obtained from the single-pole pulse profiles as shown in Sect. 3.3. It means that only a part of the emission is seen from each pole during the revolution of the neutron star. By putting the two visible parts together, we obtain the total beam pattern of the emission around one magnetic pole. In doing so, we make the assumption that the two magnetic poles have the same emission pattern. The `plus` solution (Fig. 3, upper panel) can be described as a composition of a forward directed emission (towards 0°) that is more pronounced at higher energies and an extended, relatively soft emission (~80°–180°). The harder, forward-directed emission indicates a pencil beam. The relative flux of the softer emission component is higher in the data from the observation performed near the maximum compared to the one during the decay and can be interpreted as a fan beam, in agreement with the largely accepted picture that an optically thick accretion column is formed during the giant outburst (White et al. 1983, and references therein). The `minus` solution has a soft emission at $\theta \lesssim 60°$ and a harder emission at $\theta \gtrsim 120°$ that increases for larger θ. As newest calculations by Kraus et al. (2010) have shown, reprocessing of photons in the upper accretion stream creates a significant emission component that dominates the beam pattern at higher energies and can be observed while the pole, hence the accretion column, is on the other side of the neutron star ("anti-pencil"). In addition, the emission from a halo that is formed by scattered photons at the bottom of the accretion column dominates the beam pattern at lower energies and at lower θ and is stronger in the data near the maximum of the giant outburst.

Figure 5 shows how the emission from the two poles contributes to the pulse profiles for the decompositions of the low energy band data taken at the maximum of the giant outburst in the case of the `minus` solution. Let us assume that the first magnetic pole with the polar angle Θ_1 gets closer to the line of sight than the second magnetic pole, i.e., $\Theta_0 - \Theta_1 \leq \Theta_2 - \Theta_0$. At phase 0.0, both poles are right behind the horizon of the neutron star: the first pole is going to reappear, the second pole is turning farther away from the observer. At phase ~0.1 the first pole becomes visible, and from then on the emission from the halo of the first pole makes the largest contribution until the pole disappears behind the horizon at ~0.6. When the first pole, which is closer to the observer's line of sight, is right at the horizon of the neutron star and its accretion column is seen from the side, a minimum is likely to be observed in the pulse profile (see also Sect. 4.4). At the major maximum at phase 0.15–0.25, the second magnetic pole is behind the horizon of the neutron star and the scattered and gravitationally bent photons from the upper accretion stream cause the pronounced increase in flux. The second pole that is rotating on a circle farther away from the line of sight than the first pole comes back to the front side at about phase 0.45 and is closest to the observer at about phase 0.7. However, since the line of sight is closer in latitude to the first pole than to the second pole, the observer never gets as close to the surface normal of the second pole as to that of the first pole. The main emission seen from the second pole while it is on this side of the horizon comes directly from the accretion column.

Parmar et al. (1989a) have modeled the luminosity dependent pulse profiles from the first observed giant outburst in 1985 by assuming a fan beam and a pencil beam component for the two magnetic poles based on a model by Wang & Welter (1981). They obtain a fit for all ten pulse profiles for different luminosities ranging from $0.1–10.0 \times 10^{37}$ erg s^{-1} with some residuals and find that the fan beam mainly produces the major peak at phase 0.2, whereas the peak at phase 0.95 can be ascribed to a pencil beam. The way they have chosen phase 0.0 is different

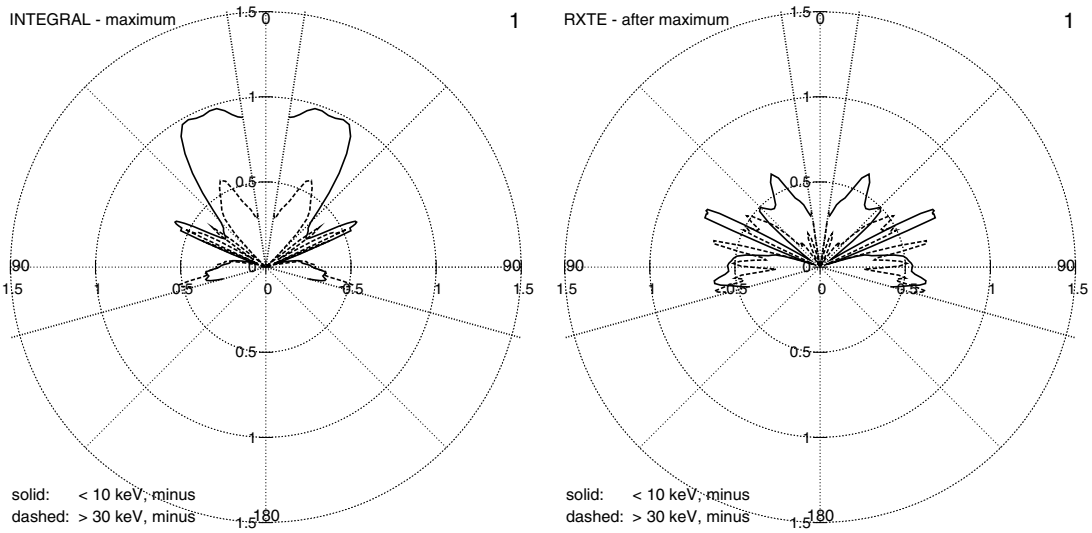

Fig. 6. Polar diagrams of the intrinsic beam pattern for the `minus` solution of solution 1 for the same observations as shown in Fig. 3, for the softest and the hardest bands for an assumed $\Theta_0 = 50°$. Dotted lines are drawn to clearly show the range in which the emission is visible for the observer.

than in our work, resulting in a shift by about 0.4. The best-fit parameters of Parmar et al. (1989a) correspond to $\Theta_1 = 70°$, $\Theta_2 = 110°$, and $\delta = 70°$, assuming $\Theta_0 = 25°$. This result is consistent with our solution 1 for the case of $\Theta_0 = 25°$ (see Fig. 4).

4.2. Comparison to phase-resolved spectral analysis

Klochkov et al. (2008) analyzed the same *INTEGRAL* data as used in this work and performed pulse phase resolved spectroscopy. For the data of the maximum, they find that the spectrum is harder at the main peak (phase 0.2). They conclude that the observer might be seeing Compton scattered photons from the optically thick accretion column. In the data taken at the end of the decay, a new peak appears at about phase 0.95. At this point, the spectrum is again harder, leading to the conclusion that the line of sight of the observer is closest to the magnetic field lines. This picture is in good agreement with the solution 1 of the decomposition, in which the emission of the upper accretion stream of the second pole, which is visible owing to gravitational light bending, has its maximum at phase ∼0.2 while the halo of the first pole also has substantial emission, thus contributing significantly to the main peak. At phase ∼0.95 the scattered emission from the upper accretion stream of the second pole starts to increase, while the emission from the accretion column of the first pole also contributes to the observed emission.

4.3. Intrinsic beam patterns

The observed asymptotic beam pattern differs from the intrinsic local beam pattern of the emission region because of relativistic light deflection near the neutron star. Making assumptions on the radius r and mass m of the neutron star, the asymptotic angle θ can be transformed into the intrinsic angle ϑ relative to the surface normal at the first magnetic pole to describe the local emission pattern. We use the canonical values $r = 10$ km and $m = 1.4\ M_\odot$, thus the ratio between r and the Schwarzschild radius r_S is $r/r_S = 2.4$. The intrinsic beam patterns of the `minus` solution are shown in Fig. 6 in polar diagrams. As can be seen in these polar diagrams, the range for the visible angle is ∼10°–105° if $\Theta_0 = 50°$ is assumed.

4.4. Possible origin of the emission

In X-ray pulsars, a strong magnetic field funnels matter accreted from the companion star onto the polar caps. The infalling particles deposit their energy in the atmosphere of the neutron star. Heating due to accretion is balanced by radiative cooling through bremsstrahlung emission, Compton scattering, and the so-called cyclotron radiation after collisional excitation of electrons. In low-luminosity states, the accreted matter is decelerated in the atmosphere of the neutron star by Coulomb scattering. Emission can be seen as pencil beams from the hot spots at polar caps (Wang & Welter 1981). In high-luminosity states, however, the accretion rate is higher, and an accretion column is believed to form. Plasma is decelerated by radiation pressure in the column, and a radiative shock forms above the neutron star surface (Davidson 1973; Basko & Sunyaev 1976). Above the radiative shock, plasma is in free fall, while below the discontinuity, there is a region of nearly stagnant plasma from which photons escape from the sides of the column in a fan beam.

In addition, a luminous halo might form around the accretion column (Davidson & Ostriker 1973; Lyubarskii & Syunyaev 1988) and radiation from the polar cap and the halo can also be scattered in the upper accretion stream (Soffel et al. 1985; Brainerd & Meszaros 1991). As the accretion stream is delimited by magnetic field lines of the neutron star, it opens up wide far from the neutron star. Therefore, the emission from the upper part of the accretion stream can dominate the observed flux and can also screen the polar caps and the halo. Due to relativistic light deflection, emission from one pole can be deflected to the antipodal direction (Pechenick et al. 1983; Riffert & Meszaros 1988; Leahy & Li 1995; Kraus 2001). All these effects can modify the local beam pattern and thus have an effect on the pulse profile of the X-ray pulsar. Wang & Welter (1981) have modeled the pulse profiles of X-ray pulsars by assuming hot spots and fan beams, although EXO 2030+375 is not included in their list of selected X-ray pulsars. They show that, in general, sharp minima can be seen in the pulse profiles at the moment when the fan beam rotates behind the horizon of the neutron star and when it reappears on the side of the neutron star facing the observer. This is exactly what seems to be happening in EXO 2030+375 at phases 0.1 and 0.6 as the decomposition method has shown.

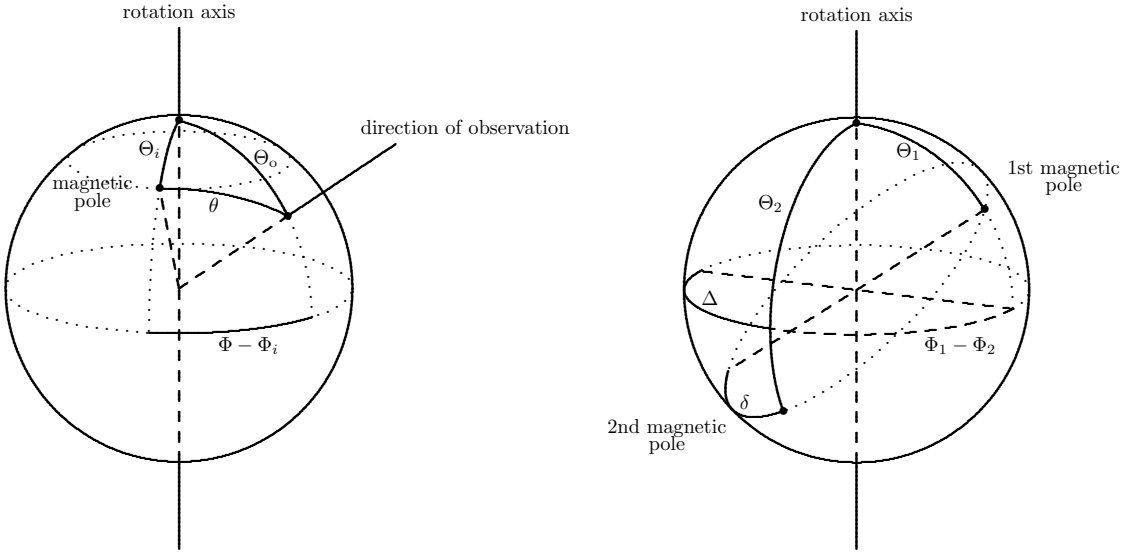

Fig. A.1. Intrinsic geometry of the neutron star. Figures taken from Kraus et al. (1995).

Kraus et al. (2003, 2010) have modeled beam patterns and pulse profiles for medium-luminosity X-ray pulsars assuming an accretion column with energy-dependent local beaming of radiation, a luminous halo formed by illumination of the neutron star surface, and magnetic scattering in the upper accretion stream. They show that the emission from the upper accretion stream can dominate the local beam pattern for $\theta > 120°$. Halo emission has a maximum at $\theta \approx 30°$–$60°$, with significant contribution to the beam pattern for photon energies below ∼5 keV. If one assumes isotropic emission from the accretion column below the discontinuity, the halo emission becomes comparable or negligible relative to the column emission at ≳10 keV. However, if the radiation below the shock is beamed downwards, the halo remains more luminous than the accretion column and the upper stream up to ∼30 keV. The decomposition has shown that the beam patterns show dominant soft emission for $\theta < 60°$, which can be interpreted as halo emission, while the emission $\theta > 150°$ most likely arises from the upper accretion stream (see Fig. 3, lower panel).

5. Summary

We performed pulse-profile decomposition with data of EXO 2030+375 taken during the giant outburst of 2006 by *RXTE* and *INTEGRAL*. This is the fourth source after Cen X-3, Her X-1, and A 0535+26 to which this method has been applied. Each of the asymmetric pulse profiles of EXO 2030+375 at different luminosities in various energy bands are decomposed in two symmetric pulse profiles that account for emission from the two emission regions of the system.

We find that the magnetic field of the neutron star is moderately distorted. The observer sees a part of the emission from each of the two emission regions, but these parts do not overlap. We suggest that the main peak at phase 0.2 in the observed pulse profiles can be attributed to harder emission from the upper accretion stream of the second pole, which can be observed while the pole is on the other side of the neutron star because of relativistic light bending around the neutron star ("anti-pencil"). However, the main peak also has a considerable contribution from the halo emission of the first pole, which is closer to the line of sight than the second. Between phases ∼0.95 and ∼0.1, both poles are located on the rear side of the neutron star. The sharp minima seen at phases 0.0 and 0.6 are caused when the first pole is about to re- and disappear at the horizon of the neutron star, and its accretion column is seen from the side.

Our analysis has disentangled the emission components of the neutron star, which in total lead to the observed asymmetric, energy-, and luminosity-dependent pulse profiles of EXO 2030+375. It will allow us to perform detailed analyses of, e.g., the pulse phase-resolved spectra with reliable interpretation of the differences in the spectral parameters, hence shedding light on the physical processes in the system responsible for the observed emission.

Acknowledgements. This research is based on observations with INTEGRAL, an ESA project with instruments and science data centre funded by ESA member states (especially the PI countries: Denmark, France, Germany, Italy, Switzerland, Spain), Poland, and with the participation of Russia and the USA. This research has made use of data obtained from the High Energy Astrophysics Science Archive Research Center (HEASARC), provided by NASA's Goddard Space Flight Center. This work was supported by DFG grant SA 1777 1/1.

Appendix A: The decomposition method

The pulse-profile decomposition method has been developed and first presented by Kraus et al. (1995). Here we quickly summarize the method and the steps in the analysis.

A.1. Decomposition into two single-pole pulse profiles

Let θ be the angle between the direction of the line of sight and the axis through one magnetic pole. Figure A.1 shows the configuration of the neutron star, showing the positions of the magnetic poles with respect to the rotation axis. The polar angles of the two magnetic poles are called Θ_1 and Θ_2. As the neutron star rotates, θ changes with rotation angle Φ. For the emission of each pole, there are two symmetry points at Φ_i and $\Phi_i + \pi$ ($i = 1, 2$). For each pole, the relation between θ, Θ_i, and Φ_i can be obtained using the spherical triangle in Fig. A.1 (left):

$$\cos\theta = \cos\Theta_0 \cos\Theta_i + \sin\Theta_0 \sin\Theta_i \cos(\Phi - \Phi_i). \quad (A.1)$$

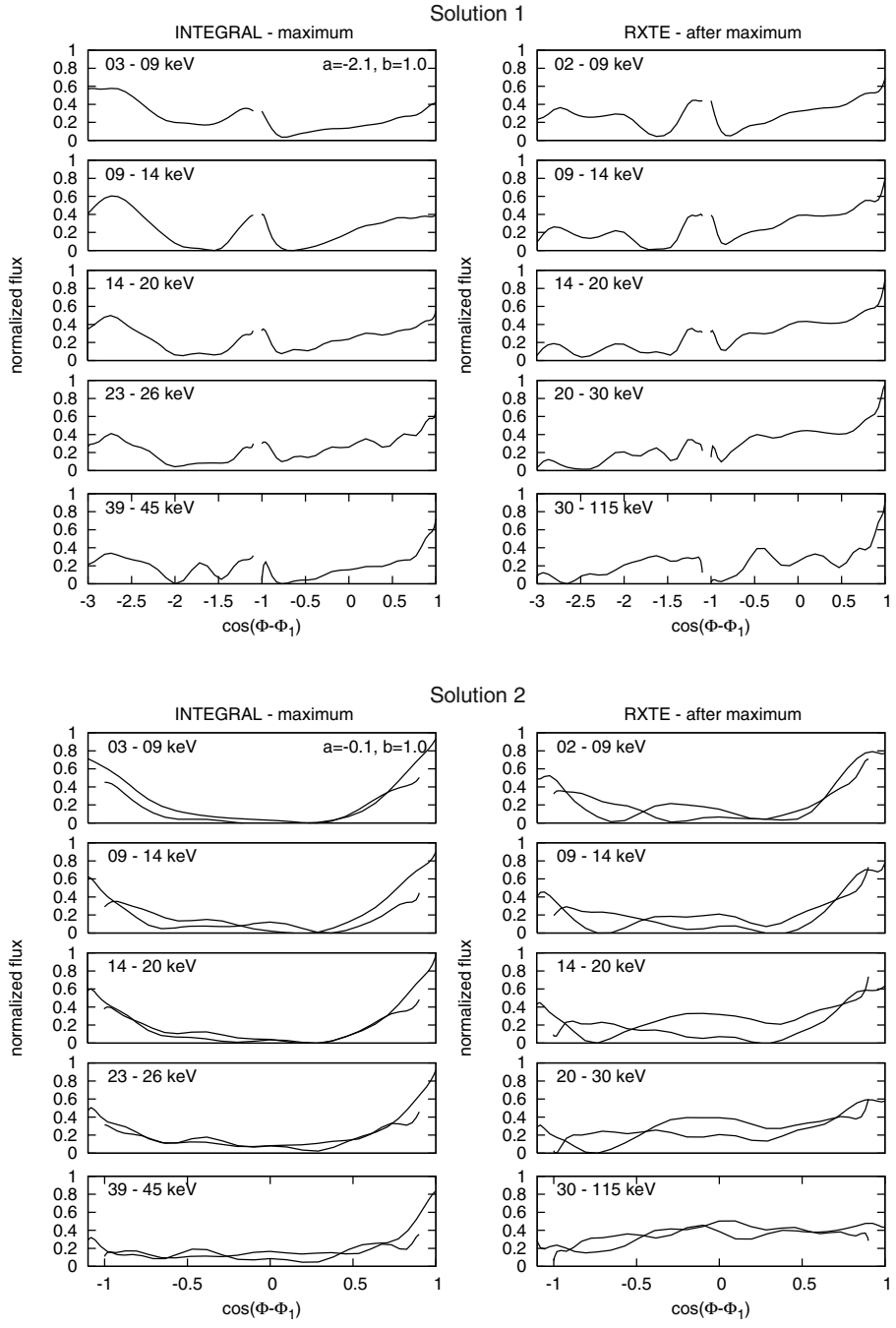

Fig. A.2. Beam patterns from the two emission regions seen by the observer plotted over $\cos(\Phi - \Phi_1)$. *The left panel* shows the beam patterns of solution 1 of the observation near maximum as shown in Fig. 2. *The right panel* shows a selection of additional data from the observation after maximum with similar energy bands. For solution 1 (*upper panel*) no overlap of the beam patterns for the two emission regions is found. For solution 2 (*lower panel*), the beam patterns seem to overlap over a wide range, but show small differences. For the parameters a, b, see Sect. 3.3.

We assume that there is an offset δ between the second magnetic pole and the antipodal position of the first magnetic pole, therefore, there will be a phase offset for the rotation angles Φ_i from a symmetric configuration which can be defined as

$$\Delta = \pi - (\Phi_1 - \Phi_2). \tag{A.2}$$

For an ideal dipole field $\Theta_1 + \Theta_2 = \pi$, $\Delta = 0$, and $\delta = 0$. With the polar angles Θ_1, Θ_2, and the offset Δ in the rotation angles, we have a complete set of parameters to describe the geometry of the neutron star.

To find the contributions from each magnetic pole, we perform Fourier analysis of the observed total pulse profiles. We model it as a sum of two symmetric functions f_1 and f_2 and search for the values for their symmetry points Φ_1 and Φ_2, respectively. In principle we are able to find a set of f_1 and f_2 for any chosen Φ_1 and Φ_2. However, since we deal with functions that describe astronomically observed emission, the following criteria need to be fulfilled:

1. *Positive flux:* The symmetric functions f_1 and f_2 must not have negative values because they model the flux of an astronomical object.
2. *No ripples:* The functions f_1 and f_2 should show no small-scale features that cancel out in the sum. As the two functions correspond to pulse profiles of single-poles that emit independently, they ought not to have features that match exactly. Also, the single-pole pulse profiles are supposedly not more complicated than the total pulse profile.
3. *Same geometry:* We have pulse profiles from one source in different energy bands and, ideally, from more than one

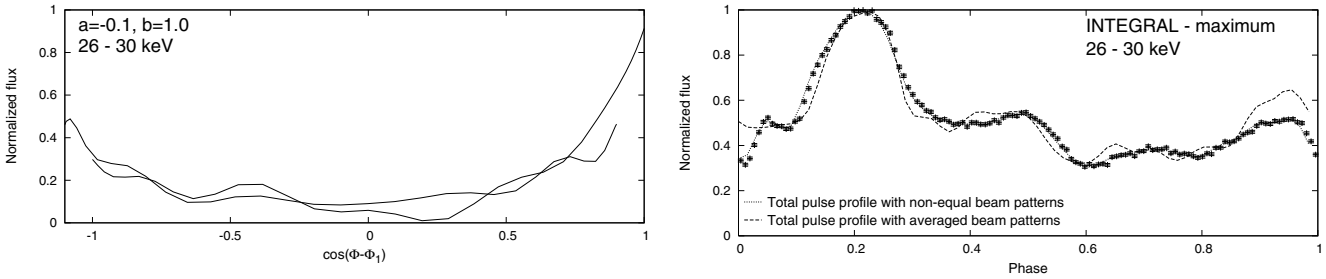

Fig. A.3. *Left*: beam patterns from the two emission regions plotted over $\cos(\Phi - \Phi_1)$ for the energy band 26–30 keV of the *INTEGRAL* observation near maximum for solution 2. For this solution, the beam patterns seem to overlap over a wide range, but show small differences between each other. *Right*: observed total pulse profile (data points with errors) with total pulse profiles reconstructed from the not perfectly matching beam patterns of solution 2 for the two emission regions (dotted) and averaged beam patterns assuming equal local emission pattern for the two regions (dashed).

observation. The observed pulse profiles are energy and luminosity dependent in most cases. Since the emission arises from only one object, the symmetry points must be the same for the decompositions of all available data.

The actual search for reasonable decompositions is performed using the parameters Φ_1 and Δ. The second symmetry point Φ_2 can then be obtained from Eq. (A.2). The decompositions of the pulse profiles of different energy bands and different observations will not yield identical values for Φ_1 and Δ. Therefore we have to define interesting regions in the parameter space of Φ_1 and Δ and look at the single-pole pulse profile for similar values of Φ_1 and Δ for each energy band and observation to decide if they can be declared as one consistent set of emission. This means that the single-pole pulse profiles have to have similar values of Φ_1 and Δ and ought to be similar from one energy band to the other in one observation. Once one has found such a set of decomposition for all energy bands and observations for similar Φ_1 and Δ, one can compute the corresponding beam patterns for each pole.

A.2. Reconstruction of the beam pattern

Two beam patterns are obtained from single-pole pulse profiles as functions of the rotation angles Φ (for one single-pole pulse profile) and $\tilde{\Phi}$ (for the other single-pole pulse profile). During one revolution of the neutron star, the angle θ between the first magnetic pole and the line of sight changes with the phase. There may be an interval during one phase, i.e., a range of the angle θ, in which the observer sees emission from both poles. The same is true for the second magnetic pole. The range covered by the angle θ is in general different for each pole. There may, however, be a certain subrange of values of θ that occur for each of the poles. Then, at some phase Φ, the observer looks onto the first pole at angle θ and at some different phase $\tilde{\Phi}$, the observer looks onto the second pole at the same angle θ. A simple example would be two antipodal poles that pass through the line of sight ($\theta = 0$) at $\Phi = 0$ and at $\tilde{\Phi} = 0.5$, respectively. If, in addition, the two emission regions of the neutron star have the same beam pattern, the emission seen at θ from the first pole (phase Φ) is the same as the emission seen at θ from the second pole (phase $\tilde{\Phi}$). This means that the visible beam patterns of the two poles must have identical parts at different pulse phases. If we find such parts of the beam patterns of the two single-pole pulse profiles we can overlay them and get a relation between $\cos(\Phi - \Phi_1)$ and $\cos(\tilde{\Phi} - \Phi_2)$. From this relation, we can derive the positions of the magnetic poles Θ_1 and Θ_2 as functions of the direction of the observation Θ_0. The angle Θ_0 needs to be determined independently in other studies of the source.

References

Angelini, L., Stella, L., & Parmar, A. N. 1989, ApJ, 346, 906
Basko, M. M., & Sunyaev, R. A. 1976, MNRAS, 175, 395
Bildsten, L., Chakrabarty, D., Chiu, J., et al. 1997, ApJS, 113, 367
Blum, S., & Kraus, U. 2000, ApJ, 529, 968
Brainerd, J. J., & Meszaros, P. 1991, ApJ, 369, 179
Bulik, T., Riffert, H., Meszaros, P., et al. 1995, ApJ, 444, 405
Caballero, I., Kraus, U., Santangelo, A., Sasaki, M., & Kretschmar, P. 2010, A&A, submitted
Coe, M. J., Payne, B. J., Longmore, A., & Hanson, C. G. 1988, MNRAS, 232, 865
Corbet, R. H. D., & Levine, A. M. 2006, The Astronomer's Telegram, 843, 1
Davidson, K. 1973, Nature, 246, 1
Davidson, K., & Ostriker, J. P. 1973, ApJ, 179, 585
Frontera, F., & Dalfiume, D. 1989, in Two Topics in X-Ray Astronomy, Vol. 1, X Ray Binaries, Vol. 2, AGN and the X Ray Background, ed. J. Hunt, & B. Battrick, ESA SP, 296, 57
Gehrels, N., Chincarini, G., Giommi, P., et al. 2004, ApJ, 611, 1005
Jahoda, K., Swank, J. H., Giles, A. B., et al. 1996, in SPIE Conf. Ser. 2808, ed. O. H. Siegmund, & M. A. Gummin, 59
Janot-Pacheco, E., Motch, C., & Pakull, M. W. 1988, A&A, 202, 81
Klochkov, D., Horns, D., Santangelo, A., et al. 2007, A&A, 464, L45
Klochkov, D., Santangelo, A., Staubert, R., & Ferrigno, C. 2008, A&A, 491, 833
Kraus, U. 2001, ApJ, 563, 289
Kraus, U., Nollert, H.-P., Ruder, H., & Riffert, H. 1995, ApJ, 450, 763
Kraus, U., Blum, S., Schulte, J., Ruder, H., & Meszaros, P. 1996, ApJ, 467, 794
Kraus, U., Zahn, C., Weth, C., & Ruder, H. 2003, ApJ, 590, 424
Kraus, U., Zahn, C., & Santangelo, A. 2010, A&A, submitted
Krimm, H., Barthelmy, S., Gehrels, N., et al. 2006, The Astronomer's Telegram, 861, 1
Leahy, D. A. 1991, MNRAS, 251, 203
Leahy, D. A., & Li, L. 1995, MNRAS, 277, 1177
Lund, N., Budtz-Jørgensen, C., Westergaard, N. J., et al. 2003, A&A, 411, L231
Lyubarskii, Y. E., & Syunyaev, R. A. 1988, SvA Lett., 14, 390
McCollough, M. L., Turler, M., Willis, D., & Shaw, S. E. 2006, The Astronomer's Telegram, 868, 1
Motch, C., & Janot-Pacheco, E. 1987, A&A, 182, L55
Parmar, A. N., White, N. E., & Stella, L. 1989a, ApJ, 338, 373
Parmar, A. N., White, N. E., Stella, L., Izzo, C., & Ferri, P. 1989b, ApJ, 338, 359
Pechenick, K. R., Ftaclas, C., & Cohen, J. M. 1983, ApJ, 274, 846
Reynolds, A. P., Parmar, A. N., & White, N. E. 1993, ApJ, 414, 302
Riffert, H., & Meszaros, P. 1988, ApJ, 325, 207
Riffert, H., Nollert, H.-P., Kraus, U., & Ruder, H. 1993, ApJ, 406, 185
Soffel, M., Herold, H., Ruder, H., & Ventura, J. 1985, A&A, 144, 485
Ubertini, P., Lebrun, F., Di Cocco, G., et al. 2003, A&A, 411, L131
Wang, Y., & Welter, G. L. 1981, A&A, 102, 97
White, N. E., Swank, J. H., & Holt, S. S. 1983, ApJ, 270, 711
Wilson, C. A., Finger, M. H., Coe, M. J., Laycock, S., & Fabregat, J. 2002, ApJ, 570, 287
Wilson, C. A., Fabregat, J., & Coburn, W. 2005, ApJ, 620, L99
Wilson, C. A., Finger, M. H., & Camero-Arranz, A. 2008, ApJ, 678, 1263
Winkler, C., Courvoisier, T. J.-L., Di Cocco, G., et al. 2003, A&A, 411, L1

A&A 540, A35 (2012)
DOI: 10.1051/0004-6361/201016304

Astronomy & Astrophysics

Analysing X-ray pulsar profiles

Geometry and beam pattern of 4U 0115+63 and V 0332+53

M. Sasaki[1], D. Müller[1], U. Kraus[2], C. Ferrigno[3], and A. Santangelo[1]

[1] Institut für Astronomie und Astrophysik, Universität Tübingen, Sand 1, 72076 Tübingen, Germany
e-mail: sasaki@astro.uni-tuebingen.de
[2] Institut für Physik, Universität Hildesheim, Marienburger Platz 22, 31141 Hildesheim, Germany
[3] ISDC Data Centre for Astrophysics, Univeristy of Geneva, Chemin d'Écogia 16, 1290 Versoix, Switzerland

Received 13 December 2010 / Accepted 17 January 2012

ABSTRACT

Aims. By analysing the asymmetric pulse profiles of the transient Be/X-ray binaries 4U 0115+63 and V 0332+53 we aim to identify the origin of the pulsed emission to understand the geometry of the accretion onto the neutron star.
Methods. We have applied the pulse-profile decomposition method, which enabled us to find two symmetric pulse profiles for the two magnetic poles of the neutron star. We derived beam patterns for different energy bands and luminosity states. This allowed us to identify the components that are responsible for the emission. The analysis and the models used for the interpretation of the results take relativistic light deflection into account.
Results. We find that the magnetic field of the neutron star is distorted in both 4U 0115+63 and V 0332+53. The beam patterns are interpreted in terms of a model for an accretion column that includes the formation of a halo at the bottom of the accretion column and scattering in the upper accretion stream.
Conclusions. In both systems, an accretion column forms while the accretion rate is high. If the accretion decreases and the sources become fainter, the emission from the halo and the accretion column disappears. In 4U 0115+63 there seems to be significant scattering of photons in the still existing accretion stream even at the end of the outburst. In V 0332+53, the scattering in the upper stream also disappears at the end and we apparently observe the emission from the hot spots on the neutron star.

Key words. accretion, accretion disks – stars: neutron – X-rays: binaries

1. Introduction

In accreting X-ray pulsars ionised gas from a normal star is accreted onto a neutron star (NS) along the magnetic field lines. This results in the production of X-rays. If the magnetic and rotation axes of the neutron star are misaligned, pulsed emission is observed. These X-ray pulsars exhibit a wide variety of pulse shapes that differ from source to source (White et al. 1983; Frontera & Dalfiume 1989; Bildsten et al. 1997, and references therein). In addition, the pulse shapes strongly depend on both the energy and the luminosity, as has been observed for Vela X-1 (Staubert et al. 1980), EXO 2030+375 (Parmar et al. 1989), Cen X-3 (Nagase et al. 1992), etc. Efforts have been made for more than three decades to improve our understanding of the physics and the geometries of the accretion and the resulting emission (e.g., Basko & Sunyaev 1976; Wang & Welter 1981; Riffert & Meszaros 1988; Brainerd & Meszaros 1991; Becker & Wolff 2007, and references therein). However, owing to the complexity of the problem, there is still no compelling model that can describe the physics of the emission and the observed pulse profiles.

The changes in pulse profiles with luminosity are believed to be related to the change of the structures formed by the accreted gas. In low-luminosity states, the accretion rate is low and the gas can fall freely onto the magnetic poles of the neutron star. It forms a mound on the surface of the neutron star from which a pencil-beam emission is expected (Wang & Welter 1981). In high-luminosity states, the accretion rate is increased and the gas funneled along the magnetic fields forms an accretion column. A radiative shock forms in the accretion column above the neutron star surface (Davidson 1973; Basko & Sunyaev 1976), above which the plasma is in free fall. X-rays are radiated from the walls of the accretion column below the shock. A luminous halo can form at the bottom of the column by scattering of photons on the neutron star surface (Davidson & Ostriker 1973; Lyubarskii & Syunyaev 1988; Kraus et al. 2003; Ferrigno et al. 2009). The luminosity dependence of the pulse profile thus reflects the transition from low to high accretion rate or vice versa, and hence the change of the emission components. From the observed pulse profiles we are able to derive the beam patterns, i.e., the flux distributions from one emission region, as seen from the distant observer. This again will allow us to derive the local beam pattern as well as the geometry of the neutron star. In doing so it is also necessary to take the relativistic light bending into account.

If the magnetic field is a dipole field and each emission region is axially symmetric with respect to the magnetic axis, the observed pulse profile should be symmetric. However, the observed pulse profiles of X-ray pulsars are in general asymmetric. Different theoretical models have been suggested to explain the observed asymmetry of the pulse profiles. A distorted magnetic dipole field in which the two magnetic poles are not located opposite to each other has been suggested as a possible reason for the asymmetry of pulse profiles (Parmar et al. 1989; Leahy 1991; Riffert et al. 1993; Bulik et al. 1995). Another way to explain the

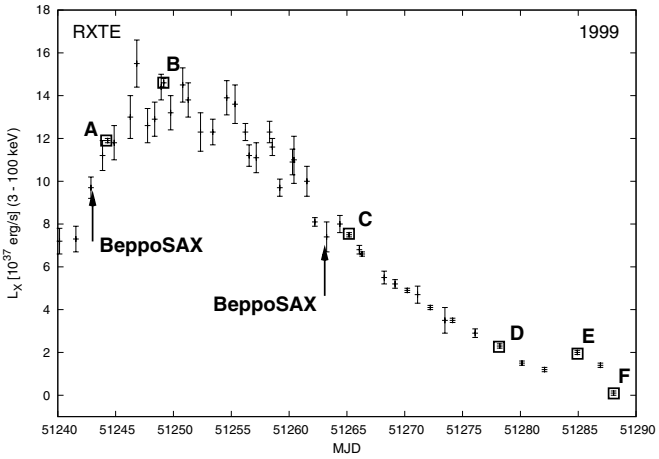

Fig. 1. Light curve obtained from the RXTE observations of 4U 0115+63 during the giant outburst in 1999. Data used in this work are indicated.

asymmetric shape of pulse profiles is an asymmetric accretion stream (Basko & Sunyaev 1976; Wang & Welter 1981; Miller 1996), which has also been discussed for other types of accreting neutron stars, e.g., the "Bursting Pulsar" GRO J1744–28, which shows pulse profiles changes during type II bursts caused by instabilities in accretion (e.g., Kouveliotou et al. 1996; Lewin et al. 1996).

Based on the assumption of distorted magnetic fields, Kraus et al. (1995) developed the decomposition method that allows us to find two symmetric contributions from the two poles to the observed total pulse profiles. Using this pulse profile decomposition method, we have successfully analysed the pulse profiles of the X-ray pulsars Cen X-3 (Kraus et al. 1996), Her X-1 (Blum & Kraus 2000), EXO 2030+375 (Sasaki et al. 2010), and A 0535+26 (Caballero et al. 2011).

In this paper, we present the results of the pulse profile decomposition analysis of the transient sources 4U 0115+63 and V 0332+53.

2. Data

2.1. 4U 0115+63

4U 0115+63 is an accreting X-ray pulsar, which has been known and was extensively studied since the early 1970s. Observations of the Uhuru satellite yielded detections of this X-ray transient in 1970 and 71 (Forman et al. 1976). The subsequent analysis of the archival data of the Vela 5B satellite revealed that the source had also been detected in 1969 (Whitlock et al. 1989). Rappaport et al. (1978) measured the orbital motion of the source from observations with the SAS 3 satellite in 1978, obtaining an orbital period of 24.3 d, while Cominsky et al. (1978) detected pulsations with a pulse period of 3.61 s. Soon thereafter, a strongly reddened Be-star V635 Cas was found as its optical counterpart (Johns et al. 1978; Hutchings & Crampton 1981; Kholopov et al. 1981). This star was later classified as a B0.2Ve star at a distance of 7–8 kpc (Negueruela & Okazaki 2001). Pulse profiles from *HEAO-1* observations were presented by Johnston et al. (1978).

In 1999 4U 0115+63 underwent a giant outburst, which is believed to be caused by an enhanced mass loss activity of the Be star. During this outburst the Rossi X-ray Timing Explorer (RXTE) monitored 4U 0115+63 extensively (Fig. 1). The source was also observed by *BeppoSAX* on March 06 and 26, 1999 before and after the maximum. Observations with *BeppoSAX* revealed that the spectrum of 4U 0115+63 shows four cyclotron resonance scattering features (CRSFs) at 12.7, 24.2, 35.7, and 49.5 keV (Santangelo et al. 1999), which was the first discovery of multiple absorption lines due to cyclotron resonant scattering ever. Additional analyses of the RXTE and *BeppoSAX* data of the giant outburst of 4U 0115+63 in 1999 have been published by Nakajima et al. (2006), Tsygankov et al. (2007), Ferrigno et al. (2009), and Baushev (2009).

The pulse profiles of 4U 0115+63 and also other accreting X-ray pulsars are strongly luminosity- and energy-dependent. Because we aim to understand the reason for the evolution of the pulse shapes with luminosity and energy, it is crucial to have statistically useful pulse profiles of the source in different luminosity states, hence different observations during an outburst, as well as for different energy bands. Moreover, the more pulse profiles we have, the better will be the determination of the symmetry points and thus the determination of the geometry parameters of the neutron star (see Sect. 3).

We used the data of six RXTE observations taken with the Proportional Counter Array (PCA, Jahoda et al. 1996) and two *BeppoSAX* observations (Ferrigno et al. 2009). For the *BeppoSAX* data, we used the same energy bands as in Ferrigno et al. (2009) and divided the RXTE data into similar bands. The selected bands are approximately <5 keV, 5–10 keV, 10–15 keV, 15–20 keV, 20–30 keV, and >30 keV. If the statistics were not good enough (observations D, E, and F), we combined the harder energy bands, e.g., creating pulse profiles for the band 15–115 keV. For the same reason, we did not use the hardest band (>15 keV) in the last and thus faintest observation F for the pulse profile analysis. Table 1 lists the data used in our work. All used pulse profiles are shown in Figs. 2 and 3.

First, the light curves were corrected for barycentric and orbital motions and folded with pulse periods of ~3.61 s derived for each observation. The light curves were binned into 128 phase bins in most cases. Only for observations E and F we created pulse profiles with 64 phase bins because of poor statistics. In the next step, ideally, the pulse profiles should be phase-connected. However, the high degree of timing noise and the sparse nature of the observations prevented us from doing this. Therefore, the pulse profiles were then shifted by using their common morphological properties. In particular, we focused on the two sharp minima immediately before the major peak and used them as reference points. These minima are seen at phase 0.0 and 0.1 in Figs. 2 and 3, best visible in the softest band (top row) and in the 10–15 keV band data of the observation F. All profiles were then normalised to their maximum

Table 1. Data used for the pulse profile decomposition analysis and the luminosities of 4U 0115+63 when the data were obtained.

ID	ObsID	MJD	$L_{3-100\ \mathrm{keV}}$
	006534	51 243	9.4×10^{37} erg s^{-1}
A	40070-01-01-00	51 244	1.2×10^{38} erg s^{-1}
B	40070-01-03-00	51 249	1.5×10^{38} erg s^{-1}
	006631	51 263	6.3×10^{37} erg s^{-1}
C	40070-01-04-00	51 265	7.5×10^{37} erg s^{-1}
D	40051-05-12-00	51 278	2.3×10^{37} erg s^{-1}
E	40411-01-24-00	51 285	2.0×10^{37} erg s^{-1}
F	40411-01-26-00	51 288	0.1×10^{37} erg s^{-1}

Notes. Data with ID A – F were taken by RXTE, the first and the fourth data-sets are from *BeppoSAX*. The luminosity was calculated assuming a distance of 7 kpc.

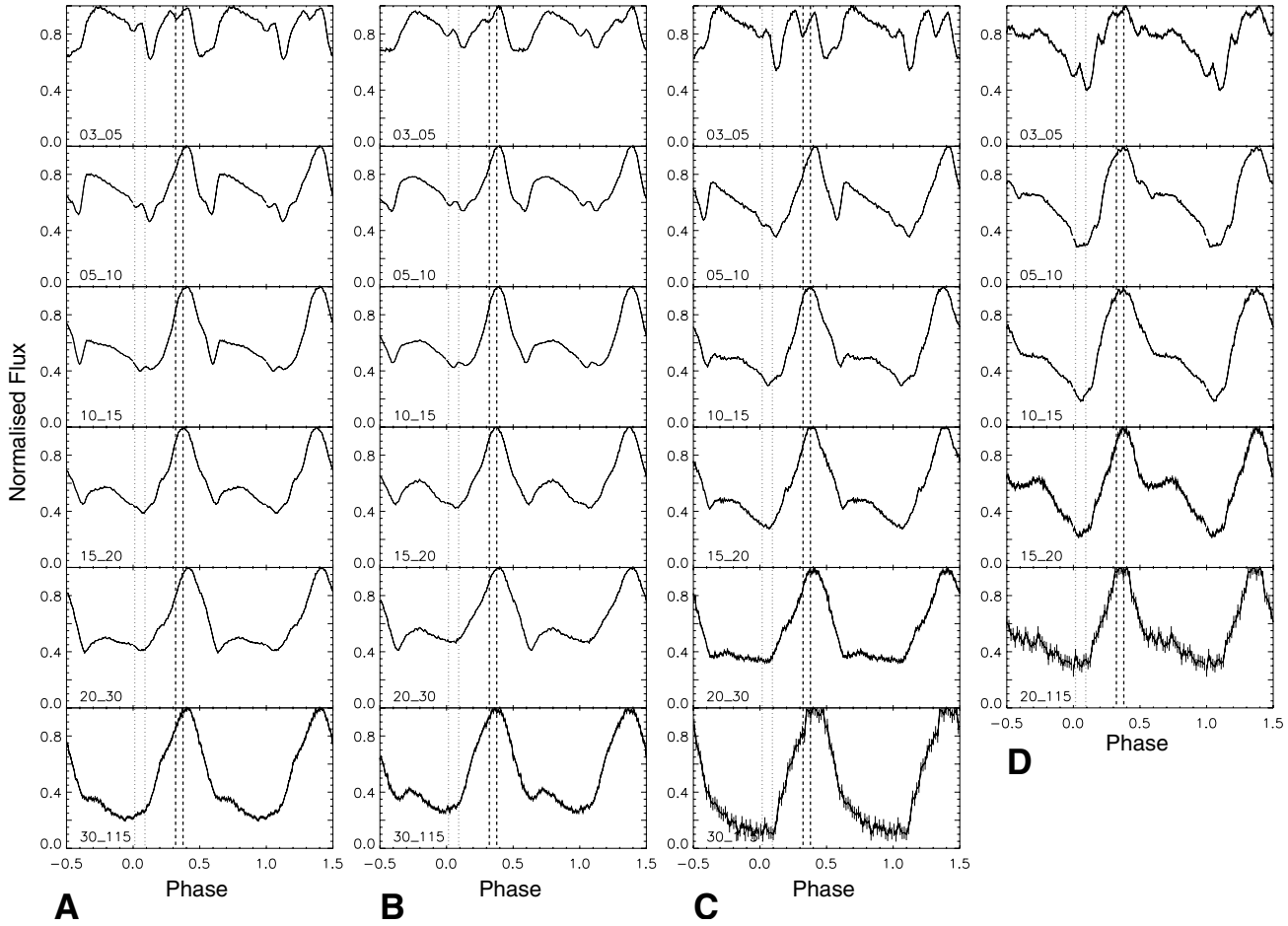

Fig. 2. Pulse profiles of 4U 0115+63 during the giant outburst in 1999 observed with RXTE for the observations A–D. Energy bands are soft to hard from top to bottom for each observation. The numbers in the plots indicate the bands (lower energy – upper energy in keV). The dotted and dashed lines show the ranges in which the symmetry points Φ_1, Φ_2 are found (see Sect. 3).

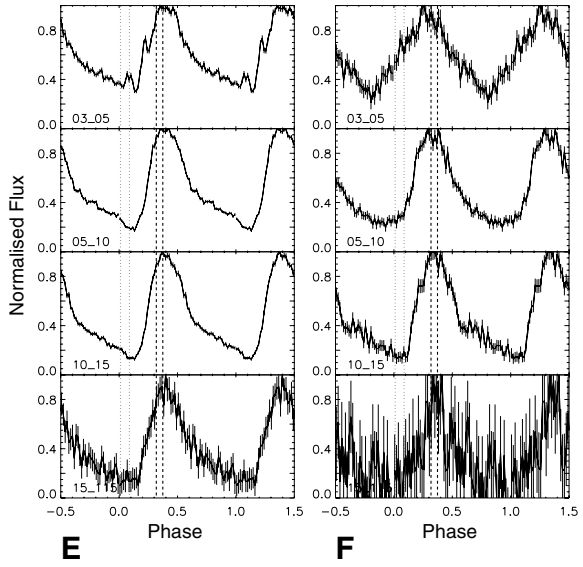

Fig. 3. Same as in Fig. 2 but for observations E and F.

value. Using fairly broad energy bands limits the impact of the different energy resolution and therefore the combined data-set of different instruments can be safely used in the analysis.

For energies higher than ∼5 keV, the pulse profiles have a major maximum at phase = 0.4 and an additional hump that follows the maximum. This hump is stronger for lower energies and is visible only during the giant outburst (observations A–D). It seems that it has disappeared in the data-sets E and F at the end of the outburst.

The most intriguing band is the softest band below 5 keV. The major peak has an additional component at phase = 0.25 in the data near the maximum of the giant outburst (A, B, C, see also Fig. 1 in Ferrigno et al. 2009). Furthermore, the height of the hump at phase = 0.6–1.1 is comparable to the double peak at 0.4. The hump and the additional peak seem to be caused by the change of emission characteristics due to the increased accretion during the giant outburst.

For the subsequent analysis we used the following identifier for the pulse profiles with the format LNNNN. The letter L is the ID for the observations as given in Table 1. The next two following numbers indicate the lower energy of the energy band, the last two numbers for the upper energy. For example, A0305 is the beam pattern belonging to the pulse profile from the A (40070-01-01-00) data for the energy band of 3 to 5 keV. The number 11 for the upper energy in the highest energy bands stands for 115 keV. For the *BeppoSAX* data, we used the identifiers "b" for the observation before the maximum and "s" for after maximum.

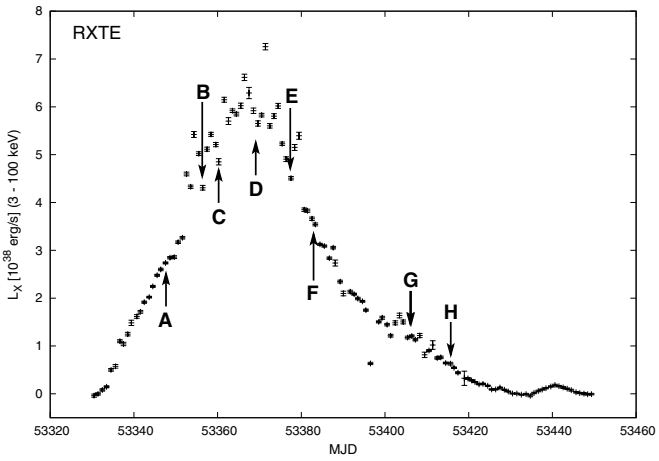

Fig. 4. Light curve of V 0332+53 during the 2004/2005 outburst obtained with the All-Sky Monitor on RXTE. The selected observations for the pulse profile decomposition are marked.

2.2. V 0332+53

V 0332+53 was discovered in 1973 by the Vela 5B satellite during a type II, i.e., a giant outburst (Terrell & Priedhorsky 1984). The pulse period was determined to a value of 4.4 s, while an orbital period of 34 d was measured (Stella et al. 1985). Its optical counterpart was identified as the O8-9Ve star BQ Cam (Bernacca et al. 1984; Negueruela et al. 1999) with a distance of ~7 kpc. Ten years later, there was a second outburst, this time of type I corresponding to a periastron passage of the neutron star, detected with the *Tenma* satellite (Inoue 1985). The source became again active in 1989 in form of a type II outburst, and the next outburst of type II was measured at the end of 2004 (December 2004 to February 2005, Zhang et al. 2005; Mowlavi et al. 2006, see Fig. 4). About a year before each outburst, one could observe a brightening of the optical companion that was most likely triggered by a sudden increase of the mass ejection rate from the companion star (Mowlavi et al. 2006). Similar to 4U 0115+63, this source is one of the few sources that show multiple cyclotron lines in their spectra. V 0332+53 is the second X-ray accreting pulsar that has at least three CRSFs, the main harmonic at $E_{\rm cycl,1} = 25$ keV and the first and second harmonics at $E_{\rm cycl,2} = 51$ keV and $E_{\rm cycl,3} = 72$ keV, respectively (Coburn et al. 2005; Kreykenbohm et al. 2005; Pottschmidt et al. 2005).

The pulse profiles of V 0332+53 are highly asymmetric and lumimosity-dependent (Zhang et al. 2005; Tsygankov et al. 2006, see Fig. 5). One can observe a change in the structure of the profiles from double-peaked to single-peaked and also a change of the phase separation of the double pulses with the source luminosity. While the source was bright, the separation of the two main peaks in the pulse profile remained nearly constant at a value of about 0.47 and decreased to 0.37 within a short time of about three days during which the luminosity declined after the maximum intensity was reached (Zhang et al. 2005). Significant changes of the double-peaked structure of the pulse profiles can be seen as the intensity of the source decreases. For a luminosity of about $L \approx 7 \times 10^{37}$ erg s^{-1} the profiles become asymmetrically single-peaked at energies below the energy of the main harmonic cyclotron line, while it seems to remain double-peaked above this energy (Tsygankov et al. 2006). However, the low statistics make detailed analyses at these low luminosities difficult.

Table 2. Data used for the pulse profile decomposition analysis of V 0332+53.

ID	Observation ID	MJD	$L_{3-100\ \rm keV}$
A	90089-11-02-08	53 346	2.6×10^{38} erg s^{-1}
B	90089-11-03-04	53 353	4.1×10^{38} erg s^{-1}
C	90089-11-04-03	53 358	4.6×10^{38} erg s^{-1}
D	90427-01-01-01	53 368	4.8×10^{38} erg s^{-1}
E	90427-01-02-02	53 376	3.9×10^{38} erg s^{-1}
F	90014-01-01-04	53 381	3.4×10^{38} erg s^{-1}
G	90014-01-05-01	53 407	1.1×10^{38} erg s^{-1}
H	90427-01-04-04	53 414	7.9×10^{37} erg s^{-1}

Notes. The luminosity was calculated assuming a distance of 7 kpc.

For the pulse profile decomposition we selected a set of RXTE observations covering the whole time span of the 2004/2005 outburst from the beginning of December 2004 until mid February 2005. These observations are listed in Table 2. The selected observations are also marked in the light curve of the 2004/2005 outburst taken by the RXTE All-Sky Monitor (ASM, see Fig. 4). The data are mainly available as binned-mode data. Therefore, after the event arrival time was corrected for barycentric and orbital motions, pulse profiles were created with phase bins of 128 for four different energy bands: 3–7 keV, 7–20 keV, 20–30 keV, and 30–115 keV. As was discussed before, the pulse profiles of V 0332+53 have two distinct minima that become stronger if the source becomes brighter. In addition, the two maxima have different shapes, one showing a slightly increasing plateau (at phase 0.1–0.4 in Fig. 5) while the other is flat or has a decreasing plateau (at phase 0.6–0.9). By identifying these two minima and two maxima, we shifted the pulse profiles by defining the minimum before the maximum that shows an increase as phase 0. For the pulse profiles of V 0332+53 we used the same scheme for the identifiers as for 4U 0115+63: the ID given in Table 2 together with the lower and upper energies gives the total identifier, e.g., the pulse profile of the softest band of the observation 90089-11-02-08 is called A0307.

3. The analysis

A detailed description of the pulse profile decomposition method can be found in Kraus et al. (1995). A short summary of the method is also given in our papers on EXO 2030+375 (Sasaki et al. 2010) and A 0535+26 (Caballero et al. 2011). In Fig. 6 we show the assumed geometry of the neutron star and the angles used for the analysis. The polar angles of the two magnetic poles are Θ_1 and Θ_2. We assumed that there is an offset angle δ between the second magnetic pole and the antipodal position of the first magnetic pole. The inclination angle of the observer with respect to the rotation axis of the neutron star is Θ_0. The angle between the line of sight and the axis through one magnetic pole is called $\theta_{\rm obs}$. As the neutron star rotates, $\theta_{\rm obs}$ changes with the rotation angle Φ. Since the observed X-ray emission most likely arises from regions close to the magnetic poles as well as directly above, and we assumed that the emission is symmetric in shape, there should be two symmetry points in the emission of each magnetic pole at Φ_i and $\Phi_i + \pi$ ($i = 1, 2$), each corresponding to the pulse phase at which the pole is either closest or farthest from the line of sight. The non-antipodal positions of the two

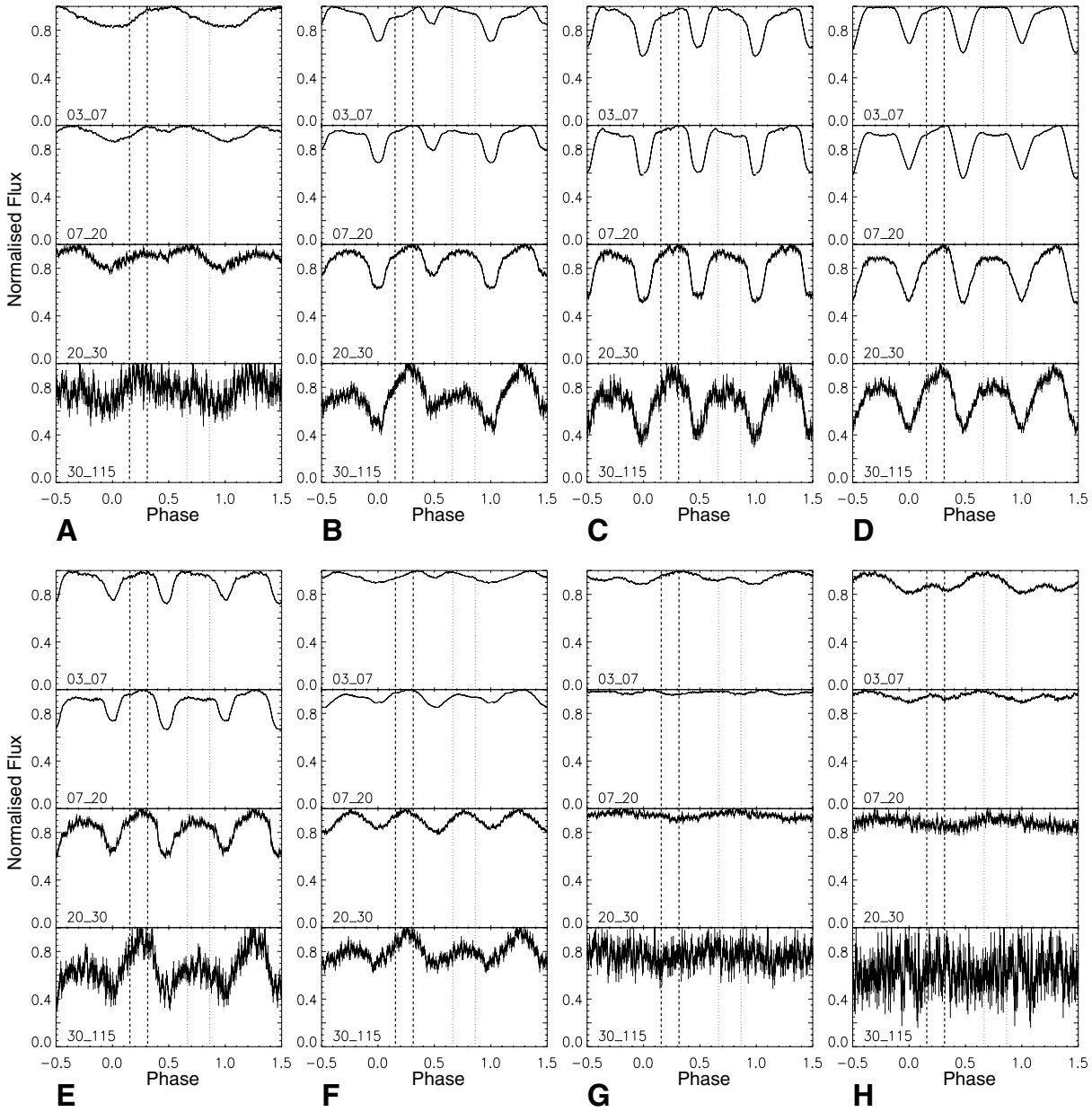

Fig. 5. Pulse profiles of V 0332+53 during the giant outburst in 2004/2005 observed with RXTE. The pulse profiles are sorted chronologically from left to right in the upper panel, then left to right in the lower panel. Energy bands are soft to hard from top to bottom for each observation. The bands (lower energy – upper energy in keV) are given in the diagrams. The letters at the botton of each panel give our identifiers for the observations. The dotted and dashed lines show the ranges in which the symmetry points Φ_1, Φ_2 are found (see Sect. 3).

poles result in an offset $\Delta = \pi - (\Phi_1 - \Phi_2)$ in rotation angle between the symmetry points Φ_1 and Φ_2.

The decomposition method is in principle a backward-tracing of the emission. The basic assumption is that the two magnetic poles of the neutron star have the same emission characteristics and that a sum of the two symmetric single-pole pulse profiles result in the observed asymmetric pulse profile. We are interested in the shape and the change of the shape of the beam patterns with energy and luminosity. This gives information about the relative fluxes of the different emission regions of the source (see Sect. 4) that contribute to the observed total emission. Therefore, the observed total pulse profiles are first normalised so that the maximum in the pulse profile is equal to one.

To decompose the observed asymmetric pulse profiles into two symmetric pulse profiles, each of these normalised asymmetric pulse profiles F can be represented by its Fourier expansion:

$$F(\Phi) = \frac{1}{2}u_0 + \sum_{k=1}^{n/2-1} [u_k \cos(k\Phi) + v_k \sin(k\Phi)] + u_{n/2} \cos\left(\frac{n}{2}\Phi\right), \quad (1)$$

where n is the number of phase bins, which we divide the pulse profiles into (64 or 128, depending on the strength of the signal in each observation). As shown by Kraus et al. (1995), we can express $F(\Phi)$ by means of two symmetric functions f_1 and f_2 for

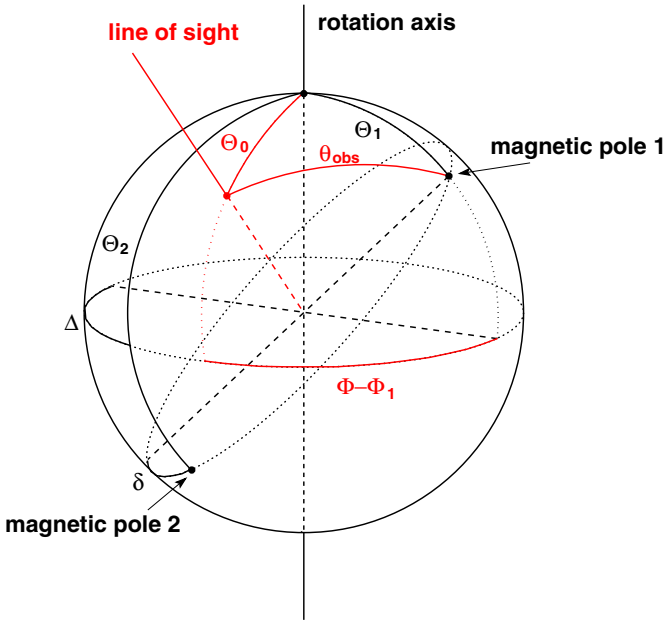

Fig. 6. Intrinsic geometry of the neutron star.

virtually any choice of two symmetry points Φ_1 and Φ_2. Because f_1 and f_2 should be symmetric, the sine terms vanish and we can write

$$f_1(\Phi) = \frac{1}{2}c_0 + \sum_{k=1}^{n/2} c_k \cos[k(\Phi - \Phi_1)], \quad (2)$$

$$f_2(\Phi) = \frac{1}{2}d_0 + \sum_{k=1}^{n/2} d_k \cos\{k[\Phi - (\Phi_2 - \pi)]\}. \quad (3)$$

The parameters c_0 and d_0 are subject to the constraint that their sum equals u_0. They are determined in two steps: in the decomposition, minimum values $c_{0,\min}$ and $d_{0,\min}$ are determined such that the symmetric functions do not become negative at any phase. The remaining constant flux $u_0 - c_{0,\min} - d_{0,\min}$ is divided up when the two beam patterns are combined to obtain the total beam pattern (as described in Sect. 3.1.1). It is distributed among the two beam patterns so that the quadratic deviation in the overlap region is minimised. The mean square devitaion function $Q(a, b)$ is computed with the optimum flux distribution for each pair of values a and b (see Sect. 3.1.1). We assumed that F is well-defined by the n data points and is thus limited to frequencies below $n/2$. This is confirmed by verifying that the power of the Fourier transform of F approaches zero if the frequency approaches $n/2$. As sugested by Kraus et al. (1995), we used less than n Fourier coefficients, omitting the highest coefficients that may be affected by aliasing and may also have fairly large statistical errors. This results in a certain smoothing of the pulse profile. In practice, we performed the decomposition with 20 to 30 Fourier coefficients. In addition, we used $\Delta = \pi - (\Phi_1 - \Phi_2)$ for convenience instead of Φ_2, i.e., searching for parameters (Φ_1, Δ).

For each pulse profile, we then selected the symmetry points that yield a "good" decomposition according to the following criteria.

1. *Positive flux:* the Fourier analysis yields two symmetric functions f_1 and f_2 for each pulse profile. These functions must be positive because they represent the emitted flux of an astronomical object.
2. *No ripples:* the functions f_1 and f_2 describe the emission of two poles that emit independently from each other, therefore, one expects that they do not show features that match exactly. Also, we do not expect the single-pole pulse profiles to be more complex than the observed total pulse profiles. Therefore, the two functions are not supposed to have small-scale fluctuations that cancel out in the sum.
3. *Same geometry:* we used several pulse profiles from different observations and energy ranges. It is crucial to find a small region in the parameter space that is allowed for all cases, because the emission arises from only one object that has one special geometry. Therefore, the symmetry points must be the same for the decompositions of all available data.

Table 3. Parameters obtained from the decomposition analysis of the pulse profiles of 4U 0115+63 and V 0332+53.

	4U 0115+63	V 0332+53
Decomposition parameters		
Φ_1	115°–135°	91°–110°
Φ_2	5°–30°	277°–311°
Δ	60°–75°	6°–21°
a	–1.2 (+1.0, –1.6)	–0.95 (+0.35, –1.05)
b	1.8 (+0.2, –1.3)	1.0 (+0.5, –0.5)
Pulsar geometry		
Θ_1	148° (+12°, –57°)	142° (+18°, –22°)
Θ_2	74° (+31°, –44°)	38° (+8°, –12°)
δ	65° (+14°, –26°)	12° (+24°, –1°)
Θ_0 (assumed)	60°	70°

Notes. The ranges in which decompositions were found to be consistent for all analysed observations and energy bands are given for Φ_1, Φ_2, and Δ. The main uncertainty comes from the poorly known or unknown value of Θ_0.

For each observed pulse profile, Φ_1 and Δ (and thus Φ_2) were determined independently. The comparison of the possible solutions in the parameter space of Φ_1 and Δ for different energy bands and different observations, thus luminosity states, then yields a few, or, ideally only one region in the Φ_1-Δ parameter space with pairs of Φ_1 and Δ, which have similar values for all pulse profiles. These Φ_1 and Δ values were used for the subsequent analysis for each pulse profile. By means of the resulting two symmetry points, we reconstructed the single-pole pulse profiles for each observed pulse profile.

Each single-pole pulse profile obtained in the decomposition has two symmetry points that correspond to the rotation angles at which the pole is closest to, or farthest from, the line of sight, respectively. Since there is no way to decide which symmetry point corresponds to which end of the range in viewing angle, two groups of solutions are obtained that we call `plus` and `minus` solutions. From these single-pole pulse profiles of the two groups of solutions we derived the beam patterns and interpreted them in terms of emission originating from the accretion column, halo, and/or the upper accretion stream. Comparisons of the beam patterns to theoretically calculated models for the emission from an accreting neutron star (e.g., Kraus et al. 2003, in prep., see Sect. 4) will tell us which of these two groups of solutions are more reasonable.

We summarised the parameters that we obtained from the decomposition analysis and those derived for the geometry of the neutron star for 4U 0115+63 and V 0332+53 in Table 3.

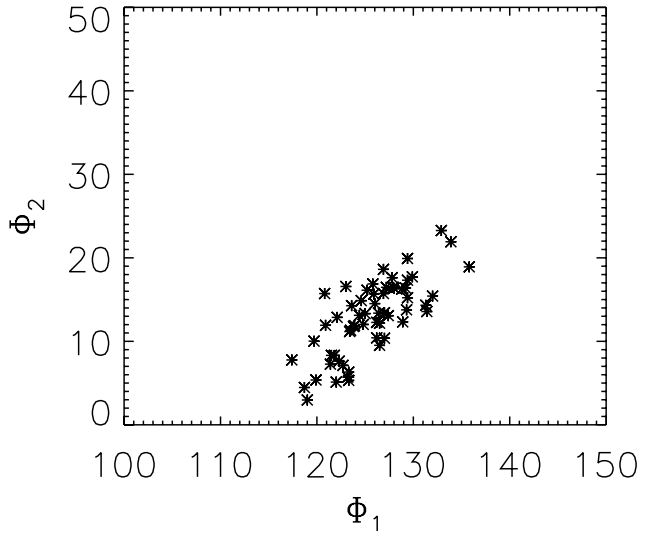

Fig. 7. Diagram showing the values of Φ_1 and Φ_2 for each pulse profile for the solution of 4U 0115+63.

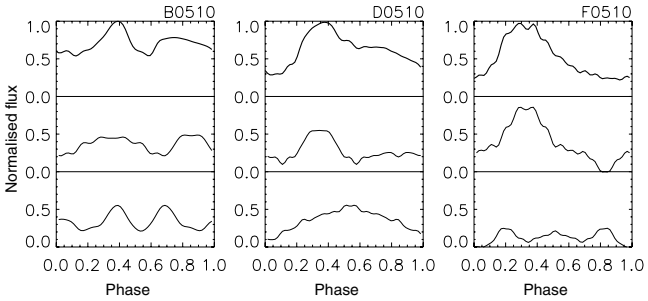

Fig. 8. Single-pole pulse profiles of 4U 0115+63 for one pole (lower curve) and the other (middle) for the observations B (maximum), D (decay), F (end of decay) in the 5–10 keV band. The upper thick curve shows the total pulse profile, which is the sum of the two single-pole pulse profiles.

3.1. 4U 0115+63

The decomposition of all pulse profiles has yielded one set of solutions that can be regarded as consistent for all observed pulse profiles: the first symmetry point is found in the range of $\Phi_1 = 115°–135°$ and the offset of the second symmetry point from $\Phi_1 + \pi$ (i.e., an antipodal configuration) has the range of $\Delta = 60°–75°$. A diagram with the obtained values for Φ_1 and Φ_2 for each pulse profile is shown in Fig. 7. Figure 8 shows an example of the two single-pole pulse profiles obtained from the Fourier decomposition (middle and bottom rows) and their sum, which is the total pulse profile (top). We can derive the geometric parameters Θ_1, Θ_2, and δ from this set of solutions, with $\Theta_{1,2}$ being the polar angles of the magnetic poles with respect to the rotation axis and δ being the offset of the second magnetic pole from the antipodal position of the first magnetic pole. To obtain these geometrical parmeters of the neutron star and also for the reconstruction of the beam patterns, we need to know the inclination angle Θ_0 of the observer with respect to the rotation axis of the neutron star. However, this number is not known for most of the accreting X-ray pulsars. For 4U 0115+63, Negueruela & Okazaki (2001) have derived a companion mass of $\sim$18 $M_\odot$ from the optical spectrum, corresponding to an inclination angle of the binary system $i \approx 40–60°$. We assumed that the rotation axis of the neutron star is perpendicular to the orbital plane, i.e., $\Theta_0 \approx i$. For the pulse profile analysis, we will assume $\Theta_0 = 60°$.

3.1.1. Asymptotic beam patterns

From the single-pole pulse profiles obtained by decomposing the observed pulse profiles, we can calculate the beam patterns for each pole as seen by the distant observer. One of our basic assumptions was that the two poles of the NS have the same beam patterns. Therefore, while the NS rotates, we see emission from pole 1 at phase Φ and the angle $\theta_{\rm obs}$ to pole 1, which may be the same as the emission from pole 2 at the same angle $\theta_{\rm obs}$ to pole 2 but at a different phase $\tilde{\Phi}$. For pole 1 the angle $\theta_{\rm obs}$ varies between $\theta_{\rm obs,min} = |\Theta_1 - \Theta_0|$ and $\theta_{\rm obs,max} = \Theta_1 + \Theta_0$ over the entire range of $\Phi/2\pi = 0–1$ (see Fig. 6). The pulse profile of pole 1 therefore displays the section of the beam pattern between $\theta_{\rm obs,min}$ and $\theta_{\rm obs,max}$. The same holds for pole 2 from which we see a different fraction of the beam pattern, which however might be partly identical with the visible fraction of the beam pattern of pole 1. If we find such identical parts of the two poles, we can overlay and connect the beam patterns and derive the relation between $\cos(\Phi - \Phi_1)$ and $\cos(\tilde{\Phi} - \Phi_2)$

$$\cos(\Phi - \Phi_1) = a + b\ \cos(\tilde{\Phi} - \Phi_2), \quad b > 0, \tag{4}$$

by determining the parameters a and b (see Kraus et al. 1995, for details).

This step of the analysis is based on the assumption that the two emission regions have identical beam patterns. There might also be some cases for which this is incorrect. However, in such cases we should see an inconsistency between the two beam patterns derived from the two single-pole pulse profiles and it will not be possible to reconstruct the total asymptotic beam pattern from the decomposition. If we obtain two parts of beam patterns that can be connected, we believe that the assumption of identical beam patterns is viable.

We shifted and scaled the two beam patterns computed from the decomposed pulse profiles as shown in Fig. 8 to obtain the best match of the two parts for a certain range of $\theta_{\rm obs}$ for all observations and all energy bands. For different values of the parameters a and b we computed the mean square deviation Q between the two beam patterns in the overlapping part. The minimum of the function $Q(a, b)$ was determined to obtain a and b for the best overlap for all observations and energy bands. The scattering of a and b obtained for each data-set represents the uncertainties of these parameters. For the pulse profiles of 4U 0115+63, we obtained $a = -1.2\ (+1.0, -1.6)$, $b = 1.8\ (+0.2, -1.3)$. The reconstructed asymptotic beam patterns seen by the distant observer are shown in Fig. 9.

The asymptotic beam patterns in Fig. 9 are plotted over the angle $\theta_{\rm obs}$ between the normal at the first magnetic pole and the line of sight. The difference between the `plus` and `minus` solutions is the assignment of the angle $\theta_{\rm obs}$: replacing $\theta_{\rm obs}$ with $\pi - \theta_{\rm obs}$ transforms the beam patterns of the `plus` solution into those of the `minus` solution, and vice versa. Therefore, the features that are seen in the `plus` solution for, e.g., lower $\theta_{\rm obs}$ are found for higher $\theta_{\rm obs}$ in the `minus` solution. The most prominent features in the beam patterns are the maximum for lower $\theta_{\rm obs}$ and the steep rise for higher $\theta_{\rm obs}$ for the `minus` solution (or the steep rise in flux for lower $\theta_{\rm obs}$ and the maximum seen in the softer bands for higher $\theta_{\rm obs}$ for the `plus` solution). In a system where a large amount of matter is accreted and the major part of the emission is caused by scattering, it is unlikely to obtain dominant flux for low $\theta_{\rm obs}$ (i.e., a pencil beam) for this wide range

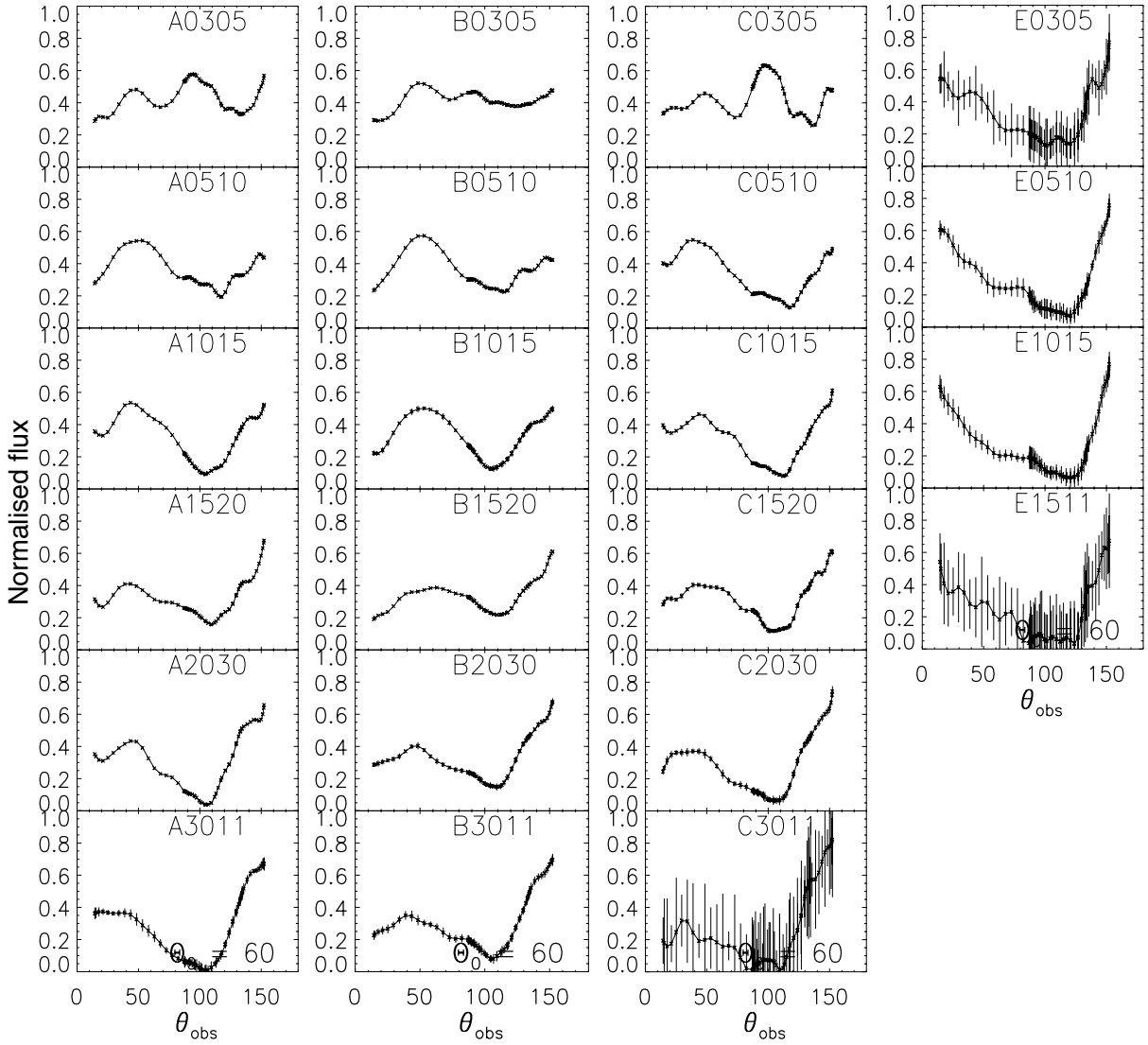

Fig. 9. Asymptotic beam patterns of 4U 0115+63 as seen by the distant observer plotted over the angle $\theta_{\rm obs}$ between the first magnetic pole and the line of sight for the observations A (before maximum), B (maximum), C (after maximum), and E (end of decay). Errors are propagated statistical errors of the pulse profiles. Only the `minus` solution is shown, which is the physically reasonable solution (see Sect. 3.1.1). The `plus` solution can be obtained by transforming $\theta_{\rm obs}$ to $\pi - \theta_{\rm obs}$.

of energy bands and luminosity, as is suggested in the `plus` solution. Also, the maximum at $\theta_{\rm obs} \approx 40°$ in the `minus` solution observed in the softer bands indicates halo emission at the base of the accretion stream, which one expects for lower $\theta_{\rm obs}$ instead of values like $\theta_{\rm obs} > 100°$ in the `plus` solution. Therefore, it is difficult to describe the `plus` solution in a physical sense and we conclude that the `minus` solution is more appropriate for the emission of 4U 0115+63. Our remaining study is performed using the `minus` solution.

3.1.2. Intrinsic beam patterns and geometry

The radiation seen by a distant observer has suffered relativistic light deflection. To understand the local emission pattern we imagined the radiation to originate from a point source at the pole and determined the intrinsic beam patterns of this hypothetical point source by relating the local direction of photon emission with the direction of propagation far away from the neutron star. To obtain these intrinsic beam patterns, we needed to make assumptions about the neutron star and remove the effects of the relativistic light deflection. We assumed a standard neutron star with $R_{\rm NS} = 10$ km and $M_{\rm NS} = 1.4\ M_\odot$. In Fig. 10 we plotted polar diagrams of the intrinsic beam patterns during the maximum and at the end of the decay. We only show the softest and the hardest bands for clarity.

The reconstruction of the total beam pattern provides us with two contraints on the pulsar geometry:

$$a = \frac{\cot\Theta_0(\cos\Theta_2 - \cos\Theta_1)}{\sin\Theta_1}, \quad b = \frac{\sin\Theta_2}{\sin\Theta_1} \tag{5}$$

(see Kraus et al. 1995). The inclination angle Θ_0 of the observer with respect to the rotation axis of the neutron star is a crucial number for the analysis. The Θ_0-dependence of the position angles of the magnetic poles Θ_1 and Θ_2 and the offset δ from the antipodal configuration of the magnetic poles is shown in Fig. 11. The errors in Fig. 11 represent the uncertainty of the determination of a and b for the reconstruction of the beam patterns,

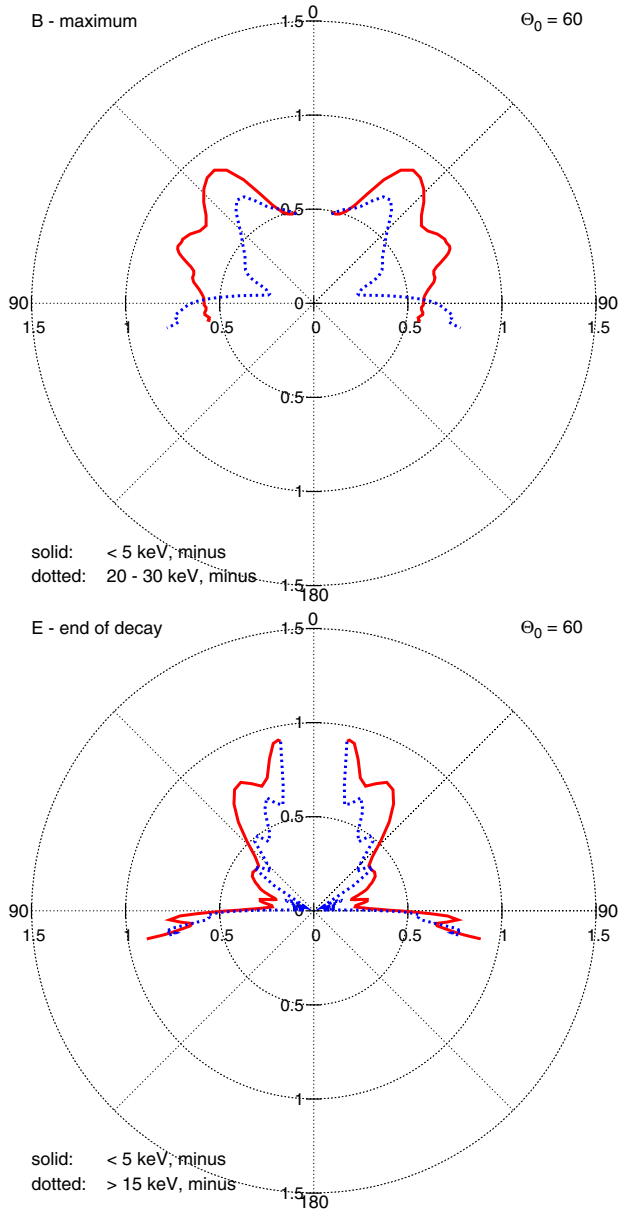

Fig. 10. Polar diagrams of the intrinsic beam patterns of 4U 0115+63 for the observations B (maximum) and E (end of decay) for the softest band and the hard band above ~20 keV. Up (0°) is the direction straight up from the magnetic pole, 90° and 270° are the directions tangential to the neutron star surface at the magnetic pole. These beam patterns correspond to the asymptotic beam patterns of the `minus` solution shown in Fig. 9.

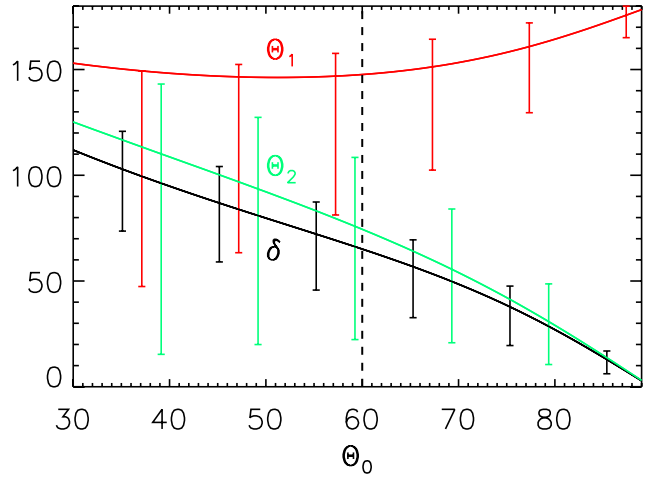

Fig. 11. Relation between the observing angle Θ_0 and the angles Θ_1 (red), Θ_2 (green), and δ (black) for 4U 0115+63. The vertical dashed line indicates $\Theta_0 = 60°$. For errors see Sect. 3.1.2.

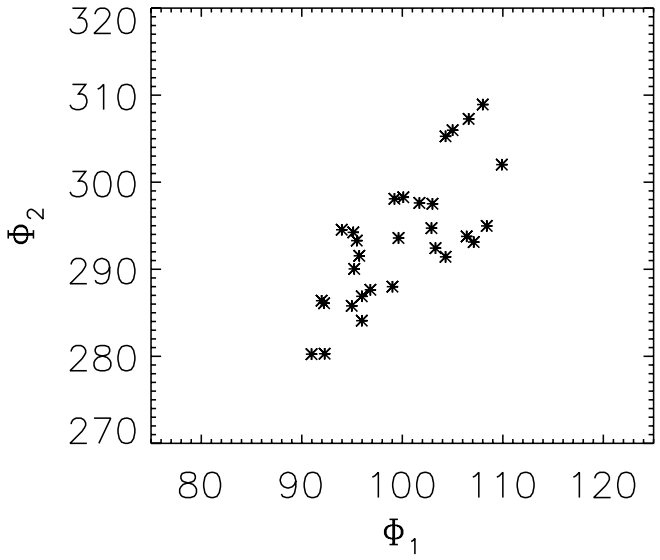

Fig. 12. Diagram showing the values of Φ_1 and Φ_2 for each pulse profile for the solution of V 0332+53.

which was made simultaneously for all analysed pulse profiles. If we determine a and b separately for each pulse profiles, the values lie within the shown errors (see Sect. 3.1.1). For an assumed $\Theta_0 = 60°$, we obtain $\Theta_1 = 148°$ $(+12°, -57°)$, $\Theta_2 = 74°$ $(+31°, -44°)$, and $\delta = 65°$ $(+14°, -26°)$.

3.2. V 0332+53

The pulse profiles of V 0332+53 were decomposed in the same way as those of 4U 0115+63. After rejecting decompositions based on the criteria listed at the beginning of this section, we obtained a region in the parameter space of $(\Phi_1, \Delta) = (91°–110°, 6°–21°)$. The resulting values for Φ_1 and Φ_2 for each pulse profile are plotted in Fig. 12. The parameters used for the reconstruction of the beam patterns are $a = -0.95$ $(+0.35, -1.05)$, $b = 1.0$ $(+0.5, -0.5)$. Because there are no measurements of the inclination angle of V 0332+53, we needed to assume an angle for the next steps of the analysis. The important features in the beam patterns (e.g., prominent maximum or minimum, increase towards lower or higher observation angles) do not change if we use different Θ_0. Only the range of the angle for the intrinsic beam patterns discussed in Sect. 3.2.2 vary slightly with assumed Θ_0. We chose to use an inclination angle of $\Theta_0 = 70°$.

3.2.1. Asymptotic beam patterns

The single-pole pulse profiles of three pulse profiles of V 0332+53 are shown in Fig. 13. Similar to the case of 4U 0115+63 discussed in Sect. 3.1.1, the `minus` solution is reasonable for V 0332+53. If we look at the asymptotic beam

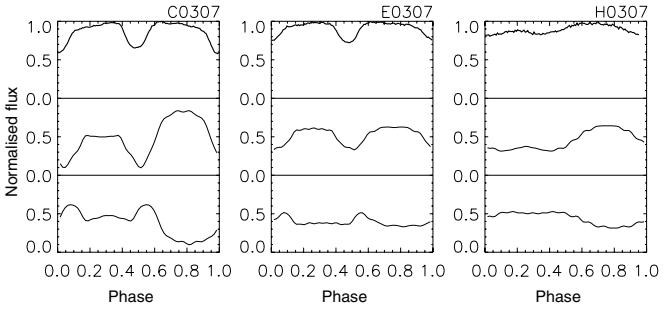

Fig. 13. Single-pole pulse profiles of V 0332+53 for one pole (lower curve) and the other (middle) for the observations C (before maximum), E (after maximum), and H (end of decay) in the softest band. The upper thick curve shows the total pulse profile, which is the sum of the two single-pole pulse profiles.

patterns of the `minus` solution in Fig. 14, the main emission is found for low $\theta_{\rm obs}$ if the source is faint (A0307 – A2030 at the beginning and H0307, H0720 at the end of the giant outburst). If the source becomes brighter we find additional components for $\theta_{\rm obs} \approx 50$–$90°$ and distinct minima at ∼50° and 110°. These shapes of beam patterns can be adequately described using accretion column models (see below).

3.2.2. Intrinsic beam patterns and geometry

Intrinsic beam patterns were calculated assuming canonical values for the neutron star ($R_{\rm NS} = 10$ km and $M_{\rm NS} = 1.4\ M_\odot$) and an observing angle of $\Theta_0 = 70°$. The beam patterns are shown in Fig. 15. Clearly, at the beginning of the giant outburst, the emission of V 0332+53 is mostly directed along the magnetic axis, indicating a pencil beam-like emission (Fig. 15, upper diagram).

Again, these results depend on the assumed observing angle Θ_0. The position angles of the magnetic poles of V 0332+53 are plotted over Θ_0 in Fig. 16. For an assumed angle of $\Theta_0 = 70°$, we obtain $\Theta_1 = 142°$ $(+18°, -22°)$, $\Theta_2 = 38°$ $(+8°, -12°)$, and $\delta = 12°$ $(+24°, -1°)$.

4. Discussion

Kraus et al. (2003, in prep.) have performed model calculations of beam patterns and pulse profiles of X-ray pulsars in a luminosity range in which a radiative shock forms in the accretion column. The authors showed that in general three main components contribute to the observed flux: the first component is radiation observed directly from the accretion column. It forms a fan beam that is bent backwards towards the observer by relativistic light deflection while the corresponding pole and thus the accretion column is located on the back side of the neutron star. For standard neutron star parameters ($R_{\rm NS} = 10$ km and $M_{\rm NS} = 1.4\ M_\odot$) the observed flux from the column peaks at $\theta_{\rm obs} > 140°$. Secondly, the illumination of the neutron star surface creates a luminous halo that produces a broad pencil beam. Since the halo is shadowed when the accretion stream passes through the line of sight, the pencil beam is suppressed for low values of $\theta_{\rm obs}$. The maximum of this "hollow pencil" is at $\theta_{\rm obs} = 30$–$50°$ for accretion funnel half widths of 5–10° at the neutron star surface. For a hollow accretion column, there is an additional peak at $\theta_{\rm obs} \approx 0°$ when the observer looks down into the hollow funnel. Thirdly, the upper accretion stream is irradiated by the column and the halo. Owing to advection in the accretion stream and gravitational light deflection, the reprocessed radiation forms a narrow anti-pencil, which is emission produced in the stream and is visible while the accreting pole is on the back side of the neutron star. The relative importance of these three components is energy-dependent; the halo is expected to dominate at low energies, the radiation reprocessed in the accretion stream is expected to dominate at the highest energies.

Cen X-3 was the first accreting X-ray pulsar to which the decomposition method was applied (Kraus et al. 1996) and for which a distorted geometry with a small offset δ was found. The derived beam patterns are a combination of a pencil and fan beam. Blum & Kraus (2000) analysed Her X-1 and again found indications for a distorted magnetic field. They have also shown that in this source, a warped and tilted accretion disk attenuates the emission from one pole of the neutron star. In the case of A 0535+26 studied by Caballero et al. (2011), the most characteristic feature of the reconstructed beam pattern at all energies is the minimum in the flux at $\theta_{\rm obs} \approx 30°$. The authors performed model calculations to interpret the beam patterns for different parameters and found that a model including a hollow column emitting black body radiation plus a thermal halo created by radiation from the column walls, which was scattered on the neutron star surface, was able to reproduce the observations well. The results show that a hollow accretion column with an half-opening angle of 0.2 rad (∼11°) and column thickness of 0.06 rad with a halo around the base can well explain the deduced beam patterns. Based on the analysis of EXO 2030+375 we showed that a considerable fraction of its emission arises from a halo while the pole is facing the observer and from the accretion stream of the other pole while it is behind the neutron star (Sasaki et al. 2010). Even if the emission regions are behind the neutron star, gravitational light bending makes the emission visible to us.

The two sources analysed in this paper also fit in this scheme. The decompositions of the pulse profiles of the above-mentioned accreting neutron stars indicate that the magnetic fields of these neutron stars are likely distorted to some extent. This is not so surprising because they might have experienced some anisotropic conditions during their birth depending on the environment in which the progenitor was located.

4.1. 4U 0115+63

We have already discussed in Sect. 3.1.1 that the `minus` solution is the likely solution for 4U 0115+63. The comparison with the synthetic beam patterns of Kraus et al. (2003, in prep.) shows that the asymptotic and intrinsic beam patterns (Figs. 9 and 10, respectively) obtained at and near the maximum of the giant outburst (A and B data) can be interpreted in terms of an accretion stream with a column and a halo at the bottom. The halo component with a maximum at around $\theta_{\rm obs} = 50°$ in the asymptotic beam patterns (Fig. 9) is most prominent in the softer bands around 10 keV (the second and the third diagrams from the top in Fig. 9). This component fades above ∼15 keV or if the luminosity drops to $\sim 10^{37}$ erg s^{-1}. The emission from the accretion column is expected for higher $\theta_{\rm obs}$. The halo and column components are also well reproduced for $\theta_{\rm intr} \approx 30$–$90°$ in the intrinsic beam patterns (Fig. 10, upper diagram). For $\theta_{\rm obs} \approx 180°$ (corresponding to $\theta_{\rm intr} \approx 90°$) there is a steep increase of the flux, which can be assigned to scattering in the accretion stream. This component is more prominent for higher energies (>20 keV) and in particular in the end-of-decay data (Fig. 10, lower diagram).

The shape of the pulse profiles becomes simpler at the end of the giant outburst (E, F data), i.e., when the luminosity drops to about or less than the tenth of that during the maximum. The

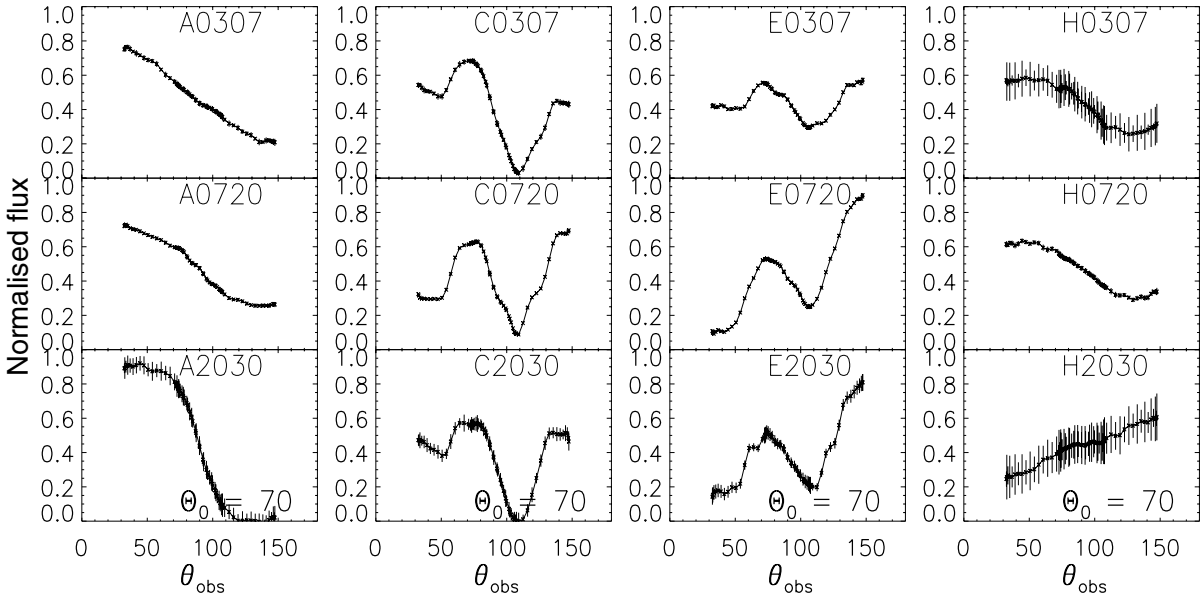

Fig. 14. Asymptotic beam patterns of V 0332+53 for the observations A (rise), C (before maximum), E (after maximum), and H (end of decay). Errors are propagated statistical errors of the pulse profiles. Only the `minus` solution is shown (see Sect. 3.2).

beam patterns are simpler as well and show no extra maxima at $\theta_{obs} \approx 50$ or 100°. The accretion has decreased so much that the accretion column and also the halo have disappeared and we now see the emission from the hot spot as a pencil beam (Fig. 10, lower panel). This emission, however, can also be scattered in the upper accretion stream. Therefore, the rise for θ_{obs} >120° may be caused by the scattering in the accretion stream.

4.2. V 0332+53

The beam patterns obtained from the analysis of the pulse profiles of V 0332+53 can also be interpreted in terms of an accretion column with halo emission and scattering in the upper accretion stream. The soft halo emission for $\theta_{obs} < 60°$ is obvious in the data around the maximum (C, D, E), while in these data, the scattering in the upper stream is prominent in the harder bands (observations C and E in Fig. 14). These components are also seen in the intrinsic beam patterns (Fig. 15, lower diagram), i.e., as halo emission for $\theta_{intr} < 70°$ and emission from the accretion stream for $\theta_{intr} > 90°$. In contrast to 4U 0115+63, there is a pronounced minimum at $\theta_{obs} = 50°$, which might indicate a hollow column. If more matter is funneled along the outer parts of the accretion column, the column can be optically thin in the center and regarded as a hollow column (Kraus 2001; Caballero et al. 2011). Because photons can also escape from the inner wall of the column, one sees emission for low θ_{obs}. If the magnetic pole turns away from the observer, there is a point where the observer looks directly down on the top of the hollow column, i.e. on the shock front. No emission is observed directly from the column, like at the minimum at $\theta_{obs} = 50°$. For even higher θ_{obs}, the emission rises again because the observer now also sees emission from the outer wall of the accretion column.

However, shadowing of the halo emission by the upper stream can also cause reduced flux in the beam patterns. The emission that is directed perpendicular to the surface of the neutron star, and thus seen for lower θ_{obs}, can be most likely attributed to the halo. The fact that the minimum is more pronounced for higher energies than for lower energies (e.g., in the E data) is in fact in favour of the shadowing of the halo emission because low-energy photons are scattered less than high-energy photons.

The most interesting result for V 0332+53 is that we can directly observe the transition from a pencil-beam emission for low luminosities, hence low accretion rate (A), to a fan-beam emission from accretion column and scattered photons for higher luminosities (C, E), and again back to a pencil beam at the end of the giant outburst (H, see Figs. 14, 15). Only the shape of one beam pattern, i.e. that of H2030, is different from that of a pencil beam, but one should consider that the statistics for this data-set are very low (see Figs. 4, 5). This is the first observational proof for the accretion models that predict emission from a hot spot at the magnetic pole of the neutron star if the accretion rate is low, whereas an accretion column is formed for increased accretion rates.

5. Conclusions

We have studied the pulse profiles of the accreting X-ray pulsars 4U 0115+63 and V 0332+53 using *BeppoSAX* and RXTE data. For both sources, we analysed pulse profiles in different energy bands for many observations during one giant outburst to examine their energy and luminosity dependence. The pulse profiles were each decomposed into two symmetric single-pole pulse profiles. Using these two emission components we reconstructed the beam patterns of the X-ray pulsars for various energies and luminosity states.

The origin of the emission of 4U 0115+63 during the high-luminosity state can be interpreted as a combination of the accretion column, the halo at the bottom of the accretion column, and the scattering of photons in the upper accretion stream. The scattering in the upper accretion stream that causes the dominant emission for energies above ~30 keV also occurs for lower luminosities and creates the major peak in the observed total pulse profile. This emission is visible to the observer while the accretion stream is on the other side of the neutron star because of relativistic light bending.

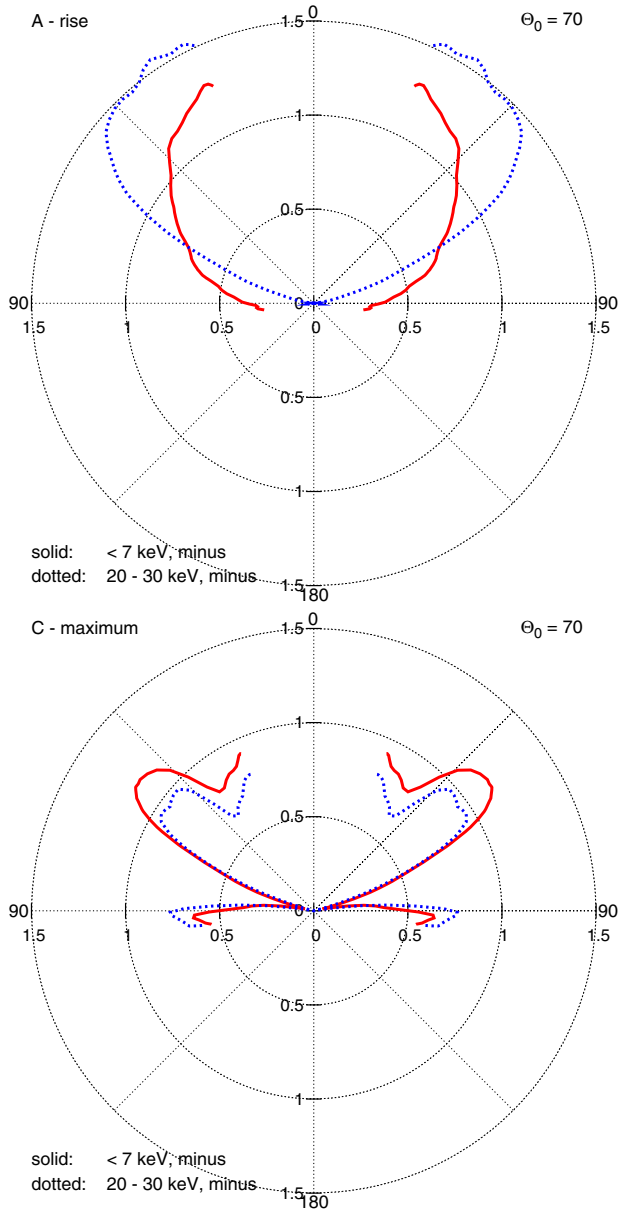

Fig. 15. Polar diagrams of the intrinsic beam patterns of V 0332+53 for the observations A (rise) and C (maximum) for <7 keV and 20–30 keV, assuming an inclination angle of $\Theta_0 = 70°$ between the line of sight and the rotation axis of the neutron star. Like in Fig. 10, up (0°) is the direction straight up from the magnetic pole, 90° and 270° are the directions tangential to the neutron star surface at the magnetic pole.

The analysis of the pulse profiles of V 0332+53 showed that its beam patterns agree also with emission from the accretion column, the halo, and the upper accretion stream while the source is bright, and hence the accretion rate is high. For this source we found a minimum in the asymptotic beam patterns at $\theta_{obs} = 50°$, which is indicative of a hollow column or shadowing by the accretion stream.

The most important result for V 0332+53 is that we found pencil-beam emission from the magnetic poles at the beginning and the end of the outburst, while other emission components are predominant during the outburst. By decomposing the observed pulse profiles into single-pole components, we showed for the first time that the change of the pulse profiles during the giant outburst of V 0332+53 is due to the transition from low accretion rate resulting in a mound, to higher accretion rate with the formation of a column and additional reprocessing on the neutron star surface as well as in the upper accretion stream, and back again to a mound when the accretion rate decreases.

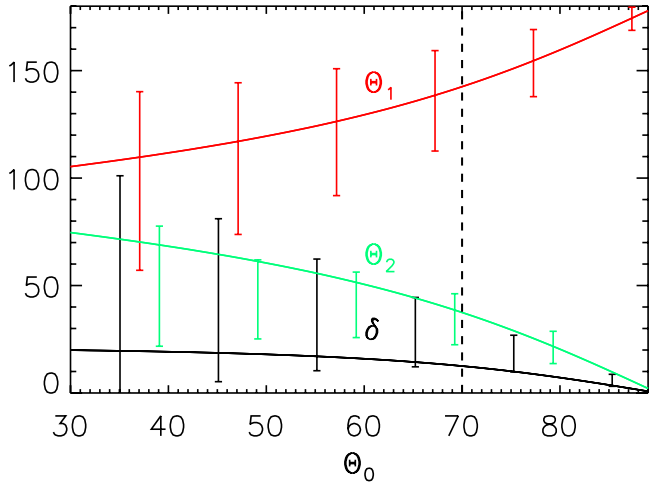

Fig. 16. Relation between the observing angle Θ_0 and the angles Θ_1 (red), Θ_2 (green), and δ (black) for V 0332+53. The vertical dashed line indicates $\Theta_0 = 70°$. For errors see Sect. 3.1.2.

Acknowledgements. This research has made use of data obtained from the High Energy Astrophysics Science Archive Research Center (HEASARC), provided by NASA's Goddard Space Flight Center. Quick-look results of the ASM are provided by the ASM/RXTE team. The *BeppoSAX* data have been provided by the Science data center of the Agenzia Spaziale Italiana (ASDC). This work was supported by DFG grant SA 1777 1/1.

References

Basko, M. M., & Sunyaev, R. A. 1976, MNRAS, 175, 395
Baushev, A. N. 2009, Astron. Rep., 53, 67
Becker, P. A., & Wolff, M. T. 2007, ApJ, 654, 435
Bernacca, P. L., Iijima, T., & Stagni, R. 1984, A&A, 132, L8
Bildsten, L., Chakrabarty, D., Chiu, J., et al. 1997, ApJS, 113, 367
Blum, S., & Kraus, U. 2000, ApJ, 529, 968
Brainerd, J. J., & Meszaros, P. 1991, ApJ, 369, 179
Bulik, T., Riffert, H., Meszaros, P., et al. 1995, ApJ, 444, 405
Caballero, I., Kraus, U., Santangelo, A., Sasaki, M., & Kretschmar, P. 2011, A&A, 526, A131
Coburn, W., Kretschmar, P., Kreykenbohm, I., et al. 2005, The Astronomer's Telegram, 381, 1
Cominsky, L., Clark, G. W., Li, F., Mayer, W., & Rappaport, S. 1978, Nature, 273, 367
Davidson, K. 1973, Nature, 246, 1
Davidson, K., & Ostriker, J. P. 1973, ApJ, 179, 585
Ferrigno, C., Becker, P. A., Segreto, A., Mineo, T., & Santangelo, A. 2009, A&A, 498, 825
Forman, W., Tananbaum, H., & Jones, C. 1976, ApJ, 206, L29
Frontera, F., & Dalfiume, D. 1989, in Two Topics in X-Ray Astronomy, Vol. 1: X Ray Binaries, Vol. 2: AGN and the X Ray Background, ed. J. Hunt, & B. Battrick, ESA SP, 296, 57
Hutchings, J. B., & Crampton, D. 1981, ApJ, 247, 222
Inoue, H. 1985, Space Sci. Rev., 40, 317
Jahoda, K., Swank, J. H., Giles, A. B., et al. 1996, in SPIE Conf. Ser. 2808, ed. O. H. Siegmund, & M. A. Gummin, 59
Johns, M., Koski, A., Canizares, C., et al. 1978, IAU Circ., 3171, 1
Johnston, M., Bradt, H., Doxsey, R., et al. 1978, ApJ, 223, L71
Kholopov, P. N., Samus', N. N., Kukarkina, N. P., Medvedeva, G. I., & Perova, N. B. 1981, Info. Bull. Var. Stars, 2042, 1
Kouveliotou, C., van Paradijs, J., Fishman, G. J., et al. 1996, Nature, 379, 799
Kraus, U. 2001, ApJ, 563, 289
Kraus, U., Nollert, H.-P., Ruder, H., & Riffert, H. 1995, ApJ, 450, 763
Kraus, U., Blum, S., Schulte, J., Ruder, H., & Meszaros, P. 1996, ApJ, 467, 794

Kraus, U., Zahn, C., Weth, C., & Ruder, H. 2003, ApJ, 590, 424
Kreykenbohm, I., Mowlavi, N., Produit, N., et al. 2005, A&A, 433, L45
Leahy, D. A. 1991, MNRAS, 251, 203
Lewin, W. H. G., Rutledge, R. E., Kommers, J. M., van Paradijs, J., & Kouveliotou, C. 1996, ApJ, 462, L39
Lyubarskii, Y. E., & Syunyaev, R. A. 1988, Sov. Astron. Lett., 14, 390
Miller, G. S. 1996, ApJ, 468, L29
Mowlavi, N., Kreykenbohm, I., Shaw, S. E., et al. 2006, A&A, 451, 187
Nagase, F., Corbet, R. H. D., Day, C. S. R., et al. 1992, ApJ, 396, 147
Nakajima, M., Mihara, T., Makishima, K., & Niko, H. 2006, ApJ, 646, 1125
Negueruela, I., & Okazaki, A. T. 2001, A&A, 369, 108
Negueruela, I., Roche, P., Fabregat, J., & Coe, M. J. 1999, MNRAS, 307, 695
Parmar, A. N., White, N. E., & Stella, L. 1989, ApJ, 338, 373
Pottschmidt, K., Kreykenbohm, I., Wilms, J., et al. 2005, ApJ, 634, L97
Rappaport, S., Clark, G. W., Cominsky, L., Li, F., & Joss, P. C. 1978, ApJ, 224, L1
Riffert, H., & Meszaros, P. 1988, ApJ, 325, 207
Riffert, H., Nollert, H.-P., Kraus, U., & Ruder, H. 1993, ApJ, 406, 185
Santangelo, A., Segreto, A., Giarrusso, S., et al. 1999, ApJ, 523, L85
Sasaki, M., Klochkov, D., Kraus, U., Caballero, I., & Santangelo, A. 2010, A&A, 517, A8
Staubert, R., Kendziorra, E., Pietsch, W., et al. 1980, ApJ, 239, 1010
Stella, L., White, N. E., Davelaar, J., et al. 1985, ApJ, 288, L45
Terrell, J., & Priedhorsky, W. C. 1984, ApJ, 285, L15
Tsygankov, S. S., Lutovinov, A. A., Churazov, E. M., & Sunyaev, R. A. 2006, MNRAS, 371, 19
Tsygankov, S. S., Lutovinov, A. A., Churazov, E. M., & Sunyaev, R. A. 2007, Astron. Lett., 33, 368
Wang, Y., & Welter, G. L. 1981, A&A, 102, 97
White, N. E., Swank, J. H., & Holt, S. S. 1983, ApJ, 270, 711
Whitlock, L., Roussel-Dupre, D., & Priedhorsky, W. 1989, ApJ, 338, 381
Zhang, S., Qu, J., Song, L., & Torres, D. F. 2005, ApJ, 630, L65

A&A 546, A80 (2012)
DOI: 10.1051/0004-6361/201220200

Astronomy & Astrophysics

Observations of the post-shock break-out emission of SN 2011dh with *XMM-Newton*⋆ *(Research Note)*

M. Sasaki and L. Ducci

Institut für Astronomie und Astrophysik, Universität Tübingen, Sand 1, 72076 Tübingen, Germany
e-mail: sasaki@astro.uni-tuebingen.de

Received 10 August 2012 / Accepted 16 September 2012

ABSTRACT

Context. After the occurrence of the type cIIb SN 2011dh in the nearby spiral galaxy M 51 numerous observations were performed with different telescopes in various bands ranging from radio to γ-rays.
Aims. We analysed the *XMM-Newton* and *Swift* observations taken 3 to 30 days after the SN explosion to study the X-ray spectrum of SN 2011dh.
Methods. We extracted spectra from the *XMM-Newton* observations, which took place ∼7 and 11 days after the SN. In addition, we created integrated *Swift*/XRT spectra of 3 to 10 days and 11 to 30 days.
Results. The spectra can be well-fitted with a power-law spectrum absorbed with Galactic foreground absorption. In addition, we find a harder spectral component in the first *XMM-Newton* spectrum taken at $t \approx 7$ d. This component is also detected in the first *Swift* spectrum of $t = 3$–10 d.
Conclusions. While the persistent component can be explained as inverse Compton emission from radio synchrotron emitting electrons or emission of the reverse shock, the harder component is most likely bremsstrahlung emission from the shocked stellar wind. Therefore, the harder X-ray emission that fades away after $t \approx 10$ d can be interpreted as emission from the shocked circumstellar wind of SN 2011dh.

Key words. shock waves – circumstellar matter – supernovae: individual: SN2011dh

1. Introduction

Massive stars at the end of their lives have undergone phases of more or less strong mass loss. The evolution of the stars and thus also the way their supernovae (SNe) evolve, depend strongly on their mass loss rates. The interaction of the SN shock wave with the stellar wind creates a hot region around the SN site in which electrons are accelerated and produce radio synchrotron emission. The hot plasma around the SNe can be observed in X-rays. Strong X-ray emission is in particular expected when the SN shock wave breaks out of the star and starts propagating into the circumstellar material (Chevalier & Irwin 2011, 2012, and references therein). Owing to prompt observations with the *Swift* or the *Chandra* telescope, X-rays from the interaction of the SN shock with the circumstellar matter have been detected for a number of SNe (e.g., SN 2006jc or SN 2010jl, Immler et al. 2008; Chandra et al. 2012, respectively). Soderberg et al. (2008) detected a transient X-ray source with *Swift*, which was then identified as SN 2008D in the galaxy NGC 2770. The X-ray outburst was ascribed to the shock break-out of the SN.

On May 31, 2011, a supernova explosion was observed (Silverman et al. 2011) in the nearby galaxy M 51 located at a distance of 8.4 ± 0.7 Mpc (Vinkó et al. 2012). It was classified as a type IIb SN (Arcavi et al. 2011a). Several radio, optical, and X-ray observations followed to study the SN evolution, which also allowed to constrain the nature of the progenitor, suggesting a compact progenitor star with a radius of $\sim 10^{11}$ cm and thus the classification of SN 2011dh as a type cIIb SN (Arcavi et al. 2011b; Soderberg et al. 2012).

Soderberg et al. (2012) studied SN 2011dh using *Swift* and *Chandra* data in X-rays and the Submillimeter Array, the Combined Array for Research in Millimeter-wave Astronomy, and the Expanded Very Large Array in radio in the following weeks. They showed that the observed radio emission is synchrotron radiation of electrons, accelerated in the forward shock of the SN explosion, while inverse Compton (IC) scattering of these electrons produced X-rays. The authors estimated that the break-out of the shock out of the compact progenitor must have occured at $R_{\rm br} \approx 4 \times 10^{11}$ cm with a rise time for the break-out pulse of $t_{\rm br} \approx 1$ min. However, the shock break-out pulse was not detected by any X-ray or γ-ray observatory.

We report the detection of a hard X-ray component in the early spectra of SN 2011dh observed with *XMM-Newton* and *Swift*. The comparison of the spectra taken at different times after the SN event ranging from $t = 3$ to 30 d allows us to consider this component as emission from the interaction of the SN shock with the circumstellar material in the immediate surroundings of the progenitor star.

2. Data

2.1. XMM-Newton data

Shortly after SN 2011dh occured, two observations with *XMM-Newton* were initiated. The first observation with the

⋆ Based on observations obtained with *XMM-Newton*, an ESA science mission with instruments and contributions directly funded by ESA Member States and NASA.

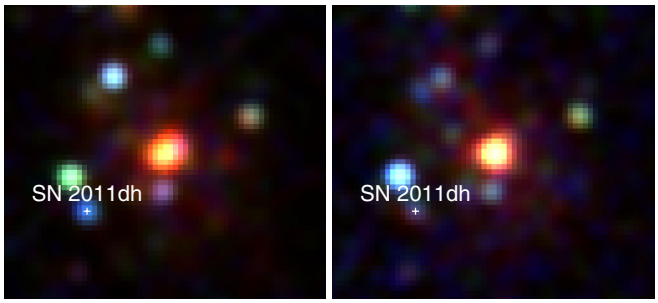

Fig. 1. *XMM-Newton* EPIC-pn images ~7 d (*left*) and ~11 d (*right*) after the SN explosion in the colours red (0.3–1.0 keV), green (1.0–2.0 keV), and blue (2.0–8.0 keV).

ObsID 0677980701 was performed at $t \approx 7$ d after the SN explosion from 2011/06/07, 5:19:56 to 2011/06/07, 8:30:40 (UTC) with an exposure of ~11 ks. All European Photon Imaging Cameras (EPICs, Strüder et al. 2001; Turner et al. 2001) were operated in full-frame mode and used with the thin filter. The next observation took place from 2011/06/11, 5:05:03 to 2011/06/11, 8:15:38 (UTC) at $t \approx 11$ d with ~10 ks exposure. The EPICs were used in the same configuration as in the observations before. After filtering good time intervals, only 4 and 2.6 ks of useful data remained for the observations 0677980701 and 0677980801, respectively.

Owing to low statistics, the MOS1/2 data are not useful for further analysis. Therefore, we created images from the EPIC-pn data in the bands 0.3–1.0 keV, 1.0–2.0 keV, and 2.0–8.0 keV (Fig. 1). As can be seen in the EPIC-pn images, the X-ray source at the position of SN 2011dh is brighter on 2011/06/07 than on 2011/06/11 and also appears to be more blue. The red-orange appearing source in the centre is the nucleus of M 51 together with an unresolved ultra-luminous X-ray source (ULX). The other brighter blue or green sources are also ULXs in M 51 (Dewangan et al. 2005).

We extracted EPIC-pn spectra of SN 2011dh in a circular region with a radius of 20″ around the optical position. The background spectrum was extracted in a 30″ radius circle close to the source, where no X-ray source was detected. Hereafter, we call the EPIC-pn spectrum of 2011/06/07 spectrum XMM1 and that of 2011/06/11 spectrum XMM2.

2.2. Swift data

SN 2011dh was also observed with the *Swift* satellite in a large number of observations to study the evolution of the X-ray emission. Soderberg et al. (2012) derived the X-ray fluxes of SN 2011dh from *Swift* observations taken with the X-ray telescope (XRT) from 2011/06/03 to 29 and analysed the integrated spectrum from the observations of 2011/06/03 to 17. Since we aim to study the *Swift* spectra at times comparable to the *XMM-Newton* observations, we collected XRT observations of SN 2011dh starting ~3 d after the SN explosion, in the time period from 2011/06/03 12:04:02 (UT) to 2011/06/10 17:08:32 (total exposure time of ~44 ks) and in a later period from 2011/06/11 04:55:01 to 2011/06/30 12:33:50 (total exposure time of ~85 ks). The XRT data obtained in photon-counting (PC) mode were processed with the standard procedures (XRTPIPELINE v.0.12.6, Burrows et al. 2005). Standard grade filtering (0–12) and screening criteria were applied.

Events for the spectral analysis were accumulated within the same circular regions as for the *XMM-Newton* spectra, i.e., with 20″ radius centred on the optical position of the SN for the source spectrum and from a source-free circular region of radius 30″ close to the SN for the background. We used version v.013 of the response matrices in HEASARC calibration database (CALDB) and the corresponding ancillary response files created using the task XRTMKARF. We call the integrated spectrum of 2011/06/03 to 10 spectrum *Swift*1 and that of 2011/06/11 to 30 spectrum *Swift*2.

3. Spectral analysis

The spectrum *Swift*1 is merged from the data of 2011/06/03 to 10 and thus represents an average spectrum of before 2011/06/10. Similarly, spectrum *Swift*2 is an average spectrum of after 2011/06/11. Therefore, the four analysed spectra have the following chronological order: *Swift*1, XMM1, XMM2, and *Swift*2, with *Swift*1 and XMM1 corresponding to spectra taken at similar times.

3.1. The longer persistent soft X-ray emission

We analysed the two *XMM-Newton* and two *Swift* spectra simultaneously to search for changes in the spectral components. Pooley (2011) reported that the *Chandra* spectrum taken on 2011/06/12 can be fitted with a power-law spectrum with a photon index of $\Gamma = 1.4 \pm 0.3$, absorbed by the Galactic foreground $N_{\rm H} = 1.8 \times 10^{20}$ cm^{-2}. For the *Swift* spectra from 2011/06/03 to 17, Soderberg et al. (2012) determined a photon index of $\Gamma = 0.9$–1.8. We therefore fitted the spectra first with a single power-law model, also assuming foreground absorption by Galactic $N_{\rm H} = 1.8 \times 10^{20}$ cm^{-2}. The first two spectra *Swift*1 and XMM1 can be fitted with a lower photon index of $\Gamma = 1.1$ (1.0–1.3)[1] with red. $\chi^2 = 1.1$ and d.o.f. = 33, whereas the spectra XMM2 and *Swift*2 taken after 2011/06/11 are fitted well with $\Gamma = 1.8$ (1.5–2.0) with red. $\chi^2 = 1.1$ and d.o.f. = 23. Therefore, the spectra taken on the first ~10 days after the SN are significantly different from the subsequent spectra.

We also fitted all spectra with a single thermal bremsstrahlung model. While the temperatures fitted for the first two spectra ($t < 10$ d) are unconstrained ($kT_{\rm brems,\mathit{Swift}1} > 9$ keV and $kT_{\rm brems,XMM1} > 22$ keV, respectively), the two later spectra ($t > 11$ d) are both fitted well with temperatures of $kT_{\rm brems,XMM2} = 3(1-18)$ keV and $kT_{\rm brems,\mathit{Swift}2} = 3(2-8)$ keV (red. $\chi^2 = 1.1$ at d.o.f. = 56).

3.2. The fading hard X-ray emission

A likely origin of the additional harder component in the earlier spectra is free-free emission from the shocked circumstellar wind (Chevalier & Fransson 2003). If we keep the power-law component and include an additional free-free emission component for the earlier spectra *Swift*1 and XMM1, the photon indices of their power-law component become higher with $\Gamma = 2.0$ (1.6–2.5) (red. $\chi^2 = 1.1$ at d.o.f. = 32). Moreover, we obtain an additional absorbing column density of $N_{\rm Hintr} = 7.2$ (1.3–15.0) $\times 10^{20}$ cm^{-2}. The flux of the power-law component is the same for all four spectra with the unabsorbed flux being $F_{\rm pow}(0.3-8.0\ {\rm keV}) = 1.1(0.8-1.5) \times 10^{-13}$ erg cm^{-2} s^{-1}. The temperature of the bremsstrahlung component is poorly constrained and we can only determine a lower limit of $kT_{\rm brems} > 42$ keV. Figure 2 shows

[1] All errors in this paper given in brackets are at 90% confidence level.

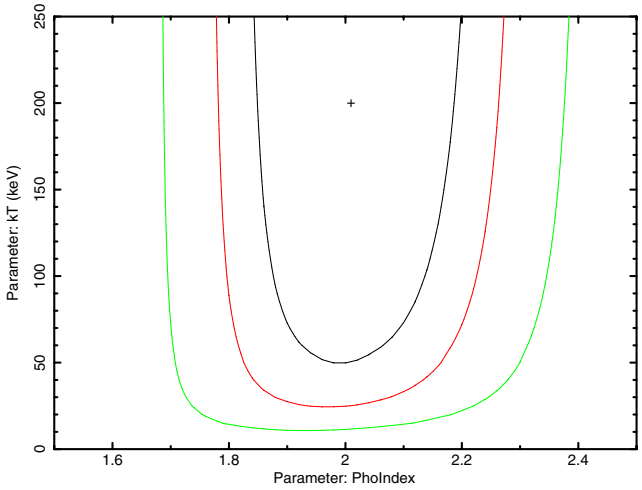

Fig. 2. Confidence level contours (63, 90, and 99%) for the parameters $kT_{\rm brems}$ and Γ.

the confidence contours for the parameters $kT_{\rm brems}$ and Γ. The unabsorbed flux of the bremsstrahlung component is $F_{\rm brems}(0.3{-}8.0\ {\rm keV}) = 1.3(0.9{-}1.7) \times 10^{-13}$ erg cm^{-2} s^{-1} and $1.1(0.7{-}1.6) \times 10^{-13}$ erg cm^{-2} s^{-1} for *Swift*1 and XMM1, i.e., for $t < 10$ d and $t = 7$ d, respectively. While this component has disappeared at $t = 11$ d with an upper limit of the unabsorbed flux of $F_{\rm brems}(0.3{-}8.0\ {\rm keV}) < 0.6 \times 10^{-13}$ erg cm^{-2} s^{-1}, the power-law component seems to represent emission that is persistent up to 30 d or longer. Figure 3 shows the first two spectra *Swift*1 and XMM1 with a model consisting of a bremsstrahlung and a power-law component (upper diagram), while the later spectra XMM2 and *Swift*2 are shown with the single power-law fits (lower diagram).

Immler & Lewin (2003), on the other hand, discussed the presence of a blackbody continuum of the shocked hot circumstellar gas. If we fit the spectra *Swift*1 and XMM1 with a blackbody model for the additional hard component, we obtain a temperature of $kT_{\rm BB} = 1.6(1.7{-}2.8)$ keV. The luminosities are $L_{\rm BB}(< 10\ {\rm d}) = 1.6(0.8{-}3.7) \times 10^{39}$ erg s^{-1} and $L_{\rm BB}(7\ {\rm d}) = 1.6(0.8{-}3.1) \times 10^{39}$ erg s^{-1} for *Swift*1 and XMM1, respectively. From the fits of the spectra XMM2 and *Swift*2, we obtain the following upper limits: $L_{\rm BB}(11\ {\rm d}) < 0.8 \times 10^{39}$ erg s^{-1} and for XMM1, $L_{\rm BB}(11{-}30\ {\rm d}) < 0.3 \times 10^{39}$ erg s^{-1}.

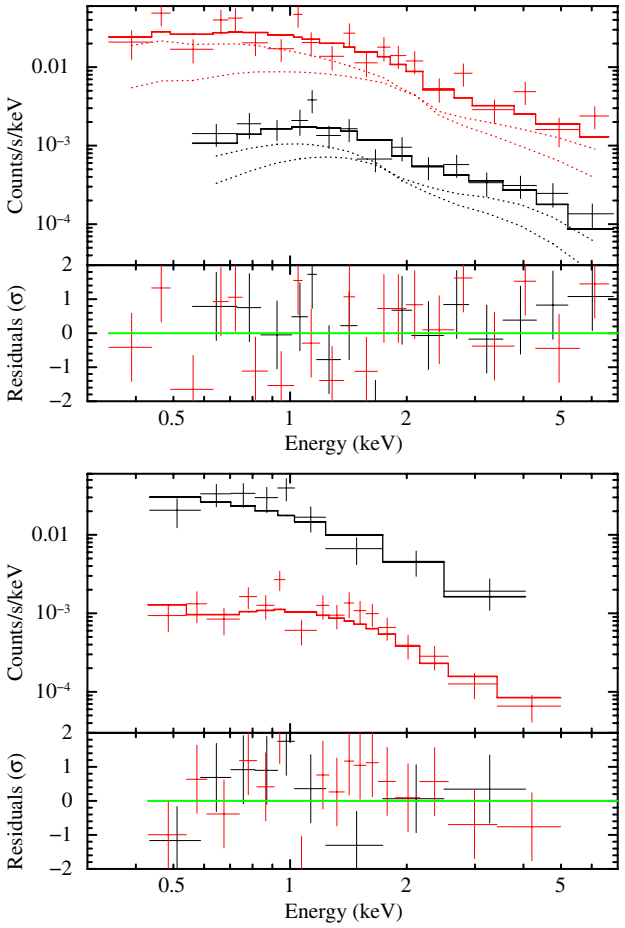

Fig. 3. X-ray spectra of SN 2011dh: stacked *Swift* spectrum for $t < 10$ d (Swift1, black in the *upper* diagram), *XMM-Newton* EPIC-pn spectrum taken at $t \approx 7$ d (XMM1, red in the *upper* diagram), *XMM-Newton* EPIC-pn spectrum taken at $t \approx 11$ d (XMM2, black in the *lower* diagram), and stacked *Swift* spectrum for $11 < t < 30$ d (Swift2, red in the *lower* diagram). The spectra in the *upper* diagram are fitted with a combined power-law + bremsstrahlung spectrum, while the spectra in the *lower* diagram are fitted with a power-law spectrum only. The *Swift* spectra appear at a lower countrate per energy bin due to the lower effective area of the detector.

4. Discussion

Many SNe show a softening of their X-ray spectrum days to months after the SN event (e.g., Immler & Kuntz 2005, and references therein). If the X-ray emission is mainly caused by an IC process, as proposed for SN 2011dh by Soderberg et al. (2012), one expects $dL_X/dE \propto E^{-(p-1)/2}$, with p being the spectral index of the energy of the injected electrons responsible also for the radio synchrotron emission (e.g., Chevalier et al. 2006). This, of course, is based on the simple assumption that the particle spectrum does not change over a broad spectral range. In reality, some acceleration processes or particle losses can modify the spectrum. As the power-law fits of XMM1 and *Swift*1 vs. *Swift*2 and XMM2 have shown, the photon indices are significantly different ($\Gamma = 1.1$ [1.0–1.3] and 1.8 [1.5–2.0], respectively) and indicate a temporal change in the X-ray spectrum. Assuming that the particle spectrum does not change its shape significantly, the softening of the X-ray spectrum is most likely not caused by the change of the slope of the non-thermal spectrum, but rather by the change of the emission components. The X-ray emitting gas behind the blast wave of the SN shock is expected to have high temperatures of 100 keV or higher, while the gas behind the reverse shock is cooler (~1–10 keV, Immler 2003). Hence a likely explanation for the softening of the X-ray spectrum is that the reverse shock emission becomes more dominant.

The analysis of the *XMM-Newton* EPIC-pn and *Swift* XRT spectra of SN 2011dh have shown that the X-ray spectrum changes during ~10 d after the SN event. If we assume that the longer persistent X-ray emission component can be interpreted as thermal bremsstrahlung, we obtain a temperature of ~3 keV after $t \approx 11$ d, i.e., $\sim 3 \times 10^7$ K, corresponding to a shock velocity of ~1500 km s^{-1}, which is far lower than what was measured in the optical spectra at these times (~10 000 km s^{-1}, Arcavi et al. 2011b). Therefore, this component is better identified as reverse shock emission or IC emission. In this case, the additional hot component observed only until ~10 d after the SN event might be emission from circumstellar gas shocked by the forward shock.

A similar X-ray emission was also detected for SN 1993J with ROSAT a few days after the SN explosion, which occured in the galaxy M 81 at a distance of 3.6 kpc (Zimmermann et al. 1994). This emission was fitted well with a power-law spectrum with $\Gamma = 1.0 \pm 0.25$ or a bremsstrahlung spectrum with $kT_{\rm brems} > 7$ keV, and decreased exponentially during the ~40 d in which it was observed.

Assuming free-free emission for the hard component, we obtain a lower limit for the temperature of $kT_{\rm brems} > 42$ keV. The flux at $t = 7$ d is $F_{\rm brems}(0.3-8.0\ {\rm keV}) = (1.1 \pm 0.5) \times 10^{-13}$ erg cm^{-2} s^{-1}, corresponding to $L_{\rm brems}(0.3{-}8.0\ {\rm keV}) \approx 9.3 \times 10^{38}$ erg s^{-1}. Using the lower limit for the temperature, we obtain a lower limit for the shock velocity of

$$v_{\rm s} = \sqrt{\frac{16 kT_{\rm brems}}{3\bar{m}}} > 9800\ {\rm km\ s^{-1}}, \quad (1)$$

with a mean mass per free particle for fully ionised plasma of $\bar{m} = 0.61\ m_{\rm p}$. Soderberg et al. (2012) estimated $v_{\rm s} \approx 0.1\ c$, which is about three times higher than this lower limit. The *XMM-Newton* and *Swift* spectra that only extend up to ~10 keV do not allow us to constrain the temperature for a bremsstrahlung model. Using $v_{\rm s} \approx 0.1\ c$ derived by Soderberg et al. (2012), we estimate that at $t = 7$ d, the shock must have reached a radius of $R_{\rm s} \approx v_{\rm s} t \approx 1.8 \times 10^{15}$ cm. Therefore, from the bremsstrahlung spectrum at $t = 7$ d, we derive a down-stream density of $n = 6.4 \times 10^7$ cm^{-3} at $R_{\rm s} \approx 1.8 \times 10^{15}$ cm.

On the other hand, we can also estimate the stellar wind density based on the assumption made about the progenitor star. SN 2011dh was classified as a type IIb SN with a compact progenitor, making a Wolf-Rayet (WR) star a likely progenitor candidate (Chevalier & Soderberg 2010). The number density of the wind at a distance r from the WR star is given by the continuity equation:

$$n(r) = \frac{\dot{M}}{4\pi\mu m_{\rm p} r^2 v(r)}, \quad (2)$$

where $\dot{M}$ is the mass-loss rate, μ is the mean atomic weight of the wind material, and $v(r)$ is the β-velocity law (Castor et al. 1975):

$$v(r) = v_\infty \left(1 - \frac{bR_*}{r}\right)^\beta. \quad (3)$$

R_* is the stellar radius, v_∞ the terminal velocity, $b = 0.9983$ a parameter that ensures that $v(R_*) > 0$, and $\beta = 4$–8 for WR stars (Schmutz 1997). The volume integral of equation (2) over a shell with radii $R_{\rm br}$ and $R_{\rm s}$ centred at the position of the WR star gives the total number of particles:

$$N = \int_V n(r) {\rm d}r. \quad (4)$$

Thus, from Eq. (4), it is possible to obtain the average number density in that shell:

$$\bar{n} = N \times \left[\frac{4}{3}\pi \left(R_{\rm s}^3 - R_{\rm br}^3\right)\right]^{-1}. \quad (5)$$

Soderberg et al. (2012) estimated a stellar radius of $R_* = 10^{11}$ cm, a shock break-out radius of $R_{\rm br} = 4 \times 10^{11}$ cm, and a mass loss rate of $\dot{M} = 3 \times 10^{-5}\ M_\odot\ {\rm yr}^{-1}$. With a typical wind velocity of $v_\infty = 10^3\ {\rm km\ s^{-1}}$ and $R_{\rm s} = 1.8 \times 10^{15}$ cm at $t = 7$ d, we obtain a mean stellar wind density of $\bar{n} \approx 8 \times 10^5$ cm^{-3} from Eq. (5). This calculation is based on the assumption that the stellar wind density is highest close to the stellar surface and decreases with $\sim r^{-2}$. However, the stellar wind material might as well form a dense shell around the star at a certain distance, as was most likely the case for SN 2006jc (Immler et al. 2008). This SN showed an increase in X-rays about 100 days after the explosion, which was interpreted as emission from shock-heated shell at $R_{\rm s} \approx 10^{16}$ cm with a thickness of $\Delta R \approx 2 \times 10^{15}$ cm. A similar condition may have been the case also for SN 2011dh, but with a shell located closer to the star, which resulted in an earlier rise and decay of the X-ray emission.

5. Summary

Two *XMM-Newton* observations of SN 2011dh performed ~7 and 11 days after the discovery revealed that the X-ray spectrum changes significantly at about 10 days after the explosion. The analysis of the *XMM-Newton* EPIC-pn spectra and additional stacked *Swift*/XRT spectra extracted from many observations of similar periods supports the existence of two spectral components, of which the harder disappeared after ~10 days. The softer component can be identified either as IC emission, as suggested by Soderberg et al. (2012), or as reverse shock emission with an unabsorbed flux of $F_{\rm soft}(0.3{-}8.0\ {\rm keV}) \approx 1 \times 10^{-13}$ erg cm^{-2} s^{-1} up to $t \approx 30$ d. The flux of the hard component, if we assume that it is bremsstrahlung emission, is $F_{\rm brems}(0.3{-}8.0\ {\rm keV}) = (1.1 \pm 0.5) \times 10^{-13}$ erg cm^{-2} s^{-1} at $t = 7$ d, and therefore comparable to the soft component, and decreases quickly thereafter. This indicates that this emission has its origin in the circumstellar matter that extends to ~10^{15} cm and was heated by the SN shock.

Acknowledgements. This research has made use of data obtained from the High Energy Astrophysics Science Archive Research Center (HEASARC), provided by NASA's Goddard Space Flight Center. This work was support by the Deutsche Forschungsgemeinschaft through the Emmy Noether Research Grant SA 2131/1.

References

Arcavi, I., Gal-Yam, A., Polishook, D., et al. 2011a, The Astronomer's Telegram, 3413, 1
Arcavi, I., Gal-Yam, A., Yaron, O., et al. 2011b, ApJ, 742, L18
Burrows, D. N., Hill, J. E., Nousek, J. A., et al. 2005, Space Sci. Rev., 120, 165
Castor, J. I., Abbott, D. C., & Klein, R. I. 1975, ApJ, 195, 157
Chandra, P., Chevalier, R. A., Irwin, C. M., et al. 2012, ApJ, 750, L2
Chevalier, R. A., & Fransson, C. 2003, in Supernovae and Gamma-Ray Bursters, ed. K. Weiler, Lect. Notes Phys. (Berlin: Springer Verlag), 598, 171
Chevalier, R. A., & Soderberg, A. M. 2010, ApJ, 711, L40
Chevalier, R. A., & Irwin, C. M. 2011, ApJ, 729, L6
Chevalier, R. A., & Irwin, C. M. 2012, ApJ, 747, L17
Chevalier, R. A., Fransson, C., & Nymark, T. K. 2006, ApJ, 641, 1029
Dewangan, G. C., Griffiths, R. E., Choudhury, M., Miyaji, T., & Schurch, N. J. 2005, ApJ, 635, 198
Immler, S. 2003, in High Energy Processes and Phenomena in Astrophysics, eds. X. D. Li, V. Trimble, & Z. R. Wang, IAU Symp., 214, 113
Immler, S., & Kuntz, K. D. 2005, ApJ, 632, L99
Immler, S., & Lewin, W. H. G. 2003, in Supernovae and Gamma-Ray Bursters, Lect. Notes Phys. (Berlin: Springer Verlag), ed. K. Weiler, 598, 91
Immler, S., Modjaz, M., Landsman, W., et al. 2008, ApJ, 674, L85
Pooley, D. 2011, The Astronomer's Telegram, 3456, 1
Schmutz, W. 1997, A&A, 321, 268
Silverman, J. M., Filippenko, A. V., & Cenko, S. B. 2011, The Astronomer's Telegram, 3398, 1
Soderberg, A. M., Berger, E., Page, K. L., et al. 2008, Nature, 453, 469
Soderberg, A. M., Margutti, R., Zauderer, B. A., et al. 2012, ApJ, 752, 78
Strüder, L., Briel, U., Dennerl, K., et al. 2001, A&A, 365, L18
Turner, M. J. L., Abbey, A., Arnaud, M., et al. 2001, A&A, 365, L27
Vinkó, J., Takáts, K., Szalai, T., et al. 2012, A&A, 540, A93
Zimmermann, H.-U., Lewin, W., Predehl, P., et al. 1994, Nature, 367, 621

The Astrophysical Journal, 617:322–338, 2004 December 10

XMM-NEWTON OBSERVATIONS OF THE GALACTIC SUPERNOVA REMNANT CTB 109 (G109.1−1.0)

Manami Sasaki, Paul P. Plucinsky, Terrance J. Gaetz, Randall K. Smith,
Richard J. Edgar, and Patrick O. Slane
Harvard-Smithsonian Center for Astrophysics, 60 Garden Street, Cambridge, MA 02138; msasaki@cfa.harvard.edu
Received 2004 April 28; accepted 2004 August 27

ABSTRACT

We present the analysis of the *X-ray Multimirror Mission* (*XMM-Newton*) European Photon Imaging Camera (EPIC) data of the Galactic supernova remnant (SNR) CTB 109 (G109.1−1.0). CTB 109 is associated with the anomalous X-ray pulsar (AXP) 1E 2259+586 and has an unusual semicircular morphology in both the X-ray and the radio and an extended X-ray bright interior region known as the "Lobe." The deep EPIC mosaic image of the remnant shows no emission toward the west where a giant molecular cloud complex is located. No morphological connection between the Lobe and the AXP is found. We find remarkably little spectral variation across the remnant given the large intensity variations. All spectra of the shell and the Lobe are well fitted by a single-temperature nonequilibrium ionization model for a collisional plasma with solar abundances [$kT \approx 0.5$–0.7 keV, $\tau = \int n_e\, dt \approx (1\text{–}4) \times 10^{11}$ s cm^{-3}, $N_{\rm H} \approx (5\text{–}7) \times 10^{21}$ cm^{-2}]. There is no indication of nonthermal emission in the Lobe or the shell. We conclude that the Lobe originated from an interaction of the SNR shock wave with an interstellar cloud. Applying the Sedov solution for the undisturbed eastern part of the SNR and assuming full equilibration between the electrons and ions behind the shock front, the SNR shock velocity is derived as $v_s = 720 \pm 60$ km s^{-1}, the remnant age as $t = (8.8 \pm 0.9) \times 10^3 d_3$ yr, the initial energy as $E_0 = (7.4 \pm 2.9) \times 10^{50} d_3^{2.5}$ ergs, and the preshock density of the nuclei in the ambient medium as $n_0 = (0.16 \pm 0.02) d_3^{-0.5}$ cm^{-3}, at an assumed distance of $D = 3.0 d_3$ kpc. Assuming that CTB 109 and 1E 2259+586 are associated, these values constrain the age and the environment of the progenitor of the SNR and the pulsar.

Subject headings: ISM: individual (CTB 109) — shock waves — supernova remnants — X-rays: individual (CTB 109)

1. INTRODUCTION

The Galactic supernova remnant (SNR) CTB 109 (G109.2−1.0) was discovered in X-rays with *Einstein* by Gregory & Fahlman (1980). In the radio band, it was identified as an SNR by Hughes et al. (1981) in the Galactic plane survey at $\lambda 49$ cm with the Westerbork Synthesis Radio Telescope. CTB 109 is the host remnant of the anomalous X-ray pulsar (AXP) 1E 2259+586 with a spin period of $P = 6.98$ s (Fahlman & Gregory 1981, 1983) and a spin-down rate of $(3\text{–}6) \times 10^{-13}$ s s^{-1} (Iwasawa et al. 1992). In 2002, an outburst of 1E 2259+586 occurred with bursts similar to soft gamma repeaters and with a sudden spin-up of $\delta\nu/\nu = 4 \times 10^{-6}$ (Kaspi et al. 2003; Gavriil et al. 2004; Woods et al. 2004).

The distance to the SNR has been estimated from various observations as 3–6 kpc (Sofue et al. 1983; Hughes et al. 1984; Kothes et al. 2002 and references therein). A distance of 3.0 ± 0.5 kpc has been derived by Kothes et al. (2002) by measuring the spectroscopic distances and radial velocities of H II regions and comparing those values to the radial velocity of CTB 109 measured by Tatematsu et al. (1990). The remnant is embedded in a large complex of H II regions that extends over 400 pc along the Galactic plane.

At radio frequencies, Hughes et al. (1984) have derived a spectral index of $\alpha = 0.50 \pm 0.04$, for flux density $S_\nu \propto \nu^{-\alpha}$ and frequency ν, which does not vary across the remnant. The remnant shell is incomplete in the west, in both radio and X-rays (see Fig. 1). Bright spots are found around the rim, but the features do not correlate in the two bands. No radio point source is found at the position of the X-ray pulsar, which is displaced by $3\farcm6$ from the geometrical center of the radio shell.

CTB 109 is located near a giant molecular cloud (GMC) complex (Israel 1980) that contains five H II regions. Heydari-Malayeri et al. (1981) and Tatematsu et al. (1985) have suggested that this GMC complex is associated with the SNR based on CO and ^{13}CO observations. Data from the *ROSAT* PSPC confirm that there is no X-ray emission in the west (Rho & Petre 1997). The SNR shell does not extend farther to the west behind the GMC in either radio or X-rays; because absorption is negligible in the radio continuum, this implies that the semicircular shape of the remnant is not due to absorption. More likely, the SNR shock has been stopped by the GMC complex on one side. To the east, the interstellar medium (ISM) density appears to be lower, as indicated in the H I map of Kothes et al. (2002). In CO ($J = 1$–0) and ^{13}CO ($J = 1$–0) observations, Tatematsu et al. (1987) have found an armlike CO ridge ("CO arm") that is anticorrelated with the X-ray emission.

CTB 109 has a strikingly bright region in X-rays in the interior, the "X-ray blob" or the "Lobe." Gregory & Fahlman (1983) have suggested that the AXP emits a jet and that the bright Lobe is material excited by a jet or the jet itself. However, Rho & Petre (1993, 1997) have shown that the *ROSAT* PSPC spectrum of the Lobe is thermal in origin and shows no evidence of synchrotron emission, arguing against a jet interpretation. Hurford & Fesen (1995) have found no morphological evidence to support a pulsar jet origin for the Lobe in the *ROSAT* High Resolution Imager (HRI) data and conclude that the bright X-ray emission from the Lobe is most likely caused by a density enhancement in material stripped from the cloud complex. Finally, the *Chandra* image (Patel et al. 2001) reveals no morphological connection between the Lobe and the AXP. Rho & Petre (1997) show that for parts of the shell, the X-ray spectrum is well fitted by a single-component thermal model, whereas for the Lobe and the northern and southern parts of the shell, two thermal components are required. A *BeppoSAX*

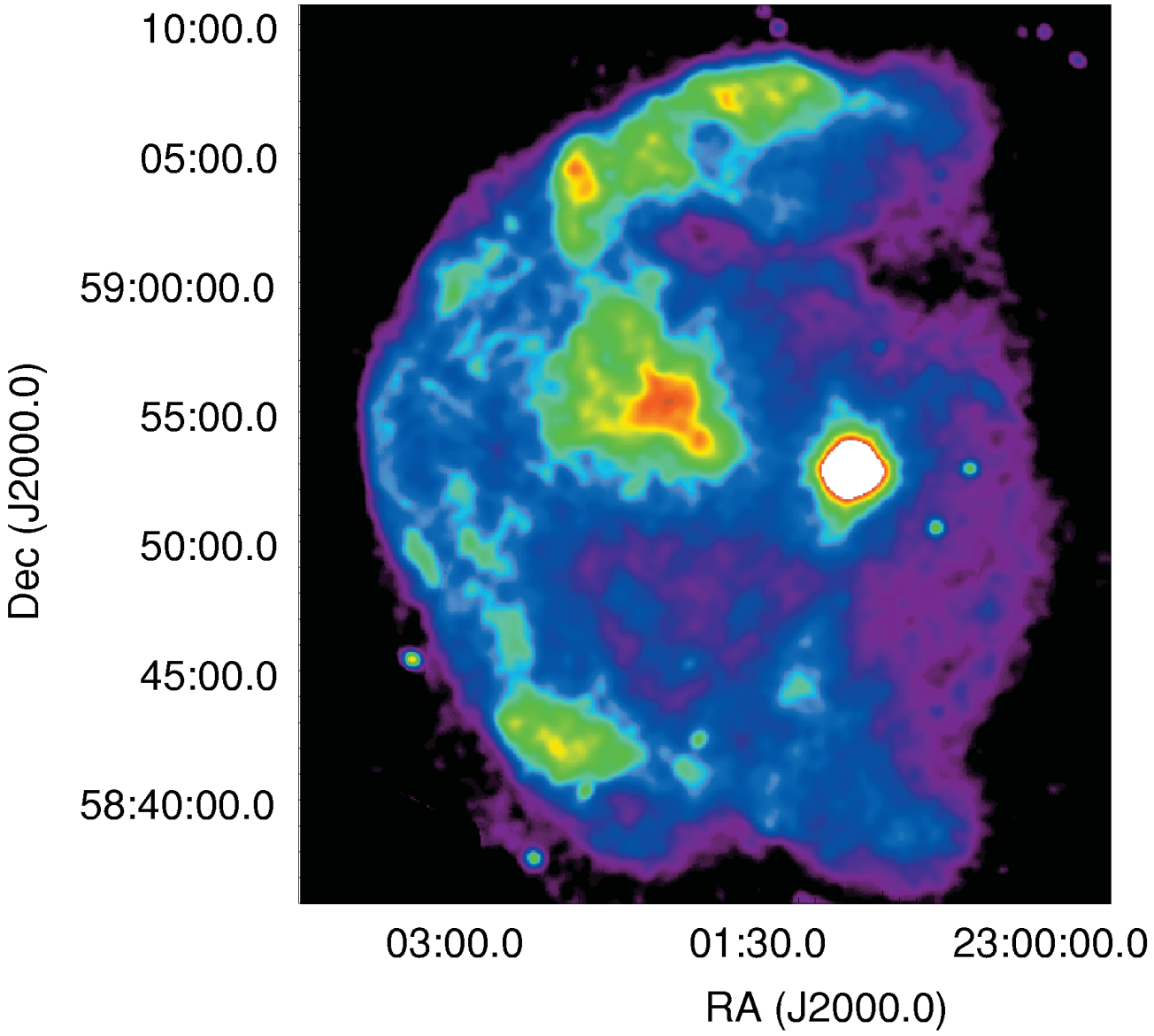

FIG. 1.—Intensity map (0.3–4.0 keV) of CTB 109 in false color. It has been created as a mosaic of smoothed images from the *XMM-Newton* EPIC data in full frame and extended full frame mode. In the fainter parts (*blue to light blue*), some linelike features caused by the CCD gaps are visible. The very bright point source is the pulsar 1E 2259+586, and the diffuse emission at R.A. $= 23^{h}02^{m}$, decl. $= +58^{\circ}55'$ (J2000.0) with an extent of $\sim 7'$ is the Lobe. The lowest count rates are $\sim 5 \times 10^{-5}$ counts s^{-1} around the SNR, and the count rate in the brightest part of the Lobe (*dark red*) is 7.4×10^{-4} counts s^{-1}, using a linear intensity scale. There is no morphological connection between the Lobe and the pulsar evident in this image.

TABLE 1
XMM-Newton Data Used for the Analysis

ObsID[a]	Pointing Direction R.A. (J2000.0)	Pointing Direction Decl. (J2000.0)	Instrument[b]	Mode[c]	Start Time (UT)	Effective Exposure (ks)
00575401 (south, S)	23 01 25.2	58 41 45	PN	E. Full	2002 Jan 22 17:03:34	8.0
			M1	Full		11.0
			M2	Full		11.0
00575402 (north, N).....	23 00 48.8	59 05 27	PN	E. Full	2002 Jul 09 07:58:03	6.0
			M1	Full		11.0
			M2	Full		11.0
00575403 (east, E).....	23 02 23.1	58 53 30	PN	E. Full	2002 Jul 09 13:34:48	9.0
			M1	Full		11.0
			M2	Full		12.0
00381401 (P1)	23 00 57.6	58 53 43	M1	Full	2002 Jun 11 09:05:01	34.0
			M2	Full		34.0
01553503 (P2)	23 00 57.4	58 53 37	M2	Full	2002 Jun 21 09:35:31	17.0

Note.—Units of right ascension are hours, minutes, and seconds, and units of declination are degrees, arcminutes, and arcseconds.
[a] Throughout the paper, the observations are called S, N, E, P1, and P2, as indicated in the table.
[b] Instruments: PN—EPIC PN; M1—EPIC MOS1; M2—EPIC MOS2. All the analyzed data were obtained with the medium filter.
[c] Full: full window mode; E. Full: extended full window mode.

Low-Energy Concentrator Spectrometer (LECS) spectrum of the whole SNR excluding the pulsar and the Lobe has been analyzed by Parmar et al. (1998). The parameters of the best fit to the LECS data with a nonequilibrium model are $kT = 0.95^{+0.65}_{-0.27}$ keV and the ionization timescale $n_e t = 3.8^{+3.8}_{-1.6} \times 10^{11}$ cm^{-3} s.

Surveys of Galactic SNRs have been performed with the *Infrared Astronomical Satellite* (*IRAS*), revealing infrared emission from CTB 109 (Arendt 1989; Saken et al. 1992). The data in the wavelength bands of 12, 25, 60, and 100 μm show a dense dust cloud that is correlated with bright H II regions, located in the south and west of the remnant (Coe et al. 1989). Furthermore, an enhancement in infrared emission is found between the Lobe and the northeast shell.

Optical emission is detected mainly near the bright northeastern and southern radio emission (Hughes et al. 1981). Spectra of filamentary structures in the south confirm their shock origin (Blair & Kirshner 1981). Hα and [O III] images of Fesen & Hurford (1995) reveal previously unknown filaments, e.g., faint filaments near the projected center of the remnant, along the southwestern edge of the bright Lobe. From the filament spectra, they derive a shock velocity of $\sim$100 km s^{-1} and preshock cloud densities of 5–20 cm^{-3}.

We have undertaken observations of CTB 109 with the *XMM-Newton* observatory to provide the deepest X-ray image of this SNR and to provide the highest quality X-ray spectral data to date. The primary objectives of our analysis are to determine the evolutionary parameters of the remnant assuming that it is in the Sedov phase and to determine the nature of the Lobe emission. The deep X-ray images are used to study the morphology of this remnant in comparison to the data at other wavelengths and to search for any morphological connection between the pulsar and the Lobe. The high-quality spectral data are used to determine the evolutionary parameters of the remnant (age, shock velocity, ambient density) and to search for spectral variations within the remnant. The evolutionary parameters determined from the X-ray spectral fits provide useful constraints not only on the age and the environment in which the remnant formed but also for the pulsar. This is particularly useful for the AXP since there is no other reliable technique for estimating the age of this object (Kaspi et al. 2003; Woods et al. 2004). The detailed spectral fits of the shell and the Lobe provide useful insights into the nature of the Lobe emission. In particular, the high-quality spectra of the Lobe are used to determine if the abundances are enhanced (evidence of ejecta), if there is a nonthermal component, and if the temperature and ionization state of the plasma are similar to those of the shell.

2. *XMM-NEWTON* DATA

We have observed CTB 109 with three pointings of *XMM-Newton*, (Jansen et al. 2001; Aschenbach et al. 2000) in the AO1 period covering the southern (hereafter pointing S), northern (pointing N), and eastern (pointing E) parts. We analyze data from the European Photon Imaging Cameras (EPIC) PN (Strüder et al. 2001), EPIC MOS1, and EPIC MOS2 (Turner et al. 2001). The exposure times, after removing flares and periods of high background, are $\sim$10 ks. Furthermore, we have access to observation 0038140101 (PI V. Kaspi, hereafter pointing P1), with a net integration time of 34 ks for MOS1/2. We also analyze the target of opportunity (ToO) data set of the pulsar 1E 2259+586 in the *XMM-Newton* Archive (ObsID 0155350301, hereafter P2) with 17 ks of MOS2 data in full frame mode. The MOS1 was in partial window mode, covering only the pulsar. In observations P1 and P2, the PN was in small window mode. Therefore, we do not consider the PN data of the observation P1 and the PN and MOS1 data of observation P2 in our analysis. Observation details of the data sets used are listed in Table 1. Starting from the observational data files (ODFs), the data are processed with *XMM-Newton* Science Analysis System (XMMSAS) version 5.4.1. For EPIC PN, only single and double pattern events are used, whereas for the MOS1 and MOS2, singles to quadruples are selected.

2.1. *Intensity Map*

The SNR has been fully covered in five pointings with different directions (three for the shell and two centered on the pulsar). We therefore merge the images from the different pointings to obtain complete exposure-corrected images of the remnant using the procedure *emosaic*. For all the pointings, events are selected in the energy bands 0.3–0.9, 0.9–1.5, 1.5–4.0, and 4.0–12.0 keV. Images are created with a bin size of 4″ and

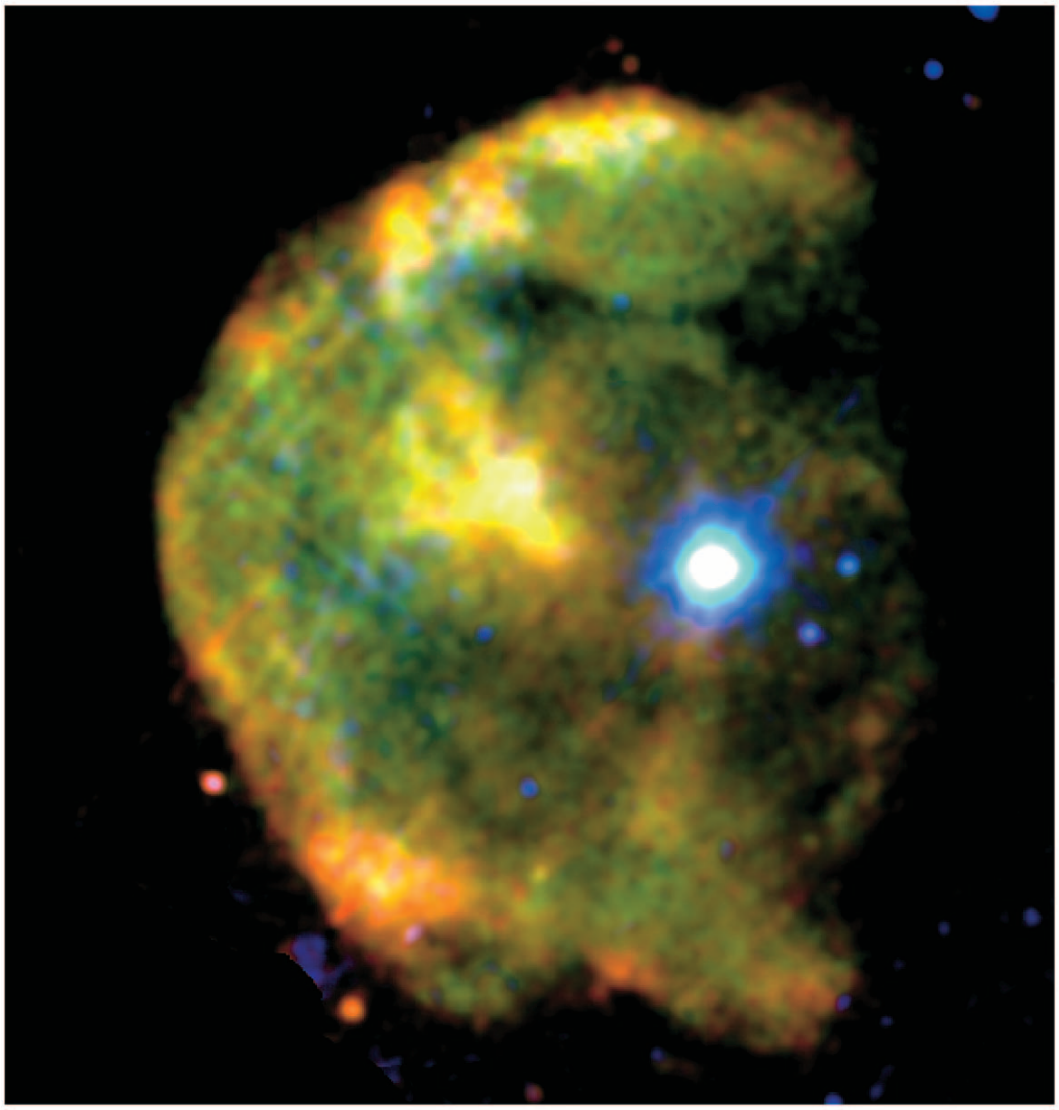

FIG. 2.—Mosaic RGB image created from EPIC data of the pointings E, N, S, and P2 obtained in full frame and extended full frame mode: $R = 0.3-0.9$ keV, $G = 0.9-1.5$ keV, $B = 1.5-4.0$ keV. The image is smoothed (see § 2.1).

smoothed with a circular Gaussian function that has a sigma of 3 pixels in both right ascension and declination. In the 4.0–12.0 keV images, only significant emission from the pulsar is seen, but not from the rest of the SNR.

Figure 1 shows a mosaic image in the energy band of 0.3–4.0 keV in false color. The remnant's X-ray emission fades off to the west, lacking a clearly defined edge. In the interior, the Lobe is brighter than any part of the shell and there are dark regions north and south of the Lobe. The Lobe emission is well separated from the pulsar. We estimate the distance of the shell from the pulsar in the mosaic image by fitting a circle centered on the pulsar to each sector and obtain 18.′5 for the eastern shell, 17.′3 for the southern shell, and 16.′6 for the northern shell. Thus, the eastern shell has the largest projected distance from the pulsar.

2.2. *RGB Composite Image*

As no emission from the remnant is found above 4 keV except from the pulsar, we create images in the energy bands below 4 keV in order to identify possible spectral variations within the remnant. The images in the red ($R = 0.3$–0.9 keV), green ($G = 0.9$–1.5 keV), and blue ($B = 1.5$–4.0 keV) bands are combined into an RGB mosaic image (Fig. 2). We then use this image to guide our selection of regions to be examined more closely through detailed spectral fitting. The selected regions are shown in Figure 3.

The shell is slightly redder than the interior and has some red clumps. There is a small sector of the shell with lower emission in the northeast, coinciding with a bright region in the radio continuum (Kothes et al. 2002). Next to this region, there are red knots in the RGB composite image of the X-ray shell (regions 5 and 6 in Fig. 3). Furthermore, there is a larger red spot in the south (region 15). There are also color variations within the Lobe, the outskirts being redder than the central part of the Lobe.

In addition to the very bright pulsar, fainter point sources are found in and around the remnant. Two point sources located southeast of the remnant appear red in the RGB composite

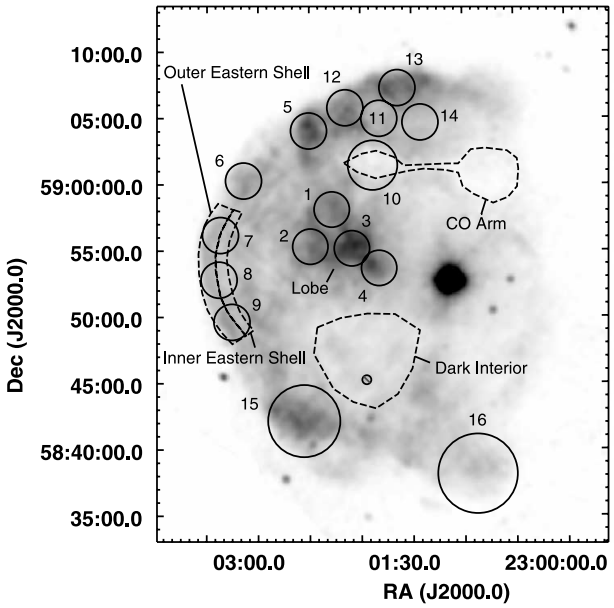

FIG. 3.—Mosaic of all five pointings toward CTB 109 in the energy band of 0.3–4.0 keV with analyzed regions. For circular regions, numbers as used in the paper are given, and the noncircular regions analyzed with *evigweight* are shown with dashed lines. A point source is excluded in the region "Dark Interior" (*small circle with slash*).

image. The one farther east at R.A. = $23^{h}03^{m}19\overset{s}{.}6$, decl. = $+58^{\circ}45'29''$ (J2000.0) is a star of the spectral type G5.5 V (USNO-A2.0 1425-14515707; Monet et al. 1998) and is coincident with source 3 in Rho & Petre (1997). The other source at R.A. = $23^{h}02^{m}43\overset{s}{.}7$, decl. = $+58^{\circ}37'46''$ (J2000.0) is coincident with source 4 in Rho & Petre (1997); it is also coincident with a point source in the Digitized Sky Survey (DSS) image. Presumably, it is also a Galactic star. The point sources close to the pulsar (in projection) have blue or violet colors. The source at R.A. = $23^{h}00^{m}33\overset{s}{.}3$, decl. = $+58^{\circ}52'45''$ (J2000.0) located west of the pulsar is USNO-A2.0 1425-14436845 (source 1 in Rho & Petre 1997), a star of the spectral type G9.5 III–IV. The source at R.A. = $23^{h}00^{m}43\overset{s}{.}3$, decl. = $+58^{\circ}50'28''$ (J2000.0) south of USNO-A2.0 1425-14436845 is only known as an X-ray source (source 2 in Rho & Petre 1997). There is an optical point source on the DSS image at the X-ray position. Therefore, these hard point sources seem to be Galactic stars as well. Enhanced column density in the foreground or high intrinsic absorption seems to be responsible for the hard spectrum. We extracted spectra for these point sources, but the low number of counts does not allow detailed spectral fitting.

2.3. *Background*

Since CTB 109 is a relatively faint diffuse object, a good knowledge of the background is crucial for the spectral analysis. We studied the background properties of the EPIC cameras based on the treatments of Lumb (2001), Lumb et al. (2002), and Read & Ponman (2003).

In the case of a point source a local background extracted from another region of the same data as the source can be used. For extended objects, it is not possible to obtain background data at small distances from the source, i.e., a few arcseconds away from the source as for point or pointlike sources. Instead, one has to extract the background data far from the target, from a part of the detector that is not illuminated by source emission. In this case the distance between the source and the background region is large (few arcminutes) and the difference of the detector background at the two positions could become significant (see next paragraph). In the case of a diffuse source that fills the entire field of view, it is even impossible to estimate the local background from the same data. If one selects a background region far from the source itself, many effects can produce an inappropriate background due to the different chip position. First, the effective area of the mirrors depends on the off-axis angle. Photons are subject to vignetting, but particles are not. Second, high-energy particles that interact with material surrounding the detector produce fluorescence; the magnitude of this fluorescence emission can vary significantly with position on the detector, especially for the PN detector. Third, the spectral response depends on the position on the detector, especially for the PN.

The internal "quiescent" background of the EPIC cameras consists of fluorescence lines and events produced by charged particles. The fluorescence depends on the camera body materials and the incident flux of high-energy charged particles. Therefore, the fluorescent component varies with position on the detector and with time. In addition, the high-energy charged particles can produce background events directly in the detector. Finally, low-energy protons can reflect off of the mirror surfaces and reach the detectors in the focal plane. The background produced by low-energy protons is highly variable in time for the *XMM-Newton* instruments.

There are two types of background template files available that can be used for the analysis of EPIC data: "closed" data and blank sky data. Closed data have been obtained with the filter wheel in the closed position; these data include only the internal detector background. However, this instrument configuration is not representative of the usual observation where the CCDs are exposed to photons and low-energy charged particles. For the blank sky data, data sets for different pointings have been merged for each EPIC camera after eliminating sources from the data. These data sets comprise the detector background and an average cosmic X-ray background. Since the background component due to high-energy charged particles is included in these data at an unknown level, we need to model it using the spectral shape determined from the closed data.

2.4. *Extraction of EPIC Spectra*

2.4.1. *Circular Regions*

Although the cosmic X-ray background is a significant uncertainty in the blank sky data, we decide to use the blank sky instead of the closed data because the latter have poor photon statistics and are therefore not suitable for extracting small regions. We use the blank sky data of the background analysis group in Birmingham, UK[1] because they have data for both the medium and the thin filters, as well as for the full frame and extended full frame PN modes. The Birmingham group has also developed scripts that can be used for the background analysis. The script *skycast* converts the detector coordinates of the template background data sets into sky coordinates using the pointing direction of the observation to be analyzed and adds sky coordinates to the background data. The script *createspectra* extracts spectra in specified circular (or annular) regions from the data and background file. Ancillary response files (ARFs) and redistribution matrix files (RMFs) are produced for the corresponding detector regions using the XMMSAS commands

[1] See http://www.sr.bham.ac.uk/xmm3.

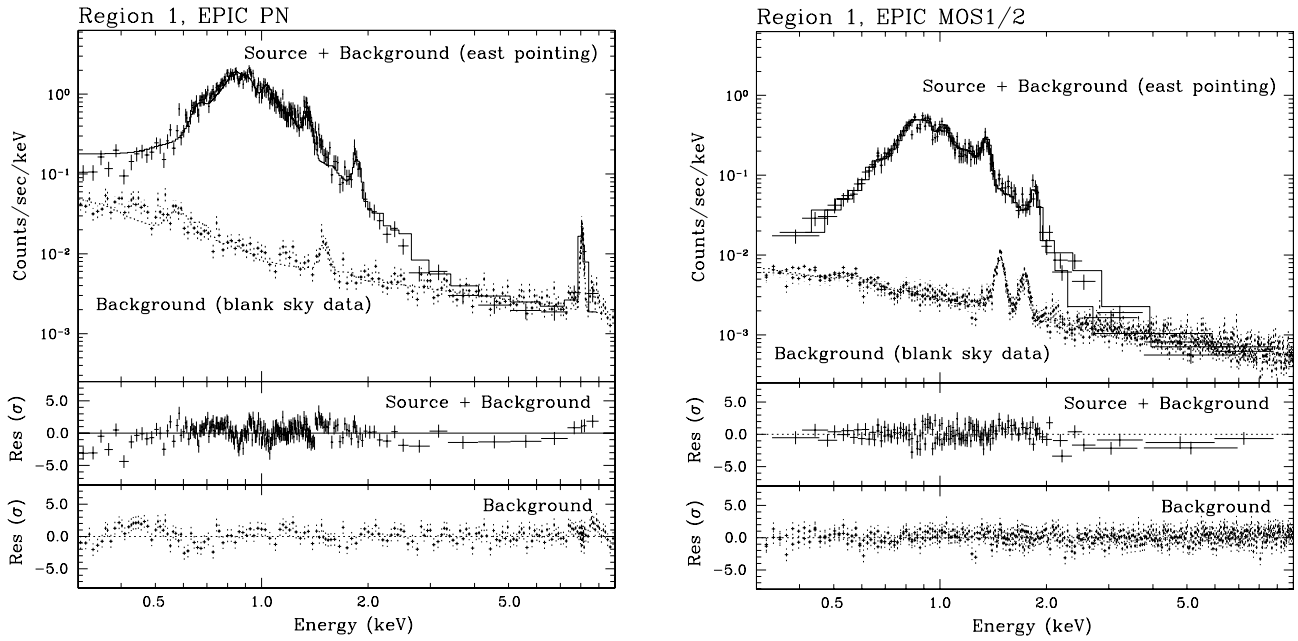

FIG. 4.—*XMM-Newton* EPIC spectra of the Lobe region 1 extracted from the pointing E data shown with VNEI model fits for PN and MOS1/2. The solid line is for source plus background spectrum, dashed line for background spectrum. The background spectrum has not been subtracted from the source spectrum but has been modeled simultaneously and is included in the spectral model of the source spectrum. Strong fluorescence lines are visible in the background spectra: Al-K line at 1.5 keV and Cu-Ni-Zn-K line complex around 8 keV in the PN spectrum (*left*), and Al-K at 1.5 keV and Si-K at 1.7 keV in the MOS spectra (*right*).

arfgen and *rmfgen*. Since the source spectrum and associated blank sky background spectrum are created at the same position of the detector, the ARF and RMF are correct for both source and background.

Spectra are analyzed with XSPEC version 11.3. We read in the source and the blank sky background spectra as two data sets: source (1) and background (2). We model the background spectrum as a combination of a power-law component and two Raymond & Smith (1977) components with temperatures $kT = 0.08$ and 0.2 keV (Lumb 2001; Lumb et al. 2002). Zero-width Gaussians are used to reproduce the fluorescence lines of the detector. The detector background is modeled with a power-law component and Gaussians using the XSPEC option "/b" to suppress the application of the ARF. An additional thermal component is used to model the SNR emission (set to zero for the background data set). In Figure 4, the EPIC PN and MOS1/2 spectra of region 1 (see Fig. 3) extracted from the E pointing are displayed together with the corresponding blank sky background spectra. We show the spectrum from region 1 since this is the faintest part of the Lobe and hence the most sensitive to the background subtraction.

In order to convince ourselves that the background in the source spectrum can be well estimated from the blank sky data, we compare the spectra extracted as source (from observations) and background (from blank sky data) in a region outside the SNR. For both PN and MOS1/2, the off-remnant spectrum from observations matches the blank sky spectrum very well in the softer ($<$0.6 keV) and harder ($>$1.5 keV) bands, as well as for the fluorescence lines. There is a small excess in the off-remnant spectrum between $\sim$0.6 and 1.5 keV. This faint emission is well fitted with a thermal model component and is likely Galactic diffuse X-ray emission. Since the remnant spectrum dominates the background spectrum in the 0.6–1.5 keV band (see Fig. 4), using the blank sky data as background introduces only a small systematic uncertainty in the derived parameters for the remnant spectra. We verify this by modeling the spectra of regions in the remnant shell including an additional thermal component for the local diffuse X-ray background, as derived from the off-remnant spectrum. The parameters of the model component for the remnant emission (foreground absorption, temperature, and ionization timescale; see § 3) are consistent with results from the fit using only the blank sky data as background. The abundances of the elements with emission lines in this energy band (O, Ne, and Mg) also yield fit results that agree well with the results without the additional component, i.e., solar abundances. Consequently, the use of the blank sky data as background should have little effect on our determination of the neutral hydrogen column density and on the temperature of the thermal component.

2.4.2. *Arbitrary Extraction Region Shape*

Since the existing version of *arfgen* only computes ARF files for circular and annular extraction regions, our analysis has been largely limited to circular regions. However, the XMMSAS command *evigweight* calculates the vignetting correction for each event; thus, one can use the on-axis ARF. In order to subtract the nonvignetted events from the observation data, it is better to use the closed data for the background, as this data set only consists of the nonvignetted component, which is the internal detector background, and thus includes no additional external background emission. Compared to the blank sky data, the closed data have far poorer statistics. Therefore, we use this method only for noncircular extraction regions.

After computing the weight factor for the vignetting correction for each event, spectra are extracted from the new event files and RMFs are created with *rmfgen*. The source data still include the nonvignetted events that have not passed through the X-ray telescope but now have a weighting factor applied. This misapplication of the weighting factor to nonvignetted events can be compensated for by applying the same weights to

the closed background data. Coordinates of the closed data are converted into the corresponding sky position using *skycast*. The vignetting correction weights are computed for the closed data. Finally, spectra are extracted in the same regions as for the observed source data. Again the background spectrum is used as a second data set and modeled as in § 2.4.1.

2.4.3. *Comparison of the Two Methods*

In order to check for consistency between the two methods for creating spectral data, spectra of the Lobe regions (see § 3.4), extracted from the pointing E data, are analyzed using both methods and compared. For the first method, we use the blank sky data as background data and create the ARF with *arfgen*. For the second method, the event files are vignetting corrected with *evigweight* and on-axis ARF and closed background data are used. All the fitted parameters derived from the two methods agree within 90% confidence limits. Therefore, we are confident that either method may be used without introducing systematic errors that dominate over the statistical errors.

3. THE SPECTRAL ANALYSIS

The *XMM-Newton* EPIC data allow us to perform spatially resolved spectral analysis of the SNR. Extraction regions are shown in Figure 3 on the 0.3–4.0 keV mosaic image. Data sets and extraction regions are selected as follows:

1. As we have shown in § 2.1, the eastern part of the shell is farthest from the pulsar. Since it is located opposite to the GMC complex in the west, the eastern shell segment most likely indicates a blast wave propagating into a lower density ISM (Kothes et al. 2002). For the spectral analysis, we cover the eastern shell with three circular regions (7–9) and also arc regions for comparison. In addition, we extract spectra for regions next to the radio bright knot in the northeast (regions 5 and 6). Data set E is used for all these analyses.
2. The shell is brightest in the northern part; it has been covered completely by pointing N. We select circular regions from this data set centered on the brighter knots (regions 12 and 13) and also analyze interior regions close to the northern shell for comparison (regions 11 and 14).
3. In the southern part of the shell, which does not have as clearly a defined edge as the eastern or the northern portions of the shell, we study the EPIC spectra (using observation S) for two regions (15 and 16) with soft emission (see RGB composite image, Fig. 2).
4. In CO observations, an enhancement of CO gas has been found that extends from the GMC in the west across the northern part of the remnant (Tatematsu et al. 1987). This dense material is called the CO arm. Its position and shape coincide well with an X-ray–faint interior region, north of the pulsar and the Lobe (see Fig. 1). Spectra are analyzed for a large circular region (10), as well as for a noncircular region that follows the shape of the very low emission region. Data from observations N and P1 are used.
5. The interior of the remnant has remarkably low surface brightness in the south ("Dark Interior"). This region is analyzed using the P1 data, which have the longest exposure time.
6. We extract spectra for four regions of the Lobe (regions 1–4 in Fig. 3) from the observations E, P1, and P2, in order to look for spectral variations.

All the EPIC spectra are analyzed in XSPEC using an energy range of 0.3–10.0 keV. The spectra are grouped with a minimum of 20 counts bin^{-1} and the χ^2 statistic is used. The errors quoted are 90% confidence limits. As can be seen in Figure 4, the emission above ~4 keV is mainly background emission and is crucial for estimating the background. Although we select the energy range of 0.3–10.0 keV for spectral fitting, we only show the spectrum below 4 keV in the following figures in order to clearly display the SNR emission.

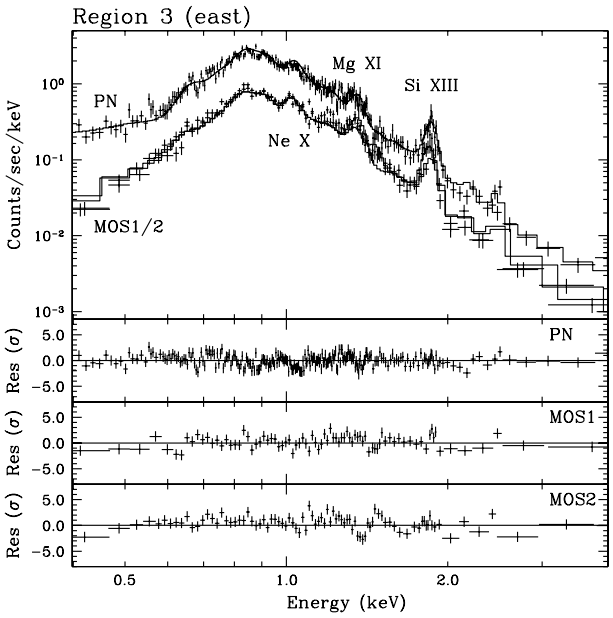

FIG. 5.—*XMM-Newton* EPIC spectra of the Lobe region 3 extracted from the pointing E data, with VNEI model fits. The position of the Ne X, Mg XI, and Si XIII lines is indicated. Instead of subtracting the background spectrum from the source spectrum, it has been modeled simultaneously. The displayed source spectrum and its fitted model include the background spectrum components. Background spectra are not plotted in this and the following spectrum figures.

For analyzing the *XMM-Newton* EPIC spectra we use the following models: VMEKAL, which describes an emission spectrum for hot ionized gas in collisional ionization equilibrium with variable abundances (Mewe et al. 1985, 1986; Kaastra 1992; Liedahl et al. 1995), and VNEI, which is a model for a nonequilibrium ionization (NEI) collisional plasma, again with variable abundances (Hamilton et al. 1983; Borkowski et al. 1994, 2001; Liedahl et al. 1995). The VNEI model includes a parameter for the ionization timescale, $\tau = \int n_e\, dt$, an integral over the time since the gas was shocked. In addition, we modeled some regions in the shell with the model VPSHOCK for a constant-temperature, plane-parallel shock that includes a range of ionization timescales, parameterized by the lower limit and the upper limit of the τ range (Borkowski et al. 2001 and references therein).

The *XMM-Newton* EPIC spectra of region 3 in the Lobe extracted from the pointing E data (with VNEI model fits) are presented in Figure 5. Emission-line features corresponding to the Mg XI triplet and the Si XIII triplet are easily visible. Moreover, the Ne X Lyα line can be clearly seen in the MOS data, as the energy resolution of MOS is slightly better than that of PN.

We first fit the spectra with free abundances. For all the spectra, the abundances for all the elements are consistent with solar abundances. We thereupon fix the abundances to solar values in order to reduce the number of free parameters and hopefully to better constrain the remaining free parameters. Only Mg and Si are still kept free because these abundances have appeared to differ slightly from solar values for some regions and the line features are evident in the EPIC spectra. We allowed the

TABLE 2

XMM-Newton Spectral Results of Circular Regions Using the Spectral Model VNEI with Solar Abundances except for Mg and Si

Region	Pointing	N_H (10^{22} cm^{-2})	kT (keV)	Mg (solar)	Si (solar)	nt (10^{11} s cm^{-3})	χ^2/dof
1	P1	$0.60^{+0.02}_{-0.10}$	$0.55^{+0.04}_{-0.03}$	$1.0^{+0.2}_{-0.1}$	$0.9^{+0.2}_{-0.1}$	$1.4^{+1.1}_{-0.1}$	896.1/702 = 1.3
2	P1	$0.51^{+0.05}_{-0.02}$	$0.59^{+0.02}_{-0.02}$	$0.9^{+0.1}_{-0.1}$	$1.2^{+0.2}_{-0.2}$	$2.0^{+0.1}_{-0.2}$	896.6/684 = 1.3
3	P1	$0.49^{+0.04}_{-0.03}$	$0.55^{+0.02}_{-0.01}$	$0.9^{+0.1}_{-0.1}$	$1.6^{+0.2}_{-0.2}$	$2.0^{+0.3}_{-0.2}$	904.3/721 = 1.3
4	P1	$0.49^{+0.04}_{-0.05}$	$0.53^{+0.03}_{-0.01}$	$0.9^{+0.1}_{-0.1}$	$1.2^{+0.2}_{-0.2}$	$2.8^{+1.0}_{-0.5}$	896.5/676 = 1.3
5	E	$0.82^{+0.07}_{-0.07}$	$0.29^{+0.03}_{-0.03}$	$0.7^{+0.2}_{-0.2}$	$1.9^{+0.9}_{-0.7}$	$4.0^{+4.1}_{-1.7}$	747.3/600 = 1.2
6	E	$0.51^{+0.07}_{-0.09}$	$0.64^{+0.09}_{-0.10}$	$1.3^{+0.4}_{-0.2}$	$1.0^{+0.3}_{-0.4}$	$1.0^{+0.6}_{-0.4}$	645.9/593 = 1.1
7	E	$0.68^{+0.11}_{-0.06}$	$0.63^{+0.10}_{-0.11}$	$1.1^{+0.3}_{-0.2}$	$1.0^{+0.4}_{-0.4}$	$0.8^{+0.6}_{-0.3}$	678.0/552 = 1.2
8	E	$0.67^{+0.03}_{-0.04}$	$0.62^{+0.04}_{-0.03}$	$1.0^{+0.3}_{-0.1}$	$0.8^{+0.2}_{-0.4}$	$0.7^{+0.2}_{-0.1}$	642.8/593 = 1.1
9	E	$0.54^{+0.49}_{-0.09}$	$0.57^{+0.11}_{-0.36}$	$1.0^{+0.6}_{-0.4}$	$1.2^{+0.8}_{-0.7}$	$1.4^{+1.4}_{-1.1}$	728.7/607 = 1.2
10	P1	$0.88^{+0.05}_{-0.02}$	$0.52^{+0.01}_{-0.02}$	$1.0^{+0.1}_{-0.2}$	$1.0^{+0.3}_{-0.1}$	$1.7^{+0.5}_{-0.3}$	1126.7/918 = 1.2
11	N	$0.79^{+0.22}_{-0.04}$	$0.53^{+0.05}_{-0.24}$	$0.8^{+0.1}_{-0.2}$	$0.6^{+0.2}_{-0.2}$	$0.9^{+0.5}_{-0.3}$	637.7/618 = 1.0
12	N	$0.70^{+0.26}_{-0.11}$	$0.48^{+0.13}_{-0.23}$	$1.0^{+0.1}_{-0.4}$	$1.0^{+0.3}_{-0.3}$	$1.1^{+2.8}_{-0.5}$	653.4/586 = 1.1
13	N	$0.67^{+0.33}_{-0.05}$	$0.52^{+0.05}_{-0.26}$	$1.0^{+0.1}_{-0.1}$	$0.9^{+0.3}_{-0.2}$	$1.4^{+0.3}_{-0.4}$	733.9/617 = 1.2
14	N	$0.93^{+0.14}_{-0.07}$	$0.42^{+0.05}_{-0.13}$	$0.8^{+0.3}_{-0.4}$	$0.8^{+1.7}_{-0.2}$	$1.8^{+N/A}_{-0.5}$	734.4/641 = 1.1
15	S	$0.54^{+0.01}_{-0.01}$	$0.60^{+0.02}_{-0.01}$	$1.0^{+0.1}_{-0.1}$	$1.0^{+0.2}_{-0.3}$	$0.8^{+0.1}_{-0.2}$	1549.8/1325 = 1.2
16	S	$0.57^{+0.01}_{-0.01}$	$0.60^{+0.03}_{-0.01}$	$1.1^{+0.1}_{-0.1}$	$0.9^{+0.3}_{-0.2}$	$1.0^{+0.1}_{-0.2}$	1646.6/1475 = 1.1

Notes.—Only results from the simultaneous fits of the MOS1 and MOS2 data are shown, whereas the paper discusses results from PN data as well. Blank sky data are used as background data.

Si and Mg abundances to vary independently. For other elements like Ne or S, it is too difficult to distinguish between line and continuum emission in the corresponding energy intervals.

All the EPIC spectra are fitted better by a single-temperature VNEI model than by a collisional ionization equilibrium VMEKAL model. In the following, we present only the VNEI results for all the regions and discuss the VPSHOCK results for shell spectra where we expect the least disturbed plane-parallel shock. Tables 2 and 3 summarize the results of the spectral analysis of MOS1/2 data, using the VNEI model. Spectra of some selected regions with the best-fit VNEI model are displayed in the following figures: Figure 5 shows the PN and MOS1/2 spectra of the brightest part of the Lobe (region 3), the spectra in Figure 6 are extracted from a bright region in the shell (region 5), and Figure 7 shows the heavily absorbed spectra of the CO arm. In all these plots, the non–background-subtracted source spectra are shown, but not the simultaneously modeled background spectra.

The parameters of the VNEI model for the Lobe data of the pointing E, with the spectra from the two EPIC detector types PN and MOS fitted separately, are consistent with the MOS results of the Lobe regions in Table 2 except that the Mg and Si abundances from the PN fits turn out to be subsolar in some regions. The most likely explanation for this discrepancy between PN and MOS is the calibration issue addressed in the EPIC calibration status documentation of 2003 April (Kirsch 2003): in the range 0.3–1.0 keV, the PN flux is up to 10% higher than the MOS flux, whereas above 1.5 keV, the MOS flux is up to 10% higher. In the EPIC spectra, most of the emission lines cannot be resolved as a result of moderate spectral resolution. This complicates the determination of the continuum. Assuming the same temperature and absorption, the flux inconsistency between the MOS and the PN can mimic lower abundances for the PN data for elements like Mg and Si with lines above $\sim$1 keV because the unresolved lines cannot be distinguished from the continuum. Although most of the fit parameters (absorption, temperature, ionization timescale) for the PN, MOS1, and MOS2 spectra are consistent, the discrepancy between the abundances makes us conclude that the results from the MOS data (MOS1 and MOS2 data fitted simultaneously, if data of both instruments are available) are more reliable than the PN results in terms of abundances. Therefore, we list the MOS1/2 results in Tables 2 and 3.

3.1. *Shell*

3.1.1. *Eastern Part of the Shell*

The eastern part of the remnant shell is farthest from the pulsar 1E 2259+586 and has a more circular shape. The density of the ambient ISM is apparently lower on this side (Kothes et al. 2002). Thus, the eastern portion of the shell seems to be the best region to study the least perturbed shock-ISM interaction.

The spectral analysis of regions in the eastern shell (regions 6–9) yields a temperature of $\sim$0.6 keV for the VNEI model,

TABLE 3

XMM-Newton Spectral Results of the Arc-shaped Region in the Eastern Part of the Shell, the CO Arm, and the Low Surface Brightness Region in the Southern Interior, Using *evigweight*

Region	Pointing	N_H (10^{22} cm^{-2})	kT (keV)	Mg (solar)	Si (solar)	nt (10^{11} s cm^{-3})	χ^2/dof
Outer E. shell	E	$0.59^{+0.02}_{-0.01}$	$0.68^{+0.02}_{-0.02}$	$1.1^{+0.2}_{-0.1}$	$0.9^{+0.2}_{-0.2}$	$0.7^{+0.1}_{-0.2}$	566.7/405 = 1.4
Inner E. shell	E	$0.67^{+0.04}_{-0.06}$	$0.60^{+0.05}_{-0.04}$	$1.1^{+0.1}_{-0.2}$	$0.9^{+0.2}_{-0.2}$	$1.1^{+0.3}_{-0.3}$	347.8/267 = 1.3
CO arm	P1	$0.97^{+0.02}_{-0.01}$	$0.54^{+0.01}_{-0.01}$	$0.9^{+0.1}_{-0.2}$	$0.9^{+0.2}_{-0.1}$	$1.5^{+0.4}_{-0.2}$	918.5/732 = 1.3
Dark interior	P1	$0.66^{+0.03}_{-0.07}$	$0.53^{+0.05}_{-0.03}$	$1.0^{+0.1}_{-0.2}$	$0.9^{+0.1}_{-0.2}$	$1.5^{+0.4}_{-0.3}$	1452.5/1074 = 1.4

Notes.—The fit results are from the analysis of MOS1/2 data using the VNEI model; abundances are fixed to solar values except for Mg and Si. "Closed" data are used as background data.

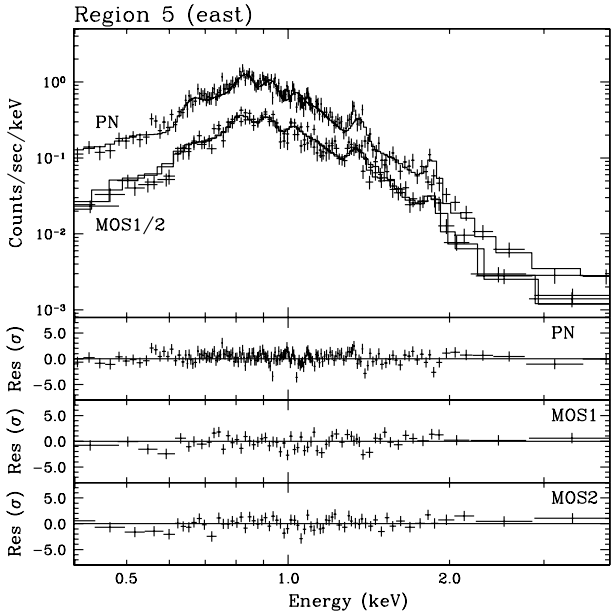

FIG. 6.—*XMM-Newton* EPIC spectra of region 5 in the eastern part of the shell extracted from the pointing E data, with VNEI model fits. For background spectrum see the caption of Fig. 5.

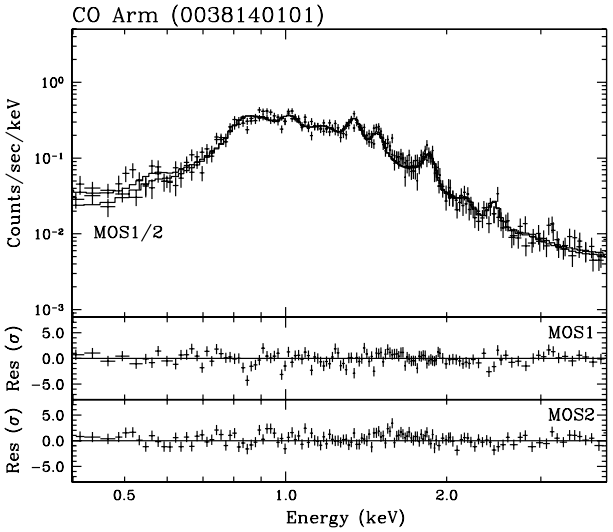

FIG. 7.—*XMM-Newton* EPIC MOS1/2 spectra of the CO arm (from pointing P1) with VNEI model fit. For background spectrum see the caption of Fig. 5.

which is slightly higher than those in the Lobe and the northern portion of the shell, although not significantly. The Mg and Si abundances are consistent with solar, and the ionization timescale is $\sim 1 \times 10^{11}$ s cm^{-3}, similar to that in the northern part of the shell (see § 3.1.2). The absorbing column density is $N_{\rm H} = (5\text{–}7) \times 10^{21}$ cm^{-2}. We also analyze the spectra of the regions in the eastern shell using the model VPSHOCK. The values for $N_{\rm H}$, kT, and the abundances agree well with the results of the VNEI model in all four regions. The lower limit of τ has been set equal to zero. The upper limit of the ionization timescale τ is $3.4^{+0.7}_{-0.3} \times 10^{11}$ s cm^{-3} for region 6, $4.8^{+7.2}_{-2.5} \times 10^{11}$ s cm^{-3} for region 7, $3.5^{+30.0}_{-1.7} \times 10^{11}$ s cm^{-3} for region 8, and $6.8^{+10.0}_{-1.1} \times 10^{11}$ s cm^{-3} for region 9, all higher than and therefore consistent with the average values obtained from the VNEI model.

No indication of nonthermal emission is found in these spectra. We model the spectra with an additional power-law component and obtain an upper limit for the flux of the power-law component. Studies of nonthermal emission from the shells of SNRs yield photon indices of around 2.0: $\Gamma = 1.8$ for Cas A (below 16 keV; Allen et al. 1997) and $\sim$2.2 for SN 1006 (Bamba et al. 2003; Allen et al. 2004). Therefore, we assume a photon index of $\Gamma = 2.0$ and obtain upper limits of the nonthermal flux (0.3–10 keV, 90% confidence level): 1.7×10^{-14} ergs cm^{-2} s^{-1} in region 6, 1.3×10^{-13} ergs cm^{-2} s^{-1} in region 7, 3.0×10^{-14} ergs cm^{-2} s^{-1} in region 8, and 1.5×10^{-14} ergs cm^{-2} s^{-1} in region 9, i.e., less than 0.2%, less than 1.6%, less than 0.4%, and less than 0.2% of the unabsorbed VNEI flux, respectively. Gotthelf et al. (2001) have studied the emission from the forward shock in the northern part of Cas A and report that the flux of the nonthermal emission is 50%–70% of the total 0.5–10.0 keV flux. In comparison, the upper limit of the nonthermal emission from the eastern part of the shell of CTB 109 in the energy range of 0.5–10.0 keV is 0.2%–1.4%, about 2 orders of magnitude lower than in Cas A.

In radio continuum, CTB 109 has a very bright extended region approximately where the connecting line from the pulsar through the Lobe intersects the shell in the northeast (see, e.g., Fig. 1 in Kothes et al. 2002). In region 5, which lies north of this radio-bright region, the column density $N_{\rm H}$ ($\sim 8 \times 10^{21}$ cm^{-2}) and the ionization timescale τ (6×10^{11} s cm^{-3} from the joint fit of PN and MOS1/2 data, 4×10^{11} s cm^{-3} from the fit of MOS1/2 data; see Table 2) are higher compared to the eastern shell regions south of the radio-bright region, whereas the temperature is significantly lower: $kT = 0.29 \pm 0.03$ keV at the 90% level, as obtained from both the PN and MOS1/2 fit and the MOS1/2 fit. The kT value for region 5 differs from that in other regions also at the 99% confidence level. The spectra are shown in Figure 6. Fitting a model similar to other shell spectra ($N_{\rm H} = 6 \times 10^{21}$ cm^{-2}, $kT = 0.6$ keV, $\tau = 1 \times 10^{11}$ s cm^{-3}) results in a modeled spectrum with lower flux below 0.9 keV and flatter continuum above 2 keV, compared to the observed spectrum. The optical image of Fesen & Hurford (1995) shows that this region covers two bright optical filaments with an [S II]/Hα ratio typical for shocked gas rather than photoionized gas; they derive a preshock density of 10–20 cm^{-3}, higher than for other optical filaments seen in CTB 109. This might indicate that a shock-cloud interaction is occurring in region 5. The ionization timescale for this region is $\sim$4–6 times higher than in other parts of the remnant shell. Since the regions are all located at similar radii, the time that has elapsed after these regions have interacted with the shock front can be assumed to be comparable. Therefore, the higher τ in region 5 is consistent with the shock having encountered a density enhancement.

Although we assume that the undisturbed eastern part of the remnant can be reproduced by a model based on the Sedov–Taylor–von Neumann similarity solution (Sedov 1959; Taylor 1950; von Neumann 1947), the fit results are not satisfactory if we use the SEDOV model (Borkowski et al. 2001) in XSPEC. This is presumably due to inhomogeneities in the ISM that result in flux and spectral variations in the remnant. Therefore, we focus on smaller shell segments and analyze arc-shaped regions of the eastern shell (see Fig. 3 and Table 3) using the *evigweight* method. As the VNEI fit results show, the spectra in the outer and inner shell seem to be different: the best-fit temperature is slightly higher in the outer shell, whereas the ionization timescale is lower. The foreground absorption is lower for the outer shell than for the inner shell. However, if we compare the confidence contours of $N_{\rm H}$ versus kT and kT

versus τ for the two shell regions, the 90% confidence regions are fully separated, but the 99% regions overlap. Thus, there is only a marginal inconsistency between the temperatures and the ionization timescales of the outer shell and the inner shell.

For a Sedov phase remnant expanding into a homogeneous medium, the temperature and ionization timescale both increase radially inward. This is an idealized case, however. If the kT and τ differences are real, we may be seeing the effects of nonuniformities in the ambient medium. If the shock (as seen in projection) encountered a density enhancement, that could cause a larger ionization timescale and lower temperature and reduce the flux in the inner shell region relative to the outer shell region.

3.1.2. *Northern Part of the Shell*

For the northern portion of the shell (regions 12 and 13) $N_{\rm H} \approx 7 \times 10^{21}$ cm^{-2}, $kT \approx 0.5$ keV, and $\tau \approx 1 \times 10^{11}$ s cm^{-3}. The temperature seems to be lower and the column density $N_{\rm H}$ higher than in the eastern portion of the shell. For regions inside the northern shell segment (regions 11 and 14), the column density $N_{\rm H}$ seems to be slightly higher [$(8–9) \times 10^{21}$ cm^{-2}], perhaps indicating a gradual increase of the foreground absorption in the direction of the CO arm.

3.1.3. *Southern Part of the Shell*

In the southern portion of the shell, there are two diffuse spots that appear red in the RGB composite image (Fig. 2): a bright region in the southeast (region 15) and the western tip of the shell in the south (region 16). The temperature is 0.6 keV and the ionization timescale $\tau \approx 1 \times 10^{11}$ s cm^{-3}, comparable to the eastern part of the shell. Rather than being a result of a lower temperature plasma, the red color of these regions appears to be a result from a lower $N_{\rm H}$ ($\sim 5 \times 10^{21}$ cm^{-2}, as derived from a joint fit of PN and MOS1/2 data, and $\sim 5.5 \times 10^{21}$ cm^{-2}, from MOS1/2 data only).

3.2. CO *Arm*

We analyze a circular region covering the extended tip of the CO arm (region 10). The column density $N_{\rm H}$ is higher than in the eastern part of the shell and the Lobe, $N_{\rm H} > 8 \times 10^{21}$ cm^{-2}, but the temperature, the Mg and Si abundances, and the ionization timescale are comparable to the shell of the remnant [$kT = 0.5–0.6$ keV, $\tau = (1–2) \times 10^{11}$ s cm^{-3}, as derived from PN and MOS1/2 data].

We also study a noncircular X-ray–faint region corresponding to the CO arm (see Fig. 3), using *evigweight*. Figure 7 shows the spectra of this region obtained with the EPIC MOS1/2 of the pointing P1; the flux falls off more rapidly below 1 keV compared to other regions of the SNR, consistent with the presence of additional absorption. The result of the spectral fit of the MOS1/2 data is given in Table 3; it confirms that the column density $N_{\rm H}$ is almost 10^{22} cm^{-2}, higher than in other regions of the remnant. The intrinsic spectrum seems to be the same as in most of the other regions of the remnant. Therefore, we conclude that this region appears fainter because of additional absorption.

3.3. *Dark Interior*

There is a low surface brightness region south of the Lobe inside the remnant shell. No enhanced CO emission is found in the observations by Tatematsu et al. (1990) that coincide with this X-ray–faint region. We extract the X-ray spectrum of this region using the *evigweight* method excluding the point source that is located within this region. The parameters kT, Mg and Si abundances, and τ of the dark region are all consistent with the parameters of the CO arm (Table 3), indicating that the intrinsic spectra of these two regions are similar. Only the column density $N_{\rm H}$ is higher in the CO arm. The spectral parameters also agree well with the parameters of region 1 (northern tip of the Lobe), which has about the same distance to the pulsar as this region. Although $N_{\rm H}$ does not differ significantly from that in region 1, it seems to be higher in this dark region, indicating a higher absorption.

3.4. *Lobe*

There are three observations that we can use to study the Lobe: pointings E, P1, and P2. The results from pointings E and P2 are consistent with that from pointing P1. The largest number of counts is obtained from observation P1 because the exposure time is 2–3 times longer than in other observations. We also fit all the spectra (PN and MOS1/2 data of pointing E, MOS1/2 data of pointing P1, and MOS2 data of pointing P2) simultaneously for each of the regions 1–4. The results of these simultaneous fits are all consistent with the results of the fit of the MOS 1/2 data of pointing P1 (shown in Table 2).

In all the Lobe regions, the best-fit temperatures, kT, range from 0.53 to 0.59 keV (from simultaneous fit of PN and MOS1/2, as well as from the fit of MOS1/2 data; see Table 2). For Lobe regions 2–4, the column density $N_{\rm H} \approx 5 \times 10^{21}$ cm^{-2} and the ionization timescale $\tau = (2–3) \times 10^{11}$ s cm^{-3}. The rather small differences in temperature, ionization timescale, and $N_{\rm H}$ seem to be responsible for the apparent spectral differences seen as color variations in the RGB composite image (Fig. 2). However, the detailed spectral analysis indicates that there are no statistically significant differences among the four regions. In the bright central part of the Lobe, Si appears to be slightly overabundant (1.6 ± 0.2 times solar), while the Mg abundance is consistent with solar. This is not what we would expect if the by-products of dust destruction were contributing to the X-ray–emitting material because the Mg and Si abundances should track each other (Itoh 1989; Vancura et al. 1994 and references therein). Since the other three regions have Si abundances consistent with solar and all regions have Mg abundances consistent with solar, there is no compelling evidence for ejecta material in these regions. Furthermore, the global NEI fits that have all other elemental abundances set to solar values produce good fits with no large residuals around elemental emission lines.

3.4.1. *Line Emission Analysis*

All the EPIC spectra for the Lobe show line features that can be attributed to Mg XI, Mg XII, and Si XIII lines, whereas the Si XIV line is too faint to be visible. Therefore, we use the Mg XI triplet and Mg XII Lyα line as line diagnostics of the NEI conditions of the plasma. We analyze the Lobe spectra from MOS1/2 data of pointing P1 and from MOS2 data of pointing P2. The spectrum is modeled using a modified "APEC" (Smith et al. 2001) model that excludes all emission lines[2] for the continuum and Gaussians for the lines, over the energy range of 1.15–3.0 keV. The fitted parameters for the Gaussians are used to determine the line centroids and fluxes. The line energies for the Gaussians are modeled as follows: 1.211 keV for Ne X Lyβ, $\sim$1.340 keV for Mg XI triplet, 1.472 keV for Mg XII Lyα, $\sim$1.850 keV for Si XIII triplet, and $\sim$2.440 keV for S XV.

[2] Contact R. Smith for a copy of this model.

TABLE 4
RESULTS OF THE Mg LINE ANALYSIS FROM *XMM-Newton* EPIC MOS DATA (POINTINGS P1 AND P2) OF THE LOBE

REGION	Mg XI TRIPLET		Mg XII Lyα NORM[a]	Mg XI TRIPLET/Mg XII Lyα LINE RATIO
	E (keV)	Norm[a]		
P1, MOS1/2				
1 (north)	$1.337^{+0.009}_{-0.002}$	$1.1^{+0.1}_{-0.5}\times10^{-4}$	$2.0^{+0.4}_{-0.5}\times10^{-5}$	$5.5^{+2.5}_{-3.0}$
2 (east)	$1.338^{+0.008}_{-0.003}$	$9.7^{+1.3}_{-2.0}\times10^{-5}$	$0.1^{+0.7}_{-0.1}\times10^{-5}$	$97^{+\infty}_{-87}$
3 (center)	$1.337^{+0.004}_{-0.002}$	$1.2^{+0.1}_{-0.2}\times10^{-4}$	$7.7^{+5.3}_{-4.0}\times10^{-6}$	16^{+19}_{-8}
4 (southwest)	$1.340^{+0.006}_{-0.010}$	$7.2^{+1.8}_{-2.0}\times10^{-5}$	$0.1^{+1.4}_{-0.1}\times10^{-5}$	$72^{+\infty}_{-69}$
P2, MOS2				
1 (north)	$1.335^{+0.011}_{-0.010}$	$9.4^{+2.6}_{-6.1}\times10^{-5}$	$1.8^{+0.8}_{-1.7}\times10^{-5}$	$5.2^{+114.8}_{-3.9}$
2 (east)	$1.343^{+0.013}_{-0.008}$	$1.2^{+0.2}_{-0.3}\times10^{-4}$	$0.8^{+1.8}_{-0.8}\times10^{-5}$	$15^{+\infty}_{-12}$
3 (center)	$1.335^{+0.006}_{-0.005}$	$1.3^{+0.5}_{-0.2}\times10^{-4}$	$1.1^{+0.7}_{-1.0}\times10^{-5}$	12^{+168}_{-7}
4 (southwest)	$1.340^{+0.011}_{-0.010}$	$8.2^{+1.8}_{-4.0}\times10^{-5}$	$0.3^{+0.8}_{-0.3}\times10^{-5}$	$27^{+\infty}_{-23}$

NOTE.—The spectral model is "APEC No Line" plus Gaussians.
[a] Norm = total number of photons cm^{-2} s^{-1} per extraction area in the line.

With the spectral resolution of the EPIC detectors, we are not able to resolve the lines in the Mg XI triplet. Therefore, we model the Mg XI line feature with one Gaussian and determine the line centroid. Variations in the line centroid from region to region would be indicative of different relative strengths of the resonance, intercombination, and forbidden lines. However, the line centroids of Mg XI are equal for all four Lobe regions within the 90% confidence intervals (Table 4). The data simply are not of high enough quality to determine such a small shift. However, the EPIC spectral resolution is sufficient to resolve the Mg XI triplet from the Mg XII Lyα line. From the fluxes of the Mg line complexes, the ratio Mg XI triplet/Mg XII Lyα is calculated. In Table 4, the line energy in keV and the flux in photons cm^{-2} s^{-1} per extraction area are given for the Mg XI triplet and the Mg XII Lyα line, as well as the derived ratio of Mg XI triplet/Mg XII Lyα.

The resulting line fluxes and line ratios are compared to NEI plasma models obtained using *neiline* (see Appendix A). The calculation provides line emissivities for different temperatures and ionization timescales. In Figure 8, the Mg XI triplet/Mg XII Lyα line ratio of region 3 for P1 data derived from the spectral analysis and error estimate based on the 90% confidence intervals for the line fluxes is plotted as a function of the ionization timescale τ and temperature kT. We also plot the best-fit values from the global VNEI fit for kT and τ and the 90% errors. Since region 3 has the best statistics, it gives the narrowest band in the kT-τ diagram. Within the errors, the VNEI value lies within the allowed region resulting from the line ratio analysis. From the diagram, we can derive the kT range for region 3 as $kT > 0.32$ keV. This lower limit is consistent with the results from the VNEI fit of the EPIC spectra in the total energy range of 0.3–10.0 keV (Table 2). The ratio of the Mg XI triplet to Mg XII Lyα does not provide a constraint on the ionization timescale.

These results show that line diagnostics are possible with CCD spectra. Compared to global fits, they suffer from fewer systematic uncertainties, while it is difficult to quantify the systematic errors of global fits. Line diagnostics are independent of foreground absorption and offer an additional method to constrain the plasma parameters. In our analysis the spectral resolution and the photon statistics only allow us to set a lower limit on the temperature. However, the results obtained from fitting the lines only and from fitting the entire EPIC spectrum are consistent with each other. This method is a promising technique of analyzing plasma conditions and can be applied for brighter SNRs, as well as for future missions with higher spectral resolution and larger collecting area.

3.4.2. *Nonthermal Emission*

In order to check if there is nonthermal emission from the Lobe that would be associated with a pulsar jet, we fit the spectra of regions 1–4 in the energy range of 0.3–10.0 keV with a model including a VNEI component and an additional power-law component for the Lobe emission. The fit does not improve significantly, and the flux of the power-law component is consistent with zero. Therefore, we derive an upper limit for the flux of the power-law component, assuming a photon index of $\Gamma = 1.5$; typical photon indices for pulsar jets are $\sim$1.2–1.7 (Lu et al. 2002; Gaensler et al. 2002; Pavlov et al. 2003). The nonthermal flux of the Lobe (0.3–10 keV) is less than 9.2×10^{-15} ergs cm^{-2}

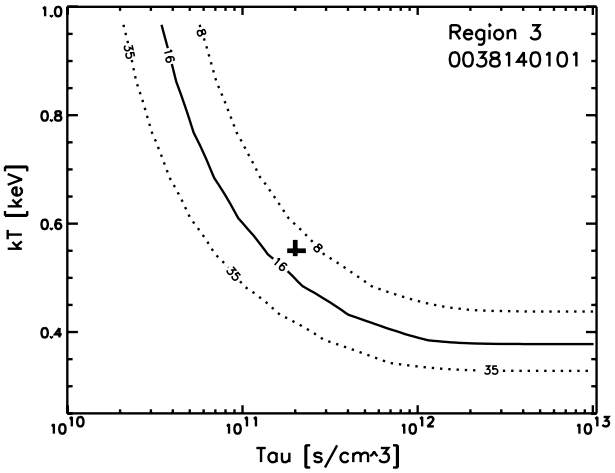

FIG. 8.—Line ratio Mg XI/Mg XII for region 3 derived from the spectral fits of P1 data plotted as a function of τ and kT (*solid line*). The estimated range for the error is shown with dotted lines. The kT and τ values resulting from the global spectral analysis (0.3–10.0 keV with VNEI model) are plotted with 90% confidence errors.

s^{-1} in region 1 (90% confidence level), less than 8.0×10^{-15} ergs cm^{-2} s^{-1} in region 2, less than 7.0×10^{-15} ergs cm^{-2} s^{-1} in region 3, and less than 6.1×10^{-15} ergs cm^{-2} s^{-1} in region 4, i.e., less than 0.05%, less than 0.08%, less than 0.05%, and less than 0.07% of the unabsorbed VNEI flux in regions 1–4, respectively. For the entire Lobe, the upper limit for the nonthermal emission is 6.9×10^{-14} ergs cm^{-2} s^{-1}, corresponding to 8.2×10^{-6} photons keV^{-1} cm^{-2} s^{-1} at 1 keV. For comparison, the intensity of the Vela pulsar jet is $\sim 4 \times 10^{-5}$ photons keV^{-1} cm^{-2} s^{-1} at 1 keV (Pavlov et al. 2003).

4. ESTIMATES BASED ON THE SEDOV SOLUTION

The morphology of CTB 109 and the existence of the GMC complex in the west suggest that the shock wave expanded into a dense cloud and decelerated very quickly. To the east, the shock wave is expanding into a lower density medium. CTB 109 seems to be confined by denser material in the north and south (Fesen & Hurford 1995), which might be responsible for the smaller radii of the northern and southern X-ray shells compared to that of the eastern shell (§ 2.1). However, the difference is relatively small (∼5%–10%) and overall the X-ray shell of CTB 109 can be considered as a semicircle. Calculations for the evolution of SNRs adjacent to a molecular cloud show that the shock propagation on the low-density side is almost unaffected by the presence of the molecular cloud (e.g., Tenorio-Tagle et al. 1985; Wang et al. 1992) and can be modeled as a spherical problem. The X-ray temperature of $\sim(3–8) \times 10^6$ K and the bright and well-defined X-ray rim of the remnant, as well as the lack of optical emission except in a few particular regions with higher density, indicate that the remnant has not yet reached the radiative phase. To estimate physical parameters for the remnant, we apply the shock jump conditions and the Sedov–Taylor–von Neumann similarity solution (Sedov 1959; Taylor 1950; von Neumann 1947). We assume a distance, D, to CTB 109 of 3.0 ± 0.5 kpc as estimated by Kothes et al. (2002) and introduce a scaling factor $d_3 = D/3.0$ kpc. For the mass and densities, the following relations apply: Assuming cosmic abundances (Anders & Grevesse 1989), the gas density (excluding electrons) is $n = 1.1 n_{\rm H}$, where $n_{\rm H}$ is the atomic H number density. The electron number density depends on the ionization state of the gas; if we assume at least single ionization for each element, $n_e = (1.1–1.2) n_{\rm H}$, and the total number density, including electrons, is $n_{\rm tot} = n_e + n = (2.2–2.3) n_{\rm H}$. The corresponding mass per free particle is $\bar{m} = (0.64–0.61) m_p$, with proton mass $m_p = 1.67 \times 10^{-24}$ g. The mean mass per nucleus in any ionization stage is $\bar{m}_n = 1.4 m_p$. In the following, subscript "0" denotes preshock values, and subscript "s" denotes postshock values.

For the radius of the blast wave, we use the distance of the eastern shell from the pulsar as estimated from the EPIC image: $R_s = 18\farcm5 \pm 1\farcm0 = (16 \pm 1) d_3$ pc $= (5.0 \pm 0.3) \times 10^{19} d_3$ cm. If a supernova occurs near a molecular cloud, the shock can be reflected at the cloud surface and cause the center of divergence of the velocity field to move away from the cloud (Tenorio-Tagle et al. 1985). The pulsar might also have a proper motion. Consequently, in the case of CTB 109 the distance of the eastern part of the shell to the pulsar is only an estimate of the radius. An alternative way to estimate the radius of the remnant is to measure the half of the extent of the shell in the north-south direction. However, as there is dense matter both north and south of the remnant that might interact with the shock front, the north-south extent rather provides a lower limit for the size of the remnant.

For the temperature, we use the result from the VNEI fits of the spectra in regions 7–9. The weighted mean of the temperature is calculated from the results that have been obtained by fitting the PN and MOS1/2 spectra separately and from the results of the simultaneous fits of the PN and MOS1/2 spectra. As the comparison of these results with the values for the eastern shell (Table 3) shows, there is a discrepancy of $\lesssim 0.08$ keV between the average temperature derived from the circular regions and the temperature obtained for the outer shell. To allow for the variation between the kT estimates, we increase the error estimate to 0.10 keV for this calculation and obtain for the temperature of the eastern part of the remnant shell $T_{\rm X} = 0.62 \pm 0.10$ keV $= (7.2 \pm 1.2) \times 10^6$ K.

At the discontinuity of the shock front, the density jump is $n = 4 n_0$, with n_0 being the preshock ambient density of nuclei. Inside the shock front, the density decreases toward the center because of the adiabatic expansion of the remnant (Heiles 1964; Cox & Anderson 1982). In order to derive further parameters, we use the distribution of the normalized density of the nuclei, $n(R)/n_0 = n_{\rm H}(R)/n_{\rm H,0}$, as calculated by Cox & Anderson (1982) and compute the emissivity numerically. The emitting volume is modeled as a cylinder intersecting a spherical remnant with the long axis of the cylinder running along the line of sight through the remnant. The radius of the cylinder is simply the radius of the extraction region, which, in this case, is $r = 80'' = 1.2 d_3$ pc for $D = 3.0 d_3$ kpc.

From the spectral fits of the EPIC data of regions 7–9 with the VNEI model, we derive the normalization in XSPEC as $K = (10^{-14}/4\pi D^2) \int 1.2 n_{{\rm H},s}^2 \, dV = (1.6 \pm 0.5) \times 10^{-3}$ cm^{-5}. Since the integral of the normalized density $n(R)/n_0$ over the volume can be calculated numerically, the ambient ISM density n_0 is estimated from the normalization K:

$$K = \frac{1.2 \times 10^{-14} n_{\rm H,0}^2}{4\pi D^2} \int \left(\frac{n_{\rm H}}{n_{\rm H,0}} \right)^2 dV. \quad (1)$$

The projected volume is $V = 42 d_3^3$ pc^3, and the integral is $\int (n_{\rm H}/n_{\rm H,0})^2 \, dV = 240 d_3^3$ pc^3. Thus, the preshock H density is $n_{\rm H,0} = (0.14 \pm 0.02) d_3^{-0.5}$ cm^{-3}, and the preshock density of nuclei $n_0 = 1.1 n_{\rm H,0} = (0.16 \pm 0.02) d_3^{-0.5}$ cm^{-3}.

In the case of full equilibration between the electrons and the nuclei, the shock velocity is related to the postshock temperature as

$$T_{\rm X} \approx T_s = \frac{3\bar{m}}{16k} v_s^2, \quad (2)$$

where $k = 1.38 \times 10^{-16}$ ergs K^{-1} is Boltzmann's constant. With a mean mass per free particle of $\bar{m} = 0.61 m_p$ for a fully ionized plasma, the shock velocity is estimated as $v_s = [(16 k T_{\rm X})/(3 \times 0.61 m_p)]^{1/2} = 720 \pm 60$ km s^{-1}.

It is possible that the electrons and ions are not fully equilibrated in the shock, in which case the ion temperature $T_{\rm ion}$ may be higher and the electron temperature T_e much lower than the mean plasma temperature $T \approx T_{\rm ion}$. The electrons and ions would then equilibrate slowly through Coulomb collisions. The plasma X-ray emissivity depends primarily on the electron temperature, and the deduced velocity would be larger. Ghavamian et al. (2003) and Rakowski et al. (2003) have analyzed the blast wave of the SNR DEM L71 in the Large Magellanic Cloud and find values for $T_e/T_{\rm ion}$ at different locations ranging from 0.01 (almost no equilibration) to 1.0 (full equilibration). The evolution of the electron temperature and its ratio to the mean postshock temperature in two-fluid phase SNR shocks has been studied by Itoh (1978). Applying the Sedov similarity solution

to the energy equation and the equation of state for the electron gas and assuming Coulomb interactions between the electron and the ion gas, he shows that the ratio $g = T_e/T$ is a function of a reduced time variable $\nu = t_3(n_0^8/E_{51}^3)^{1/14}$ that describes the thermal structure of the blast wave; t_3 is the time elapsed since the explosion (in units of 10^3 yr), n_0 is the preshock density of the nuclei (in units of cm^{-3}), and E_{51} is the initial blast energy (in units of 10^{51} ergs). From X-ray measurements one obtains the X-ray temperature, T_X, the ambient density, n_0, and the radius, R_s, of the SNR. Since these three values are related to each other as $f = T_X/T = 0.043T_X(R_s n_0)^{-1/2}\nu^{7/5}$, Itoh (1978) derives the value of $f = T_X/T$ from the intersection of the curve $f(\nu)$ with the theoretical curve for Coulomb equilibration $g(\nu) = T_e/T$. Based on this method, we determine a lower limit for the ratio $T_e/T_s \approx T_X/T_s \approx 0.4$ and an upper limit for the velocity $v_s = [(16kT_X)/(3 \times 0.4 \times 0.61m_p)]^{1/2} = 1140 \pm 90$ km s^{-1}.

The age of the remnant can be estimated from the shock velocity using the similarity solution:

$$v_s = \dot{R}_s = \frac{2R_s}{5t}. \tag{3}$$

Under the assumption of full equilibration of electron and ion temperatures, this yields an age estimate of $t = (2.8 \pm 0.3) \times 10^{11} d_3$ s $= (8.8 \pm 0.9) \times 10^3 d_3$ yr. If equilibration in the shock is incomplete, the age estimate would be lower. For the lower limit of $T_e/T_s = 0.4$, the age would be $t = (1.8 \pm 0.2) \times 10^{11} d_3$ s $= (5.6 \pm 0.6) \times 10^3 d_3$ yr.

We estimate the initial energy of the explosion from

$$R_s = \left(\frac{2.02 E_0 t^2}{\bar{m}_n n_0}\right)^{1/5}, \tag{4}$$

where the mean mass of the nuclei is $\bar{m}_n = 1.4m_p$. Solving for E_0 gives $E_0 = (1/2.02)R_s^5 \bar{m}_n n_0 t^{-2} = (7.4 \pm 2.9) \times 10^{50} d_3^{2.5}$ ergs, assuming full equilibration between the electrons and ions, and $E_0 = (18.5 \pm 7.3) \times 10^{50} d_3^{2.5}$ ergs, assuming partial equilibration with a lower limit of the temperature ratio of $T_e/T_s = 0.4$. The mass swept up by the SNR shock wave is $M = (4\pi/3) R_s^3 1.4 m_p n_0 = (97 \pm 23) d_3^{2.5} M_\odot$ if we assume a uniform ambient medium.

Wang et al. (1992) have numerically modeled an SNR next to a dense molecular cloud, using the Kompaneets (1960) approximation. They obtain a geometry comparable to that of CTB 109, 1.3×10^4 yr after the explosion in an ISM with a density of $n_0 = 0.13$ cm^{-3}. This value for the ambient density agrees well with the result we obtain from the *XMM-Newton* data. The assumed initial energy is $E = 3.6 \times 10^{50}$ ergs, 2–5 times lower than the energies we derive in our calculations. Consequently, the age estimate of Wang et al. (1992) is higher.

Rho & Petre (1997) have fitted a two-temperature Raymond & Smith model to the *ROSAT* PSPC spectrum of the northern shell, but the eastern shell is well fitted with a single-temperature model with a relatively low temperature of $kT = 0.21^{+0.05}_{-0.04}$ keV. They derive a shock velocity of $v_s = 380$ km s^{-1}, which is much lower than the EPIC result, and a remnant age of 1.9×10^4 yr assuming a distance of 4 kpc. This age is 2–4 times higher than our estimate. If we assumed a larger distance of 4 kpc, the calculation for the full equilibration case would yield 1.2×10^4 yr.

5. DISCUSSION

5.1. *X-Ray Spectrum*

ROSAT PSPC and Broad Band X-Ray Telescope (BBXRT) spectra of CTB 109 have been analyzed by Rho & Petre (1997). Assuming nonequilibrium ionization, they derive $kT = 1.7$ keV and $n_e t = 1.4 \times 10^{10}$ cm^{-3} s for the southern part of the remnant. A fit of the Lobe spectrum with a two-component Raymond & Smith model yields $kT_{\rm low} = 0.16^{+0.03}_{-0.04}$ keV and $kT_{\rm high} = 0.56^{+0.20}_{-0.10}$ keV. Their estimate for the column density, $N_{\rm H}$, for foreground absorption is $9.2^{+1.0}_{-1.5} \times 10^{21}$ cm^{-2}. No spectral lines can be resolved in the *ROSAT* PSPC spectrum, whereas the improved spectral resolution of *XMM-Newton* EPIC allows lines to be identified, and the continuum can also be better determined. Therefore, with the *XMM-Newton* EPIC data we can show that the emission is arising from a plasma out of ionization equilibrium and also determine the temperature more accurately. In contrast to the *ROSAT* results, we obtain a good fit of the EPIC spectra of the Lobe with a single NEI model with a temperature comparable to that of the high-temperature component of Rho & Petre (1997). The column density $N_{\rm H}$ of the EPIC fit is lower than that from the *ROSAT* data ($\sim 5 \times 10^{21}$ cm^{-2}). Presumably, the lower spectral resolution data of *ROSAT* PSPC allowed successful fits to two equilibrium plasma models, but with a higher absorbing column density.

Parmar et al. (1998) have fitted the *BeppoSAX* LECS spectrum of the whole remnant shell with a nonequilibrium ionization model and obtain $kT = 0.95^{+0.65}_{-0.27}$ keV, $n_e t = 3.8^{+3.8}_{-1.6} \times 10^{11}$ cm^{-3} s, and $N_{\rm H} = 6.9^{+0.7}_{-1.2} \times 10^{21}$ cm^{-2}. The analyzed spectrum does not include the emission from the pulsar and the Lobe but encompasses the rest of the remnant. The large errors of the fit parameters of the *BeppoSAX* spectrum are presumably caused by the lower spectral resolution compared to *XMM-Newton* EPIC, as well as the large extraction region including emission from various parts of the SNR.

For the *XMM-Newton* EPIC data of CTB 109, we use an NEI model for a collisional plasma with variable abundances for Mg and Si, while fixing the abundances of other elements to solar values. In the shell and in the Lobe, the temperature is $kT = 0.50$–0.70 keV, the ionization timescale $\tau \approx (1$–$3) \times 10^{11}$ s cm^{-3}, and the column density $N_{\rm H} = (5$–$7) \times 10^{21}$ cm^{-2}, with the exception of region 5 in the northeastern shell, where the temperature is low (~ 0.3 keV) and the ionization timescale is high [$(4$–$6) \times 10^{11}$ s cm^{-3}]. In the region corresponding to the CO arm, the absorption seems to be higher with $N_{\rm H} = (1.0 \pm 0.1) \times 10^{22}$ cm^{-2}, indicating that there is additional material along the line of sight to the SNR. Abundances are consistent with solar values in the whole remnant, except for one region (the bright central region of the Lobe), where Si appears to be overabundant ($\sim 1.6 \pm 0.2$ times solar). Since this marginal indication of overabundance is obtained only for Si in one region within the Lobe, while all the other abundances are consistent with solar, we conclude that there is no compelling evidence for ejecta emission. Given the large intensity variations within the remnant, it is somewhat surprising that none of the brighter regions show evidence of enhanced abundances. It may be the case in CTB 109 that the ejecta mass is relatively low and the current amount of swept-up matter is relatively high such that the ejecta will be difficult to detect. Although X-ray emission from ejecta is generally observed in SNRs up to an age of a few times 10^3 yr, there are remnants younger than CTB 109 that show no evidence for ejecta. For example, Kes 79 is estimated

to be ~6000 yr old and has no obvious emission from ejecta (Sun et al. 2004).

5.2. *Interaction between the SNR and the Giant Molecular Cloud*

As Tatematsu et al. (1985) have shown, the CO emission stretches from the GMC both north and south of CTB 109. In the optical band, filamentary structures have been found that are located at the rim of faint H II regions north and southeast of the SNR. At the position of the filaments, the H II regions overlap with the remnant in projection. This suggests that the optical emission is mainly caused by the interaction of the remnant with dense material harboring the H II regions (Fesen & Hurford 1995). The diffuse H II regions are probably associated with the outskirts of the molecular cloud complex to the west. From [S II] line ratios, Fesen & Hurford (1995) derive preshock cloud densities of up to ~20 cm^{-3} for the optical filaments. New H I and CO data (Kothes et al. 2002) make it clear that the remnant is located in a density gradient: very high density in the molecular cloud in the west and low density in the emission gap in the east of the SNR. As Kothes et al. (2002) point out, the H I map indicates that the SNR is not expanding inside a stellar wind bubble, since there is no evidence for a lower density cavity in H I with a pronounced rim.

Tenorio-Tagle et al. (1985) have performed two-dimensional numerical hydrodynamical calculations for the evolution of an SNR in or near a molecular cloud. If a supernova with an initial energy of $E \approx 10^{51}$ ergs occurs in a low-density ISM (1 cm^{-3}), the remnant shell becomes radiative after $\sim 5 \times 10^4$–10^5 yr when it has reached a radius of $R \approx 30$ pc. However, if the explosion occurs in a molecular cloud that has a higher density (10^3 cm^{-3}), the Sedov phase is shorter (~10^3 yr) and R smaller (~1–6 pc, Shull 1980; Tenorio-Tagle et al. 1985; Chevalier 1999). In the case of a supernova explosion inside a molecular cloud, a breakout occurs if the shock reaches the edge of the cloud. For CTB 109, the position of the pulsar and the shell relative to the GMC complex, as well as the semicircular shape of the shell, indicates that the supernova explosion was presumably located outside and close to a GMC. As Tenorio-Tagle et al. (1985) make clear in their calculations, a reflected shock forms from the cloud surface if the explosion takes place outside the cloud, but the shock transmitted into the cloud is weak and has a minor effect on the cloud surface. The reflected shock can cause an additional velocity component to the expansion of the SNR, directed away from the cloud. Wang et al. (1992) have modeled CTB 109 as a supernova explosion near (2 pc) a large molecular cloud, assuming an initial energy of $E = 3.6 \times 10^{50}$ ergs, an ISM density of $n_0 = 0.13$ cm^{-3}, and a cloud density of $n = 36$ cm^{-3}. They reproduce a semicircular shell of the observed size at the age of 1.3×10^4 yr.

The deep EPIC mosaic image of CTB 109 confirms that there is no emission in the western part of the remnant. In combination with the morphology of the remnant in the radio, this indicates that the shock wave has been stopped completely in the west. However, no indication has been found for a molecular shock in the GMC (Koralesky et al. 1998 and references therein). It is possible that there is enough material in unshocked parts of the GMC that lie in front of the interaction region such that any emission from this region could be absorbed. Hard point sources discovered in the X-ray–faint parts of the SNR (§ 2.2) also suggest the existence of absorbing material in front of the SNR.

5.3. *Lobe as Shocked Cloud*

Our analysis of the *XMM-Newton* EPIC data shows that the spectral properties of the Lobe are very similar to those of the remnant shell. Moreover, the merged *XMM-Newton* image (Fig. 1) corroborates that the Lobe and the pulsar are not related morphologically, confirming that the Lobe is not a jet phenomenon. Rho & Petre (1997) have suggested that, as a result of the interaction between the SNR and the GMC in the west, a reflected shock has propagated into the SNR. Rayleigh-Taylor instabilities might have formed between the thin SNR plasma and the dense GMC, possibly producing a structure such as the Lobe. Another possibility is that there are denser clouds in the outer parts of the GMC complex that have been shocked by the SNR blast wave. In projection, the Lobe and the bright knots in the northern part of the remnant seem to trace the outer boundary of the CO arm and therefore might be emission from shocked interstellar clouds on the outskirts of the GMC complex.

Tatematsu et al. (1990) point out that a density fluctuation in the preshock gas might have resulted in a local excess of the postshock emission measure seen as the Lobe. They estimate that a cloud with a density 2–5 times higher than the average preshock density in the ambient medium could have produced the Lobe. However, they find no evidence of CO gas accelerated by the SNR shock wave. In the far-infrared, Coe et al. (1989) have found a region with bright emission northeast of the Lobe. This region also coincides with the eastern edge of the CO arm extending from the western molecular cloud complex, which suggests that this emission is caused by a shocked cloud. Fesen & Hurford (1995) have found optical filaments at the southwestern edge of the Lobe, i.e., closer to the center of the remnant. All the other optical filaments detected in their observations are located along the northern and southern shell of the remnant and seem to be the result of the SNR interacting with material associated with the H II regions in the north and south. Usually, optical filaments are believed to be thin, shocked regions tangent to the line of sight. Since the diffuse optical emission in the north extends southward to the position of the Lobe, they suggest that the central filamentary emission arises from shocked gas along the projected edge of an interstellar cloud. Assuming a shock velocity of 100 km s^{-1}, the observed [S II] line ratio corresponds to a preshock cloud density of $n_{\rm cloud} = 5$ cm^{-3} (Fesen & Hurford 1995).

The interaction between a shock wave and a density enhancement like an interstellar cloud has been studied theoretically by many authors. Two-dimensional hydrodynamical calculations give information about the dynamical evolution of an interaction between the SNR blast wave and a dense cloud (e.g., Bedogni & Woodward 1990; Mac Low et al. 1994; Klein et al. 1994). The cloud fragments as a result of the interaction. This is also observed in three-dimensional simulations by Xu & Stone (1995), who in addition show that the morphology of the cloud after the interaction depends strongly on the initial shape of the cloud. Klein et al. (2003) have performed a laboratory experiment using the Nova high-energy density laser at Lawrence Livermore National Laboratory in order to study the interaction of a shock wave with a high-density sphere located in a low-density medium. They confirm that the evolution of the sphere after the interaction depends on the density ratio of the high-density to low-density medium, χ, and the Mach number of the shock wave, as shown by Klein et al. (1994). The high-density sphere ($\chi = 10$) is destroyed by the interaction with a shock wave with a Mach number of 10.

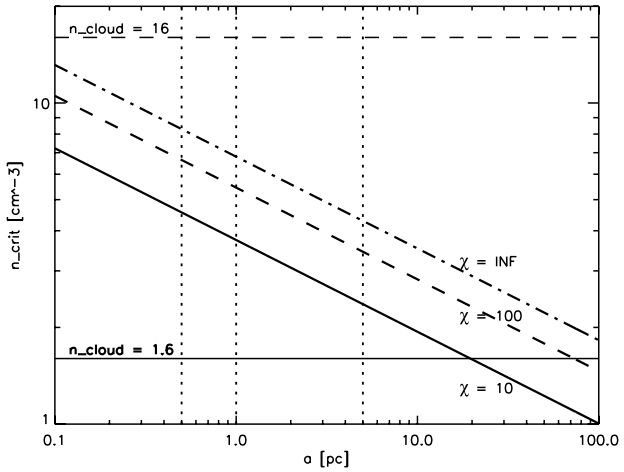

FIG. 9.—Critical density $n_{\rm crit}$ (Sgro 1975) as a function of cloud size a for $v_s = 720$ km s^{-1} and $n_0 = 0.16$ cm^{-3} (*thick lines*). The solid line is for $\chi = 10$, dashed line for $\chi = 100$, and dot-dashed line for $\chi = \infty$. For $\chi = 10$ and 100, the corresponding cloud density is shown with thin lines for $n_0 = 0.16$ cm^{-3}. The dotted lines indicate $a = 0.5$, 1, and 5 pc.

In order to better understand the possible origin of the Lobe emission in CTB 109, we estimate cloud densities from the results of *XMM-Newton* observations based on analytical estimates by Sgro (1975) for a planar shock-cloud interaction. There are two limiting cases, the "cold" cloud case and the "hot" cloud case, depending on the cooling timescale in the postshock cloud gas relative to the crossing time for the transmitted cloud shock. A critical density is estimated by equating the cooling time and the shock crossing time:

$$n_{\rm crit} = 5.8 \times 10^{-4} \beta^{5/7} v_s^{10/7} n_0^{5/7} a^{-2/7}, \qquad (5)$$

where β is the ratio of the pressure behind the transmitted cloud shock and the pressure in the shocked ambient ISM, v_s is the shock velocity (in km s^{-1}), n_0 is the ambient preshock density (in cm^{-3}), and a is the size of the cloud (in pc). For a density contrast of $\chi = n_{\rm cloud}/n_0 = 10$, 100, and ∞, β is 2.6, 4.4, and 6.0, respectively (Sgro 1975). If the cloud is denser than $n_{\rm crit}$, the shocked cloud gas cools rapidly (cold cloud) and, after having reached a temperature below $\sim 10^4$ K, produces line emission of lower ionization stages of the constituent elements. In the hot cloud case, the cloud density is lower than $n_{\rm crit}$ and the temperature is still higher than $\sim 10^6$ K when the transmitted shock reaches the end of the cloud. The cloud emits X-rays and optical lines of higher ionization stages. However, there will be no region that has cooled down to $\sim 10^4$ K; therefore, no Hα emission will be detected.

To estimate the properties of a hypothetical uniform cloud in the Lobe region, we use the values obtained in § 4 from the Sedov analysis of the EPIC data, i.e., $v_s = 720$ km s^{-1}, under the assumption of full equilibration between electrons and ions behind the shock, and $n_0 = 0.16$ cm^{-3}. The critical density $n_{\rm crit}$ as a function of the cloud size a (eq. [5]) is plotted in Figure 9 for three different values for the density contrast $\chi = 10$, 100, and ∞. The region below the line corresponds to the hot cloud case, whereas the region above is the cold cloud case. Assuming an ambient density of $n_0 = 0.16$ cm^{-3}, the initial cloud density $n_{\rm cloud} = 1.6$ and 16 for $\chi = 10$ and 100, respectively. Parameter $n_{\rm cloud}$ is also indicated in the diagram with thin horizontal lines. As can be seen in Figure 9, for $\chi = 100$ we would have the cold cloud case for all clouds with $a > 0.1$ pc. However, the observed soft X-ray emission from the Lobe indicates a hot cloud case. If we assume a cloud size $a = 1$ pc and a density contrast $\chi = 10$, equation (5) yields a critical density of $n_{\rm crit} = 3.7$ cm^{-3}, while a cloud size of $a = 0.5$ pc with $\chi = 10$ results in $n_{\rm crit} = 4.6$ cm^{-3}. For a likely cloud size $a \approx 1$ pc, $\chi = 10$ would result in a hot cloud. Therefore, the Lobe emission is indicative of an interaction between the shock wave of CTB 109 ($v_s = 720$ km s^{-1}, $n_0 = 0.16$ cm^{-3}) and an interstellar cloud with a density $n_{\rm cloud} \lesssim 5$ cm^{-3}.

6. SUMMARY

We have studied the Galactic SNR CTB 109 using EPIC data of five *XMM-Newton* pointings. The deep EPIC image, created from all of these observations, shows no emission in the western part of the shell. This confirms that the remnant has its semicircular morphology because the progress of the shock wave has been stopped by the GMC. We find no morphological evidence for a connection between the Lobe and the pulsar. The mosaic RGB image reveals some regions and clumps within the remnant that appear to have harder or softer spectra than the average spectrum. However, a detailed spectral analysis indicates that only two regions have significantly different fitted values for the $N_{\rm H}$, temperature, or ionization timescale. The Lobe region appears to have rather small spectral variations.

Using the RGB composite image as a guide, we extract spectra for different parts of the remnant in circular regions and polygon regions. Best-fit results are obtained with a single-temperature nonequilibrium ionization model for a collisional plasma. Abundances are determined for Mg and Si, while the abundances of the other elements are fixed to solar values. As the spectra show no indication of nonthermal emission, we derive upper limits in the energy range of 0.3–10.0 keV. In the eastern part of the shell, where emission is believed to arise from the forward shock, the upper limit of nonthermal emission is less than 2% of the thermal emission.

Analysis of the spectra of four regions in the Lobe indicates that the spectral variations seen in the RGB composite image are caused by small differences in temperature, ionization timescale of the plasma, and $N_{\rm H}$. None of these differences are significant at the 90% confidence level. There is no significant evidence for nonthermal emission from the Lobe. The upper limits of the nonthermal emission are low; the flux upper limit for the entire Lobe in the energy range of 0.3–10.0 keV is 6.9×10^{-14} ergs cm^{-2} s^{-1} with an average surface brightness of 1.1×10^{-15} ergs cm^{-2} s^{-1} arcmin^{-2}, about 5 times lower than the flux from the X-ray jet of the Vela pulsar. The detailed spectral analysis shows that the spectra of the Lobe and the remnant shell are remarkably similar, with $kT = 0.50$–0.70 keV, $\tau = (1$–$3) \times 10^{11}$ s cm^{-3}, and $N_{\rm H} = (5$–$7) \times 10^{21}$ cm^{-2}. Mg and Si abundances turn out to be consistent with solar values in almost all analyzed regions of the SNR except in the bright central part of the Lobe where the Si abundance is slightly higher than solar ($\sim 1.6 \pm 0.2$ times solar). This marginal indication of overabundance, only seen in one region of the SNR, is not indicative of ejecta emission. The small color variations seen in the RGB composite image do not result in significant differences in the fitted spectral parameters. We use the Mg line emission as an NEI line diagnostic. We fit the Mg XI triplet and Mg XII Lyα line features with Gaussians and derive a lower

limit for kT that is consistent with the results from the global NEI fits of the EPIC spectra.

The detailed spectral analysis does confirm significant spectral variations for two locations within the remnant. The northeastern part of the shell, right next to a radio bright knot, contains a bright spot with lower temperature ($kT \approx 0.3$ keV) and higher ionization timescale [$\tau = (4\text{–}6) \times 10^{11}$ s cm^{-3}]. In this region, Fesen & Hurford (1995) have found two bright optical filaments. The high value for τ indicates a region with a possibly higher density; it seems that the shock wave of the SNR has encountered a particularly dense cloud in this part of the shell. The region just north of the pulsar corresponding to the CO arm has a significantly higher $N_{\rm H}$ ($\sim 1.0 \times 10^{22}$ cm^{-2}) than other regions in the remnant. The temperature and ionization timescale are mostly consistent with the rest of the remnant. We conclude that the underlying spectrum in this region is not significantly different from the spectrum of the rest of the remnant, but the column density of material in front of this part of the remnant is higher. We note that this larger value of $N_{\rm H}$ is consistent with what Woods et al. (2004) find for their fits to the spectrum of 1E 2259+586 and hence strengthens the already strong case for an association between the remnant and the pulsar. In addition, there is marginal evidence for a spectral variation with radius in the eastern shell of the SNR. The temperature is higher in the outer eastern shell, whereas the $N_{\rm H}$ and τ values are higher for the inner shell. This might indicate that the outer part of the shell (seen in projection) expands into a medium with lower density, while in the inner regions the shock is affected by density enhancements in the ISM.

From the result of the spectral analysis, we estimate an SNR blast wave velocity of $v_s = 720 \pm 60$ km s^{-1} assuming that the remnant is in the Sedov phase and that there is full equilibration of the electron and ion temperatures right behind the shock front and a remnant age of $t = (8.8 \pm 0.9) \times 10^3 d_3$ yr, at an assumed distance of $D = 3.0 d_3$ kpc. In the case of partial equilibration with $T_e/T_s = 0.4$ as the lower limit, the blast wave velocity would be $v_s = 1140 \pm 90$ km s^{-1} and the remnant age $t = (5.6 \pm 0.6) \times 10^3 d_3$ yr. We also calculate a preshock density of the nuclei $n_0 = (0.16 \pm 0.02) d_3^{-0.5}$ cm^{-3}, initial energy $E_0 = (7.4 \pm 2.9) \times 10^{50} d_3^{2.5}$ ergs (full equilibration) or $E_0 = (18.5 \pm 7.3) \times 10^{50} d_3^{2.5}$ ergs ($T_e/T_s = 0.4$), and swept-up mass of $M = (97 \pm 23) d_3^{2.5}\ M_\odot$.

The thermal nature of the X-ray emission of the Lobe and the optical filaments found at the southwestern edge of the Lobe are clear indications that the Lobe is the result of the SNR shock wave encountering an interstellar cloud ($n_{\rm cloud} \lesssim 5$ cm^{-3}). We infer from derived shock velocities and densities that the shock wave traveled through the cloud on a timescale that was comparable to the cooling time of the shocked gas in the cloud. The cloud was heated to temperatures of $\sim 10^6$ K and has not yet cooled down substantially, resulting in little optical emission.

We are grateful to V. Kaspi for providing the *XMM-Newton* data (ObsID 0038140101) of 1E 2259+586. We would like to thank A. Read and M. Freyberg for useful discussion about the *XMM-Newton* EPIC background analysis. This work was supported by the NASA *XMM-Newton* grant NAG5-9914, NASA contracts NAS8-39073 and NAS8-03060, and in part NASA grants GO0-1127X and GO1-2060X. This research has made use of the SIMBAD database, operated at CDS, Strasbourg, France.

APPENDIX

CALCULATING NONEQUILIBRIUM LINE EMISSIVITIES

The tool *neiline* calculates line emissivities (using the Raymond & Smith 1977 code in its update by Brickhouse et al. 1993) for certain nonequilibrium conditions, specifically an ionizing or recombining plasma with astrophysical abundances. We used the code to calculate the line ratio diagnostics described herein and feel it could be of general interest to the SNR community.

The code is quite simple. After reading in the input values, it initializes the Raymond & Smith (1977; update by Brickhouse et al. 1993) plasma code, evolves the plasma, and outputs the requested emission. The user can set the abundances, the initial electron and ionization temperatures (the initial ionization temperature is used to set the initial ionization balance), the pressure, and the maximum time, ionization timescale, or minimum temperature for the model. The plasma evolution can be isothermal, isobaric, isochoric, or a special case in which the plasma is isobaric until the temperature drops to a specified value after which it is isothermal. Except in the isothermal case, the electron temperature drops by a user-defined factor (default 2%), and the cooling, ionization balance evolution, and line emissivities are calculated by the Raymond & Smith code at each step in the evolution.

The code is written in C and FORTRAN and is available at http://cxc.harvard.edu/cont-soft/software/NEIline.1.00.html.

REFERENCES

Allen, G. E., Houck, J. C., & Sturner, S. J. 2004, Adv. Space Res., 33, 440
Allen, G. E., et al. 1997, ApJ, 487, L97
Anders, E., & Grevesse, N. 1989, Geochim. Cosmochim. Acta, 53, 197
Arendt, R. G. 1989, ApJS, 70, 181
Aschenbach, B., et al. 2000, Proc. SPIE, 4012, 731
Bamba, A., Yamazaki, R., Ueno, M., & Koyama, K. 2003, ApJ, 589, 827
Bedogni, R., & Woodward, P. R. 1990, A&A, 231, 481
Blair, W. P., & Kirshner, R. P. 1981, Nature, 291, 132
Borkowski, K. J., Lyerly, W. J., & Reynolds, S. P. 2001, ApJ, 548, 820
Borkowski, K. J., Sarazin, C. L., & Blondin, J. M. 1994, ApJ, 429, 710
Brickhouse, N. S., Raymond, J. C., & Smith, B. W. 1993, BAAS, 25, 864
Chevalier, R. A. 1999, ApJ, 511, 798
Coe, M. J., Davies, S. R., Fahlman, G. G., & Gregory, P. C. 1989, MNRAS, 238, 649
Cox, D. P., & Anderson, P. R. 1982, ApJ, 253, 268
Fahlman, G. G., & Gregory, P. C. 1981, BAAS, 13, 533
Fahlman, G. G., & Gregory, P. C. 1983, in IAU Symp. 101, Supernova Remnants and Their X-Ray Emission, ed. J. Danziger & P. Gorenstein (Dordrecht: Kluwer), 445
Fesen, R. A., & Hurford, A. P. 1995, AJ, 110, 747
Gaensler, B. M., Arons, J., Kaspi, V. M., Pivovaroff, M. J., Kawai, N., & Tamura, K. 2002, ApJ, 569, 878
Gavriil, F. P., Kaspi, V. M., & Woods, P. M. 2004, ApJ, 607, 959
Ghavamian, P., Rakowski, C. E., Hughes, J. P., & Williams, T. B. 2003, ApJ, 590, 833
Gotthelf, E. V., Koralesky, B., Rudnick, L., Jones, T. W., Hwang, U., & Petre, R. 2001, ApJ, 552, L39
Gregory, P. C., & Fahlman, G. G. 1980, Nature, 287, 805
———. 1983, in IAU Symp. 101, Supernova Remnants and Their X-Ray Emission, ed. J. Danziger & P. Gorenstein (Dordrecht: Kluwer), 429
Hamilton, A. J. S., Chevalier, R. A., & Sarazin, C. L. 1983, ApJS, 51, 115
Heiles, C. 1964, ApJ, 140, 470

Heydari-Malayeri, M., Kahane, C., & Lucas, R. 1981, Nature, 293, 549
Hughes, V. A., Harten, R. H., Costain, C. H., Nelson, L. A., & Viner, M. R. 1984, ApJ, 283, 147
Hughes, V. A., Harten, R. H., & van den Bergh, S. 1981, ApJ, 246, L127
Hurford, A. P., & Fesen, R. A. 1995, MNRAS, 277, 549
Israel, F. P. 1980, AJ, 85, 1612
Itoh, H. 1978, PASJ, 30, 489
———. 1989, PASJ, 41, 853
Iwasawa, K., Koyama, K., & Halpern, J. P. 1992, PASJ, 44, 9
Jansen, F., et al. 2001, A&A, 365, L1
Kaastra, J. S. 1992, An X-Ray Spectral Code for Optically Thin Plasmas, Internal SRON-Leiden Rep., Version 2.0
Kaspi, V. M., Gavriil, F. P., Woods, P. M., Jensen, J. B., Roberts, M. S. E., & Chakrabarty, D. 2003, ApJ, 588, L93
Kirsch, M. 2003, EPIC Status of Calibration and Data Analysis, XMM-SOC-CAL-TN-0018, Issue 2.1
Klein, R. I., Budil, K. S., Perry, T. S., & Bach, D. R. 2003, ApJ, 583, 245
Klein, R. I., McKee, C. F., & Colella, P. 1994, ApJ, 420, 213
Kompaneets, A. S. 1960, Soviet Phys. Dokl., 5, 46
Koralesky, B., Frail, D. A., Goss, W. M., Claussen, M. J., & Green, A. J. 1998, AJ, 116, 1323
Kothes, R., Uyaniker, B., & Yar, A. 2002, ApJ, 576, 169
Liedahl, D. A., Osterheld, A. L., & Goldstein, W. H. 1995, ApJ, 438, L115
Lu, F. J., Wang, Q. D., Aschenbach, B., Durouchoux, P., & Song, L. M. 2002, ApJ, 568, L49
Lumb, D. H. 2001, EPIC Background Files, XMM-SOC-CAL-TN-0016, Issue 2.0
Lumb, D. H., Warwick, R. S., Page, M., & De Luca, A. 2002, A&A, 389, 93
Mac Low, M., McKee, C. F., Klein, R. I., Stone, J. M., & Norman, M. L. 1994, ApJ, 433, 757
Mewe, R., Gronenschild, E. H. B. M., & van den Oord, G. H. J. 1985, A&AS, 62, 197
Mewe, R., Lemen, J. R., & van den Oord, G. H. J. 1986, A&AS, 65, 511
Monet, D. B. A., et al. 1998, VizieR Online Data Catalog, 1252
Parmar, A. N., Oosterbroek, T., Favata, F., Pightling, S., Coe, M. J., Mereghetti, S., & Israel, G. L. 1998, A&A, 330, 175
Patel, S. K., et al. 2001, ApJ, 563, L45
Pavlov, G. G., Teter, M. A., Kargaltsev, O., & Sanwal, D. 2003, ApJ, 591, 1157
Rakowski, C. E., Ghavamian, P., & Hughes, J. P. 2003, ApJ, 590, 846
Raymond, J. C., & Smith, B. W. 1977, ApJS, 35, 419
Read, A. M., & Ponman, T. J. 2003, A&A, 409, 395
Rho, J.-H., & Petre, R. 1993, BAAS, 25, 1442
———. 1997, ApJ, 484, 828
Saken, J. M., Fesen, R. A., & Shull, J. M. 1992, ApJS, 81, 715
Sedov, L. I. 1959, Similarity and Dimensional Methods in Mechanics (New York: Academic)
Sgro, A. G. 1975, ApJ, 197, 621
Shull, J. M. 1980, ApJ, 237, 769
Smith, R. K., Brickhouse, N. S., Liedahl, D. A., & Raymond, J. C. 2001, ApJ, 556, L91
Sofue, Y., Takahara, F., & Hirabayashi, H. 1983, PASJ, 35, 447
Strüder, L., et al. 2001, A&A, 365, L18
Sun, M., Seward, F. D., Smith, R. K., & Slane, P. O. 2004, ApJ, 605, 742
Tatematsu, K., Fukui, Y., Iwata, T., Seward, F. D., & Nakano, M. 1990, ApJ, 351, 157
Tatematsu, K., Fukui, Y., Nakano, M., Kogure, T., Ogawa, H., & Kawabata, K. 1987, A&A, 184, 279
Tatematsu, K., Nakano, M., Yoshida, S., Wiramihardja, S. D., & Kogure, T. 1985, PASJ, 37, 345
Taylor, G. I. 1950, Proc. R. Soc. London A, 201, 159
Tenorio-Tagle, G., Bodenheimer, P., & Yorke, H. W. 1985, A&A, 145, 70
Turner, M. J. L., et al. 2001, A&A, 365, L27
Vancura, O., Raymond, J. C., Dwek, E., Blair, W. P., Long, K. S., & Foster, S. 1994, ApJ, 431, 188
von Neumann, J. 1947, Los Alamos Sci. Lab. Tech. Series, Vol. 7
Wang, Z., Qu, Q., Luo, D., McCray, R., & Mac Low, M. 1992, ApJ, 388, 127
Woods, P. M., et al. 2004, ApJ, 605, 378
Xu, J., & Stone, J. M. 1995, ApJ, 454, 172

The Astrophysical Journal, 642: L149–L152, 2006 May 10

EVIDENCE FOR SHOCKED MOLECULAR GAS IN THE GALACTIC SUPERNOVA REMNANT CTB 109 (G109.1−1.0)

Manami Sasaki,[1] Roland Kothes,[2,3] Paul P. Plucinsky,[1] Terrance J. Gaetz,[1] and Christopher M. Brunt[4]

Received 2006 February 10; accepted 2006 April 3; published 2006 April 24

ABSTRACT

We report the detection of molecular clouds around the X-ray-bright interior feature in the Galactic supernova remnant (SNR) CTB 109 (G109.1−1.0). This feature, called the "lobe," has been previously suggested to be the result of an interaction of the SNR shock wave with a molecular cloud complex. We present new high-resolution X-ray data from the *Chandra X-Ray Observatory* and new high-resolution CO data from the Five College Radio Astronomy Observatory that show the region of interaction with the cloud complex in greater detail. The CO data reveal three clouds around the lobe in the velocity interval -57 km s$^{-1} < v < -52$ km s^{-1}. The velocity profiles of ^{12}CO in various parts of the east cloud are well fit with a Gaussian; however, at the position at which the CO cloud and the lobe overlap, the velocity profile has an additional component toward higher negative velocities. The molecular hydrogen density in this part of the cloud is relatively high ($N_{\rm H_2} \approx 1.9 \times 10^{20}$ cm^{-2}), whereas the foreground absorption in X-rays ($N_{\rm H} \approx 4.5 \times 10^{21}$ cm^{-2}), obtained from *Chandra* data, is lower than in other parts of the cloud and in the north and south clouds. These results indicate that the east cloud has been hit by the SNR blast wave on the western side, forming the bright X-ray lobe.

Subject headings: ISM: clouds — shock waves — supernova remnants — X-rays: individual (CTB 109)

Online material: color figure

1. INTRODUCTION

The progenitor stars of core-collapse supernova explosions form in giant molecular clouds (GMCs). Since these massive stars have a short lifetime many of them end their lives while the parental clouds are still nearby and may even still harbor small star-forming regions that produce stars of lower mass. According to Cappellaro et al. (1999), in galaxies like ours about 70% of all supernova explosions are of Type II and should explode close to the dense clouds from which they were formed. After these stars explode, strong shocks are driven into the clouds, heating, compressing, dissociating, and accelerating the gas leading, to a large variety of observable effects. A picture-book example is the Galactic supernova remnant (SNR) IC 443, on which most studies of SNR–molecular cloud interactions have been focused (Seta et al. 1998; Bocchino & Bykov 2000; Kawasaki et al. 2002 and references therein). But recently more and more SNRs have been discovered interacting with molecular clouds, e.g., W28, W44, 3C 391 (e.g., Reach & Rho 2000; Yusef-Zadeh et al. 2003 and references therein), and many others, among them the Galactic SNR CTB 109 (G109.1−1.0).

CTB 109 was first discovered as an SNR in X-rays with *Einstein* (Gregory & Fahlman 1980) and in radio in the Galactic plane survey at 610 MHz (Hughes et al. 1981). It has a semicircular morphology in both the X-ray and the radio and is located next to a GMC complex in the west. This semicircular morphology suggests that the SNR shock has been stopped entirely by the GMC complex and that the appearance is not simply due to absorption. A linear feature in CO (the "CO arm") extends from the GMC complex to the local X-ray minimum in the northern half (Tatematsu et al. 1987), implying that part of the GMC complex extends in front of the remnant (see Fig. 1). The cold interstellar medium in which the remnant is embedded has been studied in detail by Kothes et al. (2002). The most puzzling X-ray morphological feature in CTB 109 is the bright, extended, interior region known as the "lobe." The X-ray spectrum from the lobe obtained with *XMM-Newton* is completely thermal (Sasaki et al. 2004). The lobe could be the result of a hole in the GMC allowing the X-ray emission through with little or no absorption, or it could be the result of intrinsically brighter emission due to an interaction between the shock and the cloud. In order to investigate the latter hypothesis, we have obtained new high-resolution X-ray and CO data.

2. OBSERVATIONS

2.1. CO *Data*

Observations of the ^{12}CO and ^{13}CO $J = 1$–0 spectral lines, at 45″ resolution, were obtained using the Five College Radio Astronomy Observatory (FCRAO) 14 m antenna in 2003 March. The telescope was equipped with the 32 element SEQUOIA focal plane array (Erickson et al. 1999). The data were acquired through on-the-fly mapping, in which the telescope was scanned continuously across the sky while reading out the spectrometers at regular intervals of 11.″25. Calibration to the T_A^* scale was done using the chopper wheel method (Kutner & Ulich 1981), and the data were converted to the radiation temperature scale (T_R^*) by correcting for forward scattering and spillover losses ($\eta_{\rm fss} = 0.7$). The 1024 channel spectrometers were set to a total bandwidth of 25 MHz (~65 km s^{-1}) centered on -45 km s^{-1}. Following recording of the data, the spectra were converted onto a regular grid of 22.″5 pixel spacing using the FCRAO `otftool` software.

The new data have higher sensitivity than the Canadian Galactic Plane Survey data (Kothes et al. 2002) and are fully Nyquist-sampled. The higher sensitivity and the full sampling

[1] Harvard-Smithsonian Center for Astrophysics, 60 Garden Street, Cambridge, MA 02138; msasaki@cfa.harvard.edu, pplucinsky@cfa.harvard.edu, tgaetz@cfa.harvard.edu.

[2] National Research Council of Canada, Herzberg Institute of Astrophysics, Dominion Radio Astrophysical Observatory, P.O. Box 248, Penticton, BC V2A 6J9, Canada; roland.kothes@nrc-cnrc.gc.ca.

[3] Department of Physics and Astronomy, University of Calgary, 2500 University Drive NW, Calgary, AB T2N IN4, Canada.

[4] School of Physics, University of Exeter, Stocker Road, Exeter EX4 4QL, UK; brunt@astro.ex.ac.uk.

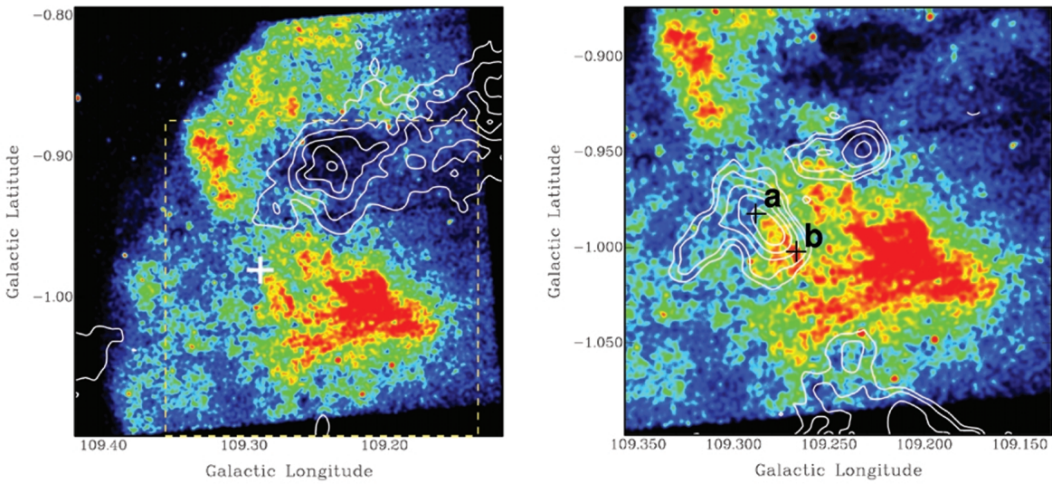

FIG. 1.—Distribution of molecular gas in the vicinity of the X-ray lobe as seen in the light of the ^{12}CO (1–0) line (*white contours*) overlaid on a *Chandra* image of the X-ray emission between 0.35 and 10.0 keV. *Left*: The CO data are averaged over the velocity range from −51 to −44.5 km s^{-1} and show the absorbing CO in the foreground. Contours levels are at 0.5, 1.0, 1.5, 2.0, and 2.5 K. The white cross marks the position of the IR source IRAS 23004+5841. The yellow dashed box shows the extent of the region shown in the right panel. *Right*: The CO data are averaged over the velocity range from −57 to −52 km s^{-1}. Contours levels are at 0.15, 0.25, 0.5, 0.8, and 1.2 K. Three clouds are seen Galactic north (up), east (left), and south (down) of the lobe. The positions at which the velocity profiles in Fig. 2 are taken are marked with crosses.

allow us to detect the faint clouds around the lobe and study them in great detail.

2.2. *Chandra Data*

The *XMM-Newton* observations have shown that the X-ray-bright lobe is thermal and seem to indicate an interaction between the shock wave and a molecular cloud (Sasaki et al. 2004). Therefore, we proposed an additional deep observation with *Chandra* to probe the shock-cloud interaction region at higher angular resolution. The observation was performed using the Advanced CCD Imaging Spectrometer (ACIS) in full-frame, timed-event mode with an exposure of 80 ks (ObsID 4626). The data were taken in the energy band of ~0.3–10.0 keV. The ACIS-I array covered the northeast part of the SNR, and the northern tip of the lobe was observed at the aim point. The data are analyzed with CIAO 3.2.2 and CALDB 3.1.0. The complete analysis of these data, including a detailed spectral analysis of the whole area, will be presented in a different paper.

Here we present the high-resolution X-ray image of the lobe of CTB 109 obtained with *Chandra* ACIS-I. The image is binned with a size of 4 pixels (1 pixel = 0.″492) and smoothed with a Gaussian with a sigma of 2 pixels (the original pixels binned by 4). X-ray spectra that are extracted at regions corresponding to CO clouds are also discussed, in order to obtain the absorbing foreground hydrogen column density ($N_{\rm H}$). The spectra are binned with a minimum of 50 counts per bin and analyzed using the X-ray spectral analysis tool XSPEC. To fit the spectra, we use a model of a thermal plasma in nonequilibrium ionization with variable abundances (VNEI), and hydrogen column density, $N_{\rm H}$, for the foreground absorption.

TABLE 1

CALCULATED CLOUD CHARACTERISTICS AND THE FOREGROUND HYDROGEN COLUMN DENSITY

	VALUE					
	Cloud					
PARAMETER	North	East	Eastern Tail	South	CO Arm	Lobe
r	8.1	7.6	12.0	13.0	3.5	...
τ_{12}	2.2	2.2	1.7	1.6	3.2	...
τ_{13}	0.13	0.14	0.076	0.068	0.47	...
$N_{\rm H_2}$ (cm^{-2})	7.0E19	1.9E20	2.9E19	3.4E19	1.3E21	...
$n_{\rm H_2}$ (cm^{-3})	10	40	5	2	100	...
Mass ($M_\odot$)	13	50	3	25	350	...
$N_{\rm H}$ (cm^{-2})	6.3E21	5.9E21	5.0E21	6.8E21	...	4.5E21

3. DISCUSSION

3.1. CO, *Infrared, and X-Ray Data*

In Figure 1 we display the distribution of molecular gas in the vicinity of the X-ray lobe. In the left image, the CO arm discovered by Tatematsu et al. (1987) is shown. The anticorrelation of the CO emission with the *Chandra* image nicely demonstrates that this molecular cloud is located in the foreground and absorbs the X-ray emission from CTB 109 coming from behind it. In the right panel we average the CO emission over a velocity range more negative than that of the CO arm. We can identify three small molecular clouds surrounding the eastern part of CTB 109's X-ray lobe, with the brightest to the Galactic east (on the left side of the lobe in Fig. 1, hereafter east), a fainter one to the Galactic north (above the lobe, hereafter north), and another one in the Galactic south (below the lobe, hereafter south), which is not fully covered by our observations. The noise level in the image is ~40 mK. Assuming that the progenitor star exploded at or close to the current position of the anomalous X-ray pulsar 1E 2259+586, the location of these clouds is suggestive of an interaction of the SNR shock wave with those molecular clouds, resulting in the X-ray lobe.

Most of the molecular clouds are rather faint in the ^{13}CO line, which is why we cannot perform a detailed comparison with the ^{12}CO measurements. However, we can estimate an average brightness ratio for each of the clouds (see Table 1). The value for the southern cloud is a bit difficult to interpret since it is not fully covered by our observations and it seems to consist of a number of small clouds. We find brightness ratios between 3.5 in the dense part of the CO arm and 13 in

the southern clouds. According to Langer & Penzias (1990), at the galactocentric radius of CTB 109 the ^{12}C to ^{13}C isotope ratio r should be about 63. This indicates that we miss some of the ^{12}CO emission and this line is optically thick.

In the following we assume local thermodynamic equilibrium and the same excitation temperature for both isotopic species and all molecules along the line of sight in each cloud. We determine an average optical depth for each cloud in both lines by the following procedure: We use the ^{12}CO to ^{13}CO ratio for each cloud to determine how much ^{12}CO emission we are missing by assuming the ^{13}CO line is optically thin. This can be translated to a first iteration for the optical depth τ_{12}. If both species have the same excitation temperature the ^{12}CO to ^{13}CO brightness temperature ratio r can be written as $r = (1 - e^{-\tau_{12}})/(1 - e^{-\tau_{13}})$. From this we determine a first iteration for the optical depth τ_{13} of the ^{13}CO line. This is again used to determine a better value for the missing ^{12}CO emission and so on. This iterative procedure converges usually after just a few iterations. The results for τ_{12} and τ_{13} are listed in Table 1. To integrate the ^{13}CO column density we actually use the ^{12}CO data scaled to ^{13}CO by the brightness ratios for each individual cloud since the signal-to-noise ratio is higher in our ^{12}CO data. The ^{13}CO column density is then scaled by 5×10^5 to determine the column density of the H_2 molecules N_{H_2} (Dickman 1978). We also estimate H_2 number densities and masses of the clouds (Table 1). While the northern cloud, the southern cloud, and the faint eastern tail of the eastern cloud have comparable H_2 column densities ($<10^{20}$ cm^{-2}), the bright part of the eastern cloud that overlaps the lobe has a higher $N_{H_2} \approx 1.9 \times 10^{20}$ cm^{-2}. It is interesting to note that we calculate a peak H_2 column density of 2.2×10^{21} cm^{-2} for the CO arm, which compares nicely with the value of 2.0×10^{21} cm^{-2} determined by Tatematsu et al. (1987).

In order to compare with these results, we extract spectra from the *Chandra* data in regions corresponding to the CO clouds and derive the atomic H column density N_H in the foreground by fitting the spectrum with a model including a thermal nonequilibrium ionization model and a foreground absorption. For the northern cloud, we obtain $N_H = 6.3$ (5.6–7.0) $\times 10^{21}$ cm^{-2} (90% confidence range in parentheses). For the larger eastern cloud, the foreground absorption of the part inside the lobe is $N_H = 4.5$ (4.2–4.9) $\times 10^{21}$ cm^{-2}, outside the lobe, we get $N_H = 5.9$ (5.5–6.4) $\times 10^{21}$ cm^{-2}, and in the eastern tail the foreground absorption is $N_H = 5.0$ (4.2–5.4) $\times 10^{21}$ cm^{-2}. Although the N_{H_2} column density is largest in the bright part of the eastern cloud, the foreground N_H is the lowest. Therefore, the eastern cloud is not located in front of the lobe. The foreground absorption in the region of the southern cloud is $N_H = 6.8$ (5.8–7.3) $\times 10^{21}$ cm^{-2}. The X-ray absorption is significantly higher in the regions corresponding to the northern cloud and the southern cloud than in the eastern tail of the eastern cloud. It seems that these two clouds are located in front of the remnant and absorb some of the X-ray emission.

As the SNR is believed to be located next to the GMC, we assume that both have a systematic velocity of -51 km s^{-1} (Tatematsu et al. 1987; Kothes et al. 2002). The three clouds (radial velocities between -52 and -57 km s^{-1}) are slightly blueshifted from the GMC to the west, indicating that these clouds are moving toward us relative to the GMC complex. As the bright eastern cloud seems to be related to the X-ray lobe, we study the velocity profiles of the ^{12}CO emission in different parts of the eastern cloud. This cloud contains the infrared (IR) source IRAS 23004+5841, which has IR colors of a star-forming region according to Wouterloot & Brand (1989). Figure 2 compares the profiles taken at the center of

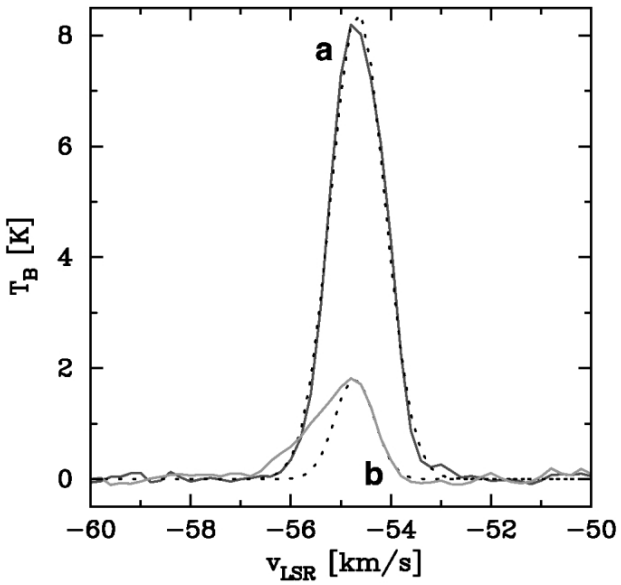

FIG. 2.—Velocity profile of the eastern CO cloud at the position of IRAS 23004+5841 (*a*) and in the lobe (*b*). Solid lines show the data, dotted lines the Gaussian fits. [*See the electronic edition of the Journal for a color version of this figure*.]

IRAS 23004+5841 (position *a*) and in the interior of the lobe (position *b*, as marked in the right panel of Fig. 1). While the first appears Gaussian, the latter has an additional component toward higher negative velocities. The asymmetry observed in the spectrum suggests that the material has been accelerated by the shock wave of the SNR that traveled into the cloud. The CO line profile is only broadened by a few kilometers per second, which indicates that the acceleration is mostly perpendicular to the line of sight.

The estimated mass of the part of the cloud with the high-velocity wing is 3–4 $M_\odot$. We have also taken profiles from parts of the east cloud that do not overlap with the lobe. The velocity profiles of the northern end of the east cloud and the faint tail in the east show that there is a velocity gradient. The center of the profile changes from -54.8 to -53.5 km s^{-1} with increasing distance to the lobe; i.e., the eastern part of the cloud is redshifted relative to the western part. This gradient indicates an acceleration of the gas in the faint tail away from the eastern cloud. As the gradient starts at the position of IRAS 23004+5841, it might be an outflow from the star-forming region.

3.2. *The Shocked Cloud*

The column densities of H_2 and the X-ray-absorbing hydrogen indicate that the northern cloud and the southern cloud are located in front of the X-ray emission. The eastern cloud, however, seems to be linked to the lobe. Moreover, the CO velocity profile shows an additional blueshifted component in the eastern cloud where it overlaps the lobe, suggesting that the cloud has been hit by a shock. The eastern tail of the eastern cloud does not show such an additional velocity component and seems to be redshifted relative to the interacting part of the cloud.

Figure 3 illustrates how the bright eastern CO cloud and the lobe are possibly located within the remnant. As in such a configuration the cloud would have a significant velocity component toward us at position *b* whereas the acceleration is directed perpendicular to the line of sight at position *a*, a high-

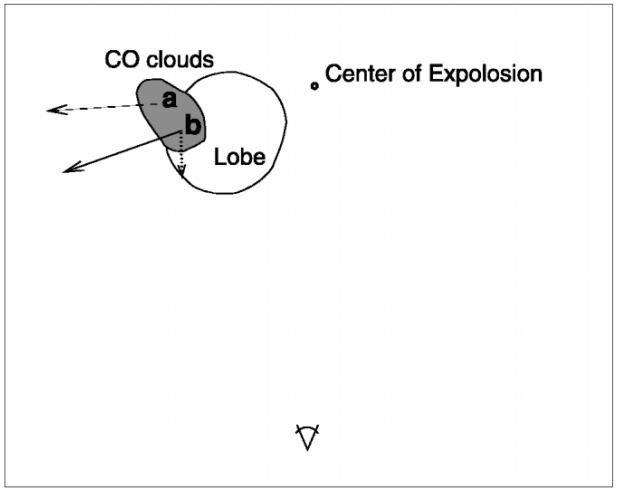

FIG. 3.—Schematic view of CTB 109 showing the lobe and the eastern cloud. The solid arrow shows the directions to which the part of the cloud at position *b* has been accelerated. The velocity component directed toward us is shown with a dotted line. As it is not certain how the cloud component at position *a* is moving in reality, the possible movement of position *a* is shown with a dashed arrow.

velocity wing in the velocity profile of the cloud is only observed at position *b*.

As we believe that the X-ray lobe was formed by evaporation of a cloud, we estimate the cloud mass from the X-ray emission. We assume that the emission is coming only from the lobe and that the evaporated cloud now fills a sphere with a radius of 3′. The XSPEC model VNEI that we use for the spectral fits gives the normalization $K = [10^{-14}/(4\pi D^2)] \int n_e n_{\rm H} dV$. The mean K per arcsec^2 in the lobe is 2.0×10^{-7} cm^{-5} arcsec^{-2}. For a distance $D = 3$ kpc (Kothes et al. 2002) and $n_e = 1.2 n_{\rm H}$, we get $n_{\rm H} = 0.9$ cm^{-3} and a mass of $M = 5\ M_\odot$ for the X-ray gas of the lobe. The mass of the observed CO clouds are higher than the estimated mass of the evaporated cloud. This could be the reason why the clouds still exist.

4. SUMMARY

We performed ^{12}CO and ^{13}CO observations, as well as a *Chandra* observation, of the region around the X-ray lobe of CTB 109. We have discovered three CO clouds around the lobe. All three clouds are blueshifted relative to the GMC in the west of CTB 109. The foreground $N_{\rm H}$ indicates that two clouds in the north and in the south of the lobe are located in front of the bright X-ray lobe, whereas the east cloud might be connected to the lobe. Therefore, the east CO cloud and the X-ray lobe seem to be evidence for an interaction between the SNR shock wave and a dense cloud. The velocity profiles of the ^{12}CO emission in the east cloud show that there is a velocity gradient in the faint tail in the east, indicating that the eastern part of the cloud is redshifted. The bright western part of the cloud overlaps with the X-ray lobe. The ^{12}CO velocity profile at this position has an negative velocity wing indicating an additional acceleration in this part of the cloud. At this position where the CO and the bright X-ray emission overlap, there is also an extended IR source (IRAS 23004+5841) that might be emission from a star-forming region. From the new CO and X-ray data we conclude that we have found strong evidence for a shock-cloud interaction at the northeast end of the X-ray lobe.

Support for this work was provided by the National Aeronautics and Space Administration through *Chandra* award G04-5068X issued by the *Chandra X-Ray Observatory* Center, which is operated by the Smithsonian Astrophysical Observatory for and on behalf of the National Aeronautics Space Administration under contract NAS8-03060. The Dominion Radio Astrophysical Observatory is a National Facility operated by the National Research Council of Canada. The Five College Radio Astronomy Observatory is supported by NSF grants AST 01-00793 and AST 02-28993.

REFERENCES

Bocchino, F., & Bykov, A. M. 2000, A&A, 362, L29
Cappellaro, E., Evans, R., & Turatto, M. 1999, A&A, 351, 459
Dickman, R. L. 1978, ApJS, 37, 407
Erickson, N. R., Grosslein, R. M., Erickson, R. B., & Weinreb, S. 1999, IEEE Trans. Microwave Theory Tech., 47, 2212
Gregory, P. C., & Fahlman, G. G. 1980, Nature, 287, 805
Hughes, V. A., Harten, R. H., & van den Bergh, S. 1981, ApJ, 246, L127
Kawasaki, M. T., Ozaki, M., Nagase, F., Masai, K., Ishida, M., & Petre, R. 2002, ApJ, 572, 897
Kothes, R., Uyaniker, B., & Yar, A. 2002, ApJ, 576, 169
Kutner, M. L., & Ulich, B. L. 1981, ApJ, 250, 341
Langer, W. D., & Penzias, A. A. 1990, ApJ, 357, 477
Reach, W. T., & Rho, J. 2000, ApJ, 544, 843
Sasaki, M., Plucinsky, P. P., Gaetz, T. J., Smith, R. K., Edgar, R. J., & Slane, P. O. 2004, ApJ, 617, 322
Seta, M., et al. 1998, ApJ, 505, 286
Tatematsu, K., Fukui, Y., Nakano, M., Kogure, T., Ogawa, H., & Kawabata, K. 1987, A&A, 184, 279
Wouterloot, J. G. A., & Brand, J. 1989, A&AS, 80, 149
Yusef-Zadeh, F., Wardle, M., Rho, J., & Sakano, M. 2003, ApJ, 585, 319

A&A 552, A45 (2013)
DOI: 10.1051/0004-6361/201220836

Astronomy & Astrophysics

Chandra observation of the Galactic supernova remnant CTB 109 (G109.1–1.0)

M. Sasaki[1], P. P. Plucinsky[2], T. J. Gaetz[2], and F. Bocchino[3]

[1] Institut für Astronomie und Astrophysik, Universität Tübingen, Sand 1, 72076 Tübingen, Germany
e-mail: sasaki@astro.uni-tuebingen.de
[2] Harvard-Smithsonian Center for Astrophysics, 60 Garden Street, Cambridge, MA 02138, USA
[3] INAF – Osservatorio Astronomico di Palermo, Piazza del Parlamento 1, 90134 Palermo, Italy

Received 3 December 2012 / Accepted 4 February 2013

ABSTRACT

Context. We study the X-ray emission of the Galactic supernova remnant (SNR) CTB 109 (G109.1−1.0), which is well-known for its enigmatic half-shell morphology both in radio and in X-rays and is associated with the anomalous X-ray pulsar (AXP) 1E 2259+586.
Aims. We want to understand the origin of the X-ray bright feature inside the SNR called the Lobe and the details of the interaction of the SNR shock wave with the ambient interstellar medium (ISM).
Methods. The Lobe and the northeastern part of the SNR were observed with *Chandra* ACIS-I. We analysed the spectrum of the X-ray emission by dividing the entire observed emission into small regions. The X-ray emission is best reproduced with one-component or two-component non-equilibrium ionisation models depending on the position. In the two-component model, one emission component represents the shocked ISM and the other the shocked ejecta.
Results. We detect enhanced element abundances, in particular for Si and Fe, in and around the Lobe. There is one particular region next to the Lobe with a high Si abundance of 3.3 (2.6–4.0) times the solar value. This is the first, unequivocal detection of ejecta in CTB 109.
Conclusions. The new *Chandra* data confirm that the Lobe was created by the interaction of the SNR shock and the supernova ejecta with a dense and inhomogeneous medium in the environment of SNR CTB 109. The newly calculated age of the SNR is $t \approx 1.4 \times 10^4$ yr.

Key words. shock waves – ISM: supernova remnants – X-rays: ISM – X-rays: individuals: SNR CTB 109

1. Introduction

The Galactic supernova remnant CTB 109 (G109.1−1.0) is the host of the anomalous X-ray pulsar (AXP) 1E 2259+586 (Fahlman & Gregory 1981) and represents one of the most exotic and interesting objects in the X-ray sky. The study of an SNR associated with an AXP provides valuable information on the environment in which it formed and an independent estimate of the age of the objects. Given that there are only three firm associations of SNRs with AXPs (Mereghetti 2008), detailed studies of each association will produce progress in our understanding not only of SNRs but also of the AXPs.

The SNR CTB 109 has a spectacular semi-circular morphology in both the X-ray and the radio. At a distance of 3.2 ± 0.2 kpc (Kothes & Foster 2012), it is located next to a giant molecular cloud (GMC) complex and is one of the most striking examples of an interaction of an SNR with a molecular cloud. Since there is neither X-ray (see Fig. 1 in Sasaki et al. 2004) nor radio emission (Hughes et al. 1981) where the western part of the shell would be expected, the semi-circular morphology of CTB 109 implies that the shock has been greatly impeded or even stopped entirely by the GMC complex in the west. A linear feature in CO ("CO arm") extends from the GMC complex to the local X-ray minimum in the northern half of the SNR (Tatematsu et al. 1987). Therefore, at least a part of the GMC complex extends in front of the remnant. CTB 109 has an X-ray bright interior region known as the "Lobe". The Lobe is brighter than any part of the shell. Although it has been suggested that this feature is a jet associated with the AXP 1E 2259+586 (Gregory & Fahlman 1983), high-resolution images from ROSAT HRI (Hurford & Fesen 1995), *Chandra* (Patel et al. 2001), as well as *XMM-Newton* (Sasaki et al. 2004), show no morphological connection with the pulsar. Furthermore, the X-ray spectrum from the Lobe obtained with *XMM-Newton* is completely thermal (Sasaki et al. 2004).

We believed that the bright X-ray emission is the result of the interaction between the SNR shock and a molecular cloud complex and therefore performed an observation with the *Chandra* X-ray Observatory (Weisskopf et al. 2002) using the Advanced CCD Imaging Spectrometer (ACIS, Garmire et al. 2003) in order to study this interaction region in more detail. The first analysis of the high resolution data obtained with ACIS-I in combination with new high resolution CO data from the Five College Radio Observatory has revealed regions with signs of interaction between the SNR shock and CO clouds (Sasaki et al. 2006). In this paper we present the results of the spectral analysis of the entire northeastern part of the SNR, which was observed with ACIS-I.

2. *Chandra* data

We observed the northeast part of the SNR in an 80 ksec pointing of *Chandra* with ACIS-I as the prime instrument (ObsID 4626). The Lobe and the northeastern part of the remant shell were completely covered by the ACIS-I array (Fig. 1). The data were analysed with CIAO 4.4. and CALDB 4.4.8.

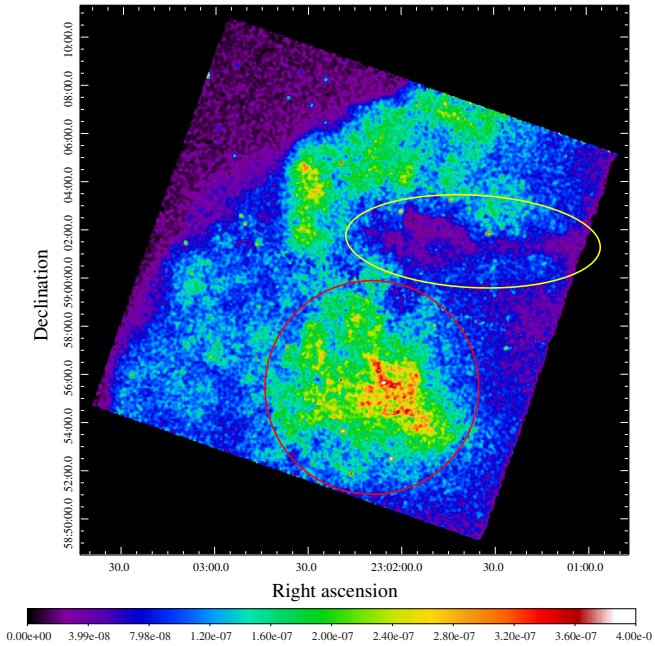

Fig. 1. Exposure-corrected *Chandra* ACIS-I intensity map (0.35−8.0 keV). The big red circle indicates the position of the Lobe, the yellow ellipse that of the CO arm.

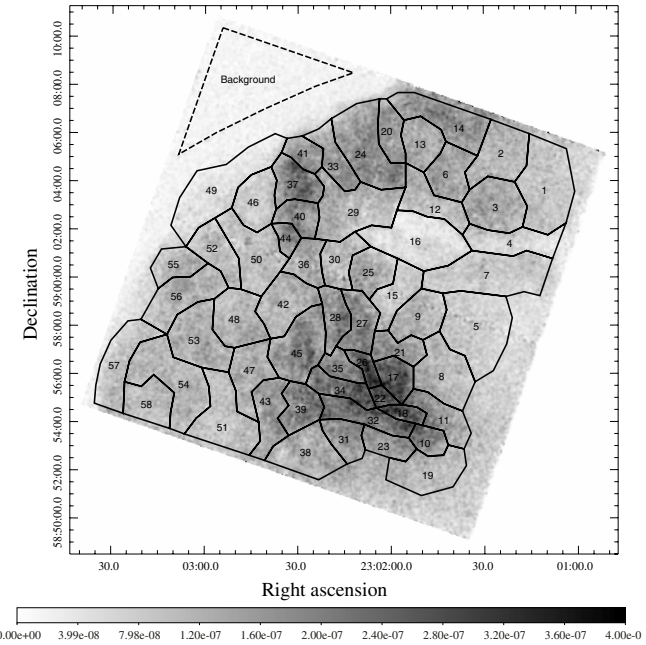

Fig. 3. Extracted regions overlaid on the intensity map. Point sources are removed.

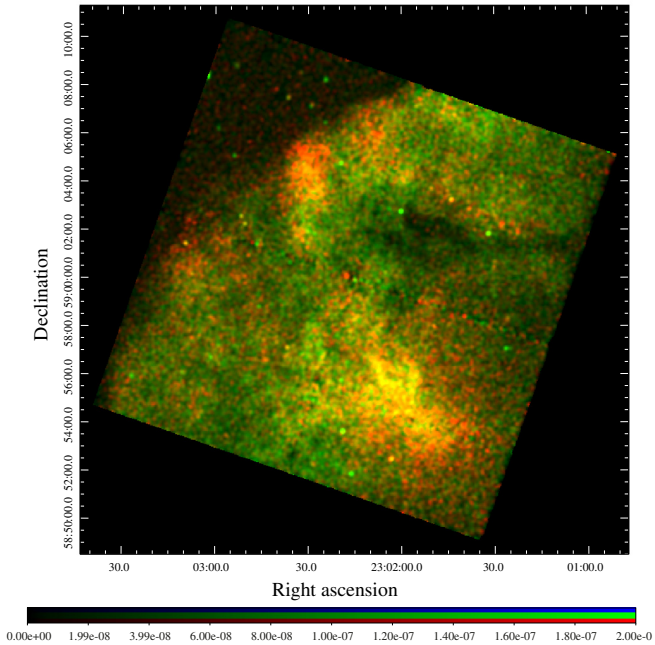

Fig. 2. Two-colour image with red (0.35−0.8 keV) and green (1.0−8.0 keV).

2.1. Images

Figure 1 shows the exposure-corrected intensity map of the ACIS-I data (0.35−8.0 keV). The events were binned with a bin size of 4 pixels and the image has been smoothed with a Gaussian kernel of 3 and 4 pixels in Figs. 1 and 2 (see below), respectively.

Compared to the *XMM-Newton* image (Sasaki et al. 2004), the *Chandra* image reveals more point sources. Also, structures in the dark region absorbed by the CO arm, as well as filamentary structures in the Lobe, are resolved. The two-colour image (Fig. 2), in which the soft band (0.35−0.8 keV) is presented in red and the hard band (1.0−8.0 keV) in green, shows colour variations in the Lobe. There is a bright yellow structure in the central part of the Lobe, while the outer diffuser parts are green (harder) in the east and red (softer) in the west. The two-colour image shows spectral variations that are either intrinsic or due to absorption or perhaps a combination of the two. The diffuse emission in the CO arm appears to have harder spectra consistent with higher absorption. A detailed spectral analysis would possibly distinguish between intrinsic spectral variations and variable absorption.

For further analysis, we divided the diffuse emission of the SNR into small regions with similar surface brightness and X-ray colour, and extract spectra for each region. To study the spectra of only the diffuse emission, we first performed source detection on the whole data (`wavdetect`) and excluded all detected point and point-like sources in each region. The regions used are shown in Fig. 3. The number of counts in the regions varies from ∼4000−20 000 cts. The spectra are binned with a minimum of 20 counts per bin so that Gaussian statistics may be assumed in the fitting.

2.2. Spectral analysis

We analysed the spectra using the X-ray spectral fitting package XSPEC Ver. 12.7.1. The analysis of *XMM-Newton* data showed that the emission from CTB 109 is thermal with no indication of nonthermal emission (Sasaki et al. 2004). Furthermore, the thermal emission suggests that the plasma is not in collisional ionisation equilibrium (CIE). Therefore, we fitted the extracted ACIS-I spectra with non-equilibrium ionisation (NEI) models. The foreground absorbing column density $N_{\rm H}$ was modeled using `TBABS` (Wilms et al. 2000). We used abundances relative to solar values reported by Wilms et al. (2000).

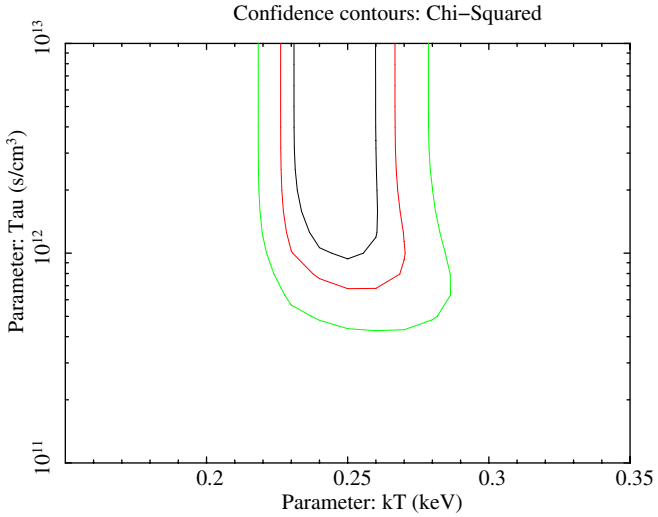

Fig. 4. Contour diagram of the parameters kT and τ for the fit with one VNEI model of region 49. The contours correspond to confidence levels of 60%, 90%, and 99%.

2.2.1. One-component NEI model

First, we fitted all spectra assuming one VNEI component, similar to what was used to analyse the *XMM-Newton* data (Sasaki et al. 2004). Initially, the abundances were all fixed to solar values. In regions 49 and 57, which correspond to the outer shock, we get relatively good fits with $N_{\rm H}$ = 9.6(8.8–10.5)[1] × 10^{21} cm^{-2}, 1.2(1.1–1.3) × 10^{22} cm^{-2}, kT = 0.25 (0.22–0.27) keV, 0.25 (0.23–0.26) keV, and $n_{\rm e}t$ > 7.2 × 10^{11} s cm^{-3}, > 2.3 × 10^{10} s cm^{-3}, with reduced χ^2 = 1.4 for 107 and 99 degrees of freedom for regions 49 and 57, respectively (see Fig. 4). The best fit values for the ionisation timescale are $n_{\rm e}t$ = 4.9 × 10^{13} s cm^{-3} and 2.1 × 10^{13} s cm^{-3} indicating CIE in these regions.

We also freed the abundances, but the one-component description of the data is not satisfactory in about 25% of the regions with reduced χ^2 > 1.5, ranging up to reduced χ^2 = 2.0 (see Fig. 5, upper left diagram).

2.2.2. Two-component NEI model

Therefore, in the next step we assumed two thermal VNEI components: 1) to model the emission of the shocked ISM and 2) to verify the existence of emission from shocked ejecta. This two-component model improves the fits in a number of regions (see below), especially in region 39, which had a reduced χ^2 = 2.0 (103 degrees of freedom) for the one-component VNEI model and can be fitted with a reduced χ^2 = 1.1 (100 degrees of freedom) with a two-component VNEI model (Fig. 5, left panels).

For the ISM component, we use kT_1 = 0.25 keV and $n_{\rm e}t_1$ = 1 × 10^{12} s cm^{-3} as starting values, representing the best fit parameters of the single-component VNEI model for regions 49 and 57. All abundances of this component were fixed to solar values. The second component, which was introduced to model the ejecta emission, was fitted with variable abundances for elements showing strong emission lines. The fits required a higher temperature of kT_2 ≈ 0.6 keV. The ejecta component with the higher temperature dominates the spectrum for energies higher than ∼1 keV in most of the spectra (see Fig. 5, middle panels). The abundances of Mg, Si, S, for which emission lines are visible in the spectra, as well as Fe, were freed for the second (ejecta) model component and fitted. In some regions, higher abundances are found for Si and Fe in particular (see Fig. 5, right panels).

2.2.3. F-test

To verify how much the fits improve by including a second VNEI component, we performed an F-test for the one-component VNEI and two-component VNEI models for all regions. In 27 out of 58 regions, the two models differ with probabilities higher than 99.9%. In order to visualise the variations of the spectral properties, we created a map of the spectral parameters by filling each region with the corresponding parameter value. In the top row of Fig. 6 we show the distribution of the temperature parameter kT of the one-component VNEI model for regions in which the F-test indicated no necessity of an additional component (left) and the distributions of kT_1 (ISM) and kT_2 (ejecta) of the two-component VNEI model (middle and right, respectively). Regions in which the F-test confirmed an improvement of the fits after including the second VNEI component are marked with white crosses. The middle and bottom rows in Fig. 6 show the same for the ionisation timescales τ (left) and τ_2 (right) and the foreground column densities $N_{\rm H}$ for the one-component (left) and two-component (right) fits.

3. Discussion

The analysis of the *Chandra* ACIS spectra of the northeastern part of the SNR CTB 109, divided into small regions, has shown that the spectra can be well fitted by a one-component VNEI model in many regions. However, in 50% of the regions a two-component model consisting of two thermal VNEI models with two different temperatures improves the fit significantly. In this model, the first component is used to describe the emission from the shocked ISM, while the second component reproduces the emission from the ejecta. Therefore, we believe that there are at least two emission components in all regions. In cases in which the one-component model yields a sufficiently good fit, the temperature and the ionisation timescale most likely tend towards values of the component of the multi-temperature spectrum that dominates the emission. We base our discussion on the results obtained with the two-component spectral fits for all regions. The diagrams in Fig. 7 show the relations between some parameters derived from the fits (see following subsections for further discussion).

The temperature of the ISM component (Fig. 6, upper middle) is comparable in all regions and is low (∼0.1–0.3 keV), while the temperature of the ejecta component is higher (∼0.4–0.9 keV, Fig. 6, upper right). The ionisation timescale of the ejecta component is τ_2 = 10^{11-12} s cm^{-3} (Fig. 6, middle right panel) except for regions at and around the CO arm, in which τ_2 tends to be higher. The higher values for τ_2 in the CO arm regions indicate a higher density as we can assume that these regions have been shocked at a similar time to the rest of the remnant.

The $N_{\rm H}$ images (Fig. 6, lower panels) show that the foreground absorption is high near the CO arm ($N_{\rm H}$ > 1.1 × 10^{22} cm^{-2}). Around and, in particular, west of the Lobe, the foreground absorption is lower ($N_{\rm H}$ < 1.0 × 10^{22} cm^{-2}), while it seems to be higher southeast of the Lobe.

[1] All errors in this paper are 90% confidence errors.

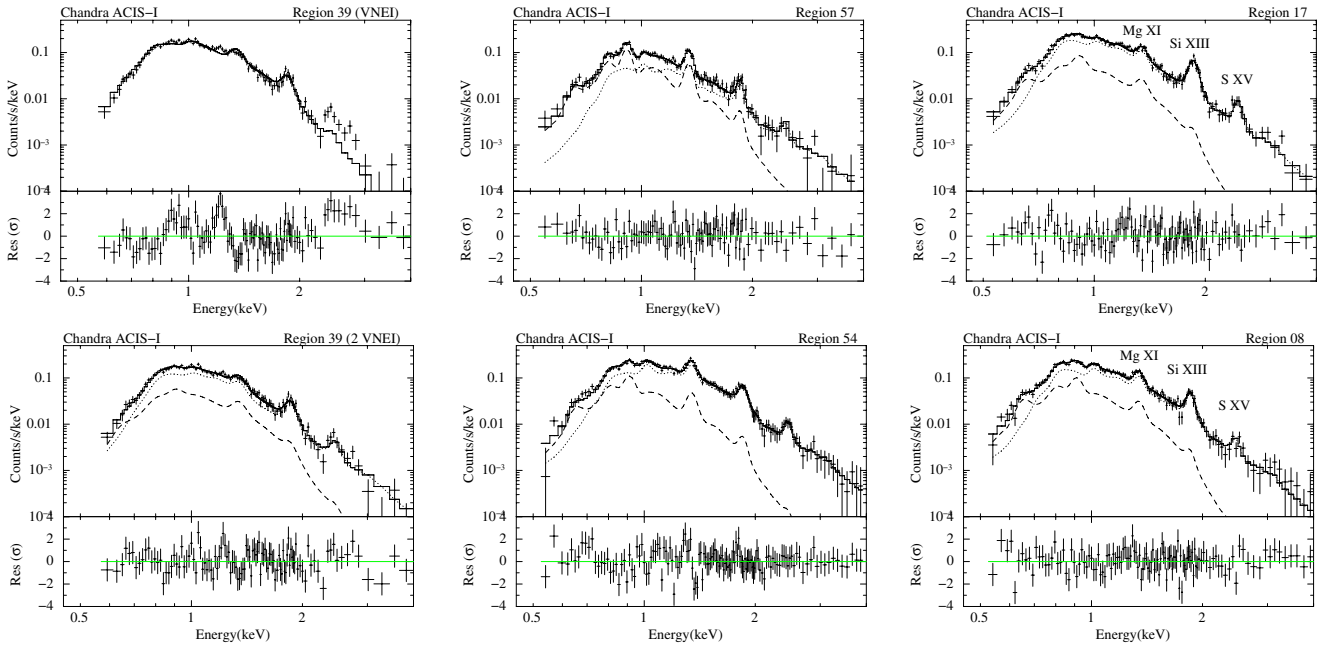

Fig. 5. *Left*: *Chandra* ACIS-I spectrum of an interior region 39 with the best fit single-component `VNEI` model (*upper diagram*, reduced $\chi^2 = 2.0$ for 103 degrees of freedom) and two-component model (*lower diagram*, reduced $\chi^2 = 1.1$ for 100 degrees of freedom). *Middle*: spectrum of the outermost region 57 in the east (*upper*) and an interior region 54 (*lower*) with the best fit 2 `VNEI` model. The relative flux of the ejecta component (dotted) with respect to the ISM component (dashed) in region 57 is lower than in most other regions. *Right*: spectrum of region 17 with enhanced Si XIII emission (*upper diagram*). The Mg XI, Si XIII, and S XV triplets are marked. For comparison, the spectrum of region 08, which is the brightest region in the Lobe next to region 17, is shown (*lower diagram*). The best fit 2 `VNEI` model is additionally plotted in the diagrams.

3.1. Filling factors and ejecta mass

CTB 109 is an evolved SNR in the Sedov phase. In such a remnant, which also shows interactions with denser molecular clouds, we can assume that the reverse shock has already propagated to the centre and thus heated most or all of the ejecta. The spectral model provides us with the normalisation parameter

$$norm_{1,2} = \frac{10^{-14}}{4\pi D^2} \times \int n_{1,2}\, n_{\mathrm{e}\ 1,2}\, f_{1,2}\, \mathrm{d}V, \quad (1)$$

with f_1 and f_2 being the filling factors of the ISM and ejecta components, respectively ($f_1 + f_2 = 1$). For the distance to the SNR, we use $D = 3.0 \pm 0.5$ kpc as estimated by Kothes et al. (2002) and confirmed by Kothes & Foster (2012, 3.2 ± 0.2 kpc). To calculate the filling factor for the ejecta component f_2 we assume pressure equilibrium between the two thermal components. Applying momentum conservation for the shock propagating through these components, we get

$$f_2 = \left(\frac{norm_1\, T_1^2}{norm_2\, T_2^2} + 1 \right)^{-1} \quad (2)$$

(see Bocchino et al. 1999).

The resulting parameter map for the filling factor of the ejecta component of the two-component `VNEI` fits is shown in Fig. 8 for all regions. We indeed see a trend in the parameter value distribution map in Fig. 8, in which the inner (western) regions tend to have higher f_2 values than the outer regions.

We can estimate the total ejected mass using the filling factor f_2 and the density n_2 derived for the ejecta component from Eq. (1). We assume that the SNR is a half sphere with a radius of $18\farcm5 \pm 1\farcm0$ as determined from the *XMM-Newton* EPIC images by Sasaki et al. (2004). For $D = 3.0 \pm 0.5$ kpc, $R = 16 \pm 3$ pc $= 5.0 \pm 0.8 \times 10^{19}$ cm. Since we have performed spectral analysis using a model with two thermal components only in regions that have been observed with *Chandra* ACIS-I, we use the median values of f_2 and n_2 from the two-component fits to estimate the total mass of the ejecta. With $f_{2,\mathrm{median}} = 0.44$ and $n_{2,\mathrm{median}} = 0.62$ cm^{-2}, the total ejecta mass under the assumption of a half sphere as seen, e.g., in the *XMM-Newton* mosaic image, is $M_{\mathrm{ejecta}} = 60\ M_\odot$. The density n_2 in the regions observed with *Chandra* varies from 0.23 to 0.81 cm^{-2}, while the filling factor f_2 has values between 0.29 and 0.91. Therefore, these estimates have uncertainties of ~50%, whereas the volume may also have an uncertainty of the same order since the X-ray emitting hot gas might not fill the entire volume applied for the estimate. In addition the ejecta might be clumped and thus not uniformly distributed in the assumed volume. If we suppose that the ejecta only fills 30% of the volume, the ejecta mass will be as low as $M_{\mathrm{ejecta}} = 20\ M_\odot$. Therefore, one should keep in mind that M_{ejecta} is a very crude estimate. However, even the lower limit of $M_{\mathrm{ejecta}} = 20\ M_\odot$ would rule out a Type Ia supernova as the origin of CTB 109.

3.2. Pressure

In the $norm_{1,2}/A$-$kT_{1,2}$ diagrams in Fig. 7 (upper two diagrams) we have plotted lines of constant pressure with $p/k = 10^6$ cm^{-3} K (blue) and 10^7 cm^{-3} K (green) for different values of filling factors and depths of the emitting volume in the SNR. These lines were calculated from the best fit parameters assuming pressure equilibrium between the ISM and ejecta components. All the data points are consistent with a thermal pressure of $p/k \approx 10^7$ cm^{-3} K, corresponding to 1.4×10^{-13} dyne cm^{-2}. The scatter is mainly due to the different filling factors and the uncertainties in the size of the emitting volume along the line of sight.

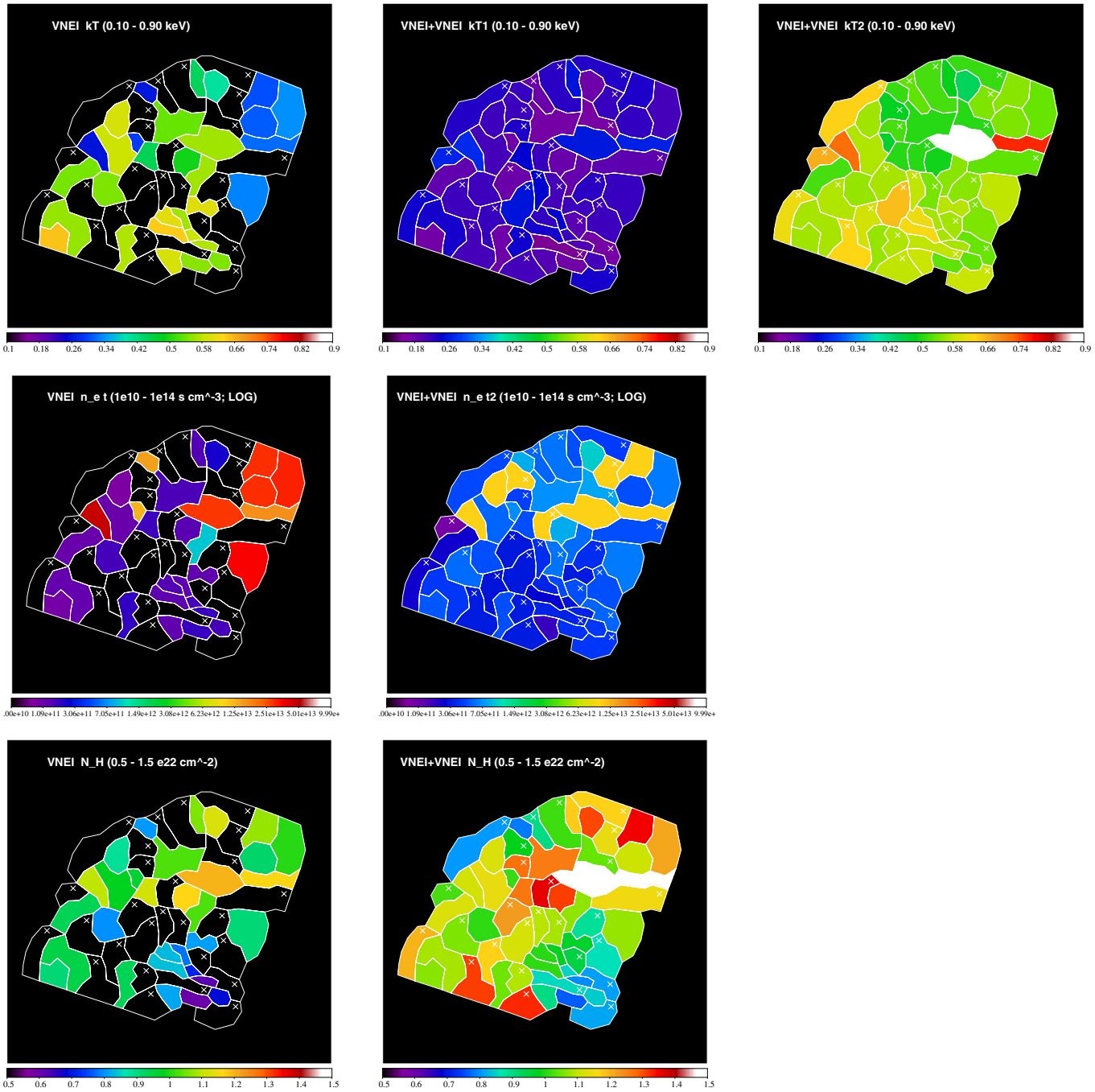

Fig. 6. *Top*: best fit temperature parameters for the one-component `VNEI` model (kT) in regions in which the F-test indicated that the one-component model fits the spectrum sufficiently well (*left*) and temperature parameters kT_1 and kT_2 for the two-component fits for all regions (*middle and right*, respectively). *Middle*: best fit values for the ionisation timescale τ for the one-component `VNEI` model (*left*) and the ionisation timescale τ_2 for the dominating ejecta component for the two-component fits (*right*). *Bottom*: best fit values for the foreground $N_{\rm H}$ for the one-component `VNEI` model (*left*) and for the two-component fits (*right*). The crosses mark the regions in which the F-test indicated that the two-`VNEI` component model yields a better fit (see Sect. 2.2.3).

3.3. Age estimate

In the τ_2-$norm_2/A$ plot in Fig. 7 (lower diagram), we plot the ionisation timescale τ_2 of the ejecta component versus the normalisation $norm_2$ per area A of each region.

To study the dependence of the X-ray surface brightness, measured as the normalisation parameter per area $norm_2/A$, and the ionisation timescale τ_2, we can replace $n_{\rm e}$ by τ/t in Eq. (1). We then get $norm_2/A$ as a function of τ for a given t. The value of $norm_2$ depends on the emitting volume, thus on the depth of the volume along the line of sight for each region. Assuming that the AXP is located at the centre of the circle corresponding to the SNR shell, we calculated the minimum and maximum distances from the AXP for each region. The calculated isochrones for different t values are also shown in the τ_2-$norm_2/A$ plot. The two lines for each time t show the possible ranges for the depth of

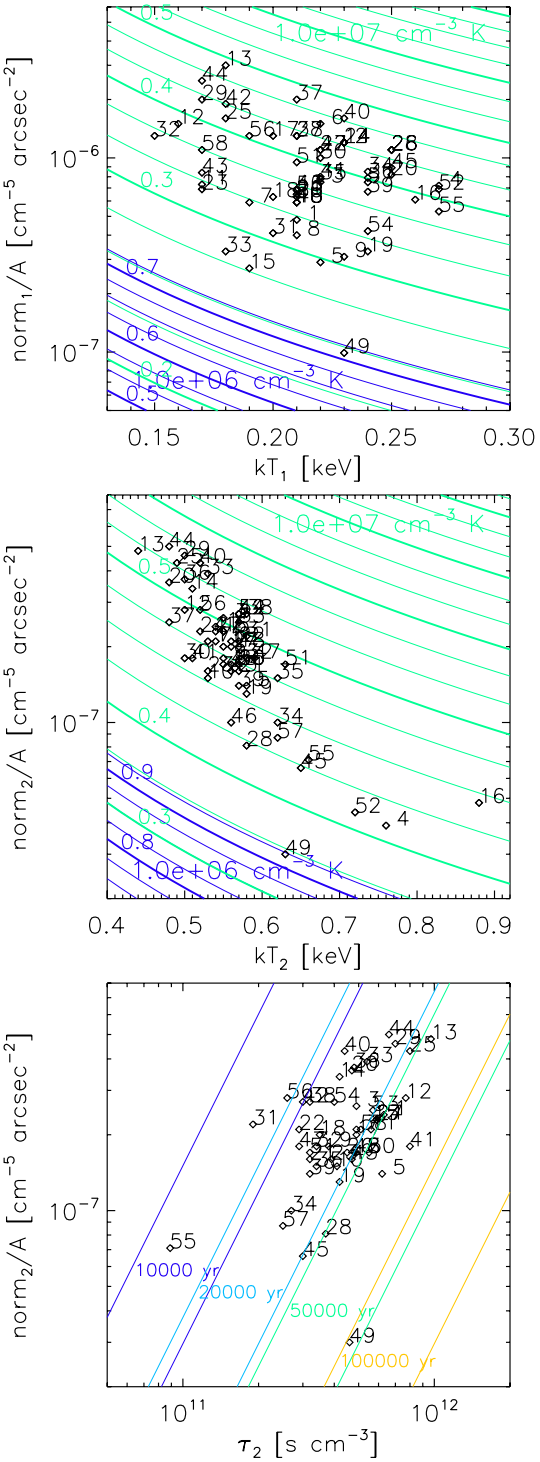

Fig. 7. Distribution of the parameter values for the fit with two `VNEI` components. The labels of the data points are region numbers. The lines in the diagrams for surface brightness $norm_{1,2}/A$ against temperature $kT_{1,2}$ (*upper and middle panels*) show the isobars for $p/k = 10^6$ cm^{-3} K (blue) and 10^7 cm^{-3} K (green) for different values of the filling factors in the remnant and the size of the emitting volume along the line of sight. The line for each filling factor with the lowest $norm_{1,2}/A$ are marked with a thicker line and labelled with the $f_{1,2}$ value. The lines in the diagram showing the surface brightness as $norm_2/A$ against the ionisation timescale τ_2 (*bottom panel*) are isochrones for $t = 10\,000$, 20 000, 50 000, and 100 000 yr. A range for all isochrones is shown for each t covering the range of variation in the depth of the emitting volume.

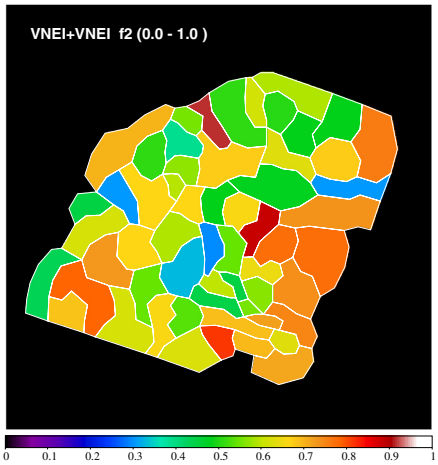

Fig. 8. Distribution of the filling factor for the ejecta component f_2 derived from the fits with the two-component `VNEI` model.

the remnant. This diagram indicates that the age of the shocked plasma, derived from the ejecta component (2) is $\sim 2 \times 10^4$ yr.

The fits have shown that the temperature of the ISM component (1) is between 0.1 keV and 0.3 keV. For the outer regions 49 and 57, the single component `VNEI` fit yields $kT = 0.25$ keV (Sect. 2.2.1). The high and not well-constrained values of the ionisation timescale τ in the single-component fits, as well as the τ_1 in the two-component fits, suggest that the plasma of the shocked ISM is close to CIE. If we assume that this temperature is more or less representative of the shocked plasma, the blast wave velocity is

$$v = \sqrt{\frac{16kT_1}{3\bar{m}}}, \tag{3}$$

with a mean mass per free particle for a fully ionised plasma of $\bar{m} = 0.61\ m_{\rm p}$. For a temperature of $kT_1 = 0.25 \pm 0.03$ keV, we get $v = 460 \pm 30$ km s^{-1}. The radius is $R = 5.0 \pm 0.8 \times 10^{19}$ cm (Sasaki et al. 2004). Using the Sedov similarity solution (Sedov 1959; Taylor 1950; von Neumann 1947), the age of the remnant can be estimated as

$$t = \frac{2R}{5v}. \tag{4}$$

We thus obtain $t = (14 \pm 2) \times 10^3$ yr from the ISM component, which is a little higher than the value obtained from the *XMM-Newton* data (Sasaki et al. 2004) for which we only assumed one spectral component. Interestingly, this new value for the age of the SNR is in agreement with the age estimate obtained from the fits of the ejecta component.

3.4. Ejecta

As can be seen in the Si-abundance and Fe-abundance distribution images in Fig. 9, the abundances measured for the ejecta emission are all comparable to or lower than solar values, except for the Lobe. While the Ne, Mg, and S abundances seem to agree with those of the other elements, Si and Fe abundances are higher, especially in and around the Lobe. The enhanced abundances in the Lobe suggest that its emission has a contribution from an ejecta clump or a conglomeration of ejecta clumps and shocked clouds. There is one particular region (region 17) with significantly enhanced Si abundance within the Lobe (3.3 [2.6−4.0], see Figs. 9b, c). The spectrum of region 17

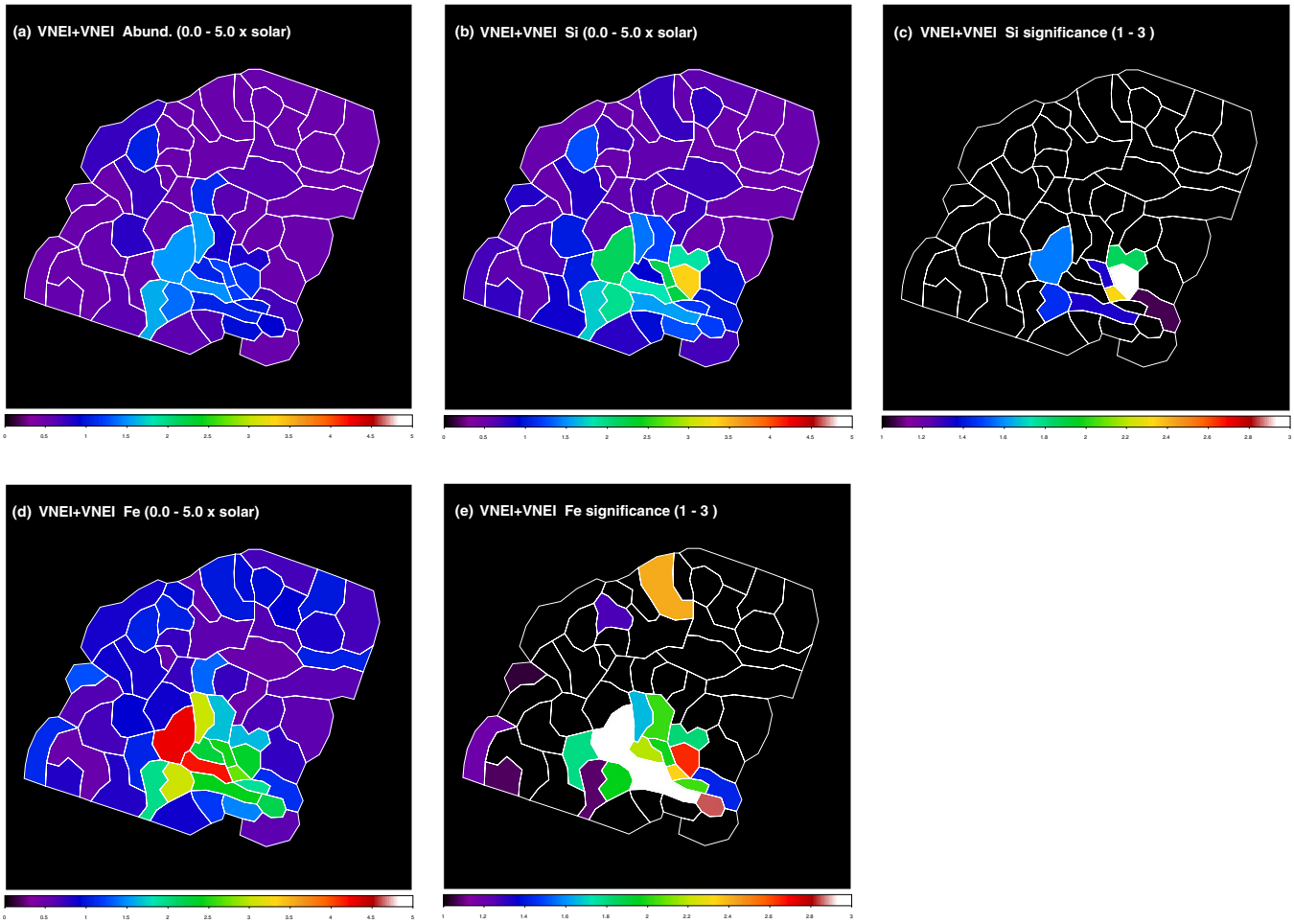

Fig. 9. Best fit abundances assuming a thermal model consisting of two `VNEI` components. The shown parameters are: abundances for elements other than Si, S, and Fe fitted for the ejecta emission **a)**, Si abundance fitted for the ejecta emission **b)** and its significance calculated as (abundance of the Si – abundance of the other elements)/error of the abundance of Si **c)**, Fe abundance and its significance (**d)** and **e)**, respectively).

is shown together with that of an adjacent region with lower Si abundance in Fig. 5 (right panels).

Another possible process that can cause enhanced emission for particular elements in thermal plasma is charge exchange. However, to produce charge exchange emission there must be a phase of cold neutral gas next to or inside the hot X-ray emitting plasma. CO data show no emission at the position of the Lobe or west of it, where the Si abundance enhancement is observed in X-rays (Sasaki et al. 2006). For a mature SNR like CTB 109 we can assume that the reverse shock has propagated all the way through the SNR and, therefore, there should be no unionised gas in the interior of CTB 109. Furtheremore, if the enhanced emission of Si is due to charge exchange, one would expect even higher indication of charge exchange for O or Ne for solar or cosmic abundances. Since no emission enhancement is observed for these lower Z elements, we can rule out that the enhanced emission of particular elements is caused by charge exchange.

The detection of ejecta emission is also very important for the study of the AXP 1E 2259+586, as it will give information on its progenitor. Together with soft gamma-ray repeaters (SGRs) and the sub-class of rotation-powered high-magnetic field pulsars, the AXPs are believed to form a class of neutron stars with extremely high magnetic fields. So far, there are only a few confirmed associations between SNRs and high-magnetic field neutron stars[2]: SNR G292.2−0.5 and the pulsar J1119−6127, SNR Kes 75 and the pulsar J1846−0258, SNR Kes 73 and AXP 1E 1841−045, SNR CTB 109 and AXP 1E 2259+586, SNR G327.2−0.1 and AXP 1E 1547.0−5408, SNR G337.0−0.1 and SGR 1627−41, SNR G042.8+00.6 and SGR 1900+14, and SNR N 49 and SGR 0526−66 in the LMC. Recently, Park et al. (2012) detected ejecta emission in a deep observation of the SNR N 49 with *Chandra* (120 ks exposure). However, the element abundance ratio derived from the emission seems to be more consistent with a Type Ia supernova, which would rule out the association between the SNR and the SGR, and requires further investigation. Lopez et al. (2011) measured enhanced abundances of Mg, Si, and S in SNR Kes 73 associated with the AXP 1E 1841−045, whereas Safi-Harb & Kumar (2012) reported on possible abundance enhancement in the X-ray spectra of SNR G292.2−0.5 and SNR Kes 73.

Ejecta emission is also detected in other middle-aged remnants, e.g., in the Galactic SNR G349.7+0.2 (Lazendic et al. 2005), which is interacting with a molecular cloud, or SNRs in the Large Magellanic Cloud (LMC) 0548−70.4, 0534−69.9 (Hendrick et al. 2003), and N49B (Park et al. 2003). Clumping of ejecta seems to be common in core-collapse SNRs. Ejecta

[2] http://www.physics.umanitoba.ca/snr/SNRcat/

clumps have also been found in evolved SNRs like the Vela, both in the interior (Miceli et al. 2008) and outside the main shell (Aschenbach et al. 1995). Kifonidis et al. (2003) have shown in two-dimensional simulations that macroscopic mixing occurs in core-collapse supernova explosions forming clumps of metals. Rayleigh-Taylor instabilities grow in the layers of metals during the expansion, and these layers fragmentate into ejecta clumps.

We created narrow band images for the elements Mg and Si, as prominent emission lines of these elements are visible in the spectra of some regions (Sect. 2.2). The continuum emission has been subtracted from the line emission. Figure 10 shows a three-colour image with red for the soft band *XMM-Newton* image (0.3−0.9 keV) presented by Sasaki et al. (2004), green for Mg emission ([1.25−1.45 keV band] – surrounding continuum), and blue for Si emission ([1.7−2.1 keV band] – continuum). There is one small region bright in Si emission, covered by the extraction region 17 with enhanced Si line emission (see Sect. 2.2). The Mg emission is distributed broadly; soft emission is bright in the Lobe and the small region in the northeast shell (region 41), which has a relatively low foreground absorption of $N_{\rm H} = 0.80\ (0.70{-}0.94) \times 10^{22}$ cm^{-2}.

Kaplan et al. (2009) measured the proper motions of the AXP 1E 2259+586 using *Chandra* ACIS-S observations in 2000 and 2006 pointed at the AXP. The suggested initial position at which the supernova occured and the AXP was born is north of the AXP and might even have been in the area coinciding with the CO arm, depending on the real age of the SNR. On the other hand, new near-infrared observations of the counterpart of the AXP with the Keck II telescope using laser guide star adaptive optics have been performed to measure the proper motion of the AXP. These data indicate that the initial position of the AXP was closer to the position of X-ray Lobe, approximately half way between today's position of the AXP and the Si clump seen in blue in Fig. 10 (Tendulkar et al., in prep.). Both results show that the position of the initial supernova explosion was located west to northwest of the Lobe and suggest that the interaction of the blast wave with a dense molecular cloud produced the X-ray Lobe and, at the same time, caused the formation of the reverse shock, which then ran into ejecta enhanced in Si or Fe. However, one has to keep in mind that the alignment of the Si enhanced region and the Lobe might well be a projection effect.

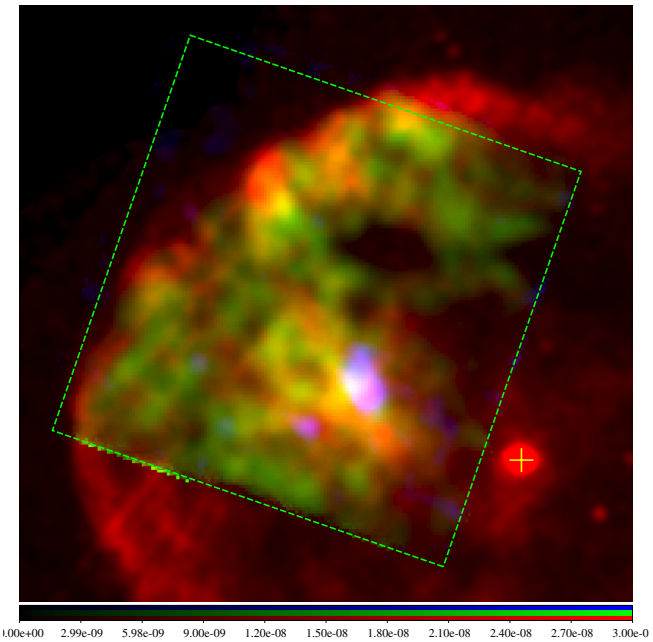

Fig. 10. Three-colour image consisting of a red image for the soft band *XMM-Newton* image (0.3−0.9 keV, Sasaki et al. 2004), a green image for Mg (1.25−1.45 keV) – continuum, and a blue image for Si (1.7−2.1 keV) – continuum. The Mg and Si images were created from the *Chandra* data. The green dashed box indicates the field of view of the *Chandra* ACIS-I. The yellow cross indicates the present position of the AXP 1E 2259+586.

4. Conclusions

Through the analysis of the deep high-resolution data of the Lobe and the northeastern part of the SNR CTB 109 taken with *Chandra* ACIS-I, we confirm ejecta emission inside the remnant. There is an enhancement in element abundances especially in the X-ray bright Lobe. We have thus unambiguously detected ejecta emission from an SNR associated with an AXP. The ISM and ejecta emission indicate an age of ∼10−20 kyr for the shocked X-ray emitting plasma.

As one can see in the *XMM-Newton* intensity image (Fig. 1, Sasaki et al. 2004) the SNR shell is brighter in the north and the south, while it is darker with diffuse structures in the outer parts of the same sector in which the Lobe is located (east-northeast). The analysis of *Chandra* data has shown that the foreground absorption $N_{\rm H}$ is lower in and around the Lobe (Fig. 6, lower panels), while the Fe L-shell emission is enhanced in the Lobe, with one smaller region with significantly enhanced Si abundance. The bright feature seen as the Lobe can be explained by the following scenario: the blast wave hit a dense cloud, evaporating and maybe encompassing it. Due to the interacton with the cloud, a reverse shock was formed and propagated towards the centre heating the ejecta. The evaporated cloud is now visible as the Lobe with stronger X-ray emission.

Castro et al. (2012) report the detection of a GeV source with *Fermi* at the position of CTB 109. The *Fermi* source is located southwest of the Lobe where the SNR appears dark, and thus most likely highly absorbed in X-rays. Assuming that the γ-rays are produced in π^0-decays caused by the interaction of the SNR shock with a dense interstellar cloud now visible as the Lobe, Castro et al. (2012) derive a density of ∼120 cm^{-3} for the cloud. They point out the discrepancy between this value and the density of 0.9 cm^{-3}, which we calculated from the X-ray data (Sasaki et al. 2006). However, as the density of the Lobe of 0.9 cm^{-3} refers to the hot shocked X-ray emitting gas, which is likely to have a lower density than the original cold cloud, the new result from Castro et al. (2012) is consistent, rather than incompatible, with our results. As we have pointed out (Sasaki et al. 2006) and confirmed in the new spectral analysis, the foreground absorption south of the Lobe (regions 38 and 51 in this work) is high with $N_{\rm H} = 1.3(1.1{-}1.5) \times 10^{22}$ cm^{-2} and comparable to that in the CO arm. Therefore, our new *Chandra* study as well as the new *Fermi* results by Castro et al. (2012) confirm that there was and still is interaction between the shock wave of CTB 109 with the ambient dense material. The remainder of this interaction is still visible as CO clouds presented in Sasaki et al. (2006).

Acknowledgements. M.S. acknowledges support by the Deutsche Forschungsgemeinschaft through the Emmy Noether Research Grant SA 2131/1. P.P.P. and T.J.G. acknowledge support from NASA contract NAS8-03060.

References

Aschenbach, B., Egger, R., & Trumper, J. 1995, Nature, 373, 587
Bocchino, F., Maggio, A., & Sciortino, S. 1999, A&A, 342, 839
Castro, D., Slane, P., Ellison, D. C., & Patnaude, D. J. 2012, ApJ, 756, 88
Fahlman, G. G., & Gregory, P. C. 1981, Nature, 293, 202
Garmire, G. P., Bautz, M. W., Ford, P. G., Nousek, J. A., & Ricker, Jr., G. R. 2003, in X-Ray and Gamma-Ray Telescopes and Instruments for Astronomy, eds. J. E. Truemper, & H. D. Tananbaum, Proc. SPIE, 4851, 28
Gregory, P. C., & Fahlman, G. G. 1983, in Supernova Remnants and their X-ray Emission, IAU Symp., 101, 429
Hendrick, S. P., Borkowski, K. J., & Reynolds, S. P. 2003, ApJ, 593, 370
Hughes, V. A., Harten, R. H., & van den Bergh, S. 1981, ApJ, 246, L127
Hurford, A. P., & Fesen, R. A. 1995, MNRAS, 277, 549
Kaplan, D. L., Chatterjee, S., Hales, C. A., Gaensler, B. M., & Slane, P. O. 2009, AJ, 137, 354
Kifonidis, K., Plewa, T., Janka, H.-T., & Müller, E. 2003, A&A, 408, 621
Kothes, R., & Foster, T. 2012, ApJ, 746, L4
Kothes, R., Uyaniker, B., & Yar, A. 2002, ApJ, 576, 169
Lazendic, J. S., Slane, P. O., Hughes, J. P., Chen, Y., & Dame, T. M. 2005, ApJ, 618, 733
Lopez, L. A., Ramirez-Ruiz, E., Huppenkothen, D., Badenes, C., & Pooley, D. A. 2011, ApJ, 732, 114
Mereghetti, S. 2008, A&ARv, 15, 225
Miceli, M., Bocchino, F., & Reale, F. 2008, ApJ, 676, 1064
Park, S., Hughes, J. P., Slane, P. O., et al. 2003, ApJ, 592, L41
Park, S., Hughes, J. P., Slane, P. O., et al. 2012, ApJ, 748, 117
Patel, S. K., Kouveliotou, C., Woods, P. M., et al. 2001, ApJ, 563, L45
Safi-Harb, S., & Kumar, H. S. 2012, ArXiv e-prints
Sasaki, M., Plucinsky, P. P., Gaetz, T. J., et al. 2004, ApJ, 617, 322
Sasaki, M., Kothes, R., Plucinsky, P. P., Gaetz, T. J., & Brunt, C. M. 2006, ApJ, 642, L149
Sedov, L. I. 1959, Similarity and Dimensional Methods in Mechanics (New York: Academic Press)
Tatematsu, K., Fukui, Y., Nakano, M., et al. 1987, A&A, 184, 279
Taylor, G. I. 1950, Proc. Roy. Soc. London A, 201, 159
von Neumann, J. 1947, Los Alamos Sci. Lab. Tech. Ser., 7
Weisskopf, M. C., Brinkman, B., Canizares, C., et al. 2002, PASP, 114, 1
Wilms, J., Allen, A., & McCray, R. 2000, ApJ, 542, 914

A&A 563, A9 (2014)
DOI: 10.1051/0004-6361/201323145

Astronomy & Astrophysics

XMM-Newton observation of the Galactic supernova remnant W51C (G49.1–0.1)⋆

Manami Sasaki, Cornelia Heinitz, Gabriele Warth, and Gerd Pühlhofer

Institut für Astronomie und Astrophysik, Universität Tübingen, Sand 1, 72076 Tübingen, Germany
e-mail: sasaki@astro.uni-tuebingen.de

Received 28 November 2013 / Accepted 15 January 2014

ABSTRACT

Context. The supernova remnant (SNR) W51C is a Galactic object located in a strongly inhomogeneous interstellar medium with signs of an interaction of the SNR blast wave with dense molecular gas.
Aims. Diffuse X-ray emission from the interior of the SNR can reveal element abundances in the different emission regions and shed light on the type of supernova (SN) explosion and its progenitor. The hard X-ray emission helps to identify possible candidates for a pulsar formed in the SN explosion and for its pulsar wind nebula (PWN).
Methods. We have analysed X-ray data obtained with *XMM-Newton*. Spectral analyses in selected regions were performed.
Results. Ejecta emission in the bright western part of the SNR, located next to a complex of dense molecular gas, was confirmed. The Ne and Mg abundances suggest a massive progenitor with a mass of >20 $M_{\odot}$. Two extended regions emitting hard X-rays were identified (corresponding to the known sources [KLS2002] HX3 west and CXO J192318.5+140305 discovered with ASCA and *Chandra*, respectively), each of which has an additional point source inside and shows a power-law spectrum with $\Gamma \approx 1.8$. Based on their X-ray emission, both sources can be classified as PWN candidates.

Key words. shock waves – HII regions – X-rays: ISM – X-rays: individuals: individual: SNR W51C

1. Introduction

Supernova remnants (SNRs) are galactic objects that are formed after a supernova (SN) explosion at the end of the life of a star. An SN explosion instantaneously releases energy and matter into the ambient interstellar medium (ISM), carving out new structures inside a galaxy and enriching it with elements that were formed inside the progenitor star and in the explosion. In the shock waves of SNRs, particles can be accelerated and become Galactic cosmic rays. Multi-frequency studies of SNRs from radio to X-rays, in some cases even to γ-rays, help to understand the physics of the shock waves and the interaction between the SNR and the ISM.

The SNR W51C (G49.1–0.1) is a Galactic SNR in the W51 complex, an extended radio source at the tangential point of the Sagittarius arm. The W51 complex comprises two additional structures, W51A and W51B, which both harbour compact H II regions. High-velocity molecular gas that runs almost parallel to the Galactic plane, known as the high-velocity stream (Mufson & Liszt 1979), has been detected on the western side of the SNR. Located in an area with a large number of H II regions and dense molecular gas, W51C is a prime example of the interaction of an SNR blast wave with the multi-phase interstellar medium in our Galaxy.

The radio continuum of SNR W51C shows a thick arc-like structure with an extent of about 30′ (Copetti & Schmidt 1991; Subrahmanyan & Goss 1995). It is open to the north and its projected western edge coincides with W51B. The distance of 6 kpc to the SNR has been estimated from molecular-line observations (Koo & Moon 1997a,b; Green et al. 1997) and places it behind the ridge of molecular gas at 5.6 kpc. Assuming a Sedov model, Koo et al. (1995) derived an SNR age of $\sim 3 \times 10^4$ yr.

On its western side, where W51C merges with W51B in the radio image, shocked atomic H I was found (Koo & Heiles 1991). Furthermore, Koo & Moon (1997b) found CO and HCO^+ emission, probably arising from molecules destroyed by a fast dissociative shock and reformed behind the shock front (Koo & Moon 1997a). Masers at 1720 MHz (OH) have also been found in W51C, between the SNR and the high-velocity stream of molecular gas (Green et al. 1997); OH (1720 MHz) emission, unaccompanied by maser emission from other OH ground-state transitions, is thought to arise in cooling gas behind non-dissociative shocks and is used to locate the site of shock-cloud interactions.

Diffuse X-ray emission was observed from W51B and W51C with the *Einstein* Imaging Proportional Counter (Seward 1990) and the Position Sensitive Proportional Counter (PSPC) of the Röntgen Satellite (ROSAT) mainly below 2 keV (Koo et al. 1995). The X-ray shell of W51C in the east and the western diffuse X-ray emission match the radio shell, while the emission gap observed in the soft X-rays between the bright central region and the western part coincides with W51B (see Fig. 1). Koo et al. (2002, hereafter KLS2002) derived a temperature of ∼0.3 keV from data taken with the Advanced Satellite for Cosmology and Astrophysics (ASCA) for the central soft SNR emission, assuming thermal emission in collisional ionisation equilibrium. The hard (2.6−6.0 keV) X-ray image of ASCA is very different from the ROSAT image with the brightest regions seeming to be associated with compact H II regions.

The remnant W51C is very likely the result of a core-collapse SN and should have an associated compact object.

⋆ Based on observations obtained with *XMM-Newton*, an ESA science mission with instruments and contributions directly funded by ESA Member States and NASA.

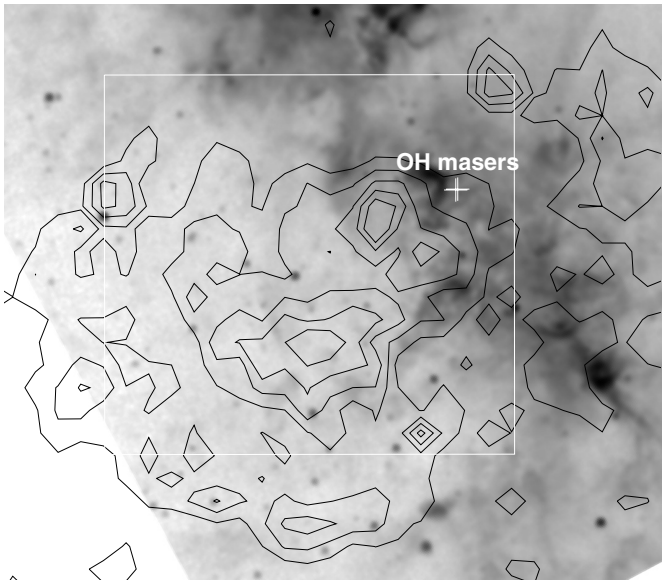

Fig. 1. A Midcourse Space Experiment (MSX, Egan et al. 2003) image in the infrared taken at 8.3 μm, together with ROSAT PSPC (0.1–2.4 keV) contours. The MSX image shows the emission from interstellar dust. The white cross marks the position of the OH (1720 MHz) masers. The white box indicates the field of the sky shown in Fig. 2.

Images taken with the *Chandra* Advanced CCD Imaging Spectrometer (ACIS) in the soft band (0.3−2.1 keV, Koo et al. 2005) show several X-ray bright clumps. The spectra of the diffuse emission suggest an enhanced abundance of sulfur. In the hard band (2.1−10.0 keV), the point-like source CXO J192318.5+140305 was found, which is surrounded by an extended emission, making it a likely candidate for a pulsar wind nebula (PWN). This structure is similar to PWNe associated with several other SNRs, which all have a ∼1 pc diameter bright core with a central pulsar or a point source. There is an indication of an unusual hardening at the ends of the envelope of this source in the *Chandra* data, but uncertainties are large. Its spectrum can be fitted with a power-law model ($\Gamma = 1.8 \pm 0.3$, Koo et al. 2005). Recently, Hanabata et al. (2013) presented the results of a study of the inner parts of the SNR W51C performed with the *Suzaku* X-ray Imaging Spectrometer (XIS).

At higher energies γ-ray emission from the W51C region has been detected with the Large Area Telescope (LAT) on board *Fermi* (Abdo et al. 2009), the High Energy Stereoscopic System (H.E.S.S.)[1], and the MAGIC telescopes (Aleksić et al. 2012). The GeV emission observed with *Fermi* is extended and seems to be consistent with the radio and X-ray extent of the remnant.

In this paper we present the analysis of the central part of the SNR W51C from a deep observation with the X-ray Multi-Mirror Mission (*XMM-Newton*, Jansen et al. 2001).

2. Data

The SNR W51C was observed with *XMM-Newton* on April 8, 2009, (obs. ID 0554690101) with the European Photon Imaging Cameras (EPICs, Strüder et al. 2001; Turner et al. 2001) as prime instruments using the medium filters. We used HEASOFT ver. 6.12 and the *XMM-Newton* Science Analysis System ver. 12.0.0 to analyse the data.

[1] Reported by Fiasson et al. (2009, Proc., 31th ICRC).

Since the emission from the SNR W51C fills almost the entire field of view (FOV) of the EPICs, we used the *XMM-Newton* Extended Source Analysis Software (ESAS)[2] to analyse the data. Using ESAS, we filtered out bad time intervals caused by soft proton flares, resulting in good exposures of 40, 51, and 54 ks for EPIC-pn, MOS1, and MOS2, respectively. In addition, we checked whether any CCD of the MOS detectors was in an anomalous state. Since CCD4 of MOS1 showed an enhancement in the background below 1 keV and was therefore in an anomalous state[3], this CCD was excluded from further analysis. The filtered events were used to perform source detection and create data with events of the extended emission. For further analysis, we selected single and double pixel events (PATTERN = 0 to 4) for the EPIC-pn and single to quadruple-pixel events (PATTERN = 0 to 12) for the EPIC-MOS1 and MOS2. To remove the detector background, data taken with the filter wheel closed (FWC) were binned to images and subtracted from the images of the observation after rescaling the FWC image using the count rates in the corners of the detectors, which are not exposed to the sky.

We are primarily interested in the extended diffuse emission of the SNR. Therefore, we ran the ESAS routines *cheese* (or *cheese-bands* for processing multiple energy bands) to detect point sources, which can then be removed in the following steps. These routines run source detection and create lists and masks of the detected point sources. The masks are used to remove the point sources from the images and the list of detected sources is used to exclude the sources in the extraction regions for spectral analysis. For the source detection we used a flux threshold of 10^{14} erg cm^{-2} s^{-1}, a signal-to-noise ratio of 2, and a minimum separation of 40″ for the point sources. In total, 48 point sources were found in the FOV, which we excluded when creating images and extracting spectra. We only checked the spectra and counterparts of the potential pulsar candidates, i.e. hard X-ray sources with associated hard extended emission around them (see Sect. 3.2).

To obtain deep images of the SNR in different energy bands, the images of the EPIC-pn and MOS1 and 2 were merged and divided by exposure maps, which take the vignetting effects into account. Figure 2 shows a three-colour presentation of the images in the bands 0.3−1.0 keV (red), 1.0−2.0 keV (green), and 2.0−8.0 keV (blue). These images, which are shown in logarithmic scale, were adaptively smoothed and then smoothed again using a Gaussian kernel of the size of 5 pixels for a better presentation of the faint diffuse emission. The holes in the images resulting from excluding point sources are not filled. The mosaicing of the three EPICs and the adaptive smoothing even out most of the holes as well as the chip gaps as can be seen in Fig. 2.

Using these images, extraction regions for the spectral analysis were defined based on surface brightness and X-ray colour (for details see Sect. 3). The spectra were rebinned with a minimum of 50 counts per bin. For a comparison of the distribution of the X-ray emission and the surrounding colder medium, we also downloaded an image from the Midcourse Space Experiment (MSX, see Fig.1, Egan et al. 2003). To estimate the local X-ray background, a background extraction region was defined north of the SNR emission. The fainter regions in the east to south-east or in the west are not appropriate as this is where the blast wave emission is expected. The background spectra were scaled to the source spectra using the areas of the extraction regions, taking into account that CCD4 in anomalous state and CCD6,

[2] http://heasarc.nasa.gov/docs/xmm/xmmhp_xmmesas.html

[3] XMM-ESAS Users Guide, Snowden & Kuntz (2012).

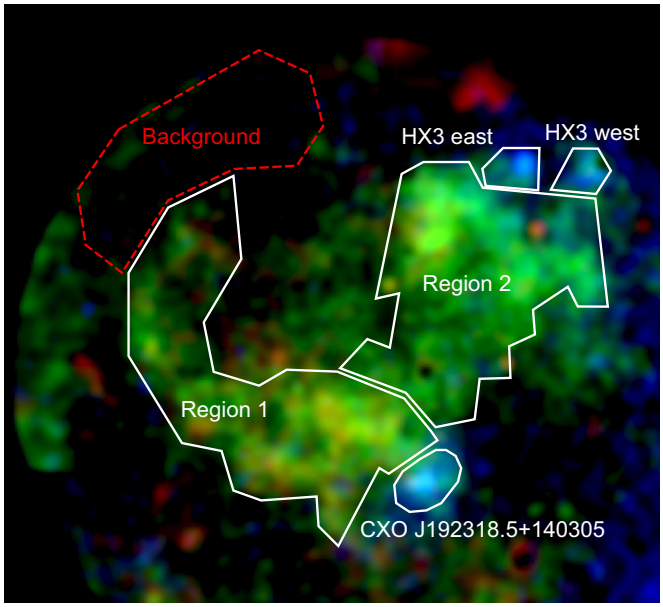

Fig. 2. Three-colour image of the mosaic images (red: 0.3–1.0 keV, green: 1.0–2.0 keV, blue: 2.0–8.0 keV). Extraction regions used for the spectral analysis are shown. Point sources are removed.

which was damaged after being hit by a micrometeorite, are excluded for MOS1.

3. Spectral analysis

The spectra were analysed using the X-ray spectral fitting package XSPEC Ver. 12.8.1 and the atomic data base AtomDB 2.0.2[4]. The emission of the SNR fills most of the FOV of the analysed observation. We divided the data into regions that are likely to have emission of similar nature based on the images in the broad band and the three-colour image (Fig. 2). Unfortunately, the statistics of the data were not high enough to analyse small regions. We were also not able to extract meaningful spectra of the fainter regions that correspond to the outer shock of the SNR, for example. We therefore focussed the spectral analysis on the inner X-ray bright region, which we divided into two, one for the arc-like structure in the south-east and one covering the region north-west of the arc region located next to a band of molecular gas showing dust emission and harbouring compact H II regions (Fig. 1). The two regions are to a certain extent consistent with the extraction regions 1 and 2 used by Hanabata et al. (2013) for the analysis of *Suzaku* XIS data and so we also call them regions 1 and 2. These two extraction regions also correspond more or less to the regions XS and XN in Koo et al. (2002).

In addition, we extracted spectra for the diffuse emission around two hard point-like sources (one at the position of CXO J192318.5+140305 and one north of the X-ray bright region, corresponding to sources [KLS2002] HX2 and HX3 west, respectively), as well as a region covering [KLS2002] HX3 east, which has been resolved into two sources in the *XMM-Newton* data (see Sect. 3.2).

The observed X-ray spectrum includes the particle background measured by the detector and the X-ray background in addition to the actual source emission. To subtract the particle background, we extracted spectra from the FWC data at the same detector positions as for the extraction regions of the analysed source data. Since the closed filter wheel blocks all X-ray emission from outside and the soft protons from solar flares, this background accounts for the contamination by cosmic rays. These FWC-background spectra are subtracted as backgrounds in XSPEC. The FWC-background subtracted spectra still show some flourescent lines coming from the instruments, which can vary from observation to observation and so cannot be completely removed by subtracting the FWC data. In addition, the spectra include the X-ray background. The time intervals with enhanced soft proton background had already been filtered out in the beginning of the data analysis. The source spectra showed no signs of residual particle-background continuum, which should otherwise have been modelled as an additional unfolded power-law component, not affected by detector response. The X-ray background was estimated by modelling the source spectrum and the local background spectrum extracted outside the SNR simultaneously. In doing so, spectra of all detectors were fitted simultaneously for each source region. The background spectra were modelled with a spectrum consisting of a component for the thermal emission from the Local Bubble, one for the thermal emission from the Galactic halo, and a power-law describing the extragalactic X-ray background. All the parameters of the background components were linked for all spectra. The assumed temperatures for the thermal X-ray background and the photon index for the extragalactic background were fixed to values suggested by Snowden et al. (2008, see also the XMM-ESAS Users Guide). Another process that can also create additional emission lines in the observed spectra is the solar wind charge exchange (SWCX, Snowden et al. 2004). Therefore, in total four Gaussians have been included to model possible SWCX emission and the fluorescent lines formed in the detector. The parameters of the Gaussians were free, as the centroids and the line fluxes can vary for the fluorescent lines between detectors and also between different positions on one detector.

3.1. Diffuse emission

To model the emission of the SNR, an additional thermal emission component was included for the source spectra. Best fit was achieved with a non-equilibrium ionisation model in both regions. We used the model VNEI which allowed us to vary the abundances. We used the solar element abundances determined by Anders & Grevesse (1989) for all fits. The best-fit parameter values are listed in Table 1.

The spectrum of region 1 is well fitted with a VNEI model assuming solar abundances (Fig. 3). If we also assume solar abundances for all elements for region 2, the fit is not sufficiently good and there are residuals especially at energies >1 keV. The fit improves if we free the abundances for Ne and Mg. The best fit indicates an overabundance of these two elements (see Table 1).

The X-ray emission from region 1 is consistent with emission from shocked ISM. This region 1 has a much higher surface brightness than the outer shock region to the east, which is seen in the radio map and is very faint in the X-rays (see the ROSAT contours in Fig. 1). The interior bright emission indicates that there was a region with higher density around the SN, i.e. circumstellar matter ejected from the progenitor. Inside this circumstellar matter, in region 2 we find enhanced abundances of selected elements (Ne, Mg), indicating emission from stellar ejecta.

[4] http://www.atomdb.org

Table 1. Fit parameters for the SNR emission.

ID	N_H [10^{22} cm^{-2}]	kT [keV]	τ [10^{11} s cm^{-3}]	Ne × solar	Mg × solar	red. χ^2	d.o.f.[a]
Region 1	1.6 (1.5–1.7)	0.68 (0.66–0.74)	1.1 (0.8–1.5)	1.0[b]	1.0[b]	1.3	1034
Region 2	2.0 (1.9–2.1)	0.59 (0.56–0.61)	8.1 (6.2–11.)	3.7 (3.5–4.2)	2.0 (1.9–2.2)	1.2	970

Notes. [(a)] Degrees of freedom. [(b)] Fixed to solar values like all the other abundances. Errors are 90% confidence limits.

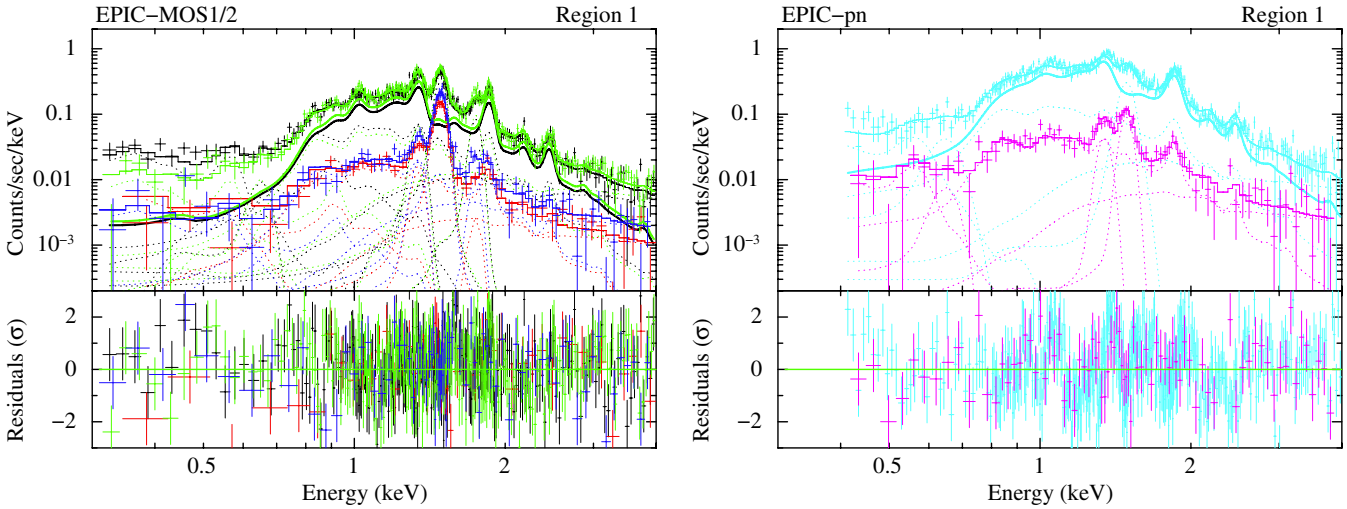

Fig. 3. EPIC spectra of region 1 (MOS1: black, MOS2: green, pn: cyan) and the background region (MOS1: red, MOS2: blue, pn: magenta) and the best-fit model. The thick solid lines show the source emission component (VNEI). The dotted lines show all the other components included in the model.

3.2. Point-like sources

There are three bright hard sources clearly visible in Fig. 2, one of which coincides with the source CXO J192318.5+140305 suggested to be a PWN by Koo et al. (2005). The two hard sources at the northern rim of the FOV of the *XMM-Newton* observation correspond to the ASCA sources [KLS2002] HX3 east and west. We extracted and analysed the spectra of the diffuse emission in these regions.

The source HX3 east has a counterpart in the radio (G49.2−0.3), which has been identified as a compact H II region (Koo & Moon 1997a) and has thus been classified as emission from massive stars in G49.2−0.3. In the presented *XMM-Newton* data, the hard emission at the position of HX3 east has been resolved into two sources that are 17″ apart (RA, Dec = 19 23 01.7, +14 16 34 and 19 23 01.8, +14 16 17) and have similar X-ray colours. We extracted the spectrum of a region that includes both sources. The spectrum was first fitted with a power-law model for the source emission. The background was modelled including the background components as described before. The resulting photon index is $\Gamma = 3.2$ (2.6–3.8)[5] and the intrinsic absorption is $N_H = 3.5(3.0–4.9) \times 10^{22}$ cm^{-2} (reduced $\chi^2 = 1.4$ for 299 degrees of freedom). A thermal emission model for a plasma in non-equilibrium ionisation instead of the non-thermal model improved the fit slightly (reduced $\chi^2 = 1.3$ for 297 degrees of freedom) and resulted in an intrinsic absorption of $N_H = 3.9(3.5–4.3) \times 10^{22}$ cm^{-2}, a temperature of $kT = 2.4(1.8–3.5)$ keV, and an ionisation timescale of $\tau = 2.0(1.2–3.3) \times 10^{10}$ s cm^{-3}. The high photon index in the non-thermal fit is indicative of a thermal emission, whereas the high column density obtained in both fits suggests an emission origin embedded in a dense medium. The temperature and the ionisation timescale are also consistent with winds of young massive stars, confirming the results of Koo et al. (2002).

The source spectra of CXO J192318.5+140305 and HX3 west were modelled with a power-law component. The results are summarised in Table 2. Both sources are well fitted with a power-law spectrum with a photon index in the range of $\Gamma = 1.7–2.0$.

4. Discussion

4.1. Ejecta mass

The well-defined emission from region 2 allows us to estimate the amount of ejecta. To do so, we fitted the spectra of region 2 with a combined source model consisting of two VNEI models. For the first VNEI component, the parameters kT and τ were fixed to the best-fit values of region 1. The abundances were all set to solar. For the second VNEI spectrum, the parameters kT, τ, and the abundances of Ne and Mg were free, while all other abundances were set to zero first. In the subsequent steps we also fitted the abundances of all other elements by additionally freeing them one by one, but no other element showed a significantly enhanced abundance. This spectral component will allow us to estimate the amount of Ne and Mg in the ejecta. The spectra of region 2 with the best-fit model is shown

[5] All errors in brackets are 90% confidence intervals throughout the paper.

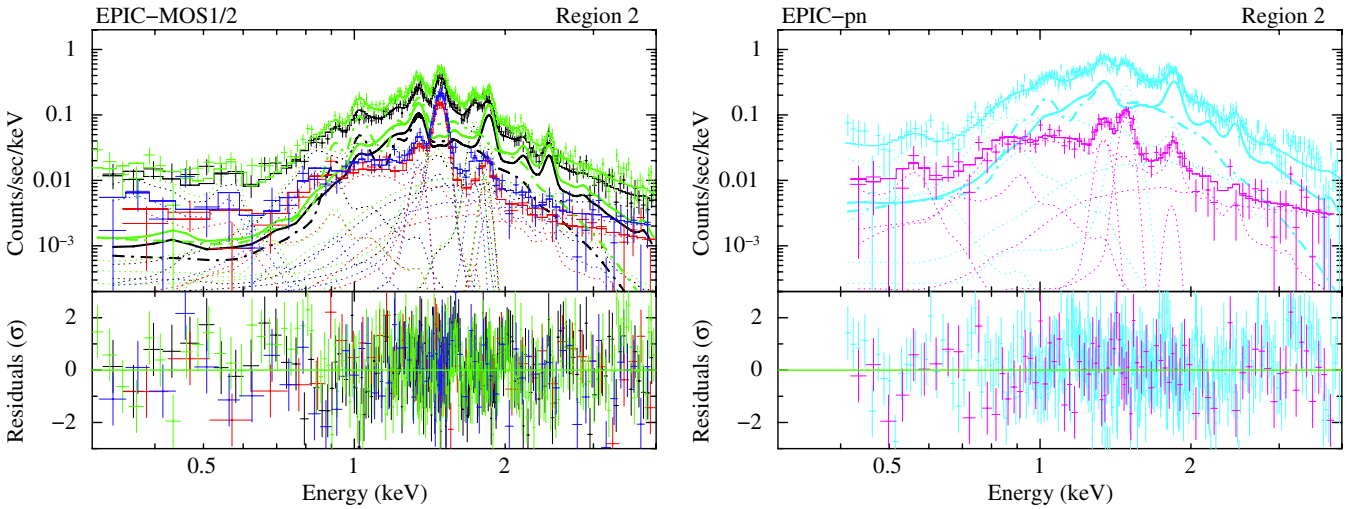

Fig. 4. EPIC spectra of region 2 (MOS1: black, MOS2: green, pn: cyan) and the background region (MOS1: red, MOS2: blue, pn: magenta) and the best-fit model, assuming two VNEI components for the source emission (see Sect. 4.1). The thick solid lines show the source emission component corresponding to shocked ISM (VNEI with solar abundances, parameters fixed to the results of region 1). The thick dash-dotted lines show the ejecta component. The dotted lines show all the other components included in the model.

Table 2. Fit parameters for the hard extended emission.

ID	RA, Dec[†] (2000.0)	$N_{\rm H}$ [10^{22} cm^{-2}]	Photon index	Unabsorbed flux (0.3–10 keV) [10^{-13} erg s^{-1} cm^{-2}]	red. χ^2	d.o.f.[*]
CXO J192318.5+140305	19 23 18.6, +14 03 03	1.00 (0.88–1.13)	1.89 (1.75–2.03)	9.7 (8.2–12.)	1.3	390
HX3 west	19 22 48.4, +14 16 27	1.79 (1.70–2.51)	1.75 (1.67–1.94)	9.0 (8.5–16.)	1.3	302

Notes. [(†)] Positions of the point sources as determined by the source detection routine of ESAS. [(*)] Degrees of freedom. Errors are 90% confidence limits.

in Fig. 4. As the best-fit parameters, we get the following values with lower 90% confidence limits for the normalisation of $norm = \frac{10^{-14}}{4\pi D^2} \times \int n_{\rm H}\, n_{\rm e}\, {\rm d}V = 1.4(>0.7) \times 10^{-3}$ cm^{-5}, with D being the distance to the source, and the abundances for Ne = 180 (>10) and Mg = 50 (>20) × solar values. Since the fit parameters for the normalisation and the abundances are correlated to each other in this model, which is dominated by emission lines, it is not possible to constrain the upper confidence limits for these values.

At X-ray emitting temperatures, we can assume that all elements are almost fully ionised. In this case, we get $n_{\rm e} = 1.21 n_{\rm H}$ for the relation between the electron and H densities. The extraction region has an extent of about 10′. For the volume of the emitting region, we take the size of the extraction region and assume a depth of 10′, corresponding to the extent of the projected volume. For the calculations, we assume a distance of D = 6 kpc. We thus get a particle number density of $n_{\rm H}$ = 0.07 (>0.05) cm^{-3}. For this density, we derive an ionisation time of $\tau/(1.21 n_{\rm H}) = 3.0 \times 10^5$ yr using the ionisation timescale obtained from the spectral fit of region 2. This time is one order of magnitude higher than the estimated age of the SNR (Koo et al. 1995, see Sect. 1). The ionisation timescale gives a characteristic number for the X-ray emitting plasma after it has been shocked and heated, and does not thus necessarily represent the real age of the SNR. As can be verified in Table 1, the ionisation timescale τ is significantly higher for region 2 than for the region 1, which is located outside region 2. This high ionisation age in the likely centre of the SNR surrounded by shocked circumstellar medium might indicate that the plasma is overionised, as observed in some mixed-morphology SNRs in our Galaxy (Lopez et al. 2013, and references therein).

Using the abundances obtained from the spectral fit, we estimate the masses of $M_{\rm Ne}$ = 2.9 (>0.16) $M_\odot$ and $M_{\rm Mg}$ = 0.30 (>0.12) $M_\odot$ for the ejecta. Because of the large uncertainties in determining the volume as well as the spectral fit parameters, these numbers only give a crude estimate of the masses. The comparison to calculated nucleosynthesis yields of SNe Type II by Nomoto et al. (1997) has shown that these mass limits for Ne and Mg point to a very massive progenitor with a mass of >20 $M_\odot$.

4.2. Pulsar wind nebula candidates

The spectral analysis of the regions around CXO J192318.5+140305 and HX3 west have shown that both sources have a power-law spectrum with photon indices that are comparable and consitent with a PWN. The flux and the extent of the diffuse emission are also similar.

The hard source at the position of HX3 west consists of an extended emission and a hard point source, which is unfortunately located at the rim of the FOV. This makes a detailed analysis of the point source impossible. The three-colour *Chandra* image presented by Koo et al. (2005, their Fig. 1) also shows a blue (thus hard) point source at the north-western rim of the extended

hard emission. As noted before, the hard sources at the positions of CXO J192318.5+140305 and HX3 west are very similar, both consisting of a diffuse emission plus a point source and the photon index of the extended emission being consistent with a PWN. The measured fluxes of the extended emission correspond to luminosities of $L_{0.3-10.0\,\mathrm{keV}} = 4.2(3.5-52.) \times 10^{33}$ erg s^{-1} and $3.9(3.7-69.) \times 10^{33}$ erg s^{-1} for CXO J192318.5+140305 and HX3 west, respectively, if we assume a distance of $D = 6$ kpc. At both positions, faint radio sources were found (Condon et al. 1998; Koo et al. 2002); therefore, we conclude that both sources are likely candidates of a PWN associated to the SNR W51C and require further investigation.

5. Summary

We have studied the Galactic SNR W51C using an observation of its central part carried out with *XMM-Newton*. It was not possible to analyse the X-ray emission of the outer blast wave as it was not covered completely by the pointing and the observed emission was too faint. However, the spectral analysis of the inner regions revealed that there are two distinct emission regions inside the SNR.

The first region has an arc-like morphology, more or less aligned to the morphology of the blast wave outside, but is much brighter. Its spectrum is well reproduced by thermal emission from plasma with non-equilibrium ionisation. The element abundances are consistent with solar values, indicating that the origin of this emission is shocked ambient medium. The shape and the higher X-ray brightness of this region suggest that the shocked material is the circumstellar medium of the progenitor.

The diffuse X-ray emission from the second region, located farther inside and in projection next to the region filled with colder gas and dust, is more highly absorbed and seems to arise from plasma close to collisional ionisation equilibium. Significantly enhanced abundances are measured for Ne and Mg. From the abundances and the density derived from the spectra, we calculated the masses of Ne and Mg in the ejecta and conclude that the progenitor was a massive star with a mass comparable to or higher than 20 $M_\odot$.

In addition, we analysed the diffuse X-ray emission detected around two hard point sources, one of which has already been studied in detail by Koo et al. (2005) using *Chandra* data. The second hard source is located north-west of the region, close to the OH (1720 MHz) masers that have been found in W51C. The extended emission of both regions is well modelled with an absorbed power-law spectrum with a photon index of $\Gamma \approx 1.8$. The luminosities are $L_{0.3-10.0\,\mathrm{keV}} \approx 4 \times 10^{33}$ erg s^{-1} for both regions; the value is rather low, but still consistent with values measured for older PWNe (e.g., Kargaltsev & Pavlov 2010). In addition, the morphology of both sources consisting of a diffuse emission with an extent of $\sim 1'$ and a point source supports their classification as PWN candidates.

The *XMM-Newton* observation has enabled us to study the diffuse emission in the SNR W51C in detail and helped us to make a step forward in the classification of the underlying components of the complex X-ray emission of the SNR. Further observations will be necessary to study the blast wave of the SNR and to identify the possibly associated pulsar/PWN.

Acknowledgements. M.S. and G.W. acknowledge support by the Deutsche Forschungsgemeinschaft through the Emmy Noether Research Grant SA 2131/1-1. This research was funded through the BMWi/DLR grant 50 OR 1009. This research made use of data products from the Midcourse Space Experiment. Processing of the data was funded by the Ballistic Missile Defense Organization with additional support from NASA Office of Space Science. This research has also made use of the NASA/ IPAC Infrared Science Archive, which is operated by the Jet Propulsion Laboratory, California Institute of Technology, under contract with the National Aeronautics and Space Administration.

References

Abdo, A. A., Ackermann, M., Ajello, M., et al. 2009, ApJ, 706, L1
Aleksić, J., Alvarez, E. A., Antonelli, L. A., et al. 2012, A&A, 541, A13
Anders, E., & Grevesse, N. 1989, Geochim. Cosmochim. Acta, 53, 197
Condon, J. J., Cotton, W. D., Greisen, E. W., et al. 1998, AJ, 115, 1693
Copetti, M. V. F., & Schmidt, A. A. 1991, MNRAS, 250, 127
Egan, M. P., Price, S. D., Kraemer, K. E., et al. 2003, Air Force Research Laboratory Technical Report AFRL-VS-TR-2003-1589
Green, A. J., Frail, D. A., Goss, W. M., & Otrupcek, R. 1997, AJ, 114, 2058
Hanabata, Y., Sawada, M., Katagiri, H., Bamba, A., & Fukazawa, Y. 2013, PASJ, 65, 42
Jansen, F., Lumb, D., Altieri, B., et al. 2001, A&A, 365, L1
Kargaltsev, O., & Pavlov, G. G. 2010, X-ray Astronomy 2009; Present Status, Multi-Wavelength Approach and Future Perspectives, AIP Conf. Ser., 1248, 25
Koo, B.-C., & Heiles, C. 1991, ApJ, 382, 204
Koo, B.-C., & Moon, D.-S. 1997a, ApJ, 475, 194
Koo, B.-C., & Moon, D.-S. 1997b, ApJ, 485, 263
Koo, B.-C., Kim, K.-T., & Seward, F. D. 1995, ApJ, 447, 211
Koo, B.-C., Lee, J.-J., & Seward, F. D. 2002, AJ, 123, 1629
Koo, B.-C., Lee, J.-J., Seward, F. D., & Moon, D.-S. 2005, ApJ, 633, 946
Lopez, L. A., Pearson, S., Ramirez-Ruiz, E., et al. 2013, ApJ, 777, 145
Mufson, S. L., & Liszt, H. S. 1979, ApJ, 232, 451
Nomoto, K., Hashimoto, M., Tsujimoto, T., et al. 1997, Nucl. Phys. A, 616, 79
Seward, F. D. 1990, ApJS, 73, 781
Snowden, S. L., Collier, M. R., & Kuntz, K. D. 2004, ApJ, 610, 1182
Snowden, S. L., Mushotzky, R. F., Kuntz, K. D., & Davis, D. S. 2008, A&A, 478, 615
Strüder, L., Briel, U., Dennerl, K., et al. 2001, A&A, 365, L18
Subrahmanyan, R., & Goss, W. M. 1995, MNRAS, 275, 755
Turner, M. J. L., Abbey, A., Arnaud, M., et al. 2001, A&A, 365, L27

A&A 539, A15 (2012)
DOI: 10.1051/0004-6361/201117881

Astronomy & Astrophysics

XMMU J0541.8-6659, a new supernova remnant in the Large Magellanic Cloud⋆

M.-H. Grondin[1], M. Sasaki[1], F. Haberl[2], W. Pietsch[2], E. J. Crawford[3], M. D. Filipović[3], L. M. Bozzetto[3], S. Points[4], and R. C. Smith[4]

[1] Institut für Astronomie und Astrophysik Tübingen, Universität Tübingen, Sand 1, 72076 Tübingen, Germany
e-mail: marie-helene.grondin@mpi-hd.mpg.de
[2] Max-Planck-Institut für extraterrestrische Physik, Giessenbachstrasse, 85748 Garching, Germany
[3] University of Western Sydney, Locked Bag 1797, Penrith South DC, NSW 1797, Australia
[4] Cerro Tololo Inter-American Observatory, Casilla 603, La Serena, Chile

Received 13 August 2011 / Accepted 12 December 2011

ABSTRACT

Context. The high sensitivity of the *XMM-Newton* instrumentation offers the opportunity to study faint and extended sources in the Milky Way and nearby galaxies such as the Large Magellanic Cloud (LMC) in detail. The ROSAT PSPC survey of the LMC has revealed more than 700 X-ray sources, among which there are 46 supernova remnants (SNRs) and candidates.
Aims. We have observed the field around one of the most promising SNR candidates in the ROSAT PSPC catalogue, labelled [HP99] 456 with *XMM-Newton*, to determine its nature.
Methods. We investigated the *XMM-Newton* data along with new radio-continuum, near infrared and optical data. In particular, spectral and morphological studies of the X-ray and radio data were performed.
Results. The X-ray images obtained in different energy bands reveal two different structures. Below 1.0 keV the X-ray emission shows the shell-like morphology of an SNR with a diameter of ∼73 pc, one of the largest known in the LMC. For its thermal spectrum we estimate an electron temperature of (0.49 ± 0.12) keV assuming non-equilibrium ionisation. The X-ray images above 1.0 keV reveal a less extended source within the SNR emission, located 1′ west of the centre of the SNR and coincident with bright point sources detected in radio-continuum. This hard component has an extent of 0.9′ (i.e. ∼13 pc at a distance of ∼50 kpc) and a non-thermal spectrum. The hard source coincides in position with the ROSAT source [HP99] 456 and shows an indication for substructure.
Conclusions. We firmly identify a new SNR in the LMC with a shell-like morphology and a thermal spectrum. Assuming the SNR to be in the Sedov phase yields an age of ∼23 kyr. We explore possible associations of the hard non-thermal emitting component with a pulsar wind nebula (PWN) or background active galactic nucleus (AGN).

Key words. Magellanic Clouds – ISM: supernova remnants

1. Introduction

The study of supernova remnants (SNRs) is crucial for a complete understanding of the chemical composition and evolution of the ISM in a galaxy because of their energy and matter inputs into the interstellar medium (ISM). The sample of SNRs studied in our Galaxy is biased because of the high absorption in the Galactic disk. Therefore, observations of nearby galaxies allow us to perform unbiased population studies and constrain the physical properties of the sources in detail. It is thus also possible to better understand the evolution and structure of the ISM in the Milky Way.

Located at a distance of ∼50 kpc to the Earth (Freedman et al. 2001; Macri et al. 2006), the Large Magellanic Cloud (LMC) offers the ideal laboratory for studying a large sample of different types of objects (such as SNRs) in greater detail than in any other galaxy. Since its first detection in X-rays (Mark et al. 1969), the LMC has been extensively observed, but the major step forward came from more than 200 observations in a 10° × 10° field centred on the LMC, which have been performed with the ROSAT position sensitive proportional counter (PSPC) from 1990 to 1994. For a description of the ROSAT mission and PSPC detectors, see Trümper (1982), Briel & Pfeffermann (1986), and Pfeffermann et al. (1987). This survey revealed 758 sources (Haberl & Pietsch 1999, hereafter labelled HP99), among which 46 sources were classified as firmly identified SNRs or candidates.

Several SNRs in the LMC have been investigated using observations with ROSAT (Filipović et al. 1998; Williams et al. 1999), *Chandra* X-ray Observatory (Hughes et al. 2006; Seward et al. 2010) and *XMM-Newton* (Williams et al. 2004; Klimek et al. 2010; Crawford et al. 2010) satellites, allowing a more detailed view of their morphologies and spectra. Badenes et al. (2010) have studied the size distribution of the SNRs in the Magellanic Clouds (MCs), which has a maximum at ∼40 pc and may extend up to sizes of ∼100 pc. With an extent of over 100 pc, SNR 0450-70.9 and SNR 0506-6542 (DEM L 72) are among the largest SNRs detected in the LMC (Williams et al. 2004; Cajko et al. 2009; Desai et al. 2010; Klimek et al. 2010), which may be highly evolved (age up to 100 kyr). The size distribution of the MC SNRs as well as those in our Galaxy or the neaby spiral galaxy M 33 cannot be explained only by the Sedov expansion model for SNRs, but seems to be largely affected by the ambient

⋆ Based on observations with *XMM-Newton*, an ESA Science Mission with instruments and contributions directly funded by ESA Member states and the USA (NASA).

ISM densities (Bandiera & Petruk 2010; Badenes et al. 2010, and references therein).

Furthermore, multi-frequency observations of several SNR candidates located in the LMC have enabled their firm identification based on morphological and spectral criteria (Bojičić et al. 2007; Crawford et al. 2010) and have revealed a strong correlation between the X-ray sources and the emission observed by the Magellanic Cloud Emission Line Survey (MCELS; Smith et al. 2000). Indeed, an enhancement of the [S II] and Hα coincident with the X-ray emission can be observed in most cases. In particular, the ratio [S II]/Hα is often higher than 0.4 (Levenson et al. 1995; Williams et al. 2004). However, several SNRs in the MCs such as LMC SNR J0528-6714 or/and SMC SNR J010505-722319 do not have any optical emission.

While the emission of the gas shocked by the shock waves of SNRs is mainly of thermal nature, there can also be a pulsar or a pulsar wind nebula (PWN) in an SNR, which produce non-thermal emission. Pulsars are rapidly rotating neutron stars characterised by short periods (up to a few 10 s) and high surface magnetic fields (Manchester et al. 2005). The dissipation of the rotational energy of pulsars via magnetised particle winds can be at the origin of PWNe (Gaensler & Slane 2006). A high percentage of PWNe known in our Galaxy have been detected in X-rays, and present a power-law spectra with a mean spectral index of $\Gamma = -1.8 \pm 0.6$ (Kargaltsev & Pavlov 2008, 2010). Sensitive X-ray observations have enabled the detection of several PWNe and candidates within the MCs, with similar properties as PWNe in the Milky Way (Gaensler et al. 2003; Williams et al. 2005; Owen et al. 2011).

There are now over 50 well-established SNRs in the LMC (Badenes et al. 2010; Klimek et al. 2010, and references therein) and some additional ~20 SNR candidates (Bozzetto et al., in prep.). This would comprise one of the most complete samples of SNRs in external galaxies. Therefore, it is of prime interest to study LMC SNRs and compare them with SNRs in other galaxies such as M 33 (Long et al. 2010), M 83 (Dopita et al. 2010), the Small Magellanic Cloud (SMC; Filipović et al. 2005; Payne et al. 2007; Filipović et al. 2008) and our Galaxy (Stupar et al. 2008; Green 2009).

The SNR candidates in the ROSAT PSPC catalogue have been classified based on the X-ray spectrum and spatial extent. Additional comparison to radio data taken with the Molonglo Observatory Synthesis Telescope (MOST; $\nu = 843$ MHz; Turtle & Mills 1984) and with optical data of MCELS has shown that there are ROSAT PSPC sources with radio or optical counterparts indicative of an SNR but with a hard X-ray spectrum and therefore no typical SNR characteristics in X-rays. The source [HP99] 456 is one of the most promising new SNR candidates of this kind, with hard emission detected by ROSAT PSPC and a possible radio or optical counterpart. It has been recently re-investigated through new observations with *XMM-Newton* and the Australia Telescope Compact Array (ATCA; Hughes et al. 2007).

In this paper, we report on the results of the analysis of new *XMM-Newton* and ATCA follow-up observations of the source [HP99] 456. Section 2 presents the observations and analysis techniques. Results of the multi-frequency analyses are presented in Sect. 3. Section 4 presents the discussion on the SNR properties and on the different scenarios to explain the non-thermal emission. In particular, we explore a possible association of this second component with a PWN or an Active Galactic Nucleus (AGN). Conclusions are presented in Sect. 5.

2. Observations and data reduction

2.1. X-rays

The *XMM-Newton* satellite is an X-ray observatory operated by the European Space Agency (ESA). The source [HP99] 456 has been proposed for observations with *XMM-Newton* (Obs. Id. 0651880101, P.I.: M. Sasaki). This paper presents results of the X-ray analysis of a 20 ks observation obtained on this source.

The source [HP99] 456 has been observed on 2010 June 06 (from 04:18:56 to 09:52:50 UT) with the European Photon Imaging Camera (EPIC) in full-frame mode and thin filters. Using the EPIC MOS1, MOS2 and pn CCDs, it offers the opportunity to perform sensitive X-ray observations of a field of the sky of diameter of 30′. More detailed technical descriptions of the EPIC cameras are presented by Turner et al. (2001) and Strüder et al. (2001).

The EPIC data were analysed with SAS v10.0.0[1]. The exposure time, after removing periods of high background, is ~11 ks. Pixels flagged as bad were not taken into account and screening on the patterns (from 0 to 12 for MOS; from 0 to 4 for pn), corresponding to the canonical set of valid X-ray events (calibrated on the ground) was applied for the image and spectral analyses. We performed source detection by using the SAS tasks *eboxdetect* and *emldetect*.

2.2. Radio-continuum

The field of [HP99] 456 was observed with the ATCA on 2010 November 29, with an array configuration 6C, at wavelengths of 3 and 6 cm (9000 and 5500 MHz), and a bandwidth of 2 GHz (ATCA project C2367). The observations were carried out in snap-shot mode, totalling about 1 h of integration over a 12 h period. PKS B1934-638 was used for flux and bandpass calibration and PKS 0530-727 was used for phase calibration. Standard calibration, editing and imaging techniques (Sault & Killeen 2011) were used. Large bandwidth multifrequency clean (Sault & Wieringa 1994) was used to deconvolve the image. We point out that interferometers such as the ATCA suffer from missing flux owing to the lack of short spacings, which significantly affects the overall detection of extended emission like that from SNRs.

We also used various other radio observations (see Table 1) including 843 MHz by Mills et al. (1984), 1377 MHz from Hughes et al. (2007) and 4800 MHz and 8640 MHz taken from the mosaic project of Dickel (2005).

2.3. Optical

The Magellanic Cloud Emission Line Survey (MCELS)[2] was carried out from the 0.6 m University of Michigan/CTIO *Curtis* Schmidt telescope, equipped with a SITE 2048 × 2048 CCD, which gave a field of 1.35° at a scale of 2.4″ pixel^{-1} (Smith et al. 2006; Winkler et al., in prep.). Both the LMC and SMC were mapped in narrow bands corresponding to Hα, [O III] (λ = 5007 Å), and [S II] (λ = 6716, 6731 Å), plus matched red and green continuum bands. All data were continuum subtracted, flux-calibrated and assembled into mosaic images (a small section of which is shown in Fig. 6).

[1] Science Analysis Software: http://xmm.esac.esa.int/sas/
[2] MCELS: http://www.ctio.noao.edu/mcels/

Table 1. Integrated radio flux densities of [HP99] 456.

ν (MHz)	λ (cm)	rms (mJy)	Beam size ($''$)	$S_{\rm Total}$ (mJy)	Reference
843	36	1.5	43.0×43.0	0.045	Mills et al. (1984)
1377	20	1.5	45.0×45.0	0.029	Hughes et al. (2007)
4800	6	0.6	30.0×30.0	0.008	Dickel (2005)
8640	3	0.6	12.0×12.0	0.004	Dickel (2005)
5500	6	0.1	2.8×2.2	–	This work
9000	3	0.1	2.8×2.2	–	This work

Table 2. Morphological details on the two emitting regions.

Emitting region	RA (hh:mm:ss.d)	Dec (°:′:″)	Size (′)	Position angle (°)	pn count rate (cts s^{-1})
Soft emission	05:41:51.5	–66:59:02.8	5.0×4.6	–45	$(18 \pm 2) \times 10^{-2}$
Hard emission	05:41:39.4	–66:58:45.8	0.9×0.45	–15	$(2.8 \pm 0.3) \times 10^{-2}$

Notes. The last column lists the count rates estimated from the analysis of EPIC-pn data between 0.3 and 5.0 keV.

3. Data analysis

3.1. X-ray morphology

The morphological analysis was performed in three energy ranges: 0.2–1.0 keV (soft band), 1.0–2.0 keV (medium band), 2.0–4.5 keV (hard band). For each energy interval, exposure-corrected images were obtained using SAS tools using the following method.

First, X-ray data were cleaned using the selection procedure described in the previous section. We computed event images and exposure maps using the filtered dataset. Then we applied a mask to remove bad pixels from the three instruments. We divided each resulting event image by the corresponding exposure map and smoothed the resulting images with a Gaussian filter using *asmooth*. Finally, we added the event images from the different instruments for each energy band.

Figure 1 shows the RGB exposure-corrected image around the unidentified source [HP99] 456 obtained with the EPIC data in the three bands defined above (red: 0.2–1.0 keV; green: 1.0–2.0 keV; blue: 2.0–4.5 keV) after subtraction of the instrumental background (see caption). The emission seen in the hardest band is similar to the medium band. This morphological analysis reveals the existence of two distinct emitting regions:

1. A soft emitting region: below 1.0 keV, the X-ray emission is dominated by a bright thermal (for more details, see Sect. 3.2) component. It presents a shell-like morphology with an extent of $\sim 5.0' \times 4.6'$.
2. A hard emitting region: above 1.0 keV, the X-ray analysis reveals a less extended harder component. Its centre is located $\sim 1'$ west from the centre of the soft shell-like emission and presents an elongated morphology of length $\sim 0.9'$. The position is consistent with the ROSAT position of [HP99] 456.

The presence of the hard emitting region coincident with the ROSAT source suggests that [HP99] 456 is unrelated to the shell-like emission region. Therefore, we designated the soft, shell-like source XMMU J0541.8-6659 according to its approximate central coordinates. Additional details on the positions and extents of both emitting regions are summarised in Table 2. The count rates of the EPIC-pn observations are listed in the last column.

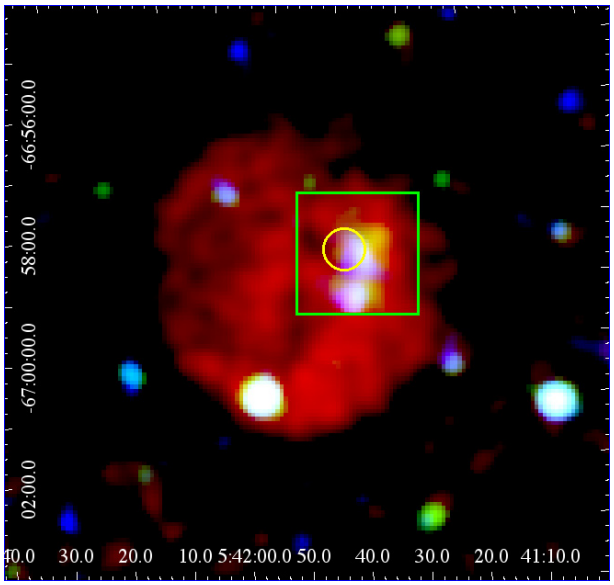

Fig. 1. Smoothed RGB three-colour image of combined exposure-corrected *XMM-Newton* EPIC pn, MOS1 and MOS2 data (red: 0.2–1.0 keV; green: 1.0–2.0 keV; blue: 2.0–4.5 keV, square root scale). The instrumental background was estimated using the method described in Sect. 3.2.1 and subtracted from the images. The renormalisation factor was derived from the shaded detector corners. The field of the radio image presented in Fig. 5 is overlaid for comparison (green square). The position of the ROSAT source [HP99] 456 is represented by a yellow circle.

3.2. X-ray spectral analysis

The following sections present the results of the subsequent spectral analyses of the two spectral components mentioned above. We first describe the method used to estimate the contribution from the intrinsic detector and X-ray background for each emitting region. The spectral analysis was performed using the XSPEC v 12.6.0 package (Arnaud 1996; Dorman & Arnaud 2001).

Point sources that were detected using the method described in Sect. 2.1 were excluded from the spectral analysis. We used data between 0.3 keV and 5.0 keV because no significant emission is detected at higher energies.

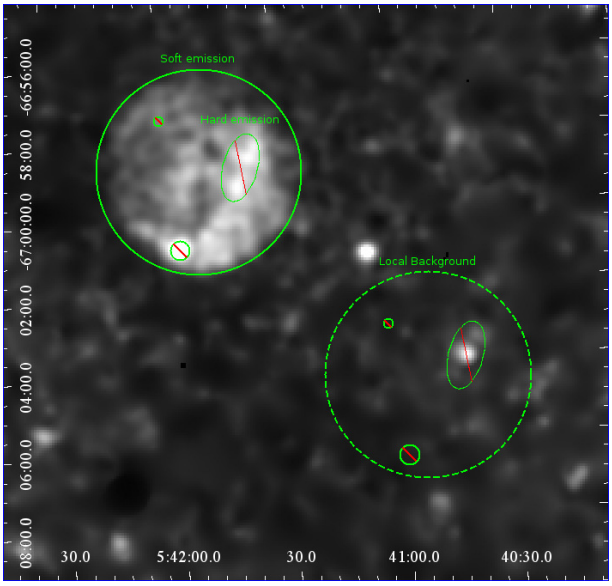

Fig. 2. Smoothed image of exposure-corrected *XMM-Newton* EPIC data in the 0.2–1.0 keV energy range. The dashed circle shows the region considered for the estimation of the local background. The thick circle represents the region used to derive the spectrum of the soft emission from the shell-like structure. Cancelled circles show the position of the bright sources excluded from the spectral analysis.

3.2.1. Estimation of the instrumental background

We estimated the contribution from the intrinsic instrumental background using the filter wheel closed (FWC) data (Freyberg et al. 2001a,b). The intrinsic background is composed of internal electronic noise as well as continuous and fluorescent X-ray emission induced by high-energy particles. This background is measured by operating the EPIC instruments in the "closed" filter wheel position, where no photons from astrophysical sources can be observed. The FWC spectrum needs to be renormalised using the continuum at higher energies.

3.2.2. Estimation of the X-ray background

The contribution of the X-ray local background emission was derived from the same observation as the source itself. We defined a region located close to our source (see Fig. 2), and extracted the spectrum from the observation and the FWC data. We estimated the renormalisation factor of the FWC spectrum with respect to the observed spectrum using the total count rates measured above 5 keV in the corners outside the field of view of the EPIC camera. The value of the renormalisation factor is 1.3.

The spectrum of the diffuse emission after subtracting the instrumental background can be modelled as a sum of the following three components:

- a soft component, modelling the emission from the local bubble with a collisional plasma, non-equilibrium model (NEI; Borkowski et al. 1994, 2001; Hamilton et al. 1983; Liedahl et al. 1995)[3] assuming a low temperature (0.1 keV);
- a hard component modelled with an absorbed NEI model with a temperature of 0.3 keV, which stands for the emission from the Galactic halo;
- an absorbed power-law of spectral index $\Gamma = 1.46$, to describe the extragalactic unresolved emission.

[3] For more details on XSPEC models, please see http://heasarc.nasa.gov/xanadu/xspec/manual/manual.html

Table 3. *XMM-Newton* spectral results of the soft thermal emitting region in the 0.3–5.0 keV energy range.

Parameter	Value
N_H ($\times 10^{21}$ cm^{-2}) in the Galaxy	0.6 (fixed)
N_H ($\times 10^{21}$ cm^{-2}) in the LMC	0 (fixed)
kT (keV)	0.49 ± 0.12
Ionisation timescale* τ (s cm^{-3})	$(1.5 \pm 0.7) \times 10^{10}$
Absorbed flux (0.3–5.0 keV, erg/cm^2/s)	2.5×10^{-13}
Absorbed luminosity (0.3–5.0 keV, erg/s)	5.1×10^{34}
Unabsorbed luminosity (0.3–5.0 keV, erg/s)	8.9×10^{34}
Reduced χ^2	1.27
Degrees of freedom	86

Notes. Model is VNEI with abundances fixed to 0.5 of the solar abundances. (*) The ionisation timescale $\tau = n_e t$, where n_e is the electron number density and t is the age of the gas.

The parameters are fixed to values similar to those used by Kuntz & Snowden (2010).

The two last components are convolved with a Tübingen-Boulder ISM absorption model (TBABS). The Galactic foreground hydrogen column density of 0.6×10^{21} cm^{-2} was derived from Stark et al. (1992) and was used for the absorption in the Galaxy.

3.2.3. Soft-emission region

The X-ray emission below 1.0 keV is dominated by a structure presenting a shell-like morphology with a maximal diameter of ~5.0′ and centred at RA(J2000) = $05^h41^m51.5^s$, Dec(J2000) = –66°59′02.8″. Photons located within the region corresponding to the hard X-ray emitting region, as defined in Table 2, were excluded from the source spectrum to avoid any contamination, as were detected point sources visible in Fig. 1.

The spectrum of the shell-like structure was obtained after the subtraction of the instrumental background. The X-ray background was estimated using a local background spectrum extracted from the same data. The source spectrum and the local background were modelled simultaneously in XSPEC by using a background model consisting of the components as explained in the previous section. All parameters of the three background components were fixed except the normalisations. The normalisations of the background components and the parameters of an additional model component for the shell emission were free fit parameters.

The spectral analysis of the soft circular emitting region reveals a thermal spectrum. It can be modelled with a single-temperature non-equilibrium ionisation collisional plasma model (VNEI; Borkowski et al. 1994, 2001; Hamilton et al. 1983; Liedahl et al. 1995) with a temperature of (0.49 ± 0.12) keV with an absorption of $N_H = 0.6 \times 10^{21}$ cm^{-2} for the Galactic foreground (with solar abundances) and a value of N_H for the absorption in the LMC. The abundances were fixed to 0.5 of the solar system abundances for the emission and absorption taking place in the LMC. This value is the standard mean value for the LMC (Russell & Dopita 1992). The value of N_H for the LMC turned out to tend towards 0 with an 90% C.L. upper limit of 0.4×10^{21} cm^{-2}. This parameter was therefore fixed to 0.

The resulting spectrum is presented in Fig. 3. The corresponding spectral parameters are given in Table 3.

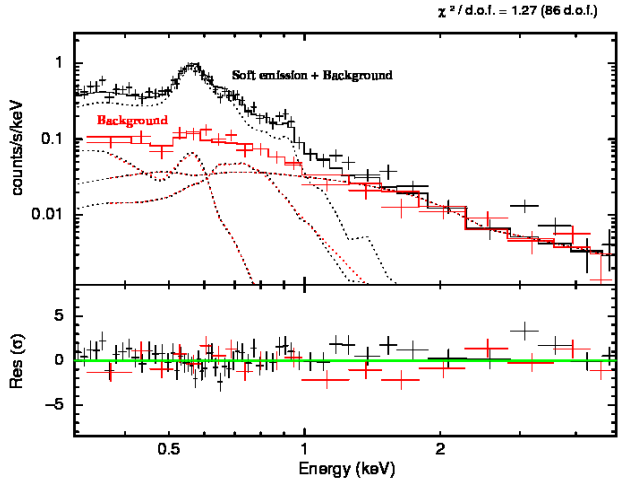

Fig. 3. *XMM-Newton* EPIC-pn spectrum and model of the soft emitting region with a VNEI model fit (black points and solid line). The estimation of the local background spectrum and model (red points and solid line) is described in Sect. 3.2.1. The background spectrum was not subtracted from the source spectrum but was modelled simultaneously and is included in the spectral model of the source spectrum. The different spectral components are shown separately (red and black dotted lines) for the background and source spectra. The bottom panel shows the residuals from the best-fit models.

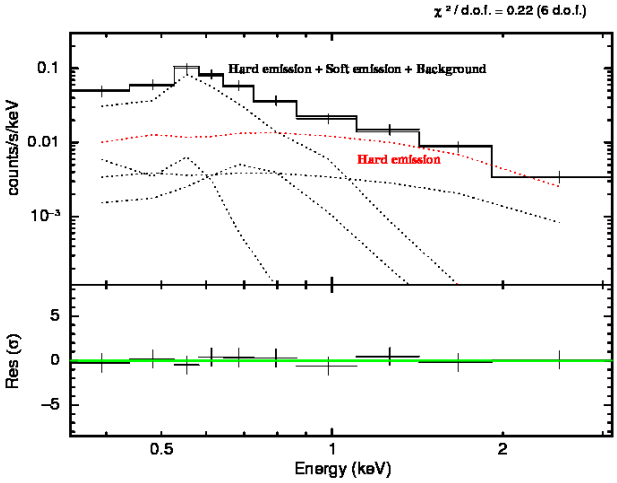

Fig. 4. *XMM-Newton* EPIC-pn spectrum of the hard emitting region with a power-law model fit. The solid line is for the hard emission plus background spectra. Here, the background is the sum of the shell emission and the local emission. The background spectrum and shell spectrum were evaluated as described in Sect. 3.2.4. The background spectrum was not subtracted from the source spectrum but was modelled simultaneously and is included in the spectral model of the source spectrum. The contribution from the hard emitting region is represented in red. The bottom panel shows the residuals from the best-fit model.

3.2.4. Hard-emission region

The X-ray emission above 1.0 keV is dominated by a narrow structure of length ∼0.9′ located ∼1′ to the west of the centroid of the shell-like thermal emission, as seen from Fig. 1. Above 1.0 keV, the hard source has a surface brightness of $\sim 5.8 \times 10^{-3}$ counts/s/arcmin^2, i.e. ∼6 times the background level, which has a surface brightness of $\sim 9.4 \times 10^{-4}$ counts/s/arcmin^2. There is indication for substructure in the X-ray image, which could be caused by multiple sources. The ROSAT source [HP99] 456 coincides with the northern part of the narrow structure.

To analyse the spectrum of this second component again the instrumental background spectrum was subtracted and the X-ray spectrum was modelled simultaneously, this time using the surrounding shell-like emission as the local background. The normalisations of the component corresponding to the X-ray background components were renormalised to the area and were fitted, along with the spectral parameters of the hard emitting region.

The spectrum of the hard emitting region is non-thermal and can be modelled in the 0.3–5.0 keV energy range with an absorbed power-law with a spectral index of $\Gamma = 1.8 \pm 0.3$, with an absorption of $N_{\rm H} = 0.6 \times 10^{21}$ cm^{-2} for the Galactic foreground (fixed, with solar abundances) and a value of $N_{\rm H}$ for the absorption in the LMC of $N_{\rm H} = (0.58 \pm 0.53) \times 10^{21}$ cm^{-2}. This yields an absorbed flux of $\sim 9.5 \times 10^{-14}$ erg/cm^2/s (reduced $\chi^2 = 0.22$ for 6 degrees of freedom). The resulting spectrum is shown in Fig. 4. In particular, the contribution from the hard X-ray emitting region is represented in red.

An alternative technique was used to derive the spectrum of the hard emitting region. Instead of using the FWC data, we extracted a background spectrum from a nearby region located within the shell and subtracted it from the source spectrum. This method yields consistent results for the hard emission.

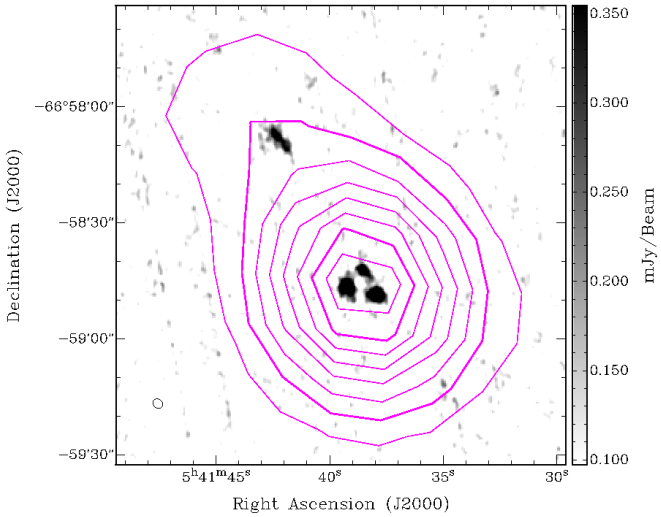

Fig. 5. High-resolution ATCA radio-continuum image at 6 cm (5.5 GHz) overlaid with 20 cm contours (violet) from the low-resolution mosaic image of the immediate surroundings of [HP99] 456. Contours are from 3 to 18 mJy/beam in steps of 1 mJy/beam and 6 cm beam size (2.8″ × 2.2″) is shown in the bottom left corner.

3.3. Radio

New high-resolution (∼2″) radio-continuum observations resolved low-resolution emission into three bright sources within the hard X-ray emitting region (Fig. 5). For comparison, the size of the radio image shown in Fig. 5 is represented in Fig. 1. In particular, three bright sources can be seen coinciding with the central position of this hard non-thermal X-ray emitting region. The brightest source (the most eastern one) has a spectral index of $\alpha = -0.5 \pm 0.1$ with integrated flux densities of (0.85 ± 0.05) mJy at 5.5 GHz and (0.67 ± 0.05) mJy at 9.0 GHz.

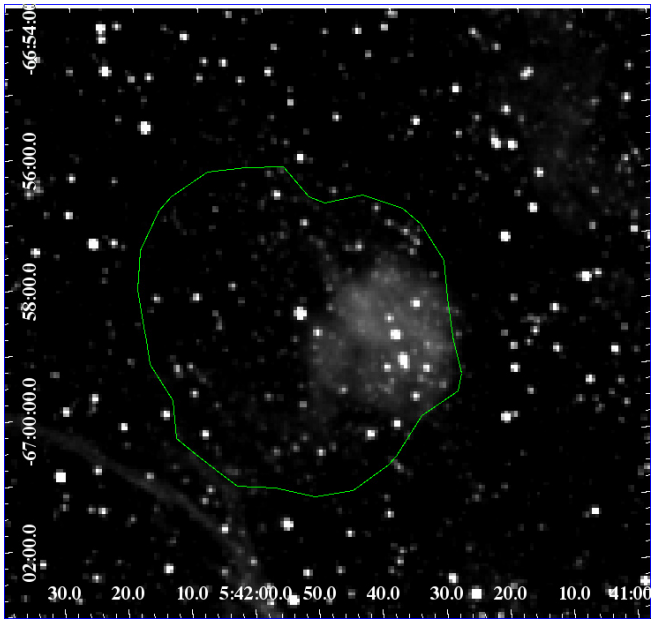

Fig. 6. Hα emission (arbitrary units) derived from the MCELS in the surroundings of [HP99] 456. A contour of the soft thermal emission of XMMU J0541.8-6659 is overlaid in green for comparison.

Our estimate of the SNR overall radio spectral index (excluding central point source; using flux densities from mosaic surveys only and listed in Table 1 i.e. observations from 843, 1377, 4800, 8640 MHz) is $\alpha = -1.0 \pm 0.2$, which is more typical for younger SNRs.

3.4. Optical

The emission from optical lines (Hα and [S II]) derived from the MCELS were considered. The Hα emission in the surroundings of [HP99] 456 are presented in Fig. 6. This image shows a possible correlation between the western part of the shell-like X-ray thermal emission observed by *XMM-Newton*, the low-resolution radio-continuum and the Hα emission line, as seen in Figs. 5 and 6. However, we acknowledge that this correlation could be a chance coincidence because the Hα "cloud" could be an unrelated HII region.

Low-resolution radio-continuum images at 36, 20, 6 and 3 cm show good alignment with the optical (MCELS) feature and also coincide with the maximum emission from the X-rays.

Supernova remnants can show significant Hα, [S II] and [O III] line emission if they are in the radiative phase. In this case, the flux ratio [S II]/Hα is a crucial parameter to distinguish between SNRs and e.g., HII regions (Levenson et al. 1995). However, the [S II]/Hα ratio around [HP99] 456 is ~0.3, which is not necessarily indicative of SNR emission.

Hα emission is spatially coincident with the hard emitting region, but additional studies are required to determine if they are associated or not.

4. Discussion

Thanks to the high sensitivity of *XMM-Newton*, a recent observation of the field of [HP99] 456 has revealed the existence of two emitting components. The softer component presents a circular morphology and is firmly identified as a new SNR, designated XMMU J0541.8-6659. The nature of the emitting region with harder spectrum is still unclear, but we examined the possible identification as a PWN or a background AGN.

4.1. Properties of the newly identified SNR XMMU J0541.8-6659

X-ray data reveal a large structure of soft emission close to the ROSAT PSPC source [HP99] 456 in the LMC. Analyses performed in different energy ranges indicate that this source dominates the X-ray emission below 1.0 keV.

The spectrum of the SNR XMMU J0541.8-6659 can be modelled with an absorbed component representing a plasma in non-equilibrium ionisation characterised by a temperature of ~0.49 keV, which is the average of the typical temperature of previously detected SNRs in the LMC. We note that the spectral parameters quoted in Table 3 are consistent with the parameters of the unambiguously identified SNRs in the LMC (Klimek et al. 2010; Levenson et al. 1995; Williams et al. 1999, 2004). It further supports the identification of this thermal emission with an SNR.

The soft emitting region is firmly identified as a new SNR, in view of its morphology and X-ray spectrum. It has a maximum diameter of ~5.0′, which corresponds to a maximum extent of ~73 pc at a distance of ~50 kpc. Therefore, XMMU J0541.8-6659 is one of the largest SNR observed in the LMC (Williams et al. 1999; Klimek et al. 2010).

However, the large extent of the source does not necessarily imply an old age for the SNR. Indeed, assuming the SNR to be in the Sedov phase, the dynamic age of the source can be estimated using the shock temperature as follows:

$$k_{\rm B}T_{\rm s} = 1.8 \times 10^5 \left(\frac{R_{\rm s}}{t}\right)^2 \ {\rm keV}, \quad (1)$$

where $k_{\rm B}$ is the Boltzmann constant, $T_{\rm s}$ is the temperature of the shock, which is comparable here to the plasma temperature estimated in Sect. 3.2.3, $R_{\rm s}$ is the radius of the shock (in pc) and t is the age of the SNR (in yr).

From the spectral fit yielding a plasma temperature of $k_{\rm B}T_{\rm s} \approx 0.49$ keV, we derived an age of ~23 kyr. This value is well below the age of previous largely-extended SNRs detected in the LMC (e.g. Klimek et al. 2010; Williams et al. 2004).

This result means that the large extent of the source is not due to its high age, but rather to an expansion in a probably rarefied ambient medium. This is not surprising knowing the position of XMMU J0541.8-6659 at the north-east part of the LMC, where the gas density is quite low.

As a legacy project of the *Spitzer* Space Telescope, a survey of the MCs has been carried out called "Surveying the Agents of Galaxy Evolution" (SAGE)[4] (Meixner et al. 2006) to obtain images and spectra of the dust emission. A uniform survey of the LMC was performed in a 7° × 7° by the Infrared Array Camera (IRAC, dedicated to near infrared observations at wavelength 3.6, 4.5, 5.8, and 8 μm) and Multiband Imaging Photometer for *Spitzer* (MIPS, mid- and far-infrared observations at wavelengths 24, 70, and 160 μm). The near-infrared emission (at 5.8 μm) in the region surrounding the source [HP99] 456 is presented in Fig. 7. *Spitzer*-SAGE observations (Meixner et al. 2006) reveal dust emission spatially coincident with the eastern half of the shell-like soft emitting region. However, there is no clear indication that this dust emission is associated to the source XMMU J0541.8-6659.

[4] *Spitzer*-SAGE: http://sage.stsci.edu/index.php

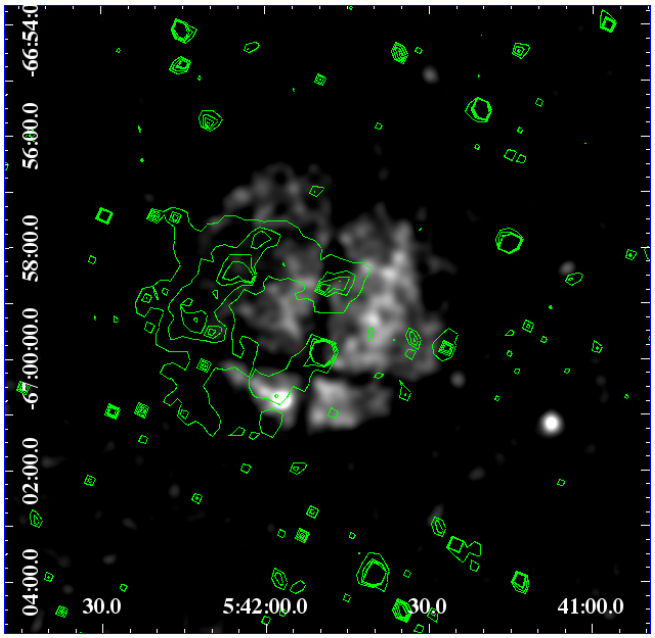

Fig. 7. Soft X-ray emission of XMMU J0541.8-6659. The contours of the near-infrared emission (*Spitzer*, 5.8 μm) are overlaid for comparison.

4.2. Hard-emission region: a PWN or background AGN?

Energy-dependent morphological studies of the X-ray emission in the surroundings of [HP99] 456 have revealed an extended elongated structure located within the SNR, which dominates the X-ray emission above 1.0 keV. Its centre is located ~1′ from the centre of the SNR. This hard emission region has an apparent extent of ~0.9′, corresponding to ~13 pc at a distance of ~50 kpc and a non-thermal spectrum. However, the angular resolution of *XMM-Newton* does not allow us to clarify if this hard source is indeed extended (with substructure) or if it is a conglomerate of point sources. A careful look at the ROSAT images reveals that the position of [HP99] 456 is consistent with the hard source detected with *XMM-Newton* and in particular with the more northern knot in the hard emission (see Fig. 1). Hence, a possible association between the soft and the hard components and the exact nature of the hard X-ray source remains unclear. The radio observations reveal several point sources at the position of the northern X-ray knot. This may point towards an identification as a pulsar with PWN. However, equivalently, one may argue for an existence of several background sources such as AGN. We investigate the different scenarios below.

Firstly, we examine the possibility that the hard X-ray emitting region is associated to background AGN. With a flux of 5.1×10^{-14} erg cm^{-2} s^{-1} (0.5–2 keV), we expect to see ~12 AGN per square degree in the sky (Rosati et al. 2002). We have an 8% probability for an AGN inside a 5.0′ × 4.5′ SNR shell. This low probability and the non-detection of any similar morphological (jet-like) structure either in radio, IR or in optical renders an association of the hard X-ray component with an AGN quite unlikely.

It is worth noticing that the different values of absorption obtained during the spectral fit of the hard and soft emitting regions may indicate that they are located at different distances from us. While the absorption of the shell is consistent with the SNR being located in the LMC, the slightly higher absorption of the hard emission suggests that the source might be located behind the SNR.

Secondly, we consider the possible association of the hard X-ray component with a PWN. Three radio sources are embedded in the hard and narrow X-ray component. The brightest radio source presents a spectrum that can be modelled with a power-law of index $\alpha \approx -1.0$ which is consistent with spectra of pulsars. If this radio source is indeed a pulsar, then it might power a PWN that would be seen in the X-ray domain. Timing observations are required to confirm or invalidate this identification. Furthermore, it is worth noticing that with a spectral index of $\Gamma = 1.8 \pm 0.3$, the spectrum of the hard X-ray emitting source is similar to spectra of PWNe in the Milky Way (spectral indices ranging from –2.5 to –1.2; Kargaltsev & Pavlov 2008, 2010) but also typical for AGN.

The multi-frequency observations along with the spectral and morphological results of our X-ray and radio data analyses do not uniquely identify the nature of the hard X-ray emission embedded in the SNR XMMU J0541.8-6659. Deeper X-ray observations with higher angular resolution are required to differentiate between the two scenarios.

5. Conclusions

A recent X-ray observation with *XMM-Newton* of [HP99] 456 previously discovered by ROSAT led to the identification of a new SNR (XMMU J0541.8-6659) in the LMC, which presents a shell-like morphology and a soft thermal spectrum. No clear correlation can be found between the X-ray and optical emission. The physical properties (temperature, size, etc.) of this new SNR are consistent with SNRs previously identified in the LMC by X-ray observations (Levenson et al. 1995; Klimek et al. 2010; Williams et al. 1999, 2004).

Additional analyses of the *XMM-Newton* data have revealed a harder and narrower emitting region within the shell, which may be a PWN or background AGN. This emission is likely the counterpart of the hard source discovered by ROSAT. Follow-up observations with ATCA revealed several radio point sources coincident with the hard emitting region, one of which could be a pulsar. Deeper observations of the hard X-ray emitting region with the *Chandra* X-ray Observatory will help to distinguish between the different scenarios and to unveil its nature.

Acknowledgements. The XMM project is supported by the Bundesministerium für Wirtschaft und Technologie/Deutsches Zentrum für Luft- und Raumfahrt (BMWI/DLR, FKZ 50 OX 0001) and the Max-Planck Society. The Australia Telescope Compact Array is part of the Australia Telescope, which is funded by the Commonwealth of Australia for operation as a National Facility managed by the CSIRO. This work is based in part on observations made with the *Spitzer* Space Telescope, obtained from the NASA/IPAC Infrared Science Archive, both of which are operated by the Jet Propulsion Laboratory, California Institute of Technology under a contract with the National Aeronautics and Space Administration. The Magellanic Clouds Emission Line Survey (MCELS) data are provided by R. C. Smith, P. F. Winkler, and S. D. Points. The MCELS project has been supported in part by NSF grants AST-9540747 and AST-0307613, and through the generous support of the Dean B. McLaughlin Fund at the University of Michigan, a bequest from the family of Dr. Dean B. McLaughlin in memory of his lasting impact on Astronomy. The National Optical Astronomy Observatory is operated by the Association of Universities for Research in Astronomy Inc. (AURA), under a cooperative agreement with the National Science Foundation. M.-H. Grondin is supported by the BMBF/DLR grant #50-0R-1009.

References

Arnaud, K. A. 1996, Astronomical Data Analysis Software and Systems V, ed. G. Jacoby, & J. Barnes, ASP Conf. Ser., 101, 17
Badenes, C., Maoz, D., & Draine, B. T. 2010, MNRAS, 407, 1301
Bandiera, R., & Petruk, O. 2010, A&A, 509, A34

Bojičić, I. S., Filipović, M. D., Parker, Q. A., et al. 2007, MNRAS, 378, 1237
Borkowski, K. J., Sarazin, C. L., & Blondin, J. M. 1994, ApJ, 429, 710
Borkowski, K. J., Lyerly, W. J., & Reynolds, S. P. 2001, ApJ, 548, 820
Briel, U. G., & Pfeffermann, E. 1986, Nuclear Instruments and Methods in Physics Research Section A, 242, 376
Cajko, K. O., Crawford, E. J., & Filipović, M. D. 2009, Serbian Astron. J., 179, 55
Crawford, E. J., Filipović, M. D., Haberl, F., et al. 2010, A&A, 518, A35
Desai, K. M., Chu, Y.-H., Gruendl, R. A., et al. 2010, AJ, 140, 584
Dickel, J. R. 2005, AAS Meeting, 207, 27, 1403
Dopita, M. A., Blair, W. P., Long, K. S., et al., 2010, ApJ, 710, 964
Dorman, B., & Arnaud, K. A. 2001, Astronomical Data Analysis Software and Systems X, ed. F. R. Harnden, Jr., F. A. Primini, & H. E. Payne, 238, 415
Filipović, M. D., Pietsch, W., Haynes, R. F., et al. 1998, A&AS, 127, 119
Filipović, M. D., Payne, J. L., Reid, W., et al. 2005, MNRAS, 364, 217
Filipović, M. D., Haberl, F., Winkler, P. F., et al. 2008, A&A, 485, 63
Freedman, W. L., Madore, B. F., Gibson, B. K., et al. 2001, ApJ, 553, 47
Freyberg, M. J., Pfeffermann, E., & Briel, U. G. 2001a, Proc. Symposium New visions of the X-ray Universe in the *XMM-Newton* and Chandra era, November 2001, ESTEC, The Netherlands
Freyberg, M. J., Briel, U. G., Dennerl, J., et al. 2001b, Proc. Symposium New visions of the X-ray Universe in the XMM-Newton and Chandra era, November, ESTEC, The Netherlands
Gaensler, B. M., & Slane, P. O. 2006, ARA&A, 44, 17
Gaensler, B. M., Hendrick, S. P., Reynolds, S. P., & Borkowski, K. J. 2003, ApJ, 594, L111
Green, D. A. 2009, BASI, 37, 45
Haberl, F., & Pietsch, W., 1999, A&AS, 139, 277
Hamilton, A. J. S., Sarazin, C. L., & Chevalier, R. A. 1983, ApJS, 51, 115
Hughes, J. P., Rafelski, M., Warren, J. S., et al. 2006, ApJ, 645, L117
Hughes, A., Staveley-Smith, L., Kim, S., Wolleben, M., & Filipović, M. 2007, MNRAS, 382, 543
Kargaltsev, O., & Pavlov, G. G. 2008, AIPC, 983, 171
Kargaltsev, O., & Pavlov, G. G. 2010, AIPC, 1248, 25
Klimek M. D., Points, S. D., Smith, R. C., Shelton, R. L., & Williams, R. 2010, ApJ, 725, 2281
Kuntz, K. D., & Snowden, S. L. 2010, ApJS, 188, 46
Long, K. S., Blair, W. P., & Winkler, P. F. 2010, ApJS, 187, 495
Levenson, N. A., Kischner, R. P., Blair, W. P., & Winkler, P. F. 1995, AJ, 110, 739
Liedahl, D. A., Osterheld, A. L., & Goldstein, W. H. 1995, ApJ, 438, L11
Macri, L. M., Stanek, K. Z., Bersier, D., Greenhill, L. J., & Reid, M. J. 2006, ApJ, 652, 1133
Manchester, R. N., Hobbs, G. B., Teoh, A., & Hobbs, M. 2005, AJ, 129, 1993
Mark, H., Price, R., Rodrigues, R., Seward, F. D., & Swift, C. D. 1969, ApJ, 155, L143
Meixner, M., Gordon, K. D., Indebetouw, R., et al. 2006, AJ, 132, 2268
Mills, B. Y., Turtle, A. J., Little, A. G., & Durdin, J. M. 1984, Austr. J. Phys., 37, 321
Owen, R. A., Filipović, M. D., Ballet, J., et al. 2011, A&A, 530, A132
Payne, J. L., White, G. L., Filipović, M. D., & Pannuti, T. G. 2007, MNRAS, 376, 1793
Pfeffermann, E., Briel, U. G., Hippmann, H., et al. 1987, Soft X-ray optics and technology, Proc. Meeting, Berlin, SPIE, 733, 519
Rosati, P., Tozzi, P., Giacconi, R., et al. 2002, ApJ, 566, 667
Russell, S. C., & Dopita, M. A. 1992, ApJ, 384, 508
Sault, B., & Killeen, N. 2011, Users Guide, Australia Telescope National Facility
Sault, R. J., & Wieringa, M. H. 1994, A&AS, 108, 585
Seward, F. D., Williams, R. M., Chu, Y.-H., Gruendl, R. A., & Dickel, J. R. 2010, AJ, 140, 177
Smith, R. C., Leiton, R., & Pizarro, S. 2000, ASP Conf. Proc., 221, 83
Smith, R. C., Points, S., & Winkler, P. F., 2006, NOAO Newsletter, 85, 6
Stark, A. A., Gammie, C. F., Wilson, R. W., et al. 1992, ApJ, 79, 77
Strüder, L., Briel, U., Dennerl, K., et al. 2001, A&A, 365, L18
Stupar, M., Parker, Q. A., & Filipović, M. D. 2008, MNRAS, 390, 1037
Trümper, J. 1982, Adv. Space Res., 2, 241
Turner, M. L. J., Abbey, A., Arnaud, M., et al. 2001, A&A, 365, L27
Turtle, A. J., & Mills, B. Y. 1984, Astronomical Society of Australia, 5, 537
Williams, R. M., Chu, Y.-H., Dickel, J. R., et al. 1999, ApJS, 123, 467
Williams, R. M., Chu, Y.-H., Dickel, J. R., et al. 2004, ApJ, 613, 948
Williams, R. M., Chu, Y., Dickel, J. R., et al. 2005, ApJ, 628, 704

A&A 544, A144 (2012)
DOI: 10.1051/0004-6361/201219025

Astronomy & Astrophysics

Supernova remnants and candidates detected in the *XMM-Newton* M 31 large survey⋆,⋆⋆

M. Sasaki[1], W. Pietsch[2], F. Haberl[2], D. Hatzidimitriou[3], H. Stiele[4], B. Williams[5], A. Kong[6], and U. Kolb[7]

[1] Institut für Astronomie und Astrophysik, Universität Tübingen, Sand 1, 72076 Tübingen, Germany
e-mail: sasaki@astro.uni-tuebingen.de
[2] Max-Planck-Institut für extraterrestrische Physik, Giessenbachstraße, 85748 Garching, Germany
[3] Department of Astrophysics, Astronomy and Mechanics, Faculty of Physics, University of Athens, Panepistimiopolis, 15784 Zografos, Athens, Greece
[4] INAF – Osservatorio Astronomico di Brera, via E. Bianchi 46, 23807 Merate (LC), Italy
[5] Department of Astronomy, Box 351580, University of Washington, Seattle, WA 98195, USA
[6] Institute of Astronomy and Department of Physics, National Tsing Hua University, 30013 Hsinchu, Taiwan
[7] Dept of Physical Sciences, The Open University, Walton Hall, Milton Keynes, MK7 6AA, UK

Received 13 February 2012 / Accepted 20 June 2012

ABSTRACT

Context. We present the analysis of supernova remnants (SNRs) and candidates in M 31 identified in the *XMM-Newton* large programme survey of M 31. Supernova remnants are among the brightest X-ray sources in a galaxy. They are good indicators of the recent star-formation activities of galaxies and the interstellar environment in which they evolve.
Aims. By combining the X-ray data of sources in M 31 with optical data as well as optical and radio catalogues, we aim to compile a complete, revised list of SNRs emitting X-rays in M 31 detected with *XMM-Newton*, study their luminosity and spatial distributions, and understand the X-ray spectra of the brightest SNRs.
Methods. We analysed the X-ray spectra of the 12 brightest SNRs and candidates that have been observed with *XMM-Newton*. Our study of the four brightest sources allowed us to perform a more detailed spectral analysis and compare different models to describe their spectrum. For all M 31 large programme sources, we searched for their optical counterparts in the Hα, [S II], and [O III] images of the Local Group Galaxy Survey.
Results. We confirm 21 X-ray sources as counterparts to known SNRs. In addition, we identify 5 new X-ray sources as X-ray and optically emitting SNRs. Seventeen sources are no longer considered as SNR candidates. We thus create a list of 26 X-ray SNRs and 20 X-ray SNR candidates in M 31 based on their X-ray, optical, and radio emission, which is the most recent complete list of X-ray SNRs in M 31. The brightest SNRs have X-ray luminosities of up to 8×10^{36} erg s^{-1} in the 0.35–2.0 keV band.

Key words. ISM: supernova remnants – galaxies: ISM – galaxies: individual: M 31 – X-rays: galaxies – X-rays: ISM

1. Introduction

The Andromeda galaxy (M 31) is the largest galaxy in the Local Group and the nearest spiral galaxy to the Milky Way. Its size and mass are comparable to those of our Galaxy. Therefore, this archetypical spiral galaxy provides a unique opportunity to study and understand the nature and the evolution of a galaxy similar to our own. Various authors have studied the star-formation histories in different regions of M 31 using observations with both the *Hubble* Space Telescope (HST) and large ground-based telescopes (e.g., the Local Group Galaxy Survey [LGGS] performed at the Kitt Peak National Observatory [KPNO] and the Cerro Tololo Inter-American Observatory, Williams 2003; Massey et al. 2006). Deep HST photometry has shown that the mean age of the disk of M 31 is ~6–8 Gyr (Brown et al. 2006) and that the average metallicity is [Fe/H] ≈ –0.6 dex (Bellazzini et al. 2003). Williams (2003) measured a mean star-formation rate of about 1 $M_\odot$ yr^{-1} in the full disk of M 31. Tabatabaei & Berkhuijsen (2010) studied the dust distribution and computed the de-reddened Hα distribution in the disk of M 31. They derived a star-formation rate of 0.27 $M_\odot$ yr^{-1} for the radial range of $6 < R < 17$ kpc with an increase to about twice the mean value at around $R = 10$ kpc. Although the current star-formation rate in M 31 is lower than that of the Milky Way, M 31 seems to have undergone more active star-formation periods. In addition to the well-known dust ring at a radius of ~10 kpc (Brinks & Shane 1984; Dame et al. 1993) that contains enhanced star formation, Block et al. (2006) found an inner dust ring with a radius of 1–1.5 kpc, which had apparently been created in an encounter with a companion galaxy, most likely M 32.

First observations of individual sources in M 31 in X-rays were performed with the *Einstein* Observatory (Giacconi et al. 1979) in the energy band of 0.2–4.5 keV and yielded the first catalogues of X-ray sources in the field of M 31 (van Speybroeck et al. 1979; Trinchieri & Fabbiano 1991). In the 1990s, ROSAT (Trümper 1982) observed M 31 in the 0.1–2.4 keV band and revealed a total of 560 sources in the field of M 31 (Supper et al. 1997, hereafter SHP97; Supper et al. 2001, hereafter SHL01). The next generation X-ray satellites *Chandra* X-ray Observatory (Weisskopf et al. 2002) and X-ray Multi-Mirror Mission (*XMM-Newton*, Jansen et al. 2001), which were both launched in 1999, have significantly improved on the spatial and spectral resolutions of the prior X-ray telescopes. They have also

⋆ Based on observations obtained with *XMM-Newton*, an ESA science mission with instruments and contributions directly funded by ESA Member States and NASA.
⋆⋆ Appendices are available in electronic form at http://www.aanda.org

performed several observations of M 31 and allowed us to obtain a comprehensive list of X-ray sources and study individual sources (e.g., Osborne et al. 2001; Kong et al. 2002b; Kaaret 2002; Pietsch et al. 2005; Stiele et al. 2008; Barnard et al. 2008). The entire galaxy M 31 was observed by *XMM-Newton* in a large programme (LP) between June 2006 and February 2008 with the European Photon Imaging Cameras (EPICs, Strüder et al. 2001; Turner et al. 2001) as prime instruments. The *XMM-Newton* source catalogue with 1897 sources was published by Stiele et al. (2011, hereafter SPH11).

Supernova remnants are the aftermath of stellar explosions releasing a large amount of energy in galaxies. The spherically expanding blast-wave shock produces a cavity in the interstellar medium with a very low-density, high-temperature interior, which emits predominantly soft X-ray radiation. In addition, relativistic electrons and heavier particles in SNRs emit synchrotron emission that can be detected in radio and in some cases in X-rays. After a few thousand years, the SNR becomes radiative, i.e., the radiative losses in SNR shocks expanding into the ambient ISM become non-negligible and the shell emits energy as both ultraviolet and optical line emission. If a neutron star is created in the supernova explosion, a pulsar and/or a pulsar wind nebula (PWN) can be found inside the SNR, in which particles are accelerated in the strong magnetic field of the neutron star and thus non-thermal emission is produced. Supernova remnants in M 31 have been mainly detected in the optical (e.g., D'Odorico et al. 1980; Dennefeld & Kunth 1981; Blair et al. 1981) and combined optical and radio studies (Braun & Walterbos 1993). The X-ray survey performed with ROSAT led to the detection of 16 X-ray SNRs (Supper et al. 2001), while 21 were detected and identified with *XMM-Newton* (Pietsch et al. 2005). Kong et al. (2002a) presented the first resolved X-ray image of an SNR in M 31 taken with *Chandra*, while Kong et al. (2003) and Williams et al. (2004b) reported on the discovery of additional SNRs in M 31 based on *Chandra* data.

In this paper, we present the study of all X-ray sources that have been proposed as SNRs or SNR candidates in M 31 based on a complete survey of M 31 performed within the framework of the LP of *XMM-Newton* (SPH11). Through a detailed study of each SNR and candidate detected by *XMM-Newton*, we obtained a more representative sample of SNRs in M 31 consisting of X-ray and optically confirmed SNRs as well as bona-fide candidates. We performed a spectral analysis of the bright SNRs and candidates in the catalogue of SPH11. Using optical data of the LGGS, we searched for the optical counterparts of the X-ray SNRs and candidates showing optical Hα, [S II], and [O III] emission from the radiative shock. We newly calibrated the LGGS data to obtain optical fluxes and computed the [S II]/Hα flux ratio, which is an indicator of SNR emission in the optical. This study has also allowed us to identify sources that are most probably not SNRs. In addition, we performed statistical studies using the revised list of SNRs and candidates in M 31 detected with *XMM-Newton*.

2. Data

2.1. X-ray data

XMM-Newton performed a survey of M 31 as a large programme between June 2006 and February 2008. The analysis of the entire data of this survey, including additional archival data taken between June 2000 and July 2004, is presented by SPH11. These observations in total covered the entire D_{25} ellipse of M 31 down to a limiting luminosity of $\sim 10^{35}$ erg s^{-1} in the 0.2–4.5 keV band. A total of 1897 sources were detected in the *XMM-Newton* survey data (SPH11). The sources were either identified or classified based on their X-ray hardness ratios, spatial extent, and variability, as well as through cross-correlations with catalogues in the X-ray, optical, infrared, and radio wavelengths. In the end, 25 sources were identified by SPH11 as known SNRs and 31 additional sources were classified as SNR candidates based on their X-ray properties. Their positions are shown on a Digitised Sky Survey (DSS) 2 blue image in Fig. 1. While the main objective of the work by SPH11 was to create a source catalogue of all *XMM-Newton* detections in the field of M 31, we are interested in one particular class of objects, namely SNRs, which are soft and intrinsically extended sources. We therefore reprocessed and analysed the data using XMMSAS version 10.0.0 to obtain the data products that are best suited to the study of SNRs. We created mosaic images of data taken from all observations between 2006 and 2010 in the bands 0.2–1.0 keV, 1.0–2.0 keV, and 2.0–4.5 keV. The images are binned with $2'' \times 2''$ pixel size and smoothed with a Gaussian of $10''$ width. The three-colour images created with the three bands zoomed in on each source are shown in Figs. 2, 3, and from Fig. A.1.

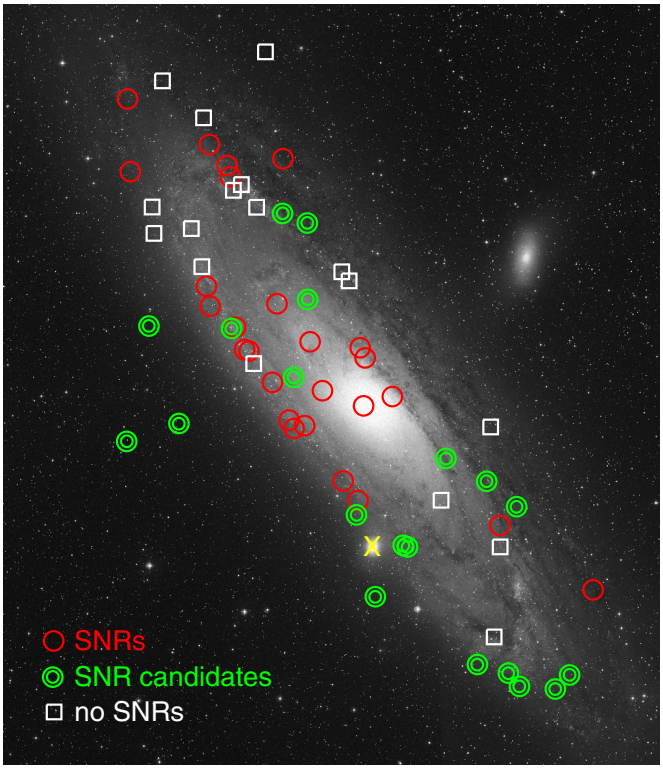

Fig. 1. The positions of X-ray SNRs and candidates detected with *XMM-Newton* are shown on a Digitised Sky Survey 2 (blue) image. The sources are marked with new classifications of this work (see Sect. 4). In addition, the position of the dwarf elliptical M 32, which is a satellite galaxy of M 31, is indicated by a yellow cross.

The X-ray energy bands used for the detection and calculation of hardness ratios by SPH11 are B_1 = 0.2–0.5 keV, B_2 = 0.5–1.0 keV, B_3 = 1.0–2.0 keV, B_4 = 2.0–4.5 keV, and B_5 = 4.5–12 keV. The hardness ratios and errors are defined as $HR_i = (C_{i+1} - C_i)/(C_{i+1} + C_i)$ and $EHR_i = 2 \times \sqrt{(C_{i+1} \times EC_i)^2 + (C_i \times EC_{i+1})^2}/(C_{i+1} + C_i)^2$, $i = 1, 2, 3, 4$. The numbers C_i and EC_i are the count rates and errors in the energy band i. Table B.1 lists the SNRs and candidates classified

Table 1. Additional X-ray sources in the *XMM-Newton* M 31 survey catalogue of Stiele et al. (2011) analysed in this work.

[SPH11] ID	RA (2000.0)	Dec (2000.0)	Pos. error [arcsec]	Rate [cts/s]	ML^a	$HR_1{}^b$	$HR_2{}^b$	$HR_3{}^b$	$HR_4{}^b$
Additional SNR candidates									
811	00 42 10.60	+40 51 49.1	6.19	3.0e–3 ± 1.0e–4	8.3	–0.46 ± 0.46	0.48 ± 0.46	–0.83 ± 0.36	
833	00 42 14.60	+40 52 04.7	4.30	3.2e–3 ± 5.0e–5	26	0.73 ± 0.17	–0.09 ± 0.17	–0.84 ± 0.23	
[c]1121	00 43 03.70	+41 37 17.2	4.47	5.4e–3 ± 1.0e–4	17		0.45 ± 0.24	0.14 ± 0.19	–0.23 ± 0.36
1286	00 43 42.08	+41 47 09.5	7.42	2.2e–3 ± 5.0e–5	8.6	0.74 ± 0.27	–0.38 ± 0.23	–0.85 ± 0.46	
[d]1461	00 44 28.62	+41 49 48.7	7.00	2.7e–3 ± 7.0e–5	8.7	0.63 ± 0.33	–0.58 ± 0.29		
[c]1468	00 44 30.56	+41 23 06.2	4.84	4.0e–3 ± 6.0e–5	38		0.82 ± 0.16	0.16 ± 0.17	–0.66 ± 0.30
[c]1611	00 45 18.44	+41 39 36.3	3.42	7.5e–3 ± 8.0e–5	94		0.85 ± 0.17	0.29 ± 0.11	–0.13 ± 0.14

Notes. Sources in this table have been studied as possible SNR candidates based on optical data (see Sect. 2.1). [(a)] Detection likelihood. [(b)] Hardness ratios. [(c)] Classified as a hard source by SPH11. [(d)] Classified as a foreground star candidate by SPH11.

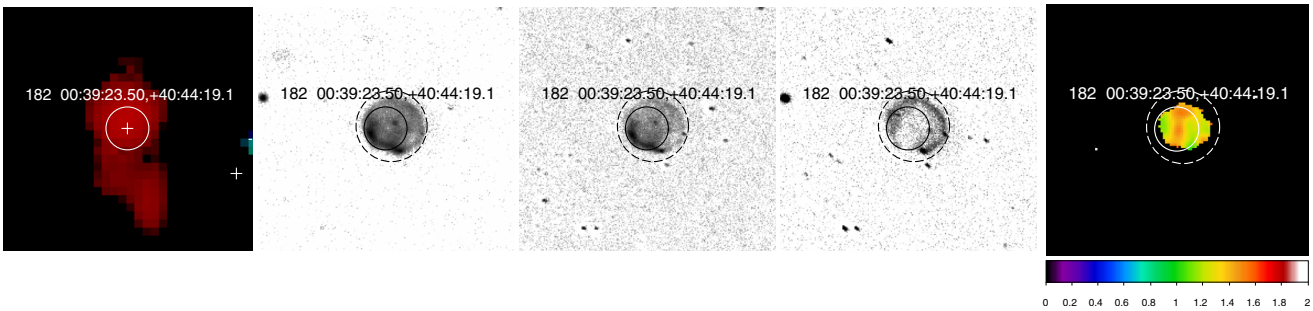

Fig. 2. *XMM-Newton* three-colour image (red 0.2–1.0 keV, green 1.0–2.0 keV, blue 2.0–4.5 keV), continuum-subtracted LGGS Hα, [S II], and [O III] images, and an [S II]/Hα ratio image with *XMM-Newton* 3σ positional error circle (solid) for source [SHP11] 182. The dashed circle shows the extraction region for the optical emission. The shown area has a size of ∼1′ × 1′. The label gives the source number of the *XMM-Newton* catalogue (SPH11) followed by the coordinates. The positions of all detected *XMM-Newton* sources are marked in the *XMM-Newton* images (left) with crosses. Figure A.1 shows images of other sources.

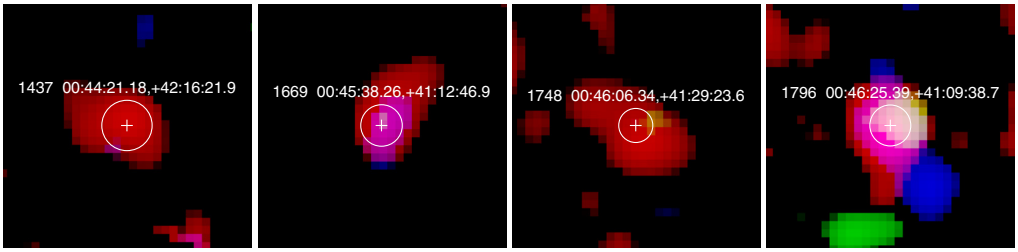

Fig. 3. *XMM-Newton* colour images (red 0.2–1.0 keV, green 1.0–2.0 keV, blue 2.0–4.5 keV) of sources 1437, 1669, 1748, and 1796, which are located outside the regions covered by LGGS (see Sect. 2.2). The area shown has a size of ∼1′ × 1′.

by SPH11, along with their positions, count rates, detection likelihoods, and hardness ratios. If a hardness ratio HR_1, HR_2, HR_3, or HR_4 is not given in Table B.1, it was not calculated owing to the low quality photon statistics in the corresponding bands. The sources in Table 1 were not classified as SNR candidates by SPH11. However, the study of optical data while planning follow-up observations of the *XMM-Newton* LP survey of M 31 revealed shell-like optical emission-line sources at the X-ray positions, indicating that these sources might be SNRs. We therefore included these sources in our analysis.

2.2. Optical data

M 31 was observed as part of the Local Group Galaxy Survey, which was carried out with the 4 m telescope at KPNO (Massey et al. 2006). Continuum images as well as narrow-band Hα, [S II], and [O III] images are available for the fields, which in total cover the entire galaxy. Each field covers ∼35′ × 35′ and the median seeing of the observations was ∼1″. Bias-corrected and flat-fielded images can be downloaded from the LGGS web site[1]. For the emission-line images, the photometric uncertainty is ∼5%, according to the LGGS web page. We subtracted scaled *R* band continuum images from the Hα and [S II] images and scaled *V* band continuum images from the [O III] images.

Figures 2 and A.1 show continuum-subtracted LGGS Hα, [S II], and [O III] images, and an [S II]/Hα ratio image with the *XMM-Newton* 3σ positional error circle for each source, along with the *XMM-Newton* images described in Sect. 2.1. Four sources ([SPH11] 1437, 1669, 1748, and 1796) are located outside the regions covered by LGGS. The *XMM-Newton* three-colour images of these sources are shown in Fig. 3. We used image data from the Data Release 8 of the Sloan Digital Sky Survey (SDSS) III[2] in order to search for possible optical counterparts to these sources. The *u*, *r*, *i*, and *z* band images are shown in Figs. 4

[1] http://www.lowell.edu/users/massey/lgsurvey.html
[2] http://www.sdss3.org/

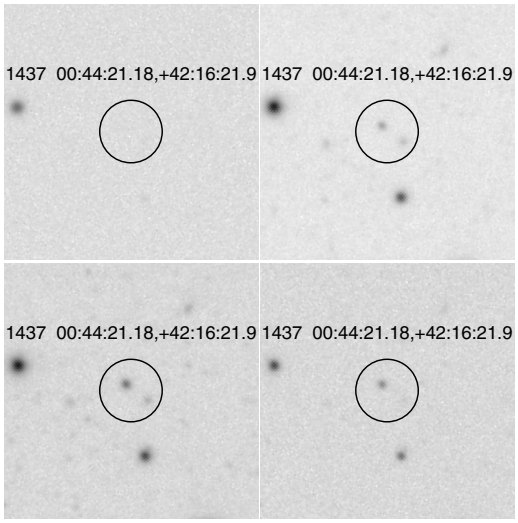

Fig. 4. SDSS-III images (*upper left*: *u* band, *upper right*: *r* band, *lower left*: *i* band, *lower right*: *z* band) of [SPH11] 1437. The shown area has a size of ∼1′ × 1′. For sources [SPH11] 1669, 1748, and 1796 see Fig. C.1.

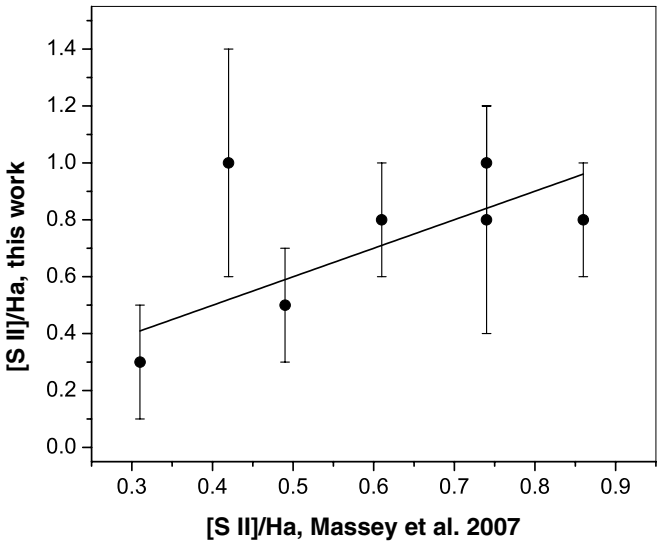

Fig. 5. [S II]/Hα flux ratios of sources, for which we computed the flux using the LGGS data and there is a corresponding entry in the emission-line source catalogue of Massey et al. (2007). The fitted line with a slope of 1.0 is shown.

and C.1. For all sources, we also checked the HST archive for optical images to search for possible counterparts. While for most sources the LGGS and SDSS images were sufficient to identify possible counterparts, in the case of [SPH11] 1505 the HST image revealed a background galaxy, which is not resolved in the LGGS images, thus allowed its classification as a background source (see Sect. 4.3.7).

The SNRs and their candidates are located in fields F2 to F9 of the LGGS survey. We first calibrated the images in fields F4, F5, and F6 based on the Hα, [S II], and [O III] fluxes of [SPH11] 883 (r2-57) and [SPH11] 1040 (r3-84) determined by Williams et al. (2004b), allowing us to calculate the flux in erg cm^{-2} s^{-1} from the count rates in the images. The publication of Williams et al. (2004b) also includes the Hα and [S II] fluxes of [SPH11] 1234. The [O III] flux for [SPH11] 1234 was obtained from the publication of Dennefeld & Kunth (1981). As the LGGS fields have a small overlap with the adjacent fields (e.g., F3 has an overlap with F2 and F4), we can, e.g., calibrate F3, if F4 is calibrated and there are sources that are observed in both F3 and F4. In addition, Hα and [S II] fluxes of the sources [SPH11] 1539 and 1599 could be obtained from Braun & Walterbos (1993). By using the fluxes of [SPH11] 1539 and 1599 in F4, which were observed in F2, F3, and F4, and comparing the values to their fluxes published by Braun & Walterbos (1993), we calibrated the fields F2 and F3. For fields F7, F8, and F9, we derived the count-rate-to-flux conversion factors by using other sources that were observed in many fields, starting with those observed in F6 and F7. For fields F8 and F9, however, we were unable to calibrate the [O III] images as there were no sources with significant [O III] emission observed in both F7 and F8. This flux calibration yields an uncertainty in the flux in the range of 3–20% in most of the fields, but up to 50% in some fields, in which there were only a few sources in overlapping areas.

We compared our list of sources to the catalogue of emission-line objects compiled by Massey et al. (2007). We find seven common objects. In Fig. 5, we plot the [S II]/Hα flux ratios that we derived (see Sect. 3.2) over the values in the Massey et al. (2007) catalogue. Except for one outlier, the correlation is very good with a coefficient of 1.002 ± 0.374 and an intercept of 0.098 ± 0.235 (Fig. 5). The outlier corresponds to LGGS J004452.98+415457.7, which is the point source visible in the *V* band image inside the positional error circle of the *XMM-Newton* source [SPH11] 1539 (Fig. 6, right). The Hα and [S II] fluxes of the optical source associated with [SPH11] 1539 (XMMM31 J004452.82+415458.1) was determined in a larger area covering the entire extended optical source (Fig. 6, left). This is most likely the reason for the discrepancy between our flux ratio and that in the catalogue of Massey et al. (2007) corresponding to the point source. In conclusion, the agreement between our flux ratios and the Massey et al. (2007) values for the small sample of common objects lends credibility to our calibration procedure.

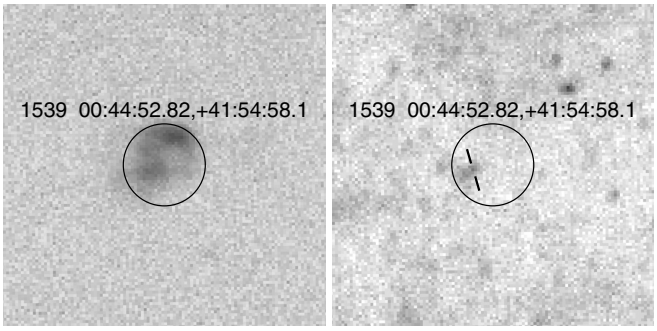

Fig. 6. Continuum-subtracted LGGS Hα (*left*) and LGGS *V* band image (*right*) of [SPH11] 1539. The shown area has a size of ∼30″ × 30″. The *XMM-Newton* positional error circle is shown. The position of LGGS J004452.98+415457.7 is indicated.

We obtained new optical spectra for three sources, [SPH11] 811, 1156, and 1712, in follow-up observations of the *XMM-Newton* LP survey undertaken in the period of 2006–2011. The spectra were acquired with the 3.5 m telescope at the Apache Point Observatory, located in the Sacramento Mountains in Sunspot, New Mexico (USA) in order to identify the optical counterparts of the *XMM-Newton* sources. These optical spectra will be published in a separate paper (Hatzidimitriou

Table 2. Spectral parameters obtained from the fits of the EPIC spectra of [SPH11] 1050, 1066, and 1234.

[SPH11] ID	$N_{\rm H}$ (TBABS2) [10^{21} cm^{-2}]	kT (APEC) [keV]	*norm* (APEC) [cm^{-5}]			Red. χ^2	d.o.f.	$F_{\rm abs}{}^a$ [erg s^{-1} cm^{-2}]
1050	1 (0–17)	0.19 (0.04–0.25)	2e–5			1.0	34	1.1e–14
1066	6 (4–7)	0.18 (0.14–0.20)	9e–4			3.2	29	3.2e–14
1234	0 (0–2)	0.25 (0.05–0.27)	4e–5			2.6	61	5.6e– 14
[SPH11] ID	$N_{\rm H}$ (TBABS2) [10^{21} cm^{-2}]	kT (NEI) [keV]	τ (NEI) [10^{10} s cm^{-3}]	*norm* (NEI) [cm^{-5}]		Red. χ^2	d.o.f.	$F_{\rm abs}{}^a$ [erg s^{-1} cm^{-2}]
1066	3 (2–4)	3.8 (2.8–4.2)	0.6 (0.4–0.8)	1e–5		2.3	26	3.5e–14
1234	0 (0–1)	2.2 (1.8–3.8)	0.9 (0.8–1.2)	4e–6		1.4	60	6.2e–14
[SPH11] ID	$N_{\rm H}$ (TBABS2) [10^{21} cm^{-2}]	kT (APEC1) [keV]	*norm* (APEC1) [cm^{-5}]	kT (APEC2) [keV]	*norm* (APEC2) [cm^{-5}]	Red. χ^2	d.o.f.	$F_{\rm abs}{}^a$ [erg s^{-1} cm^{-2}]
1234	4 (3–6)	0.23 (0.18–0.25)	2.8e–4	0.04 (0.02–0.05)	3.9	1.1	59	6.4e–14

Notes. 90% confidence ranges are given in brackets. [(a)] For 0.35–2.0 keV.

et al., in prep.). In the present work, we only use the results for these three sources to discuss their nature (see Sects. 4.2.3, 4.3.5, and 4.3.11). The telescope was equipped with the Dual Imaging Spectrograph (DIS), a medium dispersion spectrograph with separate collimators for the red and blue part of the spectrum, and two 2048 × 1028 E2V CCD cameras, with the transition wavelength at around 5350 Å.

3. Analysis

3.1. X-ray spectra

Out of the 63 sources in Tables B.1 and 1, only twelve had enough counts to obtain spectra with good statistics. We extracted spectra for these sources and created corresponding ancillary response files and response matrix files.

We analysed spectra that yielded more than five bins with more than 20 counts per bin. The *XMM-Newton* EPIC spectra were all fitted in XSPEC with a model that included two absorption components (fixed TBABS1 for the column density in the Milky Way [MW] in the direction of M 31 of $N_{\rm H}$(MW) = 0.7×10^{21} cm^{-2}, Stark et al. 1992), and a free parameter TBABS2 for additional absorption in M 31) and a thermal emission model. To begin with, we used the emission model APEC, which assumes collisional ionisation equilibrium (CIE). For most of the sources, for which we do not have high quality statistics to study the effect of non-equilibrium ionisation (NEI), this model gives us the average temperature of the hot plasma. The abundances were fixed to solar values (Anders & Grevesse 1989) in all fits. The spectra are all fitted relatively well with a low temperature of $kT \approx 0.2$ keV. The results for the fits using a single APEC model component are listed in the upper part of Table 2 for the brightest sources [SPH11] 1050, 1066, and 1234. For the faintest of the three, [SPH11] 1050, the APEC model reproduces the spectrum fairly well with reduced $\chi^2 = 1.0$ (Fig. 7, top). However, the fits yield no satisfactory results for the brighter sources. Therefore, we also modelled the spectra with a non-equilibrium ionisation model NEI or a combination of two APEC models instead of a single APEC model (see Table 2).

The brightest X-ray SNR in M 31 is [SPH11] 1234 (XMMM31 J004327.93+411830.5). The spectral analysis revealed that its spectrum consists of at least two thermal components with temperatures of $kT = 0.04(0.02–0.05)$ keV and $kT = 0.23(0.18–0.25)$ keV (Table 2 and Fig. 7, middle). It is an SNR that was first identified in the optical with a nice round shell

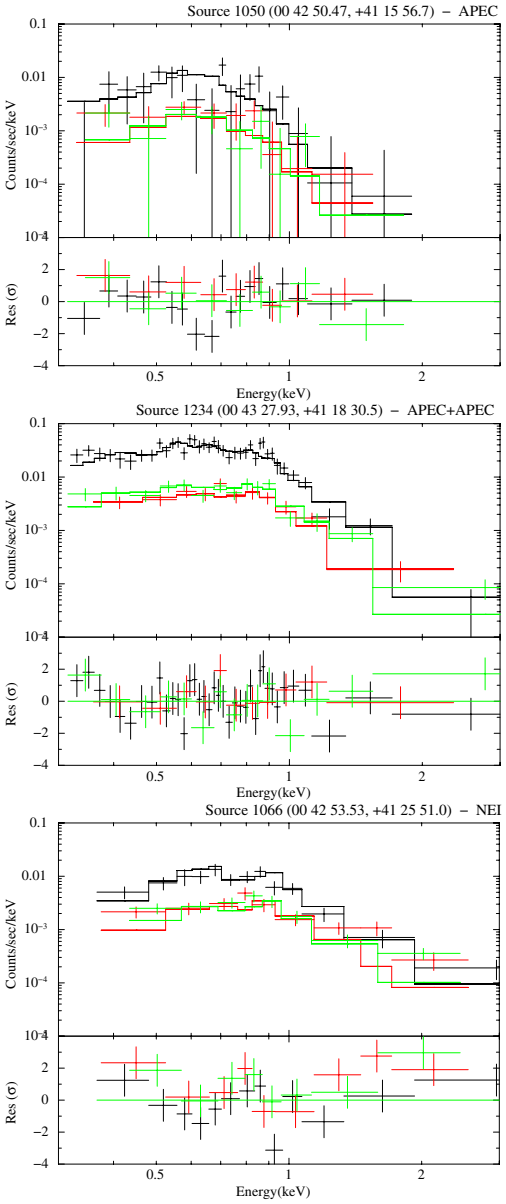

Fig. 7. Spectrum of [SPH11] 1050, 1234, and 1066 with an APEC, APEC+ APEC, and NEI model, respectively. EPIC-pn spectrum with fitted model is shown in black, MOS1 in red, and MOS2 in green.

Table 3. X-ray SNRs in M 31 detected with *XMM-Newton*.

[SPH11] ID	Hα [erg cm^{-2} s^{-1} arcsec^{-2}]	[S II] [erg cm^{-2} s^{-1} arcsec^{-2}]	[O III] [erg cm^{-2} s^{-1} arcsec^{-2}]	[S II]/Hα	L (0.35–2.0 keV)[a] [erg s^{-1}]
		Known SNRs[b]			
182	1.4e–14 ± 2.9e–15	1.5e–14 ± 7.5e–15	N/A	1.1 ± 0.6	2.2e+35
474	2.5e–14 ± 5.2e–15	2.6e–14 ± 1.3e–14	2.3e–14 ± 1.1e–14	1.0 ± 0.5	6.9e+35
883	9.7e–15 ± 5.7e–16	9.2e–15 ± 1.9e–15	2.4e–16 ± 2.7e–17	0.9 ± 0.2	4.0e+35
1040	1.1e–14 ± 6.5e–16	9.0e–15 ± 1.9e–15	1.7e–14 ± 1.9e–15	0.8 ± 0.2	1.0e+36
1050	7.5e–15 ± 4.4e–16	7.7e–15 ± 1.5e–15	0.0	1.0 ± 0.2	1.2e+36
1066	2.2e–14 ± 1.3e–15	1.9e–14 ± 3.9e–15	2.1e–14 ± 2.3e–15	0.9 ± 0.2	3.8e+36
1234	5.6e–14 ± 3.3e–15	4.2e–14 ± 8.7e–15	3.7e–14 ± 4.1e–15	0.7 ± 0.2	8.0e+36
1275	3.0e–14 ± 1.7e–15	2.8e–14 ± 5.8e–15	5.4e–14 ± 6.0e–15	0.9 ± 0.2	3.1e+36
1291	3.1e–17 ± 1.9e–18	0.0	1.8e–17 ± 2.0e–18	0.0	1.8e+36
1328	5.9e–15 ± 3.4e–16	2.5e–15 ± 5.1e–16	1.6e–14 ± 1.8e–15	0.4 ± 0.1	1.2e+36
1351	3.8e–14 ± 2.2e–15	3.1e–14 ± 6.4e–15	6.4e–14 ± 7.2e–15	0.8 ± 0.2	6.5e+35
1386	5.9e–14 ± 3.4e–15	1.3e–14 ± 2.7e–15	6.3e–15 ± 7.1e–16	0.2 ± 0.0	2.2e+35
1410	1.2e–14 ± 6.8e–16	1.1e–14 ± 2.3e–15	7.1e–15 ± 8.0e–16	0.9 ± 0.2	8.5e+35
1497	4.7e–14 ± 2.7e–15	2.5e–14 ± 5.2e–15	3.0e–14 ± 3.4e–15	0.5 ± 0.1	5.9e+35
1522	2.4e–14 ± 1.4e–15	2.5e–14 ± 5.1e–15	1.2e–14 ± 1.3e–15	1.0 ± 0.2	4.4e+35
1539	2.1e–14 ± 6.4e–15	2.1e–14 ± 4.3e–15	2.7e–15 ± 8.2e–16	1.0 ± 0.4	2.1e+35
1587	0.0	0.0	0.0	0.0	3.6e+35
1593	2.6e–14 ± 7.9e–15	2.6e–14 ± 5.4e–15	6.2e–14 ± 1.9e–14	1.0 ± 0.4	1.7e+35
1599	5.8e–14 ± 3.4e–15	5.4e–14 ± 1.1e–14	9.7e–14 ± 2.9e–14	0.9 ± 0.2	2.1e+36
1793	3.5e–16 ± 1.1e–16	2.5e–16 ± 5.2e–17	2.9e–16 ± 8.8e–17	0.7 ± 0.3	5.1e+35
1805	3.2e–17 ± 9.7e–18	9.6e–17 ± 2.0e–17	4.5e–16 ± 1.3e–16	3.0 ± 1.1	8.0e+35
		Newly confirmed SNRs based on optical and X-ray data			
1079	3.9e–15 ± 8.1e–16	3.4e–15 ± 1.7e–15	1.4e–14 ± 7.0e–15	0.9 ± 0.4	5.5e+35
1148	2.3e–16 ± 1.3e–17	1.8e–16 ± 3.7e–17	1.7e–15 ± 1.9e–16	0.8 ± 0.2	2.9e+35
1370	8.2e–17 ± 4.8e–18	6.9e–17 ± 1.4e–17	2.6e–16 ± 7.9e–17	0.8 ± 0.2	3.0e+35
1481	7.6e–14 ± 4.4e–15	6.3e–14 ± 1.3e–14	3.7e–14 ± 4.2e–15	0.8 ± 0.2	4.6e+35
1548	2.1e–15 ± 6.4e–16	2.3e–15 ± 4.8e–16	1.5e–15 ± 4.6e–16	1.1 ± 0.4	2.1e+35

Notes. No [O III] flux was calculated for sources that were only observed in fields F8 and/or F9 ([SPH11] 182; see Sect. 2.2). [(a)] See Sect. 6.1. [(b)] SNRs known from literature. The optical fluxes and the flux ratios were determined from the LGGS data but were not used for the classification.

clearly visible in Hα, [S II], and [O III] (see Sect. D.1.7). As can be seen in the Hα data, the remnant is located in an H II region. The X-ray spectrum therefore seems to be the superposition of the hot gas inside an interstellar bubble and the emission of the SNR.

The second brightest source is [SPH11] 969 (XMMM31 J004239.82+404318.8), which has been suggested to be an SNR candidate based on its soft X-ray spectrum. The spectral analysis by SPH11 revealed that its spectrum is best modelled with a non-equilibrium plasma with a low temperature $kT = 0.2$ keV and a strikingly low ionisation timescale $\tau = 2 \times 10^8$ s cm^{-3} $\approx$ 6 yr cm^{-3}, implying a very low density of $n_e = 6 \times 10^{-4}$ cm^{-3} if the SNR had an age of ~10 000 yr. The source is located at the outer rim of the optical disk of M 31 (green annulus south of M 32 in Fig. 1). Therefore, if this is an SNR it might have been expanding in a very low density medium. We tried to fit its spectrum with a model including a power-law component, which yields an unreasonably high index of $\Gamma = 6.0$ (5.2–7.0). X-ray data of higher quality statistics are necessary to understand the emission of this source.

The third brightest source [SPH11] 1066 (XMMM31 J004253.53+412551.0) is an optically identified SNR and has a rather hard spectrum in X-rays with a high temperature and low ionisation timescale (see Table 2 and Fig. 7, bottom). This spectrum is consistent with that of a young SNR. The statistics are not high enough to verify if there is a non-thermal component.

3.2. Optical flux

As mentioned earlier, except for four sources, the X-ray SNRs and candidates are located in regions covered by the LGGS data. For these sources, we determined the Hα, [S II], and [O III] fluxes and calculated the flux ratio [S II]/Hα. The [S II]/Hα flux ratio is a diagnostic tool to distinguish the shock-ionised diffuse emission of SNRs from those of photoionised H II regions or planetary nebulae. The radiative shocks in SNRs produce a larger [S II]/Hα ratio, typically higher than 0.5 (Braun & Walterbos 1993). Values around [S II]/Hα = 0.4–0.5 might be indicative of an SNR nature, although shells or filaments in H II regions can also reach similar [S II]/Hα ratios. We therefore apply the hard limit of [S II]/Hα > 0.5 for SNRs. To measure the flux, we looked at the optical images for all sources, if available, one by one. If there is optical emission that seems to be the optical counterpart of the X-ray source, the extraction region was adjusted by eye to cover the entire optical emission. For sources without obvious optical emission, the size of the 3σ error circle of the *XMM-Newton* position was used. For instance, the extraction region of [SPH11] 414 in Fig. A.1 was left as it is shown in the figures, whereas for [SPH11] 182 in Fig. 2, the extraction region was increased in size and shifted to cover the entire circular optical source seen in all optical images (dashed circle). The background emission was estimated locally for each source. On the basis of the optical fluxes and the [S II]/Hα ratio, we confirmed five sources with significant Hα, [S II], and [O III] emission and an [S II]/Hα ratio higher than 0.5 as new SNRs (see Table 3).

Table 4. X-ray SNR candidates in M 31 detected with *XMM-Newton*.

[SPH11] ID	Hα [erg cm^{-2} s^{-1} arcsec^{-2}]	[S II] [erg cm^{-2} s^{-1} arcsec^{-2}]	[O III] [erg cm^{-2} s^{-1} arcsec^{-2}]	[S II]/Hα	L (0.35–2.0 keV)[a] [erg s^{-1}]
263	1.4e–14 ± 2.9e–15	1.1e–14 ± 5.5e–15	N/A	0.8 ± 0.4	4.0e+35
294	1.4e–16 ± 2.9e–17	4.2e–17 ± 2.1e–17	N/A	0.3 ± 0.2	2.1e+36
414	0.0	2.3e–17 ± 1.2e–17	N/A	0.0	4.4e+35
419	0.0	5.6e–18 ± 2.8e–18	2.5e–16 ± 1.3e–16	0.0	2.3e+35
441	2.1e–16 ± 4.3e–17	7.5e–17 ± 3.7e–17	N/A	0.4 ± 0.2	4.0e+35
521	1.1e–12 ± 2.3e–13	2.8e–13 ± 1.4e–13	8.0e–13 ± 4.0e–13	0.3 ± 0.2	2.4e+35
560	1.8e–16 ± 3.7e–17	5.2e–17 ± 2.6e–17	N/A	0.3 ± 0.2	6.1e+35
668	1.5e–14 ± 3.1e–15	1.3e–14 ± 6.5e–15	3.1e–14 ± 1.6e–14	0.9 ± 0.5	1.1e+36
811	5.4e–15 ± 1.1e–15	7.8e–15 ± 3.9e–15	2.6e–14 ± 1.3e–14	1.4 ± 0.8	3.3e+35
833	3.3e–15 ± 6.8e–16	4.7e–15 ± 2.3e–15	6.4e–15 ± 3.2e–15	1.4 ± 0.7	3.5e+35
969	0.0	5.6e–18 ± 2.8e–18	3.4e–17 ± 1.7e–17	0.0	7.9e+36
1083	0.0	0.0	8.1e–17 ± 4.0e–17	0.0	2.2e+35
1282	4.1e–15 ± 2.4e–16	1.9e–15 ± 3.9e–16	3.9e–15 ± 1.2e–15	0.5 ± 0.1	2.6e+35
1286	4.0e–16 ± 2.3e–17	2.1e–16 ± 4.3e–17	1.3e–15 ± 4.0e–16	0.5 ± 0.1	2.4e+35
1332	2.2e–16 ± 1.3e–17	0.0	2.3e–16 ± 2.5e–17	0.0	5.1e+35
1372	6.2e–14 ± 3.6e–15	1.6e–14 ± 3.3e–15	1.1e–14 ± 3.3e–15	0.3 ± 0.1	2.2e+35
1535	2.8e–14 ± 1.6e–15	2.9e–14 ± 6.0e–15	6.2e–14 ± 6.9e–15	1.0 ± 0.2	1.6e+36
1669					3.7e+35
1748					2.6e+35
1796					1.1e+36

Notes. No [O III] flux was calculated for sources that were only observed in fields F8 and/or F9 ([SPH11] 263, 294, 414, 441, and 560; see Sect. 2.2). [SPH11] 1437, 1669, 1748, and 1796 are located outside the LGGS fields. [(a)] See Sect. 6.1.

Another class of extended soft X-ray sources are interstellar bubbles and superbubbles in the interstellar medium of a galaxy that are formed by the stellar winds of massive stars. Studies of superbubbles in the Large Magellanic Cloud by, e.g., Chu & Mac Low (1990) or Dunne et al. (2001) demonstrated that the X-ray luminosities of X-ray bright superbubbles is higher than predicted by theoretical models (e.g., the standard model by Weaver et al. 1977). This indicates that the energy sources of the X-ray bright superbubbles are not only the stellar winds of massive stars, but also supernovae, and thus the shock waves of SNRs that occurred inside the superbubble. In contrast to the shock-ionised gas of SNRs, the gas in H II regions around such superbubbles is mainly photoionised and the expansion velocities are too low to form a radiative shock. Therefore, the [S II]/Hα ratio is smaller in superbubbles than in SNRs. Some sources in our list have optical counterparts with a large extent and low [S II]/Hα ratio (~0.3). These sources are most likely superbubbles or SNRs in a superbubble. We point out that sources classified as SNR candidates in the catalogue of SPH11 can also be superbubbles since the classification was based on X-ray hardness ratios, which indicate soft sources for both superbubbles and SNRs.

4. New classifications

All sources in Tables B.1 and 1 have been studied in detail and are either (re-)classified as SNRs or SNR candidates, or rejected (see Tables 3–5).

Here, we summarise the X-ray and optical results for each source and its identification. In the SPH11 catalogue, the following criteria were applied to identify SNRs and candidates:

1. soft sources with $HR_1 > -0.1$ and $HR_2 + EHR_2 < -0.2$ are classified as SNR candidates if no foreground star was detected at the X-ray position;
2. a source that fulfilled criterion 1 and had a known SNR as a counterpart was identified as an SNR;
3. a source that did not fulfil criterion 1 but had an SNR counterpart in either radio or optical and showed no significant variability was classified as an SNR candidate.

We analysed the LGGS Hα, [S II], and [O III] data to obtain the optical emission-line flux of the sources and to study their morphology. In the following, we discuss for each source 1) why the source was classified as an SNR or a candidate by SPH11 and if there are any interesting details in the X-ray image or spectra, 2) its optical properties, and 3) a revised classification based on these new results. Specifically, we have

- *confirmed an XMM-Newton source as an SNR* if the X-ray source is soft (i.e., fulfils criterion 1 of SPH11), there is no foreground star at its position, and has either a radio counterpart classified as an SNR or an optical counterpart with [S II]/H$\alpha > 0.5$;
- *newly classified an XMM-Newton source as an SNR* if its spectrum is soft, there is no foreground star at its position, and the optical counterpart incidates an SNR ([S II]/H$\alpha > 0.5$);
- *classified an XMM-Newton source as an SNR candidate* if a source has a soft X-ray spectrum, no foreground star as a counterpart, and neither an optical nor a radio counterpart indicative of an SNR,
  OR a source has a soft X-ray spectrum, a foreground star at its position, but also an optical counterpart with [S II]/H$\alpha > 0.5$,
  OR a source had been identified as an SNR before and has a soft X-ray spectrum, but a possible foreground star together with diffuse optical emission was found in this work,
  OR a source has a hard X-ray spectrum and a radio counterpart,
  OR a hard source has an optical counterpart with [S II]/H$\alpha > 0.5$.

The new classifications are presented in the following. The details of the X-ray and optical properties for the sources,

Table 5. *XMM-Newton* sources from SPH11, which are no longer classified as X-ray SNRs or SNR candidates after a revised analysis.

[SPH11] ID	Hα [erg cm^{-2} s^{-1} arcsec^{-2}]	[S II] [erg cm^{-2} s^{-1} arcsec^{-2}]	[O III] [erg cm^{-2} s^{-1} arcsec^{-2}]	[S II]/Hα	Class. by SPH11[a]	New Class.[b]
472	2.2e–16 ± 4.5e–17	1.4e–16 ± 7.0e–17	0.0	0.6 ± 0.3	⟨SNR⟩	⟨fg star⟩
500	1.7e–14 ± 3.5e–15	5.4e–15 ± 2.7e–15	3.8e–15 ± 1.9e–15	0.3 ± 0.2	⟨SNR⟩	⟨hard⟩
509	2.3e–17 ± 4.8e–18	6.4e–17 ± 3.2e–17	0.0e-+00 ± 1.6e–17	2.8 ± 1.5	⟨SNR⟩	⟨fg star⟩
682	1.2e–17 ± 2.5e–18	3.6e–17 ± 1.8e–17	0.0	0.0	⟨SNR⟩	
1121	4.6e–14 ± 2.7e–15	9.6e–15 ± 2.0e–15	5.0e–15 ± 5.6e–16	0.2 ± 0.1	⟨hard⟩	⟨hard⟩
1156	2.2e–15 ± 1.3e–16	1.8e–15 ± 3.7e–16	1.0e–15 ± 1.1e–16	0.8 ± 0.2	⟨SNR⟩	⟨hard⟩
1437					⟨SNR⟩	
1461	5.0e–14 ± 2.9e–15	9.3e–15 ± 2.0e–15	4.3e–15 ± 1.3e–15	0.2 ± 0.1	⟨fg star⟩	⟨fg star⟩
1468	5.1e–15 ± 2.9e–16	2.1e–15 ± 4.3e–16	4.4e–16 ± 4.9e–17	0.4 ± 0.1	⟨hard⟩	⟨hard⟩
1505	2.8e–16 ± 8.5e–17	0.0	2.8e–16 ± 8.5e–17	0.0	⟨SNR⟩	⟨AGN⟩
1534	8.4e–16 ± 2.5e–16	0.0 ± 5.9e–17	7.2e–16 ± 2.2e–16	0.0	⟨SNR⟩	⟨fg star⟩
1608	2.3e–16 ± 7.0e–17	0.0	0.0 ± 7.9e–18	0.0	⟨SNR⟩	⟨fg star⟩
1611	1.8e–14 ± 1.0e–15	8.2e–15 ± 1.7e–15	2.6e–14 ± 7.9e–15	0.5 ± 0.1	⟨hard⟩	⟨hard⟩
1637	1.6e–17 ± 4.9e–18	0.0	0.0	0.0	⟨SNR⟩	⟨hard⟩
1712	1.8e–13 ± 5.5e–14	9.4e–14 ± 2.0e–14	3.4e–14 ± 1.0e–14	0.5 ± 0.2	⟨SNR⟩	
1732	7.2e–15 ± 4.2e–16	2.4e–15 ± 4.9e–16	2.1e–15 ± 6.4e–16	0.3 ± 0.1	⟨SNR⟩	⟨hard⟩
1741	1.6e–15 ± 4.9e–16	0.0	0.0 ± 3.2e–17	0.0	⟨SNR⟩	⟨fg star⟩

Notes. [a] Classification by SPH11. fg star: foreground star. The brackets ⟨⟩ indicate that these are candidates and the classifications hence need to be confirmed. [b] New classification.

for which the classification remains unchanged, are available in Appendix D. We assumed a distance of 744 kpc to M 31 (Vilardell et al. 2010). At this distance, 1″ corresponds to 3.6 pc. We use the following abbreviations for publications that we refer to in this section: Baade & Arp (1964, BA64), Braun (1990, B90), Braun & Walterbos (1993, BW93), D'Odorico et al. (1980, DDB80), Di Stefano et al. (2004, DKG04), Gelfand et al. (2004, GLG04), Gelfand et al. (2005, GLG05), Kong et al. (2002b, KGP02), Magnier et al. (1995, MPV95), Orio (2006, O06), Pellet et al. (1978, PAV78), Pietsch et al. (2005, PFH05), Shaw Greening et al. (2009, SBK09), Walterbos & Braun (1992, WB92), Williams et al. (2004a, WGK04), and Williams et al. (2004b, WSK04).

4.1. New SNRs

4.1.1. [SPH11] 1079: XMMM31 J004255.50+405946.4

[SPH11] 1079 is a soft X-ray source with no foreground star at its position. Therefore, it was classified as an SNR candidate by SPH11.

There is a diffuse optical source located at the X-ray position, which is visible in all three Hα, [S II], and [O III] images (Fig. A.1). The flux ratio is [S II]/Hα = 0.9 ± 0.4, indicating that it is an SNR. The extent of the diffuse emission is ∼9″. It has a bright concave arc-like structure in the south-west. On the basis of the X-ray hardness ratios and the optical flux ratio, we classify this source as a new SNR.

4.1.2. [SPH11] 1148: XMMM31 J004308.85+410305.4

[SPH11] 1148 is a soft X-ray source. As no foreground star was found at its position, it was classified as an SNR candidate by SPH11.

The flux ratio derived from the LGGS data is [S II]/Hα = 0.8 ± 0.2 (Table 3), suggesting that it is an SNR. It is very faint and diffuse in the optical emission-line images with an extent of ∼12″ and patchy structures (Fig. A.1). This morphology is similar to that of [SPH11] 1282 and 1328. On the basis of the X-ray colour and the optical line-flux ratio, we classify this source as an SNR.

4.1.3. [SPH11] 1370: XMMM31 J004404.55+415806.5

[SPH11] 1370 is a soft X-ray source without a foreground star at its position, which was therefore classified as an SNR candidate by SPH11.

We detected very faint Hα, [S II], and [O III] emission in the LGGS data with a flux ratio of [S II]/Hα = 0.8 ± 0.2 (see Table 3), which is hardly visible in the images (Fig. A.1). This optical line-flux ratio indicates that this source is indeed an SNR. Therefore, the source is now classified as an SNR.

4.1.4. [SPH11] 1481: XMMM31 J004434.90+412512.7

[SPH11] 1481 is a faint, soft source with no foreground star at its position. On the basis of its hardness ratios, it was classified as an SNR candidate by SPH11.

The X-ray source is coincident with the optical source [BW93] K490A located slightly to the north, which had been suggested to be an SNR candidate (Fig. A.1). The [S II]/Hα flux ratio derived from the LGGS data is 0.8 ± 0.2 and indicates that the source is an SNR. The optical source is diffuse and has an extent of ∼20″. It seems to be located in a complex of H II regions. The *XMM-Newton* source is also located in a region with extended soft X-ray emission and was not detected precisely at the position of the optical SNR. If the X-ray detection had been placed at the position of the optical SNR, the X-ray count rates would most likely have been higher (see Fig. A.1). Therefore, the count rates in the catalogue of SPH11 are rather underestimated. On the basis of the X-ray and optical properties, we classify this source as a new SNR.

4.1.5. [SPH11] 1548: XMMM31 J004455.73+415655.2

[SPH11] 1548 is a faint, soft X-ray source, which has been suggested as an SNR candidate by SPH11 based on its hardness ratios and the lack of a foreground star as a likely counterpart.

There is a faint arc-like structure in the optical with an extent of ∼8″, which is visible in Hα, [S II], and [O III] at the X-ray position (Fig. A.1). The [S II]/Hα flux ratio of 1.1 ± 0.4 suggests that this object is an SNR. We therefore identify this source as a new SNR.

4.2. New SNR candidates

4.2.1. [SPH11] 263: XMMM31 J003945.28+402949.9

[SPH11] 263 is a soft X-ray source with hardness ratios indicative of an SNR. The X-ray source is coincident with the optical SNR [BA64] 339 or [PAV78] 80 and was therefore identified as an SNR by PFH05 and SPH11.

The optical line emission of the LGGS images (Fig. A.1) shows a ring-like structure with an extent of ∼15″, which has a flux ratio of [S II]/Hα = 0.8 ± 0.4 at the position of the X-ray source, and an additional diffuse emission to the west with a lower flux ratio ([S II]/Hα ≈ 0.4). Therefore, it might be an SNR embedded in an interstellar bubble.

The LGGS *B*, *V*, *R*, and *I* band images show several faint point-like sources at the position of the X-ray source, two of which appear very red and may be late-type foreground stars. These stars might contribute to the detected X-ray emission (Fig. 8, top left). Owing to this ambiguity, we change the classification of the X-ray source to an SNR candidate. Only X-ray images with higher spatial resolution than *XMM-Newton* will allow us to resolve the contributions from the different sources of X-ray emission.

4.2.2. [SPH11] 668: XMMM31 J004135.76+410655.0

[SPH11] 668 is coincident with the optical SNR [DDB80] 1-11 ([BA64] 416), which is also a radio source ([B90] 14). The X-ray source was also detected with *Chandra* ([DKG04] s1-42). Although the hardness ratio $HR_2 = -0.30 \pm 0.15$ does not fulfil the SNR criterion, PFH05 and SPH11 classified the X-ray source as an SNR based on its positional coincidence with the optical SNR.

From the narrow-band LGGS images, we determined an [S II]/Hα flux ratio of 0.9 ± 0.5. The optical SNR has a diameter of ∼8″ and is brighter in the north and southwest (Fig. A.1).

There is a faint star to the southwest within the error radius of the *XMM-Newton* position (Fig. 8, upper middle right). We cannot rule out that the X-ray source is a foreground star. X-ray data with higher spatial resolution are necessary to separate the emission components. Therefore, we classify the *XMM-Newton* source as an SNR candidate.

4.2.3. [SPH11] 811: XMMM31 J004210.60+405149.1

[SPH11] 811 was not classified as an SNR candidate by SPH11. It is coincident with the source [PFH05] 224, which was classified as a candidate for a super-soft source. However, a look at the DSS images in the course of the preparation for optical follow-up observations revealed a ring-like structure.

A circular shell with a diameter of ∼12″, which is brighter in the east, is clearly visible in the Hα, [S II], and [O III] images of the LGGS (Fig. A.1). The flux ratio of the shell is [S II]/Hα = 1.4 ± 0.8, supporting its SNR nature.

In addition, there is a spoke-like feature extending from the centre to the south (Fig. 9, left). In the LGGS *U*, *B*, and *V* images, there is a bright point-like source at the centre of the ring with two additional fainter point-like structures northwest and southeast of the bright source (Fig. 9, right). These three sources form a line almost perpendicular to the spoke seen in the emission line images. We have derived an [S II]/Hα flux ratio of 1.15 ± 0.11 from new optical follow-up observations (Hatzidimitriou et al., in prep.), which is in good agreement with the flux ratio from the LGGS data. The spectrum also shows weak Balmer lines and He I lines in absorption, indicative of an early-type star. Therefore, the optical source is most likely a composite of an SNR and an OB star in M 31.

As the X-ray hardness ratios are not indicative of an SNR ($HR_1 = -0.46 \pm 0.46$, $HR_2 = 0.48 \pm 0.46$, $HR_3 = -0.83 \pm 0.36$), but the optical source is most likely an SNR, we classify the *XMM-Newton* source [SPH11] 811 as an SNR candidate.

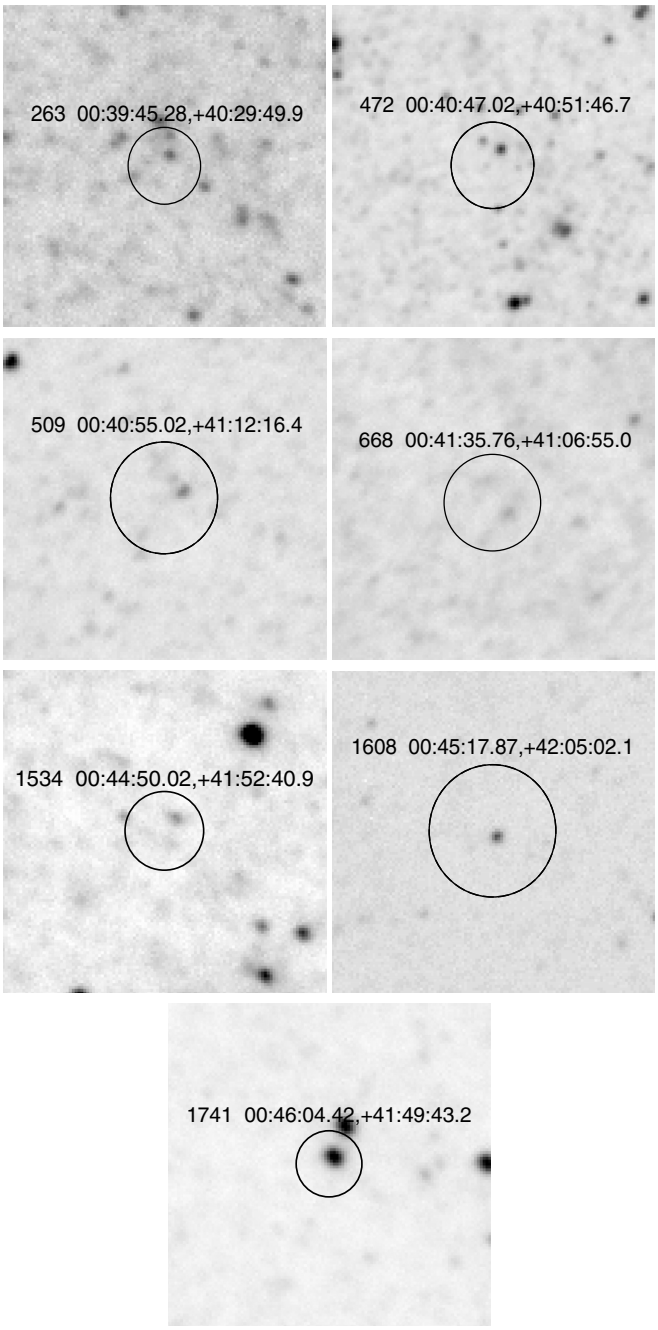

Fig. 8. LGGS *R* band images of [SPH11] 263, 472, 509, 1534, 1608, and 1741. The shown area has a size of ∼30″ × 30″. The *XMM-Newton* positional error circle is shown.

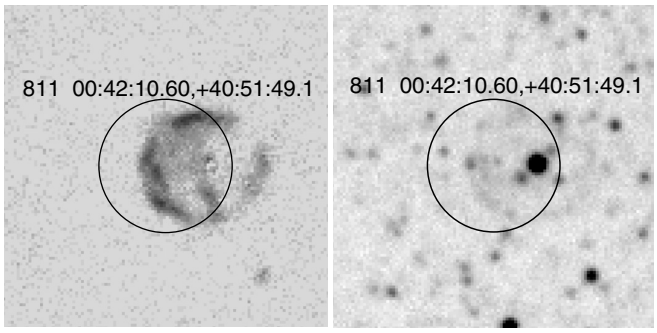

Fig. 9. Continuum-subtracted LGGS Hα (*left*) and LGGS *U* band image (*right*) of [SPH11] 811. The shown area has a size of ~30″ × 30″. The *XMM-Newton* positional error circle is shown.

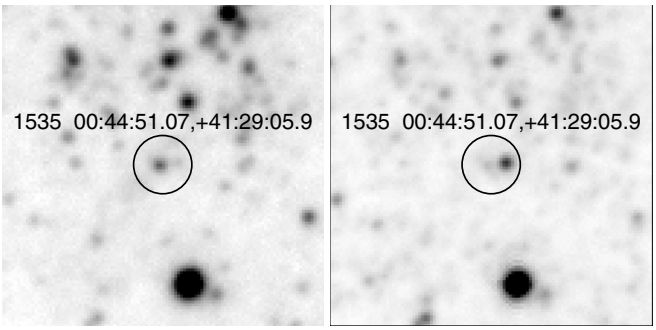

Fig. 10. LGGS *V* (*left*) and *I* (*right*) band images of [SPH11] 1535. The shown area has a size of ~30″ × 30″. The *XMM-Newton* positional error circle is shown.

4.2.4. [SPH11] 833: XMMM31 J004214.60+405204.7

[SPH11] 833 has hardness ratios that are not typical of SNRs. It is coincident with [PFH05] 234. We identified diffuse Hα, [S II], and [O III] emission and thus regarded the source as an SNR candidate.

An extended emission-line source elongated in the northeast to southwest direction (~9″ × 2″) is found on the Hα, [S II], and [O III] LGGS images (Fig. A.1). The flux ratio of [S II]/Hα = 1.4 ± 0.7 suggests that the source is an SNR. We therefore classify this source as an SNR candidate.

4.2.5. [SPH11] 1286: XMMM31 J004342.08+414709.5

[SPH11] 1286 is a soft source, which marginally did not fulfil the criterion of $HR_2 + EHR_2 < -0.2$. Diffuse Hα emission was found in the optical.

The LGGS images show a faint diffuse source in Hα, [S II], and [O III] (Fig. A.1). The [S II]/Hα flux ratio is 0.5 ± 0.1. This value is at the border between SNRs and H II regions, thus suggesting an SNR but not clearly ruling out the H II region identification. We therefore classify this source as an SNR candidate.

4.2.6. [SPH11] 1372: XMMM31 J004404.71+414846.7

[SPH11] 1372 is a faint, soft X-ray source coincident with an extended optical source [WB92] 280, which was suggested as a possible SNR candidate by [MPV95] (source 3-072). It was therefore classified as an SNR by PFH05 and SPH11.

The optical source is also visible in the LGGS images (Fig. A.1). The flux ratio derived from the LGGS data is [S II]/Hα = 0.3 ± 0.1, which is more typical of an H II region than of an SNR. The source is highly extended (~30″) and consists of an extended round region in the north and an additional arc-like structure in the southeast. We therefore classify the X-ray source as an SNR candidate, which is probably located in an H II region.

4.2.7. [SPH11] 1535: XMMM31 J004451.07+412905.9

[SPH11] 1535 is coincident with the optical SNR [BW93] K583 and its radio counterpart and was thus identified as an SNR by PFH05 and SPH11.

The optical SNR is relatively compact with an extent of ~8″ and an arc-like structure, which is open to the southwest (Fig. A.1). It has a flux ratio typical of SNRs ([S II]/Hα = 1.0 ± 0.2). The SNR seems to be embedded in a shell-like H II region extending to the northeast, which is most clearly seen in the Hα image.

A closer look at the LGGS *V*, *R*, *I* images has revealed two star-like objects within the X-ray error circle, i.e., in the projected interior of the optical SNR (Fig. 10). The object in the centre of the X-ray error circle is a star in M 31 with a *V* magnitude of 19.43 listed as source D31 J004451.1+412905.6 in the catalogue of the DIRECT Project (Mochejska et al. 2001). The redder object to the west is 2MASS 00445095+4129058 with a *J* magnitude of 16.063, listed in the 2MASS All-Sky Catalog of Point Sources (Cutri et al. 2003).

The X-ray emission of the SNR is most likely contaminated by the emission of these stellar objects. X-ray data with higher spatial resolution are necessary to separate the emission components. We therefore classfiy this *XMM-Newton* source as an SNR candidate.

4.3. Sources which are classified as no SNR candidates

4.3.1. [SPH11] 472: XMMM31 J004047.02+405146.7

[SPH11] 472 is a soft X-ray source with hardness ratios indicative of an SNR. As no foreground star was found, it was proposed as an SNR candidate by PFH05 and SPH11.

No diffuse optical line-emission was detected in the LGGS Hα, [S II], and [O III] images (Fig. A.1). The LGGS *B*, *V*, *R*, and *I* band images show a red optical point-like source inside the error circle of the *XMM-Newton* source (Fig. 8, top right). This optical source LGGS J004046.96+405148.2 has the colour $V-R$ = 1.4 and $\log(f_X/f_{opt}) = -0.6$, thus did only marginally not fulfil the criterion for stars of $V - R > 1$, $\log(f_X/f_{opt}) < -0.65$ (see Sect. 9.1 in SPH11). We therefore re-classify the source as a foreground star candidate.

4.3.2. [SPH11] 500: XMMM31 J004052.88+403624.4

[SPH11] 500 is a hard X-ray source. Owing to its positional coincidence with the optical SNR candidate with low confidence suggested by MPV95 (source 3-027), the source was classified as an SNR candidate by SPH11.

However, it is also listed in PFH05 and SBK09 as a hard source. An extended, diffuse source is visible at its position in the LGGS Hα image (Fig. A.1), although the flux ratio of [S II]/Hα = 0.3 ± 0.2 is lower than typically found for SNRs. Therefore, this hard X-ray source with an optical counterpart that is probably not an SNR, is no longer an SNR candidate.

4.3.3. [SPH11] 509: XMMM31 J004055.02+411216.4

[SPH11] 509 is a soft X-ray source and was classified as an SNR candidate based on its hardness ratios by SPH11.

However, on the LGGS B, V, R, and I band images, we find the star LGGS J004054.86+411217.1 at the X-ray position with $V - R = 1.3$ and $\log(f_X/f_{opt}) = -0.8$ (Fig. 8, upper middle left). We therefore re-classify this sources as a foreground star candidate.

4.3.4. [SPH11] 682: XMMM31 J004140.28+405947.9

[SPH11] 682 is the faintest source in our list with a detection likelihood of $ML = 7.6$. It was classified as an SNR candidate by SPH11 based on the hardness ratio criterion and the lack of a likely foreground star at its position.

However, with $HR_2 = -0.48 \pm 0.26$, the criterion $HR_2 + EHR_2 < -0.2$ is only marginally fulfilled. Furthermore, that even HR_4 was determined indicates that there is a hard component. Only faint Hα and [S II] emission and no [O III] emission is detected in the LGGS data (Table 5). No radio counterpart is known either. We therefore revise its classification and leave the source without a classification.

4.3.5. [SPH11] 1156: XMMM31 J004310.43+413850.1

[SPH11] 1156 is a hard X-ray source, which was classified as an SNR candidate by SPH11 based on the positional coincidence with the source K89A in BW93.

[BW93] K89A is seen in the LGGS Hα and [S II] images to the west of the X-ray source position (Fig. A.1). It has a very faint [O III] emission and a flux ratio of [S II]/H$\alpha \approx 1$ in the north. Therefore, the optical source was discussed as an SNR candidate. However, the *XMM-Newton* source is located east of [BW93] K89A and does not seem to be related to the optical source.

New optical follow-up observations (Hatzidimitriou et al., in prep.) have shown that the spectrum taken at the position of the *XMM-Newton* source is a composite spectrum of an early-type star and a nebular source with [S II]/H$\alpha = 0.57 \pm 0.09$. This agrees with the value derived from the LGGS images (Table 5).

Neither the X-ray emission nor the optical emission is thus clearly indicative of an SNR at the position of [SPH11] 1156. Therefore, we classify the X-ray source as hard based on the X-ray hardness ratios.

4.3.6. [SPH11] 1437: XMMM31 J004421.18+421621.9

[SPH11] 1437 is a faint soft X-ray source with low $ML = 8.5$, which was suggested as an SNR candidate based on its hardness ratios by SPH11 (see Fig. 3).

The location of this source was not covered by the LGGS. Two faint sources are found on the SDSS-III r, i, and z band images inside the *XMM-Newton* error circle (Fig. 4). These sources are not visible in the u band image. The sources are listed in the USNO-B1.0 catalogue (Monet et al. 2003), with both $R = 20.6$, 21.4 and $B = 19.6$, 19.1, respectively. The *XMM-Newton* source [SPH11] 1437 is therefore most probably either a star or an AGN. We therefore no longer classify this source as an SNR candidate.

4.3.7. [SPH11] 1505: XMMM31 J004442.73+415340.5

[SPH11] 1505 is a hard X-ray source with hardness ratios of $HR_1 = 0.50 \pm 0.27$, $HR_2 = -0.73 \pm 0.27$, $HR_3 = 0.97 \pm 0.04$, and $HR_4 = 0.50 \pm 0.04$. It was classified as an SNR candidate by SPH11 based on its hardness ratios HR_1 and HR_2 and the lack of a foreground star at its position.

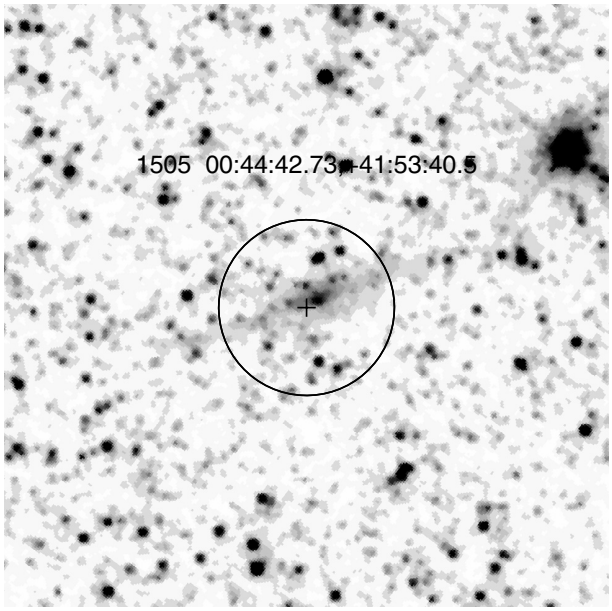

Fig. 11. *Hubble* Space Telescope ACS/WFC (F814W) image showing an extended source at the position of [SPH11] 1505, which seems to be a galaxy with an apparent extent of $\sim 6'' \times 1''$. It obviously has a nucleus located $\sim 0\farcs5$ distant from the *XMM-Newton* source position. The shown area has a size of $\sim 15'' \times 15''$.

The source is located south of the H II region [PAV78] 799 (Fig. A.1). It is obviously unrelated to the H II region. There is apparently a galaxy at its position, as can be seen in an HST image taken with ACS/WFC using the filter *F814W* (Fig. 11). This galaxy seems to have a clearly visible nucleus, which is located inside the 3σ error circle of the *XMM-Newton* source position. This source also has an extended infrared counterpart in the Wide-field Infrared Survey Explorer (WISE) All-sky data release (Cutri & et al. 2012). We therefore classify [SPH11] 1505 as an AGN candidate.

4.3.8. [SPH11] 1534: XMMM31 J004450.02+415240.9

[SPH11] 1534 is a soft X-ray source and was classified as an SNR candidate by SPH11 based on its hardness ratios.

It is located near the optical SNR [BW93] K567 and its radio counterpart [B90] 308, which is seen at the northern edge of the Hα image (Fig. A.1). However, two faint red sources are found in, e.g., the LGGS R band image at the position of the *XMM-Newton* source, which are most likely stars (Fig. 8, lower middle left). The X-ray source does not seem to be related to the SNR to the north. Because optical point sources are found, we no longer classify the X-ray source as an SNR candidate.

4.3.9. [SPH11] 1608: XMMM31 J004517.87+420502.1

[SPH11] 1608 is a faint soft X-ray source, which was classified as an SNR candidate by SPH11 based on its hardness ratios.

In the LGGS data, only faint Hα emission was detected. The LGGS R, V, and B band images show a point source at the position of the *XMM-Newton* source (Fig. 8, lower middle right). This optical source (LGGS J004517.84+420501.7) has $V-R = 1.2$ and $\log(f_X/f_{opt}) = -0.6$, thus did marginally not fulfil

the criterion for stars (Sect. 9.1 in SPH11, see also Sect. 4.3.1). However, as there is a star within the X-ray error circle and no additional extended source in the optical that is indicative of an SNR, we now classify the X-ray source as a foreground star candidate.

4.3.10. [SPH11] 1637: XMMM31 J004528.35+414605.9

[SPH11] 1637 is a hard X-ray source. It was suggested to be an SNR candidate by PFH05 and SPH11 as it is located near the SNR candidate [MPV95] 1-013.

The source [MPV95] 1-013 can be found at the top edge of the LGGS Hα and [S II] images in Fig. A.1. The X-ray source is located south of it and does not seem to be related to the SNR candidate. Therefore, we no longer classify this hard X-ray source as an SNR candidate.

4.3.11. [SPH11] 1712: XMMM31 J004556.01+421117.2

[SPH11] 1712 is a faint, hard X-ray source. It is coincident with the optical source [BW93] K884 and was therefore suggested as an SNR candidate by SPH11.

The optical source [BW93] K884, however, has been suggested to be a supershell (Fig. A.1). The [S II]/Hα ratio derived from the LGGS data is 0.5 ± 0.2, hence more consistent with an H II region.

The optical spectrum obtained in a new follow-up observation by Hatzidimitriou et al. (in prep.) indicates a composite of a most likely highly reddened Be star and nebular emission. The [S II]/Hα ratio of 0.36 ± 0.08 is consistent with the LGGS value and not indicative of an SNR.

As the X-ray source is hard and there is no optical emission that would suggest that it is an SNR, we no longer classify this source as an SNR candidate.

4.3.12. [SPH11] 1732: XMMM31 J004602.53+414513.2

[SPH11] 1732 is a hard X-ray source and was classified as an SNR candidate by PFH05 and SPH11, as it is located near the source [MPV95] 3-111, which had been suggested to be an SNR candidate.

However, [SPH11] 1732 is located at a distance of $\sim$30″ from [MPV95] 3-111. It is located at the edge of a large diffuse structure seen in Hα (Fig. A.1), but shows no clear correlation with the optical line emission. We therefore classify this X-ray source as a hard source and not as an SNR candidate.

4.3.13. [SPH11] 1741: XMMM31 J004604.42+414943.2

[SPH11] 1741 is a soft X-ray source with no optical counterpart that seems to be a foreground star. The source was therefore classified as an SNR candidate by PFH05 and SPH11. It was also detected with *Chandra* ([WGK04], [DKG04] n1-48).

We found two optical point sources in the LGGS B, V, and R band images, one inside and one right outside the error circle of the *XMM-Newton* source (Fig. 8, bottom). The optical source inside the error circle (LGGS J00460.38+414944.0) has the optical colour $V - R = 1.3 > 1$ and $\log(f_X/f_{opt}) = -1.3 < -0.65$, which are indicative of a star. We therefore classify the X-ray source as a foreground star candidate.

5. Comparison to other X-ray catalogues

5.1. Comparison to the ROSAT catalogue

In the ROSAT source catalogues of SHP97 and SHL01, 16 sources were classified as SNRs. Thirteen of the 16 sources were detected in the *XMM-Newton* survey. No counterpart was found for the ROSAT sources [SHL01] 129 (RX J0041.9+4046), [SHP97] 203 (RX J0042.8+4125), and [SHP97] 258 (RX J0043.9+4152).

The ROSAT source [SHP97] 284 (RX J0044.6+4125) is located between two *XMM-Newton* sources: [SPH11] 1497, which is an SNR with optical and radio counterparts, and 1481, which was classified as an SNR candidate by SPH11 based on its X-ray hardness ratios. On the basis of the new optical data of the LGGS, we confirmed [SPH11] 1481 as an SNR.

We classified [SPH11] 1079 ([SHP97] 212) as a new SNR based on its optical line emission. In addition, we confirmed that three *XMM-Newton* sources [SPH11] 472, 682, and 1637 with ROSAT counterparts ([SHP97] 92, [SHL01] 110, and [SHL01] 321, respectively) are not SNR candidates.

5.2. Comparison to Chandra sources

XMM-Newton detected 5 of 6 SNRs in M 31 that had been classified based on *Chandra* observations: [KGP02] r2-57 ([SPH11] 883), [KGP02] r3-84 ([SPH11] 1040), [KGP02] r2-56 ([SPH11] 1050), [KGP02] r3-69 ([SPH11] 1060), and [KGP02] r3-63 ([SPH11] 1234). The *Chandra* source CXOM31 J004247.82+411525.7, which was identified as an SNR by Kong et al. (2003, source 2), is located between two bright sources and has not been resolved by *XMM-Newton*.

Williams et al. (2004a) classified the *Chandra* source [WGK04] n1-85 (also [DKG04]) as a variable X-ray source coincident with a radio SNR ([B90] 265). In addition, this source was identified as a transient source by Williams et al. (2006). It was not detected by *XMM-Newton*, even though the position is covered by *XMM-Newton* observations, confirming its transient nature. Therefore, this source is not likely to be an SNR.

6. Discussion

6.1. Cumulative X-ray luminosity distribution

We estimated the luminosity of the SNRs and candidates listed in Tables 3 and 4 and thus obtained a cumulative luminosity distribution of the SNRs in M 31. For the M 31 SNRs, we converted the *XMM-Newton* count rates into flux by assuming a thermal spectrum with $kT = 0.2$ keV, absorbed by a foreground column density of $N_H(MW) = 0.7 \times 10^{21}$ cm^{-2} and an additional $N_H(M31) = 1.0 \times 10^{21}$ cm^{-2}, similar to the fitted values for the four brightest sources [SPH11] 969, 1050, 1066, and 1234. We simulated the flux assuming different models by varying the temperature in the range of $kT = 0.1$–0.3 keV and the foreground absorption $N_H(M31) = 0$–2×10^{21} cm^{-2} for the observed count rates and obtained an uncertainty of $\sim$20%. Assuming CIE or NEI model results in a difference in flux of $\sim$10% (see Table 2). As most of the sources are too faint to distinguish between CIE and NEI, we assume the same `APEC` model for all sources. For the cumulative luminosity distribution plot shown in Fig. 12, the luminosities in the energy band of 0.35–2.0 keV were calculated with the foreground absorption set to zero. We also included the source CXOM31 J004247.82+411525.7, which was identified as an SNR by Kong et al. (2003) but not resolved with *XMM-Newton* (see Sect. 5.2). For comparison, the luminosities

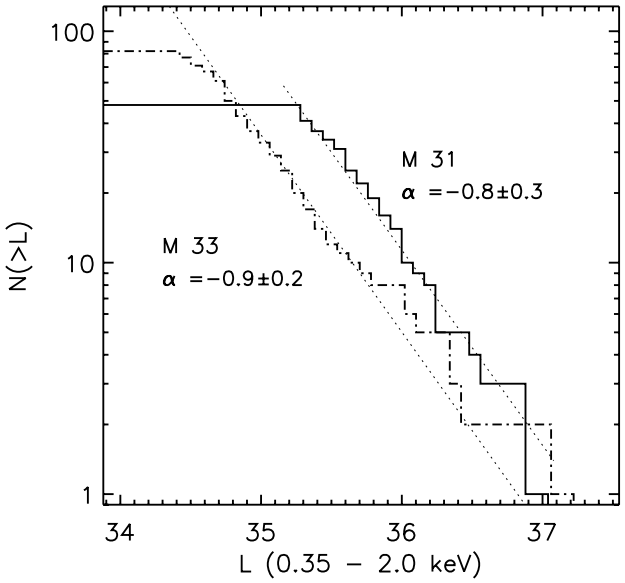

Fig. 12. Cumulative luminosity distribution of X-ray SNRs and candidates in M 31 listed in Tables 3 and 4 for the band of 0.35–2.0 keV (solid line). For comparison, the distribution of SNRs in M 33 is also shown (dash-dotted line, Long et al. 2010). The dotted lines show the power-law fits. The power-law index α is given.

for M 33 SNRs taken from Long et al. (2010) are plotted as well. These luminosities were converted from *Chandra* count rates by Long et al. (2010) assuming a thermal plasma model with $kT = 0.6$ keV and an absorbing $N_{\rm H} = 5.0 \times 10^{20}$ cm^{-2}, which correspond to the best-fit values for the brightest SNRs in M 33 observed with *Chandra*.

As one can see in Fig. 12, the slope of the cumulative luminosity distribution of X-ray SNRs in M 31 and M 33 are comparable. Both distributions can be fitted with a power law with an index of $\alpha \approx -1$. The distribution in M 33 seems to deviate from this power-law distribution for luminosities $>5 \times 10^{35}$ erg s^{-1} showing an excess. The slight difference in the shape of the cumulative luminosity distribution might indicate that the fraction of more luminous SNRs in M 33 is higher than in M 31. There are 24 sources brighter than 5×10^{35} erg s^{-1} in M 31 and 9 in M 33. Above 10^{36} erg s^{-1}, there are 13 sources in M 31 and 7 in M 33 (see also Ghavamian et al. 2005; Long et al. 2010).

The number of SNRs in M 33 is higher than expected if we simply scale with the total mass of the galaxy, as M 33 is about 10 times less massive than M 31 (Corbelli 2003; Watkins et al. 2010). M 33 is a typical flocculent spiral galaxy with discontinuous spiral arms, in which star-formation regions are found. In contrast to grand design spirals such as the Milky Way or M 31, in which density waves are believed to produce the spiral arms, gravitational instabilities together with turbulence in the interstellar medium seem to be the origin of the spiral structure and thus the ongoing star formation in flocculent galaxies (Sellwood & Carlberg 1984; Elmegreen et al. 2003, and references therein). The star-formation rate in the disk of M 31 is 0.27 $M_\odot$ yr^{-1} for $6 < R < 17$ kpc (Tabatabaei & Berkhuijsen 2010) corresponding to a star-formation rate per unit area of $\Sigma_{\rm SFR} = 0.4\ M_\odot$ Gyr^{-1} pc^{-2}. This value is about six times lower than in M 33, for which a star-formation rate per unit area of $\Sigma_{\rm SFR} = 2$–$3\ M_\odot$ Gyr^{-1} pc^{-2} has been measured (Verley et al. 2009). The higher star-formation rate implies that there is a higher probability of core-collapse SNRs occuring in M 33.

In addition, we note that our list of SNRs in M 31 is based on *XMM-Newton* observations, whereas the M 33 SNRs were detected in a survey performed with *Chandra*. Not only was the *Chandra* survey of M 33 deeper, but the superior angular resolution of *Chandra* made it possible to detect smaller and thus most likely younger SNRs in M 33, which would not have been resolved and classified as SNRs in an *XMM-Newton* observation. However, the *Chandra* M 33 survey only observed the inner part of the galaxy inside the D_{25} ellipse, whereas the *XMM-Newton* M 31 survey fully covered the D_{25} ellipse.

6.2. Radial distribution

In the shock waves of SNRs, particles can gain energies of up to 10^{15} eV or higher by means of diffusive shock acceleration (Bell 1978a,b; Blandford & Ostriker 1978; Hillas 2005). Therefore, SNRs together with pulsars are thought to be the primary sources of Galactic cosmic rays (CRs). The distribution of SNRs and pulsars in our Galaxy is a crucial basis for the understanding of the CR distribution. Stecker & Jones (1977) studied the radial dependence of the Galactic SNR surface density using the observational SNR data of Kodaira (1974) and pulsar data of Seiradakis (1977) and showed that it can be described as $\propto x^\alpha \exp(-x/R)$ with x being the radial distance to the Galactic centre. Using only Galactic shell-type SNRs, Leahy & Wu (1989) found a peak in the surface density distribution at a 4–6 kpc distance from the Galactic centre. Case & Bhattacharya (1998) re-analysed the Galactic SNR data and suggested using a dependence of the type $\propto \sin(\pi x + \theta) \exp(-x/R)$ for the radial surface density distribution. They obtained a scale length of ~7 kpc and a maximum of the distribution at about 5 kpc. Based on the obtained distribution of SNRs in our Galaxy, the spectral distribution of Galactic CRs can be modelled to explain the CR spectrum up to 10^{15}–10^{16} eV (see, e.g., Hillas 2005). However, our vantage point is not ideal for the study of the source distribution in our Galaxy. To understand the distribution of SNRs in a spiral galaxy, it is thus necessary to study the most nearby spiral galaxies M 31 and M 33.

To obtain the radial distribution of SNRs in M 31, the positions of the SNRs and candidates in Tables 3 and 4 as well as the source CXOM31 J004247.82+411525.7 were first corrected for projection and their galactocentric distances were computed. Stiele et al. (2011) also presented the radial distribution of SNRs and candidates in M 31 detected in the *XMM-Newton* LP. To compare M 31 and M 33, the radial distances were normalised to $R_{25} = D_{25}/2$. The positions of sources were binned into equidistant radial bins and the surface density was calculated for each annulus. The parameters used, i.e., distance, inclination angle, position angle, and D_{25} are listed in Table 6. The SNR surface densities are plotted against the normalised radial distance in Fig. 13. We fitted the obtained radial surface-density distribution of the SNRs in each galaxy with the model distribution introduced for the radio-selected SNRs in the Milky Way

$$f(x) = C\, x^\alpha \exp(-x/R), \qquad (1)$$

with a maximum at a radial distance of several kpc from the Galactic centre as originally suggested by Stecker & Jones (1977). The parameters of the distribution obtained by Case & Bhattacharya (1998) for our Galaxy are $C = 136.5, \alpha = 2.00$, and $R = 0.14$. The best-fit model curves according to Eq. (1) are plotted in Fig. 13 with dotted lines. This radial SNR distribution in M 31 and M 33 differs from the mass distribution of these galaxies derived from the rotation curves (e.g., Corbelli 2003; Corbelli et al. 2010, and references therein).

Table 6. Geometric parameters of M 31 and M 33 used for the calculation of the radial SNR number density distribution.

Galaxy	Distance[a] [kpc]	Position angle[b]	Inclination angle[b]	Corrected D_{25}[b]	R_{25} [kpc]
M 31	744	35°	71°	155′.5	16.8
M 33	805	23°	54°	52′.6	6.2

Notes. [(a)] Vilardell et al. (2010) for M 31 and Scowcroft et al. (2009) for M 33. [(b)] de Vaucouleurs et al. (1991).

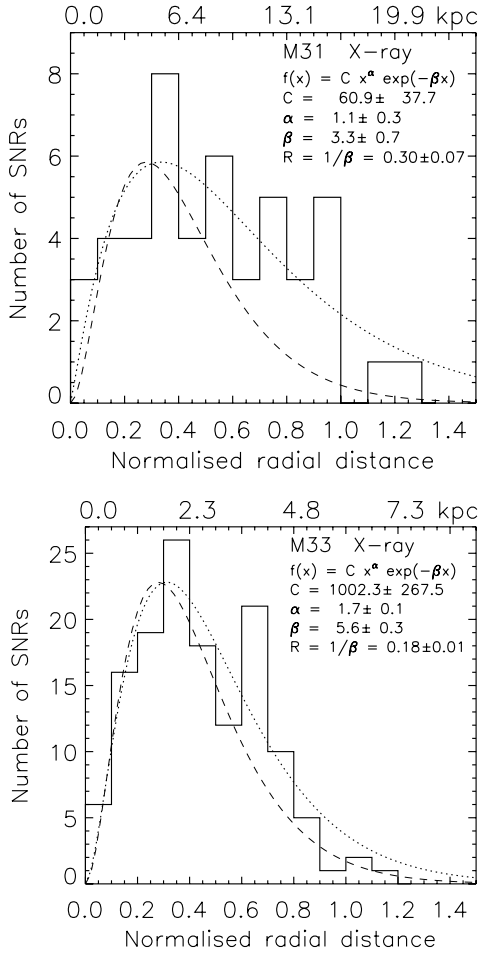

Fig. 13. Surface density of SNRs and candidates in M 31 (this work) and M 33 (Long et al. 2010) plotted over the radius normalised to $D_{25}/2$ (D_{25} = 155.5′, 52.6′ for M 31 and M 33, respectively, de Vaucouleurs et al. 1991). The radial distance in kpc is given along the upper x-axis. Dotted lines show the fitted model function $f(x) = Cx^{\alpha}\exp(-\beta x)$, dashed lines show the model function for the Milky Way normalised to the maximum of M 31 or M 33.

The SNR distribution rather seems to follow the distribution of stars and gas, similar to what had been suggested for the Milky Way. For comparison, we also plot the distribution for the Milky Way normalised to the fitted maxima of the distributions in M 31 and M 33. The fitted curve indicates a maximum at about 5.5 kpc and 2 kpc for M 31 and M 33, respectively, corresponding to ∼0.3 R_{25} for both galaxies. The distribution in M 31 seems to be almost flat for <17 kpc ≈ R_{25} and falls exponentially outside ∼1.0 R_{25}, while the distribution in M 33 falls off exponentially for >4 kpc ≈ 0.65 R_{25}. This behaviour of the SNR distribution in M 31 seems to be correlated with the distribution of gas in M 31, which is known to have ring-like structures consisting of many spiral arms between a radius of ∼5 kpc to 20 kpc, with the most prominent ring being found at a radius of ∼10 kpc (Sofue & Kato 1981; Braun 1991).

7. Summary

We have studied the X-ray and optical properties of SNRs and candidates in the source catalogue of the *XMM-Newton* LP survey of M 31. For the optical analysis, we used the Hα, [S II], and [O III] emission-line images as well as the *UBVRI* band images of the LGGS (Massey et al. 2006), which covered M 31 in ten fields.

In addition to the 56 SNRs and candidates in the *XMM-Newton* survey source catalogue of SPH11, we found 7 sources, which had not been previously classified as SNR candidates but showed optical line emission indicative of SNRs. We therefore also included these seven sources in the list of the studied sources. We extracted X-ray spectra of the 12 brightest sources. Only 4 of the sources have sufficiently high quality statistics to perform a more detailed analysis of the X-ray spectra taken with the *XMM-Newton* EPIC instruments. For the 3 brightest sources ([SPH11] 969, 1066, 1234), a collisional ionisation equilibrium model (`APEC`) does not reproduce the spectra well, while a non-equilibrium ionisation model (`NEI`) provides a closer fit. Two thermal components with two different temperatures are necessary to describe the spectrum of [SPH11] 1234 to achieve a satisfactory fit indicating that the X-ray emission is a superposition of at least two emission components.

For each SNR and candidate, we measured the Hα, [S II], and [O III] fluxes as well as the [S II]/Hα flux ratio and thus confirmed five new X-ray sources as SNRs. We point out that the final classification of this work applies to the X-ray source. Therefore, if, for example, the optical counterpart is likely an SNR but the X-ray source is either a soft source with a star in its positional error circle or a hard source, the X-ray source was classified as an SNR candidate.

We identified 17 sources, which are either hard X-ray sources with no optical counterpart indicative of an SNR or with an optical counterpart that is likely a star or a background AGN. We therefore excluded these sources from the list of SNRs or candidates. In particular, source [SPH11] 1505, for which we found a galaxy with a bright nucleus as an optical counterpart, has been classified as an AGN candidate.

From the *XMM-Newton* LP survey catalogue, we have thus obtained a list of 26 X-ray SNRs and additional 20 bona-fide X-ray SNR candidates in M 31. The brightest SNRs have X-ray luminosities of $\sim 8 \times 10^{36}$ erg s^{-1} in the 0.3–2.0 keV band.

Acknowledgements. We have made extensive use of the optical data from the Local Group Galaxy Survey, which are kindly made available by Phil Massey and his collaborators. This work has also made use of *SkyView* and images from the Sloan Digital Sky Survey (SDSS) III. Funding for SDSS-III has been provided by the Alfred P. Sloan Foundation, the Participating Institutions, the National Science Foundation, and the US Department of Energy. The SDSS-III web site is `http://www.sdss3.org/`. SDSS-III is managed by the Astrophysical Research Consortium for the Participating Institutions of the SDSS-III Collaboration including the University of Arizona, the Brazilian

Participation Group, Brookhaven National Laboratory, University of Cambridge, University of Florida, the French Participation Group, the German Participation Group, the Instituto de Astrofisica de Canarias, the Michigan State/Notre Dame/JINA Participation Group, Johns Hopkins University, Lawrence Berkeley National Laboratory, Max Planck Institute for Astrophysics, New Mexico State University, New York University, Ohio State University, Pennsylvania State University, University of Portsmouth, Princeton University, the Spanish Participation Group, University of Tokyo, University of Utah, Vanderbilt University, University of Virginia, University of Washington, and Yale University. Furthermore, this work is based on observations made with the NASA/ESA *Hubble* Space Telescope, obtained from the data archive at the Space Telescope Institute. STScI is operated by the association of Universities for Research in Astronomy, Inc. under the NASA contract NAS 5-26555. This publication makes use of data products from the Wide-field Infrared Survey Explorer, which is a joint project of the University of California, Los Angeles, and the Jet Propulsion Laboratory/California Institute of Technology, funded by the National Aeronautics and Space Administration. M.S. acknowledges support by the Deutsche Forschungsgemeinschaft through the Emmy Noether Research Grant SA 2131/1.

References

Anders, E., & Grevesse, N. 1989, Geochim. Cosmochim. Acta, 53, 197
Baade, W., & Arp, H. 1964, ApJ, 139, 1027
Barnard, R., Stiele, H., Hatzidimitriou, D., et al. 2008, ApJ, 689, 1215
Bell, A. R. 1978a, MNRAS, 182, 147
Bell, A. R. 1978b, MNRAS, 182, 443
Bellazzini, M., Cacciari, C., Federici, L., Fusi Pecci, F., & Rich, M. 2003, A&A, 405, 867
Blair, W. P., Kirshner, R. P., & Chevalier, R. A. 1981, ApJ, 247, 879
Blandford, R. D., & Ostriker, J. P. 1978, ApJ, 221, L29
Block, D. L., Bournaud, F., Combes, F., et al. 2006, Nature, 443, 832
Braun, R. 1990, ApJS, 72, 761
Braun, R. 1991, ApJ, 372, 54
Braun, R., & Walterbos, R. A. M. 1993, A&AS, 98, 327
Brinks, E., & Shane, W. W. 1984, A&AS, 55, 179
Brown, T. M., Smith, E., Ferguson, H. C., et al. 2006, ApJ, 652, 323
Case, G. L., & Bhattacharya, D. 1998, ApJ, 504, 761
Chu, Y.-H., & Mac Low, M.-M. 1990, ApJ, 365, 510
Corbelli, E. 2003, MNRAS, 342, 199
Corbelli, E., Lorenzoni, S., Walterbos, R., Braun, R., & Thilker, D. 2010, A&A, 511, A89
Cutri, R. M., Skrutskie, M. F., van Dyk, S., et al. 2003, VizieR Online Data Catalog, 2246, 0
Cutri, R. M., et al. 2012, VizieR Online Data Catalog, 2311, 0
Dame, T. M., Koper, E., Israel, F. P., & Thaddeus, P. 1993, ApJ, 418, 730
de Vaucouleurs, G., de Vaucouleurs, A., Corwin, Jr., H. G., et al. 1991, Third Reference Catalogue of Bright Galaxies, eds. G. de Vaucouleurs, et al.
Dennefeld, M., & Kunth, D. 1981, AJ, 86, 989
Di Stefano, R., Kong, A. K. H., Greiner, J., et al. 2004, ApJ, 610, 247
D'Odorico, S., Dopita, M. A., & Benvenuti, P. 1980, A&AS, 40, 67
Dunne, B. C., Points, S. D., & Chu, Y.-H. 2001, ApJS, 136, 119
Elmegreen, B. G., Leitner, S. N., Elmegreen, D. M., & Cuillandre, J.-C. 2003, ApJ, 593, 333
Gelfand, J. D., Lazio, T. J. W., & Gaensler, B. M. 2004, ApJS, 155, 89
Gelfand, J. D., Lazio, T. J. W., & Gaensler, B. M. 2005, ApJS, 159, 242
Ghavamian, P., Blair, W. P., Long, K. S., et al. 2005, AJ, 130, 539
Giacconi, R., Branduardi, G., Briel, U., et al. 1979, ApJ, 230, 540
Hillas, A. M. 2005, J. Phys. G Nucl. Phys., 31, 95
Jansen, F., Lumb, D., Altieri, B., et al. 2001, A&A, 365, L1
Kaaret, P. 2002, ApJ, 578, 114
Kodaira, K. 1974, PASJ, 26, 255
Kong, A. K. H., Garcia, M. R., Primini, F. A., & Murray, S. S. 2002a, ApJ, 580, L125
Kong, A. K. H., Garcia, M. R., Primini, F. A., et al. 2002b, ApJ, 577, 738
Kong, A. K. H., Sjouwerman, L. O., Williams, B. F., Garcia, M. R., & Dickel, J. R. 2003, ApJ, 590, L21
Leahy, D. A., & Wu, X. 1989, PASP, 101, 607
Long, K. S., Blair, W. P., Winkler, P. F., et al. 2010, ApJS, 187, 495
Magnier, E. A., Prins, S., van Paradijs, J., et al. 1995, A&AS, 114, 215
Massey, P., Olsen, K. A. G., Hodge, P. W., et al. 2006, AJ, 131, 2478
Massey, P., McNeill, R. T., Olsen, K. A. G., et al. 2007, AJ, 134, 2474
Mochejska, B. J., Kaluzny, J., Stanek, K. Z., & Sasselov, D. D. 2001, AJ, 122, 1383
Monet, D. G., Levine, S. E., Canzian, B., et al. 2003, AJ, 125, 984
Orio, M. 2006, ApJ, 643, 844
Osborne, J. P., Borozdin, K. N., Trudolyubov, S. P., et al. 2001, A&A, 378, 800
Pellet, A., Astier, N., Viale, A., et al. 1978, A&AS, 31, 439
Pietsch, W., Freyberg, M., & Haberl, F. 2005, A&A, 434, 483
Scowcroft, V., Bersier, D., Mould, J. R., & Wood, P. R. 2009, MNRAS, 396, 1287
Seiradakis, J. H. 1977, in NASA Conf. Publ. 2, eds. C. E. Fichtel, & F. W. Stecker, 265
Sellwood, J. A., & Carlberg, R. G. 1984, ApJ, 282, 61
Shaw Greening, L., Barnard, R., Kolb, U., Tonkin, C., & Osborne, J. P. 2009, A&A, 495, 733
Sofue, Y., & Kato, T. 1981, PASJ, 33, 449
Stark, A. A., Gammie, C. F., Wilson, R. W., et al. 1992, ApJS, 79, 77
Stecker, F. W., & Jones, F. C. 1977, ApJ, 217, 843
Stiele, H., Pietsch, W., Haberl, F., & Freyberg, M. 2008, A&A, 480, 599
Stiele, H., Pietsch, W., Haberl, F., et al. 2011, A&A, 534, A55 (SPH11)
Strüder, L., Briel, U., Dennerl, K., et al. 2001, A&A, 365, L18
Supper, R., Hasinger, G., Pietsch, W., et al. 1997, A&A, 317, 328 (SHP97)
Supper, R., Hasinger, G., Lewin, W. H. G., et al. 2001, A&A, 373, 63 (SHL01)
Tabatabaei, F. S., & Berkhuijsen, E. M. 2010, A&A, 517, A77
Trinchieri, G., & Fabbiano, G. 1991, ApJ, 382, 82
Trümper, J. 1982, Adv. Space Res., 2, 241
Turner, M. J. L., Abbey, A., Arnaud, M., et al. 2001, A&A, 365, L27
van Speybroeck, L., Epstein, A., Forman, W., et al. 1979, ApJ, 234, L45
Verley, S., Corbelli, E., Giovanardi, C., & Hunt, L. K. 2009, A&A, 493, 453
Vilardell, F., Ribas, I., Jordi, C., Fitzpatrick, E. L., & Guinan, E. F. 2010, A&A, 509, A70
Walterbos, R. A. M., & Braun, R. 1992, A&AS, 92, 625
Watkins, L. L., Evans, N. W., & An, J. H. 2010, MNRAS, 406, 264
Weaver, R., McCray, R., Castor, J., Shapiro, P., & Moore, R. 1977, ApJ, 218, 377
Weisskopf, M. C., Brinkman, B., Canizares, C., et al. 2002, PASP, 114, 1
Williams, B. F. 2003, AJ, 126, 1312
Williams, B. F., Garcia, M. R., Kong, A. K. H., et al. 2004a, ApJ, 609, 735
Williams, B. F., Sjouwerman, L. O., Kong, A. K. H., et al. 2004b, ApJ, 615, 720
Williams, B. F., Naik, S., Garcia, M. R., & Callanan, P. J. 2006, ApJ, 643, 356

Pages 16 to 33 are available in the electronic edition of the journal at http://www.aanda.org

Appendix A: *XMM-Newton* and LGGS images

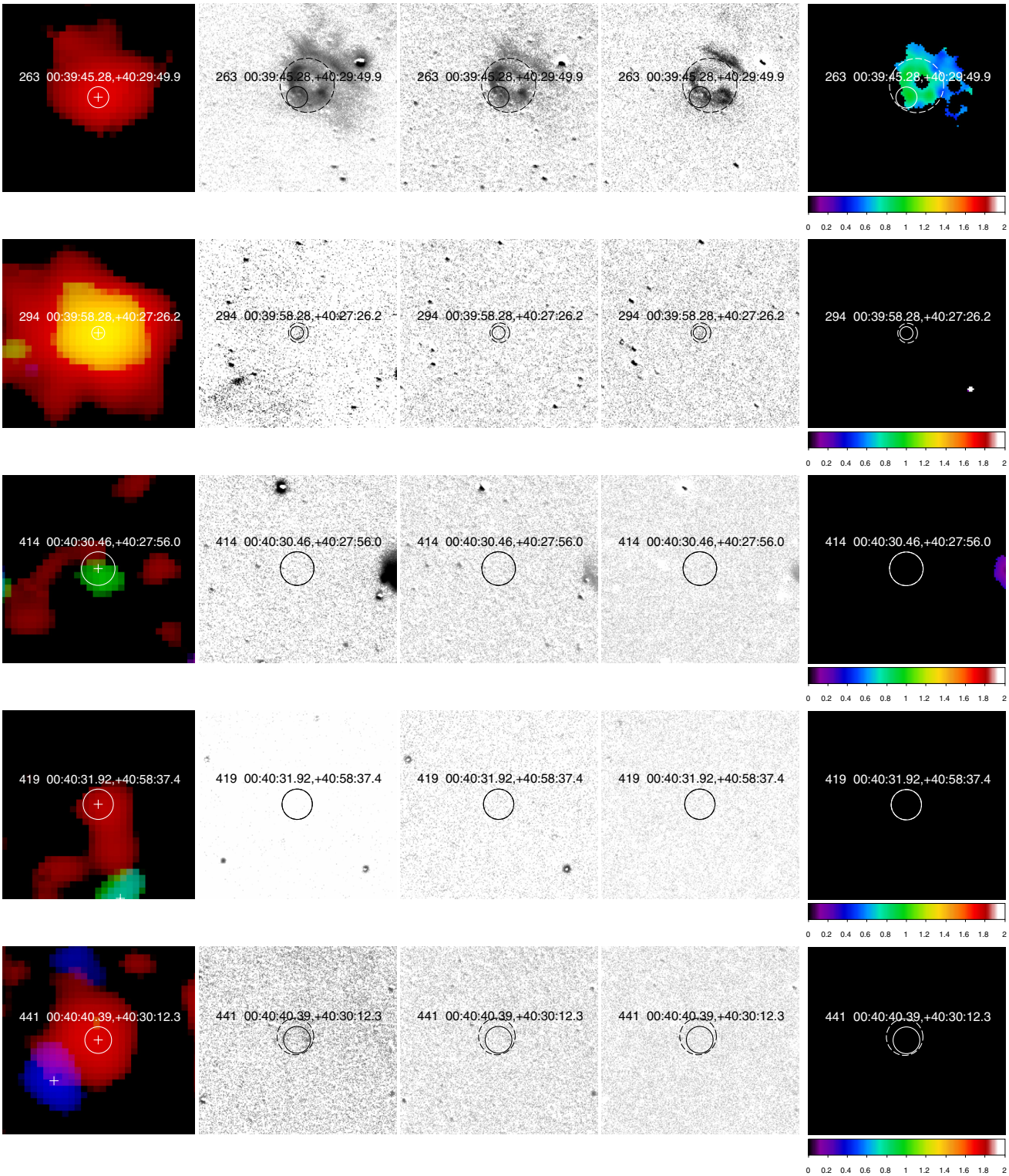

Fig. A.1. *XMM-Newton* three-colour image (red 0.2–1.0 keV, green 1.0–2.0 keV, blue 2.0–4.5 keV), continuum-subtracted LGGS Hα, [S II], and [O III] images, and an [S II]/Hα ratio image with *XMM-Newton* 3σ positional error circle (solid). The dashed circle shows the extraction region for the optical emission. If no dashed circle is shown, the X-ray error circle was used. The shown area has a size of $\sim 1' \times 1'$. The label gives the source number of the *XMM-Newton* catalogue (SPH11), followed by the coordinates. The positions of all detected *XMM-Newton* sources are marked in the *XMM-Newton* images (*left*) with crosses.

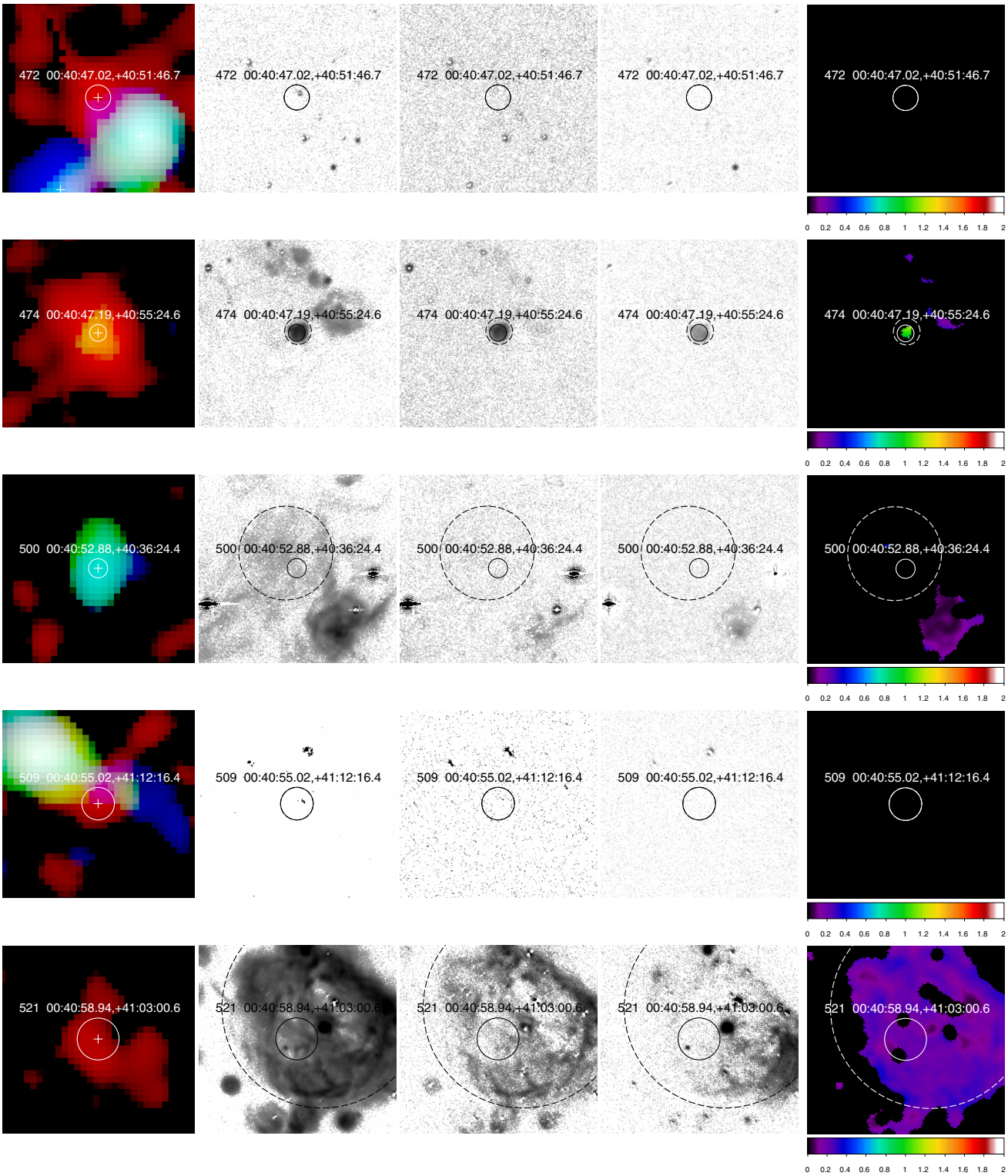

Fig. A.1. continued.

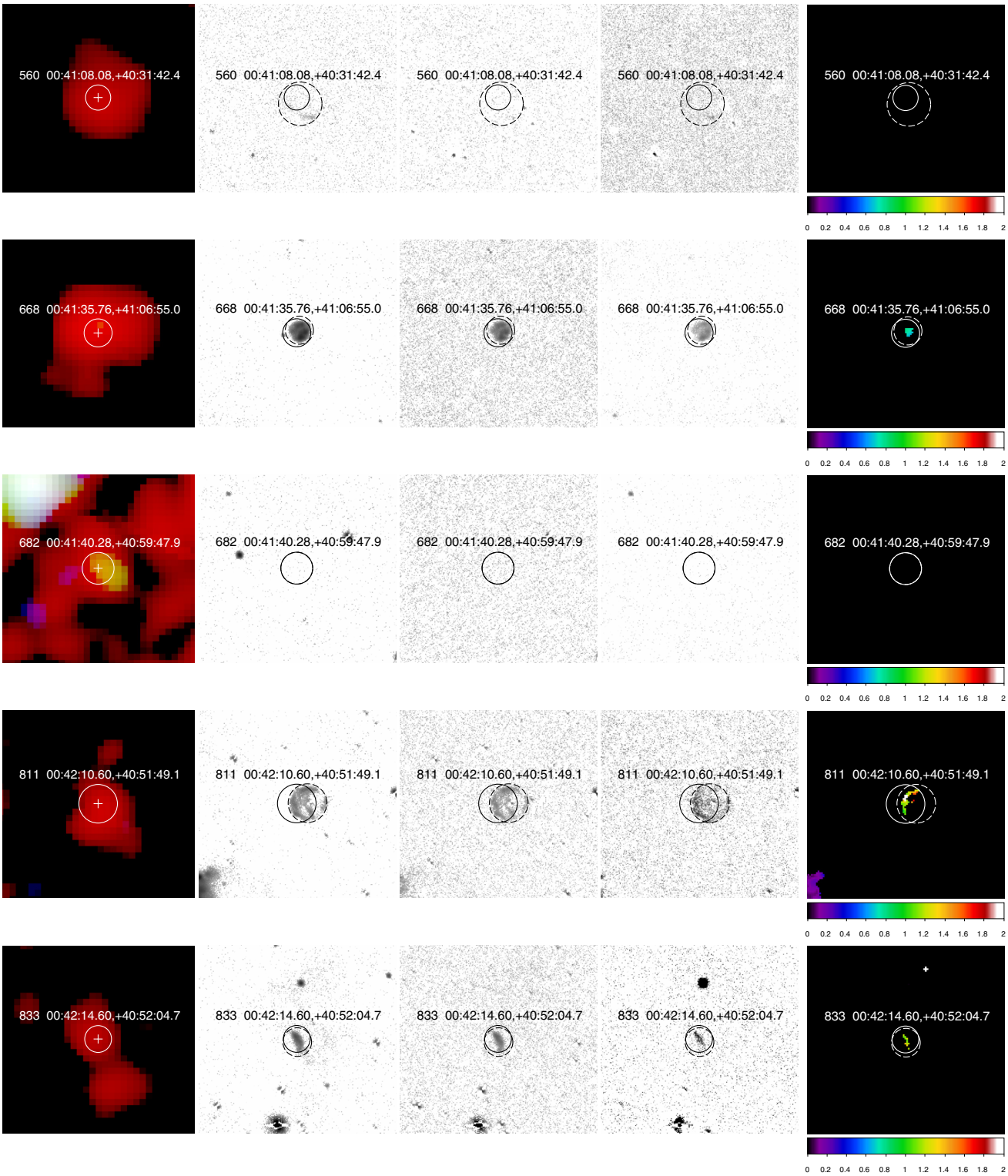

Fig. A.1. continued.

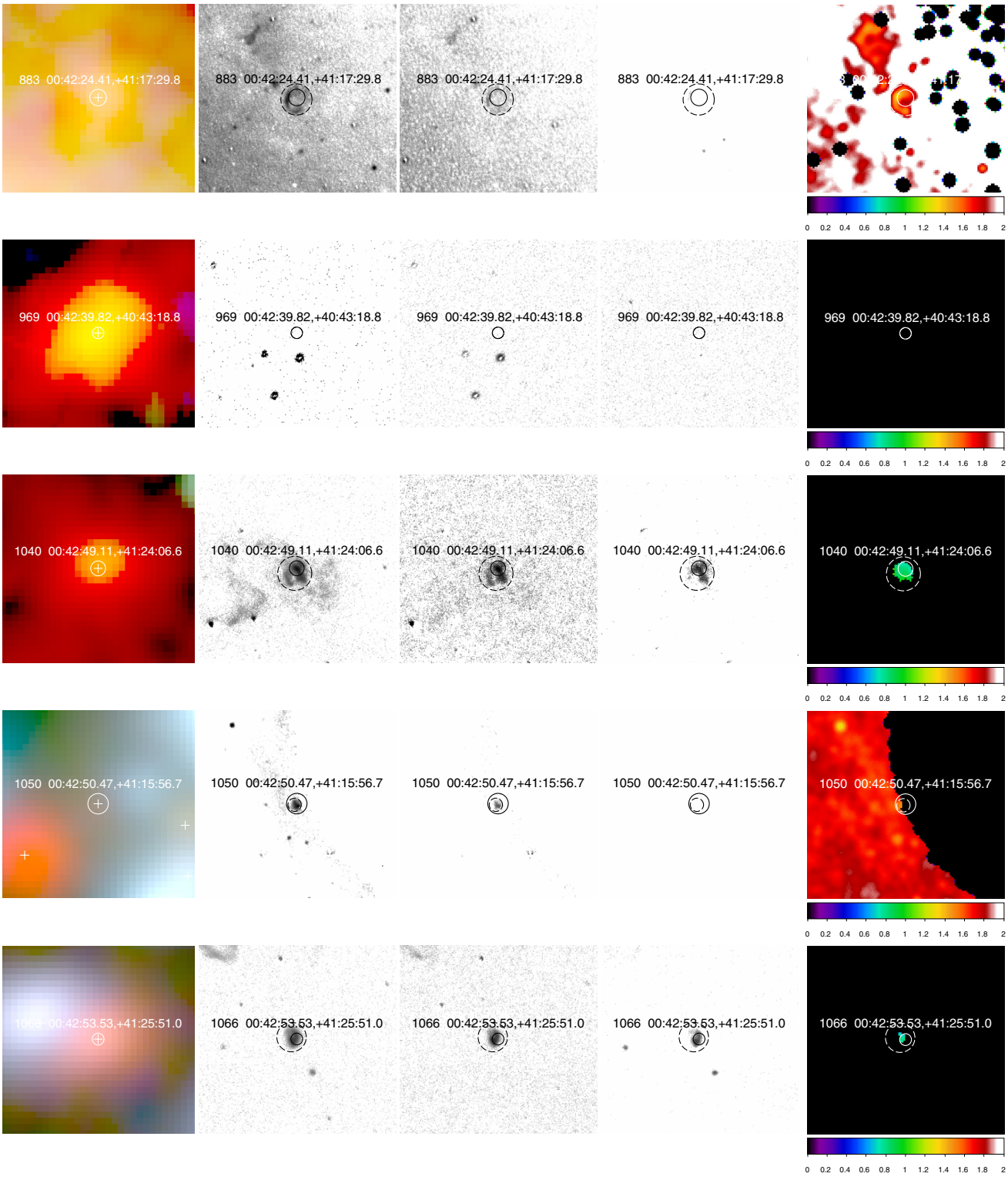

Fig. A.1. continued.

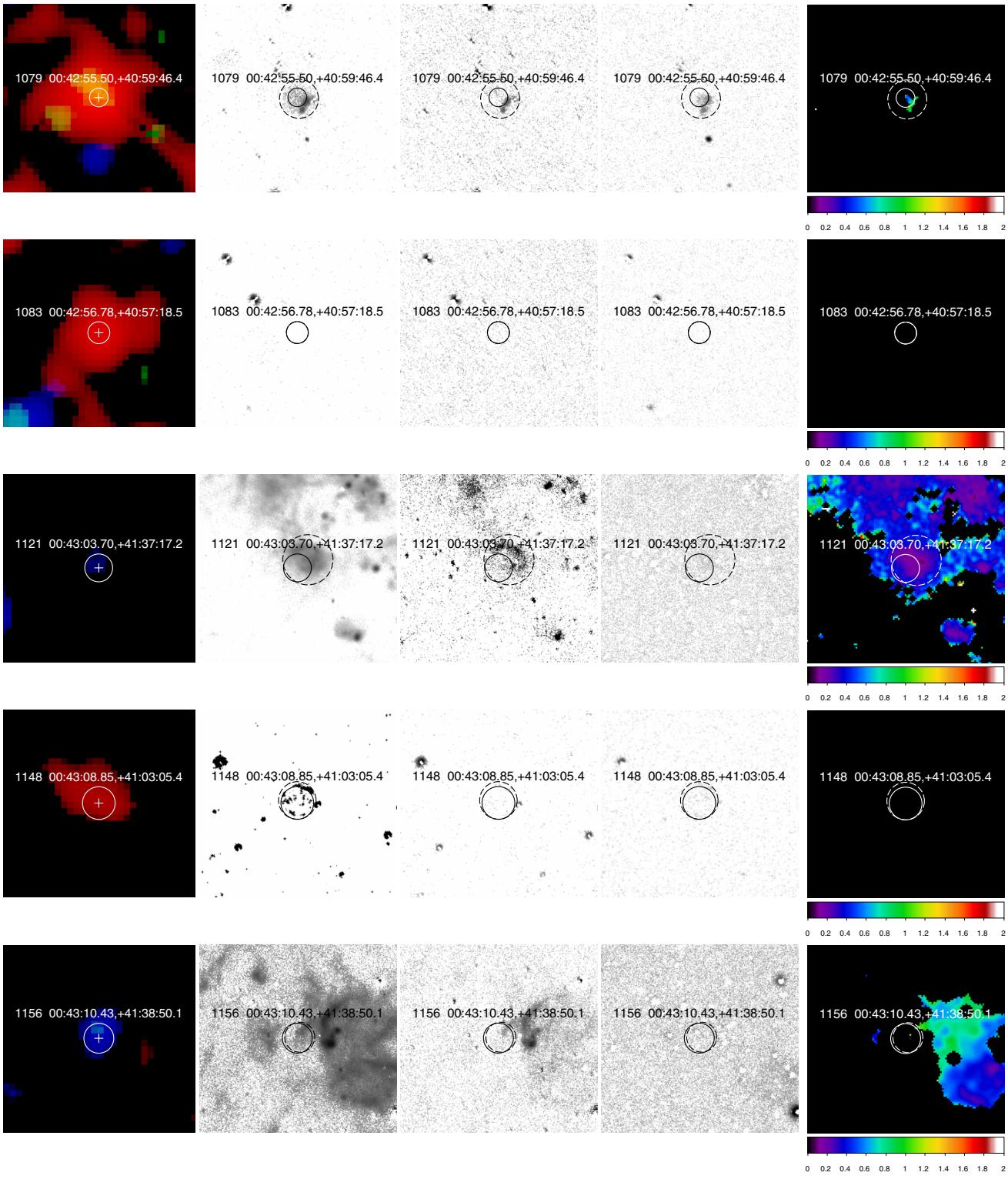

Fig. A.1. continued.

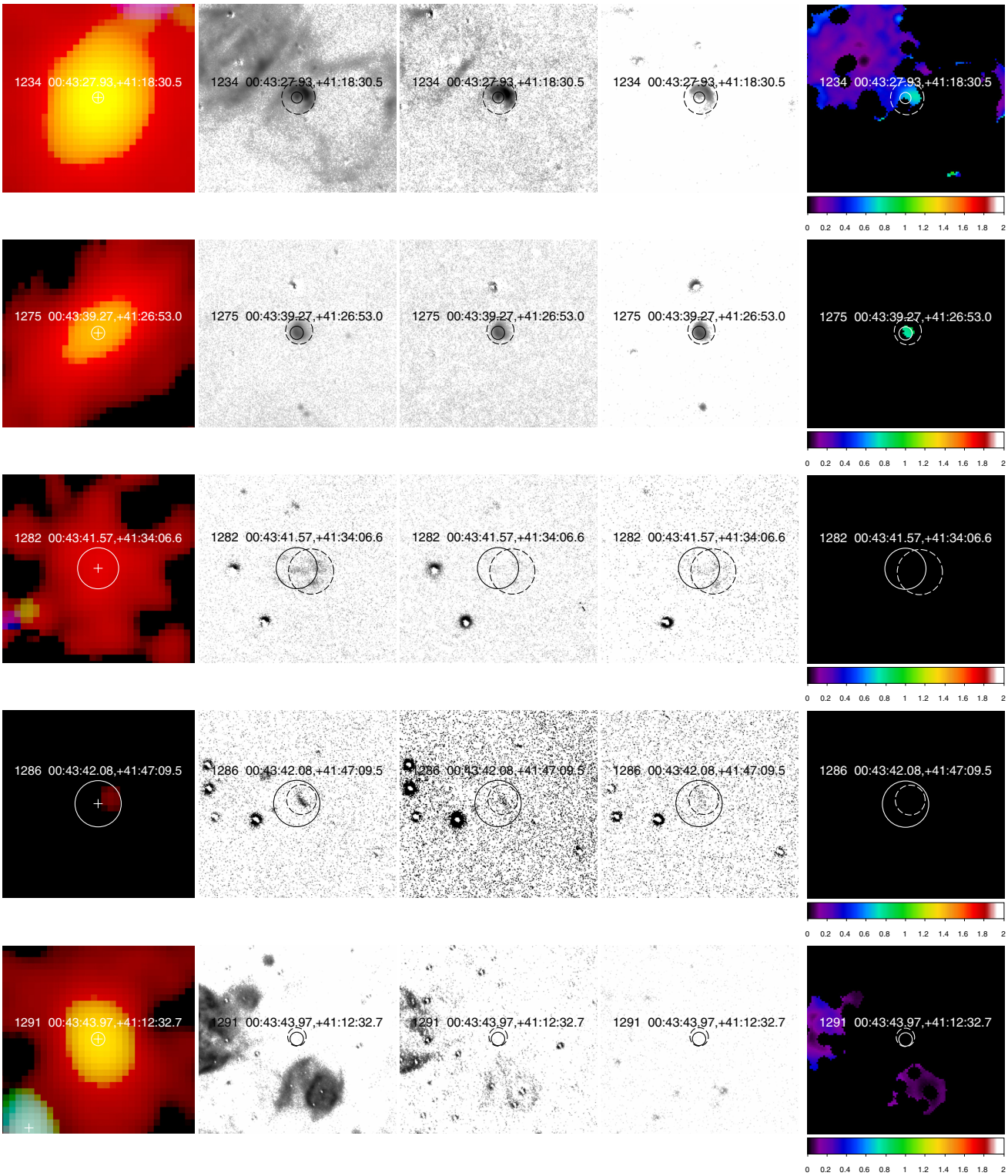

Fig. A.1. continued.

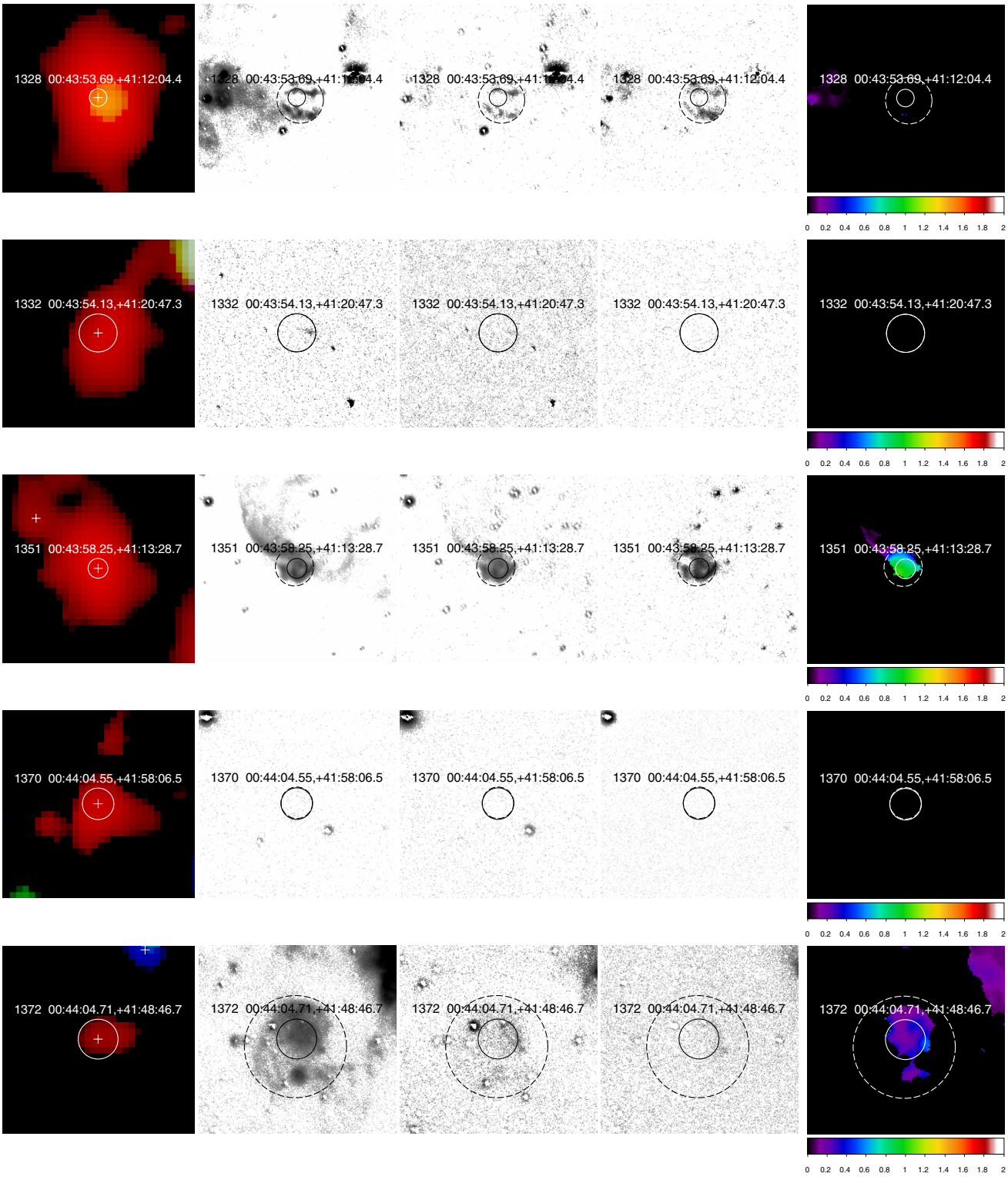

Fig. A.1. continued.

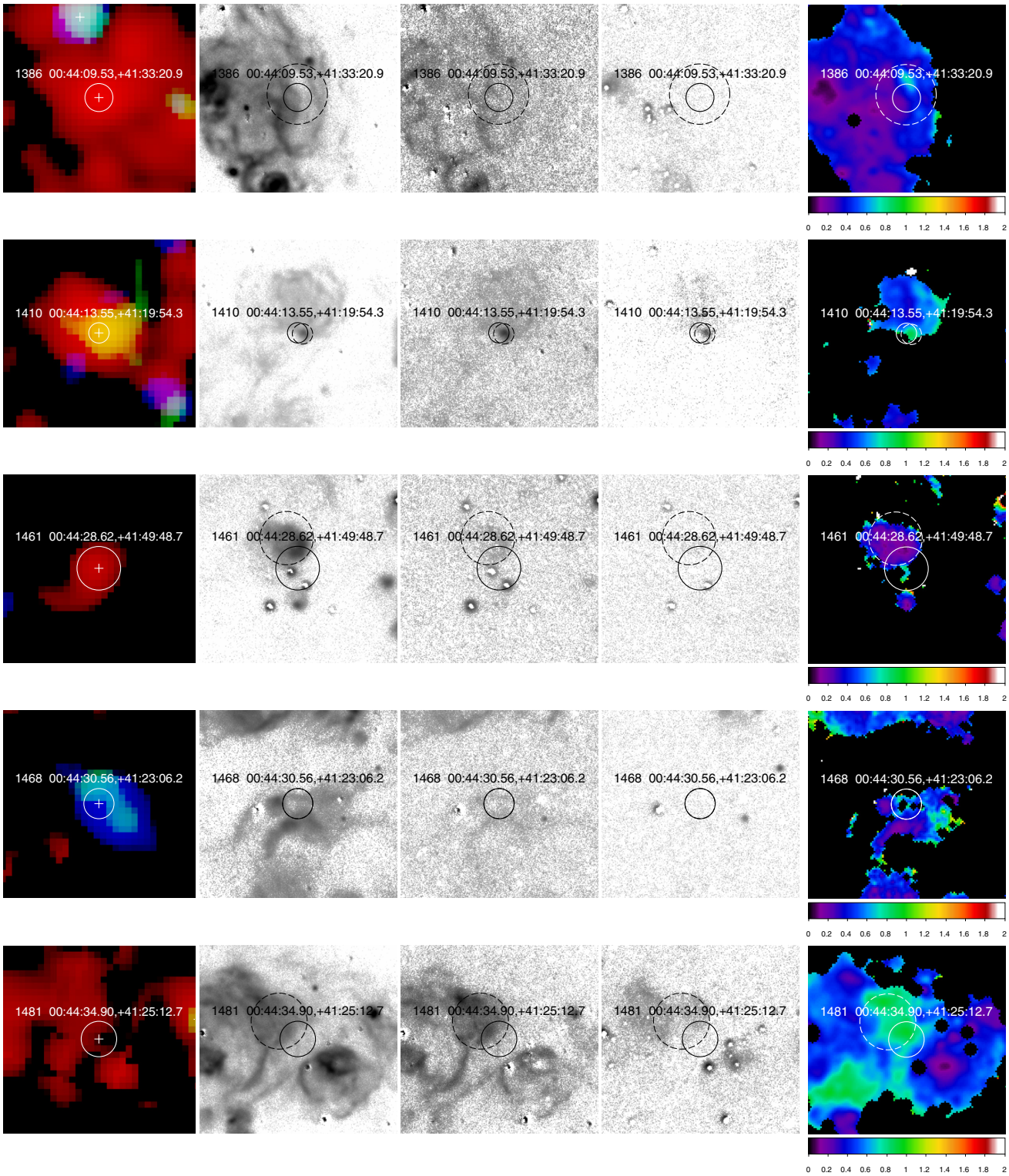

Fig. A.1. continued.

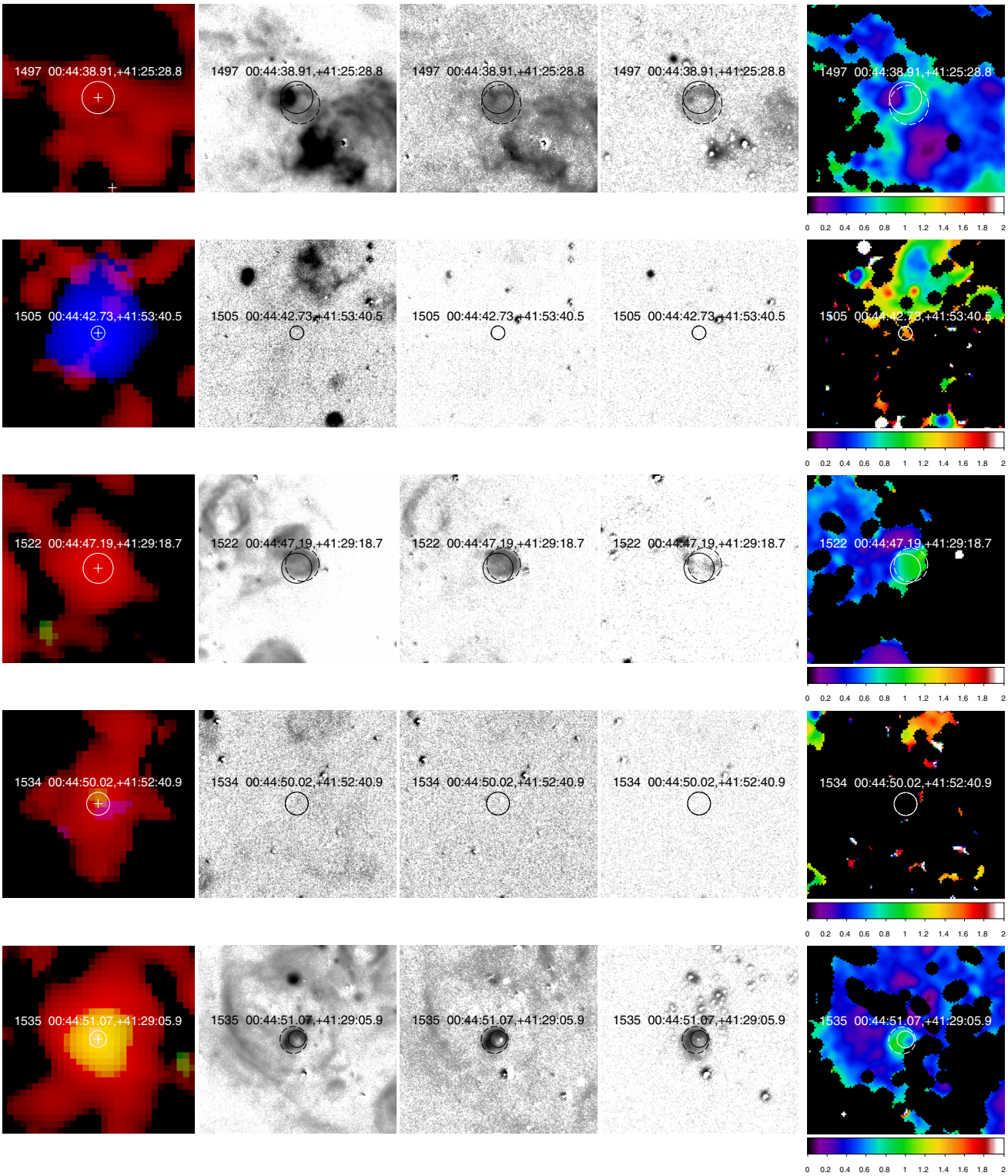

Fig. A.1. continued.

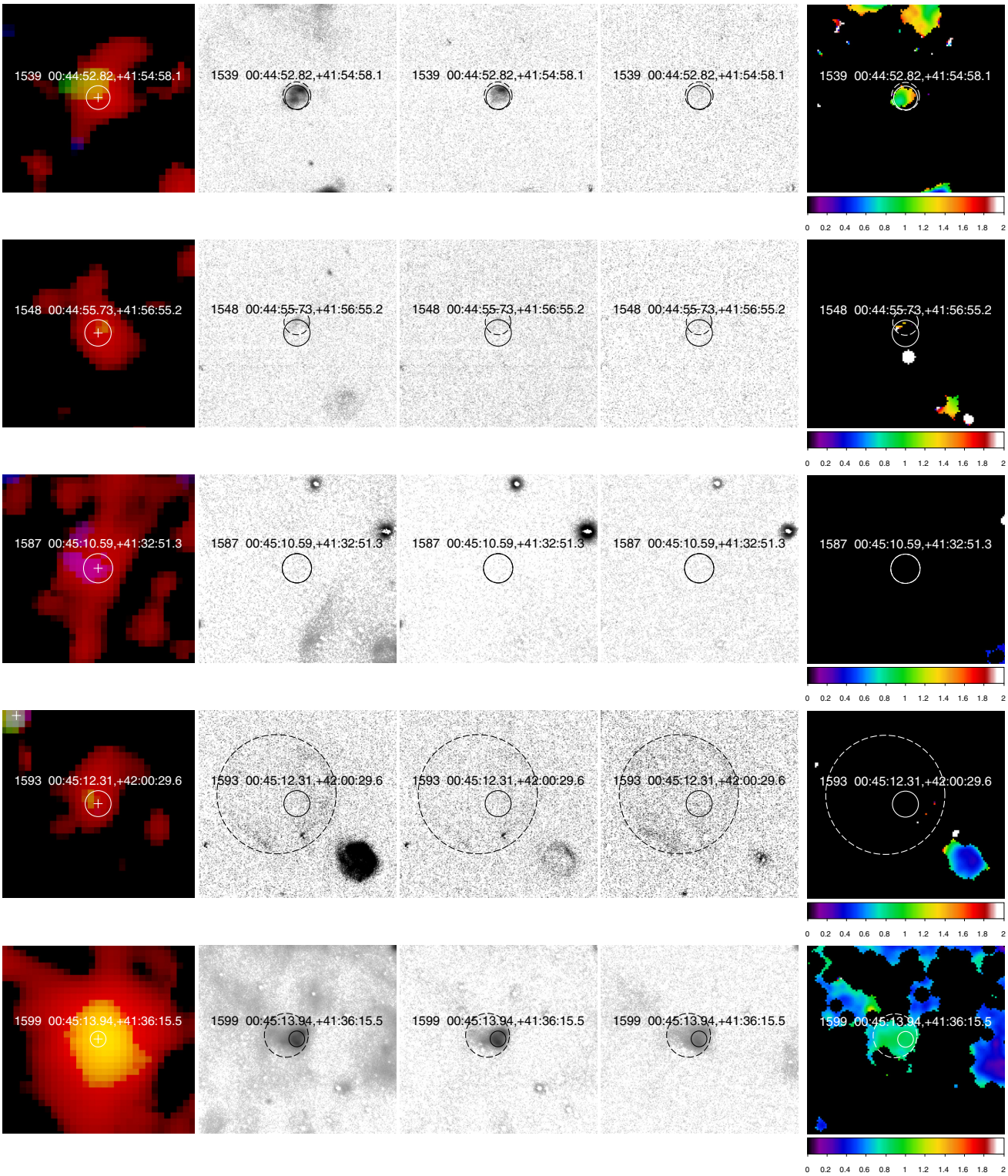

Fig. A.1. continued.

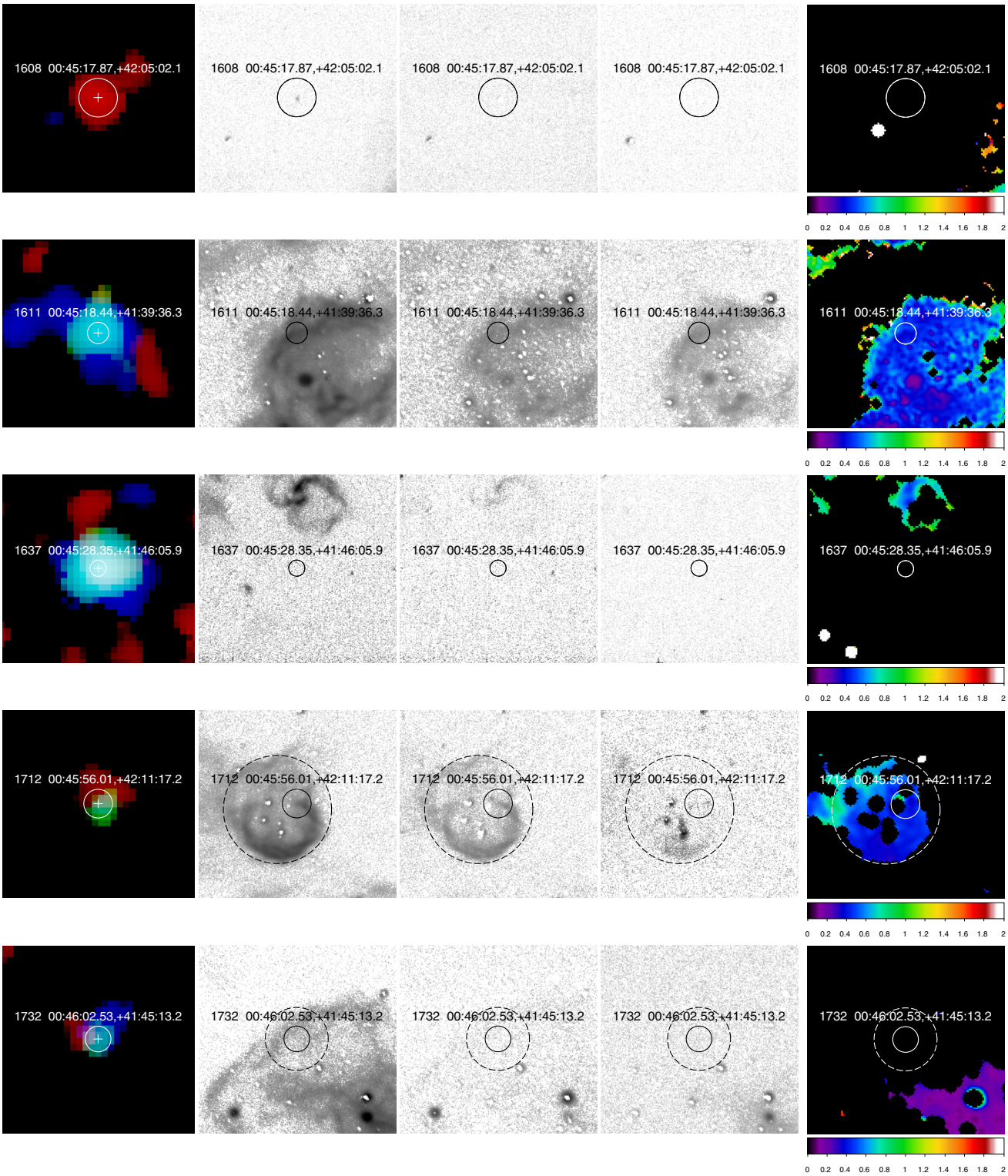

Fig. A.1. continued.

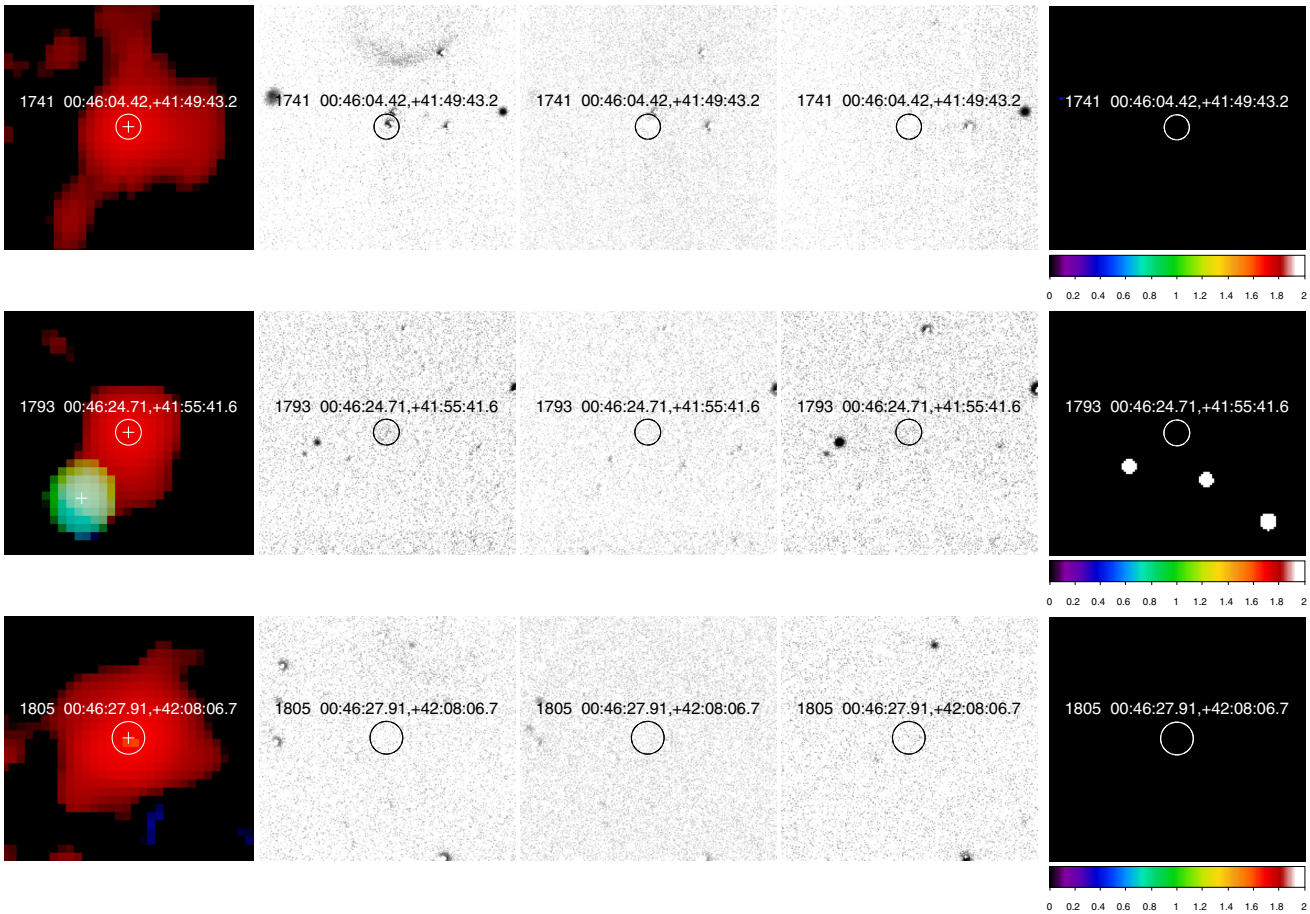

Fig. A.1. continued.

Appendix B: Supernova remnants and candidates in the *XMM-Newton* M 31 large survey catalogue

Table B.1. X-ray SNRs and candidates in the *XMM-Newton* M 31 survey catalogue by Stiele et al. (2011).

[SPH11] ID	RA (2000.0)	Dec (2000.0)	Pos. error [arcsec]	Rate [cts/s]	ML^a	$HR_1{}^b$	$HR_2{}^b$	$HR_3{}^b$	$HR_4{}^b$
				SNRs[c]					
182	00 39 23.50	+40 44 19.1	5.30	2.0e–3 ± 5.0e–5	13	0.95 ± 0.27	–0.64 ± 0.20		
263	00 39 45.28	+40 29 49.9	3.37	3.7e–3 ± 4.0e–5	96	0.42 ± 0.10	–0.93 ± 0.09		
474	00 40 47.19	+40 55 24.6	2.69	6.4e–3 ± 6.0e–5	180	0.90 ± 0.06	–0.63 ± 0.08	–0.88 ± 0.20	
668	00 41 35.76	+41 06 55.0	4.50	9.8e–3 ± 2.0e–4	62	0.71 ± 0.17	–0.30 ± 0.15	–0.80 ± 0.28	0.83 ± 0.25
883	00 42 24.41	+41 17 29.8	2.65	3.7e–3 ± 4.0e–5	52	0.80 ± 0.07	–0.98 ± 0.06		
1040	00 42 49.11	+41 24 06.6	2.38	9.2e–3 ± 5.0e–5	330	0.48 ± 0.05	–0.84 ± 0.05	–1.00 ± 0.27	
1050	00 42 50.47	+41 15 56.7	3.28	1.1e–2 ± 9.0e–5	73	0.53 ± 0.08	–0.96 ± 0.06		
1066	00 42 53.53	+41 25 51.0	1.89	3.5e–2 ± 1.0e–4	1400	0.56 ± 0.03	–0.70 ± 0.03	–0.94 ± 0.11	
1234	00 43 27.93	+41 18 30.5	1.79	7.4e–2 ± 1.0e–4	6300	0.44 ± 0.02	–0.71 ± 0.01	–0.95 ± 0.03	
1275	00 43 39.27	+41 26 53.0	2.12	2.9e–2 ± 1.0e–4	1200	0.39 ± 0.04	–0.76 ± 0.04	–0.87 ± 0.12	
1291	00 43 43.97	+41 12 32.7	2.15	1.7e–2 ± 8.0e–5	620	0.77 ± 0.04	–0.45 ± 0.04	–0.94 ± 0.06	
1328	00 43 53.69	+41 12 04.4	2.80	1.1e–2 ± 8.0e–5	270	0.53 ± 0.07	–0.58 ± 0.07	–1.00 ± 0.12	
1351	00 43 58.25	+41 13 28.7	3.17	6.0e–3 ± 6.0e–5	86	0.42 ± 0.10	–0.78 ± 0.10	–0.48 ± 0.43	
1372	00 44 04.71	+41 48 46.7	6.39	2.0e–3 ± 6.0e–5	9.0	0.78 ± 0.28	–0.55 ± 0.24		1.00 ± 0.26
1386	00 44 09.53	+41 33 20.9	4.49	2.0e–3 ± 3.0e–5	26	0.42 ± 0.17	–0.78 ± 0.13		
1410	00 44 13.55	+41 19 54.3	3.26	7.8e–3 ± 8.0e–5	120	0.92 ± 0.07	–0.37 ± 0.09	–0.72 ± 0.17	
1497	00 44 38.91	+41 25 28.8	5.17	5.4e–3 ± 1.0e–4	20	0.72 ± 0.17	–0.46 ± 0.19	–0.68 ± 0.29	
1522	00 44 47.19	+41 29 18.7	4.83	4.1e–3 ± 6.0e–5	34	0.44 ± 0.14	–0.70 ± 0.14		
1535	00 44 51.07	+41 29 05.9	2.71	1.5e–2 ± 1.0e–4	250	0.18 ± 0.08	–0.22 ± 0.09	–0.51 ± 0.12	–0.55 ± 0.53
1539	00 44 52.82	+41 54 58.1	3.81	1.9e–3 ± 3.0e–5	22	0.70 ± 0.21	–0.08 ± 0.18	–0.62 ± 0.23	
1587	00 45 10.59	+41 32 51.3	4.69	3.3e–3 ± 7.0e–5	22	0.31 ± 0.19	–0.67 ± 0.35		
1593	00 45 12.31	+42 00 29.6	4.16	1.6e–3 ± 3.0e–5	13	0.89 ± 0.16	–0.43 ± 0.18	–0.10 ± 0.32	
1599	00 45 13.94	+41 36 15.5	2.52	1.9e–2 ± 1.0e–4	590	0.71 ± 0.05	–0.55 ± 0.05	–1.00 ± 0.05	
1793	00 46 24.71	+41 55 41.6	3.18	4.7e–3 ± 5.0e–5	140	0.55 ± 0.09	–0.66 ± 0.10	–0.87 ± 0.37	
1805	00 46 27.91	+42 08 06.7	4.03	7.4e–3 ± 8.0e–5	120	0.45 ± 0.09	–0.73 ± 0.10	–1.00 ± 0.43	
				SNR candidates[c]					
294	00 39 58.28	+40 27 26.2	2.08	1.9e–2 ± 8.0e–5	1300	0.64 ± 0.03	–0.61 ± 0.04	–0.95 ± 0.07	
414	00 40 30.46	+40 27 56.0	5.38	4.1e–3 ± 8.0e–5	19		0.45 ± 0.23	–0.34 ± 0.21	–0.22 ± 0.39
419	00 40 31.92	+40 58 37.4	4.85	2.1e–3 ± 4.0e–5	15	0.20 ± 0.20	–0.82 ± 0.23		
441	00 40 40.39	+40 30 12.3	4.28	3.7e–3 ± 6.0e–5	41	0.75 ± 0.12	–0.74 ± 0.15		
472	00 40 47.02	+40 51 46.7	4.04	3.5e–3 ± 5.0e–5	44	0.61 ± 0.13	–0.70 ± 0.15		
500	00 40 52.88	+40 36 24.4	3.07	5.6e–3 ± 6.0e–5	94	0.69 ± 0.30	0.70 ± 0.11	–0.18 ± 0.10	–0.42 ± 0.23
509	00 40 55.02	+41 12 16.4	5.23	2.2e–3 ± 4.0e–5	12	0.52 ± 0.19	–0.67 ± 0.19		
521	00 40 58.94	+41 03 00.6	6.72	2.2e–3 ± 5.0e–5	10	0.80 ± 0.19	–0.46 ± 0.20	–0.88 ± 0.38	
560	00 41 08.08	+40 31 42.4	4.04	5.6e–3 ± 7.0e–5	53	0.66 ± 0.11	–0.71 ± 0.12	–0.16 ± 0.40	
682	00 41 40.28	+40 59 47.9	5.11	1.6e–3 ± 4.0e–5	7.6	0.61 ± 0.23	–0.48 ± 0.26	0.11 ± 0.38	–0.27 ± 0.57
969	00 42 39.82	+40 43 18.8	1.84	7.3e–2 ± 2.0e–4	4800	0.06 ± 0.02	–0.75 ± 0.02	–0.92 ± 0.07	
1079	00 42 55.50	+40 59 46.4	3.00	5.1e–3 ± 6.0e–5	110	0.77 ± 0.09	–0.69 ± 0.11	–0.90 ± 0.37	
1083	00 42 56.78	+40 57 18.5	3.51	2.0e–3 ± 3.0e–5	28	0.43 ± 0.14	–0.98 ± 0.09		
1148	00 43 08.85	+41 03 05.4	5.25	2.7e–3 ± 5.0e–5	16	0.66 ± 0.16	–0.60 ± 0.21		
1156	00 43 10.43	+41 38 50.1	4.80	2.3e–3 ± 4.0e–5	24		0.98 ± 0.32	0.25 ± 0.19	0.10 ± 0.19
1282	00 43 41.57	+41 34 06.6	6.59	2.4e–3 ± 3.0e–5	38	0.08 ± 0.14	–0.96 ± 0.15		
1332	00 43 54.13	+41 20 47.3	6.10	4.7e–3 ± 8.0e–5	22	0.12 ± 0.17	–0.91 ± 0.18		
1370	00 44 04.55	+41 58 06.5	5.05	2.8e–3 ± 6.0e–5	21	0.94 ± 0.14	–0.96 ± 0.14		
1437	00 44 21.18	+42 16 21.9	6.22	2.1e–3 ± 6.0e–5	8.5	0.73 ± 0.21	–0.64 ± 0.25		
1481	00 44 34.90	+41 25 12.7	5.69	4.2e–3 ± 8.0e–5	20	0.97 ± 0.11	–0.87 ± 0.17		
1505	00 44 42.73	+41 53 40.5	2.19	7.0e–3 ± 5.0e–5	840	0.50 ± 0.27	–0.73 ± 0.27	0.97 ± 0.04	0.50 ± 0.04
1534	00 44 50.02	+41 52 40.9	3.67	2.8e–3 ± 5.0e–5	26	0.59 ± 0.19	–0.39 ± 0.17	–0.54 ± 0.31	
1548	00 44 55.73	+41 56 55.2	4.24	1.9e–3 ± 4.0e–5	20	0.95 ± 0.13	–0.34 ± 0.19	–0.83 ± 0.34	
1608	00 45 17.87	+42 05 02.1	6.19	2.4e–3 ± 5.0e–5	14	0.57 ± 0.20	–0.53 ± 0.25		
1637	00 45 28.35	+41 46 05.9	2.58	5.7e–3 ± 5.0e–5	170	0.34 ± 0.33	0.70 ± 0.11	–0.06 ± 0.10	–0.06 ± 0.15
1669	00 45 38.26	+41 12 46.9	5.13	3.4e–3 ± 1.0e–4	16	0.65 ± 0.31	–0.61 ± 0.38		
1712	00 45 56.01	+42 11 17.2	4.60	3.4e–3 ± 7.0e–5	18	0.61 ± 0.26	0.04 ± 0.25	0.02 ± 0.24	–0.15 ± 0.37
1732	00 46 02.53	+41 45 13.2	4.11	4.3e–3 ± 7.0e–5	28	0.95 ± 0.64	0.52 ± 0.19	–0.13 ± 0.17	–0.16 ± 0.30
1741	00 46 04.42	+41 49 43.2	3.09	5.6e–3 ± 7.0e–5	90	0.33 ± 0.11	–0.65 ± 0.14	–0.78 ± 0.42	
1748	00 46 06.34	+41 29 23.6	4.21	2.4e–3 ± 4.0e–5	27	0.58 ± 0.19	–0.40 ± 0.21	–0.17 ± 0.35	0.54 ± 0.23
1796	00 46 25.39	+41 09 38.7	5.06	9.7e–3 ± 2.0e–4	32	0.33 ± 0.22	–0.48 ± 0.21	0.33 ± 0.27	–0.59 ± 0.43

Notes. [a] Detection likelihood. [b] Hardness ratios. [c] Classification by SPH11.

Appendix C: SDSS images

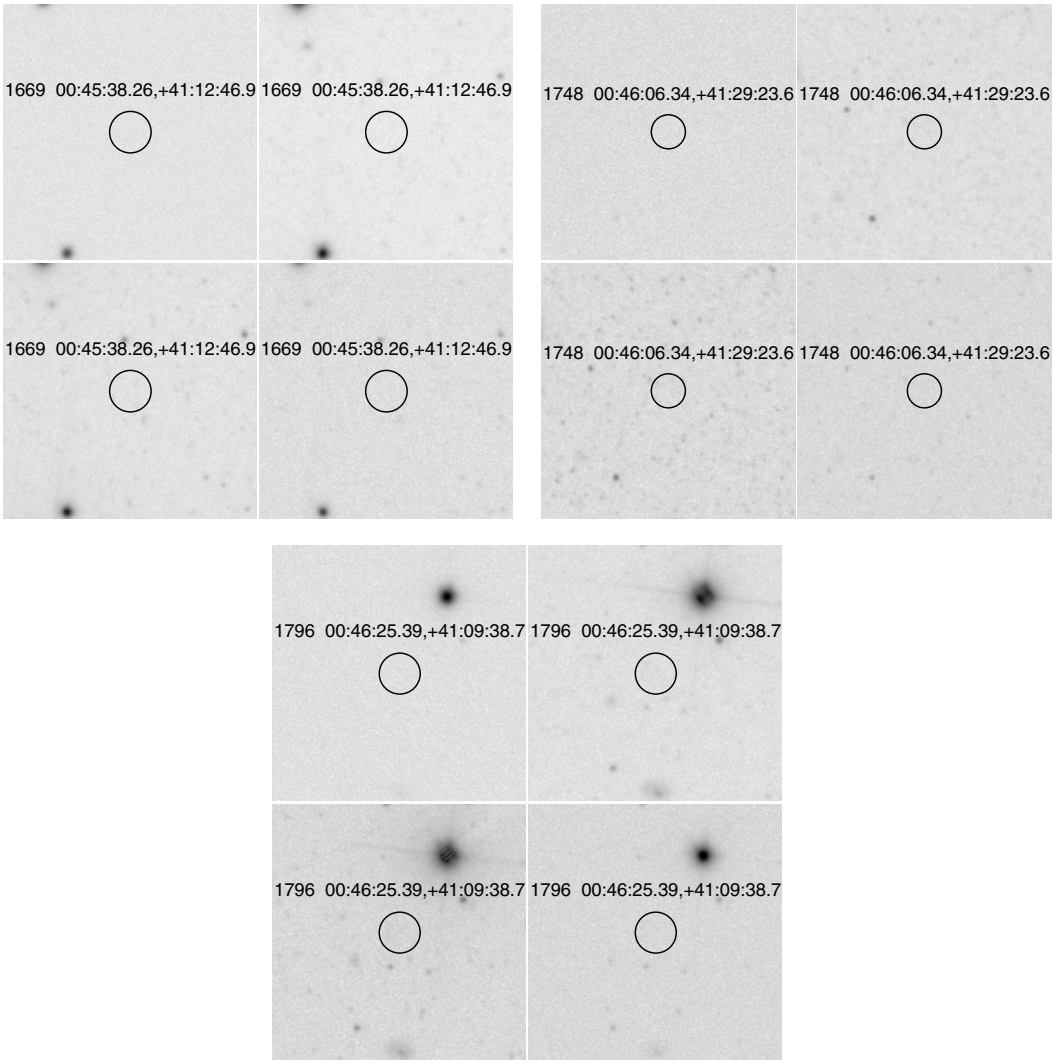

Fig. C.1. SDSS-III images (*upper left*: *u* band, *upper right*: *r* band, *lower left*: *i* band, *lower right*: *z* band) of [SPH11] 1669, 1748, and 1796. The shown area has a size of $\sim 1' \times 1'$.

Appendix D: Sources with unchanged classification

D.1. SNRs

D.1.1. [SPH11] 182: XMMM31 J003923.50+404419.1

[SPH11] 182 is a soft X-ray source with hardness ratios indicative of an SNR. No foreground star was found at its position. The X-ray source is coincident with the optical SNR [DDB80] 1-4, which corresponds to [BA64] 474 and [PAV78] 118. On the basis of these results, the source was classified as an SNR by SPH11.

The optical source is clearly visible in all three emission-line images of the LGGS (Fig. 2) and has a limb-brightened shell that is bright in the southeast. The diameter of the optical SNR is ∼16″. We confirm the SNR classification based on the [S II]/Hα flux ratio (Table 3). The LGGS *UBVRI* band images show several blue point-like sources at the position of the SNR, indicating a group of young stars.

D.1.2. [SPH11] 474: XMMM31 J004047.19+405524.6

[SPH11] 474 has hardness ratios indicative of an SNR and is coincident with the optical SNR [DDB80] 1-7. A radio counterpart [GLG04] 68 was found with $\alpha = -0.25$, which might indicate a PWN (GLG05).

From the analysis of the LGGS narrow-band images, we derived an [S II]/Hα flux ratio of 1.0 ± 0.5 (Fig. A.1), which thus confirms the SNR identification. The source is rather compact with a diameter of ∼5″, corresponding to ∼18 pc.

D.1.3. [SPH11] 883: XMMM31 J004224.41+411729.8

[SPH11] 883 has hardness ratios indicative of an SNR and is coincident with the *Chandra* source [KGP02] r2-57, which was identified as an SNR by WSK04 based on additional studies of LGGS and Very Large Array radio data.

Its optical line flux ratio is [S II]/Hα = 0.9 ± 0.2, corroborating an SNR nature. The optical source has an arc-like structure with an extent of ∼9″ (Fig. A.1). It is brightest in the east. This source is the second closest SNR to the centre of M 31 with a galactocentric distance of about 860 pc.

D.1.4. [SPH11] 1040: XMMM31 J004249.11+412406.6

[SPH11] 1040 is coincident with the *Chandra* source [KGP02] r3-84, which was identified as an SNR by WSK04, as well as the radio source [B90] 97. It was therefore classified as an SNR by PFH05 and SPH11.

There is significant Hα, [S II], and [O III] emission at its position and the flux ratio of [S II]/Hα = 0.8 ± 0.2 confirms its SNR nature (Fig. A.1). The optical SNR has a patchy, ring-like morphology with an extent of ∼6″ and is brightest in the north. It is surrounded by faint, diffuse Hα emission.

D.1.5. [SPH11] 1050: XMMM31 J004250.47+411556.7

[SPH11] 1050 is a soft source and is coincident with the *Chandra* source [KGP02] r2-56, which was identified as an SNR by Kong et al. (2003). Therefore, the *XMM-Newton* source was classified as an SNR by SPH11. The source also has an extended radio counterpart [B90] 101. It is located at a distance of about 70″ from the galactic centre (i.e., about 250 pc).

In the optical, the SNR is a rather compact source with an extent of ∼3″ (Fig. A.1). On the LGGS images, it is located at the edge of the central part of M 31 where the subtracted continuum images are saturated, as can be seen in the [S II]/Hα ratio image.

D.1.6. [SPH11] 1066: XMMM31 J004253.53+412551.0

[SPH11] 1066 is a bright X-ray source with a detection likelihood of ML = 1400. It is coincident with a *Chandra* source that was classified as an SNR by KGP02 (r3-69), the optical SNR [DDB80] 1-13 ([BA64] 521), and its radio counterpart [B90] 106. Therefore, the *XMM-Newton* source was classified as an SNR by PFH05 and SPH11.

There is significant Hα, [S II], and [O III] emission at its position and the flux ratio of [S II]/Hα = 0.9 ± 0.2 confirms its SNR nature (Fig. A.1). It is slightly elongated in the north-south direction with a size of ∼4″ × 8″, being brighter in the south. The relatively hard X-ray spectrum and the rather small extent of the source seen in the optical suggest that it is a young SNR.

D.1.7. [SPH11] 1234: XMMM31 J004327.93+411830.5

[SPH11] 1234 is the brightest source in our list with ML = 6300 and is a soft X-ray source. It is coincident with the *Chandra* source [KGP02] r3-63, which was identified as an SNR by Kong et al. (2002a), with the optical SNR [MPV95] 2-033, and the radio source [B90] 142. Therefore, it was classified as an SNR by PFH05 and SPH11.

Its *XMM-Newton* spectrum is best fitted with a combination of two thermal components (see Sect. 3.1). The soft X-ray spectrum indicates that the source is not strongly absorbed. In addition, since there is significant emission even below 0.5 keV but almost no emission above 1 keV, it might be a rather old SNR. The optical source seen in the LGGS Hα, [S II], and [O III] images has a horse-shoe shaped structure with an extent of ∼8″, corresponding to 50–60 pc (see Fig. A.1). It is brighter on one side (northwest) and open on the other side (southeast), which is typical of SNRs evolving in a medium with a density gradient. There is also significant extended diffuse emission visible in the optical emission-line images around the SNR, which indicates that the SNR might be embedded in a superbubble. The X-ray spectrum of the SNR might therefore have been contaminated by thermal emission from the interstellar gas in its environment.

D.1.8. [SPH11] 1275: XMMM31 J004339.27+412653.0

[SPH11] 1275 is a bright source (ML = 1200) embedded in a region with soft diffuse emission. The X-ray position agrees very well with the optical SNR [MPV95] 3-059, which is also a radio source ([B90] 158). Therefore, the source was classified as an SNR by PFH05 and SPH11.

Its [S II]/Hα flux ratio is 0.9±0.2. The SNR has a half-circular shape in the optical, which is open to the northwest and has an extent of ∼7″ (Fig. A.1).

D.1.9. [SPH11] 1291: XMMM31 J004343.97+411232.7

[SPH11] 1291 is a soft X-ray source and has been classified as an SNR based on its positional coincidence with the radio source [B90] 166, which is an extended continuum source. O06 also discussed the possibility of this source being an SNR ([O06] 4).

In the optical, it is located in-between two diffuse sources in the east and the south visible in Hα, which are most likely H II regions (Fig. A.1). Neither [S II] nor [O III] emission is significant. Therefore, the source is most likely a non-radiative SNR.

D.1.10. [SPH11] 1328: XMMM31 J004353.69+411204.4

[SPH11] 1328 is a soft X-ray source coincident with the optical SNR [BW93] K230A (Fig. A.1) and was thus classified as an SNR by PFH05 and SPH11. Radio emission that fills the western half of the gap between the optical line emission was also found.

In the optical, the source consists of brighter regions to the north and the south, which are both extended in the east-west direction, thus form a parallel structure. The entire structure has an extent of ∼15″.

D.1.11. [SPH11] 1351: XMMM31 J004358.25+411328.7

[SPH11] 1351 is a soft source coincident with the optical SNR [BW93] K252 ([DDB80] 18) and the radio source [B90] 199. It was therefore classified as an SNR by PFH05 and SPH11.

In the optical, the source has an extent of ∼12″ and is located on the southern edge of the more extended structure visible in the Hα image (Fig. A.1). The [S II]/Hα flux ratio of 0.8 ± 0.2 fulfils the criterion for SNRs. In the optical, the source has a half-shell structure in the south with filaments extending to the north. In general, it has a patchy morphology.

D.1.12. [SPH11] 1386: XMMM31 J004409.53+413320.9

[SPH11] 1386 is a soft X-ray source. In the catalogues of PFH05 and SPH11, it was classified as an SNR based on its positional coincidence with the radio source [B90] 217.

It is located inside the H II region [WB92] 315, which can also be seen in the LGGS images (Fig. A.1). The [S II]/Hα flux ratio at the X-ray position is low (≈0.2). Therefore, the source is likely a non-radiative SNR.

D.1.13. [SPH11] 1410: XMMM31 J004413.55+411954.3

[SPH11] 1410 is a soft source coincident with the optical SNR [BW93] K327 with the radio counterpart [B90] 224. Therefore, it was classified as an SNR by SPH11.

The X-ray position coincides with a knot with an extent of ∼4″ in the optical emission-line images located at the southern edge of a more extended diffuse emission (Fig. A.1). The extended emission is likely an H II region, whereas the optical SNR has a flux ratio of [S II]/Hα = 0.9 ± 0.2.

D.1.14. [SPH11] 1497: XMMM31 J004438.91+412528.8

[SPH11] 1497 is a faint soft source and has been classified as an SNR by PFH05 and SPH11 based on its coincidence with an SNR candidate suggested by [MPV95]. It is the counterpart of the optical and radio SNR [BW93] K506A, [B90] 278.

The morphology of its optical line emission is that of a circular shell with a diameter of ∼12″ and is most clearly seen in the [S II] image (Fig. A.1). There is a bright blob-like Hα source east to the SNR. While the SNR shell has an [S II]/Hα flux ratio of ∼1.0, the Hα blob reduces the [S II]/Hα ratio of the total SNR (0.5 ± 0.1).

D.1.15. [SPH11] 1522: XMMM31 J004447.19+412918.7

[SPH11] 1522 is a soft X-ray source and coincides with the optical SNR [BW93] K548 and was thus identified as an SNR by PFH05 and SPH11.

A shell with an extent of ∼10″ is seen in the LGGS images, which is slightly elongated in the east-west direction (Fig. A.1) and is brighter to the west. Its [S II]/Hα flux ratio of 1.0 ± 0.2 is clearly indicative of an SNR. A nebula that is bright only in Hα with a similar size is located northeast of the SNR.

D.1.16. [SPH11] 1539: XMMM31 J004452.82+415458.1

[SPH11]1539 is the X-ray counterpart of the optical SNR [BW93] K594 and its radio counterpart [B90] 316. It was therefore identified as an SNR by PFH05 and SPH11.

It has an extent of ∼8″ in the optical and is brighter in the north (Fig. A.1). Its [S II]/Hα flux ratio is 1.0 ± 0.4.

D.1.17. [SPH11] 1587: XMMM31 J004510.59+413251.3

[SPH11] 1587 is a faint, soft X-ray source and is positionally coincident with a shell-type radio source [B90] 354 with an offset of ∼3″. It was thus classified as an SNR by SPH11.

No optical emission is detected at its position. Therefore, the SNR seems to be non-radiative.

D.1.18. [SPH11] 1593: XMMM31 J004512.31+420029.6

[SPH11] 1593 is a faint, soft X-ray source and is coincident with a radio source [B90] 365 with an amorphous shape and was thus classified as an SNR by SPH11.

Faint shell-like emission can be seen in the Hα, [S II], [O III] images (Fig. A.1) that has a diameter of about 30″. Its optical flux ratio [S II]/Hα is 1.0 ± 0.4, indicative of an SNR. We therefore also classify this source as an SNR, most likely a highly evolved SNR. It is so far the largest X-ray SNR detected in M 31.

D.1.19. [SPH11] 1599: XMMM31 J004513.94+413615.5

[SPH11] 1599 is the X-ray counterpart of the optical SNR [DDB80] 19 ([BW93] K717) and the radio source [B90] 367. It was identified as an SNR by PFH05 and SPH11.

The optical SNR has an extent of ∼10″. It is bright in the west and has a diffuse extension to the east (Fig. A.1). The X-ray poisition coincides with the bright part in the optical.

D.1.20. [SPH11] 1793: XMMM31 J004624.71+415541.6

[SPH11] 1793 is a soft X-ray source coincident with the source [PFH05] 745. The X-ray source has an extended radio counterpart [B90] 472 and was thus classified as an SNR by PFH05 and SPH11.

Only faint emission is seen in the LGGS images (Fig. A.1). The optical flux ratio [S II]/Hα is 0.7 ± 0.3. On the basis of the X-ray properties and the coincidence with a radio continuum source, we also classify this source as an SNR, which is most likely non-radiative.

D.1.21. [SPH11] 1805: XMMM31 J004627.91+420806.7

[SPH11] 1805 is a soft X-ray source coincident with the radio source [B90] 476 and was thus classified as an SNR by PFH05, O06, and SPH11.

Very faint optical line-emission is detected in the LGGS images. The [S II]/Hα flux ratio of 3.0 ± 1.1 is indicative of an SNR.

D.2. SNR candidates

D.2.1. [SPH11] 294: XMMM31 J003958.28+402726.2

[SPH11] 294 is a bright X-ray source with hardness ratios typical of an SNR. As no foreground star is detected, it was proposed as an SNR candidate by PFH05 and SPH11.

We determined its Hα and [S II] fluxes from the LGGS images, even though the source is very faint (Fig. A.1). We therefore keep the classification of this source as an SNR candidate. If it is an SNR, the optical fluxes indicate that it is likely non-radiative.

D.2.2. [SPH11] 414: XMMM31 J004030.46+402756.0

[SPH11] 414 is a hard source and thus was not classified as an SNR candidate based on its hardness ratios but was instead suggested as an SNR candidate based on its positional coincidence with the radio source [GLG04] 198 with a radio spectral index of $\alpha = -0.08$. Its radio properties indicate emission from a PWN (GLG05).

We detect neither Hα, [S II], nor [O III] emission in the LGGS images (Fig. A.1). Therefore, if the source is an SNR, it has to be non-radiative. A PWN can produce hard X-ray emission. On the basis of the radio-source coincidence, we retain its identification as an SNR candidate.

D.2.3. [SPH11] 419: XMMM31 J004031.92+405837.4

[SPH11] 419 is a soft X-ray source with hardness ratios indicative of an SNR. No optical source is detected at its position that might be a foreground star. Therefore, it was classified as an SNR candidate by SPH11.

We do not detect any emission in the narrow-band filter images of the LGGS (Fig. A.1). If the source is an SNR, it has to be non-radiative. Because of a lack of additional information, we keep the SNR candidate classification.

D.2.4. [SPH11] 441: XMMM31 J004040.39+403012.3

[SPH11] 441 is a soft X-ray source with hardness ratios indicative of an SNR. No foreground star was found at its position. It was therefore classified as an SNR candidate by PFH05 and SPH11.

Faint Hα and [S II] emission was detected in the LGGS images (see Table 4 and Fig. A.1) on the northwestern side. However, this emission does not help us to classify the optical source as an SNR. Therefore, the *XMM-Newton* source remains an SNR candidate.

D.2.5. [SPH11] 521: XMMM31 J004058.94+410300.6

[SPH11] 521 is one of the faintest X-ray sources with a detection likelihood of $ML = 10$. Its hardness ratios suggest that it is an SNR candidate. No optical counterpart was found that could be a foreground star. It was therefore proposed as an SNR candidate by PFH05 and SPH11.

The X-ray source seems to be surrounded by a very extended optical source, which is visible in the Hα, [S II], and [O III] images (Fig. A.1) and has a low flux ratio [S II]/H$\alpha = 0.3 \pm 0.2$, hence is an H II region. The X-ray source therefore remains an SNR candidate.

D.2.6. [SPH11] 560: XMMM31 J004108.08+403142.4

[SPH11] 560 is a soft X-ray source, which was classified as an SNR candidate by PFH05 and SPH11 based on its hardness ratios and the lack of a foreground star as a possible optical counterpart.

Faint Hα and [S II] emission was measured at its position in the LGGS images. This source thus remains an SNR candidate.

D.2.7. [SPH11] 969: XMMM31 J004239.82+404318.8

[SPH11] 969 is a bright X-ray source with a detection likelihood of $ML = 4800$. Its hardness ratios suggest that it is an SNR candidate. As no foreground star was found, the *XMM-Newton* source was suggested to be an SNR candidate by SPH11. The X-ray source was also detected with *Chandra* ([WGK04] s1-84).

There is neither a point source nor significant extended emission in the optical at and around the source. Without any confirmation in optical or radio, this source is still classified as an SNR candidate.

D.2.8. [SPH11] 1083: XMMM31 J004256.78+405718.5

[SPH11] 1083 is a soft X-ray source with no foreground star at its position and hence has been classified as an SNR candidate by SPH11.

No optical source is detected at its position in the LGGS images. Therefore, if it is an SNR, it is non-radiative. The source remains an SNR candidate.

D.2.9. [SPH11] 1282: XMMM31 J004341.57+413406.6

[SPH11] 1282 is a soft X-ray source with no foreground star as a possible counterpart and thus was classified as an SNR candidate by SPH11. PFH05 classified the X-ray as a candidate super-soft source.

There is faint optical line-emission in the LGGS image with an extent of $\sim 14''$ (Fig. A.1). The flux ratio of 0.5 ± 0.1 is insignificantly high to classify the optical source as an SNR. It is very diffuse and patchy, similar to [SPH11] 1148 and 1328. This source still remains an SNR candidate based on its X-ray hardness ratios.

D.2.10. [SPH11] 1332: XMMM31 J004354.13+412047.3

[SPH11] 1332 is a soft X-ray source with no foreground star as a possible counterpart, which was classified as an SNR candidate by PFH05 and SPH11 based on its hardness ratios.

There is faint Hα and [O III] emission confirmed in the LGGS data, even though no [S II] emission was detected (see Table 4 and Fig. A.1). A filament in Hα is visible with an extent of $\sim 5''$. This source remains an SNR candidate.

D.2.11. [SPH11] 1669: XMMM31 J004538.26+411246.9

[SPH11] 1669 is a faint soft X-ray source, which was classified as an SNR candidate by SPH11 based on its hardness ratios and the lack of a foreground star as its possible counterpart.

The position of the X-ray source was not observed by the LGGS. No optical counterpart is found in the SDSS-III images (Fig. C.1, upper left). Radio emission has not been detected at

its position so far either. This source remains an SNR candidate based on its X-ray properties.

D.2.12. [SPH11] 1748: XMMM31 J004606.34+412923.6

[SPH11] 1748 is a faint soft X-ray source, which marginally fulfilled the hardness ratio criterion for SNR candidates and has no optical counterpart that is likely to be a star. Therefore, it was classified as an SNR candidate by SPH11.

The LGGS did not cover the position of the X-ray source. The SDSS-III images show no source at the *XMM-Newton* position inside the error circle (Fig. C.1, upper right). A radio counterpart is not known either. Therefore, this source remains an SNR candidate.

D.2.13. [SPH11] 1796: XMMM31 J004625.39+410938.7

[SPH11] 1796 was classified as an SNR candidate by PFH05 and SPH11 based on HR_1 and HR_2 and the lack of a foreground star at its position.

The source was not covered by the LGGS. The SDSS-III images show no source inside the *XMM-Newton* positional error circle (Fig. C.1, lower panel). A radio counterpart is similarly unknown. With no additional information available, this source remains an SNR candidate.

D.3. No SNRs

D.3.1. [SPH11] 1121: XMMM31 J004303.70+413717.2

[SPH11] 1121 is a hard source and was not proposed as an SNR candidate by SPH11. Nevertheless, we studied this source because of coincident diffuse optical emission seen in Hα and [S II].

Diffuse emission is seen in both the Hα and [S II] LGGS images (Fig. A.1). However, the flux ratio is [S II]/Hα = 0.2 ± 0.1, which is not indicative of an SNR. The diffuse optical source at and north of the X-ray emission is most likely an H II region. As this source is hard in X-rays and there is no optical counterpart indicative of an SNR, we do not classify it as an SNR candidate and keep the classification as a hard source.

D.3.2. [SPH11] 1461: XMMM31 J004428.62+414948.7

[SPH11] 1461 is a soft source and was classified as a foreground star candidate by SPH11 because stars with characteristic $\log(f_X/f_{opt})$ values are found in the X-ray error circle, with an optically red object located close to the centre of the X-ray error circle. However, the Hα image also revealed a diffuse source right next to the X-ray source in the north.

The diffuse optical source is visible in Hα, [S II], and [O III] emission (Fig. A.1). The flux ratio [S II]/Hα = 0.2 ± 0.1, which is typical of an H II region. Therefore, the origin of the soft X-ray emission seems to be either a star or an H II region and the source is not an SNR candidate.

D.3.3. [SPH11] 1468: XMMM31 J004430.56+412306.2

[SPH11] 1468 is a hard X-ray source. As diffuse Hα emission was found in the optical, we considered this source for further studies.

The LGGS images show an extended diffuse source in Hα and [S II] (Fig. A.1). The [S II]/Hα flux ratio is 0.4 ± 0.1. This value is at the border between SNRs and H II regions. While the more extended optical source seems to be an H II region, we cannot rule out that there is an SNR located at the same position. However, as the X-ray emission does not correspond to an SNR, we do not classify [SPH11] 1468 as an SNR candidate.

D.3.4. [SPH11] 1611: XMMM31 J004518.44+413936.3

[SPH11] 1611 is a hard X-ray source coincident with [PFH2005] 626 and [SBK2009] 220 and was classified as a hard source by SPH11. Diffuse optical Hα [S II], and [O III] emission was found around the X-ray source.

The largely extended optical source can be seen in the LGGS emission-line images (Fig. A.1). The X-ray source is located close to the northern rim of the optical source and is coincident with a brighter shell-like structure. The entire optical source has a flux ratio of [S II]/Hα = 0.4–0.5. The optical source is most likely a large H II region. The X-ray hardness ratios are not even marginally representative of an SNR. Therefore, we do not consider this source to be an SNR candidate.

A&A 528, A136 (2011)
DOI: 10.1051/0004-6361/201015866

Astronomy & Astrophysics

XMM-Newton observations of the superbubble in N 158 in the LMC

M. Sasaki[1], D. Breitschwerdt[2], V. Baumgartner[3], and F. Haberl[4]

[1] Institut für Astronomie und Astrophysik, Universität Tübingen, Sand 1, 72076 Tübingen, Germany
e-mail: sasaki@astro.uni-tuebingen.de
[2] Department of Astronomy and Astrophysics, Berlin Institute of Technology, Hardenbergstr. 36, 10623 Berlin, Germany
[3] Institut für Astronomie, Universität Wien, Türkenschanzstr. 17, 1180 Vienna, Austria
[4] Max-Planck-Institut für extraterrestrische Physik, Giessenbachstraße, 85748 Garching, Germany

Received 5 October 2010 / Accepted 1 February 2011

ABSTRACT

Aims. We study the diffuse X-ray emission observed in the field of view of the pulsar B 0540–69 in the Large Magellanic Cloud (LMC) by *XMM-Newton*. We wish to understand the nature of this soft diffuse emission, which coincides with the superbubble in the H II region N 158, and improve our understanding of the evolution of superbubbles.
Methods. We analyse the *XMM-Newton* spectra of the diffuse emission. Using the parameters obtained from the spectral fit, we perform calculations of the evolution of the superbubble. The mass loss and energy input rates are based on the initial mass function (IMF) of the observed OB association inside the superbubble.
Results. The analysis of the spectra shows that the soft X-ray emission arises from hot shocked gas surrounded by a thin shell of cooler, ionised gas. We show that the stellar winds alone cannot account for the energy inside the superbubble, but the energy release of 2−3 supernova explosions in the past ∼1 Myr provides a possible explanation.
Conclusions. The combination of high sensitivity X-ray data, which permits a spectral analysis, and analytical models for superbubbles can provide insight into the evolutionary state of interstellar bubbles, if the stellar content is known.

Key words. shock waves – ISM: bubbles – evolution – HII regions – X-rays: ISM

1. Introduction

Early observations in the radio and the optical have shown that the interstellar medium (ISM) in the Milky Way mainly consists of cool clouds ($T \lesssim 10^2$ K) of neutral hydrogen embedded in the warm ($T \simeq 10^4$ K) intercloud medium of partially ionised hydrogen. Since the 1970s, observations in the ultraviolet (UV) and X-rays have detected hot gas at coronal temperatures ($T \simeq 10^{5-6}$ K) in the ISM. The heat source of the ISM are massive OB stars, which inject energy through their radiation, stellar winds, and finally by supernova explosions. As these processes are often correlated in space and time, superbubbles with sizes of typically 100−1000 pc are created in the ISM. Therefore, supernova remnants (SNRs) and superbubbles are among the prime sources controlling the morphology and the evolution of the ISM, and their observation is of key interest to understanding the galactic matter cycle. However, they radiate copiously in the soft X-rays below 2 keV, an energy range that is difficult to study in the Milky Way because of absorption by the Galactic disk.

The LMC, which is a dwarf irregular but appear to contain spiral structure, is one of the closest neighbours of our Galaxy. Its proximity with a distance of 48 kpc (Macri et al. 2006) and modest extinction along the line of sight (average Galactic foreground $N_{\rm H} = 1.6 \times 10^{21}$ cm^{-2}) make it the ideal laboratory for exploring the global structure of the ISM in a galaxy. The well-known and well-studied extended emission region in the LMC is the 30 Doradus region and the region south of it, which harbour star-formation sites, superbubbles, and SNRs. *ROSAT* data of the superbubbles in the LMC have been studied in detail by, e.g., Chu et al. (1995) and Dunne et al. (2001).

N 158 (Henize 1956) is an H II region in these active regions of the LMC. It is elongated in the north-south direction and consists of a superbubble in the north and a more compact bright region in the south. It is known to host two OB associations LH 101 and LH 104 (Lucke & Hodge 1970). While LH 101 in the southern part of N 158 seems to power the very bright region in Hα, LH 104 is found in the superbubble in the northern part of N 158 and is dominated by B stars (Schild & Testor 1992), mainly consisting of a young population with an age of 2−6 Myr (Testor & Niemela 1998). Dunne et al. (2001) analysed the *ROSAT* data and suggested that the X-ray emission seen at the position of N 158 is associated with the H II region. N 158 is located near the X-ray bright pulsar (PSR) in the LMC B 0540−69, which had been observed for calibration purposes by the X-ray Multi-Mirror Mission *XMM-Newton* (Jansen et al. 2001; Aschenbach et al. 2000). The field of view of the European Photon Imaging Cameras (EPICs, Strüder et al. 2001; Turner et al. 2001) of these observations when performed in full frame mode, covers the northern part of N 158 and allows us to study the X-ray emission from the superbubble.

2. Data

The pulsar B 0540−69 in the LMC is a Crab-like pulsar with a pulsar wind nebula (PWN), which has been spatially resolved and studied with the *Chandra* X-ray Observatory (Petre et al. 2007). To study the diffuse emission in the vicinity of B 0540−69, we chose observations for which the EPICs were operated in full frame mode. The observation IDs are 0117510201, 0117730501, and 0125120101. The observations were all carried out using the medium filter. Starting from the observational

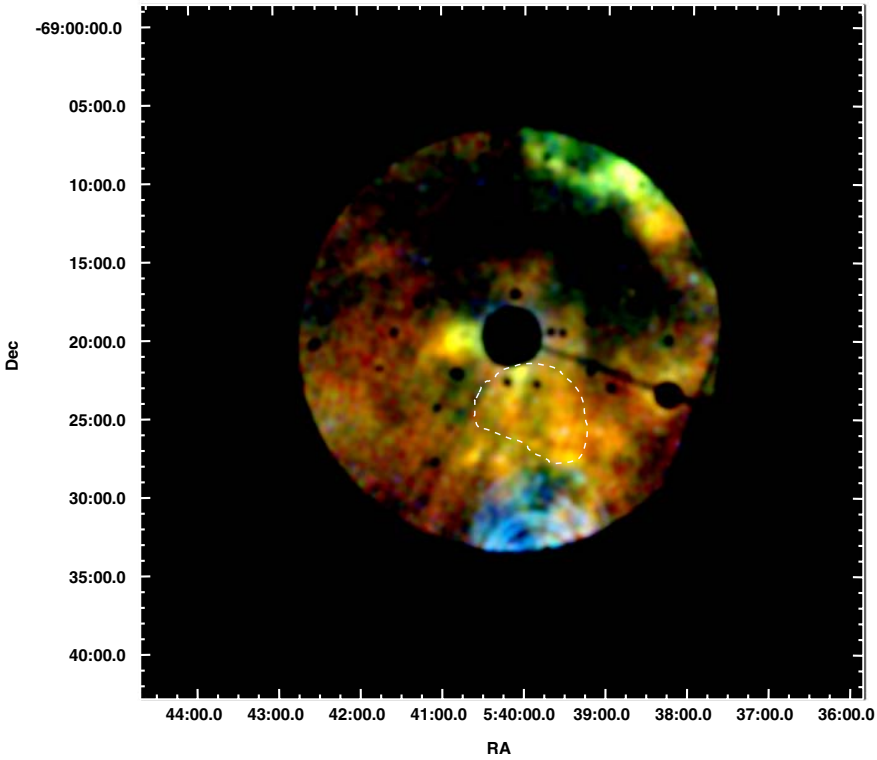

Fig. 1. *XMM-Newton* EPIC mosaic image of the PSR B 0540−69 and its surroundings in true colour presentation (red: 0.3−0.8 keV, green: 0.8−1.5 keV, blue: 1.5−2.3 keV). The bright X-ray emission from PSR B 0540−69 at ∼RA = $05^{h}40^{m}$, Dec = –69°20′, other point sources, and the out-of-time events have been removed from the data. The arc-shaped features in the south are caused by stray light from the bright X-ray source LMC X-1. The position of the superbubble in the H II region N 158 is shown with a dashed line.

Table 1. *XMM-Newton* data used for the analysis.

Obs. ID	EPIC	Start Date	Effective Exposure [ks]
01175102	PN	2000-02-11	8.3
01175102	MOS1,2		3.5
01177305	PN	2000-02-17	8.3
01177305	MOS1,2		9.8
01251201	PN	2000-05-26	29.
01251201	MOS1,2		27.

Notes. All the analysed data were obtained in full frame mode using the medium filter.

data files (ODFs), the data are processed with the *XMM-Newton* Science Analysis System (XMMSAS) version 10.0.0. For EPIC PN, only single and double pattern events are used, whereas for the MOS1 and 2, singles to quadruples are selected. The exposure times that we obtain after filtering out the time intervals with background flares are listed in Table 1.

2.1. EPIC image

After filtering out the background flares, we created a mosaic image out of the full frame mode data of EPIC PN, MOS1, and MOS2 for all three observations (Fig. 1). To enhance the not-so-bright diffuse emission, we filtered out all point sources found using a source detection routine as well as the so-called out-of-time events of EPIC PN. The images were smoothed using a Gaussian filter. The mosaic image shown in Fig. 1 is a true colour image using red colour for the 0.3−0.8 keV band, green for 0.8−1.5 keV, and blue for 1.5−2.3 keV. The extended emission of the interstellar gas is clearly soft with no emission above ∼3 keV. The comparison with the Hα image of the Magellanic Cloud emission line survey (MCELS) in Fig. 2 shows that the relatively bright extended region in the south of the PSR coincides well with a superbubble in the H II region N 158 (Henize 1956), which contains the OB association LH 104 (Lucke & Hodge 1970). To study the spectral properties of the diffuse emission, we selected two regions: region 1, which covers the brighter spot in the east of the PSR, and a region that covers the superbubble in the H II region N 158. The regions are shown in the left panel in Fig. 2. The PSR and the PWN around it have an extent of about 1′. They were completely removed from the data. The soft, extended emission east to the PSR is not directly connected to the PWN and has, as we see in Sect. 2.2.4, a perfectly thermal spectrum. We therefore assume that it is not related to the PWN.

2.2. EPIC spectra

For the spectral analysis of an extended diffuse emission the contribution of the background is significant. Since the emission fills a large part of the detector, we are unable to extract a local background close to the source emission. We note that as the effective area of the mirrors depends on the off-axis angle, photons are subject to vignetting while particles are not. The high-energy particles that interact with the material surrounding the detector, however, produce fluorescence, which varies with position on the detector, especially for the PN detector. In addition, the spectral response depends on the position on the detector. A detailed description of the *XMM-Newton* background is given by Read & Ponman (2003) and Carter & Read (2007), and a comparison of the different methods to estimate the background can be found in, e.g., Sasaki et al. (2004).

2.2.1. Blank-sky background

The *XMM-Newton* EPIC background working group has created the so-called blank-sky data for each EPIC and CCD read-out

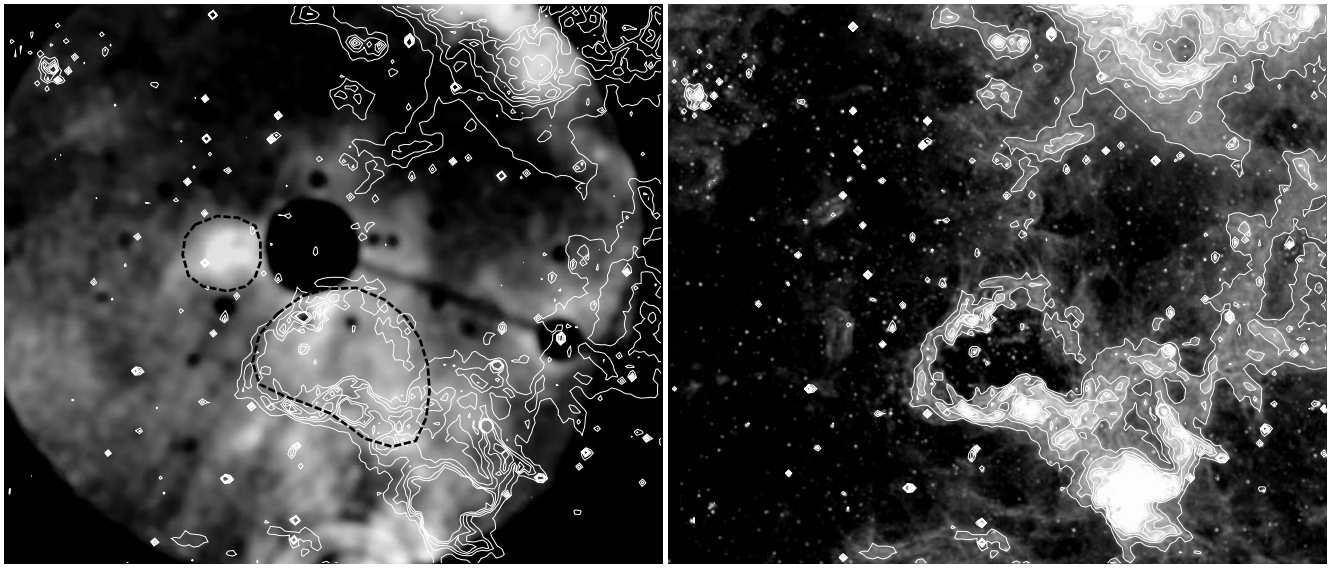

Fig. 2. A zoom-in on the *XMM-Newton* EPIC mosaic image (*left*) with regions used for the spectral analysis (black dashed line) and Hα contours (MCELS) and the Hα image with the same contours (*right*).

mode (Carter & Read 2007). The blank-sky data were merged from data of different pointings after the point sources were eliminated from the data. These data sets comprise the detector background and an average cosmic X-ray background.

Before extracting the spectra, we first corrected both the observed data and the blank-sky data for vignetting using the XMMSAS command `evigweight`. The auxiliary response file (ARF) and the response matrix file (RMF) were then created by assuming that the source is on-axis. The background spectrum was extracted from the blank-sky data at the same location on the detector as the source spectrum.

2.2.2. Background from the same data

For comparison, we also extracted a background spectrum from the same data as the source spectrum, using a region in the dark part north of B 0540−69. However, after subtracting the background, the spectrum of the soft diffuse emission still has a hard tail and is overcorrected exactly at the energies of the fluorescence lines. Therefore, as expected, extracting the background for the source spectrum from the same data at a different position on the detector seems to be inappropriate.

2.2.3. Closed filter wheel data

Another way to deal with the background is to use a local background from the same observation, but take care of the detector background by using the closed filter wheel data, as also supplied by the *XMM-Newton* EPIC background working group. To estimate the X-ray background, i.e., additional emission that is typical of the observed area and might also contribute to the spectrum of the superbubble, we extract a region next to the superbubble in the east, which shows faint diffuse emission. After subtracting the closed filter wheel spectrum extracted for each region at the corresponding position of the detector with the same shape, the spectrum of the faint diffuse emission in the east is fitted with a thermal model. This fitted spectrum is then included in the model of the spectra of the superbubble and region 1.

To verify whether the emission in the east is suitable for use as the local X-ray background, we estimated the flux for (i) the superbubble, (ii) the region east to it used as the local background, and (iii) the blank-sky background. We assumed a plane-parallel shock model for the superbubble and a non-equilibrium ionisation (NEI) model for the eastern region, and that both have LMC abundances (see Sect. 2.2.4 for details). A combination of a thermal and a non-thermal spectrum is assumed for the blank-sky background. From these spectra, we get the following fluxes, where the 90% confidence errors are given in brackets: $F_{0.2-3.0\ \mathrm{keV}}$(superbubble) = 1.4 (1.2−1.5) × 10^{-12} erg s^{-1} cm^{-2}, $F_{0.2-3.0\ \mathrm{keV}}$(east) = 4.8 (4.0−5.3) × 10^{-13} erg s^{-1} cm^{-2}, and $F_{0.2-3.0\ \mathrm{keV}}$(blank-sky) = 1.5 (1.4−1.6) × 10^{-13} erg s^{-1} cm^{-2}. The flux of the X-ray background in the blank-sky data is about 10% that of the superbubble. The emission from the ISM in the east is about three times higher than the blank sky. If we were to use the blank-sky data to estimate the X-ray background, we might underestimate the background. However, if we use the local emission, we will overestimate the background as we may also expect to find hot gas in the ISM next to the superbubble because of possible breakouts. The difference between the flux of the eastern region and the blank sky is about 20% of the superbubble flux, which needs to be taken into consideration as an additional uncertainty in the flux of the superbubble.

Otherwise, the results for the spectral fits obtained with the closed filter wheel data and those obtained with the blank-sky data are consistent with each other within the confidence range of the spectral fit parameters. Therefore, in the following, we discuss the fit results obtained with the blank-sky data.

2.2.4. Spectral fits

The spectra were fitted with thermal plasma models in XSPEC. We fitted the spectra of the different EPICs simultaneously with model parameters that are linked to each other. In both spectra, emission peaks are found in the energy interval between 0.5 keV and 1.5 keV that can be interpreted as emission lines of highly ionised elements. The X-ray emission is absorbed by the Galaxy in the foreground ($N_{\mathrm{H\,fg}}$) and by the matter in the LMC along the line of sight ($N_{\mathrm{H\,MC}}$) with abundances half of solar values

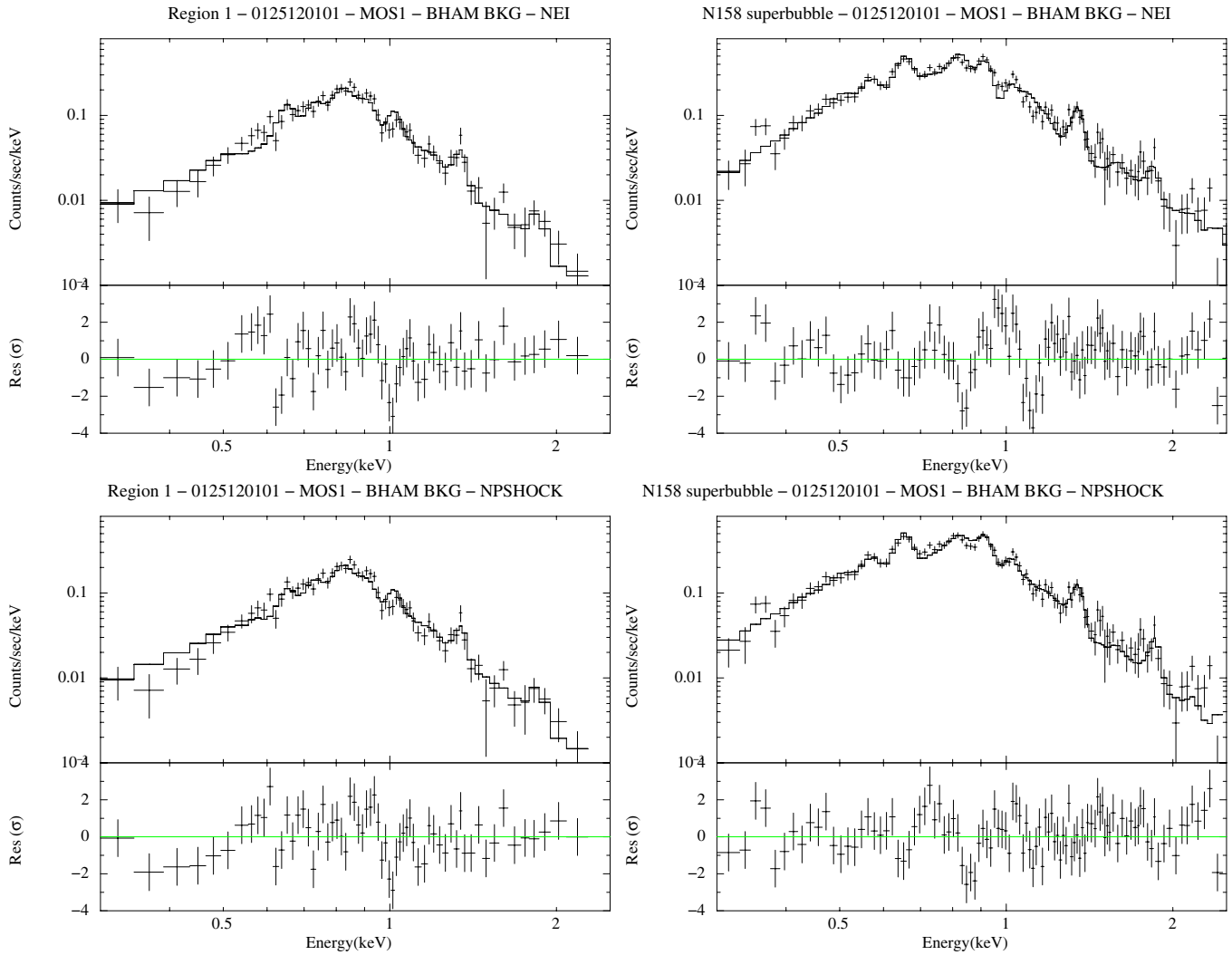

Fig. 3. Spectra of the diffuse emission in the field of view of PSR B 0540−69 extracted from the *XMM-Newton* EPIC MOS1 data of the Obs. ID 01251201. The *left panels* show the spectra of region 1 located east of the PSR, the *right panels* show the spectra of the superbubble in the H II region N 158. The upper diagrams show the fit with the NEI model, the lower diagrams with the NPSHOCK model.

(Russell & Dopita 1992). The Galactic foreground column density is $N_{\rm H\,fg} = 7.0 \times 10^{20}$ cm^{-2} in this region (Dickey & Lockman 1990). The spectra are more accurately reproduced by a NEI model (Borkowski 2000) than by the spectral models assuming collisional ionisation equilibrium (CIE). Figure 3 shows the MOS1 spectra of the Obs. ID 01251201 with the best-fit models. In the following, 90% errors are given for the parameters.

Since the first fits with CIE yielded no satisfactory results, we used the NEI model in XSPEC with the effective temperature kT, the ionisation timescale $\tau = n_{\rm e}t$, and the abundance as fit parameters. The ionisation timescale τ is an indicator of the state of the plasma after the gas has been ionised. For small ionisation timescales $\tau = n_{\rm e}t < 10^{12}$ s cm^{-3}, the electrons and ions are still not in thermal equilibrium. For this model component, we also assumed the sub-solar LMC abundance $\zeta_{\rm LMC} = 0.5$. The fit of the spectra of the superbubble emission is still not very good with a reduced χ^2 of 1.75. The emission is most likely caused by the shock from the stellar winds in the superbubble. Therefore, we also fitted the spectra using a plane-parallel shock plasma model with separate ion and electron temperatures, kT_a and kT_b, respectively (NPSHOCK, Borkowski et al. 2001). The fit parameters are given in Table 2.

As can be seen in Table 2, kT_a and kT_b for region 1 are almost equal and the χ^2 values for the NEI and the NPSHOCK fits are comparable. Therefore, the usage of the NPSHOCK model does not seem to be necessary for region 1. In addition, the value for τ is $> 10^{11}$ s cm^{-3} for both NEI and NPSHOCK models, indicating that the gas in region 1 seems to be closer to CIE than in the superbubble in N 158. The temperature of $kT = 0.54$ keV determined for region 1 is higher and more accurate than the result of the *ROSAT* PSPC analysis for this field (0.3 keV, Sasaki et al. 2002). This shows that we were only able to see the overall characteristic of a larger region with PSPC, whereas with EPIC we can now resolve smaller (few arcminutes) structures of the hot ISM.

The hot plasma in the superbubble of the H II region N 158 does not seem to be consistent with thermal equilibrium, as indicated by the low ionisation timescale $\tau = 1.4 \times 10^{10}$ s cm^{-3} of the NEI fit. The temperature of the NEI fit and the ion temperature of the NPSHOCK fit are relatively high at $kT = 0.91$ keV and $kT_a = 1.0$ keV, respectively, while the electron temperature

Table 2. Spectral parameters obtained from the fits of the EPIC data for region 1 and the superbubble.

Parameter	Region 1	Superbubble
	NEI	
$N_{\rm H\,LMC}$ [10^{22} cm^{-2}]	0.14 (0.08–0.23)	0.43 (0.38–0.51)
kT [keV]	0.54 (0.51–0.58)	0.91 (0.74–1.1)
τ [10^{11} s cm^{-3}]	2.0 (1.6–2.4)	0.14 (0.12–0.18)
norm (10^{-4})	2.0 (1.6–2.4)	9.5 (8.0–13.)
χ^2/d.o.f.	94.81/61 = 1.55	185.06/106 = 1.75
	NPSHOCK	
$N_{\rm H\,LMC}$ [10^{22} cm^{-2}]	0.19 (0.12–0.32)	0.29 (0.20–0.33)
kT_a [keV]	0.55 (0.00–0.59)	1.0 (0.74–1.2)
kT_b [keV]	0.51 (0.00–0.59)	0.13 (0.00–0.57)
τ [10^{11} s cm^{-3}]	8.8 (5.4–12.)	1.3 (1.0–2.3)
norm (10^{-4})	5.0 (4.2–6.3)	11. (9.–13.)
χ^2/d.o.f.	91.02/60 = 1.52	131.79/99 = 1.33

Notes. The numbers in brackets are 90% confidence ranges. The parameter *norm* is the normalisation of the model in XSPEC and corresponds to the emission measure. For the other parameters, see Sect. 2.2.4.

is one order of magnitude lower at $kT_b = 0.13$ keV. In addition to the Galactic foreground column density, a relatively high absorption column density of $N_{\rm H\,LMC,N158} = 4.3$ or 2.9×10^{21} cm^{-2} was determined. In comparison, the total column density in the LMC is $N_{\rm H\,LMC} = 1.0{-}5.5 \times 10^{21}$ cm^{-2} (Brüns et al. 2005). This corroborates that the diffuse X-ray emission most likely arises from inside the shell of the superbubble.

3. Discussion

To the east of PSR B 0540−69, the diffuse emission seems to arise from ionised gas close to thermal equilibrium with a temperature comparable to the value determined from the *ROSAT* PSPC spectrum. In contrast, a shorter ionisation timescale and higher temperatures are found in the south. Since the emission coincides spatially with the superbubble in the H II region N 158, we conclude that the origin of the diffuse X-ray emission is the hot gas within the interstellar bubble. The gas in the bubble interior is shocked by stellar winds, and the cooler outer rim is visible as an H II region. The total unabsorbed X-ray luminosity of the bubble is $L_{\rm X}(0.2{-}10.0\ {\rm keV}) = 1.5 \times 10^{36}$ erg s^{-1}. Stars with masses over 25 $M_\odot$ are luminous X-ray emitters with luminosities of $L_{\rm X}(0.2{-}10.0\ {\rm keV}) \approx 10^{33}$ erg s^{-1}. In LH 104, there are 16 stars with masses above 25 $M_\odot$ (Testor & Niemela 1998, see also Sect. 3.2 for details), which account for $L_{\rm X}(0.2{-}10.0\ {\rm keV}) \approx 1{-}2 \times 10^{34}$ erg s^{-1}. This is two magnitudes lower than the emission from the bubble and can be neglected in the following discussion.

The comparison of the X-ray emission with the Hα shell in Fig. 2 shows that there is additional X-ray emission outside the Hα shell, which might indicate that some hot gas escaped the superbubble. This was also suggested by Dunne et al. (2001) based on the analysis of *ROSAT* data, which had already shown that the X-ray emission is not confined by the Hα shell. However, we are unable to rule out that some projection effect might make the Hα look smaller than the extent of the X-ray emission.

3.1. Results of the spectral analysis

For more advanced studies, we used the NEI fit results for region 1 and NPSHOCK fit results for the superbubble. The emitting volume could be approximated by an ellipsoid, although it is deformed in the south. We derived the radii from the EPIC mosaic image: $a = 4' \pm 1' = (56 \pm 14)$ pc, $b = 3' \pm 1' = (42 \pm 14)$ pc ($D_{\rm LMC} = 48$ kpc). We were unable to determine the third radius of the assumed ellipsoid. Therefore, we assumed that the superbubble is oblate and has a configuration similar to that of a disk perpendicular to the plane of the sky, i.e., also perpendicular to the disk of the LMC ($c = a$). The volume of the bubble is then $V = 4/3\,\pi\,abc = (1.62 \pm 0.03) \times 10^{61}$ cm^3. With the LMC metallicity $\zeta_{\rm LMC} = 0.5$, we find that $n_{\rm e} = (1.2 + 0.013\zeta_{\rm LMC})\,n \approx 1.21\,n$, where n is the hydrogen density. Therefore, the normalisation of the spectral fit is

$$\begin{aligned} norm &= \frac{1}{10^{14} \times 4\pi D_{\rm LMC}^2} \int n_{\rm e} n \,{\rm d}fV \\ &\approx \frac{1}{10^{14} \times 4\pi D_{\rm LMC}^2}\, 1.21\, n^2\, f\, V \\ &= 4.4 \times 10^{-62}\, n^2\, f\, V \quad \left[{\rm cm}^{-5}\right], \end{aligned} \tag{1}$$

where f is the filling factor, and the gas density within the bubble can be estimated as

$$n = 4.8 \times 10^{30} \times \sqrt{\frac{norm}{f\,V}} \quad \left[{\rm cm}^{-3}\right]. \tag{2}$$

Using $norm = (1.1 \pm 0.2) \times 10^{-3}$ from the fit with the NPSHOCK model, we get $n = (4.0 \pm 0.7) \times f^{-1/2} \times 10^{-2}$ cm^{-3}. If $f < 1$, then the density of $n = 4.0 \times 10^{-2}$ cm^{-3} is a lower limit. However, the angular resolution of the X-ray data does not allow us to unambiguously determine the filling factor. For a young interstellar bubble such as in N 158, the filling factor can be assumed to be $f \approx 1$.

With temperature $T_a = (1.0 \pm 0.2)$ keV and density n given, the pressure of the gas is

$$\begin{aligned} P/k &= (n_{\rm e} + 1.1n) f^{-1/2} T_a = 2.31 n f^{-1/2} T_a \\ &= (1.1 \pm 0.3) \times f^{-1/2} \times 10^6\ {\rm cm}^{-3}\ {\rm K}. \end{aligned} \tag{3}$$

While the pressure of the Galactic ISM is thought to be $P/k = 10^{3-4}$ cm^{-3} K, star-forming regions in general have higher pressures of the order of $P/k = 10^{5-6}$ cm^{-3} K. For a galaxy such as the LMC with a high star-formation rate, Oey & García-Segura (2004) estimated an ISM pressure of $P/k \approx 10^5$ cm^{-3} K. Thus, the pressure inside the superbubble in N 158 is about ten times higher than in the surrounding hot ISM. de Avillez & Breitschwerdt (2005) performed a 3D simulation of the ISM including the effect of magnetic fields and obtained a map of the distribution of temperature, pressure, magnetic field, etc. They showed that in regions where the temperature is about 10^{5-6} K, the pressure is $P/k = 10^{4-5}$ cm^{-3} K, but can reach $P/k > 10^5$ cm^{-3} K in the interior of hot bubbles. This is in agreement with the pressure that we obtain from the X-ray spectrum of the superbubble.

The part of the LMC in which N 158 is located in general shows faint diffuse X-ray emission indicative of hot ISM. The region that we call region 1 is particularly bright and allows us to estimate the foreground column density causing the absorption of the soft X-rays. The shell of cooler gas around the superbubble should form an additional absorbing component. Using the absorbing column density determined for region 1 (besides the

Galactic column density) as the mean LMC value $N_{\rm H\,LMC,\,region1}$ = $(1.4 \pm 0.9) \times 10^{21}$ cm^{-2}, the column density of the shell around the superbubble is $N_{\rm H\,shell}$ = $N_{\rm H\,LMC,\,N158}$ − $N_{\rm H\,LMC,\,region1}$ = $(1.5 \pm 1.3) \times 10^{21}$ cm^{-2}.

3.2. Analytic estimates

With the values derived from spectral fitting for pressure and density inside the bubble, we inferred a thermal energy content of $E(t) = 3/2 \times P \times f \times V = 3.6 \times f^{1/2} \times 10^{51}$ erg. We estimated a mean shell thickness of ∼0.′5, i.e., ∼ 10% of a, corresponding to ∼7 pc from the MCELS Hα image shown in Fig. 2. From the column density $N_{\rm H\,shell}$ calculated in the last section, we obtained a density of $n_{\rm shell} \approx 70\,{\rm cm}^{-3}$ inside the shell. Since the ISM around N 158 shows Hα emission, its temperature is probably around 8000 K, typical of the warm ionised medium (McKee & Ostriker 1977), resulting in a speed of sound of ∼9.2 km s^{-1}. With the inferred pressure of $P/k = 1.1 \times f^{-1/2} \times 10^6$ cm^{-3} K from Eq. (3), we obtained a density of the ambient medium of ∼13 cm^{-3}, yielding a compression factor of the shock of ∼6. Since the cooling time behind the shock is very short because of the high density in the shell, the shock will be isothermal and, as shown below, also strong. Since we now know the radius, energy content, and density, we can use the solution for a wind blown bubble by Weaver et al. (1977) to find out the age of the bubble, which is about $t \simeq 1.1$ Myr resulting in an energy input rate over this time interval of $L_{\rm superbubble} = 2.3 \times 10^{38}$ erg s^{-1}. In addition, the mass inside a homogeneous bubble is $M = 2.31 n \times \mu \times m_{\rm H} \times V = 770\ M_\odot$, where $\mu = 0.61$ is the mean molecular weight of a fully ionised gas and $m_{\rm H}$ is the hydrogen mass. Thus, a mass-loss rate of $6.9 \times 10^{-4}\ M_\odot$ yr^{-1} over 1.1 Myr is derived. In the following, we discuss whether massive stars can account for such a large mass-loss and energy input rate.

To calculate the mass loss and energy input rates of OB stars (in cgs units), we use the mass-luminosity relation for stars with $10 \le M/M_\odot \le 50$ by Vitrichenko et al. (2007) to obtain the mass M and luminosity $L_\star$ of a star with bolometric magnitude $M_{\rm bol}$

$$M_{\rm bol} = 1.6\text{–}6.9 \log(M/M_\odot), \quad (4)$$

$$L_\star = 19 (M/M_\odot)^{2.76} L_\odot. \quad (5)$$

The radius of the star is obtained from

$$R = \sqrt{\frac{L_\star}{4\pi\sigma T_{\rm eff}^4}}, \quad (6)$$

where $T_{\rm eff}$ is the effective temperature of the star and σ is the Stefan-Boltzmann constant. Both $M_{\rm bol}$ and $T_{\rm eff}$ are taken from Table 2 of Testor & Niemela (1998). The wind velocity is determined according to the theory of radiation-driven winds (Castor et al. 1975)

$$v_\infty = a v_{\rm esc} = a \left[\frac{2GM}{R} \times (1 - L_\star/L_{\rm edd}) \right]^{0.5}, \quad (7)$$

where $a \simeq 2.5$ (Lamers et al. 1995). The parameter $v_{\rm esc}$ is the photospheric escape velocity and the Eddington luminosity is $L_{\rm edd} = 4\pi G \times M \times m_{\rm p} \times c/\sigma_{\rm T}$, where $m_{\rm p}$ is the mass of a proton and $\sigma_{\rm T}$ the Thomson cross-section for the electron. The mass loss is determined from the single-scattering limit

$$\dot{M} = \frac{L_\star}{v_\infty \times c}. \quad (8)$$

We corrected for the LMC metallicity $\zeta_{\rm LMC}$ following Leitherer et al. (1992) and obtained $\dot{M} \propto \zeta_{\rm LMC}^{0.8}$ for the mass loss and $v_\infty \propto \zeta_{\rm LMC}^{0.13}$ for the wind velocity (for hot stars with $M > 15 M_\odot$). Thus, the 67 O- and B-stars in LH 104 produce a mass loss of ∼39 $M_\odot$ or an energy input rate of $L_{\rm OB} = 3.4 \times 10^{37}$ erg s^{-1} over 1.1 Myr.

Additionally, the Wolf-Rayet (WR) stars generate ∼35 $M_\odot$ or $L_{\rm WR} = 1.8 \times 10^{38}$ erg s^{-1}, but only for 2.5×10^5 yr ≅ 0.23 t, assuming that they already went through half of their WR-lifetime of ∼5×10^5 yr (Maeder & Meynet 1987). The mass loss and wind velocity of WR-binaries are adopted from Leitherer et al. (1997) and corrected for mass losses of WC and WN types in the LMC according to Crowther (2007). Furthermore, we have to calculate the contribution of winds from WR-binaries before entering the WR-phase, i.e., for the remaining 0.85 Myr. With mass losses for O6 and O7-stars and O4-stars as WR-progenitors (PR) taken from Garmany et al. (1981) and velocities from Lamers & Leitherer (1993), we get 4 $M_\odot$ or $L_{\rm PR} = 8.0 \times 10^{36}$ erg s^{-1} for 0.85 Myr ≅ 0.77 t from these stars.

In total, we find that winds can account for ∼78 $M_\odot$ or a mechanical luminosity of $L = 8.0 \times 10^{37}$ erg s^{-1} over 1.1 Myr. Nevertheless, most of the mass (∼690 $M_\odot$) or $L_{\rm superbubble} - L = 1.5 \times 10^{38}$ erg s^{-1} corresponding to a thermal energy of 2.3×10^{51} erg is "missing", but this can be partly explained after applying an IMF to the star cluster. According to the Hertzsprung Russell diagram (HRD) of Testor & Niemela (1998, Fig. 6b) and using the masses derived from the M-L relation (Vitrichenko et al. 2007), we find that 16 stars in LH 104 have masses above 25 $M_\odot$ including all O-stars, WR-binaries, the B0V stars with Id 4–41 and 4–55, and Sk-69 259. As an upper mass limit, we take 65 $M_\odot$ as a rough estimate, since Massey et al. (2000) suggested that the progenitor masses of WR-stars in this cluster should be in excess of 60 $M_\odot$. On the other hand, by looking at the HRD of LH 104 in Massey et al. (2000, Fig. 7) we find at least 20 stars in the 25–65 $M_\odot$ interval for which spectral types or photometry are available. Comparing both HR-diagrams shows that the total number of member stars is quite uncertain, but there must be at least 70 stars with masses above 8 $M_\odot$.

Assuming that all stars formed from the same parental cloud and using an IMF with $\Gamma = -1.05$ (Testor & Niemela 1998), we obtain a total of 74 stars between 8 and 65 $M_\odot$ in the first case (16 stars with $25 < M/M_\odot < 65$) and 93 stars in the other case (20 stars with $25 < M/M_\odot < 65$). In both cases, there are about two stars in the 65–80 $M_\odot$ mass interval or about three stars in the 65–90 $M_\odot$ mass interval. This suggests that 2–3 supernovae (SNe) already exploded around 1 Myr ago and that with $E_{\rm SN} = 10^{51}$ erg per SN explosion, they can easily account for the required amount of energy. These 2–3 SNe yield approximately 150–240 $M_\odot$ of ejecta mass, thus the production of 230–310 of the 770 solar masses in the bubble can be explained. Any remaining discrepancies should be due to mass loading and the evaporation of entrained interstellar clouds and/or turbulent mixing of material from the cold shell.

With the parameters determined so far, we can further investigate the geometry of the bubble and the ambient ISM. We use an analytical model for the expansion of a wind-blown bubble in an exponentially stratified medium symmetric to the galactic midplane (Baumgartner & Breitschwerdt, in prep.) based on the approximation of Kompaneets (1960). With an energy input rate of $L_{\rm superbubble} = 2.3 \times 10^{38}$ erg s^{-1}, the bubble should reach a radius, i.e., semi-major axis, of 56 pc after ∼1.1 Myr. We calculated models with different scale heights (H = 50, 100, and 500 pc) and obtain a density of the ambient medium of n_0 = 9, 11, and 13 cm^{-3}, respectively. Values for the height of

the bubble above/below the galactic plane are $c = 80, 66$, and 58 pc. Using $b = 42$ pc, we obtain a volume of the bubble of $V = 2.4 \times 10^{51}$ cm^3, 1.9×10^{61} cm^3, and 1.7×10^{61} cm^3. Since a larger elongation, i.e., lower scale height, yields a larger volume, we argue that a larger scale height provides a close fit, otherwise the density inside the bubble is too low. With $V = 1.7 \times 10^{61}$ cm^3 and *norm* from Sect. 3.1, we derive $n = 3.9 \times 10^{-2}$ cm^{-3}. This is close to the value that was used to calculate the mass inside the bubble and the energy input rate in the beginning, whereas a volume of $V = 2.4 \times 10^{51}$ cm^3 for $H = 50$ pc yields only $n = 3.2 \times 10^{-2}$ cm^{-3}. The shell thickness in the case of $H = 500$ pc is ∼5 pc resulting in a density of the shell of 100 cm^{-3}, which is somewhat higher than the density of 70 cm^{-3} derived from the observation. Finally, we calculated the velocity of 31 km s^{-1} for the outer shock, which propagates into the ambient warm medium at the top/bottom of the bubble, and found that it agrees very well with the expansion velocity found for the wind solution of Weaver et al. (1977). This velocity corresponds to a Mach number of $M \sim 3.4$. For comparison, Dunne et al. (2001) reported an expansion velocity of the superbubble of $v_{\rm exp} \approx 45$ km s^{-1} assuming a pressure-driven bubble in an homogeneous medium. The magnetic fields in the ISM of the LMC are on the order of ∼1 μG (Gaensler et al. 2005) corresponding to an Alfvén velocity of ∼0.5 km s^{-1}. Therefore, the effects of the magnetic fields are negligible.

4. Summary

We have found significant diffuse X-ray emission in the field of view of the *XMM-Newton* observations of the pulsar B 0540−69, which is not related to the pulsar. The analysis of the spectrum of the emission has shown that it is purely thermal and can be best modelled with a hot shocked gas. The extended diffuse emission coincides spatially with the superbubble in the H II region N 158 in the LMC. Therefore, we conclude that the origin of the X-ray emission is the hot gas inside the superbubble in N 158.

From the parameters obtained from the analysis of the *XMM-Newton* spectra, we have derived a temperature of $kT = 1$ keV, a density of $n = 0.04$ cm^{-3}, and a pressure of $P/k = 10^6$ cm^{-3} K inside the superbubble. These results enable us to perform analytic calculations of the evolution of the superbubble. Since the OB association LH 104 that is located inside the superbubble has been studied in detail (Testor & Niemela 1998), the stellar population inside the superbubble is well known. Using its IMF and HRD, we have calculated the mass loss and energy input rates of the stars. We have estimated an age of ∼1 Myr and a total energy input rate of $L = 2.3 \times 10^{38}$ erg s^{-1}. The massive stars including WR-stars and binaries in LH 104 account for $L = 8 \times 10^{37}$ erg s^{-1}. Therefore, to reproduce the observations, there should have been 2−3 SN explosions in the past 1 Myr. We have also performed calculations of the expansion of the superbubble for different scale heights. We have demonstrated that a large scale height of $H = 500$ pc can closely reproduce the observed density inside the superbubble as well as the density in the shell around it. The corresponding expansion velocity of the superbubble is also in good agreement with the model of Weaver et al. (1977).

Acknowledgements. The authors thank the anonymous referee for comments that helped to improve the paper. This research is based on observations obtained with *XMM-Newton*, an ESA science mission with instruments and contributions directly funded by ESA Member States and NASA. We have also made use of preliminary data of the UM/CTIO Magellanic Cloud Emission Line Survey (MCELS) available on the web site of the project (http://www.ctio.noao.edu/mcels/). M.S. acknowledges support by the Deutsche Forschungsgemeinschaft through the Emmy Noether Research Grant SA 2131/1. V.B. is recipient of a DOC-fFORTE fellowship of the Austrian Academy of Sciences.

References

Aschenbach, B., Briel, U. G., Haberl, F., et al. 2000, Proc. SPIE, 4012, 731
Borkowski, K. J. 2000, in Rev. Mex. Astron. Astrofis. Conf. Ser., 9, 288
Borkowski, K. J., Lyerly, W. J., & Reynolds, S. P. 2001, ApJ, 548, 820
Brüns, C., Kerp, J., Staveley-Smith, L., et al. 2005, A&A, 432, 45
Carter, J. A., & Read, A. M. 2007, A&A, 464, 1155
Castor, J., Weaver, R., & McCray, R. 1975, ApJ, 200, L107
Chu, Y., Chang, H., Su, Y., & Mac Low, M. 1995, ApJ, 450, 157
Crowther, P. A. 2007, ARA&A, 45, 177
de Avillez, M. A., & Breitschwerdt, D. 2005, A&A, 436, 585
Dickey, J. M., & Lockman, F. J. 1990, ARA&A, 28, 215
Dunne, B. C., Points, S. D., & Chu, Y. 2001, ApJS, 136, 119
Gaensler, B. M., Haverkorn, M., Staveley-Smith, L., et al. 2005, Science, 307, 1610
Garmany, C. D., Olson, G. L., van Steenberg, M. E., & Conti, P. S. 1981, ApJ, 250, 660
Henize, K. G. 1956, ApJS, 2, 315
Jansen, F., Lumb, D., Altieri, B., et al. 2001, A&A, 365, L1
Kompaneets, A. S. 1960, Sov. Phys. Dokl., 5, 46
Lamers, H. J. G. L. M., & Leitherer, C. 1993, ApJ, 412, 771
Lamers, H. J. G. L. M., Snow, T. P., & Lindholm, D. M. 1995, ApJ, 455, 269
Leitherer, C., Robert, C., & Drissen, L. 1992, ApJ, 401, 596
Leitherer, C., Chapman, J. M., & Koribalski, B. 1997, ApJ, 481, 898
Lucke, P. B., & Hodge, P. W. 1970, AJ, 75, 171
Macri, L. M., Stanek, K. Z., Bersier, D., Greenhill, L. J., & Reid, M. J. 2006, ApJ, 652, 1133
Maeder, A., & Meynet, G. 1987, A&A, 182, 243
Massey, P., Waterhouse, E., & DeGioia-Eastwood, K. 2000, AJ, 119, 2214
McKee, C. F., & Ostriker, J. P. 1977, ApJ, 218, 148
Oey, M. S., & García-Segura, G. 2004, ApJ, 613, 302
Petre, R., Hwang, U., Holt, S. S., Safi-Harb, S., & Williams, R. M. 2007, ApJ, 662, 988
Read, A. M., & Ponman, T. J. 2003, A&A, 409, 395
Russell, S. C., & Dopita, M. A. 1992, ApJ, 384, 508
Sasaki, M., Haberl, F., & Pietsch, W. 2002, A&A, 392, 103
Sasaki, M., Plucinsky, P. P., Gaetz, T. J., et al. 2004, ApJ, 617, 322
Schild, H., & Testor, G. 1992, A&AS, 92, 729
Strüder, L., Briel, U., Dennerl, K., et al. 2001, A&A, 365, L18
Testor, G., & Niemela, V. 1998, A&AS, 130, 527
Turner, M. J. L., Abbey, A., Arnaud, M., et al. 2001, A&A, 365, L27
Vitrichenko, E. A., Nadyozhin, D. K., & Razinkova, T. L. 2007, Astron. Lett., 33, 251
Weaver, R., McCray, R., Castor, J., Shapiro, P., & Moore, R. 1977, ApJ, 218, 377